Self-Assembly of Organic Phosph(on)ates under Thermodynamic and Kinetic Control

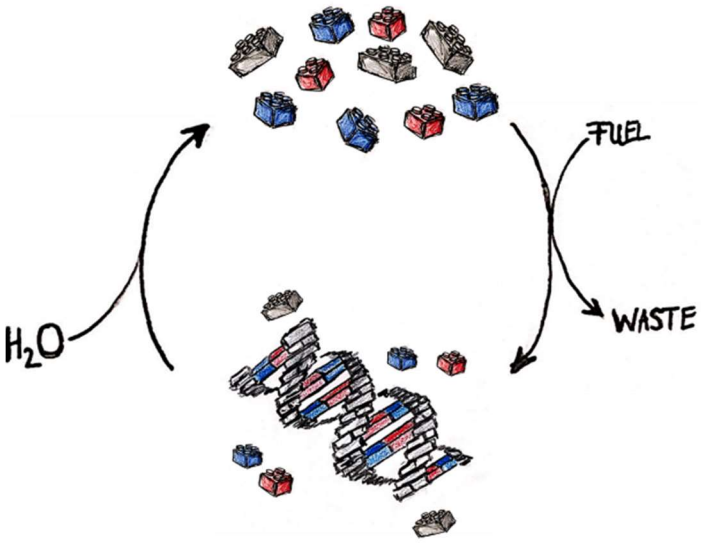

Dissertation zur Erlangung des Doktorgrades Dr. rer. nat.
der Fakultät für Naturwissenschaften der Universität Ulm

vorgelegt von
Julian Vogel
geboren in Schwäbisch Hall, Deutschland

Ulm, 2023

Dekan der Naturwissenschaftlichen Fakultät: Prof. Dr. Thorsten Bernhardt
Erstgutachter: Prof. Dr. Max von Delius
Zweitgutachter: Prof. Dr. Alexander J. C. Kühne

Tag der Promotionsprüfung: 30.06.2023

Universität Ulm, Fakultät für Naturwissenschaften, 2023

Ehrenwörtliche Erklärung:

Die vorliegende Arbeit wurde im Zeitraum von Juli 2019 bis März 2023 am Institut für Organische Chemie I der Universität Ulm unter der Leitung von Prof. Dr. Max von Delius angefertigt.
Hiermit erkläre ich, dass ich die vorliegende Arbeit selbstständig angefertigt und keine als die angegebenen Quellen und Hilfsmittel verwendet habe. Die Stellen, die dem Wortlaut oder dem Sinn nach anderen Arbeiten entnommen sind, habe ich in jedem Fall unter Angabe der Quelle als Entlehnung kenntlich gemacht. Dasselbe gilt sinngemäß für Tabellen und Abbildungen. Ich erkläre außerdem, dass ich die Satzung der Universität Ulm zur Sicherung der guten wissenschaftlichen Praxis in der aktuell gültigen Fassung vom 16.02.2022 berücksichtigt habe. Diese Arbeit hat in dieser oder ähnlicher Form noch nicht im Rahmen einer anderen Prüfung vorgelegen.

Ulm, April 2023 Julian Vogel

“Sapere aude.“
Quintus Horatius „Horaz“ Flaccus (20 BC)

“Dare to think.”
“Habe Mut, dich deines eigenen Verstandes zu bedienen.“
Immanuel Kant (1784 AD)

Contents

Preface ..... **I**

List of Abbreviations ..... **III**

1 Introduction **1**

1.1 Background and Concepts *1*

1.1.1 Systems Chemistry 1

1.1.2 Dissipative Self-Assembly 3

1.2 State of the Art: Chemically Fueled Dissipative Systems *7*

1.2.1 ATP-Fueled Phosphate Systems 7

1.2.2 Carbodiimide-Driven Carboxylic Acid Anhydrides 10

1.2.3 Transient Carboxylic Esters and Amides 13

1.2.4 Redox-Fueled Disulfides and Aldehydes 15

1.2.5 Summary of the State of the Art 18

1.3 Fundamentals of Organophosphate Chemistry *19*

2 Aims and Achievements **22**

2.1 Carbodiimide-Driven Dimerization and Self-Assembly of Artificial, Ribose-Based Amphiphiles…….22

2.2 A Ribonucleotide ↔ Phosphoramidate Reaction Network Optimized by Computer-Aided Design..25

2.3 Steric Control over the Threading of Pyrophosphonates with One or Two Cyanostar Macrocycles during Pseudorotaxane Formation *28*

3 Publications **31**

3.1 Carbodiimide-Driven Dimerization and Self-Assembly of Artificial, Ribose-Based Amphiphiles…… 31

3.2 A Ribonucleotide ↔ Phosphoramidate Reaction Network Optimized by Computer-Aided Design..99

3.3 Steric Control over the Threading of Pyrophosphonates with One or Two Cyanostar Macrocycles during Pseudorotaxane Formation *147*

4 Summary and Outlook **235**

References **239**

List of Publications **252**

Curriculum Vitae **253**

Acknowledgments / Danksagung **254**

Preface

Since the time of *Antoine Lavoisier* and *Justus von Liebig*, the founding fathers of modern chemistry in the late 18th and early 19th century, classical chemistry has investigated stable compounds and molecules that are defined by covalent bonds. Now, in the 21st century, many researchers are interested in multicomponent chemical systems, which facilitate the emergence of complex non-linear behavior. In such systems, the whole is more than the sum of its parts and they thus have far-reaching implications for the synthesis of new materials with life-like properties. Most notably, systems chemistry holds the key for the perception of how life originated from inanimate mater.

Three thermodynamic regimes can be distinguished in systems chemistry: Systems at thermodynamic equilibrium, systems in kinetically trapped states and dissipative systems, that can only maintain their out-of-equilibrium state as long as they can consume energy. Life itself is such an out-of-equilibrium phenomenon and the design of artificial dissipative systems has attracted mounting interest in the past decade. **This work** focuses on the supramolecular self-assembly in chemical systems along all three thermodynamic regimes. Inspired by the phosphate building blocks of life (like RNA), the versatile chemistry of organic phosphates and phosphonates is exploited for the design of self-assembled architectures at equilibrium and beyond (Figure i).

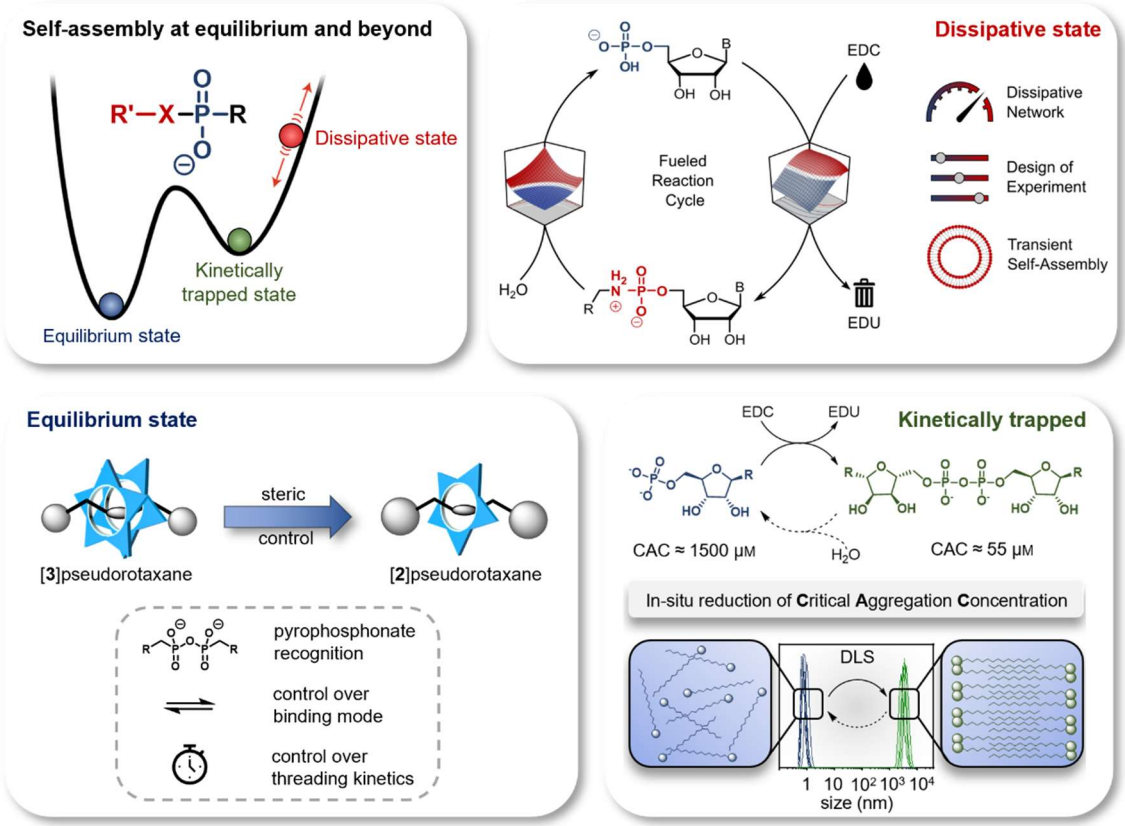

Figure i: Overview of the three projects of this work. The self-assembly of organic phosphates and phosphonates is investigated in chemical systems along all three thermodynamic regimes: At equilibrium, in kinetic traps and in dissipative reaction cycles. Adapted from Refs. 1 and 2 with a Creative Commons Attribution 4.0 International License (CC BY 4.0), https://creativecommons.org/licenses/by/4.0/.

In the **first project**[1] (chapter 2.1, Figure i, bottom right), ribonucleotide-based amphiphiles were dimerized *in situ* under the formation of a pyrophosphate bond. The high-energy carbodiimide EDC was used to facilitate this condensation (forward reaction). As the critical aggregation concentration of the dimers was up to 25 times lower compared to that of the monomers, they spontaneously self-assembled into helical fibers. The organic pyrophosphonates proofed to be exceptionally stable towards hydrolysis (backward reaction), so that the dissipative reaction cycle could not be closed. The system remained in its kinetically trapped state.

Introduction of a primary amine as a strong nucleophile, in the **second project**[2] (chapter 2.2, Figure i, top right), allowed us to overcome this kinetic trap. In an EDC-driven reaction cycle, phosphoramidates formed and readily hydrolyzed back to the starting point, when the chemical fuel was dissipated. For the first time in systems chemistry, we used the software-assisted tool "Design of Experiment" to understand and optimize the complex multi-parameter system. The use of an alkylamine in this reaction cycle enabled the dissipative self-assembly of transient vesicles.

Pyrophosphonates were supposed to function as metastable binding sites for the design of an out-of-equilibrium rotaxane, in the **third project**.[3] Under strongly acidic conditions, a phosphonate ↔ pyrophosphonate reaction cycle could be established. Complexation of the phosphonate with an anion-binding macrocycle, however, inhibited the carbodiimide activation chemistry. Therefore, the supramolecular interactions of substituted pyrophosphonates with the macrocycle were investigated at equilibrium. Control over the binding stoichiometry was gained by fine-tuned steric control (chapter 2.3, Figure i, bottom left). Remarkably, we also established steric control over the threading kinetics on a time scale of minutes, which has implications for future work on chemically fueled artificial molecular motors.

Finally, I co-authored one study on the self-assembly-driven binding and esterase-induced release of siRNA for potential applications in siRNA-based drug delivery.[4] This is not discussed in detail within this cumulative thesis.

The **introduction** of this thesis outlines the concepts of systems chemistry and dissipative self-assembly and gives an overview over the chemically fueled man-made dissipative systems that have been reported since 2010. The fundamentals of organophosphate chemistry that underlay, and in parts inspired, my own work are also described in the introduction. Chapter 2 recapitulates the **aims and achievements** and gives an overview over the main results of this work. Own **publications** or manuscripts that are currently under peer-review are included in chapter 3. In chapter 4, a **summary** is provided, that highlights the most significant findings of my work. This thesis is concluded by an **outlook**, in which I outline potential future work that is based upon the insights presented herein.

List of Abbreviations

A	adenosine
AA	adenosine phosphodiester
ADP	adenosine diphosphate
AIE	aggregation induced emission
AMP	5'-adenosine monophosphate
AppA	adenosine pyrophosphate
ATP	adenosine triphosphate
B	canonical nucleobase
CAC	critical aggregation concentration
CLSM	confocal laser scanning microscopy
CS	cyanostar
DBC	dibenzoyl-(L)-cystein
DCC	dynamic combinatorial chemistry
DCC	dicyclohexyl carbodiimde
DCL	dynamic combinatorial library
DFT	density functional theory
DIC	diisopropyl carbodiimide
DLS	dynamic light scattering
DMAP	dimethylamino pyridine
DMS	dimethyl sulfate
DNA	desoxyribonucleic acid
DoE	design of experiment
DPAC	9,14-diphenyl-9,14-dihydrodibenzo[a,c]phenazine
DSA	dissipative self-assembly
DT	dithionite
DTT	dithiothreitol
EDC	1-ethyl-3-(3-dimethylaminopropyl) carbodiimide
EDU	1-ethyl-3-(3-dimethylaminopropyl) urea
et al.	*et alii* (and others)
EtIm	1-ethylimidazole
GdL	glucono-δ-lactone
GDP	guanosine diphosphate
GTP	guanosine triphosphate
HINT 1	histidine triad nucleotide-binding protein *1*
HMTA	hexamethylenetetramine
HPLC	high performance liquid chromatography
HRMS	high resolution mass spectrometry
Ln^{III}	lanthanide(III) salt
λPP	λ-protein phosphatase
MeI	methyliodide
NHS	*N*-hydroxysuccinimide

NMR	nuclear magnetic resonance
NOE	nuclear Overhauser effect
NOESY	NOE spectroscopy
PA	phosphoramidate
PDI	perylendiimide
PEC	bis((*R/S*)-1-phenylethyl) carbodiimide
P_i	inorganic phosphate
PKA	protein kinase A
PMAA	poly(methacrylic acid)
PP	pyrophosph(on)ate
PPh_3	triphenylphosphine
ppm	parts per million
RNA	ribonucleic acid
SI	supporting information
ssDNA	single strand DNA
TACN:Zn	1,4,7-triazacyclononane:Zn^{2+}
TBA^+	tetrabutylammonium
TCEP	tricarboxyethylphosphine
TEM	transmission electron microscopy
TPE	tetraphenylethylene
VT	variable temperature

1 Introduction

1.1 Background and Concepts

1.1.1 Systems Chemistry

In order to bring the main topic of this thesis, out-of-equilibrium self-assembly, into line with a bigger picture, one has to understand the concepts of systems chemistry. As this is still a young and dynamic field of research, a dictionary definition of "systems chemistry" does not (yet) exist. If asked about a definition, the artificial intelligence language model ChatGPT,[5] that generates text output based on its input (i.e., based on the text on a specific topic available in the database) gives the following answer:

"Systems chemistry is an interdisciplinary field that combines chemistry, physics, biology, and computer science to understand the behavior of complex chemical systems. It involves the study of how molecules interact with each other and their environment to form dynamic networks, which can exhibit emergent properties that cannot be predicted from the behavior of individual molecules."[5]

This definition contains a few important concepts of systems chemistry (like complexity, emergence of properties and dynamic networks) that will be discussed in detail below. Leading scientists argue that systems chemistry studies complex networks of molecules.[6–9] Networks become complex through an increased number of interconnections between their parts, leading to non-linear behavior. More information is required to describe them as in simple systems.[6] Typical examples of complex systems include our climate, social networks or the stock market. As such, complexity can give rise to emergent properties. This are properties that go beyond the sum of their individual components and can therefore not be predicted.[6,8,9] For example, unpredictable social behavior emerges from the societies' individuals and consciousness is spawned from neurons coming together in the brain. In chemistry, oscillatory reactions,[10] such as the Belousov-Zhabotinsky reaction,[11] is an often stated example for the emergent behavior of complex chemical systems. While classical chemistry has focused on thermodynamically controlled systems of covalent bonds and the synthesis of well-defined, stable compounds for hundreds of years, the field of systems chemistry, including supramolecular[12] and out-of-equilibrium systems,[13] recently developed very fast. This development is driven by the increasing interdisciplinary nature and cooperation of the traditional branches of science (e.g., chemistry, biology, physics and computer science) and by advances in analytical methods and computational techniques.[9]

Systems chemistry can be divided into three fundamentally different regimes: Systems at thermodynamic equilibrium (A), kinetically trapped systems (B) and far-from-equilibrium systems (C).[12] This distinction is important, as self-assembly on all three different regimes is

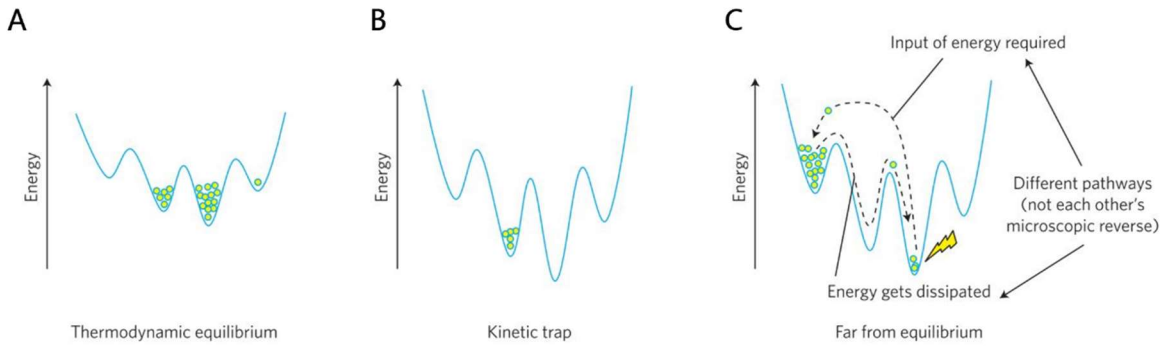

Figure 1: The three different types of thermodynamic regimes of a chemical system. **(A)** System at thermodynamic equilibrium, governed by the Boltzmann distribution. **(B)** System under kinetic control, governed by the synthetic pathway and a kinetically trapped final state. **(C)** Far-from-equilibrium system, governed by the supply of energy and an independent pathway for its dissipation. Reprinted from Ref. 12 with permission from Springer Nature, copyright 2015.

explored in this work. Therefore, the matter will be discussed in detail.

Figure 1 illustrates all three thermodynamic regimes of a chemical system. At thermodynamic equilibrium (Figure 1A) the distribution of energetically different states is determined by the Boltzmann equation and persists due to thermodynamic stability. Since this distribution can be predicted with sufficient understanding of its components, systems under thermodynamic control are unlikely to exhibit emergent properties. Nevertheless, fascinating molecules and behavior like interlocked compounds[14] and self-replication[15,16] can arise at equilibrium. In dynamic combinatorial chemistry (DCC), for example, libraries of molecules can react, interconvert and build complex networks that can respond to external stimuli according to LeChateliers principle and self-heal through their inherent reversibiliy.[17]

Under kinetic control, on the other hand, the distribution of different states is determined by the synthetic pathway and kinetically trapped in a local thermodynamic minimum. This distribution is metastable, which means that it takes either time or activation energy to convert it into a more stable distribution. On an energy landscape, more than only one kinetically trapped state with different properties like oscillation or auto-catalysis can exist (Figure 1B), which increases complexity.[12,18]

Finally, far-from-equilibrium systems require a continuous supply of energy to maintain a steady state (homeostasis). This steady state is determined by the kinetics of an activation and a deactivation reaction. As shown in Figure 1C, the energy dissipation follows a different pathway than the activation, so that there is no microscopic reversibility. When the energy supply is depleted, the transient system relaxes back to its thermodynamic ground state (or a kinetic trap). The two pathways allow continuous interaction and/or interconversion of different states (i.e., bifurcation) and thus high complexity and emergent behavior.[12] Most notably, life as we know it only exists in an out-of-equilibrium state.[13,19] Likewise, the origins of life[20–23] must have been an out-of-equilibrium process and even Darwinian evolution on a molecular level was likely a competition of chemical systems for the most efficient use of energy supplies. The emergence of life from non-living matter is arguably the most intriguing example for emergent behavior of complex chemical systems and motivates scientists to understand and mimic these processes.[24,25]

1.1.2 Dissipative Self-Assembly

The most prominent area in which scientists seek to mimic biological processes and establish life-like properties from complex chemical systems is out-of-equilibrium self-assembly. Self-assembly is the spontaneous formation of supramolecular architectures from molecules.[26,27] While classical self-assembled structures are governed by their thermodynamic stability, out-of-equilibrium self-assembly is determined by the rates of the different assembly and disassembly pathways.[8] In such systems, the self-assembled state can only be maintained as long as energy can be dissipated. In that sense, dissipative reaction systems are catalytic cycles for the depletion of a fuel coupled with some sort of function (in this case self-assembly). In artificial systems, dissipative self-assembly can rely on the energy input from light,[28,29] electricity[30,31] or from kinetically stable high-energy molecules.[32] In nature, however, self-assembly (e.g., in microtubules or actin filaments, see below) is chemically fueled.[33] This work will therefore only focus on chemically fueled dissipative self-assembly (DSA).[34–42]

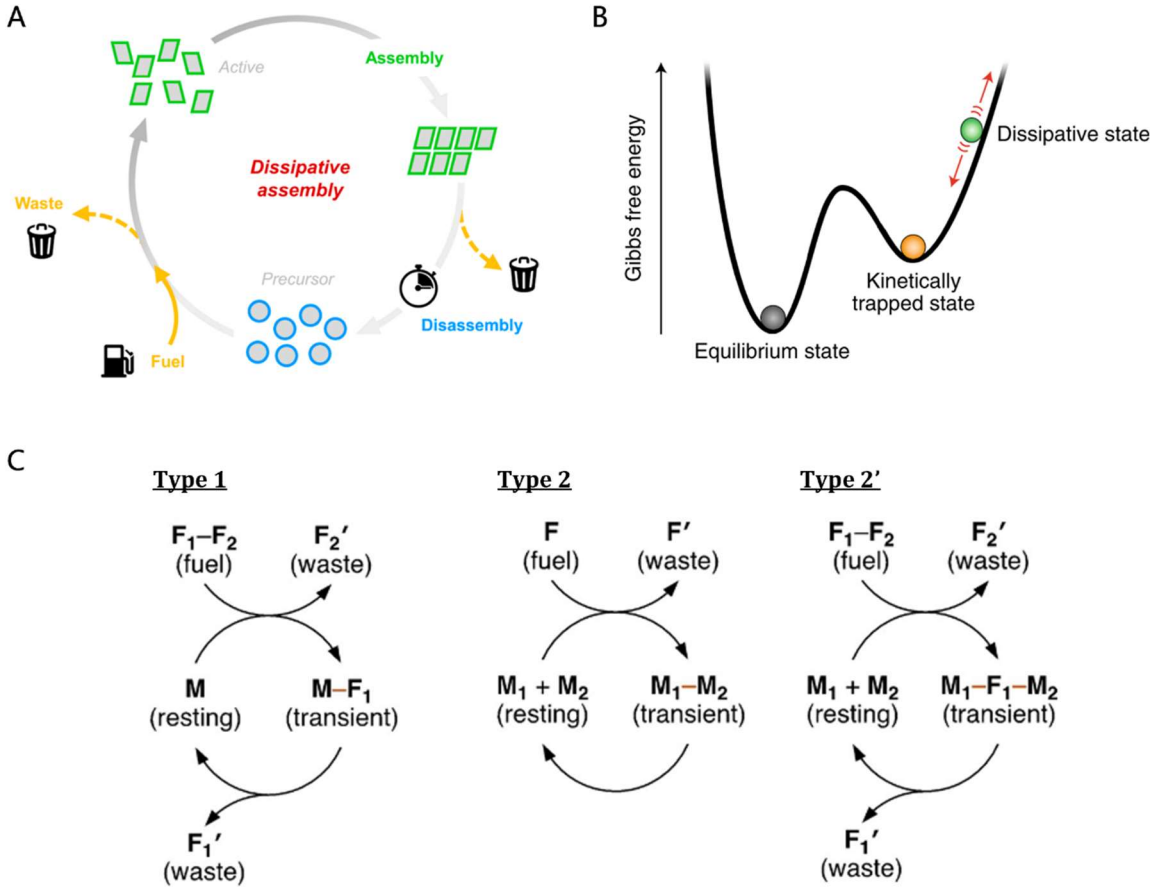

Figure 2: Dissipative self-assembly. **(A)** Schematic representation of a dissipative self-assembling cycle. A precursor is activated by a chemical fuel. The activated building blocks can form an assembled structure which is stable until the fuel is depleted, and it disassembles back to the precursors. Reprinted from Ref. 34 with a Creative Commons Attribution Non-Commercial No Derivative Works (CC-BY-NC-ND) 4.0 license, https://creativecommons.org/licenses/by/4.0/. **(B)** Distinction between the equilibrium state, the kinetically trapped state, and the dissipative steady state. Reprinted from Ref. 35 with permission from Springer Nature, copyright 2018 **(C)** Definition of the two fundamentally different types of dissipative self-assembly. Copyright (2021) Wiley. Used with permission from Ref. 36.

In all dissipative self-assembling systems, a precursor is activated and thus modified when undergoing an exergonic reaction with a chemical fuel. Up to that point, the precursor is in a non-assembled state at thermodynamic equilibrium and does not change. The activated building blocks, on the other hand, possess some kind of attractive interactions which drive them into self-assembled structures. According to the Second Law of Thermodynamics, this out-of-equilibrium steady state can only be maintained as longs as (sufficient) chemical fuel is provided, as illustrated on an energy surface in Figure 2B.[35] A subsequent deactivation reaction is crucial to close the dissipative reaction cycle. Importantly, the activation and deactivation reactions have to be independent and irreversible. Finally, deactivated building blocks spontaneously disassemble back to the precursor. From there, repeated addition of fuel can start a second cycle (Figure 2A).[34] Chemical fuels are converted to waste during the reaction cycle and the waste can be liberated during activation and/or during deactivation.

Hence, two fundamentally different types of chemically fueled transient bond formations can be distinguished (Figure 2C).[36] In "Type 1", a stable substrate (M) is chemically modified when reacting with the fuel (F_1-F_2) in a way that the fuel donates structural elements to the substrate, releasing waste F_2'. Here, the structure of the fuel directly affects the assembly properties of the activated substrate (M-F_1). Deactivation releases F1' as waste and restores the substrate M. Examples for type 1 systems are the binding of guanosine triphosphate (GTP) to microtubule substrates or *van Eschs* transient esterification (see below). "Type 2" systems are comprised of two substrates (M_1 and M_2) that only exploit the fuels energy to generate the transient species (M_1-M_2). In this case, the self-assembly properties are not directly affected by the structure of the fuel.[36] EDC-fueled anhydride formation (even intramolecularly, chapter 1.2.2) and my own work (see chapter 2.1 and 2.2) are examples for a type 2 system. "Type 2' " is a mixture of the first two fundamental types where two substrates are connected by part of the chemical fuel. Furthermore, *Prins* differentiates between such dissipative self-assembly and "self-assembly under dissipative conditions", where the building blocks are not involved in the fuel-to-waste conversion.[35] *Prins'* ATP-templated dissipative systems (see chapter 1.2.1) and *Di Stefanos* transient acid systems are the only examples for such behavior in this work.

Designing out-of-equilibrium self-assembling systems is motivated not only by the fascination to mimic biological processes but can also lead to interesting applications. Coupling reaction cycles with self-assembly facilitates spatiotemporal control over the system. Assembly will occur or be maintained only at locations where fuel is present and the lifetime of the assemblies directly depends on the amount of fuel and on the ratio of the activation and deactivation rates.[34] Moreover, the structural change across multiple length scales from nanometers (e.g., molecular activation) to micrometers (e.g., assembled structures) can lead to complex feedback loops. Thus, non-equilibrium steady states have recently been "put to work" in applications like supramolecular polymers[43] and materials.[44,45] The topic of artificial molecular motors[46] and machines[47–51] is somewhat related as it also uses chemical fuels[52,53] and kinetic asymmetry[54,55] to operate away from equilibrium. Discussing these systems in more detail, however, would exceed the scope of this work.

Biological processes rely vastly on self-organization of cellular components and the functions that are associated with them. The collective behavior that emerges from self-organization even justifies one definition of life as "a self-organized, self-reproducing process".[56] As such, the dynamic interplay between self-assembly and disassembly regulates cellular structures and allows the cell spatiotemporal control over structures and functions.[57] Adenosine triphosphate (ATP) and guanosine triphosphate (GTP) are natures chemical fuels. Most processes of self-organization in living cells such as the transient self-assembly of actin filaments[58,59] or microtubules[60–62] are controlled by their dissipation.

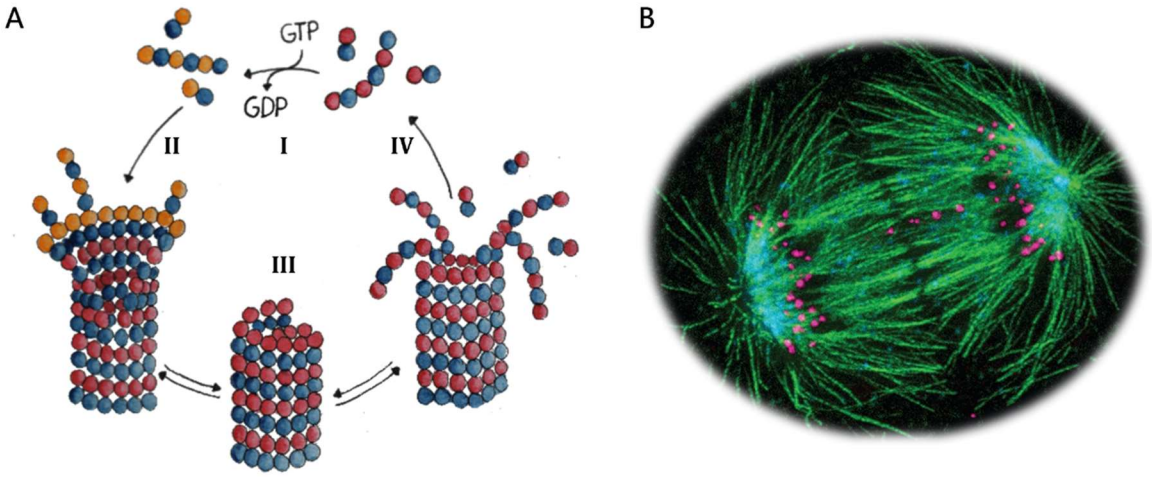

Figure 3: Dissipative self-assembly of microtubules. **(A)** Illustration of the transient self-organization of microtubules from tubulin proteins upon activation with GTP. Copyright (2019) Wiley. Used with permission from Ref. 63. **(B)** Immunofluorescence microscopy image of the mitotic spindle in anaphase in a human cell. Microtubules are colored green.[64] © 2020, L. T. Ferreira and H. Maiato. Originally published in Ref. 65.

Microtubules are present in all eukaryotic cells and play a pivotal role in cell migration,[66] intracellular transport and cell division.[67] As such, microtubules are part of the cytoskeleton and are involved in the transport of organelles throughout the cytoplasm. Furthermore, they are a vital part of a complex cell machinery called mitotic spindle, which is responsible for the separation of chromosomes during mitosis. Figure 3B shows a fluorescence microscopy image of a mitotic spindle during cell division and the large self-organized microtubules (green).[64,65]

Dynamic instability of the assemblies is crucial to the functions of microtubules and stems from the transient self-assembly driven by the hydrolysis of GTP. The process is illustrated in Figure 3A. At the beginning of the cycle, α- and β-tubulin proteins are present in a stable, soluble form in the cytoplasm (I). When they encounter a nucleating site, they start to polymerize by addition of more tubulin dimers (II). During polymerization, the β-tubulin subunit in the dimer binds to GTP, which stabilizes the structure and prevents it from depolymerizing. As more subunits are added, the microtubule grows in length until it reaches a steady state where the rate of addition is equal to the rate of loss (III). However, over time, the tubulin subunit catalyzes the hydrolysis of GTP, which is converted to guanosine diphosphate (GDP). When this deactivation outcompetes the supply of activated tubulin dimers, the microtubule is destabilized and thus depolymerizes rapidly (i.e., catastrophe phase, IV). The liberated tubulin subunits are then free to initiate a new cycle.[38,61]

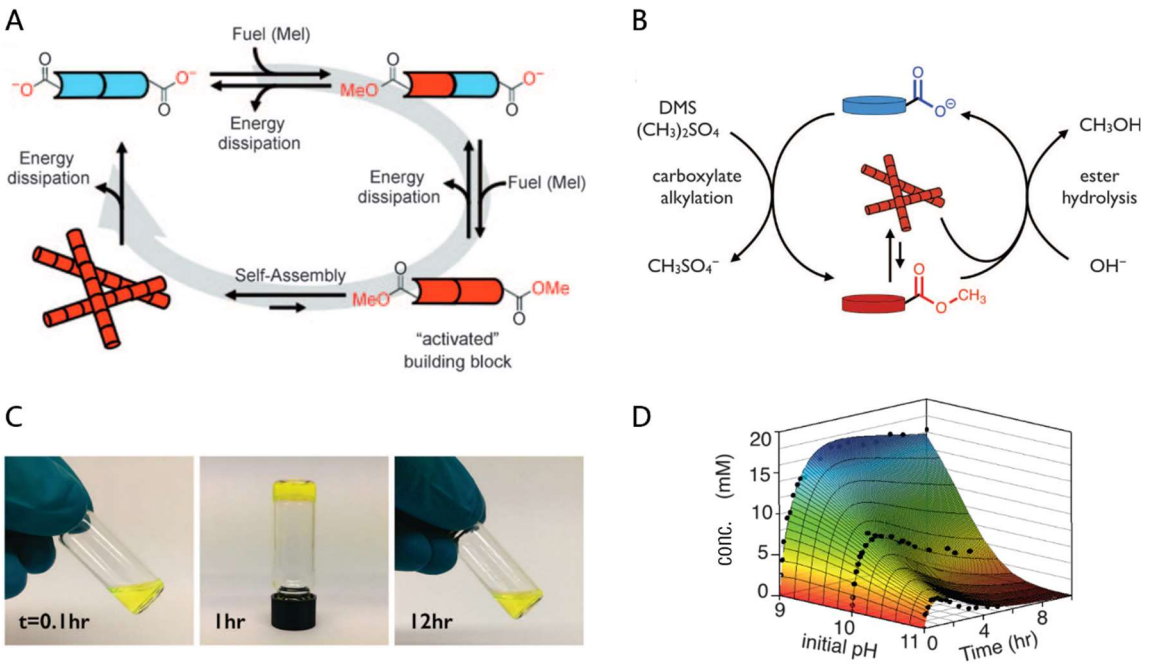

Figure 4: First examples of a man-made, chemically fueled system capable of dissipative self-assembly. **(A)** Reaction cycle in which the dicarboxylate precursor is activated by methylation with MeI.[68] Activated building blocks can assembly into hierarchical structures when the negative charge is removed. Deactivation through spontaneous hydrolysis leads to disassembly. Copyright (2010) Wiley. Used with permission from Ref. 68. **(B)** Advanced reaction cycle with dimethyl sulfate (DMS) as chemical fuel.[69] **(C)** Self-assembly leads to transient gelation. **(D)** Formation and subsequent hydrolysis of the activated species (regarding reaction cycle B) at different pH conditions. Adapted from Ref. 69 with permission from The American Association for the Advancement of Science, copyright 2015.

In the first man-made dissipative system by *Boekhoven, Eelkema,* and *van Esch*, a dicarboxylic acid (dibenzoyl-(L)-cystine, DBC) was transiently methylated with methyliodide (MeI, Figure 4A). MeI was added to the molecularly dissolved precursor as a chemical fuel and methylated both carboxylates, while iodide was released as a waste. As the negative charges of the carboxylates (and thus the repulsive forces) were removed upon methylation, the activated building blocks self-assembled into fibrous aggregates. After depletion of the fuel, the deactivation pathway (i.e., saponification) became dominant and the system returned to the thermodynamically stable non-aggregated state.[68] An advanced system used slightly modified diacid substrates and dimethyl sulfate (DMS) as a chemical fuel (Figure 4B), allowing faster kinetics of both activation and deactivation. Under the same mechanism, transient gelation was observed, as shown in Figure 4C. A close look at the concentration of the activated building block during one reaction cycle at different pH values, emphasizes the importance of fine-tuning the ratio of activation and deactivation rates in dissipative systems (Figure 4D). While the hydrolysis is fast at high pH, it is very slow at lower pH.[69] An inefficient deactivation pathway would kinetically trap the system and must therefore be avoided.

In conclusion, systems chemistry studies complex networks of molecules which exhibit emergent behavior and especially those that operate out-of-equilibrium. As such, systems chemistry could be the key to unravel the mystery of the origins of life. Dissipative self-assembly is a branch of systems chemistry that focuses on the perception of natural processes like microtubule assembly and the development of man-made systems with life-like properties and is the focus of my own research.

1.2 State of the Art: Chemically Fueled Dissipative Systems

1.2.1 ATP-Fueled Phosphate Systems

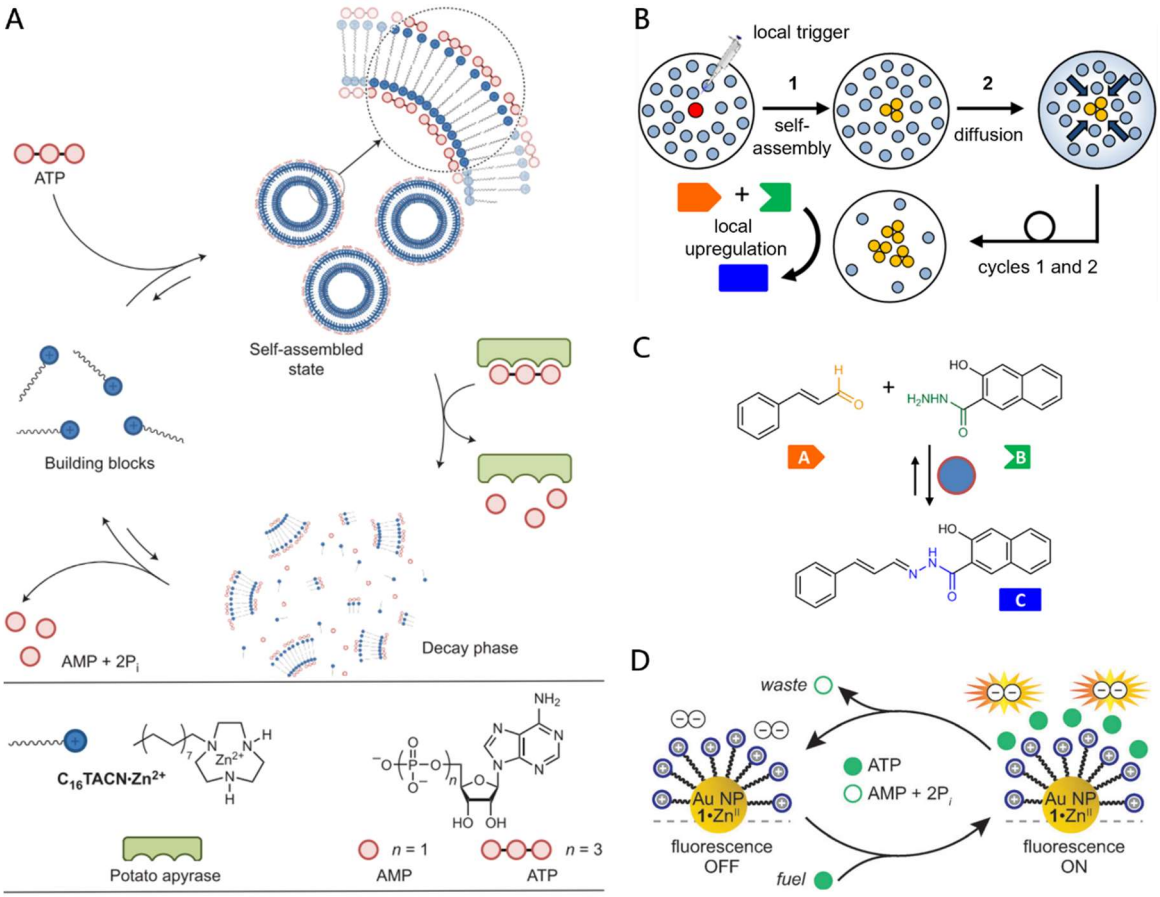

Figure 5: ATP fueled systems by *Prins* and coworkers. **(A)** Cycle of self-assembly under dissipative control and the systems components. Adapted from Ref. 70 with permission from Springer Nature, copyright 2016. **(B)** Spatiotemporal control over the self-assembly of nanoreactors by addition of ATP in a hydrogel matrix and upregulation of **(C)** a model hydrazone formation reaction from an aldehyde and a hydrazide. Adapted from Ref. 71 with a Creative Commons Attribution 4.0 International License (CC BY 4.0), https://creativecommons.org/licenses/by/4.0/. **(D)** ATP-driven dissipative displacement of a fluorescent probe allows transient signal generation. Copyright (2018) Wiley. Used with permission from Ref. 72.

As nature predominantly uses adenosine triphosphate (ATP) as fuel to regulate cellular processes (chapter 1.1.2), it is not surprising that ATP has also been employed to design man-made dissipative systems.[73] Under mild conditions, ATP is kinetically stable. Therefore, ATP-driven systems rely on enzymatic ATP hydrolysis to adenosine monophosphate (AMP) or adenosine diphosphate (ADP) to close the reaction cycle. The *Prins* group has explored self-assembly under dissipative control with amphiphiles that can be templated by ATP (or AMP[74,75]) to form large vesicular structures in aqueous media.[70] Below their critical aggregation concentration (CAC) the 1,4,7-triazacyclononane:Zn^{2+} derived amphiphiles (C_{16}TACN:Zn^{2+}) with a long apolar chain are molecularly dissolved. ATP can act as a template and pre-organize three amphiphiles by electrostatic interactions of the Zn^{2+} head group with the three-times negatively charged triphosphate. Hence, the addition of ATP leads to the formation of large vesicles (Figure 5A). In order to prevent a kinetic sink, but rather close the

dissipative reaction cycle, the ATP-hydrolysis enzyme potato apyrase is present in solution and cleaves the triphosphate to AMP and inorganic phosphate (P_i). This deactivation leads to a spontaneous decay phase and disassembly. Addition of fresh ATP can restart the cycle. In a next step, *Prins* and coworkers coupled this reaction cycle with a function. The apolar bilayer of the transient vesicles was used as an environment for a nucleophilic aromatic substitution reaction that would not occur in water. In that sense, the vesicles represent out-of-equilibrium nanoreactors that can sustain a chemical reaction, as long as the chemical fuel is present.[70] Naturally, the amount of ATP and deactivation enzyme determine the lifetime of the nanoreactor and therefore allow regulation of the reactivity in the time-domain. Similarly, this was shown for a transphosphorylation[76] and a hydrazone formation reaction,[77] as depicted in Figure 5C.

The upregulation of this reaction not only under temporal but also under spatial control was showcased in a hydrogel matrix. As depicted in Figure 5B, ATP locally triggered the self-assembly of the nanoreactors with a low diffusion rate so that unassembled amphiphiles from the surrounding diffused to the "depleted" injection point. Repetitive cycling furnished local upregulation of the reactivity.[71] Finally, *Prins* and coworkers could show that not only the reactivity in a model reaction, but also the generation of a fluorescent signal can be influenced by self-assembly under dissipative control. In the equilibrium state, a fluorescent probe was coordinated to the TACN:Zn^{2+} amphiphiles that were immobilized on gold nanoparticles. Addition of ATP lead to the displacement of the probe and thus a transient non-equilibrium turn-on of the fluorescent signal (Figure 5D).[72]

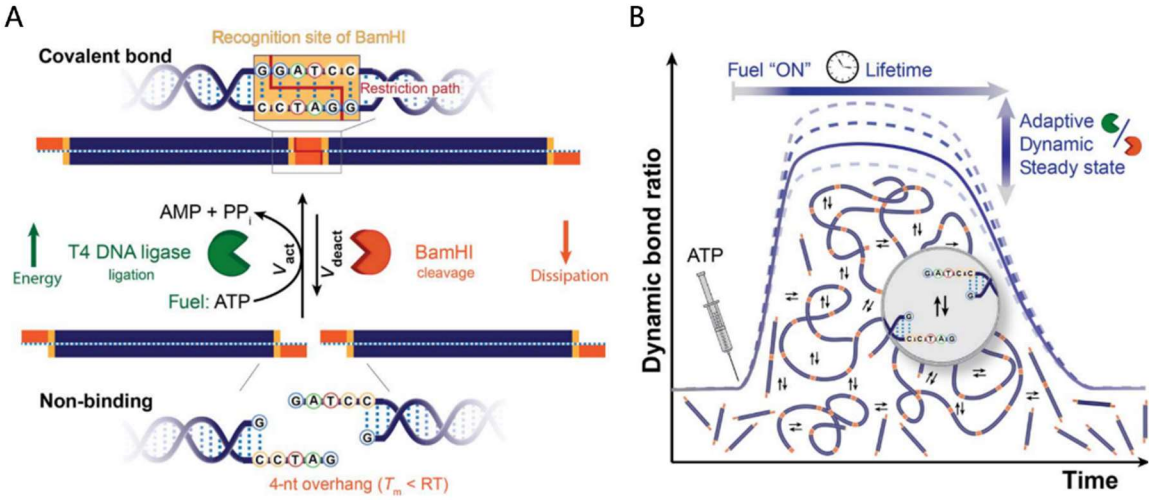

Figure 6: Steady states in an ATP-driven DNA system by the group of *Walther*. **(A)** DNA monomers with complementary ends are polymerized by ATP-fueled enzymatic ligation. Simultaneous enzymatic cleavage leads to a steady state that can only be maintained if ATP is present. **(B)** The lifetime of the dynamic steady state is coupled to the ATP fuel. Reprinted from Ref. 78 with a Creative Commons Attribution 4.0 International License (CC BY 4.0), https://creativecommons.org/licenses/by/4.0/.

Walther and coworkers have reported ATP-fueled DNA systems that heavily rely on enzyme catalysis and lead to transient DNA coacervates,[79] hierarchical DNA structures,[80] and dynamic covalent DNA polymers.[78] The mechanism of the latter is shown representatively for other examples in Figure 6. Short DNA strand monomers were strategically equipped with self-complementary ssDNA ends on either side. T4 DNA ligase enzymes consume ATP to form

phosphodiester bonds and induce polymerization by the ligation of the monomers. The newly formed DNA section is recognized by the BamHI endonuclease enzyme, which can cleave the just formed phosphodiester bond. This counteracts the activation and leads to depolymerization (Figure 6A). As, the activation reaction (i.e., ligation) is initially faster than the deactivation reaction (i.e., cleavage) the number of diester bonds increases (Figure 6B). At some point, activation and deactivation are equally fast and a non-equilibrium steady state with transient dynamic covalent diester bonds is created. This steady state is maintained until ATP runs out. As such, the energy uptake and dissipation are orthogonally synchronized, allowing control over adaptive and programmable dynamics.[78] This programmability later facilitated control over ATP-fueled DNAzymes with transient catalytic function.[81]

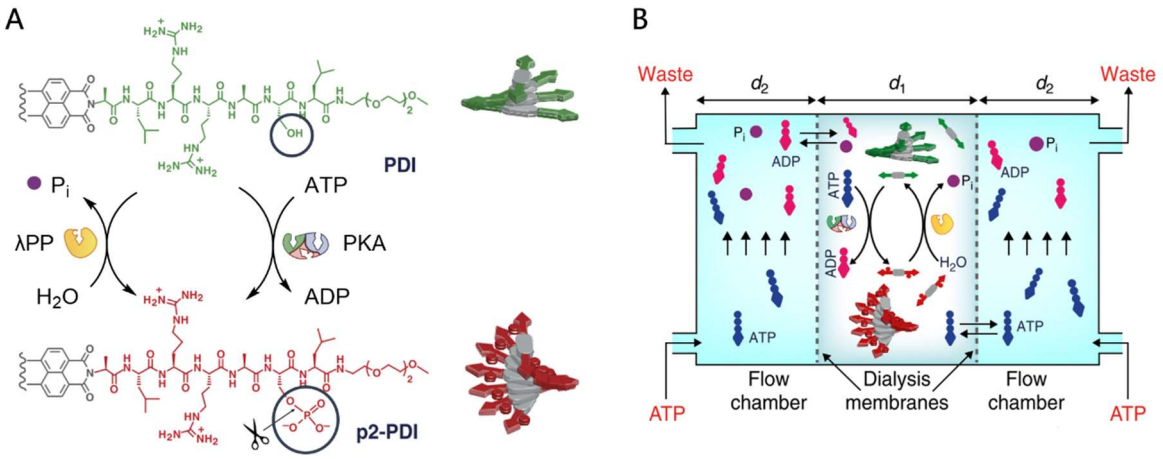

Figure 7: Transient chirality by the *Hermans* lab. **(A)** A peptide-perylenediimide (PDI) is phosphorylated by the consumption of ATP under PKA catalysis to p2-PDI and subsequently hydrolysed back by λPP. PDI and p2-PDI form supramolecular polymers with opposite helicity. **(B)** A steady state can be maintained in a flow device where fuel is added, and waste is removed continuously. Adapted from Ref. 82 with a Creative Commons Attribution 4.0 International License (CC BY 4.0), https://creativecommons.org/licenses/by/4.0/.

The group of *Hermans* introduced a system, in which ATP was used to phosphorylate the serine moiety in a peptide-perylenediimide derivative (PDI, half is shown in Figure 7A) by the enzyme protein kinase A (PKA). Both PDI (green) and the phosphorylated p2-PDI (red) form helical supramolecular polymers, but with opposite handedness (a comparable strategy was developed simultaneously by *George* and coworkers[83]) . Phosphate hydrolysis is achieved by λ-protein phosphatase (λPP), yielding the original PDI and inorganic phosphate (P_i) as waste. *Hermans* and coworkers demonstrate that they can switch the chirality of the system either in a stimuli responsive way by successive addition of ATP/PKA and λPP or in a transient way, where all the components are added simultaneously. Most remarkably, they also present a strategy, how to circumvent one of the greatest drawbacks of chemically fueled systems, namely the accumulation of waste (here ADP and P_i) that eventually poisons the system. In a continuous flow device (Figure 7B) a non-equilibrium steady state was reached by constant outflux of waste and influx of ATP fuel through semipermeable dialysis membranes, that can only be passed by small molecules. This steady state was maintained for over 20 h while the (de-)phosphorylation reactions of the PDI derivatives were continuously happening under the consumption of fuel. This underpins the potential of artificial non-equilibrium steady states in dissipative self-assemblies for the development of life-like and adaptive materials.[82]

1.2.2 Carbodiimide-Driven Carboxylic Acid Anhydrides

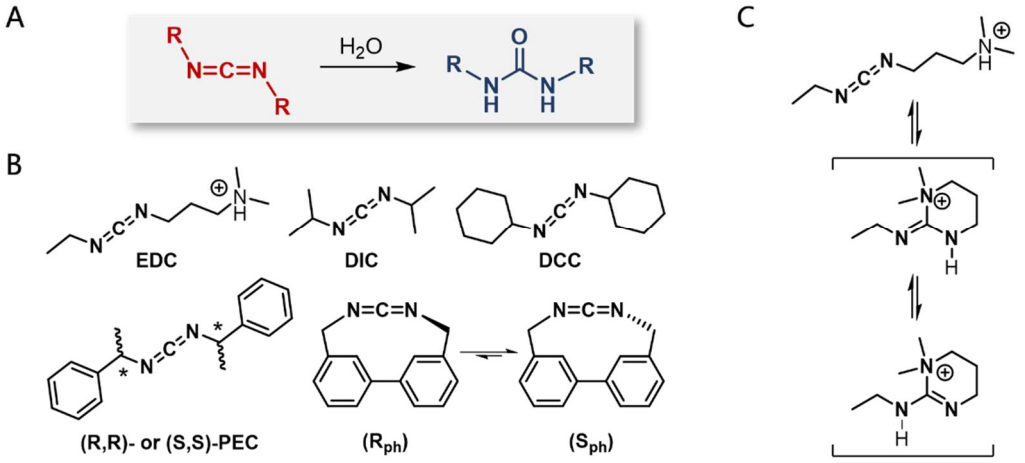

Figure 8: Carbodiimides. **(A)** Hydrolysis of carbodiimides to their urea analogue. **(B)** Different non-chiral (top) and chiral (bottom) carbodiimides that are used in reaction cycles. **(C)** Tautomeric equilibrium between the open and the cyclic form of 1-ethyl-3-(3-dimethylaminopropyl)carbodiimide (EDC) in solution.

In 2017, the groups of *Boekhoven*[84] and *Hartley*[85] simultaneously reported the carbodiimide-driven condensation of carboxylates as a new platform for dissipative reaction cycles. Since then, carbodiimides have been the most abundantly used fuels to regulate supramolecular processes in catalytic reaction cycles.[86] As carbodiimides play a major role as fuels in my own research, Figure 8 summarizes some important aspects. Classically, carbodiimides are used as condensation agents in nucleotide and peptide synthesis. They are also exceptionally well-suited for chemical reaction cycles, since their reaction profile is well-understood and their rate of background hydrolysis is relatively low.[87,88] Furthermore, they carry a lot of chemical energy that can be harvested for catalytic reaction cycles. Figure 8A shows a general structure of carbodiimides and their urea analogue. The difference in free energy ΔΔG released during this hydrolysis is approximately 80 kJ mol^{-1}.[89] In comparison, the free energy released by the hydrolysis of ATP to ADP or AMP (at pH=7 and 298 K) amounts to 30 kJ mol^{-1} or 46 kJ mol^{-1}, respectively.[90,91] The ΔΔG is comparable for different carbodiimides that have been used as chemical fuels (Figure 8B), such as 1-ethyl-3-(3-dimethylaminopropyl) carbodiimide (EDC), diisopropyl carbodiimide (DIC) and dicyclohexyl carbodiimide (DCC). Recently, chiral carbodiimides like cyclic bis-phenylene carbodiimide (R_{ph}/S_{ph}, axial chirality)[92] and bis((R/S)-1-phenylethyl) carbodiimide (PEC, central chirality)[93] have been developed. The latter has been exploited to drive autonomous molecular motors.[94,95] The most commonly used carbodiimide is the water-soluble EDC hydrochloride. It has been shown to exist as a tautomeric mixture (Figure 8C) in which both tautomers can be attacked by a nucleophile.[96]

The dissipative reaction cycle reported by *Boekhoven* and coworkers exploited the carbodiimides' unique properties like the high-energy content and the low background hydrolysis rate. EDC was irreversibly consumed to convert a peptide-based dicarboxylate into its corresponding carboxylic acid anhydride, releasing 1-ethyl-3-(3-dimethylaminopropyl) urea (EDU) as waste (Figure 9A).[84] Charge reduction upon anhydride formation allows transient self-assembly into droplets,[97] colloids, or vesicles.[98] When EDC was depleted, the metastable anhydrides spontaneously hydrolyzed to the original carboxylate.

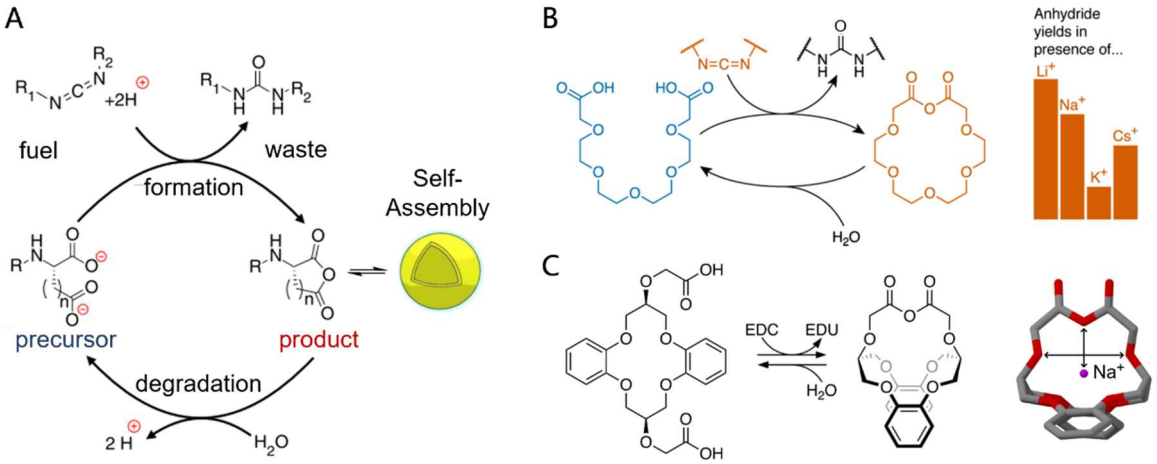

Figure 9: Carbodiimide-driven condensation of dicarboxylates. **(A)** Reaction cycle of peptide dicarboxylates by the *Boekhoven* lab. The activated product can self-assemble into supramolecular architectures. Adapted from Refs. 84 and 98 with a Creative Commons Attribution 4.0 International License (CC BY 4.0), https://creativecommons.org/licenses/by/4.0/. **(B)** EDC-fueled crown ether formation by *Hartley* and coworkers. Reprinted with permission from Ref. 85. Copyright 2017 American Chemical Society. **(C)** EDC-fueled polyether cage formation. Adapted from Ref. 99 with a Creative Commons Attribution 4.0 International License (CC BY 4.0), https://creativecommons.org/licenses/by/4.0/.

Since the behavior of these materials is not governed by thermodynamics but rather by kinetics, their lifetime can be tuned and feedback between (de-)activation and self-assembly leads to interesting, more life-like properties. In peptide-based systems,[100,101] for example, the chemical reaction cycle can be regulated by the emerging assemblies, as they change the microenvironment and affect both the activation and deactivation of the building blocks.[102] Furthermore, *Boekhoven* and coworkers used similar succinic acids, in which the peptide moieties were replaced with aliphatic chains and demonstrated that the transient phase-separation upon fueling can inhibit anhydride hydrolysis.[103,104] They gained control over this feedback mechanism by varying the length of the aliphatic chain and utilized it for drug-release with a zero-order kinetic profile.[105]

Hartley and coworkers also used EDC in aqueous media to create a system capable of transient assembly. Oligo (ethylene glycol) diacids were condensed intramolecularly to form labile crown ether analogs that bind alkali metals. Hydrolysis of the anhydride opened the macrocycle and released the guest ion (Figure 9B). Interestingly, the presence of cations that size-match the supramolecular host (like Na^+ and K^+) suppressed the anhydride formation.[85] Such a counterintuitive negative templation effect was also observed in later work with transient macrobicyclic complexes that are reminiscent of crown ether cages (Figure 9C). The authors rationalize this behavior with accelerated hydrolysis of those intermediates that were supposed to facilitate anhydride formation, when the cation is bound to the polyether and thus close to the incipient anhydride.[99]

Finally, *Hartley* and coworkers made use of the same chemistry not only intra- but also intermolecularly. Rigid diacids were dimerized under the formation of two transient anhydride bonds with EDC. The resulting shape-persistent macrocycles underwent further aggregation as long as sustained by the chemical fuel.[106] All in all, this demonstrates how well-defined architectures and materials can be assembled with temporal control and soon lead to the development of a variety of applications of EDC-fueled systems (Figure 10).

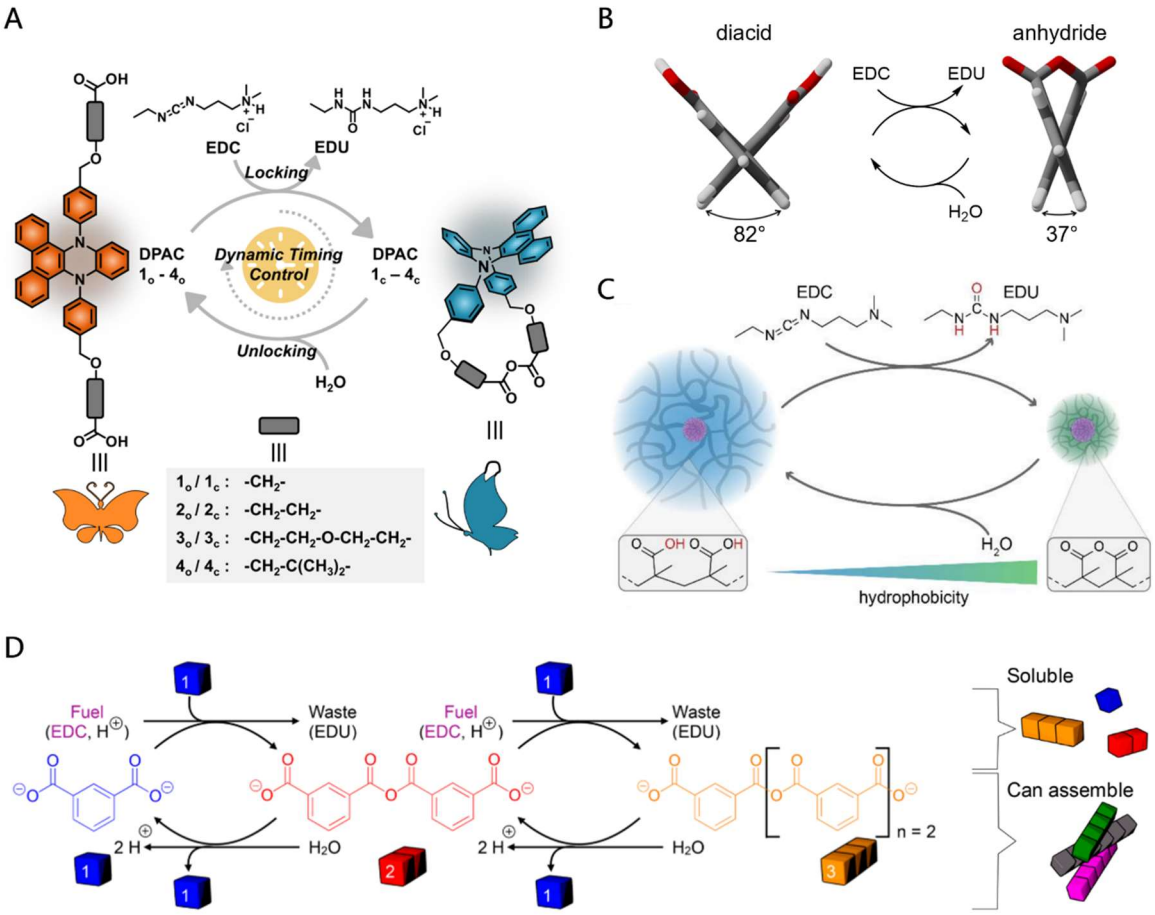

Figure 10: Applications of EDC-fueled out-of-equilibrium systems. **(A)** Control over multicolor molecular emission by chemical locking of a fluorescent dye. Copyright (2022) Wiley. Used with permission from Ref. 107. **(B)** Chemically fueled geometry changes in diphenic acid. Adapted with permission from Ref. 108. Copyright 2020 American Chemical Society. **(C)** Transient volume phase transition of a polyacid microgel. Reprinted from Ref. 109 with a Creative Commons Attribution Non-Commercial No Derivative Works (CC-BY-NC-ND) 4.0 license, https://creativecommons.org/licenses/by/4.0/. **(D)** Fuel-driven dynamic combinatorial library. Adapted with permission from Ref. 110. Copyright, 2021 American Chemical Society.

Qu and coworkers equipped a 9,14-diphenyl-9,14-dihydrodibenzo[a,c]phenazine (DPAC) fluorophore with alkyl chains, containing carboxylic acids on either side of the molecule (Figure 10A). Hence, the carboxylate ↔ anhydride reaction cycle controlled the intramolecular cyclization, which decreases the conformational freedom of the emissive unit. The chemically locked state exhibited fluorescence at a different wavelength than the unlocked state. The lifetime of the transient change in fluorescence could be tuned by the amount of fuel and by the structural information embedded in the molecule (e.g., length of alkyl chains). This underscores potential application as smart luminescent material, for example in biological imaging.[107] Another application of transient geometry changes inside a single molecule is the chemically fueled reduction of dihedral angle in a diphenic acid system, as depicted in Figure 10B. Here, the intramolecular condensation reduced the torsional angle between the two phenyl units by 45° regardless of the substitution,[108,111] mimicking conformational changes in biological systems like ATP-fueled motor proteins.[112,113]

Arguably the most broadly explored application of EDC-fueled systems is the transient cross-linking of polyacid materials that form hydrogels in aqueous solutions. Metastable anhydride cross-linking can regulate the particle size,[109] phase separation,[114–116] sol-to-gel

transition,[117,118] gel-to-gel transition[119] and the hydrogels' mechanical properties.[120–123] Exemplarily, Figure 10C illustrates how the EDC-fueled formation of hydrophobic anhydrides inside a poly(methacrylic acid) (PMAA) microgel can lead to a transient change in hydrodynamic radius of the PMAA particles. Further research in this area has the potential to yield smart colloidal materials.[109]

Traditionally, dynamic combinatorial chemistry (DCC) operates in thermodynamic equilibrium (see chapter 1.1.1).[17] *Boekhoven* and coworkers, however, created a dynamic combinatorial library (DCL) that only exists out-of-equilibrium[124] and as long as EDC is present as a chemical fuel. Isophthalic acid building blocks were reversibly oligomerized under carboxylic acid anhydride formation, as illustrated in Figure 10D. Oligomers can either decline due to hydrolysis, grow stepwise by the addition of one monomer at a time, or recombine, when existing oligomers of different sizes come together (i.e., transacylation). Hydrolysis and recondensation under non-equilibrium conditions lead to constant dynamic covalent exchange of the members of the DCL. The fact that larger oligomers are able to self-assemble, while smaller oligomers are molecularly dissolved, lead to feedback mechanisms that affected the reaction kinetics. Such a selective up- and down-regulation of certain sequences can be considered life-like behavior.[110]

1.2.3 Transient Carboxylic Esters and Amides

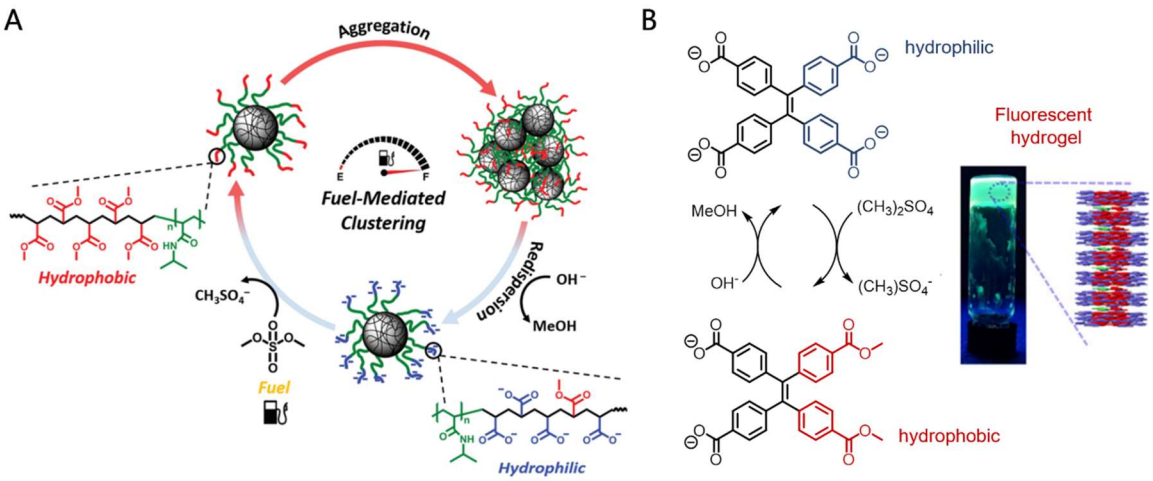

Figure 11: Transient methylation with dimethyl sulfate (DMS). **(A)** Transient clustering of colloidal building blocks. Reprinted with permission from Ref. 125. Copyright 2017 American Chemical Society. **(B)** DMS-driven gelation leads to dissipative assembly-driven emission. Adapted with permission from Ref 126. Copyright 2023 American Chemical Society.

Carboxylic acid esters are less prone to hydrolysis than carboxylic acid anhydrides. Yet, they can facilitate dissipative reaction cycles, when their hydrolysis rate is increased by a high pH value, electron-withdrawing substituents or by nucleophilic catalysis. One example is the transient methylation with MeI or dimethyl sulfate (DMS), as introduced in chapter 1.1.2.[68,69] This chemistry was used by the same group to achieve fuel-mediated clustering of colloidal particles (Figure 11A). The spherical polystyrene particles were equipped with multiple carboxylates and the electrostatic repulsion of the negative charges stabilized them in aqueous media. Addition of the methylation agent DMS converted the carboxylates into

hydrophobic esters, driving the colloids into aggregation. Repulsion was reinstated upon ester hydrolysis in the basic buffer, leading to redispersion of the particles.[125] More recently, the charge reduction of carboxylic acids upon DMS-driven esterification enabled dissipative self-assembly induced emission. The common aggregation induced emission (AIE) building block tetraphenylethylene (TPE)[127–129] was furnished with carboxylates, as depicted in Figure 11B. Esterification of the building block transformed the mixture into an emissive hydrogel via the AIE effect. The fluorescence emission was transient in nature, as the gel dissolved under spontaneous hydrolysis.[126] In another example, dissipative host-guest assembly was also regulated by transient charge reduction upon the consumption of DMS.[130]

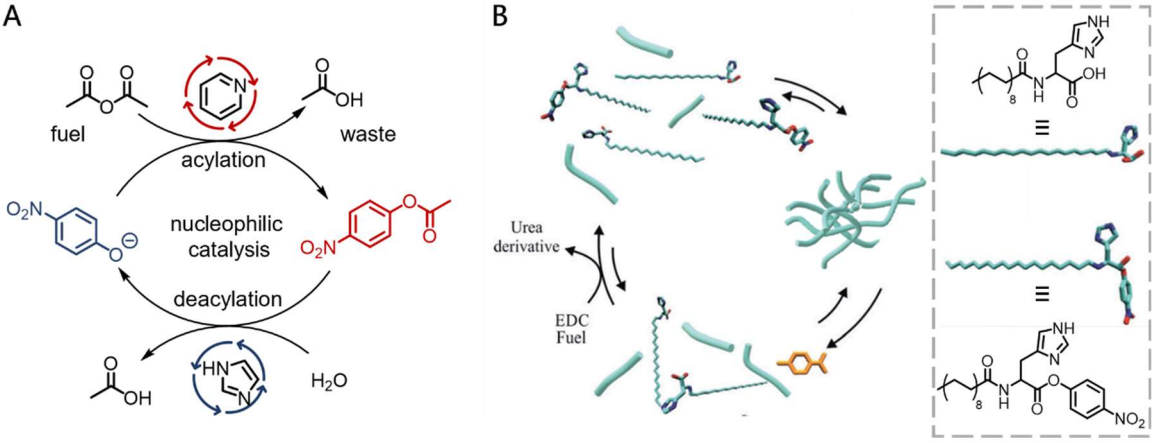

Figure 12: Transient esterification. **(A)** *Eelkema* and coworkers used acetic acid anhydride as a fuel to acylate *p*-nitrophenolate. The corresponding ester hydrolyzed under imidazole catalysis.[131] **(B)** Dissipative self-assembly of histidine containing amphiphiles through transient esterification by *Das* and coworkers. Copyright (2019) Wiley. Used with permission from Ref. 132.

Eelkema and coworkers introduced acetic acid anhydride as a chemical fuel that can transform *p*-nitrophenolate into the corresponding ester by acylation. Inspired by the enzyme-controlled signal transduction in living systems, they used pyridine and imidazole as nucleophilic catalysts for the acylation and deacylation, respectively. For the reaction cycle shown in Figure 12A, a kinetic model was developed, underpinning the effect of the organo-catalysts on the activation and deactivation reaction. Variation of the fuel concentration and use of the catalysts enabled full control over the yield and lifetime of the transient ester. The same organocatalytic control was extended to a polymer system, where transient acylation of the nitrophenolate moiety regulated the polymer chains' conformation and aggregation behavior.[131] Other reports by the *Eelkema* lab use ally acetate as a fuel to enabled transient manipulation of polymers' and coacervates' properties.[133–135]

Das and coworkers demonstrated a similar system already a year earlier. Transient self-assembly of amphiphiles containing a histidine head group was facilitated by the cooperative catalysis of the imidazole moiety of the histidine. Both the EDC-fueled ester formation, which induced self-assembly and the subsequent ester hydrolysis were intramolecularly catalyzed by the imidazole unit (Figure 12B).[132,136–138] *Boekhoven* also reported a system, in which carboxylic acids were activated with EDC and converted to a transient ester. Silicon and gold nanoparticles were equipped with carboxylates and driven into self-assembly by esterification with *N*-hydroxysuccinimide (NHS) as a nucleophile.[139,140]

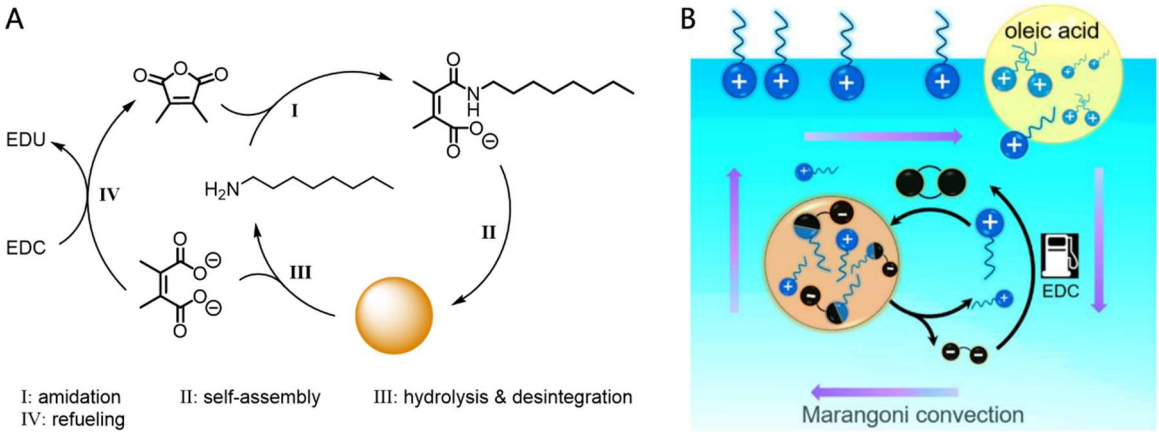

Figure 13: Transient amidation coupled with an EDC-fueled anhydride formation. **(A)** Octylamine reacts with a cyclic anhydride to form an amphiphilic amide (I) that co-assembles with the amine into droplets (II). Amide hydrolysis leads to disintegration of the droplet and release of octylamine (III). The dicarboxylate waste can be refueled with EDC to start a new cycle (IV). **(B)** EDC-fueled Marangoni convection in a source-sink system. Reprinted from Ref. 141 with a Creative Commons Attribution Non-Commercial No Derivative Works (CC-BY-NC-ND) 4.0 license, https://creativecommons.org/licenses/by/4.0/.

Otto and coworkers coupled dissipative self-assembly to a macroscopic Marangoni flow in a system comprising a transient amide bond. In this system, 2,3-dimethylmaleic acid reacts with octylamine to form the amphiphilic maleamic acid (Figure 13A, I), which can co-assembly into coacervates with remaining octylamine (II). The neighboring carboxylate renders the amide transient and spontaneous hydrolysis continuously releases octylamine and maleic acid (III). The system is refueled with EDC, which regenerates the maleic anhydride (IV) and therefore the amide-based droplets. An oleic acid droplet on the air/water interface acts as a sink and source for octylamine. Whether octylamine is free or incorporated in the transient droplets makes a difference in local octylamine concentration. This concentration gradient is determined by the reaction cycle and the resulting dynamic instability of the droplets and drives a macroscopic Marangoni convection (Figure 13B).[141] As such, this report is an example, how chemically fueled systems can operate across multiple length and time scales and how that facilitates non-linear feedback loops.

1.2.4 Redox-Fueled Disulfides and Aldehydes

While both light[142,143] and electricity[31,144] can be energy sources for redox-driven dissipative self-assembly, this chapter will focus on chemically fueled redox systems. These systems are predominantly built on reversible disulfide chemistry. *Fletcher* and coworkers developed a chemically fueled system that exhibits out-of-equilibrium self-replication of a self-assembling amphiphile. As shown in Figure 14A, the hydrophobic thiol precursor **1** and the hydrophilic disulfide precursor **2** are phase-separated and slowly transform to the metastable amphiphile **4**, releasing waste product **3**. The amphiphiles self-assemble into micelles in aqueous solution and increase the phase-mixing, which autocatalytically enhances their own rate of formation. It is therefore referred to as a self-replicator. A second thiol-disulfide exchange between the self-replicator **4** and excess precursor **1** forms additional waste **3** and **5** and eventually leads to disassembly at equilibrium. Addition of hydrogen peroxide as a chemical fuel regenerates disulfide precursor **2** from waste **3**, preventing the system from returning to equilibrium.

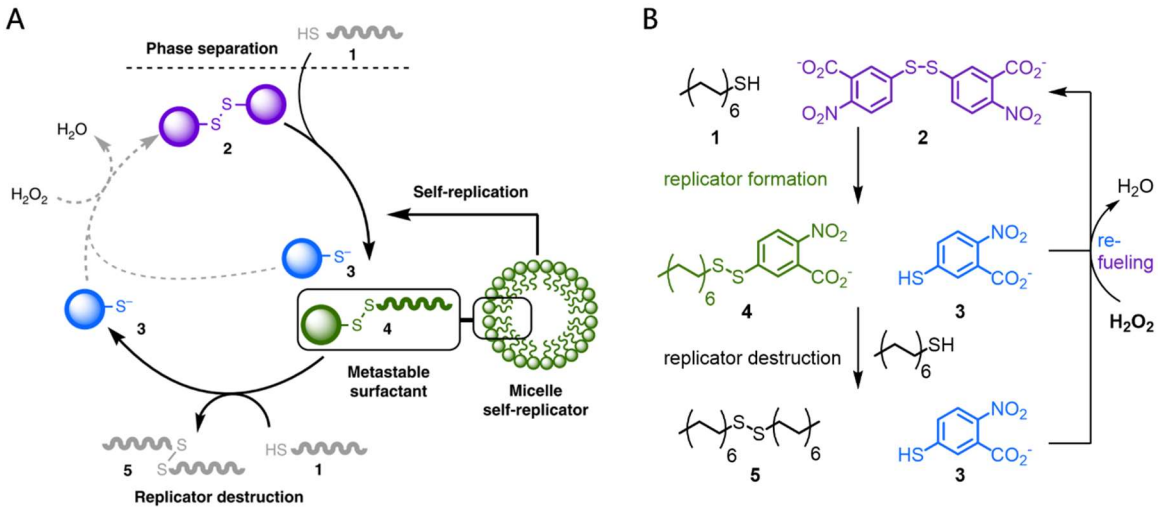

Figure 14: H_2O_2-fueled reaction cycle by *Fletcher* and coworkers. **(A)** Overview. Phase-separated precursors **1** and **2** undergo thiol-disulfide exchange to form surfactant **4**, which self-assembles into micelles. The micelles catalyze the conversion of **1** and **2** to self-replicator **4** and waste **3**. A second disulfide exchange with **4** and excess precursor **1** leads to the micelle destruction and formation of waste **5**. H_2O_2 acts as fuel by converting **3** back to precursor **2**. Adapted from Ref. 145 with a Creative Commons Attribution 4.0 International License (CC BY 4.0), https://creativecommons.org/licenses/by/4.0/. **(B)** Reaction cycle with the corresponding chemical structures.

At the resulting steady state, precursor **1** and the oxidative fuel are consumed in successive cycles and the autopoietic micelles are maintained in a higher concentration than in the non-fueled system.[145] The chemical structure of all components is shown in Figure 14B. In a similar system with different amphiphiles, the same group reported stable self-replicating vesicles that did not degrade in the same way. Only the introduction of a catalyst (*p*-dimethylamino pyridine, DMAP) closed the metabolic cycle.[146] Later, the system was further developed to enable autonomous oscillation.[147]

Guan reported similar H_2O_2-fueled disulfide formation, leading to the dimerization of building blocks. The dimers' higher aggregation propensity drives the system into transient self-assembly. Background reduction, which closes the dissipative cycle, transfers the disulfides back to the thiol precursors through irreversible oxidation of dithiothreitol (DTT) to the corresponding cyclic disulfide, as illustrated in Figure 15A.[148]

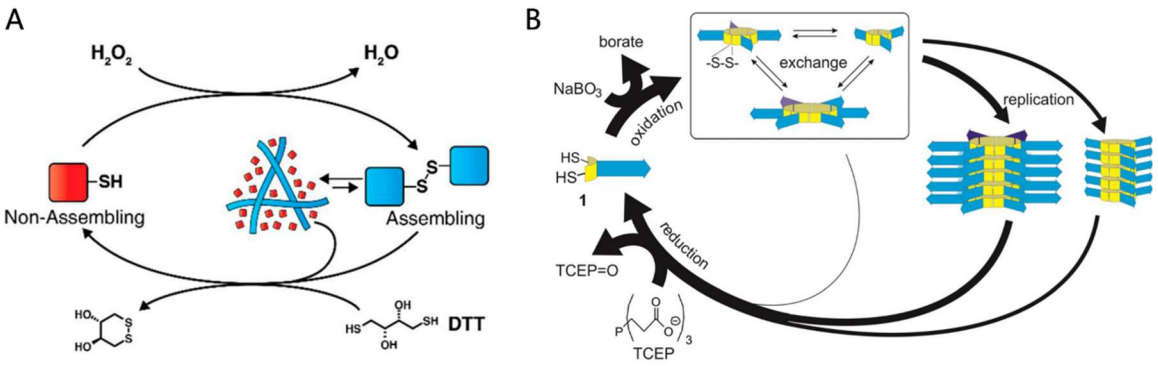

Figure 15: Redox-fueled systems by the groups of *Guan* and *Otto*. **(A)** Dissipative self-assembly of active materials governed by H_2O_2 as fuel and dithiothreitol (DTT) as background reductant. Copyright (2019) Wiley. Used with permission from Ref. 148. **(B)** Assembly-driven self-replication of disulfide macrocycles under constant simultaneous addition of oxidant ($NaBO_3$) and reductant (tricarboxyethylphosphine, TCEP). Reprinted from Ref. 149 with a Creative Commons Attribution Non-Commercial No Derivative Works (CC-BY-NC-ND) 4.0 license, https://creativecommons.org/licenses/by/4.0/.

Otto and coworkers designed a chemically fueled self-replicating system, in which more complex replicators emerged that were not accessible under thermodynamic control. Peptide-based dithiols were oxidized with $NaBO_3$ to form self-replicating macrocycles with different sizes, comprised of multiple disulfide bonds. At equilibrium, the five-membered macrocycle formed predominantly and self-assembled into fibers by *β*-sheet stacking. Simultaneous addition of the oxidant and tricarboxyethylphosphine (TCEP) as a reducing agent, facilitated a non-equilibrium steady state and opened a pathway for the more slowly forming three-membered self-replicator. In Figure 15B, the thickness of the arrows indicates the magnitude of the corresponding flux, as determined by a kinetic model. The short-circuiting redox reaction of perborate with TCEP accounted for less than 0.1% of the total flux.[149,150] Notably, out-of-equilibrium self-replication as reported by the groups of *Fletcher* and *Otto* has relevance for the origins of life and showcases dynamic life-like behavior. Other non-equilibrium disulfide exchange includes transient self-assembly of polymer-[151] and DNA-based[152] nanostructures.

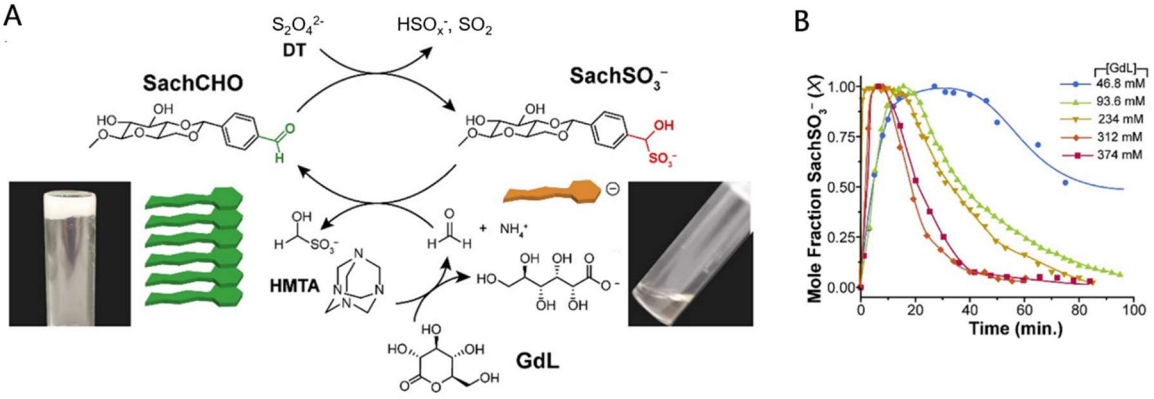

Figure 16: Dissipative (dis-)assembly by *Hermans* and coworkers. **(A)** Reaction cycle between gelating aldehyde SachCHO and non-gelating sulfonate $SachSO_3^-$, mediated by dithionite (DT) and glucono-δ-lactone (GdL) and hexamethylenetetramine (HMTA). **(B)** Mole fraction of the transient species $SachSO_3^-$ under different conditions. Adapted with permission from Ref. 153. Copyright 2020 American Chemical Society.

In a system reported by the *Hermans* lab, the aldehyde reducing agent dithionite (DT) and formaldehyde as a fuel enable dissipative (dis-)assembly. The hydrogelator SachCHO (structure in Figure 16A) is transferred to *α*-hydroxy sulfonate $SachSO_3^-$ upon addition of DT. (Even though the aldehyde is not reduced to the alcohol at 25 °C (as opposed to > 80 °C[154]), the system shall still be discussed in this chapter). Electrostatic repulsion of the sulfonates leads to disassembly of the hydrogel. In order to close the reaction cycle, formaldehyde is formed *in situ* by the pre-fuels glucono-δ-lactone (GdL) and hexamethylenetetramine (HMTA), converting the sulfonate back to the initial aldehyde hydrogelator. Figure 16B shows the mole fraction of the transient sulfonate species in the dissipative system and demonstrates how the gel-sol-gel transition can be controlled (and reprogrammed) by the amount of pre-fuel GdL.[153] The concept of a pre-fuel further increased the complexity of non-equilibrium systems. Expanding the system to three different derivatives of the hydrogelator, enabled narcissistic self-sorting of an initially random co-assembly upon fuel addition.[155]

1.2.5 Summary of the State of the Art

Figure 17 summarizes all dissipative reaction cycles, discussed in this introduction. This includes ATP fueled, enzyme-based reaction cycles[70,78,82] (A-C), carboxylic acid ↔ anhydride cycles[84,85] (D), an amine ↔ amide cycle, coupled with D[141] (E), carboxylic acid ↔ ester cycles[68,69,131,132,139] (F-H), thiol ↔ disulfide cycles[145,148,149] (I-J) and one aldehyde ↔ hydroxy sulfonate cycle[153] (K). All these catalytic reaction cycles have been exploited for dissipative self-assembly. A few systems have not been discussed in detail but need to be mentioned. That includes sugar[156] and cyclodextrin[157] fueled transient hydrogels, amino acid-fueled self-assembly,[158] out-of-equilibrium nanoparticle aggregates by *Klajn*[159] and systems under the dissipative control of transient acids by *Di Stefano*.[160–163] All in all, the discipline of dissipative chemistry has developed rapidly. More effort is needed, though, to unfold its full potential.

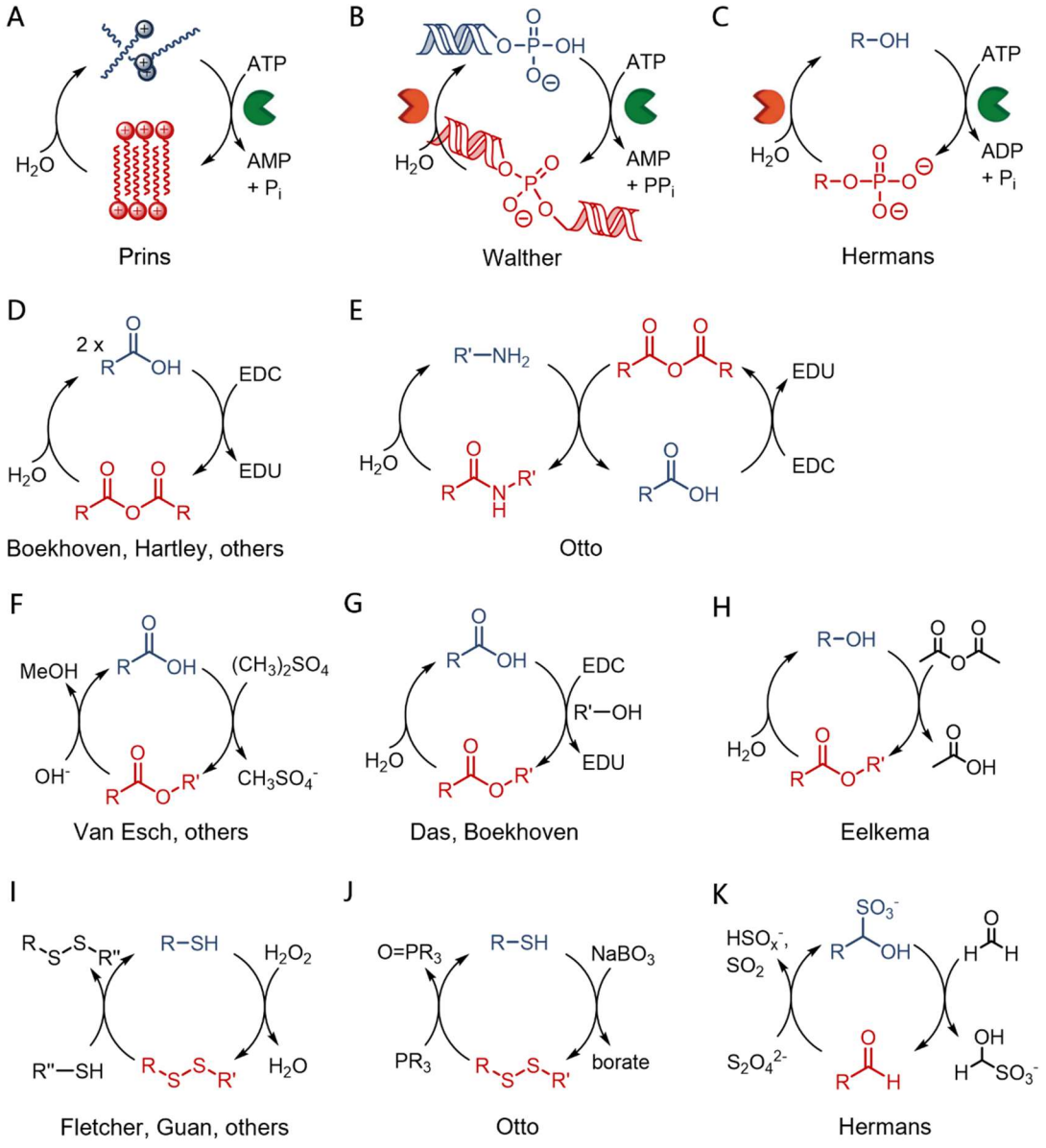

Figure 17: Overview of all dissipative reaction cycles discussed herein. **(A-C)** ATP- and enzyme-based cycles. **(D)** EDC-fueled condensation of anhydrides and **(E)** coupled transient amide. **(F-H)** Reaction cycles based on transient esterification. **(I-J)** Chemically fueled redox cycles of disulfides. **(K)** Transient sulfonation of aldehydes.

1.3 Fundamentals of Organophosphate Chemistry

As discussed in chapter 1.2, most of the artificial non-enzymatic reaction cycles rely on the transient conversion of carboxylic acids into anhydrides or esters. We figured, that reaction cycles built upon organic phosphates rather than carboxylates may have crucial advantages, like a higher affinity towards different nucleophiles,[164] multiple substitutions[165] and the flexibility to transfer the same chemistry from phosphates onto phosphonates. Furthermore, organophosphates play an important role in living systems, including metabolism (ATP), translation (DNA, RNA) and compartmentalization (phospholipids) and thus for the origins of life.[166–168] Nature chose phosphates because of their multivalency and their ability to form different bonds with tailor-made stability for specific tasks.[166] Since we set to exploit this versatility of organophosphates for dissipative reaction cycles, this chapter discusses the underlaying fundamentals of organophosphate chemistry with a focus on bond formation and hydrolysis.

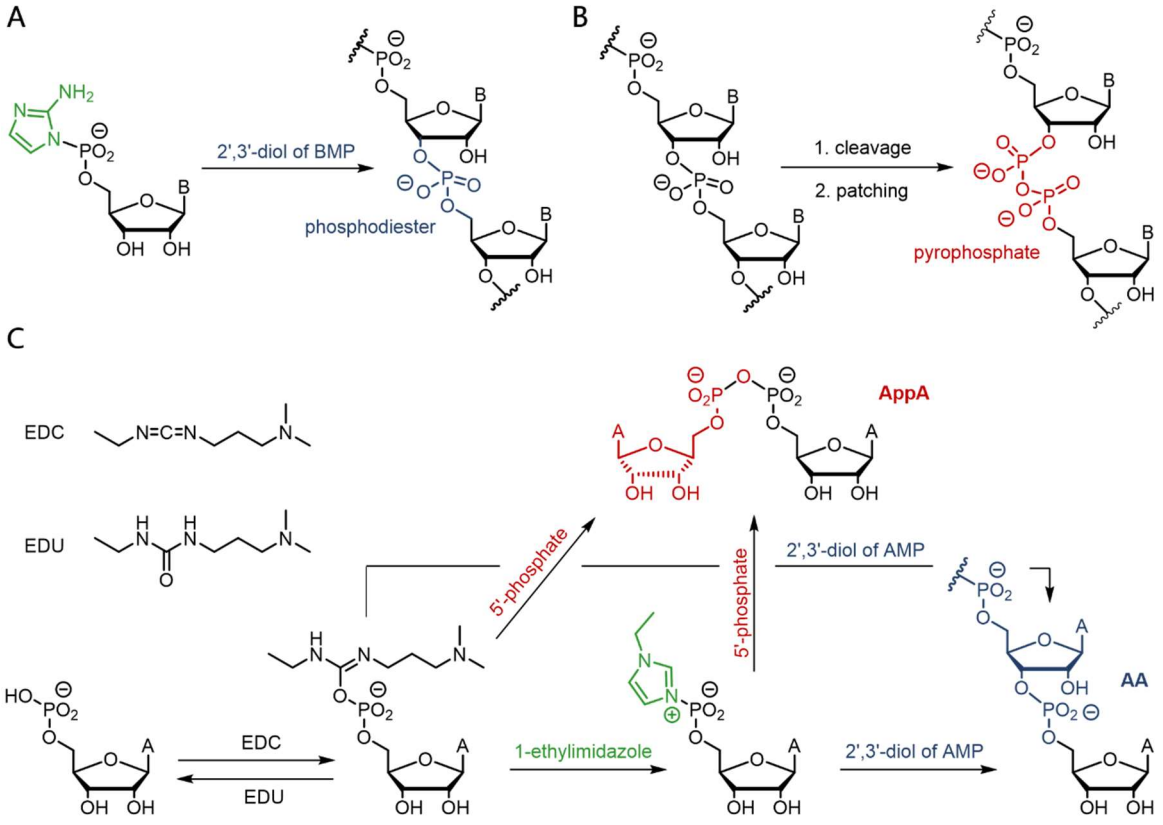

Figure 18: Formation of phosphodiesters and pyrophosphates. **(A)** Pre-activated RNA nucleotides can be oligomerized under the formation of a phosphodiester bond. **(B)** Cleavage of a phosphodiester yields 3'-phosphates, that can form pyrophosphates with a 5'-phosphate in a template-directed copying reaction. **(C)** Reaction network of *in situ* EDC-activated phosphates with 1-ethylimidazole as organo-catalyst, leading to pyrophosphates and phosphodiesters. B=nucleobase, A=adenosine, AA=diester, AppA=pyrophosphate.

In template-directed, non-enzymatic systems, RNA-primers can be extended under the formation of a phosphodiester bond, when the 3'-hydroxy group of the terminal nucleotide reacts with a pre-activated nucleotide, as demonstrated by the groups of *Richert* and *Szostak* (Figure 18A).[169–172] The confined environment of RNA-templated synthesis inhibits

pyrophosphate bond formation and yields the phosphodiester rather efficiently. Pre-activation with many different leaving groups, including imidazoles, oxyazabenzotriazolides, and other heterocycles has been investigated and 2-aminoimidazole (Figure 18, green) proofed most effective.[170,171] When phosphodiesters are cleaved in the RNA backbone, they form terminal 3'-phosphates, which can participate in a similar template-directed copying reaction with activated nucleotides to form a pyrophosphate bond (Figure 18B).[173]

Richert and coworkers reported effective copying of RNA-sequences without pre-activation of the nucleotides in a "condensation buffer".[174] Figure 18C illustrates the reaction network of *in situ* activation with EDC, leading to the formation of both phosphodiesters and pyrophosphates in a template-free oligomerization of adenosine monophosphate (AMP). AMP is first activated with EDC and then "organocaptured" by 1-ethylimidazole to form a species reminiscent of the pre-activated nucleotides discussed above. This second activated phosphate is less prone to hydrolysis and can therefore undergo a reaction with either the 2'- or 3'-hydroxy group of another AMP to form a phosphodiester bond (AA) or with a second 5'-phosphate to form a phosphoric acid anhydride, i.e., pyrophosphate (AppA). A kinetic model of the network revealed that AppA is formed an order of magnitude faster than AA, so that the pyrophosphate bond accounts for approx. 90% of the final bonds.[175]

A

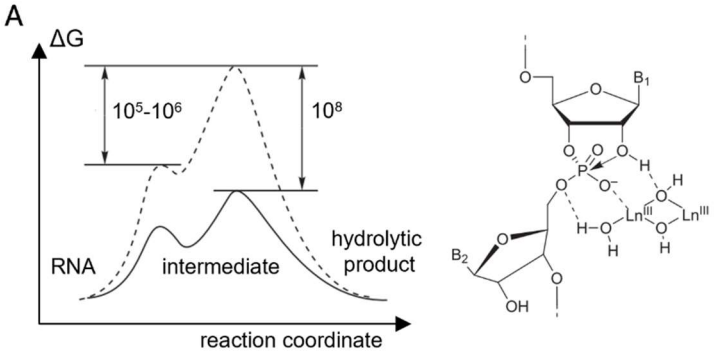

B

Conditions	% PP hydrolyzed	
Incubation	30 d	120 d
pH = 4.5	3.6	13.8
pH = 6.5	1.7	4.4
pH = 8.5	1.1	2.9
T = 25 °C	2.0	8.7
T = 45 °C	3.2	9.7

Figure 19: Hydrolysis of phosphodiester and pyrophosphate bonds. **(A)** Mechanism of lanthanide salt (Ln^{III}) catalyzed RNA diester hydrolysis, including the corresponding energy diagram. Adapted with permission from Ref. 176. Copyright 1999 Royal Society of Chemistry. **(B)** Table summarizing the hydrolysis of inorganic pyrophosphate (PP) under different conditions.[177]

The non-enzymatic hydrolysis of phosphodiesters in RNA derivatives[178] can either be catalyzed by Brønsted acids[179] or Lewis acids, like lanthanide(III) salts.[176,180,181] Ln(III) salts form bimetallic clusters $[Ln^{III}_2(OH_2)]^{4+}$ that act as base catalysts for the intramolecular attack of the 3'-hydroxy group on the phosphorous and as acid catalysts for the subsequent rate-determining break-down of the 2'-3'-cyclic penta-coordinated intermediate. Figure 19A illustrates that mechanism with a chemical structure and in an energy diagram. The dotted line shows a comparison to alkaline hydrolysis and reveal a 10^6-fold increase in hydrolysis rate by Ln(III)-catalysis.[176] Phosphodiesters that lack a neighboring nucleophile, like in DNA, are more stable, but can also be hydrolyzed, for instance by Ce(IV)-catalysis.[176,182]

Pyrophosphates are exceptionally stable towards hydrolysis, as illustrated in Figure 19B. In a reported study, only 10% of the initial inorganic pyrophosphate (PP) was hydrolyzed after 120 days at 45 °C (neutral pH). Only harsh conditions like elevated temperatures and especially strong acidic media facilitate the break-down of the pyrophosphate bond.[177,183]

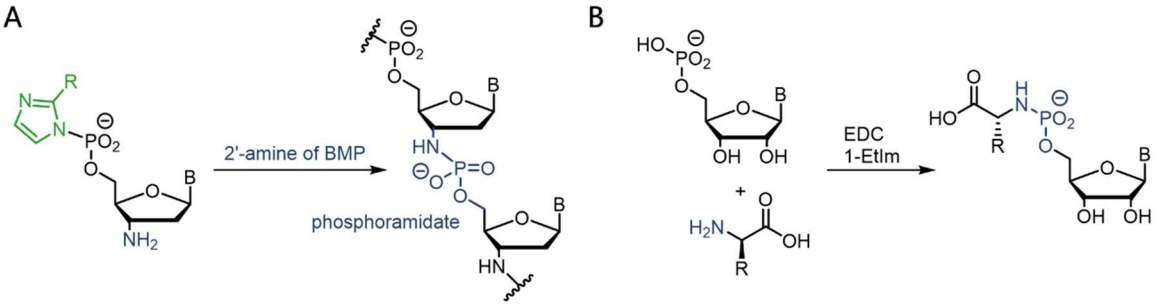

Figure 20: Formation of phosphoramidates. **(A)** Pre-activated RNA nucleotides can be oligomerized under the formation of a phosphoramidate bond**. (B)** *In situ* activation of a phosphate with EDC and 1-ethylimidazole (EtIm) and reaction with an amino acid forms peptido-RNA. B=nucleobase

When introducing different nucleophiles into the systems discussed above, different phosphate species can be formed. Introduction of an amine, for instance, enables the synthesis of phosphoramidates.[184,185] When replacing the 2'-hydroxy group with a 2'-amine, artificial DNA derivatives with all canonical nucleobases can be polymerized in a template-directed synthesis. Szostak and coworkers reported this for pre-activated phosphates, similar to the phosphodiester formation (Figure 20A).[186–188] *Richert* and coworkers exploited the condensation buffer method with *in situ* EDC-activation for the synthesis of peptido-RNA, where the 5'-phosphate of an RNA-nucleotide and the amine of an amino acid form a phosphoramidate bond (Figure 20B). Whether the phosphoramidate or the pyrophosphate forms, was dependent on the nucleophilicity of the corresponding amino acid.[175,189] Organic phosphoramidates were exploited for the design of an artificial ribosome by the *Richert* lab[190] and the prebiotic synthesis of aminoacyl-RNA by *Sutherland* and coworkers.[191]
Compared to phosphodiesters (and pyrophosphates) phosphoramidates are more readily hydrolyzed under moderate conditions. This includes mildly acidic conditions[192–194] and in case of cyclic phosphoramidates also alkaline hydrolysis.[195] Nucleophilic heterocycles (like imidazoles) are known to catalyze the phosphoramidate hydrolysis, as histidine is part of the catalytic center of phosphoramidate hydrolase enzymes (like HINT 1).[196,197] Just like the nucleophilicity of the amine dictates the phosphoramidate formation, the nature of the amine as a leaving group has also been shown to affect the corresponding rate of hydrolysis.[198]

In summary, the formation of different phosphate derivatives is enabled by the reaction of an activated phosphate with a nucleophile under release of water. In competing scenarios with more than one nucleophile, the product distribution depends on the strength of the corresponding nucleophiles. The reaction with amines or hydroxides leads to the formation of phosphoramidates or phosphodiesters, respectively. However, pyrophosphate formation by condensation of two phosphates is a common side-reaction. While phosphoramidates are readily hydrolyzed under mild conditions and phosphodiester hydrolysis can be catalyzed with Lewis and Brønsted acids, pyrophosphates are kinetically stable, and their hydrolysis requires harsh conditions. The versatility of organic phosphates and their derivatives is exploited in this work (see chapter 2) for the design of self-assembling systems under thermodynamic and kinetic control.

2 Aims and Achievements

2.1 Carbodiimide-Driven Dimerization and Self-Assembly of Artificial, Ribose-Based Amphiphiles

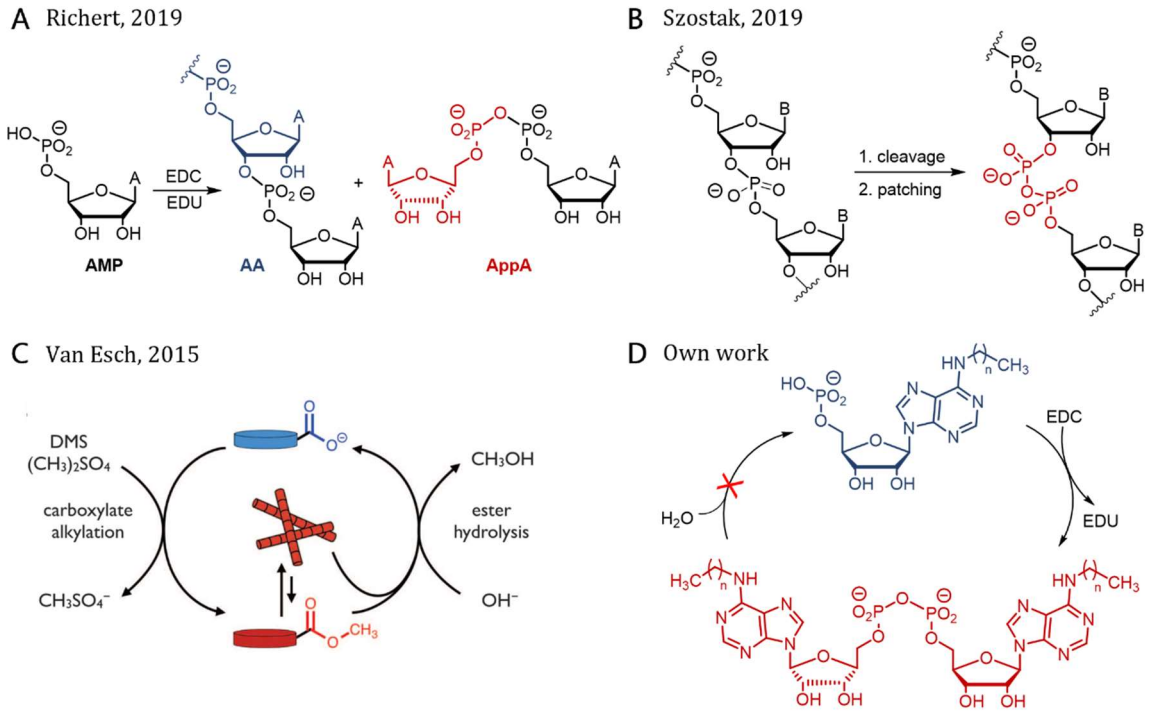

Figure 21: Foundation for own work. **(A)** *Richert* and coworkers showed that *in situ* activation with EDC and the organo-catalyst EtIm can form diester oligomers and preferentially pyrophosphates from adenosine monophosphate (AMP). **(B)** *Szostak* and coworkers formed pyrophosphates by condensation of pre-activated phosphates. **(C)** The first example of a reaction cycle with dissipative self-assembly. Reprinted from Ref. 69 with permission from The American Association for the Advancement of Science, copyright 2015. **(D)** The goal of our project was to establish a dissipative reaction cycle, based on ribonucleotide amphiphiles, but the pyrophosphates could not be hydrolyzed, and the resulting system was therefore kinetically trapped.

Inspired by two independent fields of research (origins of life and systems chemistry), we attempted to develop a new dissipative reaction cycle based on ribose- and ribonucleotide-derived amphiphiles. *Richert* and coworkers have reported the formation of oligonucleotides from adenosine monophosphate (AMP) in a "condensation buffer" (Figure 21A). As a main byproduct, they observed the formation of pyrophosphates.[175] The group of *Szostak* used the propensity of activated organophosphates to form pyrophosphates to "patch" cleaved RNA strands (Figure 21B).[173] The backwards reaction, namely the hydrolysis of these pyrophosphates, however, was widely underexplored. Motivated by recent advances in man-made dissipative reaction cycles (Figure 21C),[69] the goal of this project was to use the pyrophosphate formation chemistry and render it transient by developing a corresponding hydrolysis chemistry. Phosphate-based dissipative reaction cycles would significantly broaden the scope of the field and have important implications for the origins of life. We thus investigated whether EDC-activation of functionalized RNA derivatives with aliphatic chains and subsequent hydrolysis can lead to the transient formation of vesicles (Figure 21D).[1]

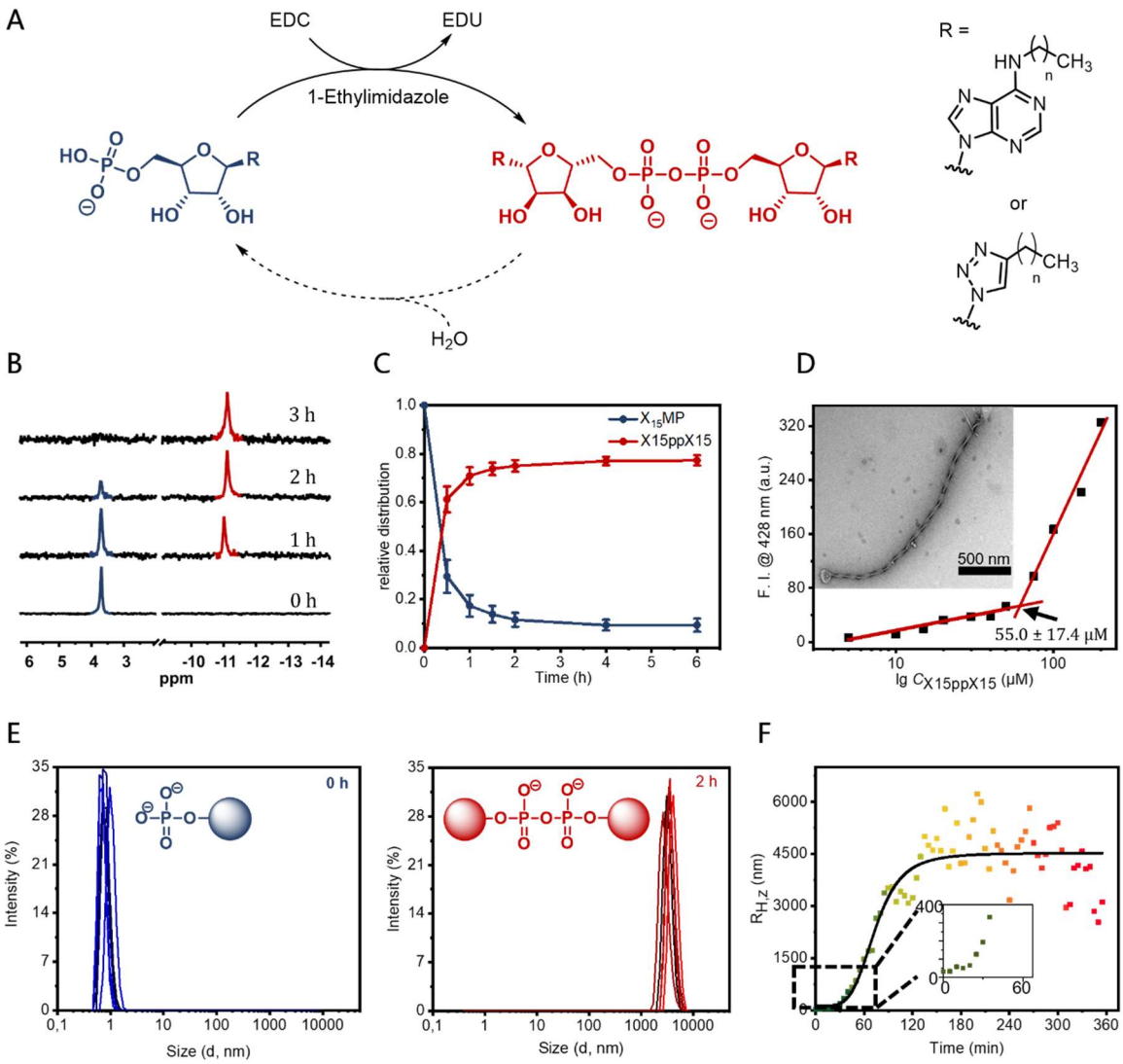

Figure 22: Results of own work. **(A)** Ribose- and ribonucleotide-based amphiphiles were dimerized upon addition of EDC. **(B)** Formation of the pyrophosphate dimer monitored by ^{31}P NMR and **(C)** by HPLC. **(D)** Determination of the critical aggregation concentration (CAC) of the dimer (25 times below that of the monomer) and TEM image of the corresponding aggregates. **(E)** DLS measurements before and 2 h after addition of EDC. **(F)** The dimerization leads to *in situ* formation of large aggregates as determined by DLS. Adapted from Ref. 1 with a Creative Commons Attribution 4.0 International License (CC BY 4.0), https://creativecommons.org/licenses/by/4.0/.

To allow a broad investigation, we first synthesized a library of nine different ribose- and ribonucleotide-based amphiphiles with a phosphate head group and aliphatic tails of different chain lengths and explored their aggregation properties. We found that they vary in their propensity to aggregate, as quantified by the critical aggregation concentration (CAC), depending on their chain length and observed that the amphiphiles self-assemble in various superstructures with different shapes and sizes on the nanometer and micrometer scale. Furthermore, we were surprised to see that the amphiphiles exhibit aggregation-induced emission (AIE)[127–129,199] both in solid-state and solution.

As expected (based on previous reports[173,175]) addition of EDC as a chemical fuel lead to the rapid formation of pyrophosphates and thus, dimerization of the amphiphiles as monitored by ^{31}P-NMR and HPLC (Figure. 22A-C). One amphiphile in particular showed spontaneous aggregation after dimerization and was therefore identified as a perfect candidate for further studies. We found that the CAC of the dimer is 25 times lower than that of the monomer and

that it self-assembles into 3 µm long helical fibers (Figure 22D). When we fueled a solution of this amphiphile at a concentration where it was molecularly dissolved (i.e., below CAC) with EDC, we could observe the formation of aggregates upon dimerization by dynamic light scattering (DLS, Figure 22E). Precise kinetic monitoring by DLS revealed an interesting sigmoidal behavior (Figure 22F), indicating cooperative effects between self-assembly and pyrophosphate formation by an increase of effective molarity inside the aggregates. Unfortunately, the pyrophosphates proofed to be stable towards hydrolysis under applicable conditions, preventing the system from relaxing back to equilibrium.

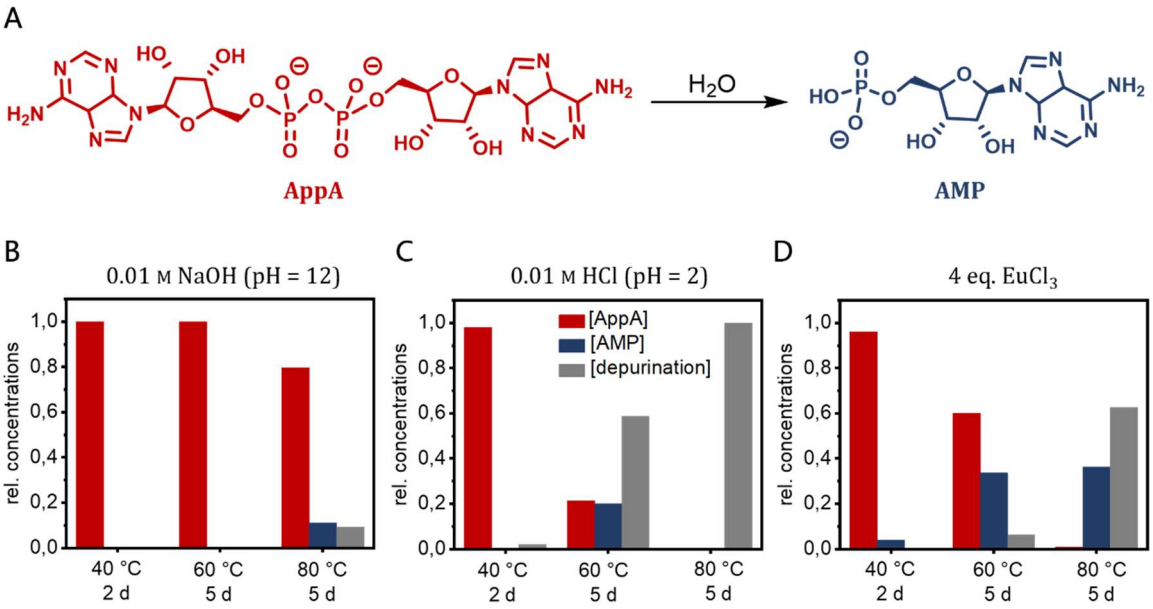

Figure 23: Systematic study of pyrophosphate hydrolysis. **(A)** Adenosine pyrophosphate (AppA) was used as a model compound for the hydrolysis to adenosine monophosphate (AMP). **(B)** Under basic conditions (pH = 12) almost no changes were observed. **(C)** Under acidic conditions (pH = 2) some pyrophosphate hydrolyzed, but most of the AppA decomposed by depurination. **(D)** $EuCl_3$ catalyzed the hydrolysis, but depurination took over at elevated temperatures. Adapted from Ref. 1 with a Creative Commons Attribution 4.0 International License (CC BY 4.0), https://creativecommons.org/licenses/by/4.0/.

Naturally, we were interested to overcome the kinetic trap and to close the dissipative reaction cycle. Therefore, we conducted a systematic study on the hydrolysis of the non-aggregating adenosine pyrophosphate (AppA) model compound (Figure 23). We found that it is essentially stable under neutral and basic conditions even at elevated temperatures of 80 °C over more than ten days. Under acidic conditions (pH = 2) and slightly elevated temperatures (60 °C), we observed some hydrolysis to AMP, but mostly decomposition in form of depurination by cleavage of the hemiaminal ether. The Lewis acid catalyst $EuCl_3$ gave the most promising results. At temperatures below 60 °C the hydrolysis was, however, too slow and at higher temperatures depurination became dominant.

In conclusion, we introduced new ribonucleotide-based amphiphiles from prebiotically plausible building blocks and showed that their *in situ* dimerization with EDC leads to the self-assembly of large aggregates. Even though we were not able to close the dissipative reaction cycle (yet), this work contains valuable lessons for those who work on the RNA world hypothesis[200–204] and on out-of-equilibrium systems alike. Finding a suitable hydrolysis catalyst for pyrophosphates is part of future research and possibly has far-reaching implications on our understanding of prebiotic RNA synthesis and “error correction”.

2.2 A Ribonucleotide ↔ Phosphoramidate Reaction Network Optimized by Computer-Aided Design

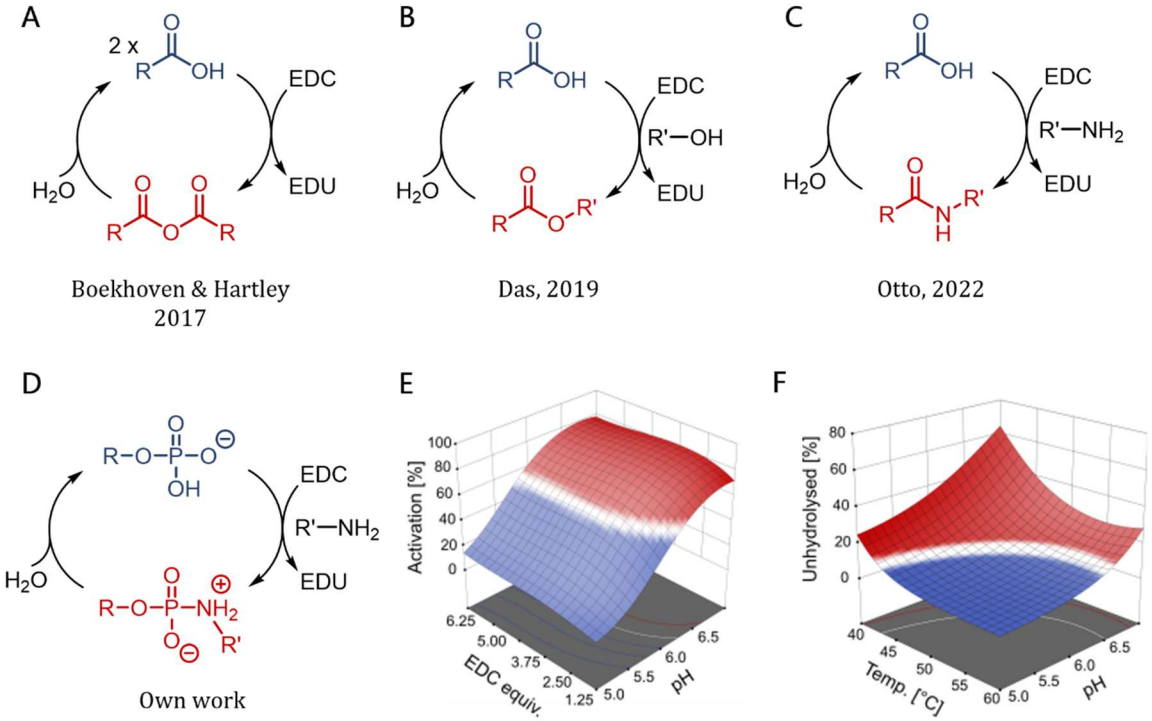

Figure 24: State of the art and own work. **(A)** Carbodiimide-driven reaction cycles based on the condensation of carboxylates were simultaneously developed by the groups of *Boekhoven* and *Hartley*. **(B)** Transient EDC-driven esterification developed by *Das* and coworkers. **(C)** Transient EDC-driven amidation developed by the *Otto* lab. Backwards hydrolysis of the carboxylic amide is only possible, due to a neighboring carboxylate. **(D)** We reported the EDC-driven formation of transient phosphoramidates (PA) from organophosphates. **(E-F)** Predicted response surfaces of the activation (i.e., PA formation) **(E)** and deactivation (i.e., PA hydrolysis) **(F)** as a function of EDC equivalents, temperature, and pH. Adapted from Ref. 2 with a Creative Commons Attribution 4.0 International License (CC BY 4.0), https://creativecommons.org/licenses/by/4.0/.

The chemical energy stored in carbodiimides such as EDC has been exploited to drive a variety of different chemical reaction cycles. Notably, EDC it is the most widespread chemical fuel for man-made dissipative self-assemblies. In all reaction cycles so far, however, EDC has only been used to activate carboxylic acids, most commonly for the formation of (intramolecular) carboxylic acid anhydrides. This strategy was developed independently by the groups of *Boekhoven*[84] and *Hartley*[85] (Figure 24A). Carboxylates are activated towards nucleophilic attack when reacted with EDC and a neighboring carboxylate can thus convert the dicarboxylate into metastable anhydrides, releasing EDU as waste. Subsequent hydrolysis closes the dissipative reaction cycle. Similarly, *Das* and coworkers reported a transient esterification by utilizing the catalytic effect of imidazole on the ester bond formation and cleavage. Here, a histidine derivative is activated with EDC at the carboxylate moiety and transferred to the corresponding ester with *p*-nitrophenol, before it hydrolyzes back to the starting materials under imidazole-catalysis (Figure 24B).[132] In a third example, *Otto* and coworkers formed amides from succinic anhydrides and amines. The neighboring carboxylate renders the amides transient and the dicarboxylate waste can be converted back to the anhydride with EDC.[141] Therefore, the net reaction cycle, comprised of two coupled

reaction cycles, can be formulated as depicted in Figure 24C. In all three examples, the reaction cycles were used to establish transient self-assemblies. Notably, they all rely on the activation of carboxylic acids with EDC. Motivated by this previous work, we strived to transfer the EDC-activation chemistry from carboxylates onto more versatile organophosphates. While this ended in a kinetic sink, when allowing the formation of pyrophosphates (see Chapter 2.1), we found that addition of amines as a strong nucleophile yielded phosphoramidates (PA) that spontaneously hydrolyze under mild conditions (Figure 24D).[2] As both the forward reaction (i.e., PA formation) and the backwards reaction (i.e., hydrolysis) are governed by a multitude of interconnected parameters, we introduced the use of the software-assisted tool "Design of Experiments" (DoE)[205–207] to understand and optimize complex reaction networks. With its help, we were able to predict the systems response to changes in parameters like temperature, pH, equivalents of EDC, or concentration (Figures 24E-F).

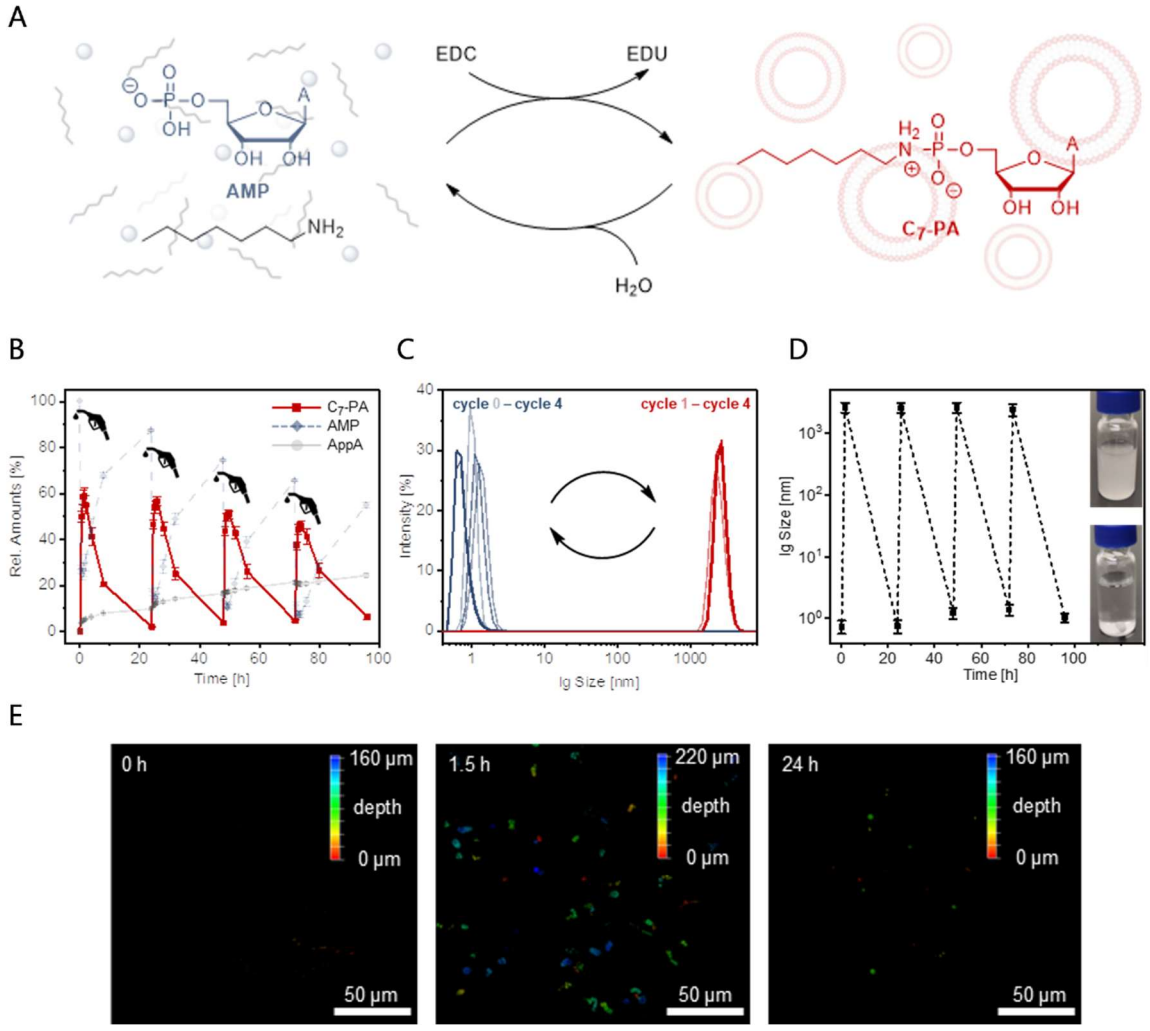

Figure 25: Results of own work **(A)** Phosphoramidates (C_7-PA) were formed from adenosine monophosphate (AMP) and heptylamine when activated with EDC and spontaneously hydrolyzed in aqueous media. **(B)** Four cycles of PA formation and hydrolysis as measured by HPLC. **(C-D)** EDC-activation and PA formation lead to the transient growth of aggregates according to dynamic light scattering (DLS). **(E)** The transient formation of aggregates was corroborated by confocal laser scanning microscopy (CLSM). Adapted from Ref. 2 with a Creative Commons Attribution 4.0 International License (CC BY 4.0), https://creativecommons.org/licenses/by/4.0/.

Most notably, we revealed the strong effect of the nucleophilic catalyst 1-ethylimidazole (EtIm) on the hydrolysis of phosphoramidates, that is reminiscent of the histidine group in phosphoramidase enzymes[197] and carboxylic ester hydrolysis.[132] With DoE, we found a "sweet spot" set of reaction conditions for a model reaction with guanosine monophosphate (GMP) and benzylamine, where the PA hydrolysis is complete within 24 h and the PA formations is still effective. From there, we developed a dissipative self-assembling system, comprised of the natural ribonucleotide AMP and heptylamine. Upon addition of EDC as a chemical fuel, up to 60% of the AMP was converted to the corresponding phosphoramidate (C_7-PA), that hydrolyzed within 24 h under mild conditions (55 °C, 5 equiv. EtIm, pH = 6.5), as depicted in Figure 25A. We could cycle this reaction for at least four times with minor loss of efficiency due to the formation of pyrophosphates as a side-reaction. On a molecular level, this was monitored by HPLC (Figure 25B). While the simple starting materials were molecularly dissolved (at 25 °C), we observed the formation of about 2.6 µm large, spherical aggregates after addition of EDC, indicated by an increase in turbidity. Aggregation was monitored by DLS and showed that we could switch the system between a non-assembled and a self-assembled state (Figures 25C-D). Furthermore, confocal laser scanning microscopy (CLSM) directly visualized the transient self-assembly (Figure 25E). In the beginning, no aggregates could be observed, while many aggregated were visible 1.5 h after addition of EDC. When the fuel was depleted and the system was allowed to hydrolyze for 24 h, almost all aggregates have vanished, corroborating their transient nature.

In summary, we developed a new dissipative reaction cycle on the basis of transient phosphoramidates and introduced a computer-assisted methodology (i.e., DoE) for the optimization of fuel-driven systems. We used this to demonstrate dissipative self-assembly, based on the prebiotically plausible building blocks AMP[208] and heptylamine.[209] While self-replication[187,191] and metabolism[190] have been reported recently, this is the first example of the third requirement for the *de novo* synthesis of life,[21] namely transient compartmentalization, with phosphoramidate chemistry, underscoring its potential importance for the origins of life.

2.3 Steric Control over the Threading of Pyrophosphonates with One or Two Cyanostar Macrocycles during Pseudorotaxane Formation

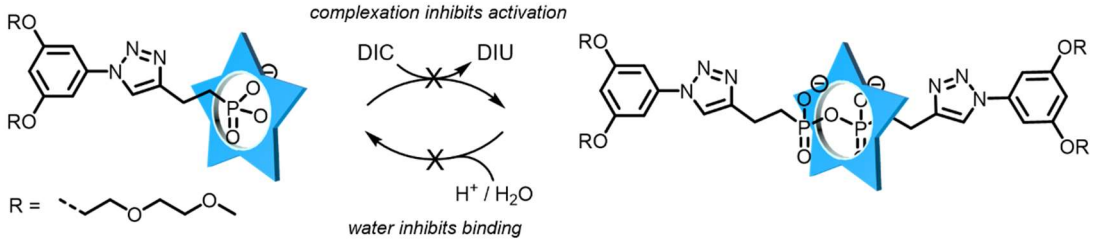

Figure 26: Initial idea for a transient rotaxane. A half-thread with a stopper group and a terminal phosphonate supramolecularly binds to the cyanostar macrocycle (cyan). Pyrophosphonate formation was supposed to be fueled with DIC and its hydrolysis catalyzed by an organic acid, to enable transient formation of a [2]rotaxane. However, complexation of the phosphonate inhibited the activation with DIC and thus the dimerization.

Based on the chemistry developed in the first two projects, we initially planned to dissipatively self-assemble a rotaxane with a labile bond incorporated in the binding site of the thread. While there are examples of rotaxanes that are operating out-of-equilibrium,[162,210–212] this would, to the best of our knowledge, be the first example of a rotaxane that only exists while it can dissipate chemical energy. Thus, a phosphonate half-thread was synthesized (Figure 26) that can be recognized by *Floods* anion binding cyanostar macrocycle (CS, cyan).[213] Preliminary results (unpublished) showed that this half-thread can be dimerized upon formation of a pyrophosphonate thread with carbodiimides. While pyrophosphates proofed to be a kinetic sink in RNA-derived systems due to depurination, we found that the use of formic acid or trifluoroacetic acid can render the pyrophosphonates used herein transient. However, complexation of the phosphonate by the CS macrocycle prevented the DIC activation chemistry and the corresponding pyrophosphonate rotaxane did not form. Moreover, we found that the supramolecular binding of the cyanostar to the pyrophosphonates is inhibited by small amounts of water, due to competitive hydrogen bonding (i.e., solvation). The project was therefore not pursuit as envisioned initially.

For a benzyl pyrophosphonate that was initially used as a model compound, we serendipitously discovered an interesting 1:1 binding stoichiometry with cyanostar that was illusive before. This third project is thus concerned with the thermodynamic self-assembly of pseudorotaxanes comprised of cyanostar and pyrophosphonates with a fine-tuned steric profile. The field of supramolecular anion recognition[214–220] enabled the self-assembly of supramolecular architectures[221–224] and mechanically interlocked compounds[225,226] like (pseudo)rotaxanes. The synthesis of rotaxanes mostly relied on anion-templation, where the anion is not part of either of the two interlocked components.[227–229] After one early example with a phenolate,[230] a new strategy was developed by *Flood* and coworkers who reported the synthesis of [3]rotaxanes (Figure 26B) based on a dialkyl phosphate and the cyanostar macrocycle (Figure 26A).[213,231] The latter can bind large anions in its electropositive central cavity through multiple C-H hydrogen bonds. Notably, cyanostar has only been reported to co-assemble with anions in a dimeric fashion where two macrocycles π-stack,[232–235] except for one example with a bulky CS derivative.[236] In this project, we were able to control the binding stoichiometry of a CS:anion self-assembly by fine-tuning the steric bulk of the anion.

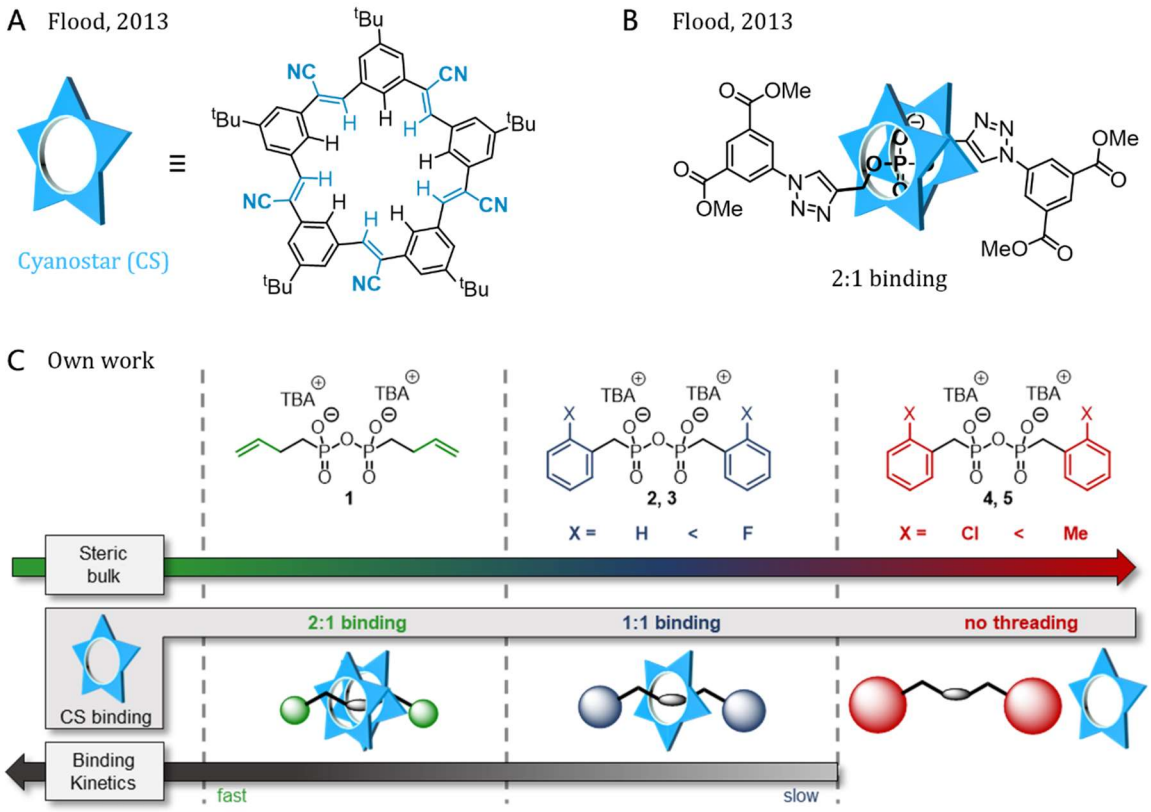

Figure 27: State of the art and own work. **(A)** Structure of the cyanostar (CS) macrocycle. **(B)** [3]Rotaxane formed by the assembly of two CS macrocycles and a dialkyl phosphate. **(C)** Overview of own work.

We synthesized a series of five dianionic pyrophosphonates (PP) with a subtle difference in steric bulk (Figure 26C) by condensation of the corresponding phosphonate with diisopropylcarbodiimde (DIC). As summarized in Figure 27C, increasing the steric demand of the pyrophosphonates enabled us to overcome the cyanostars propensity to dimerize and facilitate the self-assembly of both [3]pseudorotaxanes and [2]pseudorotaxanes. In a nuclear magnetic resonance (NMR) spectroscopy titration with CS, the small homoallyl-PP **1** showed the formation of two sets of diastereomeric peaks (Figure 28A, green), indicating the formation of a [3]pseudorotaxane (i.e., 2:1 complex). When increasing the steric bulk, however, a new set of peaks (blue) was observed that belonged to the [2]pseudorotaxane (i.e., 1:1 complex). In case of benzyl-PP **2** (Figure 28B), a mixture of 2:1 and 1:1 binding formed, whereas the bulkier F-benzyl-PP **3** exclusively self-assembled in a 1:1 binding mode. These results were further corroborated by high resolution mass spectrometry (HRMS) and two-dimensional nuclear Overhauser effect (NOE) NMR. We therefore reported an universal approach to modify the supramolecular binding mode by means of anion design.[237] Moreover, binding constants K_A were determined by ^{31}P NMR titrations, making use of the fact that the free and bound states are in slow exchange on the NMR time scale. All binding constants lay in the order of 10^3 M^{-1}. Density functional theory (DFT) calculations revealed that the cyanostar resides preferentially on one of the hydroxy groups, where the density of the negative charge is highest. As shown in Figure 28D, the first CS macrocycle binds on the pyrophosphonates, while the second one is held in place by π-π-stacking to form the [3]pseudorotaxane. For this, the macrocycle has to move onto the homoallyl thread. As this is prevented by more sterically demanding threads, only the [2]pseudorotaxane can form.

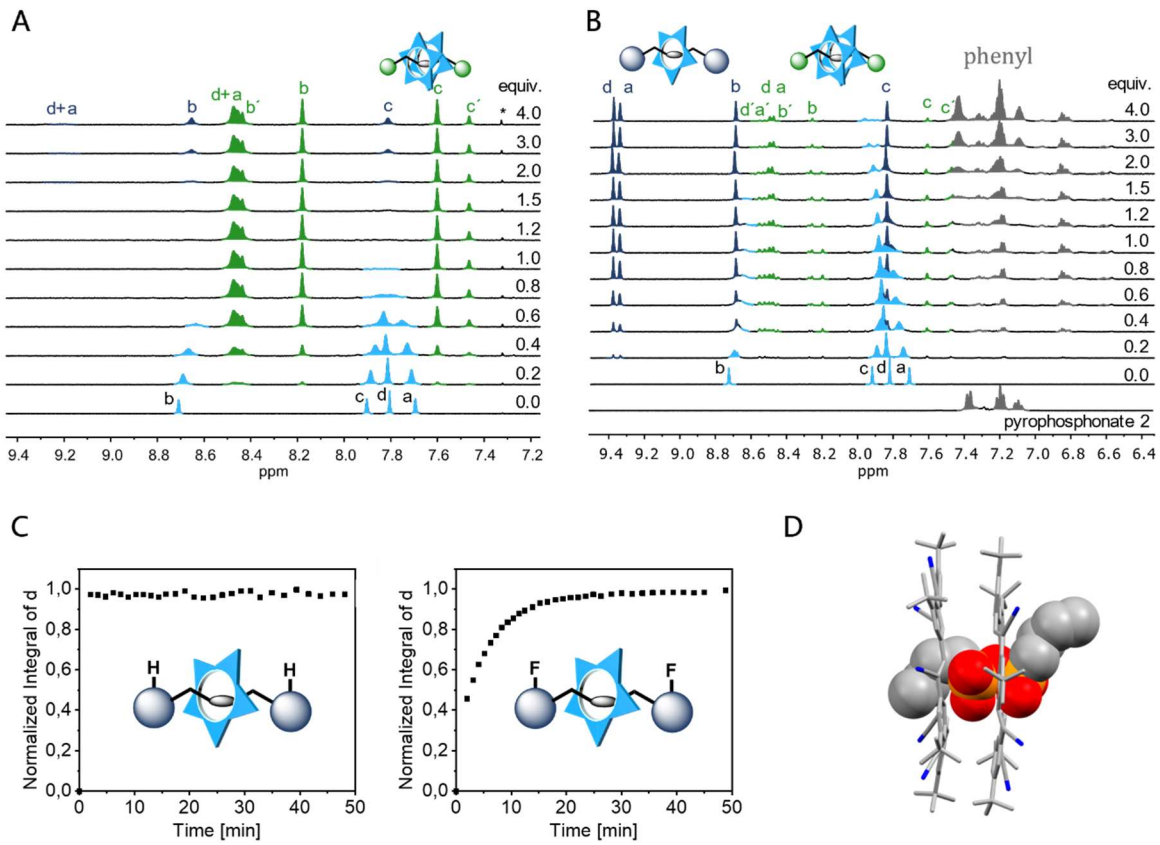

Figure 28: Results of own work. **(A)** NMR titration of homoallyl-PP **1** to CS. The formation of [3]pseudorotaxane (i.e., 2:1 complex) was observed (green signals). **(B)** NMR titration of benzyl-PP **2** to CS. The formation of both [3]pseudorotaxane (i.e., 2:1 complex) and [2]pseudorotaxane (i.e., 1:1 complex, blue signals) was observed. **(C)** Threading kinetics of CS onto benzyl-PP **2** and F-benzyl-PP **3**, respectively. **(D)** Optimized geometry of the [3]pseudorotaxane by density functional theory (DFT) calculations (RB3LYP/6-31G(D), gas-phase).

Besides the binding thermodynamics we were also interested in the threading kinetics. When monitoring characteristic peaks in an NMR kinetic experiment, we found that the threading of cyanostar onto F-benzyl-PP **3** (Figure 28C) takes about 15 minutes to reach its final equilibrium. For the less sterically demanding pseudo-stoppers homoallyl PP **1** and benzyl-PP **2** (Figure 28C), the threading kinetics were too fast to be observed in the experiment. More bulky pseudo-stoppers (Cl-benzyl-PP **4** and Me-benzyl-PP **5**) prevented the threading of the CS altogether. In variable temperature (VT) NMR experiments we found no evidence for threading even at elevated temperatures up to 403 K. These results show that not only the binding mode but also the threading kinetics are governed by the steric demand of the anion.

In conclusion, we developed a strategy to control both the binding thermodynamics and kinetics of supramolecular self-assembly by fine-tuning the steric bulk of the anion and made use of this strategy to selectively self-assemble pyrophosphonate-based pseudorotaxanes. While the recognition of phosphorylated molecules[238,239] like phosphates[240,241] and inorganic pyrophosphate[242–246] was well-reported, our results expand the scope of anion recognition by organic, dianionic pyrophosphonates. Furthermore, such tunable threading kinetics are interesting for the design of simple artificial molecular machines, where precise kinetic ratcheting with a molecular "valve" is crucial to facilitate directionality.[247–250] Future work (chapter 4) on such molecular machines will therefore build on the findings of this project.

3 Publications

3.1 Carbodiimide-Driven Dimerization and Self-Assembly of Artificial, Ribose-Based Amphiphiles

Julian Vogel, Jing Sun, Lisa Chen, A. Lennart Schleper, Tim Bergner, Alexander J. C. Kühne and Max von Delius, *Chem. Eur. J.* **2022**, *28*, e202104116. DOI: doi.org/10.1002/chem.202104116.
This article is licensed and reprinted under a Creative Commons Attribution 4.0 International License (CC BY 4.0), https://creativecommons.org/licenses/by/4.0/

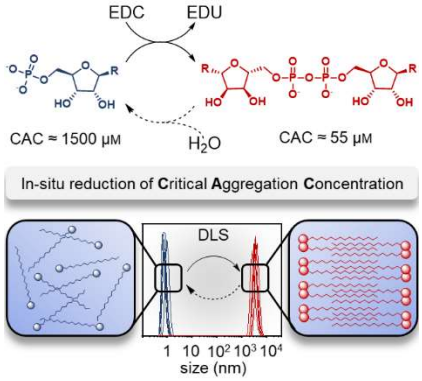

Abstract:
The aqueous self-assembly of amphiphiles into aggregates such as micelles and vesicles has been widely investigated over the past decades with applications ranging from materials science to drug delivery. The combination of characteristic properties of nucleic acids and amphiphiles is of substantial interest to mimic biological self-organization and compartmentalization. Herein, we present ribose- and ribonucleotide-based amphiphiles and investigate their self-assembly as well as their fundamental reactivity. We found that various types of aggregates are formed, ranging in size from nanometers to micrometers and all amphiphiles exhibit aggregation-induced emission (AIE) in solution as well as in the solid state. We also observed that the addition of 1-ethyl-3-(3-dimethylaminopropyl)-carbodiimide (EDC) leads to rapid and selective dimerization of the amphiphiles into pyrophosphates, which decreases the critical aggregation concentration (CAC) by a factor of 25 when compared to the monomers. Since the propensity for amphiphile dimerization is correlated with their tendency to self-assemble, our results may be relevant for the formation of rudimentary compartments under prebiotic conditions.

Own contributions:

The initial idea of this project stems from Prof. Dr. Max von Delius. This work was performed in an equal contribution with Dr. Jing Sun. I carried out the synthesis of all triazole-based nucleophiles and their characterizations (NMR, DLS, TEM, CAC, AIE) as well as the HPLC studies of the dimerization. Jing Sun synthesized and characterized the majority of the ribonucleotide-based amphiphiles. Furthermore, I conducted the systematic hydrolysis study. Lisa Chen did the CLSM measurements, Lennart Schleper did the AIE quantum yield determinations and Tim Bergner took cryo-TEM images. Writing of the first draft (incl. graphics) and the SI was equally shared by me and Jing Sun. The manuscript was edited by Alexander Kühne and Max von Delius.

Chemistry–A European Journal
Research Article
doi.org/10.1002/chem.202104116
Chemistry Europe
European Chemical Societies Publishing
www.chemeurj.org

Carbodiimide-Driven Dimerization and Self-Assembly of Artificial, Ribose-Based Amphiphiles

Jing Sun[+],[a] Julian Vogel[+],[a] Lisa Chen,[b] A. Lennart Schleper,[b] Tim Bergner,[c] Alexander J. C. Kuehne,[b, d] and Max von Delius*[a]

Abstract: The aqueous self-assembly of amphiphiles into aggregates such as micelles and vesicles has been widely investigated over the past decades with applications ranging from materials science to drug delivery. The combination of characteristic properties of nucleic acids and amphiphiles is of substantial interest to mimic biological self-organization and compartmentalization. Herein, we present ribose- and ribonucleotide-based amphiphiles and investigate their self-assembly as well as their fundamental reactivity. We found that various types of aggregates are formed, ranging in size from nanometers to micrometers and all amphiphiles exhibit aggregation-induced emission (AIE) in solution as well as in the solid state. We also observed that the addition of 1-ethyl-3-(3-dimethylaminopropyl)carbodiimide (EDC) leads to rapid and selective dimerization of the amphiphiles into pyrophosphates, which decreases the critical aggregation concentration (CAC) by a factor of 25 when compared to the monomers. Since the propensity for amphiphile dimerization is correlated with their tendency to self-assemble, our results may be relevant for the formation of rudimentary compartments under prebiotic conditions.

Introduction

Molecular self-assembly is the spontaneous equilibration of molecules into thermodynamically stable supramolecular structures.[1–10] In water, this behavior is ubiquitous and underpins the formation of a wide variety of compartments and complex biological architectures. Biomolecule-based amphiphiles and their aggregates[11–16] are currently of particular interest, because they have been used to generate self-healing materials,[17] biosensors,[18] and novel therapeutics.[12,19] Much of the biological function of DNA and RNA is based on the capability of the fundamental building blocks to form highly specific hydrogen bonds.[20,21] Thus, the structural amalgamation of nucleic acids with macrocyclic[22,23] or amphiphilic properties has the potential to generate hierarchical self-assemblies with unexpected structures and properties.

Although nucleotide/ribonucleotide-based amphiphiles have been reported previously,[24–29] the generation of a dissipative reaction network[30,31] based on the aggregation of these building blocks is still elusive. Inspired by recent work on dissipative assemblies of carboxylic anhydrides[32,33] and ATP-metal complexes,[34–37] we hypothesized that artificial ribose-based amphiphiles could exhibit similar behavior, when driven to dimerize into phosphodiesters or pyrophosphates by a chemical fuel and then left to hydrolyze after consumption of the fuel. While the forward reaction has been studied extensively by Szostak and Richert from the perspective of prebiotically plausible oligonucleotide formation and lately even translation,[38–47] the hydrolysis of phosphodiesters and pyrophosphates has received somewhat less attention.[48,49]

In this context, we report the design, synthesis, and self-assembly, of ribose- and ribonucleotide-based amphiphiles, composed of the polar ribomonophosphate or ribonucleotide head group and a nonpolar alkyl tail group. Nine different compounds with unique properties were successfully synthesized and characterized. The amphiphiles self-assemble into various superstructures ranging in size from nanometers to micrometers, which can be tuned by varying the alkyl chain length. We demonstrated that the chemical "fuel" 1-ethyl-3-(3-dimethylaminopropyl)carbodiimide (EDC) drove the dimerization of these amphiphiles selectively into pyrophosphates that were up to 25 times more prone to aggregate than the corresponding monomers. We further investigated a wide range of conditions for the hydrolysis of the pyrophosphate dimers and found that, while possible in principle, the successful conditions are too harsh to allow closing the dissipative

[a] Dr. J. Sun,[+] J. Vogel,[+] Prof. Dr. M. von Delius
Institute of Organic Chemistry, Ulm University
Albert-Einstein-Allee 11, 89081 Ulm (Germany)
E-mail: max.vondelius@uni-ulm.de
[b] L. Chen, A. L. Schleper, Prof. Dr. A. J. C. Kuehne
Institute of Macromolecular and Organic Chemistry, Ulm University
Albert-Einstein-Allee 11, 89081 Ulm (Germany)
[c] T. Bergner
Central Facility for Electron Microscopy, Ulm University
Albert-Einstein-Allee 11, 89081 Ulm (Germany)
[d] Prof. Dr. A. J. C. Kuehne
DWI – Leibniz-Institute for Interactive Materials
Forckenbeckstraße 50, 52074 Aachen (Germany
[+] These authors contributed equally to this work.
Supporting information for this article is available on the WWW under https://doi.org/10.1002/chem.202104116
© 2022 The Authors. Chemistry - A European Journal published by Wiley-VCH GmbH. This is an open access article under the terms of the Creative Commons Attribution License, which permits use, distribution and reproduction in any medium, provided the original work is properly cited.

© 2022 The Authors. Chemistry - A European Journal published by Wiley-VCH GmbH

pyrophosphate-based reaction cycle, at least for this first generation of amphiphiles.

Results and Discussion

Synthesis, characterization and aggregation of monomeric amphiphiles

To explore the self-assembly of ribonucleotide-based amphiphiles, we synthesized two different types of amphiphiles, including triazole-based ribomonophosphates, herein named **C_nMP**, and derivatives of natural ribonucleotides, named **X_nMP** (n denotes the length of the alkyl chain). These two types of amphiphiles were designed in order to explore the influence of π–π interactions and hydrogen bonding on their self-assembly, while remaining relatively close to the structure of natural nucleotides. As shown in Scheme 1, the **C_nMPs** were synthesized from commercially available 1,2,3,5-tetra-O-acetyl-β-D-ribofuranose (**1**) by acetate/azide substitution (**2**),[50] followed by copper-catalyzed 1,3-dipolar Huisgen-cycloaddition (**3**–**5**),[51] deacylation (**6**–**8**), and subsequent phosphorylation (**9**–**11**) in 50–74% yields. Similarly, the **X_nMPs** were synthesized in two steps by nucleophilic aromatic substitution of 6-chloropurine riboside (**12**) and phosphorylation (**19**–**24**) in 50–70% yields.[52] All amphiphiles were characterized by nuclear magnetic resonance spectroscopy (^{1}H NMR, ^{13}C NMR, and ^{31}P NMR) and high-resolution mass spectrometry (HR-MS) (Figures S19-S80).

The critical aggregation concentration (CAC) of ribonucleotide amphiphiles was first investigated using the nonpolar fluorescent dye 1,6-diphenyl-1,3,5-hexatriene (DPH).[36] This dye is almost non-emissive in an aqueous solution due to aggregation-caused quenching. However, once the CAC of the amphiphiles is reached, the dye will be encapsulated in the nonpolar compartment formed by the hydrophobic tails, leading to an increase in the photoluminescence intensity. To determine the CAC of each amphiphile, we carried out photoluminescence titrations of DPH (10 μM, λ_{ex} = 355 nm, λ_{em} = 428 nm) in 4-(2-hydroxyethyl)-1-piperazineethanesulfonic acid (HEPES) buffer (pH 7.0) in the presence of increasing concentrations of amphiphiles (Figures 1A and S1). As expected, it was found that the CAC decreases as the aliphatic chain length increases. However, the CAC of **X_{15}MP** was determined to be around 1.5 ± 0.2 mM, which was nearly as high as that of **X_{10}MP**. This unusual behavior might be related to an odd-even effect, which is known to occur in alkylated light-emitting dyes.[53,54] In agreement with this reasoning, the CAC of **X_{13}MP** represents an outlier within the decreasing trend from **X_{10}MP** to **X_{14}MP** (Figure 1A). The CAC of **C_6MP** could not be investigated by this method, as its aliphatic chain is presumably too short to incorporate DPH into aggregates. It was estimated, however, by making use of the AIE properties (see below). Moreover, dynamic light scattering (DLS) was used to determine the average size of aggregates in solution (Figure S2). Analysis of the data for the different amphiphile solutions (in concentrations about two times above CAC) yielded hydrodynamic diameters around 75–250 nm, indicating the formation of aggregates.

We used a variety of analytical techniques to explore the structures of these aggregates. The formation of spherical aggregates with diameters of 75–100 nm for **C_6MP** was confirmed by transmission electron microscopy (TEM) (Figur-

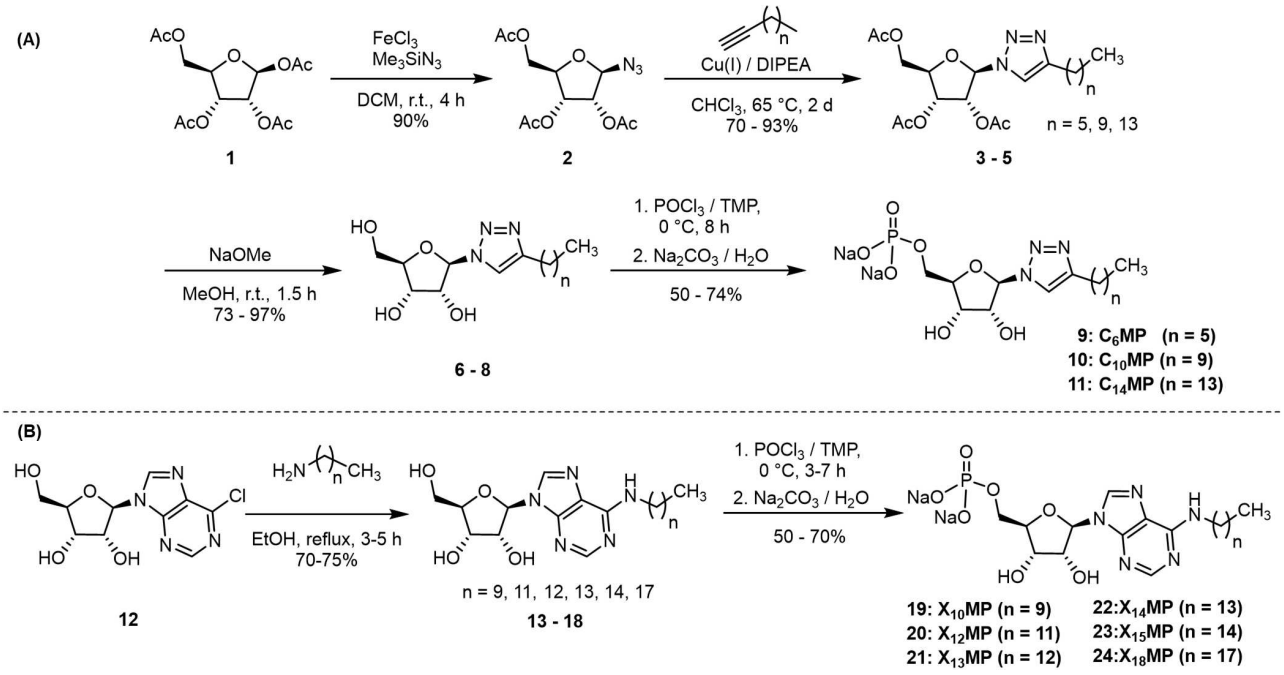

Scheme 1. Synthetic routes towards two types of amphiphiles. A) Triazole-based ribomonophosphates (**C_nMP**) and B) ribonucleotide amphiphiles (**X_nMP**), respectively.

© 2022 The Authors. Chemistry - A European Journal published by Wiley-VCH GmbH

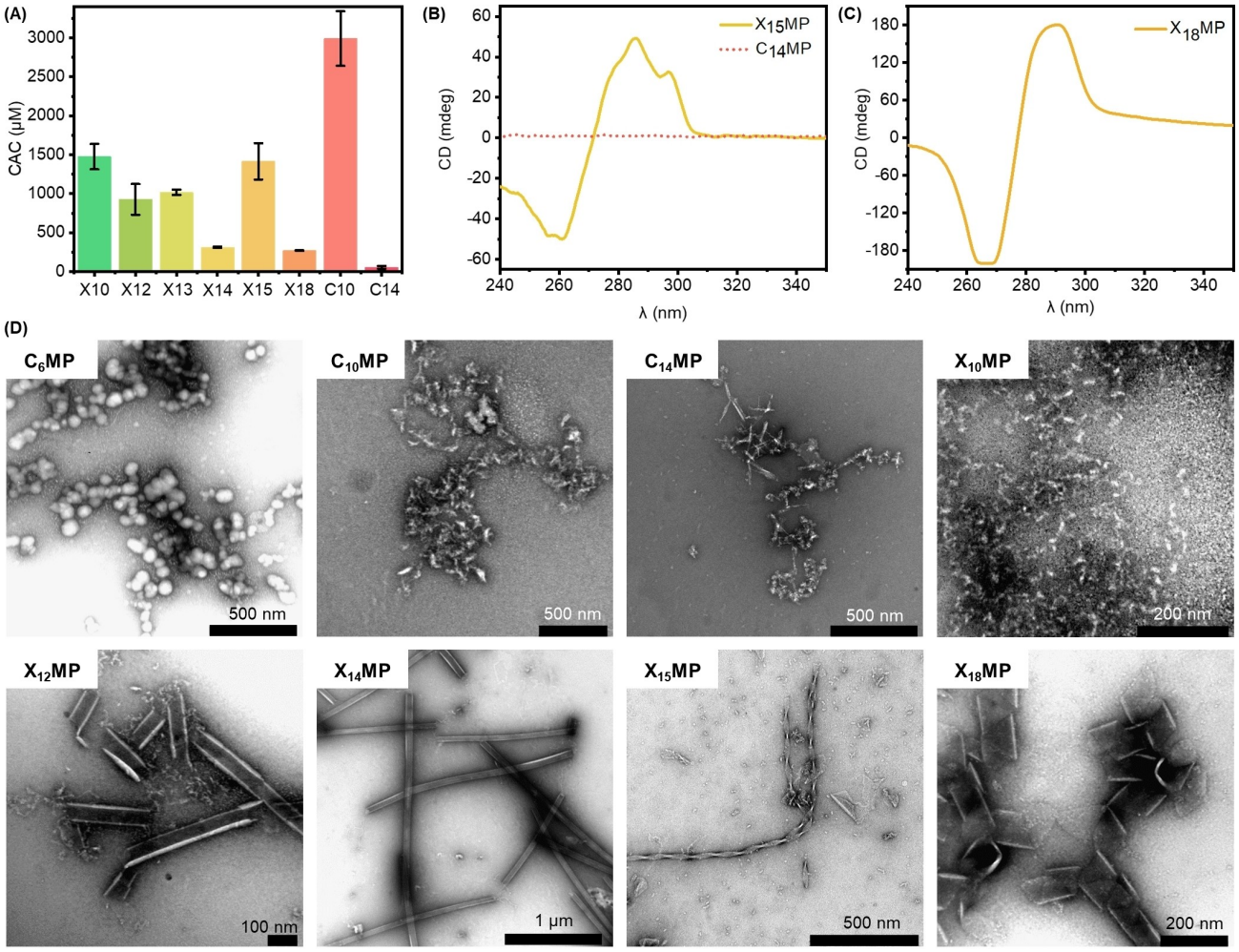

Figure 1. Characterization of amphiphiles. A) The critical aggregation concentration (CAC) of ribose-based amphiphiles was determined using 1,6-diphenyl-1,3,5-hexatriene (DPH) as a fluorescent dye. Three parallel experiments were performed to determine the average CAC values. B–C) Circular dichroism (CD) spectrum of representative amphiphiles in 5 mM HEPES buffer (pH 7.0) at 25 °C, including (B) **X_{15}MP** (2 mM) and **C_{14}MP** (0.16 mM) and (C) **X_{18}MP** (0.8 mM), respectively. D) Transmission electron microscopy (TEM) images above CAC of spherical aggregates of **C_6MP** (18 mM), ill-defined aggregates of **C_{10}MP** (6 mM), **C_{14}MP** (0.16 mM), **X_{10}MP** (2.0 mM), semi-tubes of **X_{12}MP** (1.3 mM), hollow tubes of **X_{14}MP** (2.2 mM), helical fibers of **X_{15}MP** (5.0 mM), and helical ribbons of **X_{18}MP** (0.5 mM) formed by the self-assembly of amphiphiles in 5 mM HEPES buffer (pH 7.0). All samples were negatively stained with $UO_2(OAc)_2$.

es 1D and S3). The longer alkyl chain lengths in **C_nMPs** lead to ill-defined aggregates (Figures 1D and S3). Similarly, **X_{10}MP** and **X_{13}MP** also show random aggregation above their CAC (Figures 1D and S3). However, a completely different morphology was observed for the longer **X_nMPs** in the HEPES buffer (Figure 1D), which might be due to stronger hydrophobic interactions induced by the longer alkyl chains. When the chain length was between 12 and 14, the amphiphiles formed tubular structures, including a semi-tube (**X_{12}MP**) and a hollow tube (**X_{14}MP**). This hollow tube structure of **X_{14}MP** was further confirmed by scanning electron microscopy (SEM) (Figure S4). Interestingly, helical aggregates were observed consistently for chain lengths exceeding 14, such as helical fibers (**X_{15}MP**) and helical ribbons (**X_{18}MP**) (Figure 1D). The helical characteristics were confirmed by circular dichroism (CD) spectroscopy (Figures 1B and 1C). The results corroborate helical aggregation as confirmed by the Cotton effect at wavelengths between 260–300 nm. It should be noted that the pristine adenosine monophosphate with a chiral environment of ribose, **X_{15}MP** below its CAC (Figure S5) and **C_{14}MP** above its CAC (Figure 1B) did not show any significant optical activity in the CD spectrum due to the lack of aggregation. The fact that **X_{14}MP** forms well-defined structures, while **C_{14}MP** does not, suggests that hydrogen bonding or π–π stacking are at least equally important as the hydrophobic effect for determining the aggregates' structure.[55,56] Presumably, either the larger π-surface or the hydrogen bond acceptor atoms in the purine moiety lead to the self-assembly of sheets that commonly exhibit a helical pitch.[57]

© 2022 The Authors. Chemistry - A European Journal published by Wiley-VCH GmbH

Unexpected observation of aggregation-induced emission (AIE)

It is well documented that natural nucleotides or ribonucleotides are typically not photoluminescent.[58] In stark contrast, the ribose-based amphiphiles reported herein exhibit typical AIE properties, as evidenced by their respective photoluminescence (PL) spectra measured in a solvent mixture (H_2O/acetone) with varying acetone fractions, which functions as anti-solvent. As shown in Figure 2, the solution of these amphiphiles exhibited no or relatively weak emission when the ratio of the anti-solvent f_a was below 90%. Interestingly, the emission increased significantly when f_a was increased to 90%-95% to induce aggregation. TEM confirmed the self-assembly in high acetone fractions (Figure S6). These aggregated structures were less well-defined than in pure HEPES buffer above CAC. Nevertheless, random aggregates and helical fibers were observed when f_a was above 95%. In addition, all these amphiphiles emitted light in the blue spectrum, when irradiated in the solid state with ultraviolet (UV) light (365 nm). Of note, **C_{10}MP** emitted greenish light under UV irradiation, which is different from all other amphiphiles that emitted blue light (Figure 2B). We further determined the PL quantum yield (QY) of representative amphiphiles in the solid state. Accordingly, we observed PL QYs of 13% for **C_{10}MP** and 14% for **C_6MP**, which is far below state-of-the-art AIE dyes,[59,60] but interesting for compounds lacking typical AIE motifs (Figure S7).

Beyond these studies in solid state and with varying solvent compositions, we found that the PL intensities of amphiphiles were continuously enhanced with increasing concentration in aqueous solutions (Figure S8). When the concentration is above its CAC, the photoluminescence intensities of amphiphiles are almost linearly related to their concentrations. These results further corroborate that the alkyl chain functionalized ribonucleotide amphiphiles have AIE properties. We suggest that this unexpected AIE behavior is explained by "clusteroluminescence",[61] specifically due to intermolecular through-space conjugation of the π-systems and/or electron-rich heteroatoms. In related aromatic[62] or carbohydrate[63–65] systems, this type of through-space conjugation was identified to open up radiative decay pathways. In turn, we were able to determine the CAC of our ribonucleotides by determining the change in AIE during concentration-dependent luminescence measurements in HEPES buffer and found these values to be in good agreement with the ones determined before by the addition of DPH dye (Figure S8).

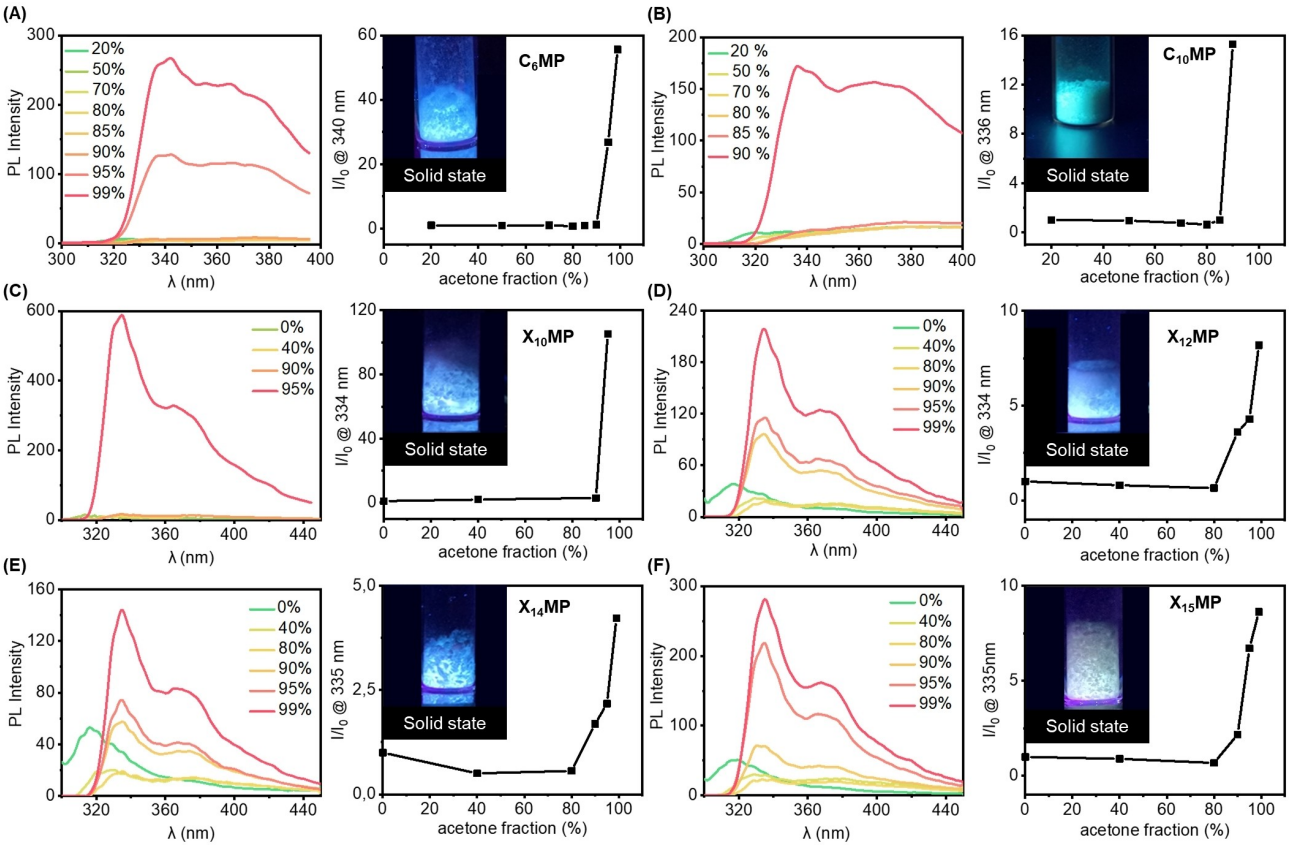

Figure 2. Unexpected aggregation-induced emission (AIE) behavior of ribose-based amphiphiles. Acetone was chosen as an anti-solvent. The PL spectra of amphiphiles and the plot of maximum emission wavelength in H_2O-acetone mixtures with different acetone fractions (f_a), including (A) **C_6MP**, (B) **C_{10}MP**, (C) **X_{10}MP**, (D) **X_{12}MP**, (E) **X_{14}MP**, (F) **X_{15}MP**. Data points in the I/I_0 plots are connected to guide the eye, I_0 and I represent the PL intensity in pure water and H_2O/acetone at the maximum emission wavelength, respectively. Excitation wavelength: 280 nm. Insets show photos of all amphiphiles in solid state under 365 nm UV lamp irradiation.

© 2022 The Authors. Chemistry - A European Journal published by Wiley-VCH GmbH

Carbodiimide-driven formation of pyrophosphate-linked amphiphile dimers

We proceeded to explore the reaction of the monomeric phosphates with the water-soluble carbodiimide EDC and nucleophilic catalyst 1-ethylimidazole (EtIm) (Figure 3A).[39,66] Initially, the different amphiphiles were compared and the amount of EDC was optimized to achieve EDC-driven dimerization. It was found that 50–100 equivalents of EDC led to rapid dimer formation, and **X_{15}MP** reacted especially efficiently when compared to other amphiphiles (Figure S9). In general, the **X_nMPs** were more prone to dimerization than the **C_nMPs**, suggesting that there is a correlation between propensity for aggregation and dimerization. Exemplarily, **X_{15}MP** (0.5 mM,

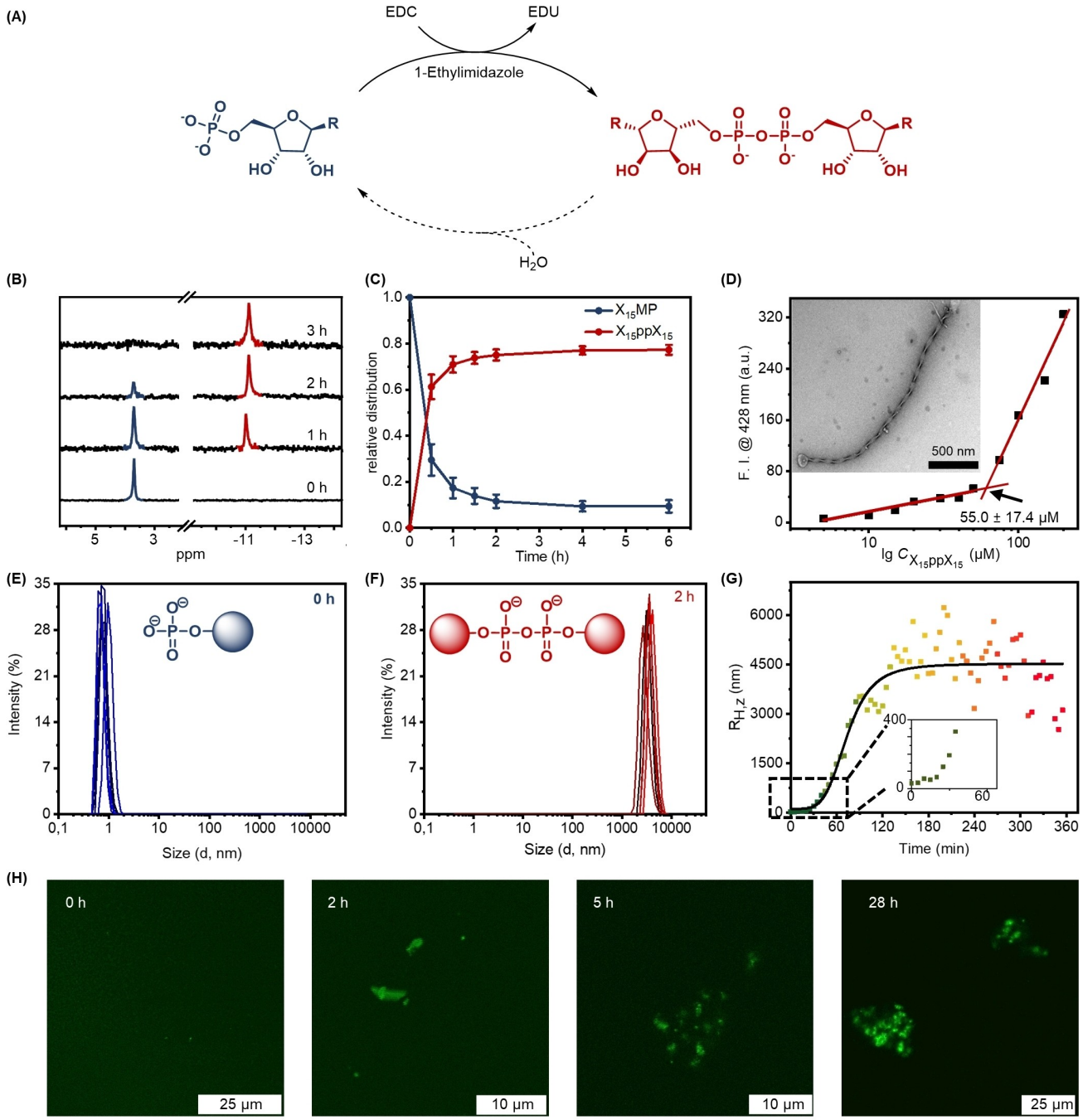

Figure 3. A) The EDC-triggered dimerization of **X_{15}MP**, yielding the formation of pyrophosphate **X_{15}ppX$_{15}$**. B) ^{31}P NMR of the dimerization reaction over time. C) The kinetics of the dimerization reaction over 6 h by HPLC. 80% of the monomer is converted to the dimer within 6 h. Three parallel experiments were performed for the HPLC kinetics study. D) CAC determination of isolated **X_{15}ppX$_{15}$**. The insert shows the assembled structure of isolated **X_{15}ppX$_{15}$** (100 µM in 0.5 mM HEPES buffer) confirmed by TEM. E–H) Characterization of the dimerization of 500 µM **X_{15}MP** in condensation buffer, driven by 50 eq. of EDC. Size distribution (E) before and (F) after dimerization monitored by DLS (data curves represent ten replicate experiments). G) Sigmoidal kinetics of aggregation as observed by DLS. H) Confocal images over time, showing the formation of aggregates. Samples were prepared using 2.5 µM C153.

© 2022 The Authors. Chemistry - A European Journal published by Wiley-VCH GmbH

below CAC) was dimerized upon addition of EDC (50 eq.) in a 0.5 mM 3-(N-morpholino)propanesulfonic acid (MOPS) buffer, containing 1-ethylimidazole (0.15 mM) and $MgCl_2$ (0.08 mM) (pH 7.5). These reaction conditions were derived from Richert and co-workers and are referred to as "condensation buffer."[46] As shown in Figure 3B, the ^{31}P NMR signal (~3.8 ppm) of **X_{15}MP** gradually decreased and vanished after 3 h. Meanwhile, a new signal around -11.0 ppm appeared and accumulated, indicating the formation of pyrophosphate **X_{15}ppX_{15}**, based on the characteristic chemical shift.[47,67] While non-substituted adenosine monophosphates also form some phosphodiesters,[47,67] we did not observe this for **X_{15}MP**. This selective transformation behavior might be attributed to steric hindrance induced by the long alkyl chains.

Subsequently, the reaction kinetics were studied by high-performance liquid chromatography (HPLC) under different temperatures, including 25 °C, 10 °C, and 0 °C (Figures 3C, S10A and S11A–C). When the dimerization was performed at room temperature (25 °C), HPLC analysis indicated that 80% of **X_{15}MP** was consumed and converted to pyrophosphate **X_{15}ppX_{15}** within 6 h. The second-order rate constant was determined to be $2.1\times10^{-6}\,M^{-1}s^{-1}$ at a concentration of **X_{15}MP** of 0.5 mM (below CAC) (Figure S10B). While the polymerization of (activated) ribonucleotides was reported to be faster at temperatures in[68] or near[66] the eutectic ice phase, we observed that the reaction rate was slowed down when decreasing the temperature. Decreasing the pH from 7.5 to 6.0 did not have any significant effect on the reaction kinetics (Figure S11). In addition, the kinetics of the hydrolysis of EDC during phosphate activation was investigated by ^{1}H NMR spectroscopy (Figure S12A). We found that EDC is consumed faster in the presence of monophosphates than in the pure buffer (Figure S12B) and that the rate of consumption is comparable for different monophosphates (Figure S12C).

To gain additional insights into EDC-triggered dimerization of **X_{15}MP**, we successfully isolated the pyrophosphate by semi-preparative HPLC (Figures S81–84). Notably, the CAC value of **X_{15}ppX_{15}** was determined to be 55.0 ± 17.4 μM, which is over 25 times lower than that of **X_{15}MP** (Figure 3D). The ultra-low CAC value of **X_{15}ppX_{15}** leads to the rapid formation of large aggregates during the reaction, yielding helical fibers (Figures 3D and S13).

We also monitored the EDC-driven dimerization of **X_{15}MP** by DLS to find out at which point of time aggregation starts to occur. In stark contrast to the non-aggregating starting material **X_{15}MP** (0.5 mM, below CAC), the formation of **X_{15}ppX_{15}** led to a significant increase in the hydrodynamic diameter (~1 μm) in aqueous solution, indicating the formation of large aggregates (Figures 3E–F). The formation of helical aggregates in solution upon dimerization was further confirmed by cryogenic TEM (cryo-TEM) (Figure S14).

The aggregation kinetics were monitored by DLS (Figure 3G), and the data shows a rapid increase in average hydrodynamic diameter ca. 30 minutes after addition of EDC (25 mM) to a solution of X_{15}MP (0.5 mM) and then entering a plateau after ca. 120 minutes. Such a sigmoidal kinetic curve typically suggests a cooperative effect, in this case between self-assembly and pyrophosphate formation. After adding EDC, pyrophosphates form slowly and start to aggregate as soon as their CAC is reached. At this point, incorporation of **X_{15}MP** into the hydrophobic aggregates accelerates pyrophosphate formation, presumably due to increased effective molarity.[69] In the absence of EDC, all control experiments (i: **X_{15}MP** + 1-ethyl-3-(3-dimethylaminopropyl)urea (EDU) in condensation buffer; ii: EDU in condensation buffer; iii: blank, pure condensation buffer) showed that the average hydrodynamic diameters remained constant over time (Figure S15), indicating that the formation of pyrophosphate is indeed responsible for the observed aggregation. Moreover, confocal laser scanning microscopy (CLSM) studies directly visualized large aggregate formation (Figure 3H). Accumulation of the coumarin 153 (C153) fluorophore in the aggregates allowed these to be detected after adding EDC. Similarly, the control experiments (i: **X_{15}MP** + EDU + C153 in condensation buffer; ii: EDU + C153 in condensation buffer; iii: blank, C153 in condensation buffer) did not show any distinguishable fluorescent structures from CLSM images over time, suggesting that the aggregates can be formed only in the presence of EDC (Figure S16).

Systematic study of pyrophosphate hydrolysis

After establishing the EDC-driven dimerization process, we investigated the hydrolysis of pyrophosphates, because suitable hydrolysis conditions could render the dimer-based aggregates described previously transient. We chose to study the hydrolysis of commercially available non-aggregating adenosine pyrophosphate (**AppA**) as a model reaction (Figure 4A) and monitored the process by HPLC-MS. The relative concentrations were obtained from the diode array detector signal under the reasonable assumption that the molar absorptivity of the pyrophosphate **AppA** is twice that of adenosine monophosphate (**AMP**). A 1 mM solution of **AppA** was subjected to various conditions, including pure water, 0.01 M HCl solution (pH 2.0), 0.01 M NaOH solution (pH 12.0), and 4 mM $EuCl_3$ solution (pH ≈ 6) (Figures 4 and S17).

Because pyrophosphates are known to be relatively stable in aqueous solution,[29,39,70] temperatures above room temperature were applied to increase the rate of hydrolysis. It was found that under neutral conditions, **AppA** is relatively inert and only starts to hydrolyze very slowly at 80 °C (Figure 4B). When incubated at 100 °C for one week, some **AppA** was converted to **AMP**, but a significant part decomposed (Figure S17A). We suspect that depurination by cleavage of the hemiaminal ether is the cause of decomposition.[71–74] Similarly, no hydrolysis occurred in the sample treated with 0.01 M NaOH solution at 40–60 °C (Figure 4C). In fact, **AppA** was mostly stable under strong basic conditions even at 100 °C for one week (Figure S17B). By contrast, depurination was the dominant reaction at 60–80 °C under acidic (0.01 M HCl) reaction conditions (Figure 4D).

As lanthanide salts have been reported to catalyze the hydrolysis of phosphodiester bonds in RNA,[75,76] $EuCl_3$ was tested and yielded more encouraging results (Figure 4E). At

© 2022 The Authors. Chemistry - A European Journal published by Wiley-VCH GmbH

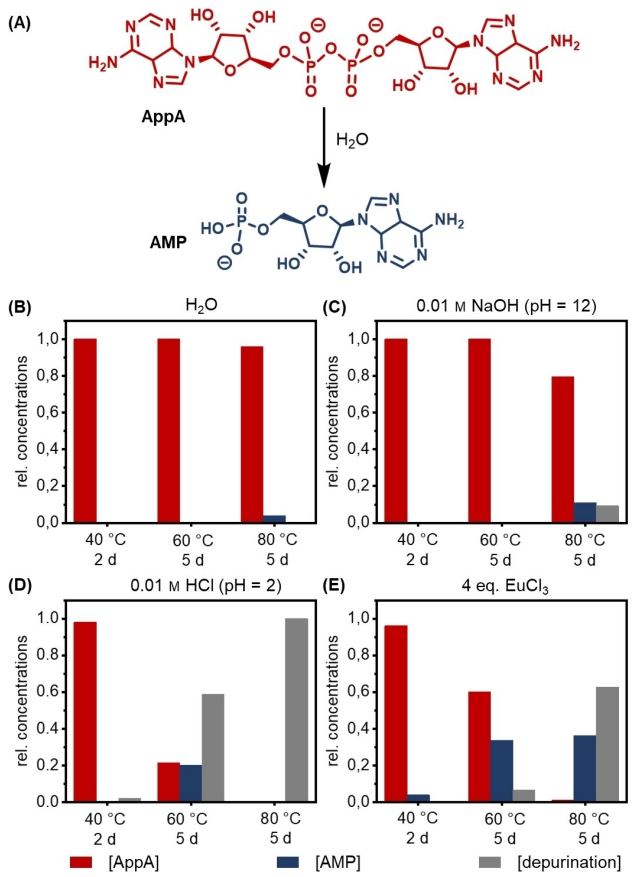

Figure 4. Investigation of pyrophosphate hydrolysis under different conditions using **AppA** as a model. A) Reaction scheme. B–E) 1 mM solutions of **AppA** were stirred at 40 °C for two days before the temperature was increased first to 60 °C and then to 80 °C for another five days each. Hydrolysis conditions were (B) H_2O, (C) 0.01 M NaOH (pH = 12), (D) 0.01 M HCl (pH = 2), (E) 4 eq. $EuCl_3$ (pH ≈ 6). Relative concentrations were obtained by HPLC.

40 °C and 60 °C, the hydrolysis was faster than depurination but still too slow to establish a dissipative reaction network, because even after five days at 60 °C there was still around 60 % of the pyrophosphate left. When increasing the temperature to 80 °C, competing depurination became dominant. Applying these conditions to the alkyl chain substituted **AppA** (namely $\mathbf{X_{15}ppX_{15}}$) led to a similar extent of depurination (Figure S18). Overall, the pyrophosphate bond in **AppA** derivatives seems too stable to be hydrolyzed under conditions where no depurination occurs, which unfortunately makes dissipative systems based on a labile pyrophosphate bond in RNA derivatives inaccessible.

As a last resort, enzymatic hydrolysis of $\mathbf{X_{15}ppX_{15}}$ was considered. It is known that pyrophosphatase can break the diphosphate bond efficiently under mild conditions.[49,77] A 365 μM solution of $\mathbf{X_{15}ppX_{15}}$ was incubated at 37 °C in a 0.5 mM HEPES buffer (pH = 7.5) with the enzyme for 3 days. To our surprise, $\mathbf{X_{15}ppX_{15}}$ was not hydrolyzed with this specific enzyme (Table S1). This behavior might be due to aggregation or the long alkyl chains that prevent inclusion into the enzyme pocket.

Conclusion

In conclusion, we report the design, synthesis, self-assembly, and dimerization of novel ribonucleotide-based amphiphiles. A family of negatively charged amphiphiles with different chain lengths were synthesized, including natural ribonucleotide-based amphiphiles and triazole-based ribonucleotide analogues. The resulting amphiphiles self-assemble into different superstructures in aqueous solutions ranging in size from nanometers to micrometers, including micelles, tubes, helical fibers, and ribbons. To our surprise, we observed that these amphiphiles, when irradiated with UV light, exhibit aggregation-induced emission. We were able to demonstrate that these monophosphate amphiphiles can be dimerized to form pyrophosphates in the presence of EDC. When carried out below the CAC of the monomer, this type of experiment therefore leads to the rapid, in situ formation of large aggregates at the micrometer scale. Unfortunately, our efforts to complete the dissipative reaction cycle by controlling the kinetics of pyrophosphate hydrolysis were unsuccessful, despite promising results using $EuCl_3$. Nevertheless, this work contains valuable lessons for those who seek to address a crucial weakness of the RNA world theory by combining fuel-driven oligomerization with compartmentalization.

Experimental Section

Dimerization of X_{15}MP and monitoring by HPLC and DLS: 0.30 mg (0.5 μmol, 500 μM) $\mathbf{X_{15}MP}$ were dissolved in 1 mL 3-(N-morpholino)propanesulfonic acid (MOPS) buffer (0.5 mM MOPS, 0.15 mM 1-ethylimidazole, 0.08 mM $MgCl_2$, pH = 7.50, filtered through a 0.45 μm syringe filter) and 4.78 mg (25 μmol, 25 mM, 50 eq.) EDC*HCl were added. The progress of dimerization and aggregation was monitored by HPLC (254 nm) and DLS (see below). For HPLC, an Ascentis C8 (100×4.6 mm, 3 μm) analytical column and a mobile phase comprising MeCN and 50 mM NH_4HCO_3 buffer (pH = 8.00) (gradient condition: 6:4 (0–3 minutes), 6:4–7:3 (3–4 minutes), 7:3 (4–15 minutes) with a flow rate of 1.0 mL min^{-1} at 60 °C was used.

Determination of critical aggregation concentration (CAC): A stock solution of the amphiphiles in buffer solution and a dilution series with the same buffer were prepared. A 1 mM solution of diphenylhexatriene (DPH) in THF was added to each sample to give a final concentration of 10 μM. The samples were vortexed and equilibrated overnight in the dark. Photoluminescence spectroscopy of each sample was recorded at $\lambda_{ex} = 355$ nm on a PerkinElmer FL 6500 spectrophotometer. The emission intensity at $\lambda_{em} = 428$ nm was monitored and plotted against the logarithmic concentration. A linear regression ($y_n = m_n x + a_n$) through the data points before and after the sudden increase in intensity were calculated, respectively. The x-value of the intersection of these two lines was used to calculate the CAC.

Aggregation induced emission (AIE): To prove that the amphiphiles exhibit an aggregation-induced emission effect, we performed an anti-solvent experiment by the addition of acetone (anti-solvent) to an aqueous solution of amphiphiles which's total concentration was kept constant and below the CAC and the emission intensity with $\lambda_{ex} = 280$ nm and $\lambda_{em} = 334$–340 nm of the amphiphiles was measured. Photoluminescence spectra in water/acetone mixtures were recorded on a PerkinElmer FL 6500

© 2022 The Authors. Chemistry - A European Journal published by Wiley-VCH GmbH

spectrophotometer. Solid state PL QYs were determined using an integrating sphere.

Transmission electron microscopy (TEM): Amphiphiles in concentrations about two times above CAC were dissolved in either H_2O or 5 mM HEPES buffer and deposited on copper grids. Negative staining with uranyl acetate was performed. Control experiments with pure water and pure HEPES buffer did not show any assembled structures. TEM measurements were performed on a Zeiss EM10 microscope with an acceleration voltage of 120 kV.

Cryogenic transmission electron microscopy (Cryo-TEM): **X_{15}MP** (below CAC) or **X_{15}MP** assembly in condensation buffer (after 2 h) were adhered to a freshly glow-discharged holey carbon grid. After blotting, the grids were vitrified in liquid ethane by a Vitrobot FP 5350/60 (FEI, Eindhoven, Netherlands). The cryo-TEM grids were analyzed in a JEM-2100F (JEOL) at 200 kV and a temperature of −150 °C using a Gatan cryo-holder. Contrast enhancement was performed with the software ImageJ and Adobe Photoshop.

Scanning electron microscopy (SEM): 5 mM X_{14}MP and X_{18}MP in 5 mM HEPES buffer were deposited on a silicon wafer and sputtered with a layer of gold after drying in vacuum before measurement. The morphology of both samples was examined by SEM (ZEISS EVO MA microscope).

Circular dichroism (CD) spectroscopy: CD spectra of 5 mM **X_{15}MP** and **X_{18}MP** in 5 mM HEPES buffer were measured at 25 °C in a 1 mm quartz cuvette on Jasco J-810 CD spectrometer equipped with Julabo F12 temperature controller.

Dynamic light scattering (DLS): The size of the amphiphiles and the assemblies were measured by DLS on a Nano-Zetasizer (Malvern Instruments) at 25 °C with a scattering angle of 173° at $\lambda =$ 633 nm.

Confocal laser scanning microscopy (CLSM): Confocal microscopy images of all samples were recorded with a TCS SP8 confocal microscope using the Leica Application Suite X (LASX) with the LIGHTNING wizard. A droplet of the mixture was placed between two glass slides for confocal measurements. The fluorescent dye (C153) was excited at a wavelength of either 405 nm or 514 nm. Image analysis was performed with the software ImageJ and Adobe Photoshop.

Acknowledgements

This work was supported by the European Union (ERCstg 802428 "SUPRANET"). A. L. S. acknowledges support through a Cusanuswerk scholarship. Prof. Paul Walther is acknowledged for advice and assistance with (cryo-)TEM. Open Access funding enabled and organized by Projekt DEAL.

Conflict of Interest

The authors declare no conflict of interest.

Data Availability Statement

The data that support the findings of this study are available from the corresponding author upon reasonable request.

Keywords: amphiphile · dimerization · hydrolysis · pyrophosphate · ribonucleotide · self-assembly

[1] J. R. Simon, N. J. Carroll, M. Rubinstein, A. Chilkoti, G. P. López, *Nat. Chem.* **2017**, *9*, 509–515.
[2] R. Freeman, M. Han, Z. Álvarez, J. A. Lewis, J. R. Wester, N. Stephanopoulos, M. T. McClendon, C. Lynsky, J. M. Godbe, H. Sangji, E. Luijten, S. I. Stupp, *Science* **2018**, *362*, 808–813.
[3] O. Shyshov, S. V. Haridas, L. Pesce, H. Qi, A. Gardin, D. Bochicchio, U. Kaiser, G. M. Pavan, M. von Delius, *Nat. Commun.* **2021**, *12*, 3134.
[4] Q. Song, Z. Cheng, M. Kariuki, S. C. L. Hall, S. K. Hill, J. Y. Rho, S. Perrier, *Chem. Rev.* **2021**, *121*, 13936–13995.
[5] E. Mattia, S. Otto, *Nat. Nanotechnol.* **2015**, *10*, 111–119.
[6] F. Späth, C. Donau, A. M. Bergmann, M. Kränzlein, C. V. Synatschke, B. Rieger, J. Boekhoven, *J. Am. Chem. Soc.* **2021**, *143*, 4782–4789.
[7] J. A. Berrocal, G. H. Heideman, B. F. M. De Waal, M. Enache, R. W. A. Havenith, M. Stöhr, E. W. Meijer, B. L. Feringa, *J. Am. Chem. Soc.* **2020**, *142*, 4070–4078.
[8] J. Leira-Iglesias, A. Tassoni, T. Adachi, M. Stich, T. M. Hermans, *Nat. Nanotechnol.* **2018**, *13*, 1021–1027.
[9] G. Singh, H. Chan, A. Baskin, E. Gelman, N. Repnin, P. Král, R. Klajn, *Science* **2014**, *345*, 1149–1153.
[10] A. Walther, M. Drechsler, S. Rosenfeldt, L. Harnau, M. Ballauff, V. Abetz, A. H. E. Müller, *J. Am. Chem. Soc.* **2009**, *131*, 4720–4728.
[11] A. Gissot, M. Camplo, M. W. Grinstaff, P. Barthélémy, *Org. Biomol. Chem.* **2008**, *6*, 1324–1333.
[12] M. P. Hendricks, K. Sato, L. C. Palmer, S. I. Stupp, *Acc. Chem. Res.* **2017**, *50*, 2440–2448.
[13] J. Baillet, V. Desvergnes, A. Hamoud, L. Latxague, P. Barthélémy, *Adv. Mater.* **2018**, *30*, 1705078.
[14] A. Sorrenti, J. Leira-Iglesias, A. Sato, T. M. Hermans, *Nat. Commun.* **2017**, *8*, 15899.
[15] C. M. LaManna, H. Lusic, M. Camplo, T. J. McIntosh, P. Barthélémy, M. W. Grinstaff, *Acc. Chem. Res.* **2012**, *45*, 1026–1038.
[16] A. Patwa, A. Gissot, I. Bestel, P. Barthélémy, *Chem. Soc. Rev.* **2011**, *40*, 5844–5854.
[17] H. Ceylan, M. Urel, T. S. Erkal, A. B. Tekinay, A. Dana, M. O. Guler, *Adv. Funct. Mater.* **2013**, *23*, 2081–2090.
[18] C. Shen, K. Zeng, J. Luo, X. Li, M. Yang, A. Rasooly, *Anal. Chem.* **2017**, *89*, 10264–10269.
[19] M. Srikanth, J. A. Kessler, *Nat. Rev. Neurol.* **2012**, *8*, 307–318.
[20] S. Hoshika, N. A. Leal, M. J. Kim, M. S. Kim, N. B. Karalkar, H. J. Kim, A. M. Bates, N. E. Watkins, H. A. SantaLucia, A. J. Meyer, S. DasGupta, J. A. Piccirilli, A. D. Ellington, J. SantaLucia, M. M. Georgiadis, S. A. Benner, *Science* **2019**, *363*, 884–887.
[21] Y. Dong, C. Yao, Y. Zhu, L. Yang, D. Luo, D. Yang, *Chem. Rev.* **2020**, *120*, 9420–9481.
[22] B. Liu, C. G. Pappas, J. Ottelé, G. Schaeffer, C. Jurissek, P. F. Pieters, M. Altay, I. Marić, M. C. A. Stuart, S. Otto, *J. Am. Chem. Soc.* **2020**, *142*, 4184–4192.
[23] B. Liu, M. A. Beatty, C. G. Pappas, K. Liu, J. Ottelé, S. Otto, *Angew. Chem. Int. Ed.* **2021**, *60*, 13569–13573; *Angew. Chem.* **2021**, *133*, 13681–13685.
[24] V. Allain, C. Bourgaux, P. Couvreur, *Nucleic Acids Res.* **2012**, *40*, 1891–1903.
[25] L. Simeone, D. Milano, L. De Napoli, C. Irace, A. Di Pascale, M. Boccalon, P. Tecilla, D. Montesarchio, *Chem. Eur. J.* **2011**, *17*, 13854–13865.
[26] C. Aimé, R. Tamoto, T. Satoh, A. Grelard, E. J. Dufourc, T. Buffeteau, H. Ihara, R. Oda, *Langmuir* **2009**, *25*, 8489–8496.
[27] F. Baldelli Bombelli, D. Berti, M. Almgren, G. Karlsson, P. Baglioni, *J. Phys. Chem. B* **2006**, *110*, 17627–17637.
[28] T. G. W. Edwardson, K. M. M. Carneiro, C. K. McLaughlin, C. J. Serpell, H. F. Sleiman, *Nat. Chem.* **2013**, *5*, 868–875.
[29] M. Kwak, A. Herrmann, *Chem. Soc. Rev.* **2011**, *40*, 5745–5755.
[30] E. Del Grosso, G. Ragazzon, L. J. Prins, F. Ricci, *Angew. Chem. Int. Ed.* **2019**, *58*, 5582–5586; *Angew. Chem.* **2019**, *131*, 5638–5642.
[31] E. Del Grosso, L. J. Prins, F. Ricci, *Angew. Chem. Int. Ed.* **2020**, *59*, 13238–13245; *Angew. Chem.* **2020**, *132*, 13340–13347.
[32] C. Donau, F. Späth, M. Sosson, B. A. K. Kriebisch, F. Schnitter, M. Tena-Solsona, H. S. Kang, E. Salibi, M. Sattler, H. Mutschler, J. Boekhoven, *Nat. Commun.* **2020**, *11*, 5167.
[33] C. M. E. Kriebisch, A. M. Bergmann, J. Boekhoven, *J. Am. Chem. Soc.* **2021**, *143*, 7719–7725.
[34] M. A. Cardona, L. J. Prins, *Chem. Sci.* **2020**, *11*, 1518–1522.

© 2022 The Authors. Chemistry - A European Journal published by Wiley-VCH GmbH

[35] P. Solís Muñana, G. Ragazzon, J. Dupont, C. Z. J. Ren, L. J. Prins, J. L. Y. Chen, *Angew. Chem. Int. Ed.* **2018**, *57*, 16469–16474; *Angew. Chem.* **2018**, *130*, 16707–16712.
[36] S. Maiti, I. Fortunati, C. Ferrante, P. Scrimin, L. J. Prins, *Nat. Chem.* **2016**, *8*, 725–731.
[37] J. L. Y. Chen, S. Maiti, I. Fortunati, C. Ferrante, L. J. Prins, *Chem. Eur. J.* **2017**, *23*, 11549–11559.
[38] L. Zhou, D. K. O'Flaherty, J. W. Szostak, *Angew. Chem. Int. Ed.* **2020**, *132*, —15682-15687; *Angew. Chem.* **2020**, *132*, 15812–15817.
[39] T. H. Wright, C. Giurgiu, W. Zhang, A. Radakovic, D. K. O'Flaherty, L. Zhou, J. W. Szostak, *J. Am. Chem. Soc.* **2019**, *141*, 18104–18112.
[40] S. C. Kim, D. K. O'Flaherty, C. Giurgiu, L. Zhou, J. W. Szostak, *J. Am. Chem. Soc.* **2021**, *143*, 3267–3279.
[41] S. J. Zhang, D. Duzdevich, J. W. Szostak, *J. Am. Chem. Soc.* **2020**, *142*, 14810–14813.
[42] K. Adamala, J. W. Szostak, *Science* **2013**, *342*, 1098–1100.
[43] H. Griesser, M. Bechthold, P. Tremmel, E. Kervio, C. Richert, *Angew. Chem. Int. Ed.* **2017**, *56*, 1224–1228; *Angew. Chem.* **2017**, *129*, 1244–1248.
[44] B. Jash, P. Tremmel, D. Jovanovic, C. Richert, *Nat. Chem.* **2021**, *13*, 751–757.
[45] D. Jovanovic, P. Tremmel, P. S. Pallan, M. Egli, C. Richert, *Angew. Chem. Int. Ed.* **2020**, *59*, 20154–20160; *Angew. Chem.* **2020**, *132*, 20329–20335.
[46] P. Tremmel, H. Griesser, U. E. Steiner, C. Richert, *Angew. Chem. Int. Ed.* **2019**, *58*, 13087–13092; *Angew. Chem.* **2019**, *58*, 13221–13226.
[47] S. Motsch, D. Pfeffer, C. Richert, *ChemBioChem* **2020**, *21*, 2013–2018.
[48] F. Ahmad, W. I. Kelso, *J. Res. Sci.* **2001**, *12*, 130–139, https://www.bzu.edu.pk/jrscience/vol12no2/4.pdf.
[49] J. Kottur, D. T. Nair, *Nucleic Acids Res.* **2018**, *46*, 5875–5885.
[50] S. B. Salunke, N. S. Babu, C. T. Chen, *Chem. Commun.* **2011**, *47*, 10440–10442.
[51] K. El Akri, K. Bougrin, J. Balzarini, A. Faraj, R. Benhida, *Bioorg. Med. Chem. Lett.* **2007**, *17*, 6656–6659.
[52] S. Wallrodt, A. Buntz, Y. Wang, A. Zumbusch, A. Marx, *Angew. Chem. Int. Ed.* **2016**, *55*, 7660–7664; *Angew. Chem.* **2016**, *128*, 7790–7794.
[53] F. Aparicio, E. Matesanz, L. Sánchez, *Chem. Eur. J.* **2014**, *20*, 14599–14603.
[54] J. Yang, H. Gao, Y. Wang, Y. Yu, Y. Gong, M. Fang, D. Ding, W. Hu, B. Z. Tang, Z. Li, *Mater. Chem. Front.* **2019**, *3*, 1391–1397.
[55] H. Yanagawa, Y. Ogawa, H. Furuta, K. Tsuno, *J. Am. Chem. Soc.* **1989**, *111*, 4567–4570.
[56] P. Barthélemy, *C. R. Chim.* **2009**, *12*, 171–179.
[57] C. D. Jones, H. T. D. Simmons, K. E. Horner, K. Liu, R. L. Thompson, J. W. Steed, *Nat. Chem.* **2019**, *11*, 375–381.
[58] J. Peon, A. H. Zewail, *Chem. Phys. Lett.* **2001**, *348*, 255–262.
[59] S. Suzuki, S. Sasaki, A. S. Sairi, R. Iwai, B. Z. Tang, G. ichi Konishi, *Angew. Chem. Int. Ed.* **2020**, *59*, 9856–9867; *Angew. Chem.* **2020**, *132*, 9940–9951.
[60] J. Qu, F. Ren, J. Shi, B. Tong, Z. Cai, Y. Dong, *Chem. Eur. J.* **2020**, *26*, 14947–14953.
[61] J. Mei, N. L. C. Leung, R. T. K. Kwok, J. W. Y. Lam, B. Z. Tang, *Chem. Rev.* **2015**, *115*, 11718–11940.
[62] H. Zhang, X. Zheng, N. Xie, Z. He, J. Liu, N. L. C. Leung, Y. Niu, X. Huang, K. S. Wong, R. T. K. Kwok, H. H. Y. Sung, I. D. Williams, A. Qin, J. W. Y. Lam, B. Z. Tang, *J. Am. Chem. Soc.* **2017**, *139*, 16264–16272.
[63] X. Dou, Q. Zhou, X. Chen, Y. Tan, X. He, P. Lu, K. Sui, B. Z. Tang, Y. Zhang, W. Z. Yuan, *Biomacromolecules* **2018**, *19*, 2014–2022.
[64] Q. Zhou, T. Yang, Z. Zhong, F. Kausar, Z. Wang, Y. Zhang, W. Z. Yuan, *Chem. Sci.* **2020**, *11*, 2926–2933.
[65] H. Zhang, Z. Zhao, P. R. McGonigal, R. Ye, S. Liu, J. W. Y. Lam, R. T. K. Kwok, W. Z. Yuan, J. Xie, A. L. Rogach, B. Z. Tang, *Mater. Today* **2020**, *32*, 275–292.
[66] M. Jauker, H. Griesser, C. Richert, *Angew. Chem. Int. Ed.* **2015**, *54*, 14559–14563; *Angew. Chem.* **2015**, *127*, 14767–14771.
[67] S. Motsch, P. Tremmel, C. Richert, *Nucleic Acids Res.* **2020**, *48*, 1097–1107.
[68] P. Monnard, A. Kanavarioti, D. W. Deamer, *J. Am. Chem. Soc.* **2003**, *125*, 13734–13740.
[69] M. T. Fenske, W. Meyer-Zaika, H. G. Korth, H. Vieker, A. Turchanin, C. Schmuck, *J. Am. Chem. Soc.* **2013**, *135*, 8342–8349.
[70] J. R. V. Wazer, E. J. Griffith, *J. Am. Chem. Soc.* **1955**, *77*, 6140–6144.
[71] J. Xu, V. Chmela, N. J. J. Green, D. A. A. Russell, M. J. J. Janicki, R. W. W. Góra, R. Szabla, A. D. D. Bond, J. D. D. Sutherland, *Nature* **2020**, *582*, 60–66.
[72] J. K. Watts, A. Katolik, J. Viladoms, M. J. Damha, *Org. Biomol. Chem.* **2009**, *7*, 1904–1910.
[73] R. An, Y. Jia, B. Wan, Y. Zhang, P. Dong, J. Li, X. Liang, *PLoS One* **2014**, *9*, 0–10.
[74] O. Amosova, R. Coulter, J. R. Fresco, *Proc. Natl. Acad. Sci. USA* **2006**, *103*, 4392–4397.
[75] C. Aimé, R. Nishiyabu, R. Gondo, K. Kaneko, N. Kimizuka, *Chem. Commun.* **2008**, *1*, 6534–6536.
[76] M. Komiyama, N. Takeda, H. Shigekawa, *Chem. Commun.* **1999**, 1443–1451.
[77] A. A. Baykov, A. S. Shestakov, *Eur. J. Biochem.* **1992**, *206*, 463–470.

Manuscript received: November 16, 2021
Accepted manuscript online: January 17, 2022
Version of record online: February 8, 2022

© 2022 The Authors. Chemistry - A European Journal published by Wiley-VCH GmbH

Chemistry–A European Journal

Supporting Information

Carbodiimide-Driven Dimerization and Self-Assembly of Artificial, Ribose-Based Amphiphiles

Jing Sun, Julian Vogel, Lisa Chen, A. Lennart Schleper, Tim Bergner, Alexander J. C. Kuehne, and Max von Delius*

Table of Contents

Experimental section. S3

General and Materials S3

Synthesis S3

2,3,5-tri-*O*-acetyl-*β*-D-ribofuranosyl azide 2 ..... S3

Deprotection to 4-Alkyl-1-(*β*-D-arabinofuranosyl)-1,2,3-triazoles 6 – 8 ..... S5

Phosphorylation to 4-Alkyl-1-(5'-disodium phosphate-β-D-arabinofuranosyl)-1,2,3-triazoles (9 - 11) S6

Amine substitution to 6-chloropurine ribosides (13-18) S7

Phosphorylation to alkyl adenosine ribosides (19-24) S10

Isolation of X15ppX15 pyrophosphate S13

Supplementary data S14

NMR spectra S24

References S57

Experimental section.

General and Materials

^{1}H NMR and ^{13}C NMR spectra were recorded on a Bruker (400 MHz or 600 MHz) Instrument. Chemical shifts (δ) are reported in ppm and referenced to the residual solvent peaks. All fluorescence spectra were measured on a PerkinElmer LS 55 spectrophotometer at 25 °C using 1 mL cuvettes. Samples were dissolved in an appropriate solvent and measured in the same solvent. Data analysis was carried out using Origin 2019b. CD spectra were measured in a 1 mm quartz cuvette on a Jasco J-810 CD spectrometer equipped with a Julabo F12 temperature controller. TEM measurements were performed on a Zeiss EM10 microscope with an acceleration voltage of 120 kV, SEM on a ZEISS EVO MA microscope. Confocal microscopy images of all samples were recorded with a TCS SP8 confocal microscope using the Leica Application Suite X (LASX). DLS measurements were performed on a Nano-Zetasizer (Malvern Instruments) at 25 °C with a scattering angle of 173° and a wavelength of λ = 633 nm.

1,2,3,5-tetra-O-acetyl-β-D-ribofuranose, 6-chloropurine riboside, trimethylsilyl azide (95%), decylamine (95%), pentadecylamine (96%), dodecylamine (99%), octadecylamine (99%), 1-hexyne (97%), 1-dodecyne (98%), 1-hexadecyne (90%), phosphorus(V) oxychloride (99%), *N*-(3-dimethylaminopropyl)-*N*'-ethylcarbodiimide hydrochloride (EDC), 1-ethylimidazole (95%), trimethyl phosphate (99%), anhydrous ethanol, sodium methoxide (5.4 M in MeOH), $FeCl_3$, and K_2CO_3 were obtained from Sigma-Aldrich (Germany) or TCI (Germany) and used without further purification. All the solvents were analytical grade and used without further purification.

Synthesis

2,3,5-tri-*O*-acetyl-β-D-ribofuranosyl azide 2

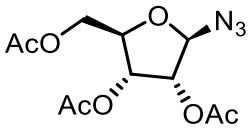

Under inert conditions, 1.00 g (3.14 mmol) **1** and 15.1 mg (0.09 mmol, 0.03 eq.) $FeCl_3$ was dissolved in 10 mL anhydrous DCM and stirred for 5 min. 0.63 mL (4.78 mmol, 1.5 eq.) Me_3SiN_3 were dissolved in 3 mL anhydrous DCM and the solution was added slowly under an inert atmosphere. The reaction was stirred at room temperature and monitored by TLC (EtOAc/Cyclohexane 1:2, R_f = 0.35). After 4 h, the reaction was quenched with a saturated $NaHCO_3$ solution. The two phases were separated, and the aqueous phase was extracted with DCM. The combined organic phases were washed with brine and

dried over $MgSO_4$ before DCM was removed. Drying under vacuum yielded 0.85 g (2.82 mmol, 90%) of a colorless oil. Spectra are in good agreement with the literature.[1]

^{1}H-NMR (400 MHz, $CDCl_3$): δ [ppm] = 2.07 (s, 3 H, OAc), 2.12 (2x s, 6 H, 2x OAc), 4.14 (dd, 1 H, *J* = 12.2 Hz, 4.3 Hz, 5'), 4.33 – 4.37 (m, 1 H, 4'), 4.41 (dd, 1 H, *J* = 12.2 Hz, 3.2 Hz, 5'), 5.13 (dd, 1 H, *J* = 4.8 Hz, 2.0 Hz, 3'), 5.31 – 5.37 (m, 2 H, 2' & 1').

^{13}C-NMR (100 MHz, $CDCl_3$): δ [ppm] = 20.6, 20.6, 20.8, 63.1, 70.6, 74.6, 79.5, 92.8, 169.5, 169.7, 170.7.

Huisgen cycloaddion to 4-Alkyl-1-(2',3',5'-tri-O-acetyl-*β*-D-ribofuranosyl)-1,2,3-triazoles 3 - 5

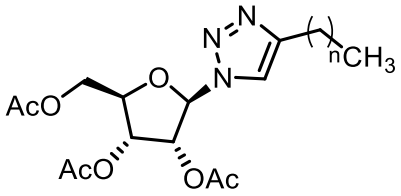

452 mg (1.50 mmol) **2** was dissolved in 20 mL anhydrous chloroform and degassed. 575 mg (3.00 mmol, 2 eq.) CuI and 1.31 mL (7.50 mmol, 5 eq.) DIPEA were added and the mixture was stirred for 5 min. 4.50 mmol (3 eq.) alkyne (1-octyne, 1-dodecyne, 1-hexadecyne, respectively) were added and the mixture was stirred for 2 d at 65 °C under an inert atmosphere. $CDCl_3$ was evaporated and direct column chromatography (DCM/EtOAc 7:1, R_f = 0.35, 0.4, 0.5, respectively) yielded between 70% and 93% of the products as colourless oils. Spectra are in good agreement with the literature.[2]

4-Hexyl-1-(2',3',5'-tri-O-acetyl-*β*-D-ribofuranosyl)-1,2,3-triazole 3 (n = 5)

^{1}H-NMR (400 MHz, $CDCl_3$): δ [ppm] = 0.87 (t, 3 H, *J* = 7.1 Hz, CH_3), 1.29-1.41 (br m, 6 H, 3 x CH_2), 1.66 (m, 2 H, CH_2), 2.08 (s, 3 H, OAc), 2.12 (2x s, 6 H, 2x OAc), 2.70 (t, 2 H, *J* = 7.9 Hz, CH_2), 4.22 (dd, 1 H, *J* = 12.2 Hz, 4.3 Hz, 5'), 4.40 (dd, 1 H, *J* = 12.2 Hz, 3.1 Hz, 5''), 4.46 (m, 1 H, 4'), 5.62 (t, 1 H, *J* = 5.4 Hz, 3'), 5.81 (dd, 1 H, *J* = 5.2 Hz, 3.9 Hz, 2'), 6.13 (d, 1 H, *J* = 3.8 Hz, 1'), 7.44 (s, 1 H, C=CH).

^{13}C-NMR (100 MHz, $CDCl_3$): δ [ppm] = 14.1, 20.5, 20.5, 22.7, 29.3, 29.4, 29.5, 29.6, 31.9, 62.9, 70.7, 74.3, 80.8, 169.3, 169.5, 170.4. Some signals overlap.

4-Decyl-1-(2',3',5'-tri-O-acetyl-β-D-ribofuranosyl)-1,2,3-triazole 4 (n = 9)

^{1}H-NMR (400 MHz, $CDCl_3$): δ [ppm] = 0.87 (t, 3 H, *J* = 7.1 Hz, CH_3), 1.22-1.33 (br m, 14 H, 7 x CH_2), 1.66 (m, 2 H, CH_2), 2.07 (s, 3 H, OAc), 2.11 (2x s, 6 H, 2x OAc), 2.70 (t, 2 H, *J* = 7.7 Hz, CH_2), 4.21 (dd, 1 H, *J* = 12.2 Hz, 4.3 Hz, 5'), 4.40 (dd, 1 H, *J* = 12.2 Hz, 3.1 Hz, 5''), 4.46 (m, 1 H, 4'), 5.61 (t, 1 H, *J* = 5.3 Hz, 3'), 5.80 (dd, 1 H, *J* = 5.2 Hz, 3.9 Hz, 2'), 6.11 (d, 1 H, *J* = 3.8 Hz, 1'), 7.44 (s, 1 H, C=CH).

^{13}C-NMR (100 MHz, $CDCl_3$): δ [ppm] = 14.1, 20.4, 20.5, 20.7, 21.2, 22.5, 22.6, 28.9, 29.1, 31.5, 62.9, 70.8, 74.3, 80.7, 169.3, 169.5, 170.4. Some signals overlap.

4-Tetradecyl-1-(2',3',5'-tri-O-acetyl-β-D-ribofuranosyl)-1,2,3-triazole 5 (n = 13)

^{1}H-NMR (400 MHz, $CDCl_3$): δ [ppm] = 0.88 (t, 3 H, *J* = 7.1 Hz, CH_3), 1.22-1.41 (br m, 22 H, 11 x CH_2), 1.67 (m, 2 H, CH_2), 2.08 (s, 3 H, OAc), 2.12 (2x s, 6 H, 2x OAc), 2.72 (t, 2 H, *J* = 7.7 Hz, CH_2), 4.22 (dd, 1 H, *J* = 12.2 Hz, 4.2 Hz, 5'), 4.41 (dd, 1 H, *J* = 12.2 Hz, 3.1 Hz, 5''), 4.46 (m, 1 H, 4'), 5.62 (t, 1 H, *J* = 5.4 Hz, 3'), 5.81 (dd, 1 H, *J* = 5.2 Hz, 3.9 Hz, 2'), 6.13 (d, 1 H, *J* = 3.8 Hz, 1'), 7.44 (s, 1 H, C=CH).

^{13}C-NMR (100 MHz, $CDCl_3$): δ [ppm] = 14.1, 20.5, 20.5, 20.7, 20.7, 25.6, 29.3, 29.3, 29.4, 29.6, 29.6, 29.7, 31.9, 62.9, 70.8, 74.3, 80.7, 89.8, 119.7, 169.3, 169.5, 170.4. Some signals overlap.

Deprotection to 4-Alkyl-1-(*β*-D-arabinofuranosyl)-1,2,3-triazoles 6 – 8

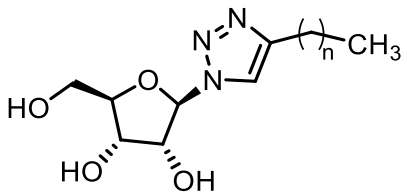

1.00 mmol of the 4-alkyl-1-(2',3',5'-tri-O-acetyl-*β*-D-ribofuranosyl)-1,2,3-triazoles **3 – 5** were dissolved in 10 – 25 mL anhydrous MeOH and 111 µL (0.60 mmol, 0.6 eq.) NaOMe in MeOH (5.4 M) were added. The mixture was stirred for 1.5 h at room temperature under an inert atmosphere before neutralizing it with 400 µL HCl/ether (2 M) (0.80 mmol, 0.8 eq.) and stirred for 15 min. Water was added and extracted with EtOAc. The organic phase was dried over $MgSO_4$. Evaporation of the solvents yielded 82 - 97% of the desired products as colorless to slightly yellow solids. Spectra were in good agreement with the literature.[3]

4-Hexyl-1-(β-D-arabinofuranosyl)-1,2,3-triazole 6 (n = 5)

^{1}H NMR (400 MHz, MeOH-d_4): δ [ppm] = 0.90 (t, 3 H, *J* = 6.9 Hz, CH_3), 1.29-1.41 (br m, 6 H, 3 x CH_2), 1.66 (m, 2 H, CH_2), 2.69 (t, 2 H, *J* = 7.7 Hz, CH_2), 3.67 (dd, 1 H, *J* = 12.2 Hz, 4.3 Hz, 5'), 3.80 (dd, 1 H, *J* = 12.2 Hz, 3.2 Hz, 5''), 4.10 (m, 1 H, 4'), 4.27 (t, 1 H, *J* = 5.0 Hz, 3'), 4.46 (t, 1 H, *J* = 4.5 Hz, 2'), 5.98 (d, 1 H, *J* = 4.1 Hz, 1'), 7.98 (1 H, s, C=CH).

^{13}C-NMR (100 MHz, MeOH-d_4): δ [ppm] = 14.2, 23.4, 26.1, 29.7, 30.3, 32.5, 62.7, 71.7, 76.8, 86.8, 94.0, 121.6, 149.2.

4-Decyl-1-(β-D-arabinofuranosyl)-1,2,3-triazole 7 (n = 9)

^{1}H NMR (400 MHz, MeOH-d_4): δ [ppm] = 0.88 (t, 3 H, *J* = 6.7 Hz, CH_3), 1.21-1.40 (br m, 14 H, 7 x CH_2), 1.66 (m, 2 H, CH_2), 2.69 (t, 2 H, *J* = 7.7 Hz, CH_2), 3.67 (dd, 1 H, *J* = 12.2 Hz, 4.3 Hz, 5'), 3.80 (dd, 1 H, *J* = 12.2 Hz, 3.1 Hz, 5''), 4.10 (m, 1 H, 4'), 4.27 (t, 1 H, *J* = 5.0 Hz, 3'), 4.46 (t, 1 H, *J* = 4.5 Hz, 2'), 5.98 (d, 1 H, *J* = 4.0 Hz, 1'), 7.98 (s, 1 H, C=CH).

^{13}C-NMR (100 MHz, MeOH-d_4): δ 14.5, 23.7, 26.3, 30.3, 30.5, 30.5, 30.5, 30.7, 30.7, 33.1, 62.9, 71.9, 77.0, 87.0, 94.2, 121.8, 149.4.

4-Tetradecyl-1-(β-D-arabinofuranosyl)-1,2,3-triazole 8 (n = 13)

^{1}H NMR (400 MHz, MeOH-d_4): δ [ppm] = 0.89 (t, 3 H, *J* = 6.8 Hz, CH_3), 1.22-1.38 (br m, 22 H, 11 x CH_2), 1.66 (m, 2 H, CH_2), 2.68 (t, 2 H, *J* = 7.7 Hz, CH_2), 3.67 (dd, 1 H, *J* = 12.2 Hz, 4.3 Hz, 5'), 3.80 (dd, 1 H, *J* = 12.2 Hz, 3.2 Hz, 5''), 4.10 (m, 1 H, 4'), 4.29 (t, 1 H, *J* = 5.0 Hz, 3'), 4.46 (t, 1 H, *J* = 4.5 Hz, 2'), 5.98 (d, 1 H, *J* = 4.1 Hz, 1'), 7.98 (s, 1 H, C=CH).

^{13}C-NMR (100 MHz, MeOH-d_4): δ [ppm] = 24.6, 23.7, 26.3, 30.3, 30.5, 30.6, 30.7, 30.8, 33.1, 62.89, 71.9, 77.0, 87.1, 94.3, 121.8, 149.4. Some signals overlap.

Phosphorylation to 4-Alkyl-1-(5'-disodium phosphate-β-D-arabinofuranosyl)-1,2,3-triazoles (9 - 11)

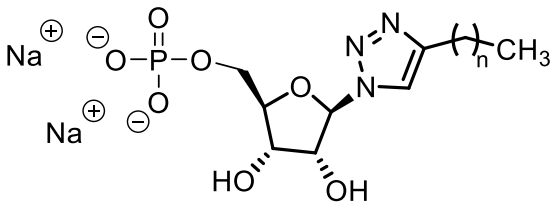

0.50 mmol of the 4-Alkyl-1-(*β*-D-arabinofuranosyl)-1,2,3-triazoles **6 - 8** were co-evaporated with MeCN three times and pre-dried in vacuo overnight. **6 - 8** were dissolved in 5 - 10 mL anhydrous $PO(OMe)_3$ (TMP) and stirred for 30 min at 0 °C. 56 µL (0.60 mmol, 1.2 eq.) $POCl_3$ were dissolved in 0.5 mL anhydrous $PO(OMe)_3$ and added to the mixture, which was stirred for 8 h at 0°C under an inert atmosphere. After 2 h another charge (0.6 mmol) of $POCl_3$ in $PO(OMe)_3$ was added. The mixture was quenched with 4 mL of H_2O, neutralized with Na_2CO_3 (pH ≈ 8) and stirred for 30 min at 0 °C. The precipitate was dissolved in H_2O. The aqueous phase was washed with ether three times. Purification was performed by MPLC (C18, H_2O/MeCN 98:2 – 5:95). Solvents were removed by lyophilization to obtain the desired products as colorless powders in 50 - 74% yield.

4-Hexyl-1-(5'-disodium phosphate-*β*-D-arabinofuranosyl)-1,2,3-triazole 9 (n = 5), C_6MP

^{1}H NMR (400 MHz, D_2O): δ [ppm] = 0.81 (t, 3 H, *J* = 6.5 Hz, CH_3), 1.19-1.31 (br m, 6 H, 3 x CH_2), 1.64 (m, 2 H, CH_2), 2.74 (t, 2 H, *J* = 7.4 Hz, CH_2), 4.00 – 4.12 (br m, 2 H, 5' & 5''), 4.37 (m, 1 H, 4'), 4.44 (t, 1 H, *J* = 4.5 Hz, 3'), 4.64 (t, 1 H, *J* = 5.1 Hz, 2'), 6.12 (d, 1 H, *J* = 5.2 Hz, 1'), 8.15 (s, 1 H, C=CH).

^{13}C-NMR (100 MHz, D_2O): δ [ppm] = 12.4, 20.9, 23.5, 26.8, 27.5, 29.8, 63.6, 69.6, 74.0, 83.4, 91.0, 120.2, 148.5.

^{31}P-NMR (162 MHz, HEPES buffer pH = 7.50, against 85% H_3PO_4): δ [ppm] = 3.78.

HRMS ESI(-) ($C_{13}H_{23}N_3O_7P$, 364.12791): m/z = 364.12794 ($[M]^-$) (Δ = 0.08 ppm).

4-Decyl-1-(5'-disodium phosphate-*β*-D-arabinofuranosyl)-1,2,3-triazole 10 (n = 9), C_{10}MP

^{1}H NMR (400 MHz, D_2O): δ [ppm] = 0.78 (t, 3 H, *J* = 6.6 Hz, CH_3), 1.13-1.30 (br m, 14 H, 7 x CH_2), 1.55 (m, 2 H, CH_2), 2.58 (t, 2 H, *J* = 7.6 Hz, CH_2), 3.93 – 4.05 (br m, 2 H, 5' & 5''), 4.28 (m, 1 H, 4'), 4.44 (t, 1 H, *J* = 5.0 Hz, 3'), 4.59 (t, 1 H, *J* = 4.7 Hz, 2'), 6.00 (d, 1 H, *J* = 4.2 Hz, 1'), 7.84 (s, 1 H, C=CH).

^{13}C-NMR (100 MHz, D_2O): δ [ppm] = 13.4, 22.1, 24.5, 28.1, 28.4, 28.5, 28.5, 28.7, 28.7, 31.2, 64.2, 70.7, 74.9, 84.5, 91.8, 121.2, 149.4.

^{31}P-NMR (162 MHz, HEPES buffer pH = 7.50, against 85% H_3PO_4): δ [ppm] = 3.73.

HRMS ESI(-) ($C_{17}H_{31}N_3O_7P$, 420.19051): m/z = 420.19070 ($[M]^-$) (Δ = 0.45 ppm).

4-Tetradecyl-1-(5'-disodium phosphate-*β*-D-arabinofuranosyl)-1,2,3-triazole 11 (n = 13), C_{14}MP

^{1}H NMR (400 MHz, D_2O): δ [ppm] = 0.83 (t, 3 H, *J* = 6.5 Hz, CH_3), 1.15-1.35 (br m, 22 H, 11 x CH_2), 1.59 (m, 2 H, CH_2), 2.69 (t, 2 H, *J* = 7.4 Hz, CH_2), 3.88 – 4.01 (br m, 2 H, 5' & 5''), 4.30 (m, 1 H, 4'), 4.45 (t, 1 H, *J* = 4.5 Hz, 3'), 4.62 (m, 1 H, 2'), 6.00 (d, 1 H, *J* = 5.2 Hz, 1'), 7.86 (s, 1 H, C=CH).

^{13}C-NMR (100 MHz, MeOH-d_4): δ 13.0, 22.3, 25.0, 29.0, 29.1, 29.1, 29.3, 29.4, 29.4, 29.4, 31.7, 64.4, 71.2, 75.8, 85.0, 92.9, 119.9, 148.8. Some signals overlap.

^{31}P-NMR (162 MHz, MeOH-d_4, against 85% H_3PO_4): δ [ppm] = 2.12.

HRMS ESI(-) ($C_{21}H_{39}N_3O_7P$, 476.25311): m/z = 476.25320 ($[M]^-$) (Δ = 0.19 ppm).

Amine substitution to 6-chloropurine ribosides (13-18)

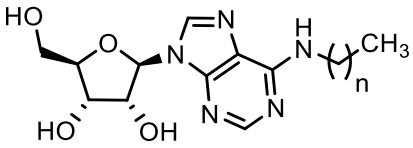

Compounds **13-18** were prepared as previously described.[4]

To a solution of 500 mg 6-chloropurine riboside **12** (1.74 mmol, 1.0 eq.) in anhydrous EtOH (10 mL), 1-alkyl amine (8.7 mmol, 5.0 eq.) was added under N_2 atmosphere and stirred at 90°C until the reaction was finished. After cooling, the crude product precipitated and was filtered off, washed with cold EtOH, and dried. The pure product was obtained either by washing the crude product with Et_2O or column chromatography with DCM:MeOH (10:1).

2-(6-(decylamino)-9H-purin-9-yl)-5-(hydroxymethyl)tetrahydrofuran-3,4-diol (n = 9)

^{1}H NMR (500 MHz, DMSO-d_6) δ [ppm] = 8.33 (s, 1H, H-8), 8.20 (s, 1H, H-2), 7.84 (s, 1H, NH), 5.90 (d, *J* = 6.2 Hz, 1H, H-1'), 5.46 (dd, *J* = 7.3, 4.3 Hz, 1H, OH-5'), 5.43 (d, *J* = 6.3 Hz, 1H, OH-2'), 5.18 (d, *J* = 4.6 Hz, 1H, OH-3'), 4.62 (q, *J* = 5.9 Hz, 1H, H-2'), 4.17 (td, *J* = 4.8, 3.0 Hz, 1H, H-3'), 3.99 (q, *J* = 3.4 Hz, 1H, H-4'), 3.69 (dt, *J* = 12.1, 3.9 Hz, 1H, H-5'), 3.57 (ddd, *J* = 11.6, 7.2, 3.5 Hz, 1H, H-5'), 3.51-3.41 (m, 2H, C$\underline{H_2}$NH), 1.58 (p, *J* = 7.0 Hz, 2H, C$\underline{H_2}$CH$_2$NH), 1.30-1.17 (m, 14H, (CH$_2$)$_7$), 0.86-0.80 (t, *J* = 6.8 Hz, 3H, CH$_3$).

^{13}C NMR (126 MHz, DMSO-d_6) δ [ppm] = 154.7 (C-6), 152.3 (C-2), 148.1 (C-4), 139.6 (C-8), 119.8 (C-5), 88.1 (C-1'), 86.0 (C-4'), 73.6 (C-2'), 70.7 (C-3'), 61.7 (C-5'), 38.9 (C$\underline{H_2}$NH), 31.3 (C$\underline{H_2}$CH$_2$NH), 29.1 (CH$_2$), 29.0 (CH$_2$), 28.9 (CH$_2$), 28.8 (CH$_2$), 28.7 (CH$_2$), 26.4 (CH$_2$), 22.1 (CH$_2$), 13.9 (CH$_3$).

2-(6-(dodecylamino)-9H-purin-9-yl)-5-(hydroxymethyl)tetrahydrofuran-3,4-diol (n= 11)

^{1}H NMR (500 MHz, DMSO-d_6) δ [ppm] = 8.34 (s, 1H, H-8), 8.20 (s, 1H, H-2), 7.84 (s, 1H, NH), 5.90 (d, *J* = 6.1 Hz, 1H, OH-5'), 5.46 (dd, *J* = 7.4, 4.4 Hz, 1H, OH-2'), 5.43 (d, *J* = 6.2 Hz, 1H, OH-3'), 5.18 (d, *J* = 4.5 Hz, 1H, H-1'), 4.63 (q, *J* = 5.8 Hz, 1H, H-2'), 4.18 (td, *J* = 4.7, 2.9 Hz, 1H, H-3'), 3.99 (q, *J* = 3.3 Hz, 1H, H-4'), 3.70 (dt, *J* = 12.1, 4.0 Hz, 1H, H-5'), 3.58 (ddd, *J* = 12.1, 7.4, 3.5 Hz, 1H, H-5'), 3.46 (dd, *J* = 7.0, 5.1 Hz, 2H, C$\underline{H_2}$NH), 1.59 (p, *J* = 7.0 Hz, 2H, C$\underline{H_2}$CH$_2$NH), 1.31-1.19 (m, 18H, (CH$_2$)$_9$), 0.87-0.81 (t, *J* = 7.5 Hz, 3H, CH$_3$).

^{13}C NMR (126 MHz, DMSO-d_6) δ [ppm] = 154.7 (C-6), 152.3 (C-2), 148.2 (C-4), 139.6 (C-8), 119.8 (C-5), 88.1 (C-1'), 86.0 (C-4'), 73.6 (C-2'), 70.7 (C-3'), 61.7 (C-5'), 38.9 (C$\underline{H_2}$NH), 31.3 (C$\underline{H_2}$CH$_2$NH), 29.1 (CH$_2$), 29.0 (CH$_2$), 28.9 (CH$_2$), 28.9 (CH$_2$), 28.8 (CH$_2$), 28.8 (CH$_2$), 28.7 (CH$_2$), 26.4 (CH$_2$), 22.1 (CH$_2$), 13.9 (CH$_3$).

2-(6-(tridecylamino)-9H-purin-9-yl)-5-(hydroxymethyl)tetrahydrofuran-3,4-diol (n= 12)

^{1}H NMR (400 MHz, DMSO-d_6) δ [ppm] = 8.33 (s, 1H, H-8), 8.19 (s, 1H, H-2), 7.86 (s, 1H, NH), 5.88 (d, *J* = 6.1 Hz, 1H, OH-5'), 5.43 (m, 1H, OH-2'), 5.43 (m, 1H, OH-3'), 5.18 (m, 1H, H-1'), 4.62 (m, 1H, H-2'), 4.16 (m, 1H, H-3'), 3.97 (q, *J* = 3.3 Hz, 1H, H-4'), 3.68 (d, *J* = 12.1, 1H, H-5'), 3.55 (m, 1H, H-5'), 3.45 (m, 2H, C$\underline{H_2}$NH), 1.58 (p, *J* = 7.0 Hz, 2H, C$\underline{H_2}$CH$_2$NH), 1.33-1.16 (m, 20H, (CH$_2$)$_{10}$), 0.87-0.81 (t, *J* = 7.5 Hz, 3H, CH$_3$).

^{13}C NMR (100 MHz, DMSO-d_6) δ [ppm] = 154.7 (C-6), 152.4 (C-2), 148.2 (C-4), 139.6 (C-8), 119.8 (C-5), 88.0 (C-1'), 85.9 (C-4'), 73.5 (C-2'), 70.7 (C-3'), 61.7 (C-5'), 31.3 (C$\underline{H_2}$CH$_2$NH), 29.1 (CH$_2$), 29.0 (CH$_2$), 28.9 (CH$_2$), 28.7 (CH$_2$), 26.4 (CH$_2$), 22.1 (CH$_2$), 13.9 (CH$_3$). Some signals overlap.

2-(hydroxymethyl)-5-(6-(tetradecylamino)-9H-purin-9-yl)tetrahydrofuran-3,4-diol (n = 13)

^{1}H NMR (500 MHz, DMSO-d_6) δ [ppm] = 8.33 (s, 1H, H-8), 8.19 (s, 1H, H-2), 7.83 (s, 1H, NH), 5.90 (d, *J* = 6.1 Hz, 1H, H-1'), 5.46 (dd, *J* = 7.4, 4.4 Hz, 1H, OH-5'), 5.42 (d, *J* = 6.3 Hz, 1H, OH-2'), 5.17 (d, *J* = 4.7 Hz, 1H, OH-3'), 4.62 (q, *J* = 5.9 Hz, 1H, H-2'), 4.17 (td, *J* = 4.8, 2.9 Hz, 1H, H-3'), 3.99 (q, *J* = 3.3 Hz, 1H, H-4'), 3.69 (dt, *J* = 12.2, 4.0 Hz, 1H, H-5'), 3.57 (ddd, *J* = 11.6, 7.4, 3.5 Hz, 1H, H-5'), 3.46 (m, 2H, CH_2NH), 1.58 (p, *J* = 7.1 Hz, 2H, CH_2CH_2NH), 1.21 (m, 22H, $(CH_2)_{11}$), 0.83 (t, *J* = 6.8 Hz, 3H, CH_3).
^{13}C NMR (126 MHz, DMSO-d_6) δ [ppm] = 154.7 (C-6), 152.3 (C-2), 148.2 (C-4), 139.6 (C-8), 119.8 (C-5), 88.1 (C-1'), 86.0 (C-4'), 73.6 (C-2'), 70.7 (C-3'), 61.7 (C-5'), 39.0 (CH_2NH), 31.3 (CH_2CH_2NH), 29.2 (CH_2), 29.1 (CH_2), 28.9 (CH_2), 28.9 (CH_2), 28.8 (CH_2), 28.7 (CH_2), 28.69 (CH_2), 28.6 (CH_2), 26.5 (CH_2), 22.1 (CH_2), 22.0 (CH_2),13.9 (CH_3).

2-(hydroxymethyl)-5-(6-(pentadecylamino)-9H-purin-9-yl)tetrahydrofuran-3,4-diol (n = 14)

^{1}H NMR (600 MHz, DMSO-d_6) δ [ppm] = 8.33 (s, 1H, H-8), 8.21 (s, 1H, H-2), 7.83 (s, 1H, NH), 5.87 (d, J = 6.2 Hz, 1H, H-1'), 5.43 (s, 2H, OH-5' and OH-2'), 5.23 - 5.12 (m, 1H, OH-3'), 4.61 (t, J = 5.6 Hz, 1H, H-2'), 4.14 (dd, J = 5.0, 3.0 Hz, 1H, H-3'), 3.96 (q, J = 3.4 Hz, 1H, H-4'), 3.67 (dd, J = 12.1, 3.6 Hz, 1H, H-5'), 3.55 (dd, J = 12.1, 3.6 Hz, 1H, H-5'), 3.49 – 3.42 (m, 2H, CH_2NH), 1.57 (p, J = 7.1 Hz, 2H, CH_2CH_2NH), 1.23 (d, J = 3.3 Hz, 24H, $(CH_2)_{12}$), 0.84 (t, *J* = 6.9 Hz, 3H, CH_3).
^{13}C NMR (151 MHz, DMSO-d_6) δ [ppm] = 154.7 (C-6), 152.4 (C-2), 148.2 (C-4), 139.6 (C-8), 119.7 (C-5), 88.0 (C-1'), 85.9 (C-4'), 73.5 (C-2'), 70.7 (C-3'), 61.7 (C-5'), 39.1 (CH_2NH), 31.3 (CH_2CH_2NH), 29.1 (CH_2), 29.0 (CH_2), 28.8 (CH_2), 28.7 (CH_2), 26.4 (CH_2), 26.3 (CH_2), 22.1 (CH_2), 13.9 (CH_3).

2-(6-(heptadecylamino)-9H-purin-9-yl)-5-(hydroxymethyl)tetrahydrofuran-3,4-diol (n = 17)

^{1}H NMR (500 MHz, DMSO-d_6) δ [ppm] = 8.33 (s, 1H, H-8), 8.19 (s, 1H, H-2), 7.88 (s, 1H, NH), 5.87 (d, *J* = 6.2 Hz, 1H, H-1'), 5.44 (dd, *J* = 9.1, 5.3 Hz, 2H, OH-2' & OH-5'), 5.18 (d, *J* = 4.6 Hz, 1H, OH-3'), 4.60 (q, *J* = 5.7 Hz, 1H, H-2'), 4.14 (td, *J* = 4.8, 2.9 Hz, 1H, H-3'), 3.96 (q, *J* = 3.4 Hz, 1H, H-4'), 3.67 (dt, *J* = 12.1, 4.1 Hz, 1H, H-5'), 3.55 (ddd, *J* = 11.6, 7.2, 3.6 Hz, 1H, H-5'), 3.51-3.40 (m, 2H, CH_2NH), 1.57 (p, *J* = 6.8 Hz, 2H, CH_2CH_2NH), 1.22 (m, 30H, $(CH_2)_{15}$), 0.88-0.80 (t, *J* = 6.0 Hz, 3H, CH_3).
^{13}C NMR (126 MHz, DMSO-d_6) δ [ppm] = 154.6 (C-6), 151.9 (C-2), 148.5 (C-4), 139.0 (C-8), 119.3 (C-5), 87.9 (C-1'), 85.6 (C-4'), 73.4 (C-2'), 70.3 (C-3'), 61.4 (C-5'), 38.8 (CH_2NH), 30.9 (CH_2CH_2NH), 28.9 (CH_2-CH_2), 28.6 (CH_2-CH_2), 28.5 (CH_2-CH_2), 28.5 (CH_2-CH_2), 28.4 (CH_2-CH_2), 28.4 (CH_2-CH_2), 28.3 (CH_2-CH_2), 28.2 (CH_2-CH_2), 28.2 (CH_2-CH_2), 28.1 (CH_2-CH_2), 26.9 (CH_2-CH_2), 26.0 (CH_2-CH_2), 25.5 (CH_2-CH_2), 21.6 (CH_2-CH_2), 21.5 (CH_2-CH_2), 13.3 (CH_3).

Phosphorylation to alkyl adenosine ribosides

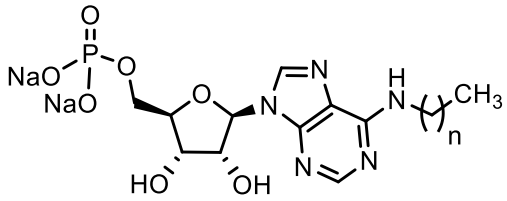

0.50 mmol of the compound **13 - 18** were co-evaporated with MeCN three times and pre-dried in vacuo overnight. **13 - 18** were dissolved in 10 mL anhydrous TMP and stirred for 30 min at 0 °C. 1.5-2.0 eq. $POCl_3$ were added to the mixture and stirred for 3-8 h at 0°C under an inert atmosphere. After the starting material was consumed completely (monitored by TLC), the reaction mixture was quenched with 5 mL of H_2O, neutralized with Na_2CO_3, stirred for 30 min at 0 °C, and washed with Et_2O (5 × 10 mL). The aqueous phase was further purified by MPLC (C18, H_2O/MeCN 95:5 – 5:95). Solvents were removed by lyophilization to obtain the desired products as white powders in 50 - 70% yield.

Note: The chemical shift and the signal broadness (and multiplicity) of compounds **19 - 24** depend strongly on the concentration and may therefore vary.

X_{10}MP

^{1}H NMR (400 MHz, D_2O) δ [ppm] = 8.23 (s, 1H, H-8), 8.04 (s, 1H, H-2), 5.91 (d, *J* = 4.8 Hz, 1H, H-1'), 4.53 (t, *J* = 5.0 Hz, 1H, H-2'), 4.37 (t, *J* = 4.8 Hz, 1H, H-3'), 4.22 (q, *J* = 4.0 Hz, 1H, H-4'), 4.02 (q, *J* = 7.3, 6.7 Hz, 2H, H-5'), 3.31 (s, 2H, CH_2NH), 1.48 (q, *J* = 8.0, 7.5 Hz, 2H, C$H_2$$CH_2$NH), 1.15 (d, *J* = 20.0 Hz, 14H, $(CH_2)_7$), 0.77 (t, *J* = 6.6 Hz, 3H, CH_3).

^{13}C NMR (101 MHz, D_2O) δ 154.1 (C-6), 152.7 (C-2), 147.4 (C-4), 138.4 (C-8), 118.5 (C-5), 87.1 (C-1'), 83.5 (C-4'), 74.5 (C-2'), 70.1 (C-3'), 64.1 (C-5'), 40.6 (CH_2NH), 31.8 (C$H_2$$CH_2$NH), 29.7 ($CH_2$), 29.6 ($CH_2$), 29.4 ($CH_2$), 29.3 ($CH_2$), 29.1 ($CH_2$), 26.9 ($CH_2$), 22.5 ($CH_2$), 13.7 ($CH_3$).

^{31}P NMR (162 MHz, D_2O) δ [ppm] = 1.88.

HRMS ESI(-) ($C_{20}H_{33}N_5O_7P^-$, 486.2123): m/z = 486.2136 ($[M]^-$) (Δ = 2.67 ppm).

X_{12}MP

^{1}H NMR (400 MHz, D_2O) δ [ppm] = 8.26 (s, 1H, H-8), 8.03 (s, 1H, H-2), 5.91 (d, J = 4.7 Hz, 1H, H-1'), 4.55 (t, J = 5.0 Hz, 1H, H-2'), 4.35 (t, J = 4.8 Hz, 1H, H-3'), 4.22 (q, J = 4.3 Hz, 1H, H-4'), 3.94 (tt, J = 12.7, 5.2 Hz, 2H, H-5'), 3.32 (dt, J = 23.4, 10.3 Hz, 2H, CH_2NH), 1.51 (p, J = 7.4, 6.8 Hz, 2H, C$H_2$$CH_2$NH), 1.18 (s, 18H, $(CH_2)_9$), 0.81 (t, J = 6.6 Hz, 3H, CH_3).

^{13}C NMR (101 MHz, D_2O) δ [ppm] = 154.2 (C-6), 152.8 (C-2), 147.46 (C-4), 138.6 (C-8), 118.5 (C-5), 87.0 (C-1'), 83.7 (C-4'), 74.3 (C-2'), 70.3 (C-3'), 63.8 (C-5'), 40.6 (CH_2NH), 31.9 (C$H_2$$CH_2$NH), 29.9 ($CH_2$),

29.8 (CH_2), 29.8 (CH_2), 29.5 (CH_2), 29.4 (CH_2), 29.2 (CH_2), 29.1 (CH_2), 27.0 (CH_2), 22.6 (CH_2), 13.8 (CH_3).

^{31}P NMR (162 MHz, D_2O) δ [ppm] = 4.02.

HRMS ESI(-) ($C_{22}H_{37}N_5O_7P^-$, 514.2436): m/z = 514.2465 ($[M]^-$) (Δ = 5.64 ppm).

X_{13}MP

^{1}H NMR (600 MHz, D_2O) δ [ppm] = 8.34 (s, 1H, H-8), 8.10 (s, 1H, H-2), 5.98 (s, 1H, H-1'), 4.62 (s, 1H, H-2'), 4.41 (s, 1H, H-3'), 4.27 (s, 1H, H-4'), 3.97 (s, 2H, H-5'), 3.41 (d, J = 32.0 Hz, 2H, CH_2NH), 1.55 (s, 2H, C$H_2$$CH_2$NH), 1.18 (s, 20H, $(CH_2)_{10}$), 0.80 (s, 3H, CH_3).

^{13}C NMR (150 MHz, D_2O) δ [ppm] = 154.4 (C-6), 152.8 (C-2), 147.6 (C-4), 138.7 (C-8), 118.7 (C-5), 87.0 (C-1'), 83.8 (C-4'), 74.3 (C-2'), 70.4 (C-3'), 63.7 (C-5'), 40.6 (CH_2NH), 31.8 (C$H_2$$CH_2$NH), 29.7 ($CH_2$), 29.3 ($CH_2$), 29.1 ($CH_2$), 26.8 ($CH_2$), 22.5 ($CH_2$), 13.8 ($CH_3$). Some signals overlap.

^{31}P NMR (243 MHz, D_2O) δ [ppm] = 4.02.

HRMS ESI(-) ($C_{22}H_{37}N_5O_7P^-$, 528.25930): m/z = 528.25931 ($[M]^-$) (Δ = 0.02 ppm).

X_{14}MP

^{1}H NMR (400 MHz, D_2O) δ [ppm] = 8.16 (s, 1H, H-8), 7.94 (s, 1H, H-2), 5.81 (s, 1H, H-1'), 4.44 (s, 1H, H-2'), 4.25 (s, 1H, H-3'), 4.12 (s, 1H, H-4'), 3.84 (d, J = 15.3 Hz, 2H, H-5'), 3.22 (s, 2H, CH_2NH), 1.43 (s, 2H, C$H_2$$CH_2$NH), 1.14 (s, 22H, $(CH_2)_{11}$), 0.75 (t, J = 6.1 Hz, 3H, CH_3).

^{13}C NMR (101 MHz, D_2O) δ [ppm] = 154.2 (C-6), 152.8 (C-2), 147.5 (C-4), 138.6 (C-8), 118.5 (C-5), 87.0 (C-1'), 83.7 (C-4'), 74.3 (C-2'), 70.3 (C-3'), 63.8 (C-5'), 40.7 (CH_2NH), 32.0 (C$H_2$$CH_2$NH), 30.0 ($CH_2$), 30.0 ($CH_2$), 29.7 ($CH_2$), 29.6 ($CH_2$), 29.5 ($CH_2$), 29.44($CH_2$), 29.4 ($CH_2$), 29.3 ($CH_2$), 29.2 ($CH_2$), 27.1 ($CH_2$), 22.6 ($CH_2$), 13.8 ($CH_3$).

^{31}P NMR (162 MHz, D_2O) δ [ppm] = 4.07.

HRMS ESI(-) ($C_{24}H_{41}N_5O_7P^-$, 542.2749): m/z = 542.2742 ($[M]^-$) (Δ = 1.29 ppm).

X_{15}MP

^{1}H NMR (400 MHz, D_2O) δ [ppm] = 8.28 (s, 1H, H-8), 8.06 (s, 1H, H-2), 5.93 (s, 1H, H-1'), 4.56 (s, 1H, H-2'), 4.36 (s, 1H, H-3'), 4.23 (s, 1H, H-4'), 3.95 (s, 2H, H-5'), 3.34 (s, 2H, CH_2NH), 1.53 (s, 2H, C$H_2$$CH_2$NH), 1.22 (s, 24H, $(CH_2)_{12}$), 0.83 (s, 3H, CH_3).

^{13}C NMR (101 MHz, D_2O) δ [ppm] = 154.2 (C-6), 152.8 (C-2), 147.5 (C-4), 138.6 (C-8), 118.6 (C-5), 87.0 (C-1'), 83.7 (C-4'), 74.3 (C-2'), 70.3 (C-3'), 63.8 (C-5'), 40.6 (CH_2NH), 32.0 (C$H_2$$CH_2$NH), 30.0 ($CH_2$), 29.9 ($CH_2$), 29.5 ($CH_2$), 29.2 ($CH_2$), 27.0 ($CH_2$), 22.6 ($CH_2$), ($CH_3$). Some signals overlap.

^{31}P NMR (162 MHz, D_2O) δ [ppm] = 4.08.

HRMS ESI(-) ($C_{25}H_{43}N_5O_7P^-$, 556.2906): m/z = 556.2901 ($[M]^-$) (Δ = 0.90 ppm).

X_{18}MP

^{1}H NMR (400 MHz, D_2O) δ [ppm] = 8.20 (s, 1H, H-8), 8.01 (s, 1H, H-2), 5.85 (s, 1H, H-1'), 4.47 (s, 1H, H-2'), 4.30 (s, 1H, H-3'), 4.16 (s, 1H, H-4'), 3.91 (s, 2H, H-5'), 3.30 (s, 2H, C$\underline{H_2}$NH), 1.54 (s, 2H, C$\underline{H_2}$$CH_2$NH), 1.29 (s, 30H, $(CH_2)_{15}$), 0.88 (s, 3H, CH_3).

^{13}C NMR (101 MHz, D_2O) δ [ppm] = 154.1 (C-6), 152.7 (C-2), 147.4 (C-4), 138.4 (C-8), 118.5 (C-5), 87.0 (C-1'), 83.5 (C-4'), 74.3 (C-2'), 70.2 (C-3'), 63.8 (C-5'), 40.7 ($\underline{C}H_2$NH), 32.2 ($\underline{C}H_2CH_2$NH), 30.5 (CH_2), 29.8 (CH_2), 29.2 (CH_2), 27.30 (CH_2), 22.8 (CH_2), 13.86 (CH_3). Some signals overlap.

^{31}P NMR (162 MHz, D_2O) δ [ppm] = 4.18.

HRMS ESI(-) ($C_{28}H_{49}N_5O_7P^-$, 598.3375): m/z = 598.3399 ($[M]^-$) (Δ = 3.68 ppm).

Isolation of X15ppX15 pyrophosphate

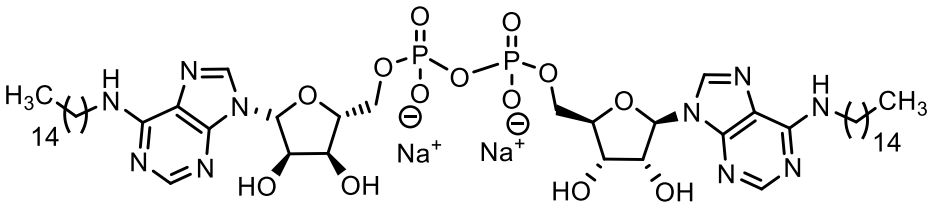

After dimerization of $X_{15}MP$ with 50 eq. EDC in condensation buffer for 6 h (according to the standard procedure), **X15ppX15** was pre-purified by MPLC on an Interchim PF-15C18HP-F0025 reverse phase column and finally purified by semi-preparative HPLC on a Supelco Ascentis C8 (25cm x 10 mm, 5 µm) column with a mobile phase of MeCN / 50 mM NH_4HCO_3 (7:3) and a flow rate of 3.0 mL/min at 60 °C (retention time: 9-12 min). The product was dried by lyophilization.

^{1}H NMR (600 MHz, MeOH-d_4) δ [ppm] = 8.71 (s, 2H, H-8), 8.46 (s, 2H, H-2), 6.29 (d, J=4.8 Hz, 2H, H-1'), 5.72 (s, 2H, NH), 4.83 (s, 2H, H-2'), 4.73 (t, ^3J=4.1 Hz, 2H, H-3'), 4.56 (m, 4H, H5'), 4.51 (m, 2H, H-4'), 3.87 (m, 4H, CH_2), 1.91 (m, 4H, CH_2), 1.69 – 1.45 (m, 48 H, CH_2), 1.14 (t, ^3J=7.1 Hz, 6H, CH_3).
^{13}C NMR (150 MHz, MeOH-d_4) δ [ppm] = 140.8, 120.3, 89.7, 85.6, 76.7, 71.8, 66.5, 54.8, 33.1, 30.9, 30.7, 30.6, 30.5, 28.1, 23.8. 14.5. Some quartinary carbon signals are not visible due to poor solubility of the compound, some signals overlap.
^{31}P NMR (243 MHz, MeOH-d_4) δ [ppm] = -11.01.
HRMS ESI(-) ($C_{50}H_{84}N_{10}O_{13}P_2^-$, 1095.5773): m/z = 1095.5841 ($[M]^-$) (Δ = 6.21 ppm).

Supplementary data

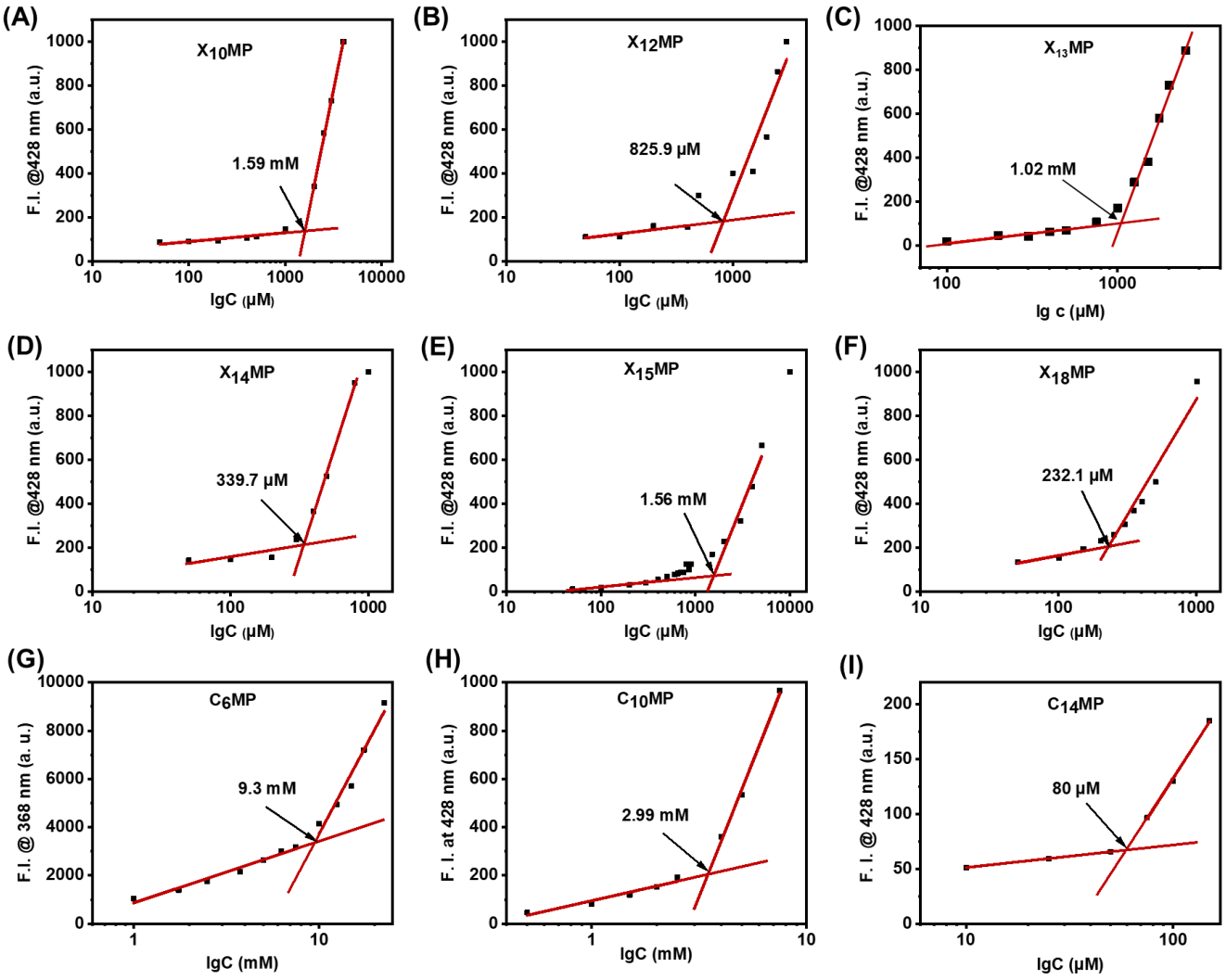

Figure S1. The CAC of all ribonucleotide-based amphiphiles was determined by monitoring the fluorescence intensity of DPH dye (10μM) at 428 nm in a dilution series of amphiphiles. Aggregation of the amphiphiles leads to incorporation of the dye in the apolar regions of the aggregates and hence leads to increasing fluorescence.

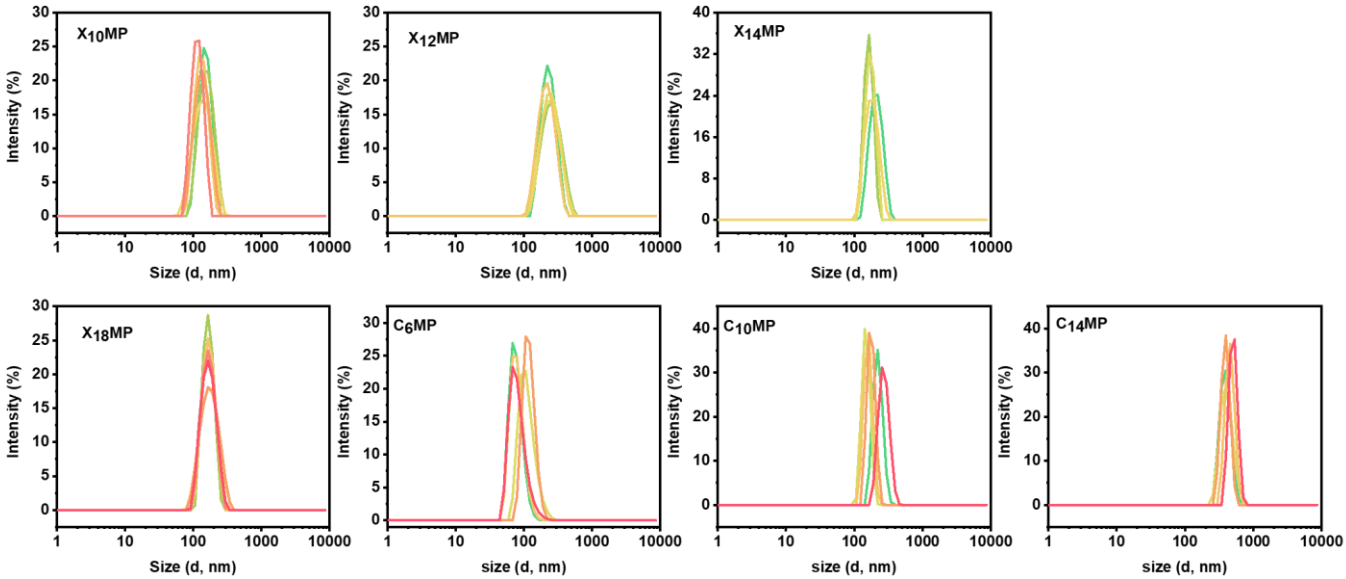

Figure S2. The hydrodynamic diameters of ribonucleotide-based amphiphiles were determined by DLS. Amphiphiles were dissolved in 5 mM HEPES buffer in concentrations above the respective CAC (**C_6MP**: 18 mM, **C_{10}MP**: 6 mM, **C_{14}MP**: 160 µM, **X_{10}MP**: 2.0 mM, **X_{12}MP**: 1.3 mM, **X_{14}MP:** 2.2 mM, **X_{18}MP**: 0.5 mM).

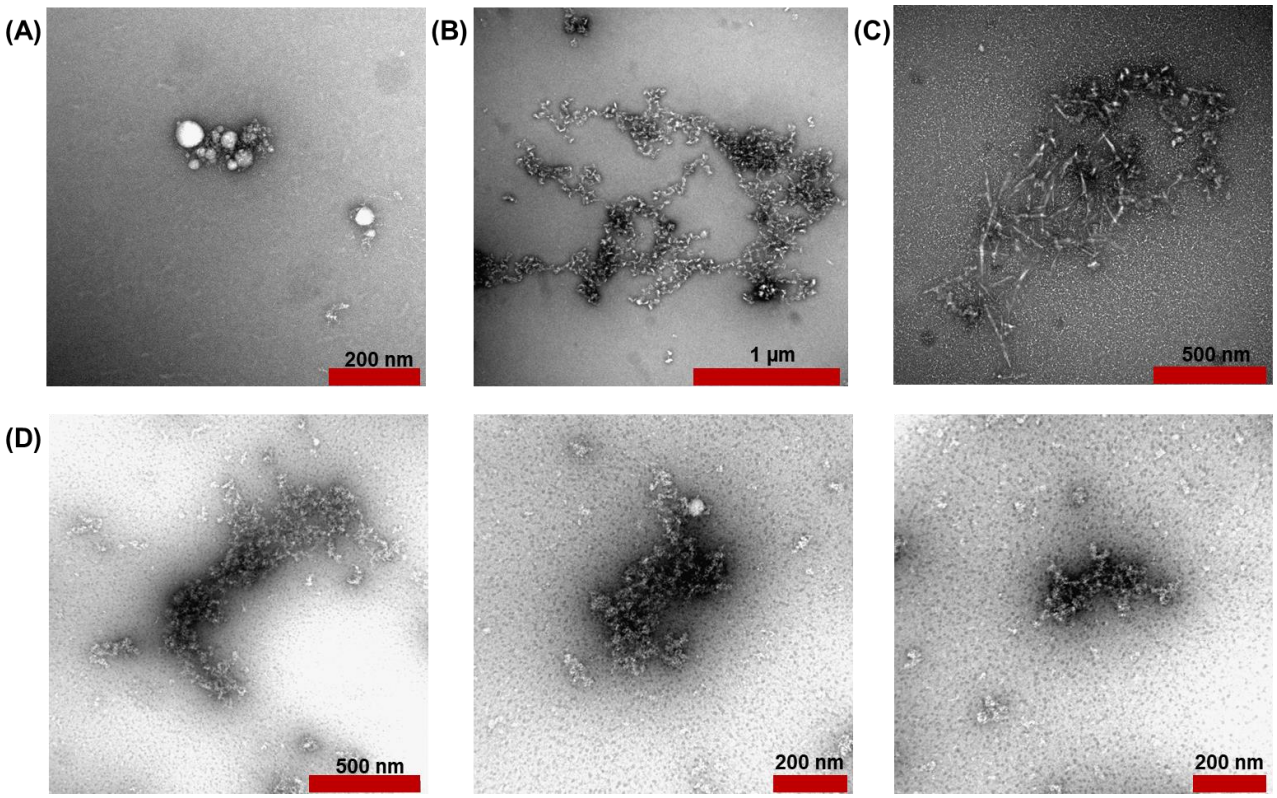

Figure S3: The additional TEM images of (**A**) C_6MP, (**B**) C_{10}MP, (**C**) C_{14}MP and (**D**) X_{13}MP in HEPES buffer (pH = 7.50).

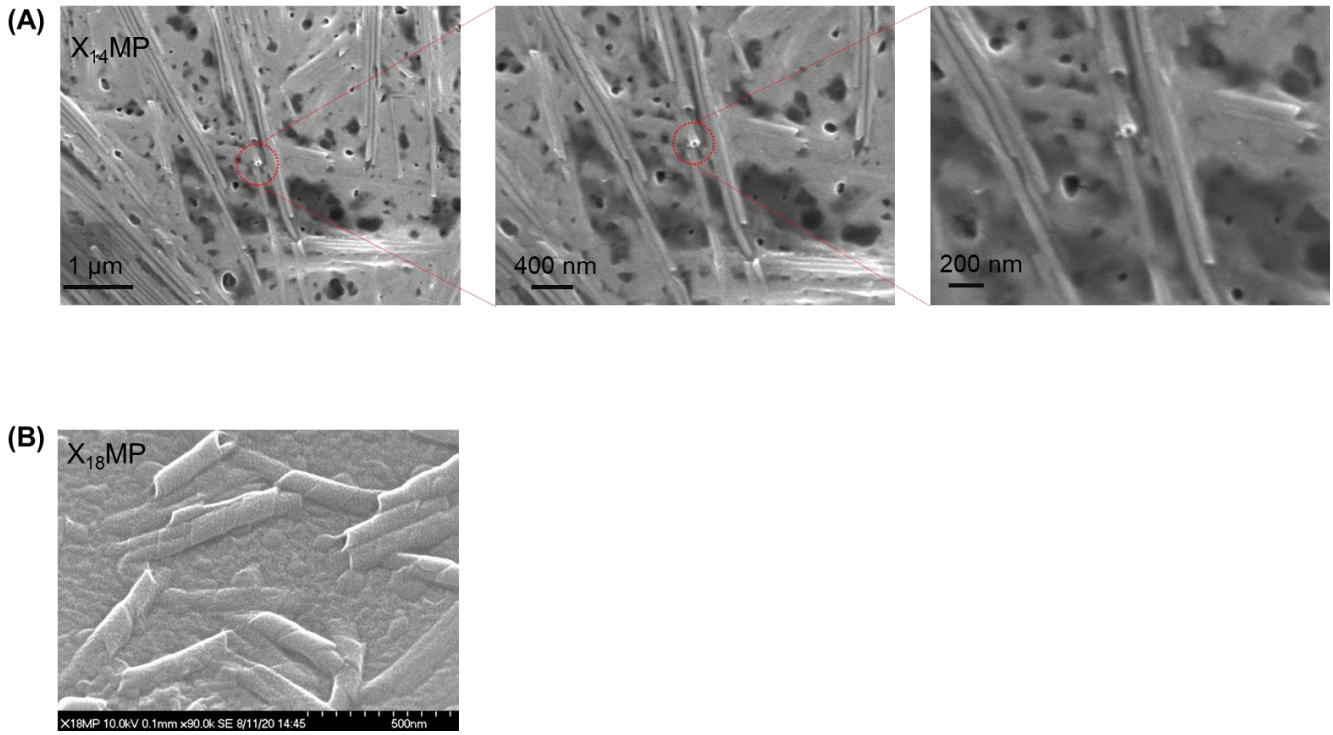

Figure S4. SEM images of (**A**) X_{14}MP and (**B**), X_{18}MP, respectively. The SEM images clearly indicate that X_{14}MP self-assembles into hollow tube structures and X_{18}MP self-assembles into helical ribbons.

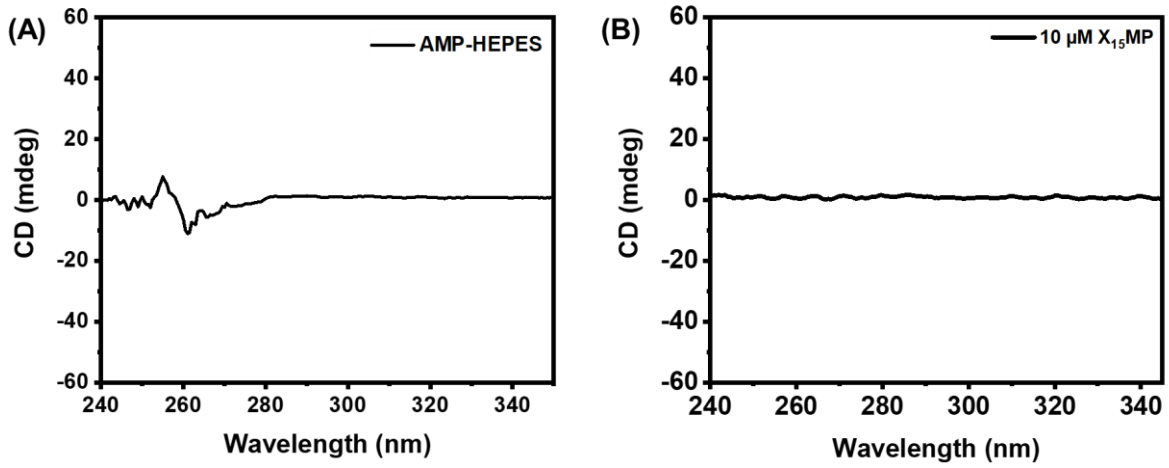

Figure S5. The CD spectrum of (**A**) pristine AMP and (**B**) X_{15}MP (10 µM) in HEPES buffer. The result suggests that AMP and X_{15}MP (below CAC) do not exhibit any CD signal under the test conditions.

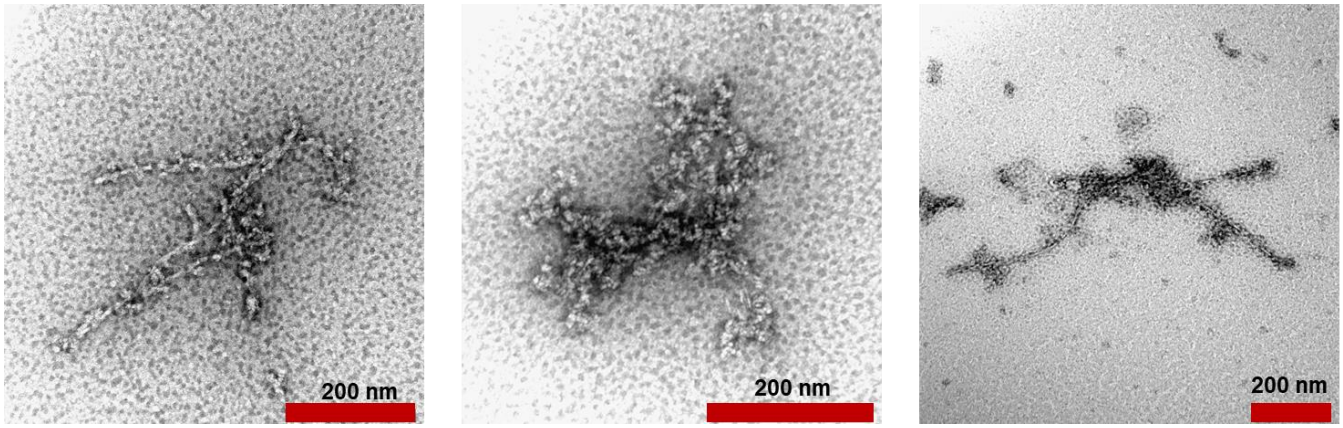

Figure S6. TEM images of X_{15}MP (0.5 µmol, total concentration 0.5 mM, below CAC) in 50 µL H_2O, precipitated with 950 µL acetone (f_a = 95%) show a mixture of random aggregates and helical fibers.

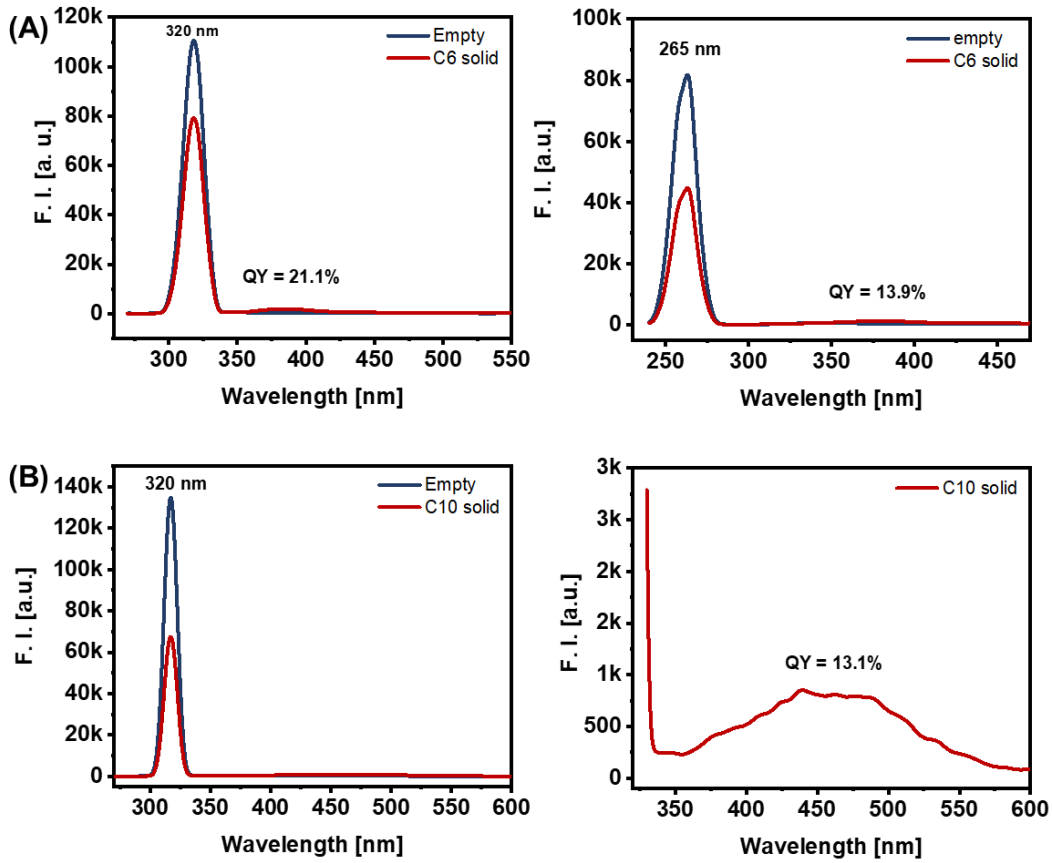

Figure S7. The fluorescence quantum yield (QY) of (**A**) C_6MP at 320 nm or 265 nm excitation wavelength and (**B**) C_{10}MP in solid state was calculated around 21.1 %, 13.9% and 13.1%, respectively. The blue curve resembles the empty cuvette measurement and the red curve shows the spectrum of the C_nMP solids. The excitation intensity was calculated as the difference between the blue and the red curve area at the excitation wavelength. The emission intensity was obtained as the integral of the whole emission band between 350 and 550 nm. The QY was calculated as follows: $\Phi = \frac{\int excitation\ wavelength\ (empty) - \int excitation\ wavelength\ (CnMP)}{\int emission\ band\ (CnMP)}$.

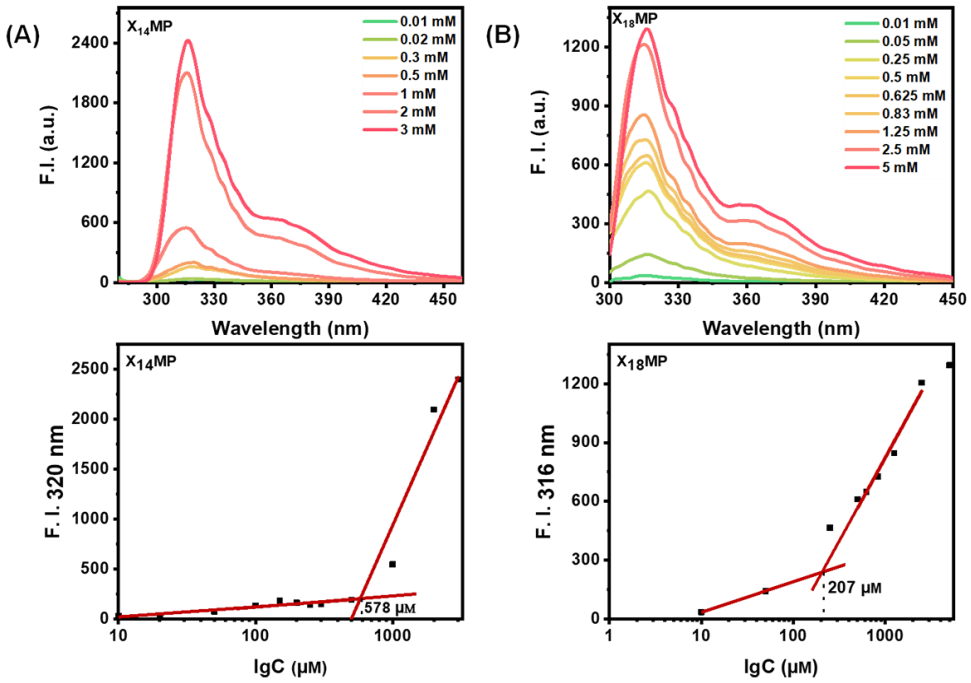

Figure S8. The concentration-dependent fluorescence behavior of (**A**) X_{14}MP and (**B**) X_{18}MP. The results show that the fluorescence intensity increases as the concentration of the monomer increases. In addition, the data can be used to determine the CAC of corresponding amphiphiles.

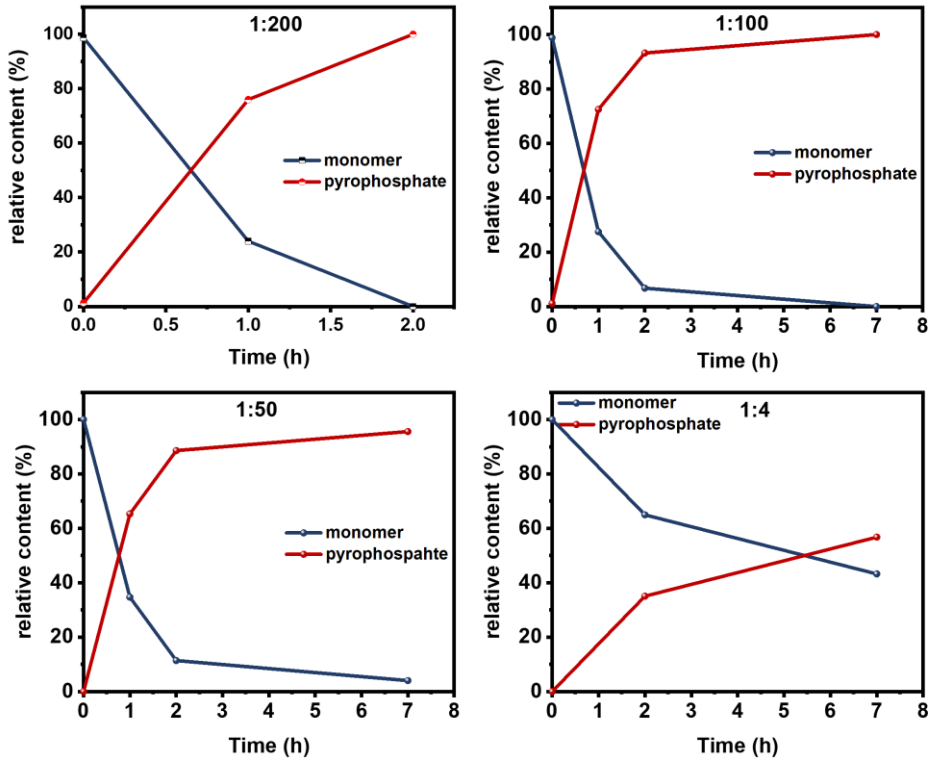

Figure S9. The molar ratio (X_{15}MP:EDC) effect on the EDC-triggered dimerization reaction of X_{15}MP was evaluated, including 1:200, 1:100, 1:50, and 1:4. X_{15}MP concentration was 500 μM in condensation buffer.

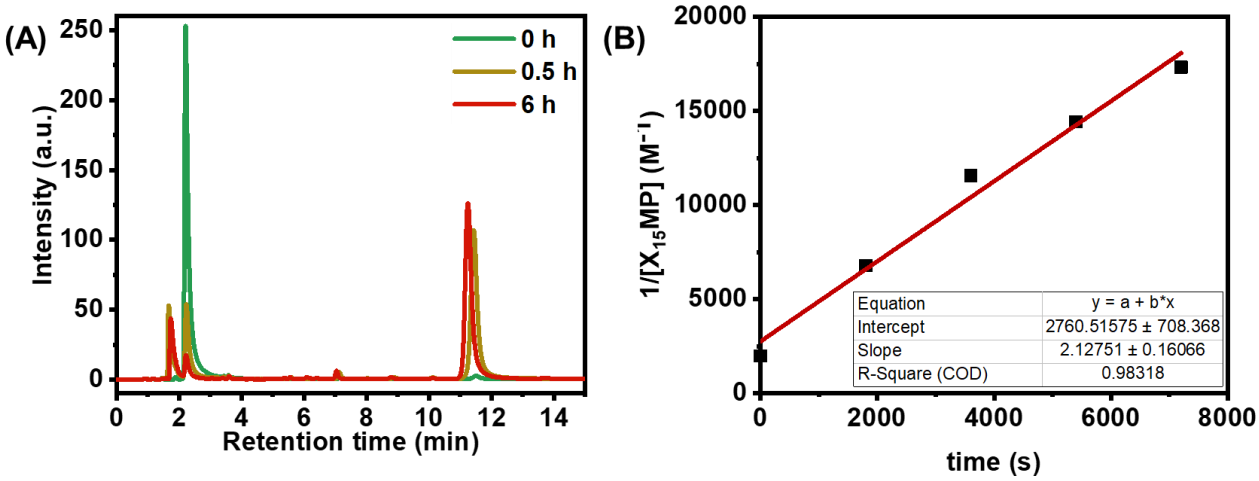

Figure S10. The reaction kinetics of the dimerization of X_{15}MP. (**A**) The HPLC chromatogram of the dimerization of X_{15}MP in the presence of EDC over 6 h. The X_{15}MP peak (2.2 min) decreases while the X15ppX15 (11.5 min) forms. (**B**) Experimental determination of the second-order rate constant of the reaction between X_{15}MP (0.5 mM) and EDC (25 mM), where $\frac{1}{[X15MP][M-1]}$ is plotted against the reaction time (s) and the slope equals the rate constant.

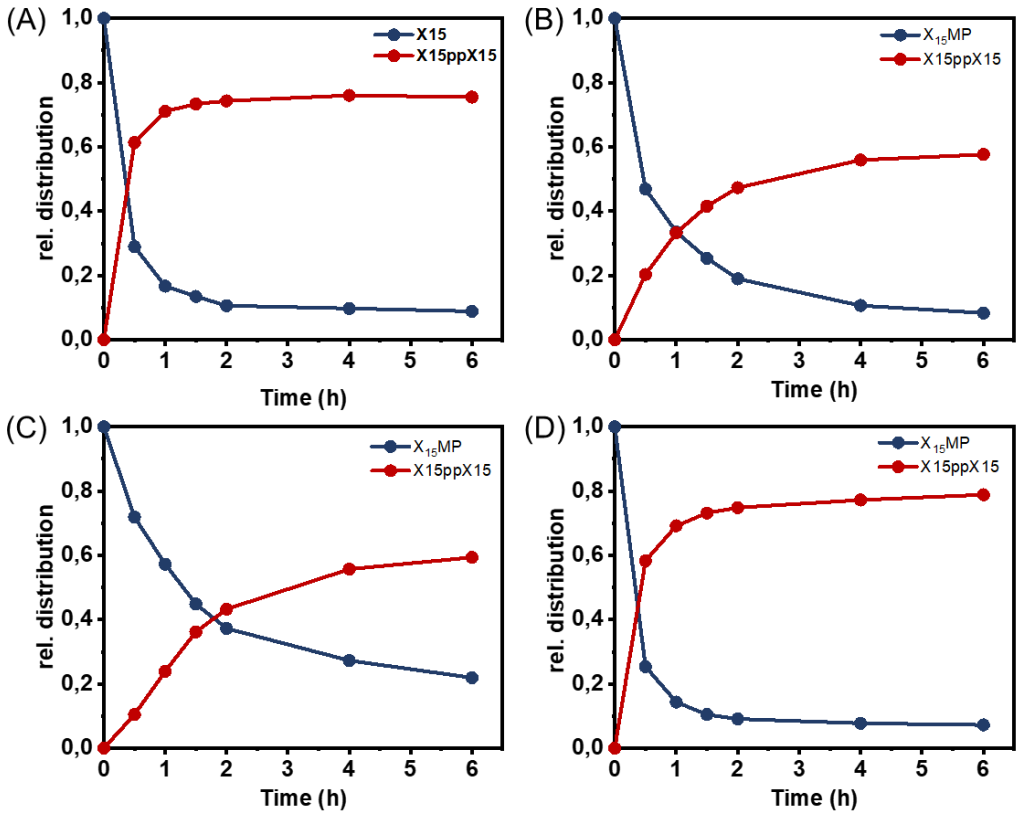

Figure S11. Further kinetic studies of the dimerization of **X_{15}MP** (0.5 mM, below CAC) in condensation buffer (**A**) at 25 °C (pH = 7.5) (these are the standard conditions), (**B**) at 10 °C (pH = 7.5), (**C**) at 0 °C (pH = 7.5) and (**D**) at pH = 6.0 (T = 25 °C), . respectively

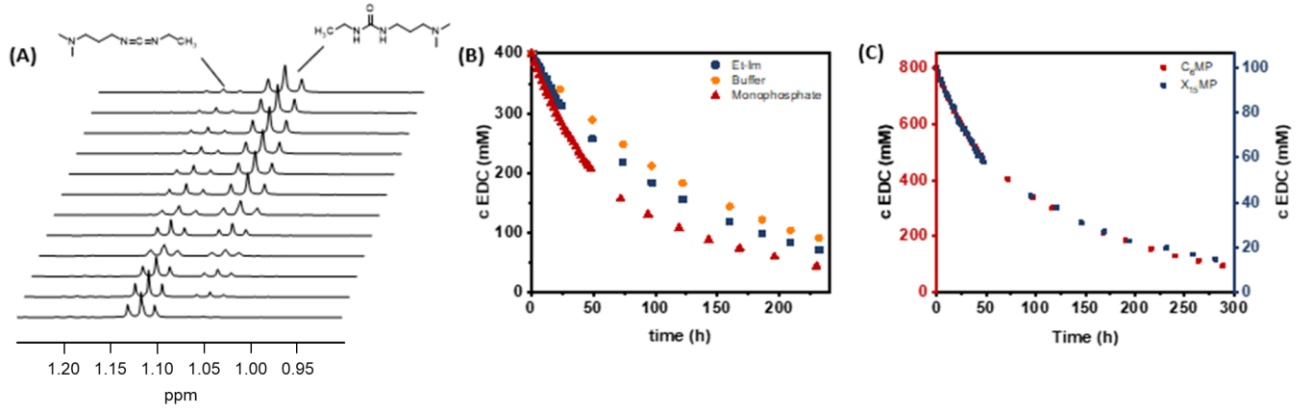

Figure S12. The hydrolysis kinetics of EDC. (**A**) The ^{1}H NMR shows how EDC is used up and EDU forms over time. (**B**) Comparison of three different conditions: Hydrolysis of EDC (0.4 M) in pure MOPS buffer (0.5 M MOPS, 0.08 M MgCl2, 10% D_2O) (orange), hydrolysis in the buffer containing 1-ethylimidazole (0.5 M MOPS, 0.15 M EtIm, 0.08 M $MgCl_2$) (blue), hydrolysis due to monophosphate activation (5 mM C_6MP) (red). The data show that a major part of the EDC in the system is consumed by the activation of the monophosphate. (**C**) Comparison of consumption of EDC (160 eq. compared to the monophosphates, respectively) in a system with different monophosphates, C_6MP (red) and X_{15}MP (blue). The activation chemistry of different monophosphates is similar.

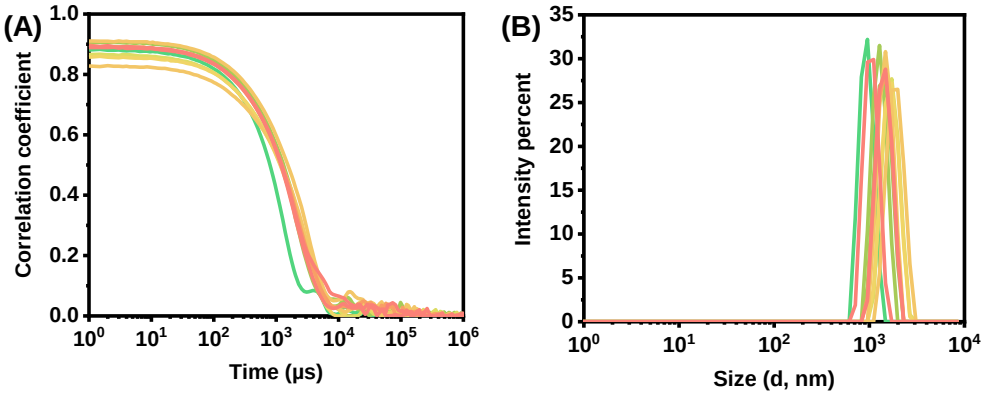

Figure S13. Characterization of isolated X15ppX15 (200 µM) by DLS. (**A**) Correlograms (**B**) Size distribution. The results indicated that X15ppX15 formed large aggregates when the concentration of X15ppX15 was above its CAC.

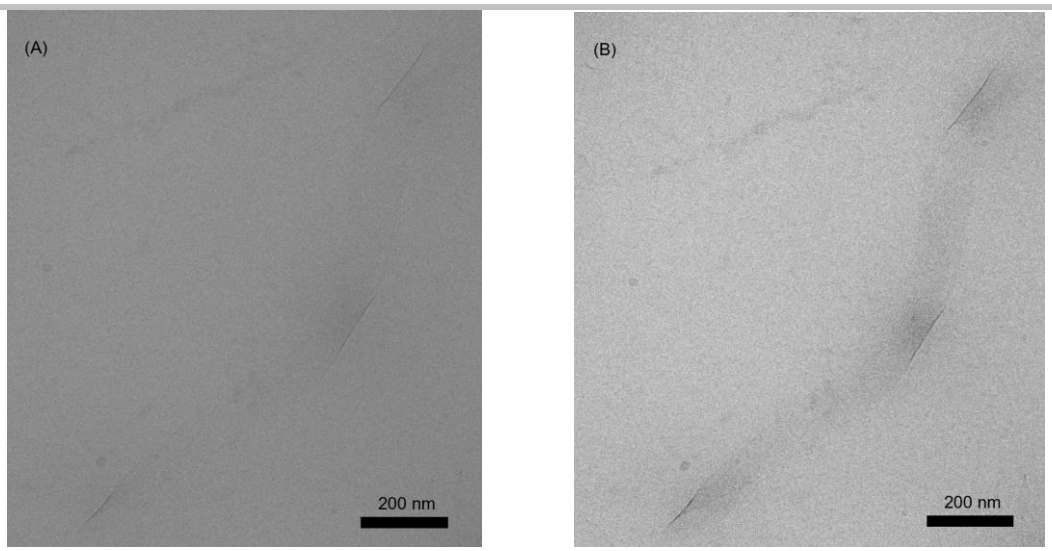

Figure S14. Cryo-TEM of the X_{15}MP dimerization. A 500 μM (below CAC) solution of X_{15}MP in condensation buffer was dimerized with 50 eq. EDC and cryo-TEM was measured after 2 h. (**A**) Original image and (**B**) image after enhancing the contrast with the softwares ImageJ and Adobe Photoshop. The formation of helical aggregates in solution is confirmed.

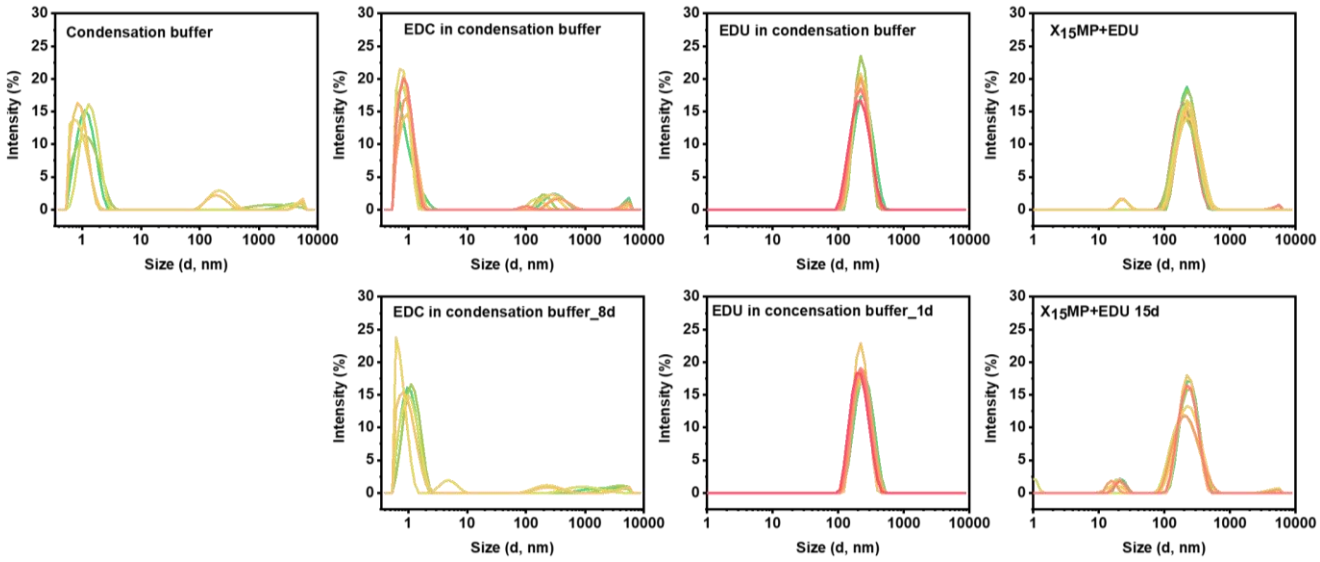

Figure S15. The control DLS experiments, including (i) condensation buffer, (ii) EDC in condensation buffer over different times, (iii) EDU in condensation buffer over different times, (iv) X_{15}MP+EDC in condensation buffer over different time. All the results indicate that the control experiments do not form large aggregates.

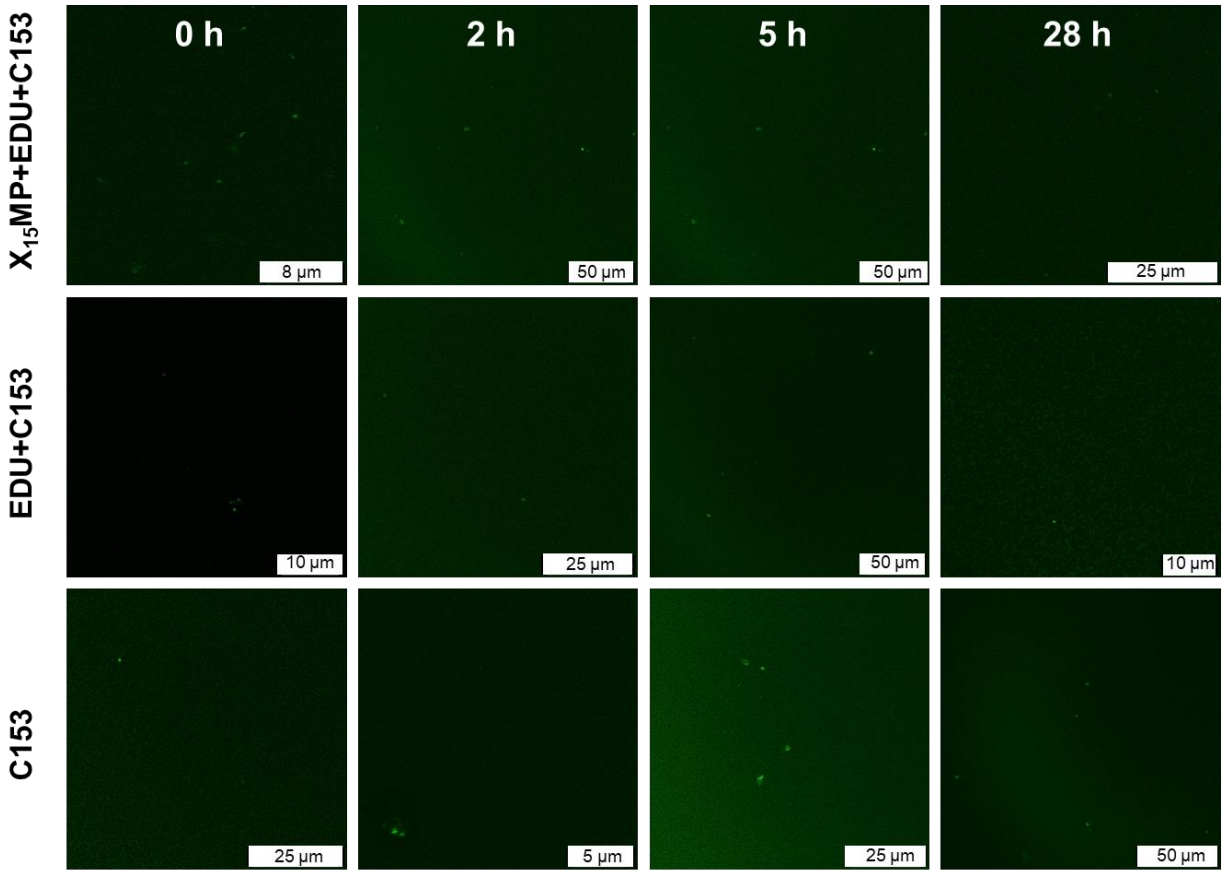

Figure S16. The control CLSM experiments, including (i) X_{15}MP+EDU+C153, (ii) EDU+C153, (iii) C153. The CLSM images over time indicate that there is no aggregation formed under these control conditions. (C153: Coumarin-153 dye).

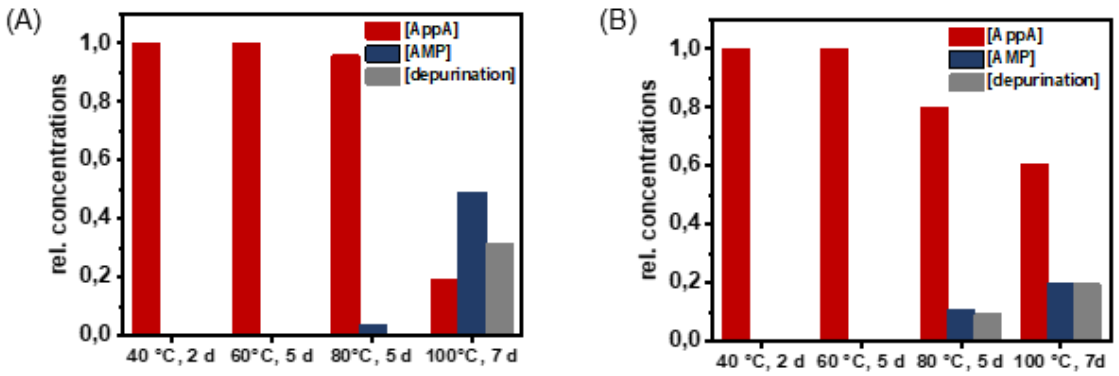

Figure S17. Additional data on the hydrolysis of AppA under (**A**) neutral and (**B**) alkaline (0.02 M NaOH) conditions.

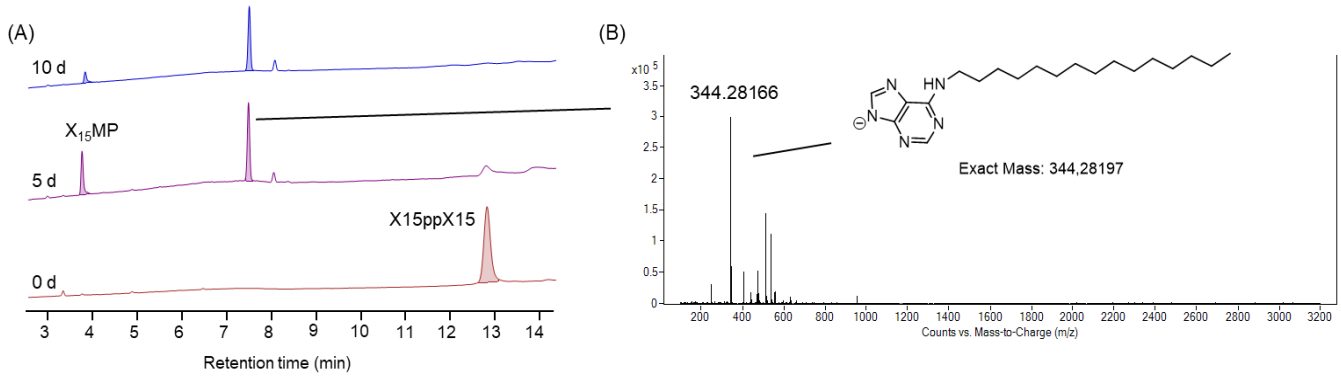

Figure S18. Hydrolysis of X15ppX15 monitored by HPLC-MS. (**A**) Stacked chromatograms after 0, 5 and 10 days. (**B**) Mass spectrum of the depurination product. A 1 mM solution of X15ppX15 in aqueous solution containing 4 eq. $EuCl_3$ (pH ≈ 6) was stirred at 60 °C. HPLC was performed on an Agilent Infinity Lab Poroshell 120 EC-C18 column (3.0 x 100mm, 2.7 µm).

Table S1. The hydrolysis studies of X15ppX15 under different conditions, including pH, lanthanide salt, temperature, and enzyme.

	Conditions	Product
	MES buffer, pH 5.87, 25°C	pyrophosphate
	MES buffer, pH 5.87, 37°C	pyrophosphate
	MES buffer+100µM Tb^{3+}, pH 6.04, 25°C	pyrophosphate
X15:EDC = 1:50	MES buffer+100µM Tb^{3+}, pH 6.04, 37°C	pyrophosphate
	MES buffer+100µM Eu^{3+}, pH 5.92, 25°C	pyrophosphate
	MES buffer+100µM Eu^{3+}, pH 5.92, 37°C	pyrophosphate
	HEPES buffer, pH 7.46+Enzyme, 37°C	pyrophosphate
X15ppX15	HEPES buffer, pH 7.46+Enzyme, 37°C	pyrophosphate

NMR spectra

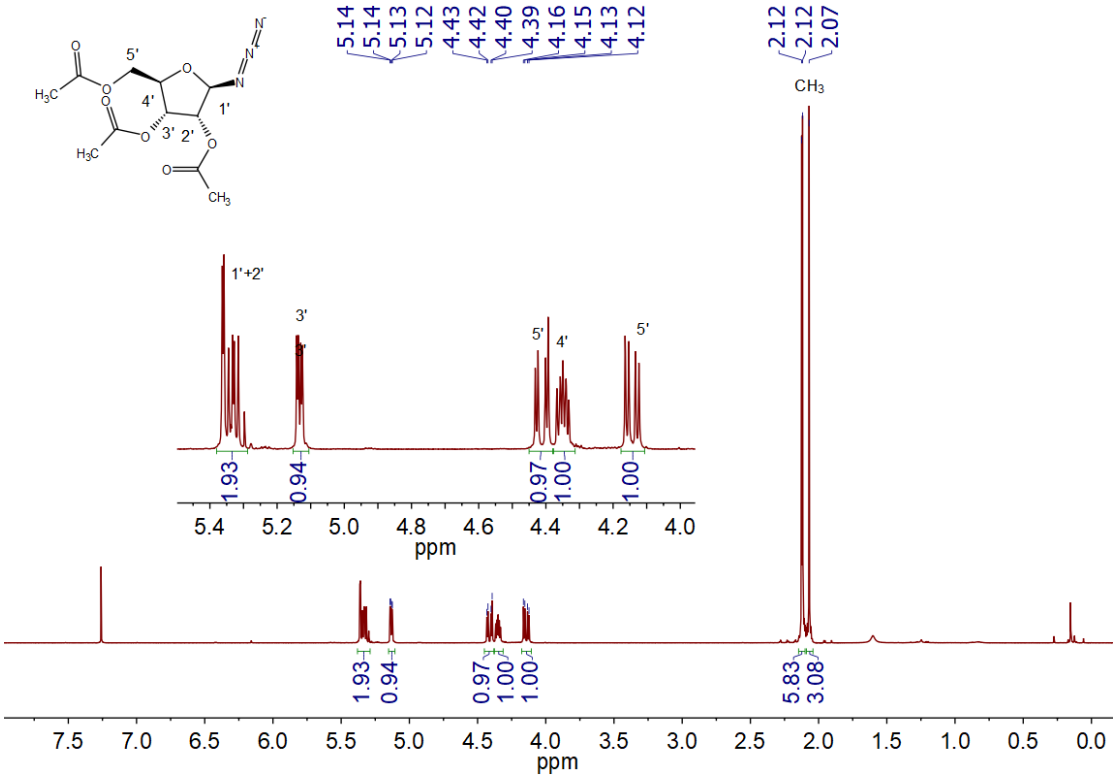

Figure S19. ^{1}H NMR spectrum of compound **2** ($CDCl_3$, 400 MHz, 295 K).

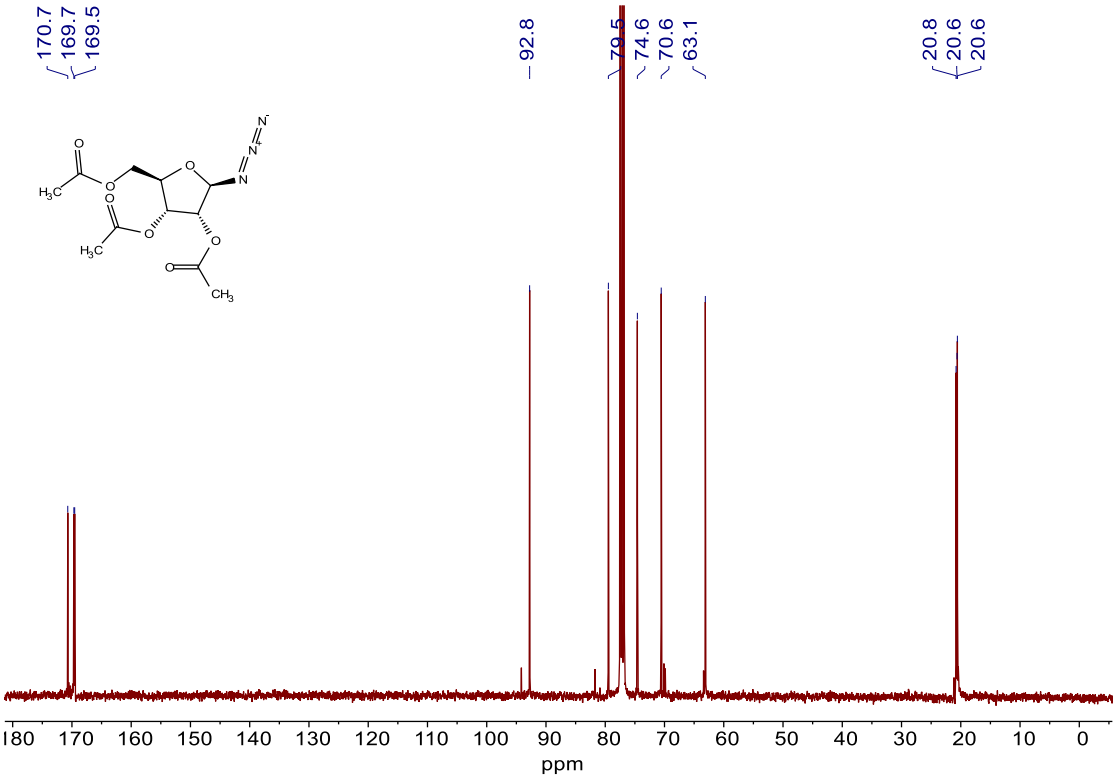

Figure S20. ^{13}C NMR spectrum of compound **2** ($CDCl_3$, 101 MHz, 295 K).

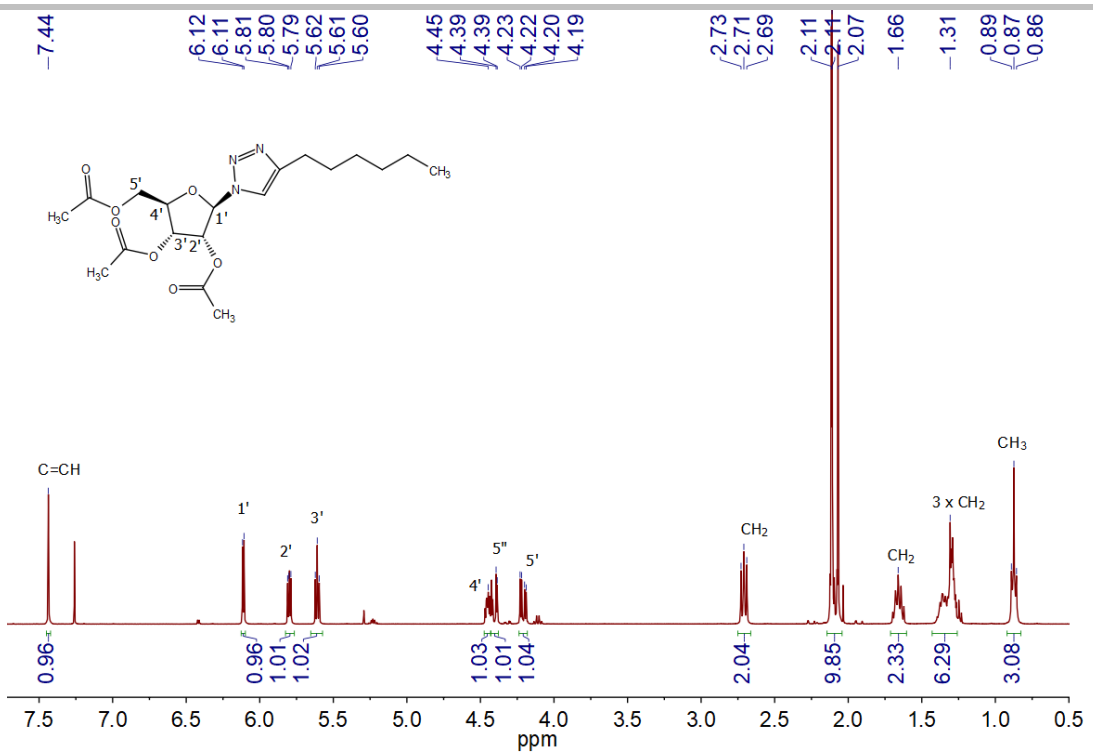

Figure S21. ^{1}H NMR spectrum of compound **3** ($CDCl_3$, 400 MHz, 295 K).

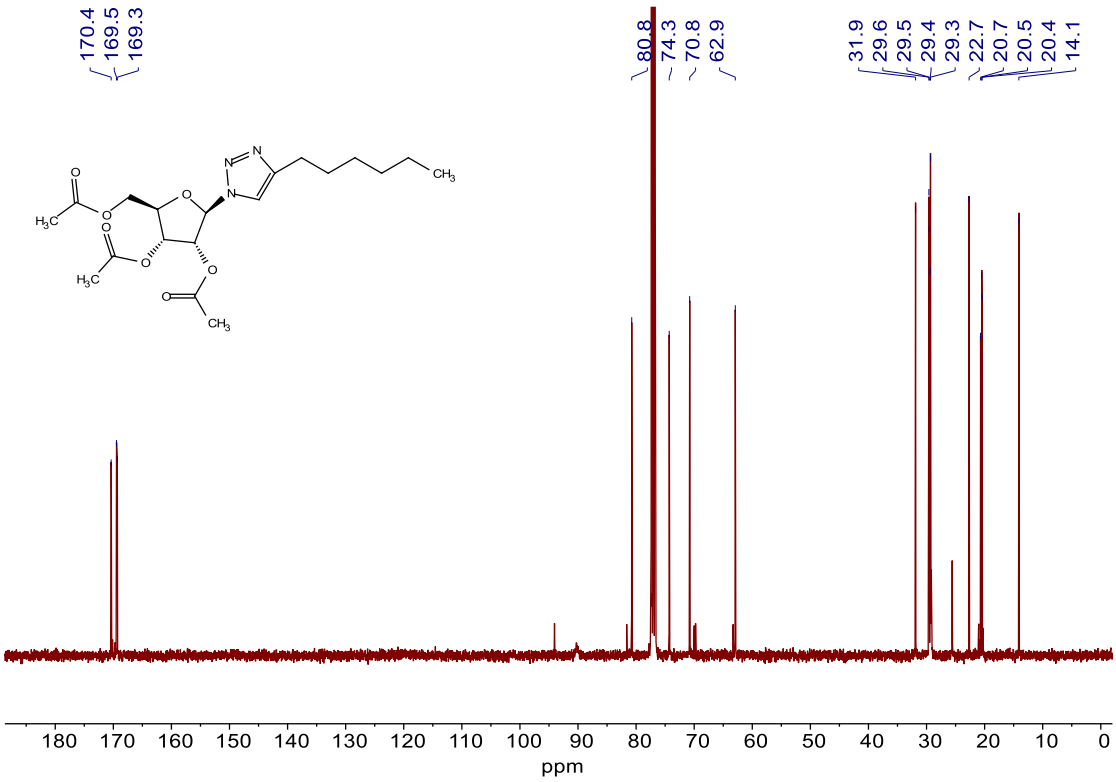

Figure S22. ^{13}C NMR spectrum of compound **3** ($CDCl_3$, 101 MHz, 295 K).

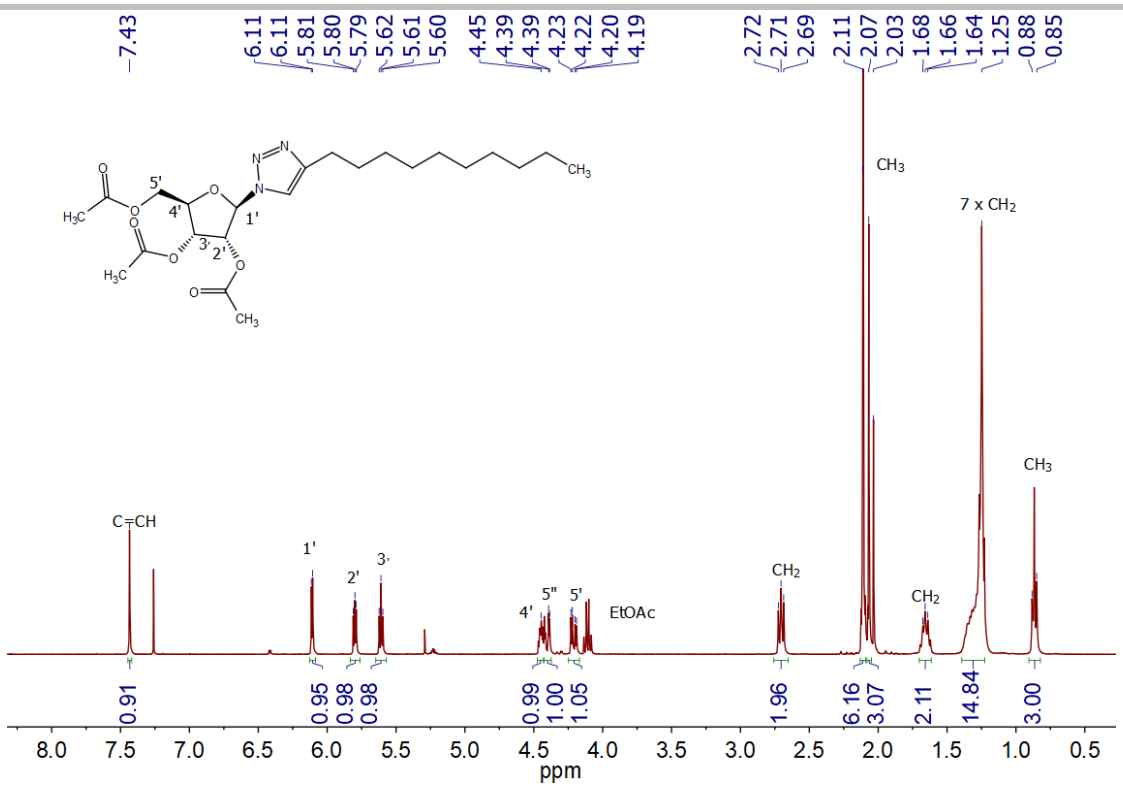

Figure S23. ^{1}H NMR spectrum of compound **4** ($CDCl_3$, 400 MHz, 295 K).

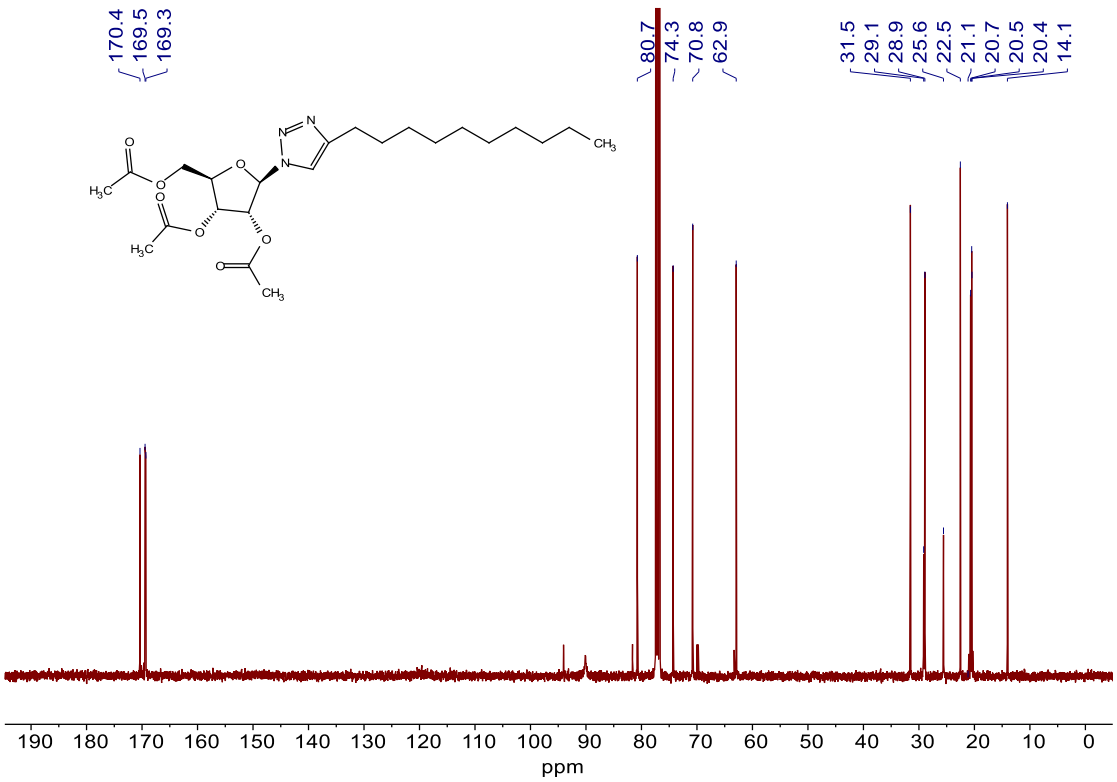

Figure S24. ^{13}C NMR spectrum of compound **4** ($CDCl_3$, 101 MHz, 295 K).

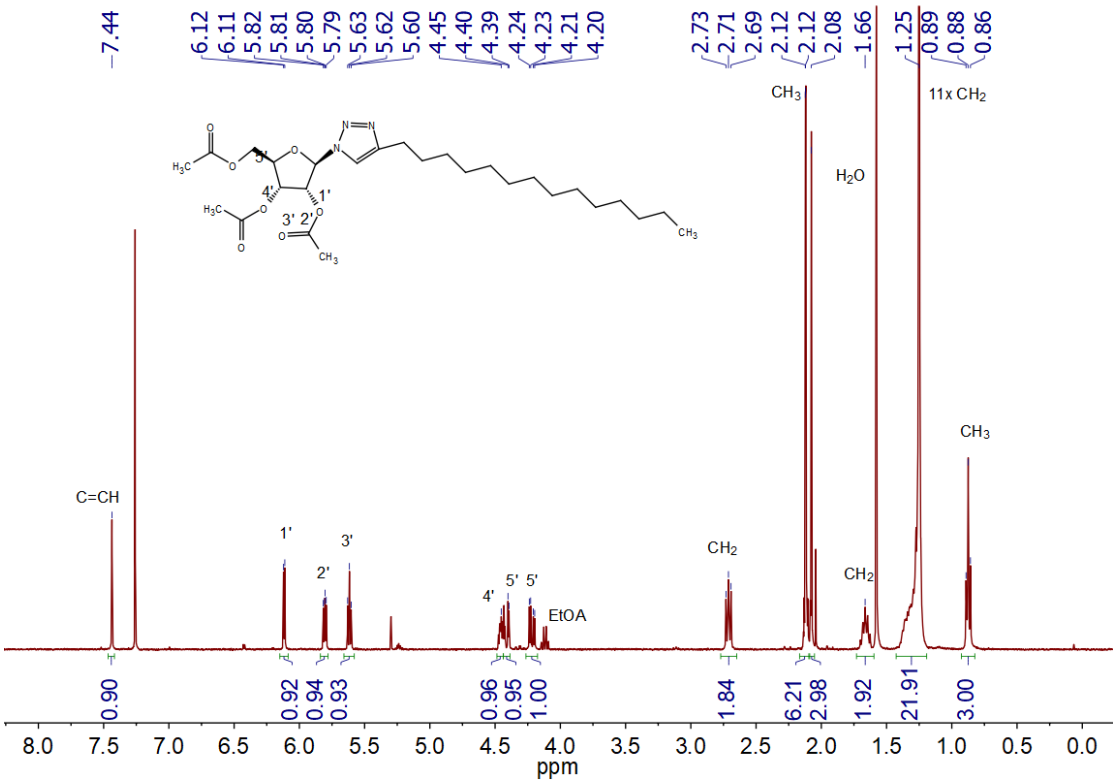

Figure S25. ^{1}H NMR spectrum of compound **5** ($CDCl_3$, 400 MHz, 295 K).

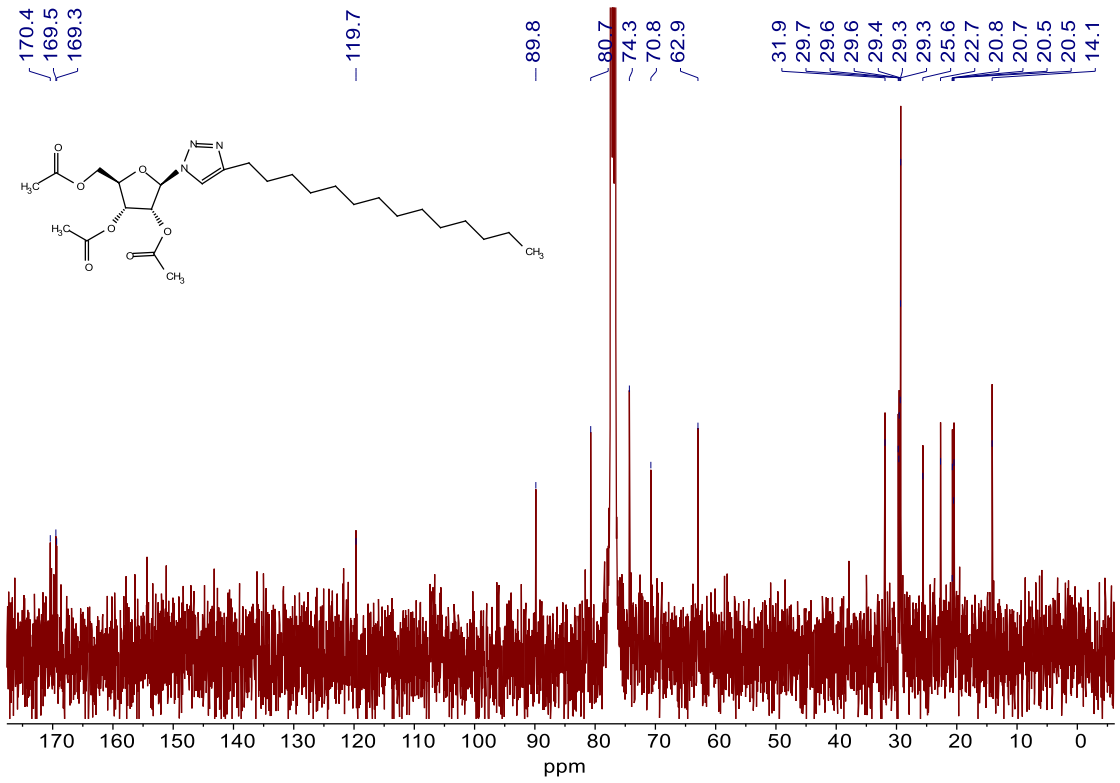

Figure S26. ^{13}C NMR spectrum of compound **5** ($CDCl_3$, 101 MHz, 295 K).

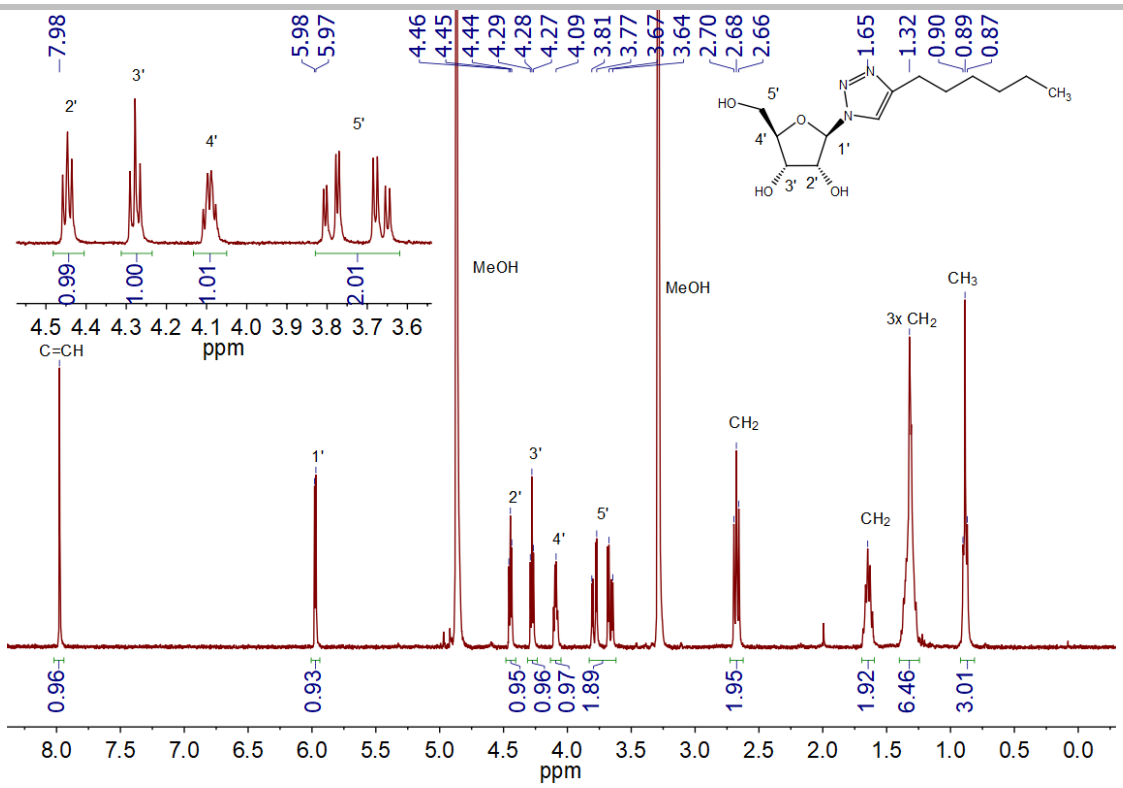

Figure S27. ^{1}H NMR spectrum of compound **6** ($CDCl_3$, 400 MHz, 295 K).

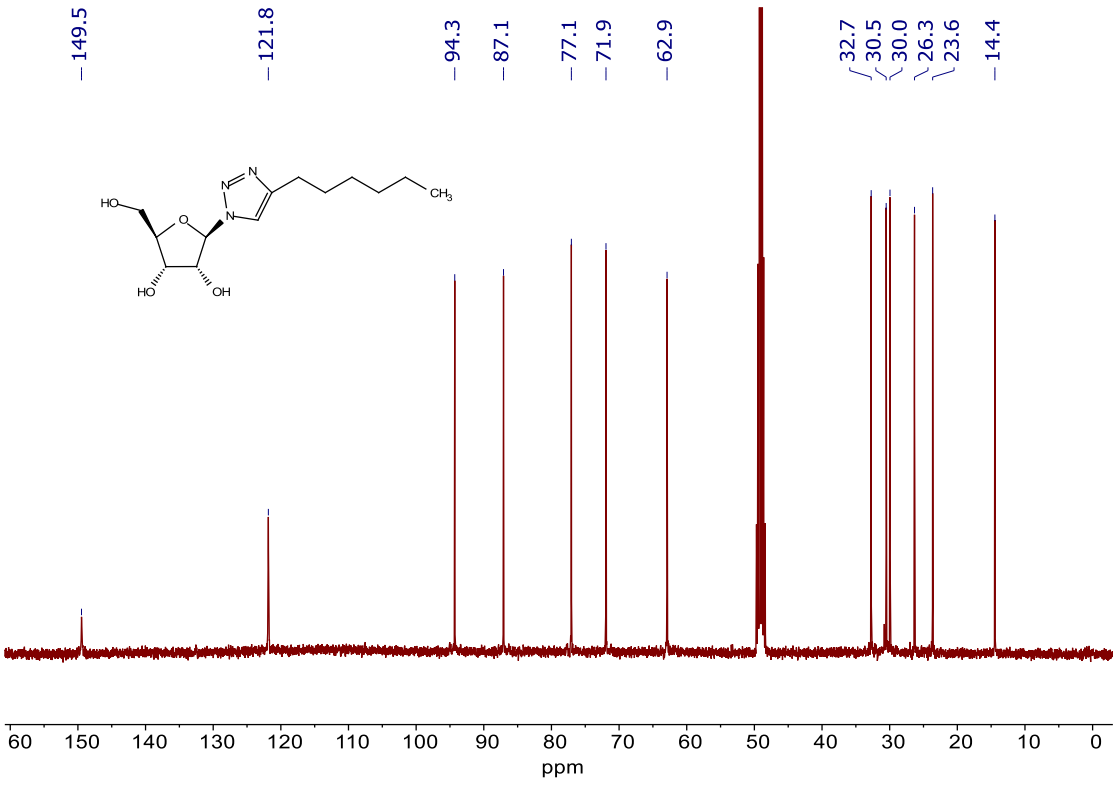

Figure S28. ^{13}C NMR spectrum of compound **6** ($CDCl_3$, 101 MHz, 295 K).

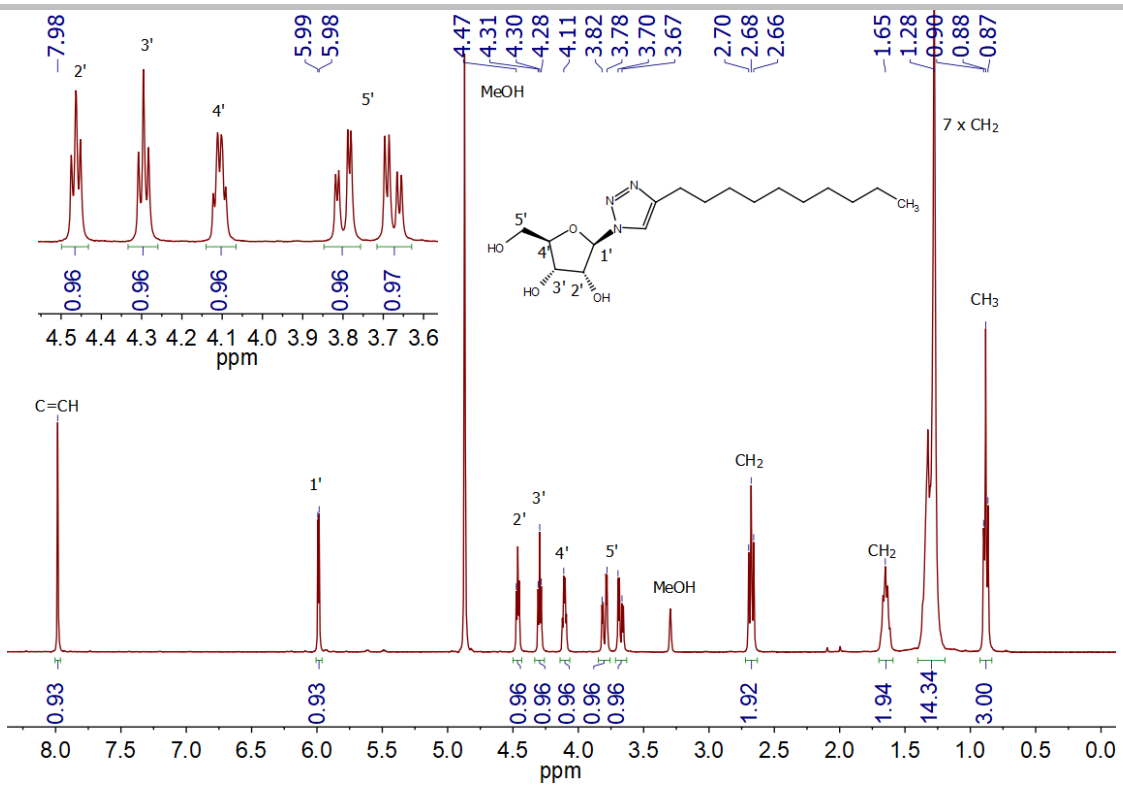

Figure S29. ^{1}H NMR spectrum of compound **7** ($CDCl_3$, 400 MHz, 295 K).

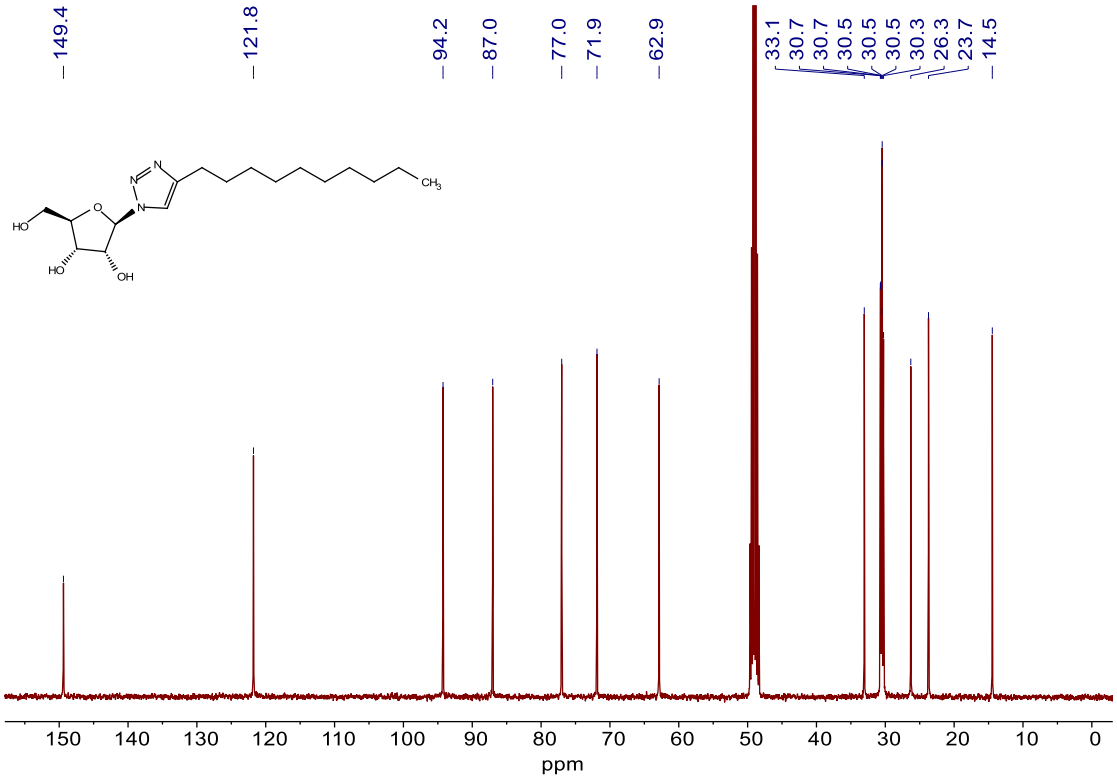

Figure S30. ^{13}C NMR spectrum of compound **7** ($CDCl_3$, 101 MHz, 295 K).

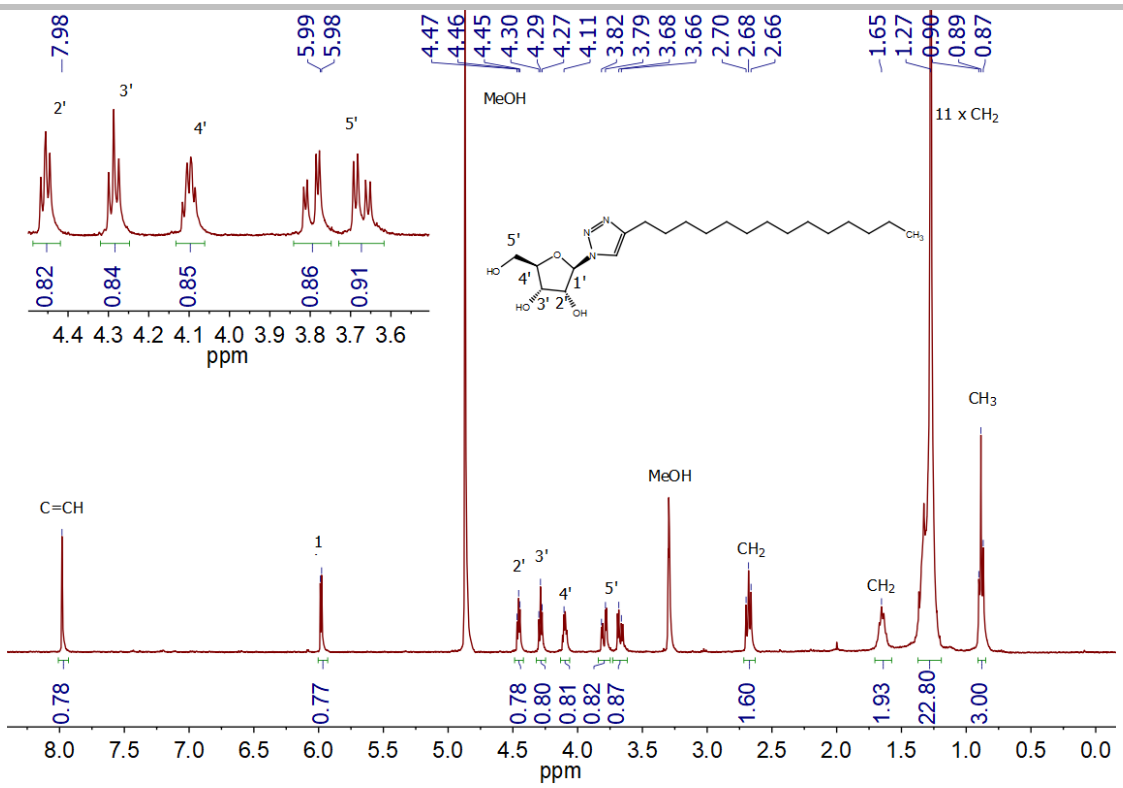

Figure S31. ^{1}H NMR spectrum of compound **8** ($CDCl_3$, 400 MHz, 295 K).

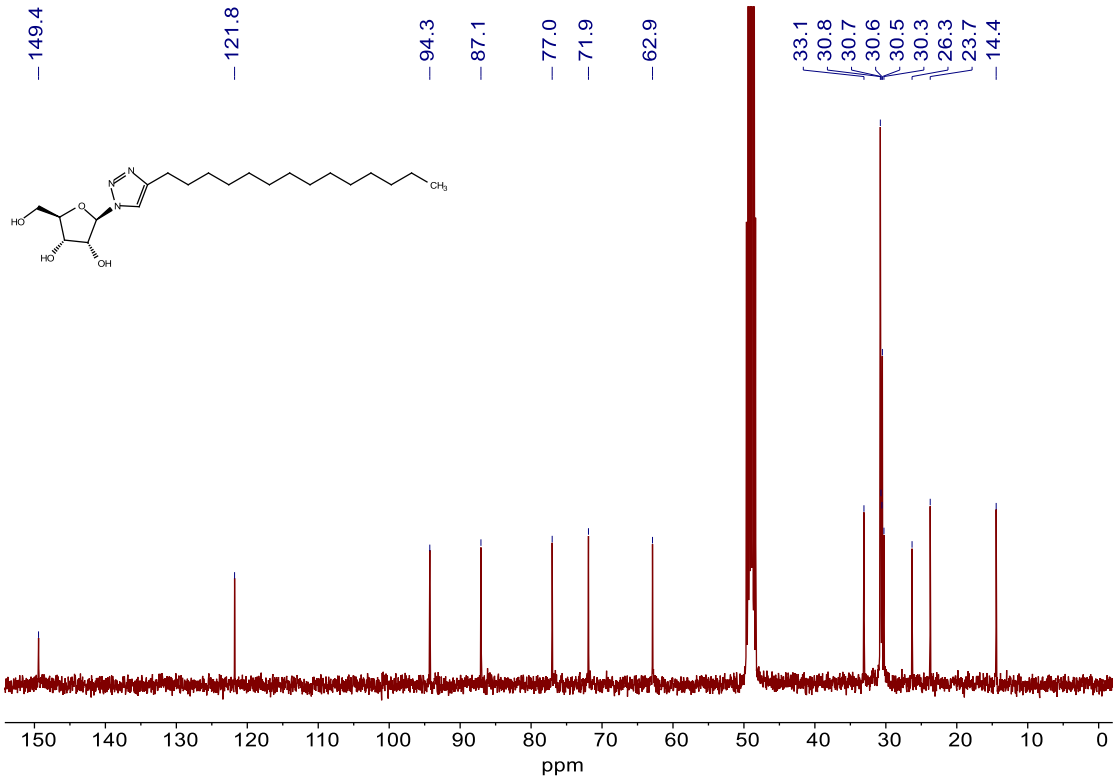

Figure S32. ^{13}C NMR spectrum of compound **8** ($CDCl_3$, 101 MHz, 295 K).

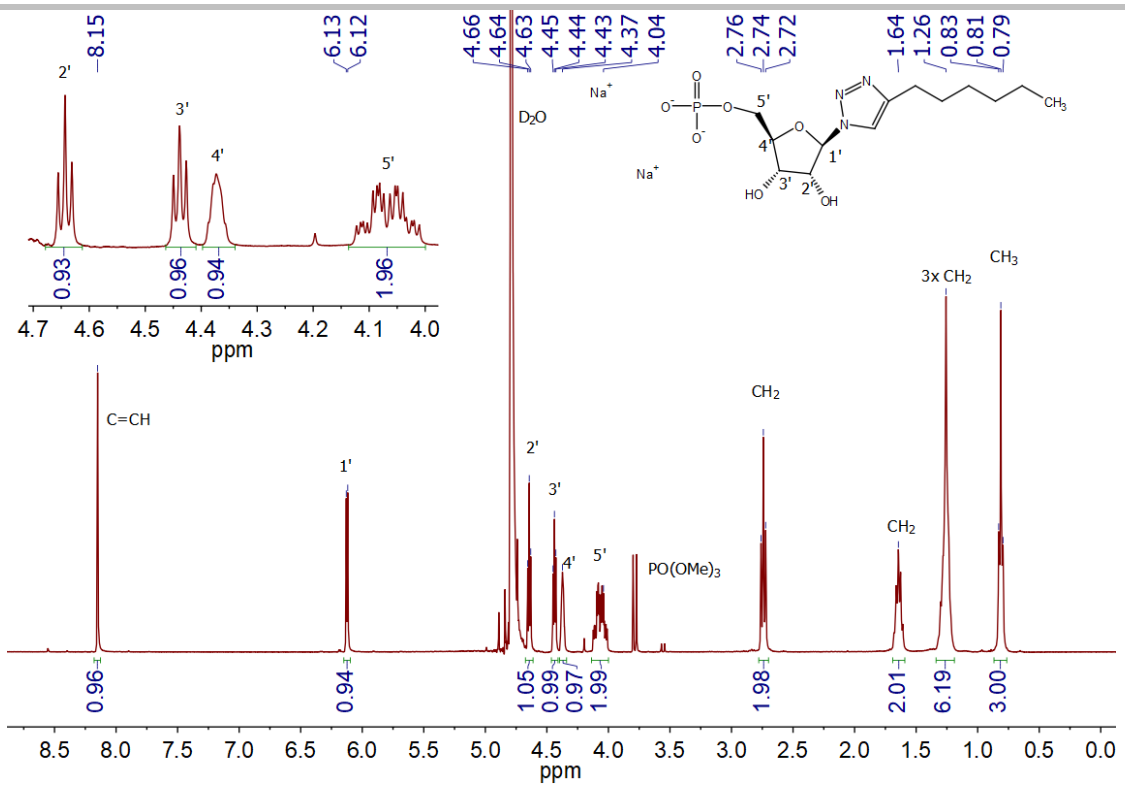

Figure S33. ^{1}H NMR spectrum of compound **9** ($CDCl_3$, 400 MHz, 295 K).

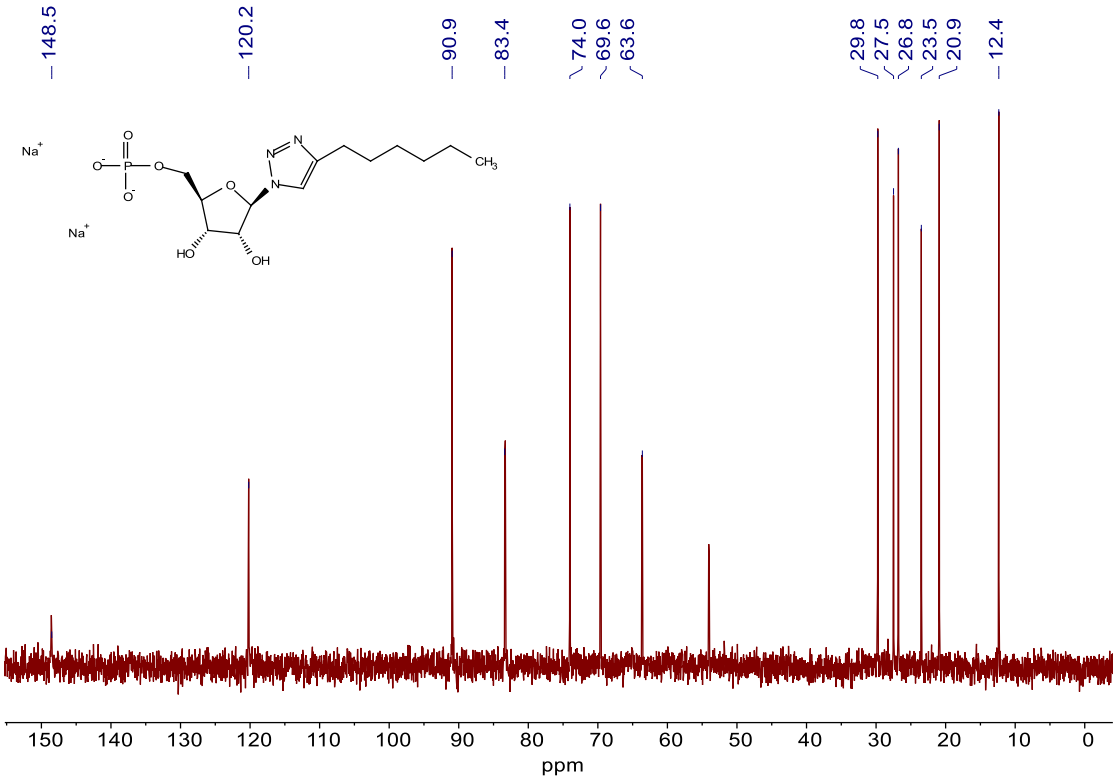

Figure S34. ^{13}C NMR spectrum of compound **9** ($CDCl_3$, 101 MHz, 295 K).

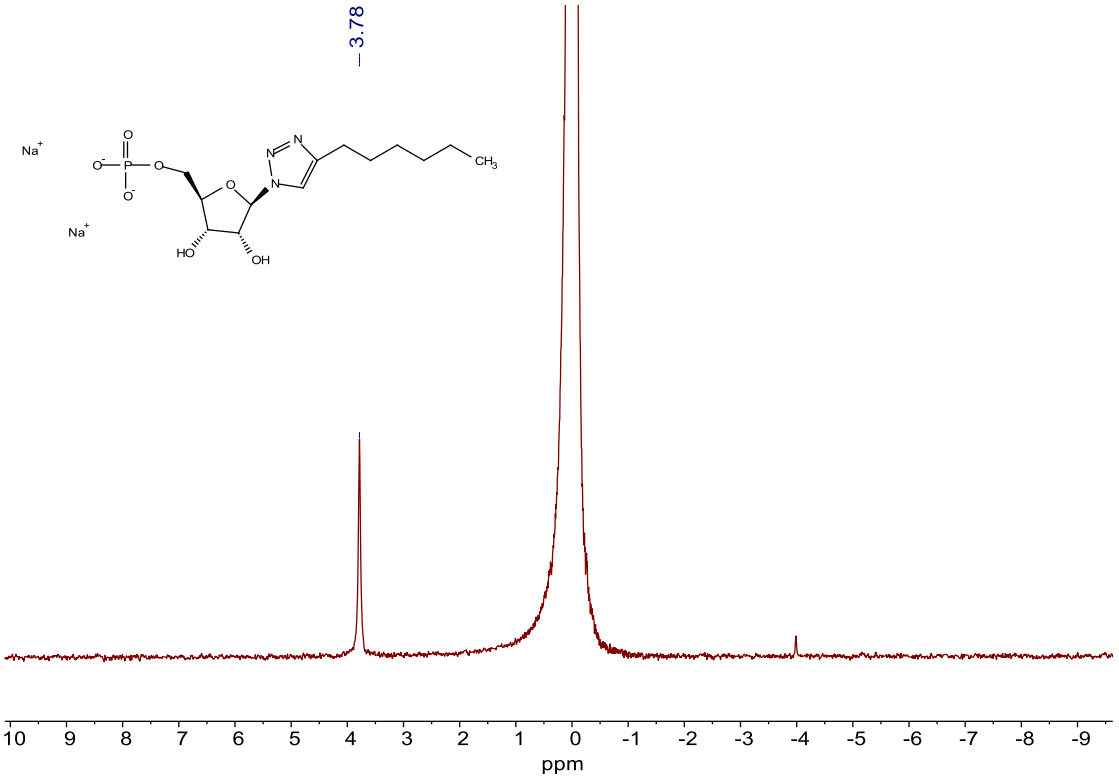

Figure S35. ^{31}P NMR spectrum of compound **9** (HEPES buffer pH = 7.50 (10% D_2O), against 85% H_3PO_4, 162 MHz, 295 K)

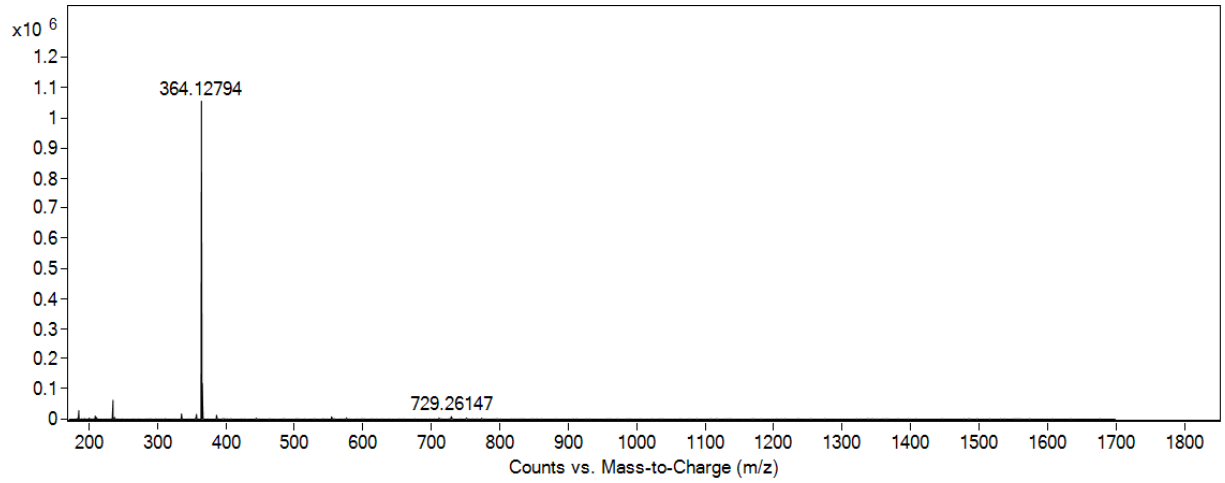

Figure S36. HR-MS (-) of compound **9**.

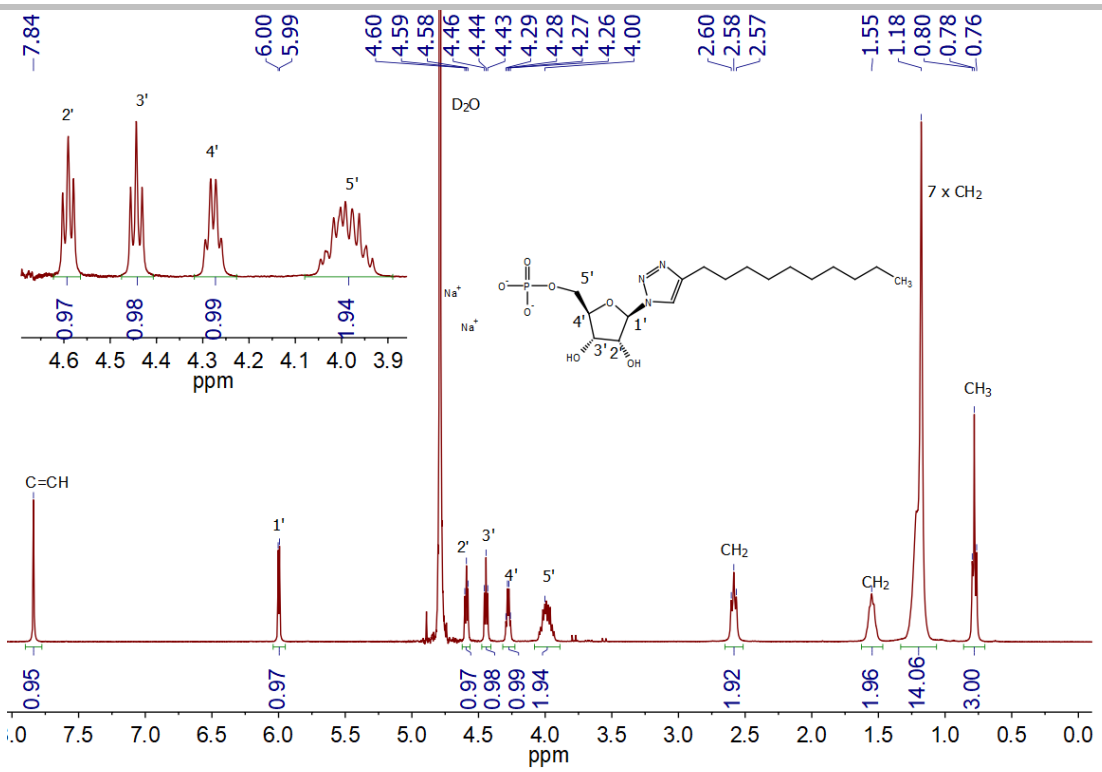

Figure S37. ^{1}H NMR spectrum of compound **10** (D_2O, 400 MHz, 295 K).

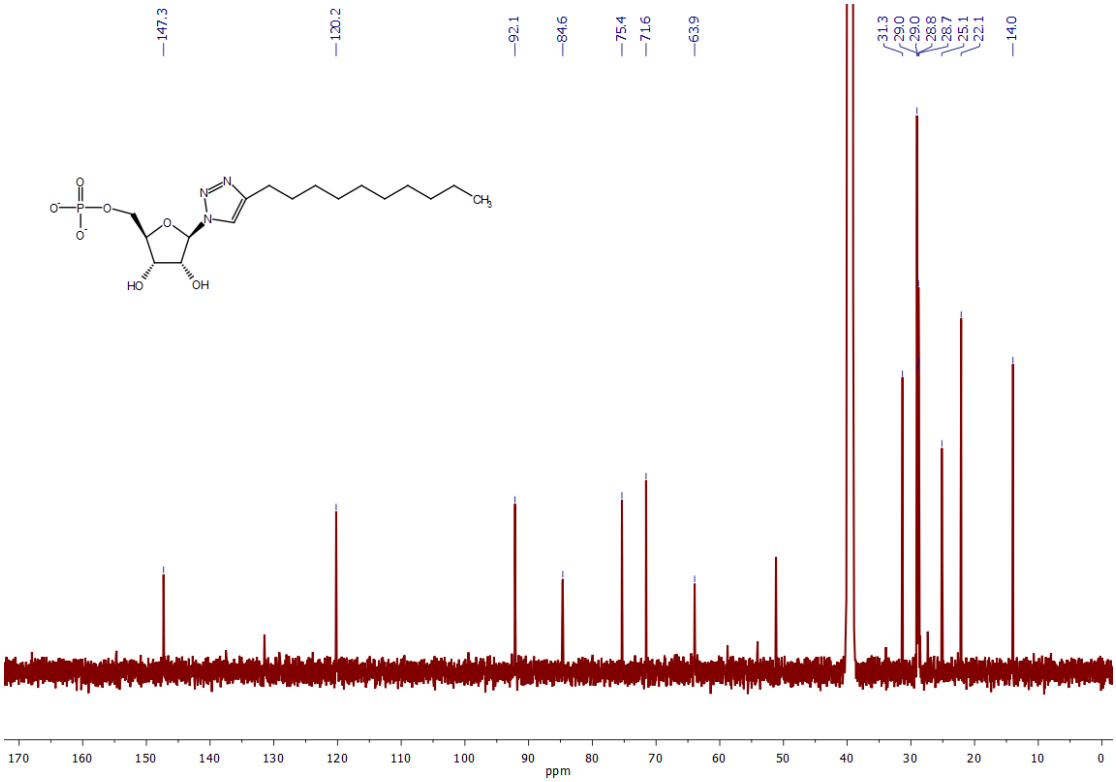

Figure S38. ^{13}C NMR spectrum of compound **10** (DMSO-d_6, 101 MHz, 295 K).

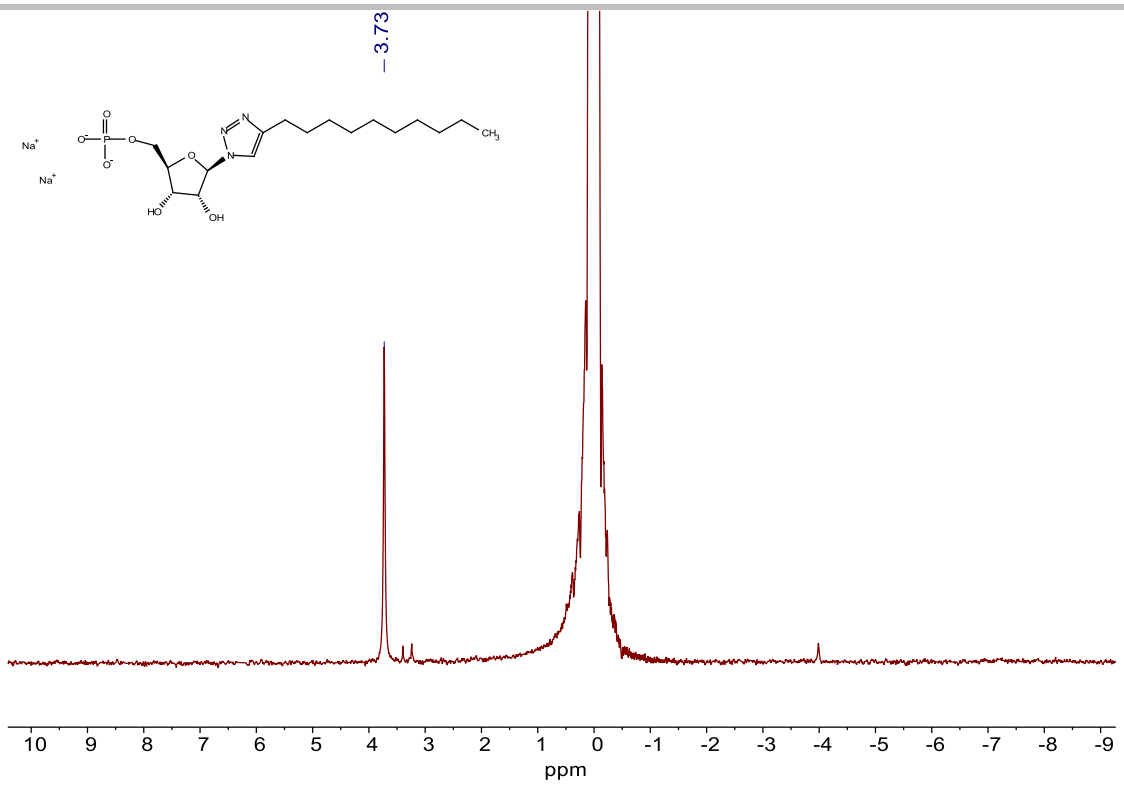

Figure S39. **^{31}P NMR** spectrum of compound **10** (HEPES buffer pH = 7.50 (10% D_2O), against 85% H3PO4, 162 MHz).

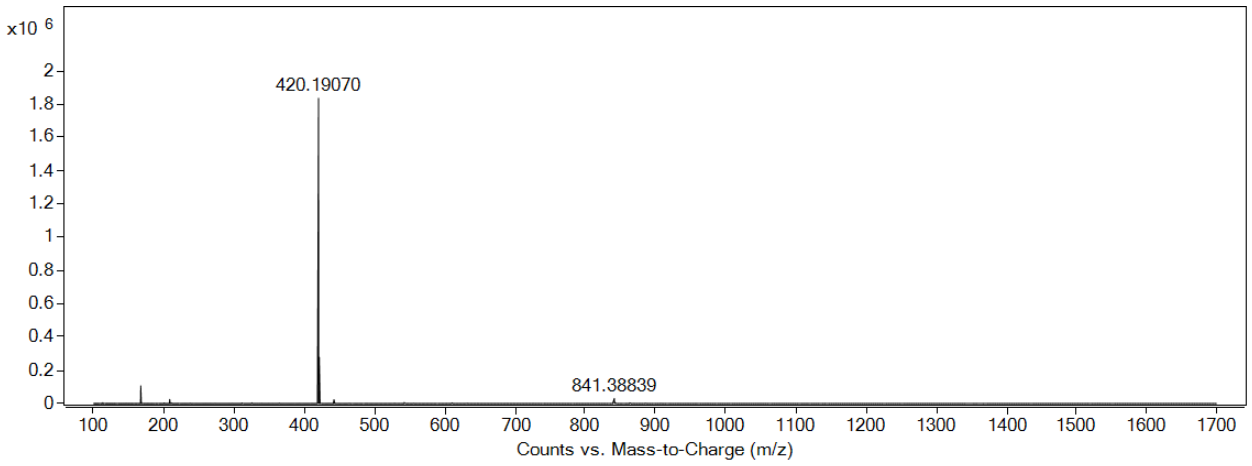

Figure S40. HR-MS (-) of compound **10**.

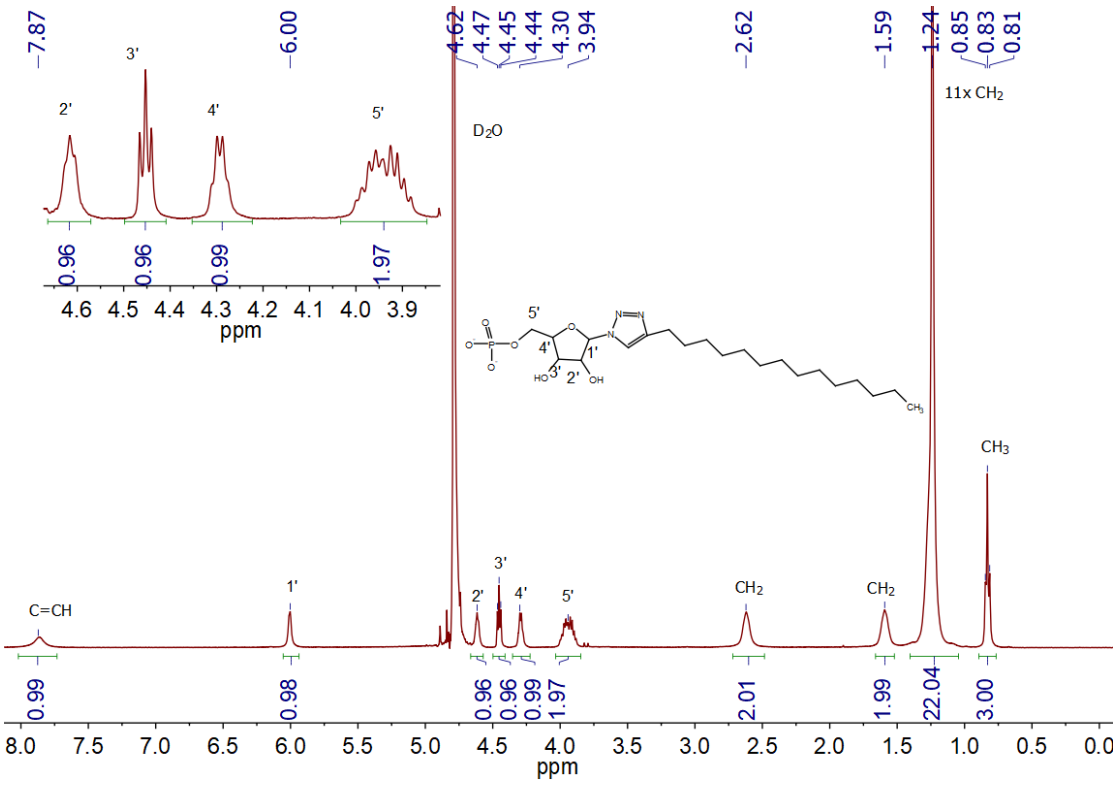

Figure S41. ^{1}H NMR spectrum of compound **11** (D_2O, 400 MHz, 295 K).

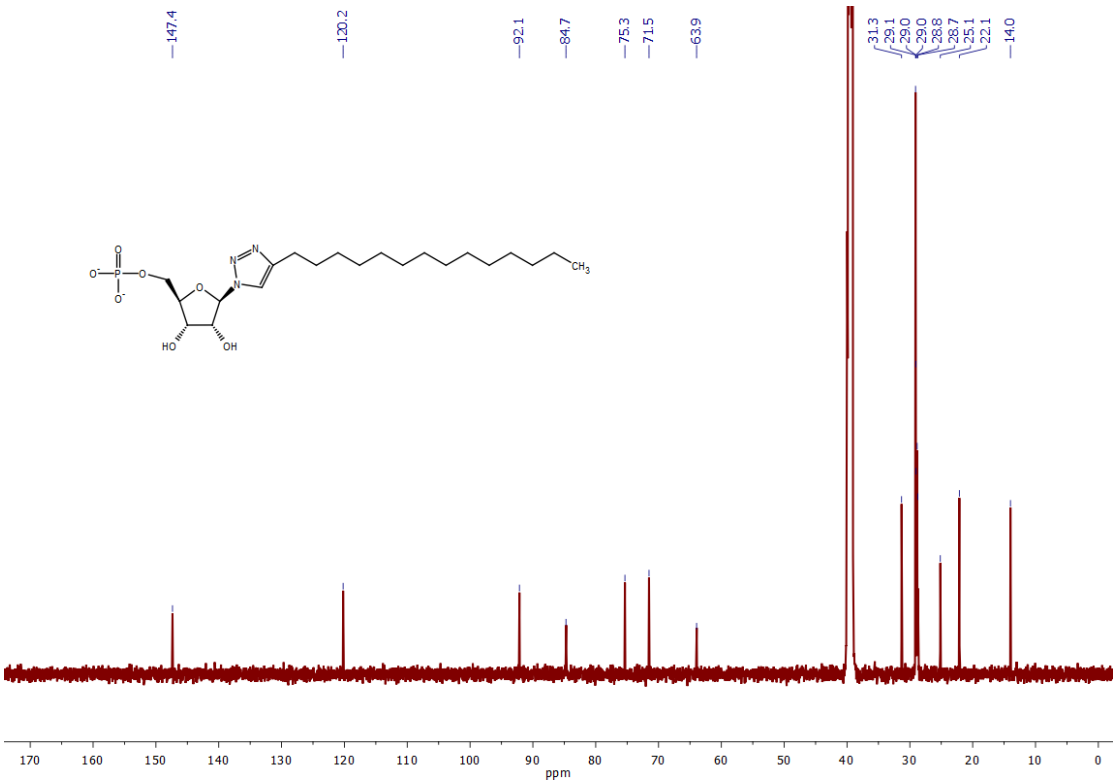

Figure S42. ^{13}C NMR spectrum of compound **11** (DMSO-d_6, 101 MHz, 295 K).

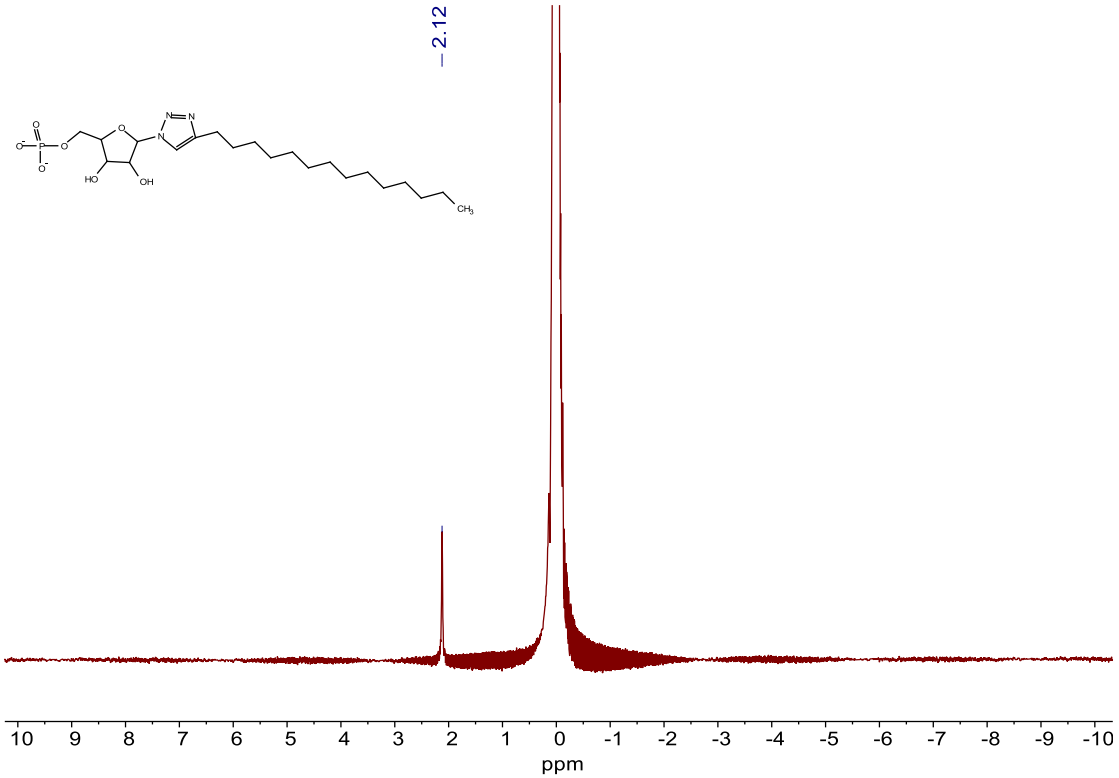

Figure S43. ^{31}P NMR spectrum of compound **11** (MeOH-d_4, against 85% H_3PO_4, 162 MHz, 295 K)

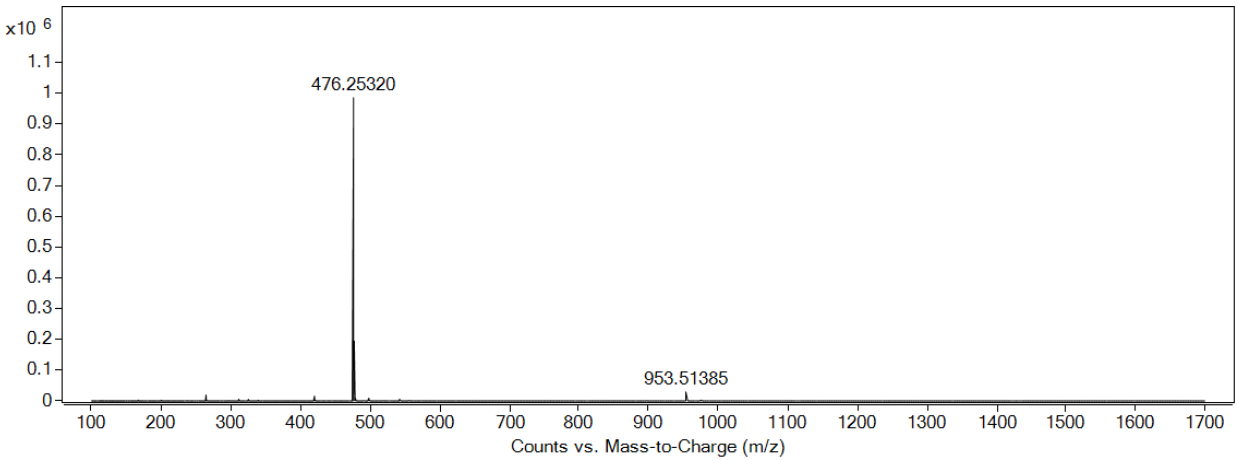

Figure S44. HR-MS (-) of compound **11**.

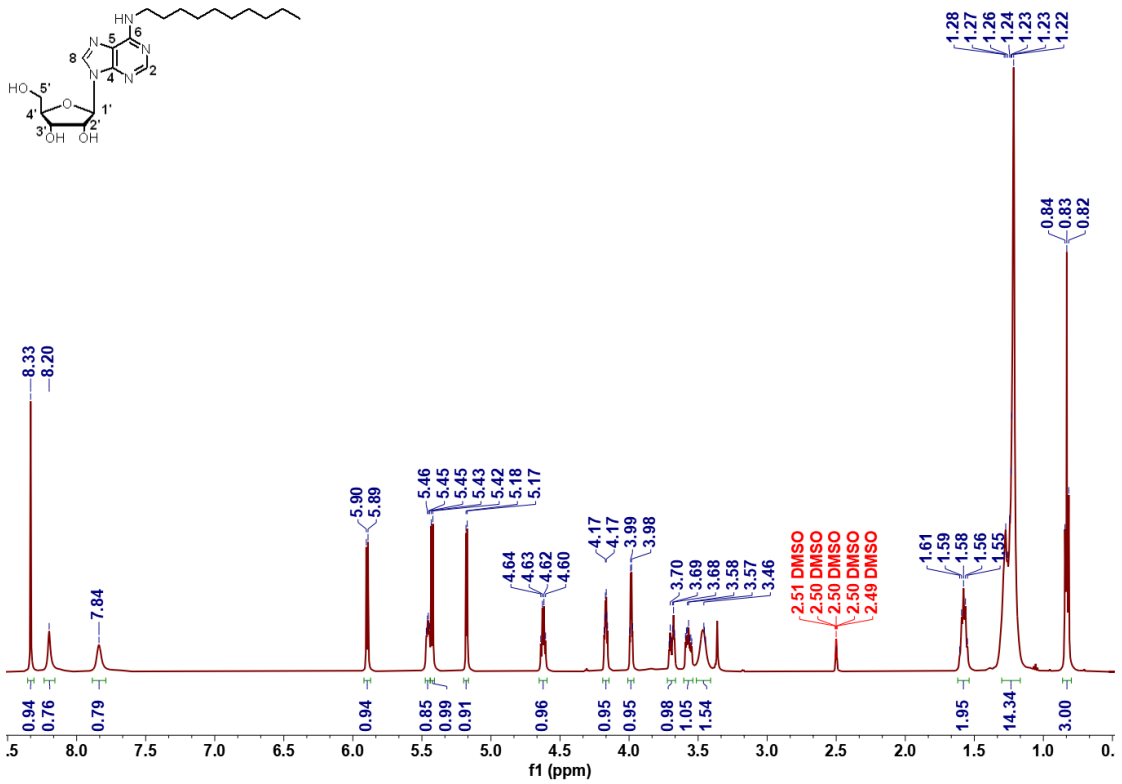

Figure S45. ^{1}H NMR spectrum of compound **13** (DMSO-d_6, 400 MHz, 295 K).

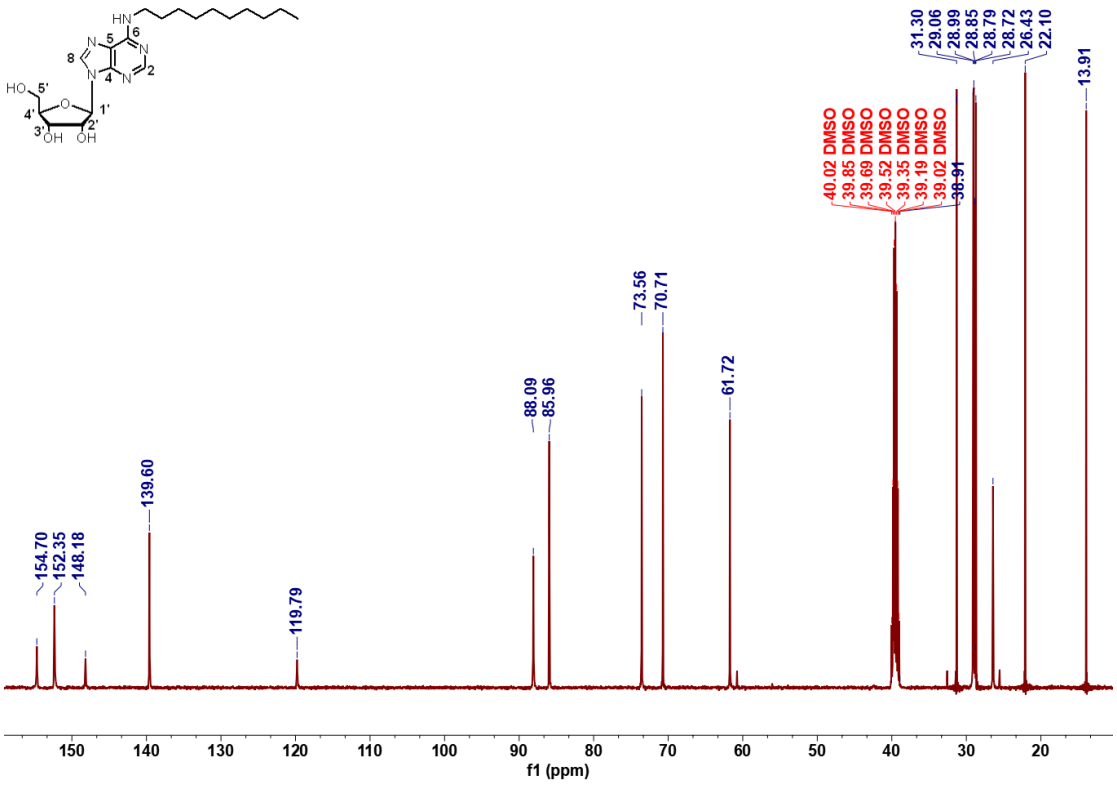

Figure S46. ^{13}C NMR spectrum of compound **13** (DMSO-d_6, 100 MHz, 295 K).

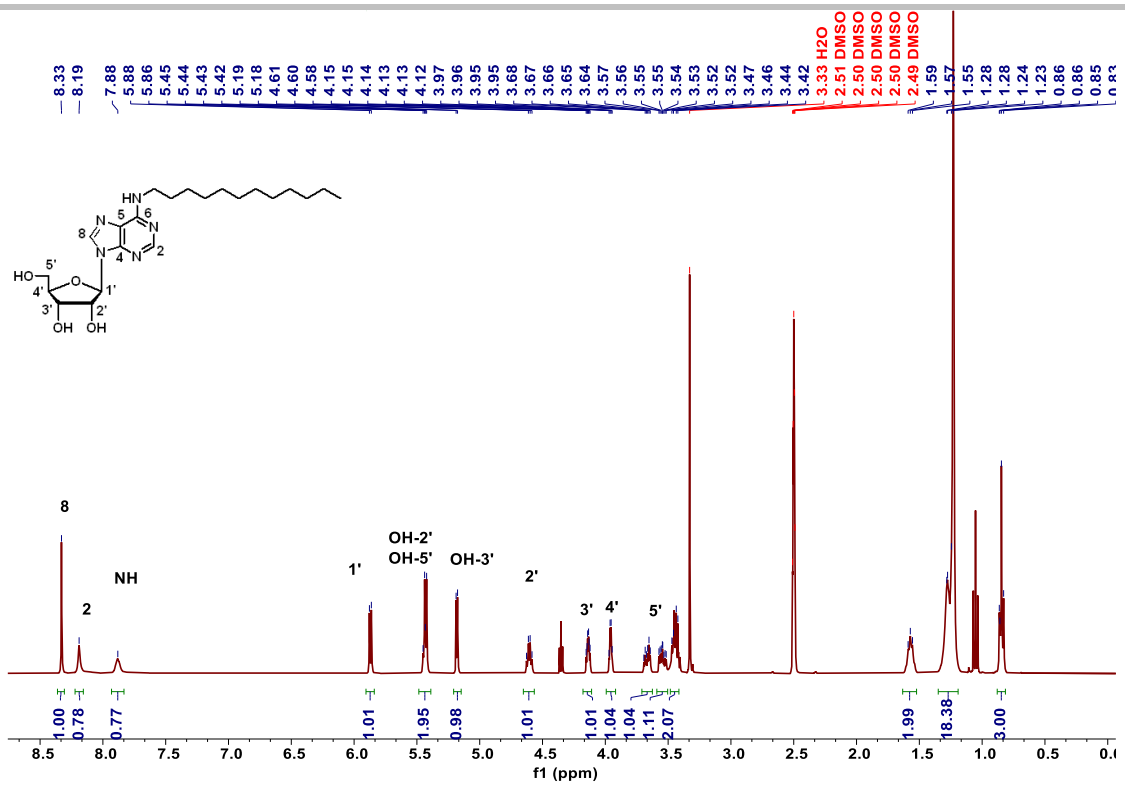

Figure S47. ^{1}H NMR spectrum of compound **14** (DMSO-d_6, 400 MHz, 295 K).

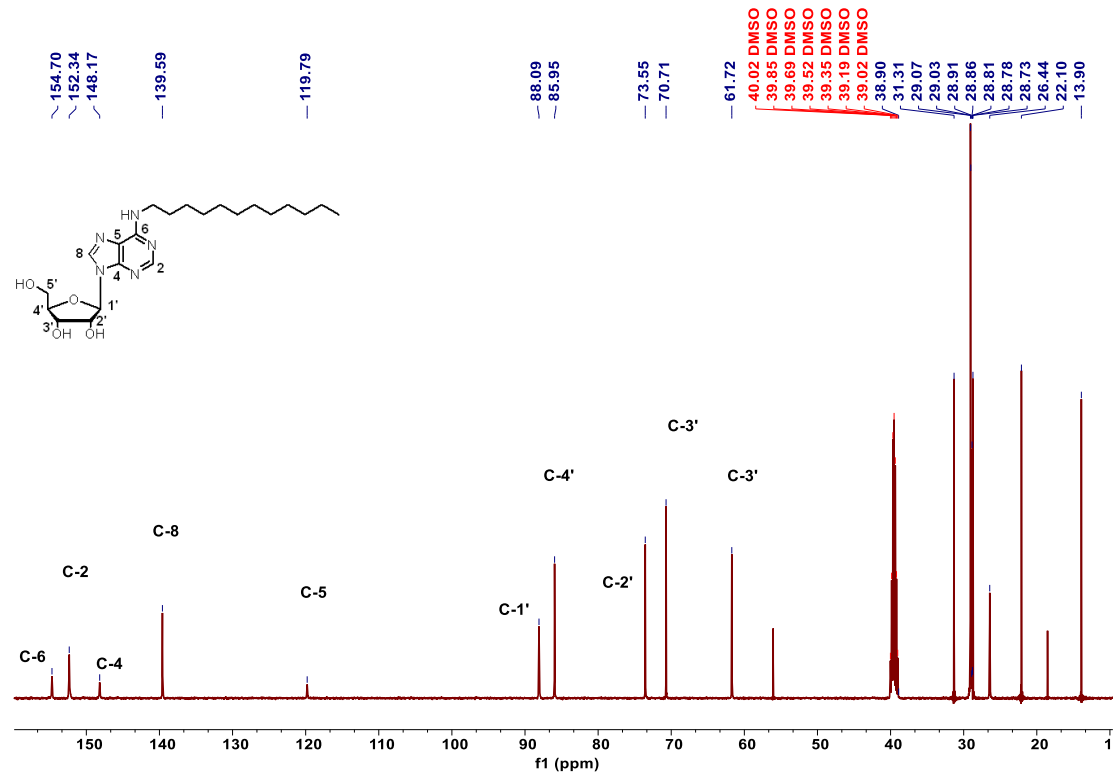

Figure S48. ^{13}C NMR spectrum of compound **14** (DMSO-d_6, 100 MHz, 295 K).

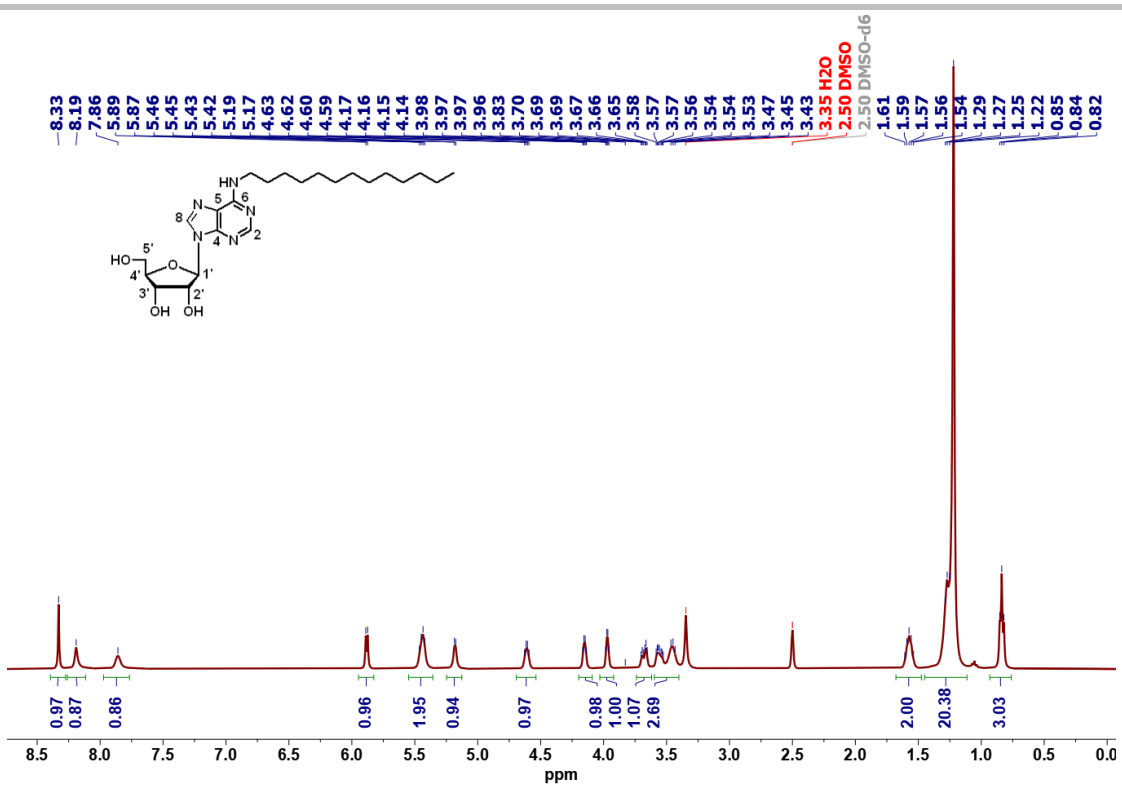

Figure S49. ^{1}H NMR spectrum of compound **15** (DMSO-d_6, 400 MHz, 295 K).

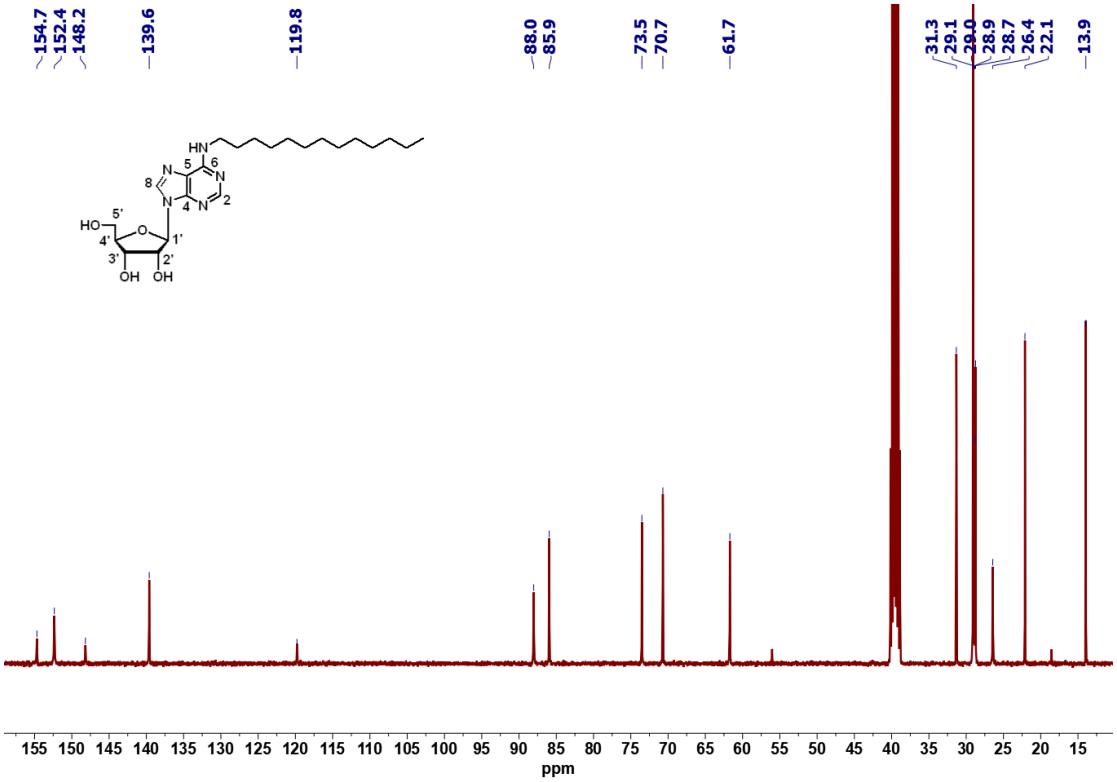

Figure S50. ^{13}C NMR spectrum of compound **15** (DMSO-d_6, 100 MHz, 295 K).

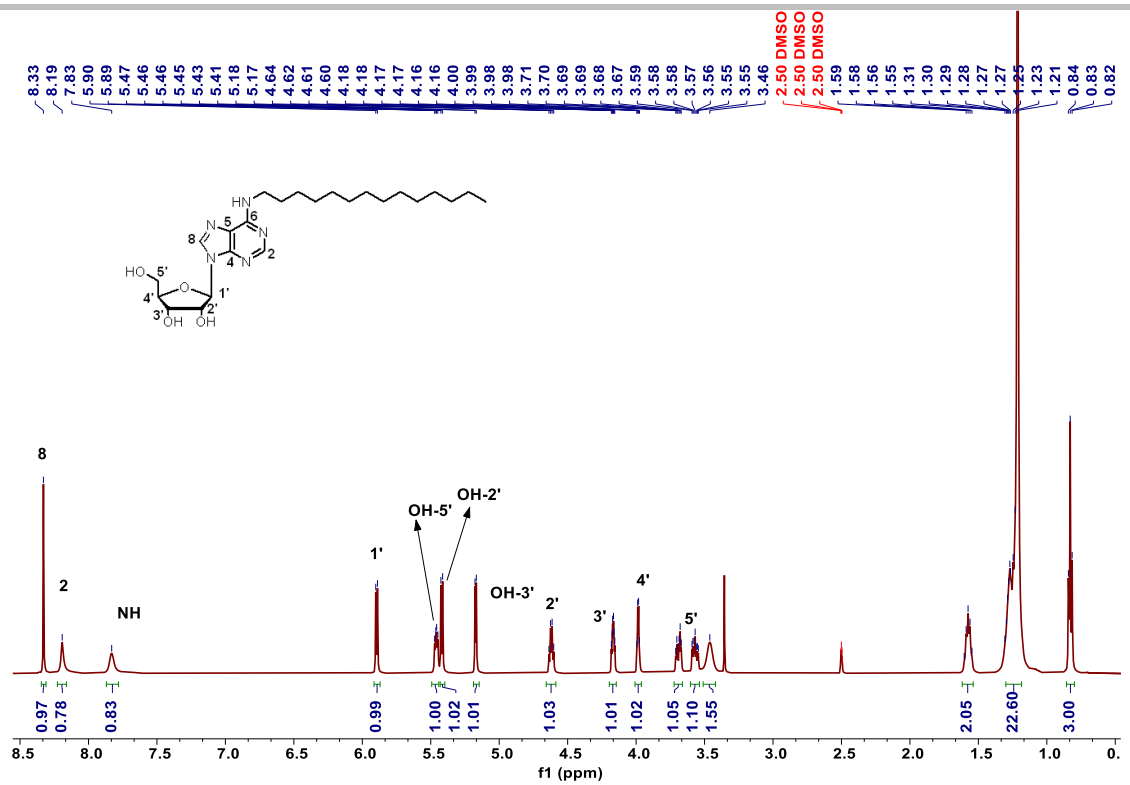

Figure S51. ^{1}H NMR spectrum of compound **16** (DMSO-d_6, 400 MHz, 295 K).

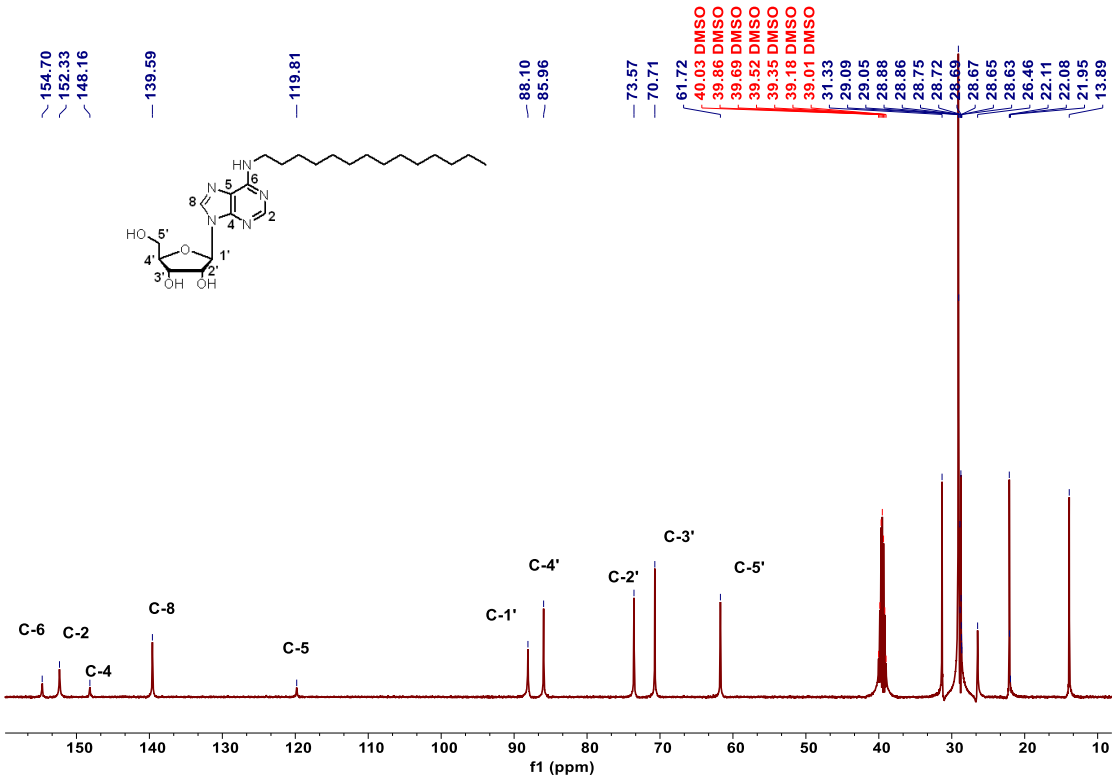

Figure S52. ^{13}C NMR spectrum of compound **16** (DMSO-d_6, 100 MHz, 295 K).

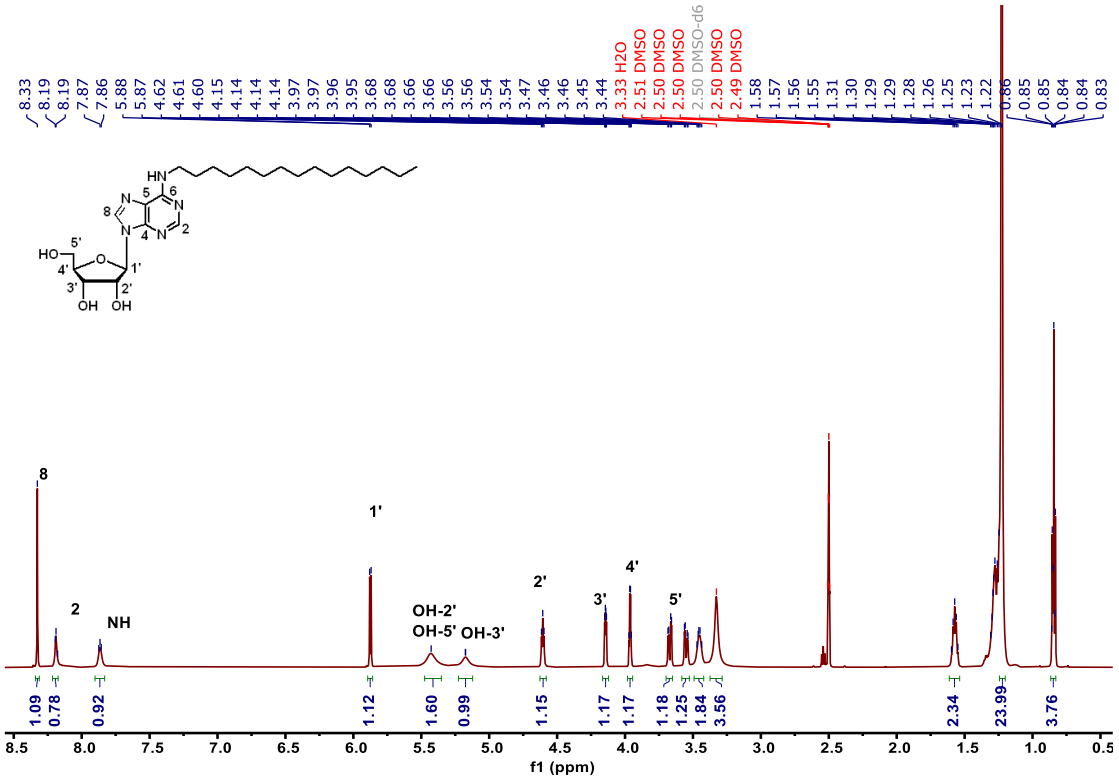

Figure S53. ^{1}H NMR spectrum of compound **17** (DMSO-d_6, 400 MHz, 295 K).

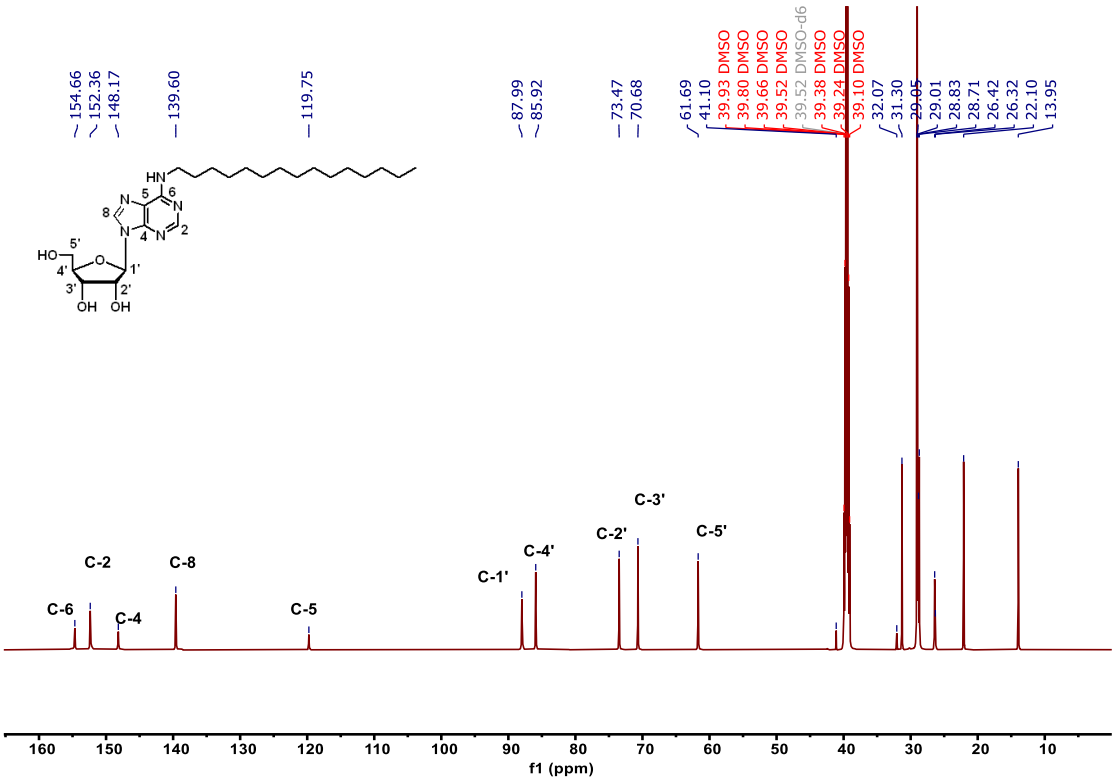

Figure S54. ^{13}C NMR spectrum of compound **17** (DMSO-d_6, 100 MHz, 295 K).

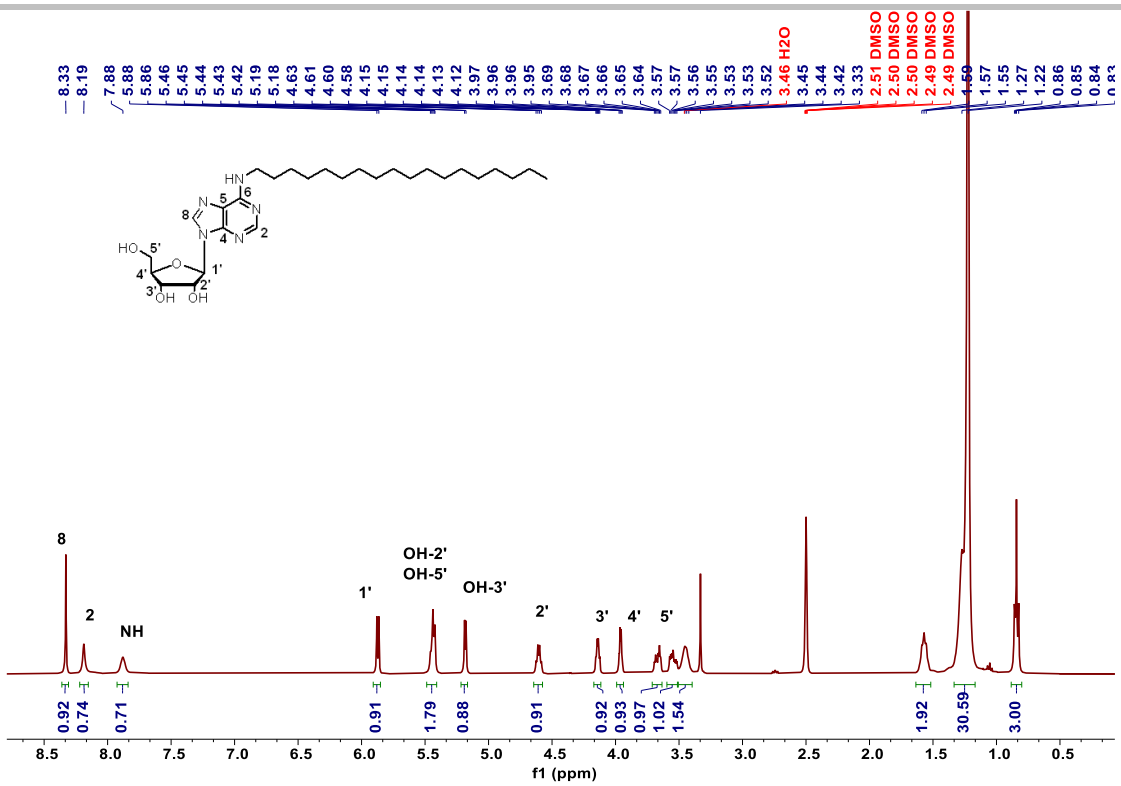

Figure S55. ^{1}H NMR spectrum of compound **18** (DMSO-d_6, 400 MHz, 295 K).

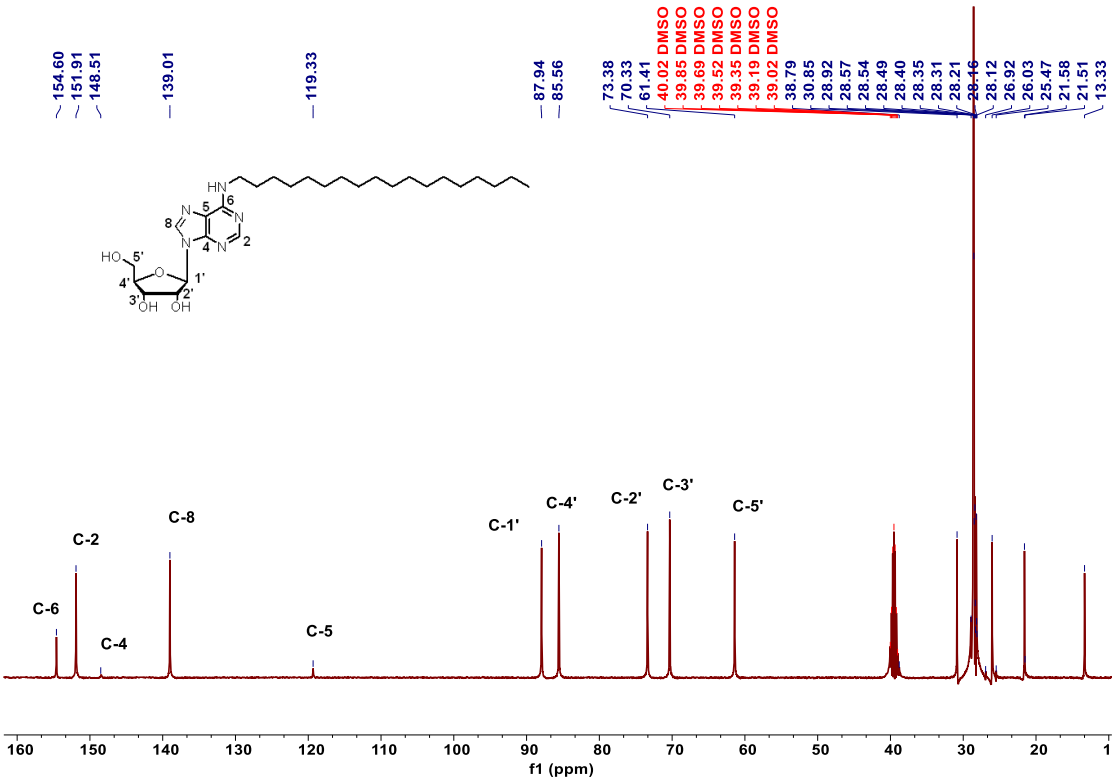

Figure S56. ^{13}C NMR spectrum of compound **18** (DMSO-d_6, 100 MHz, 295 K).

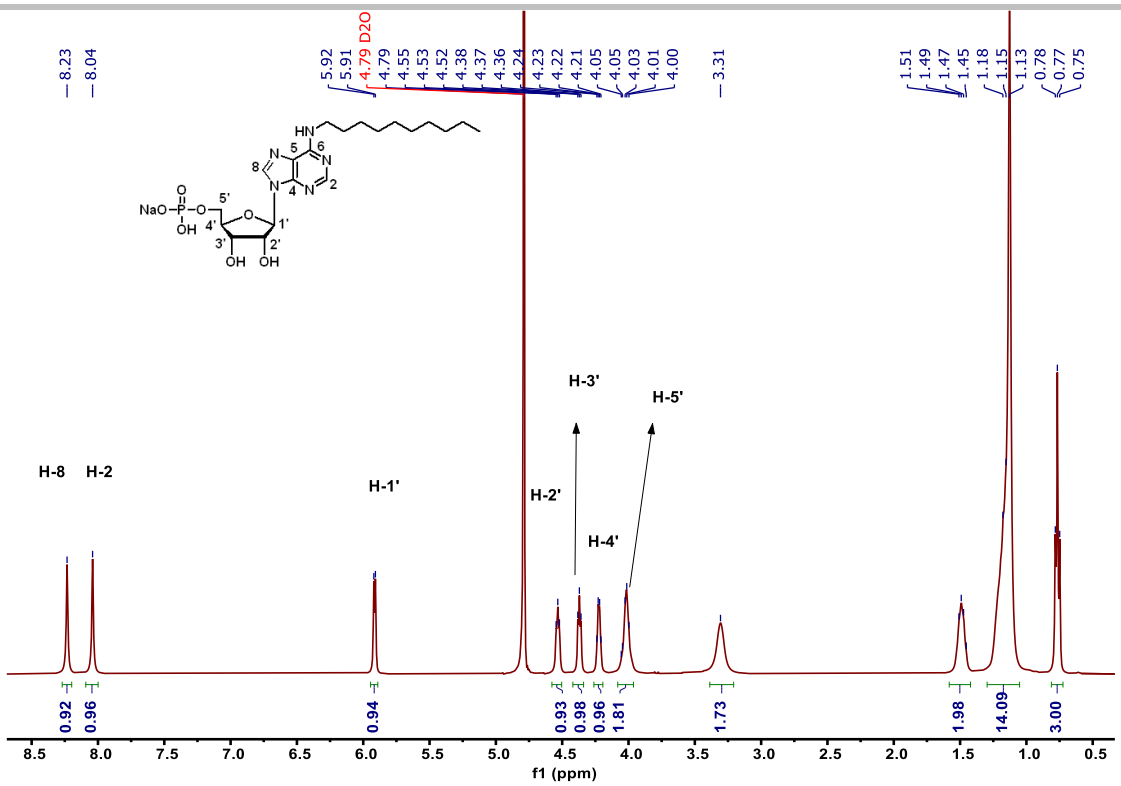

Figure S57. ^{1}H NMR spectrum of compound **19** (D_2O, 400 MHz, 295 K).

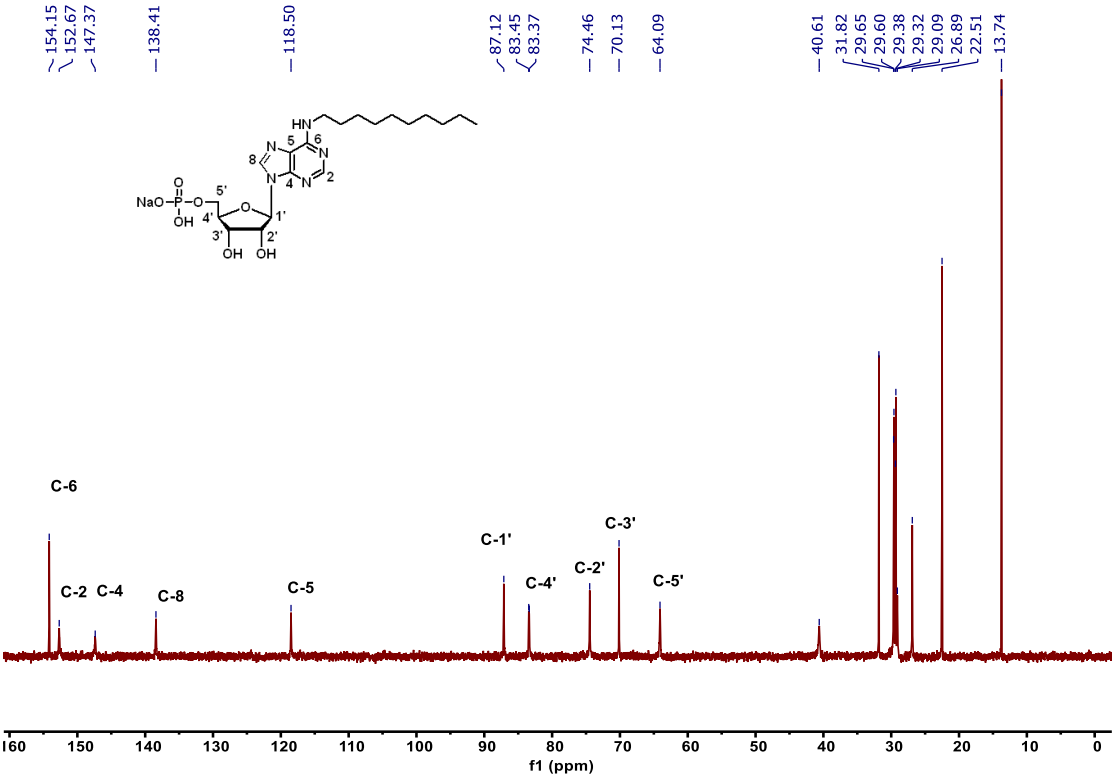

Figure S58. ^{13}C NMR spectrum of compound **19** (D_2O, 100 MHz, 295 K).

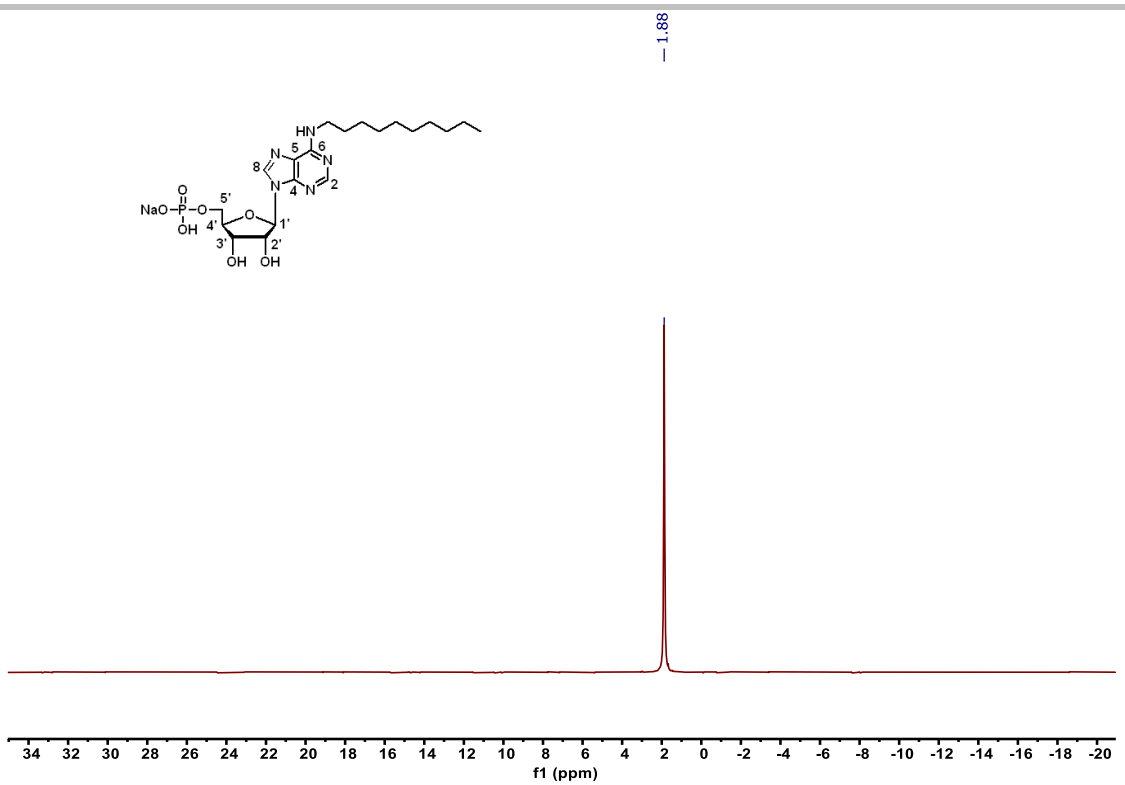

Figure S59. ^{31}P NMR spectrum of compound **19** (D_2O, 162 MHz, 295 K).

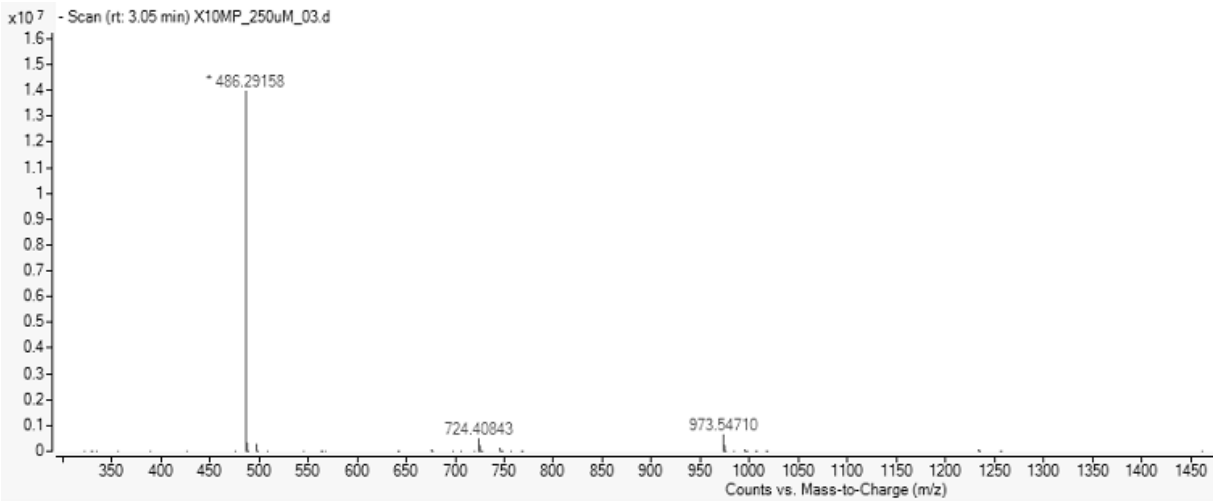

Figure S60. HR-MS (-) of compound **19**.

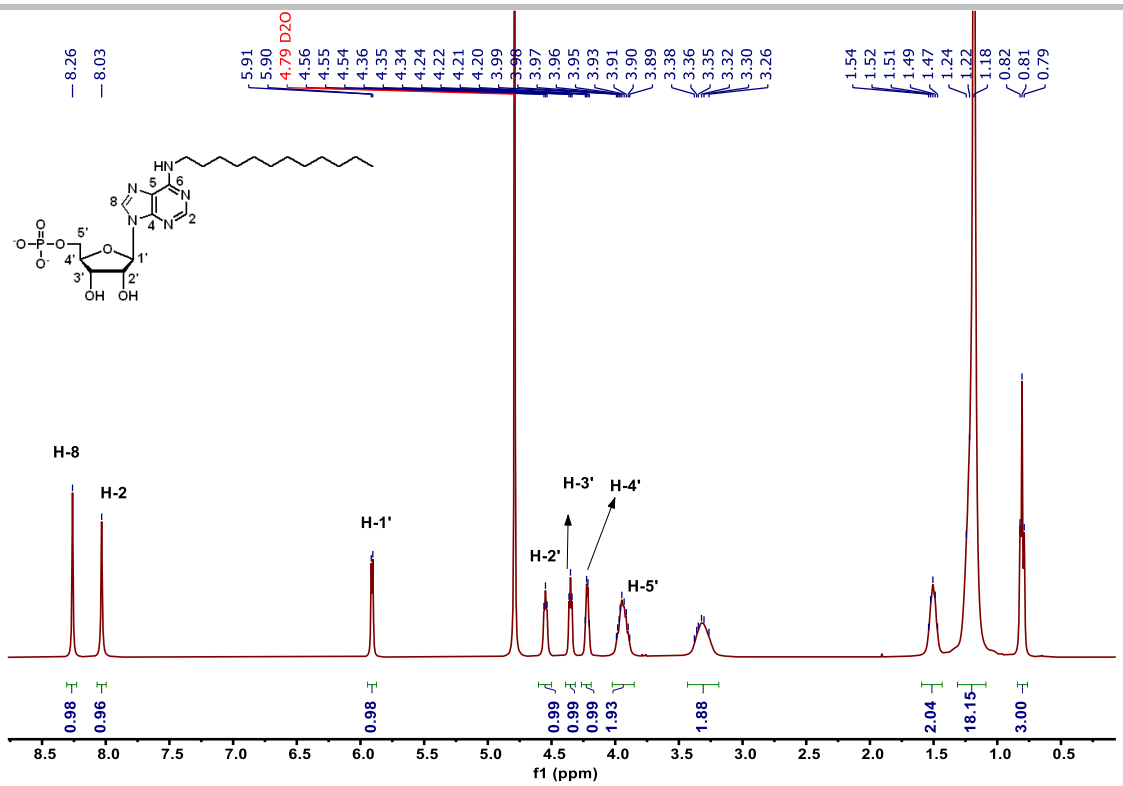

Figure S61. ^{1}H NMR spectrum of compound **20** (D_2O, 400 MHz, 295 K).

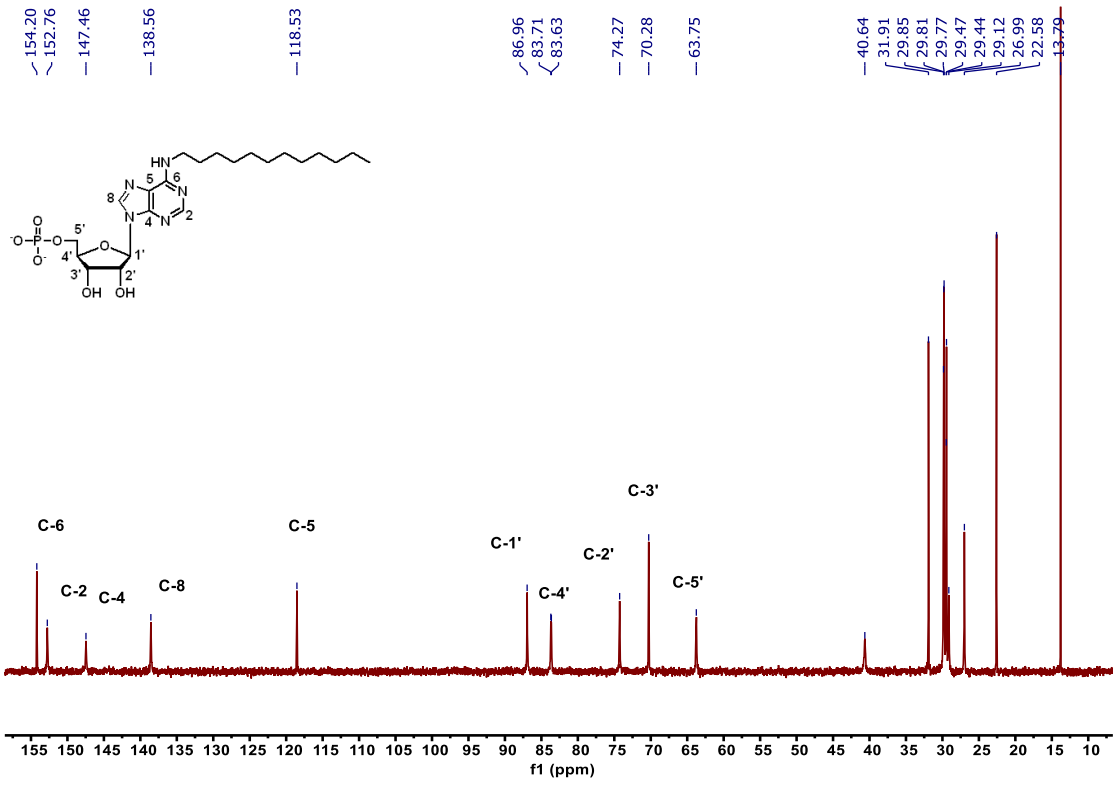

Figure S62. ^{13}C NMR spectrum of compound **20** (D_2O, 100 MHz, 295 K).

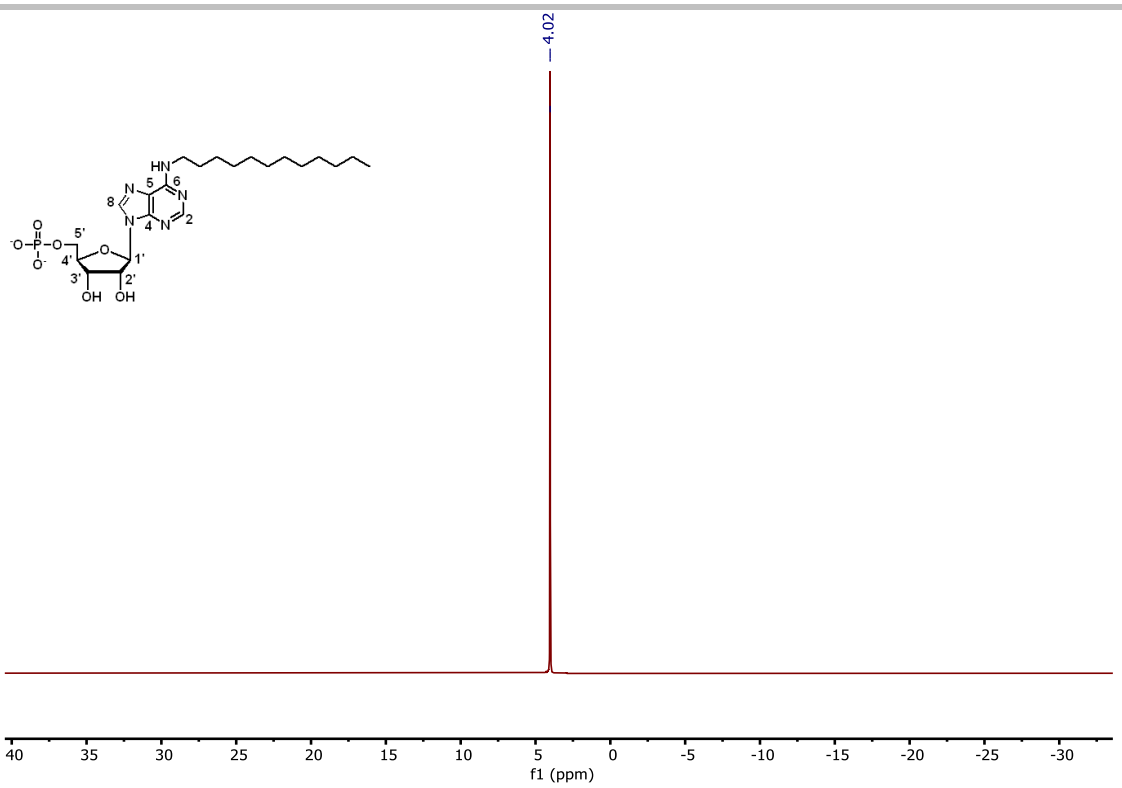

Figure S63. ^{31}P NMR spectrum of compound **20** (D_2O, 162 MHz, 295 K).

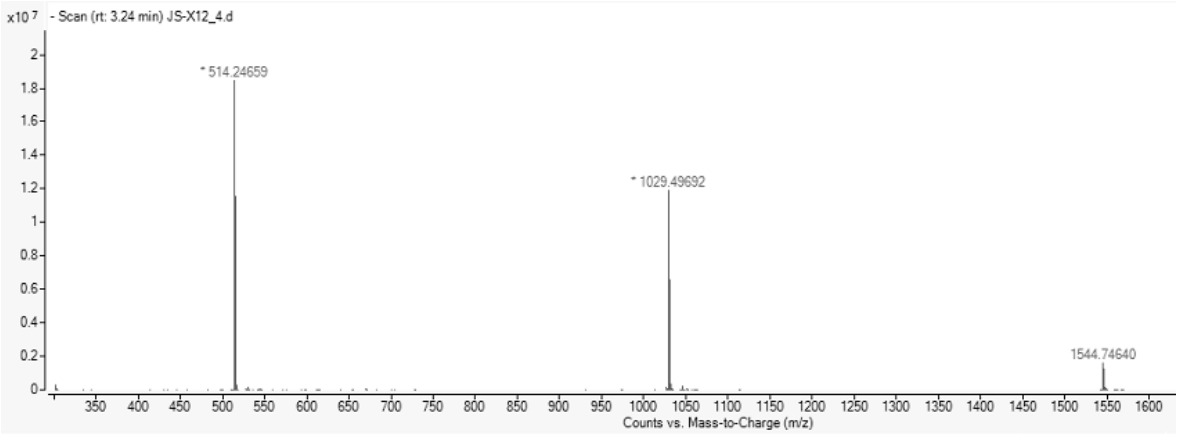

Figure S64. HR-MS (-) of compound **20**.

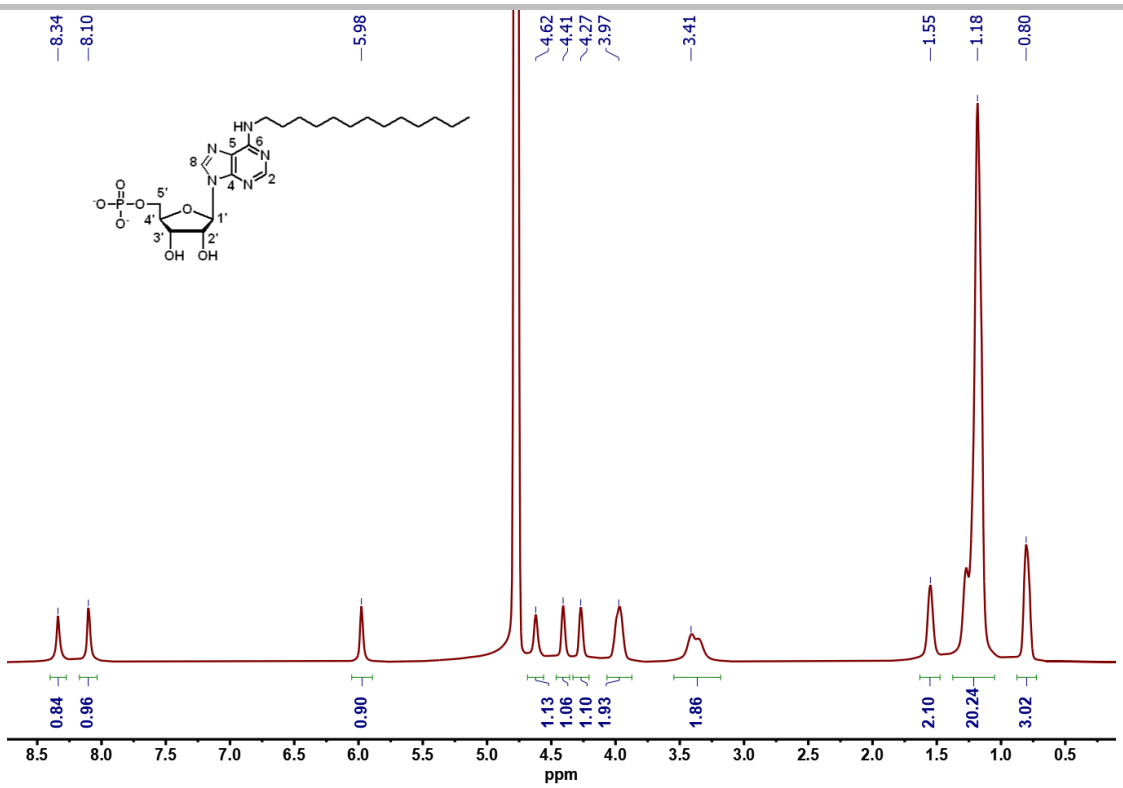

Figure S65. ^{1}H NMR spectrum of compound **21** (D_2O, 600 MHz, 295 K).

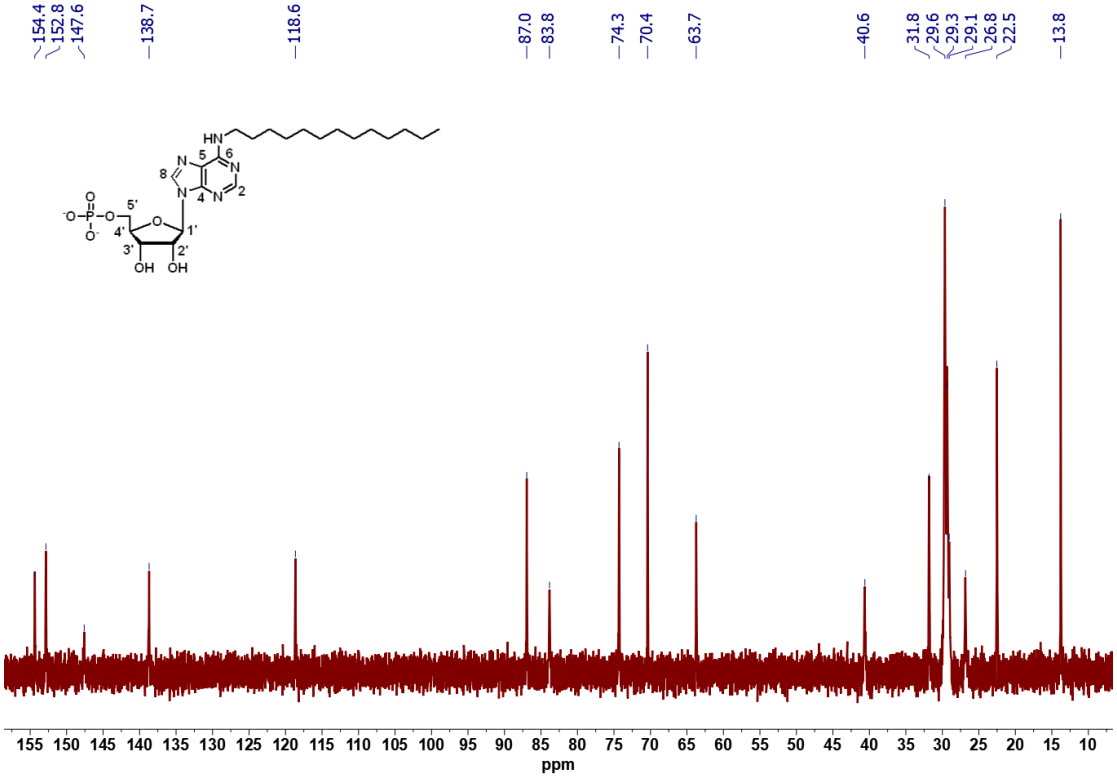

Figure S66. ^{13}C NMR spectrum of compound **21** (D_2O, 150 MHz, 295 K).

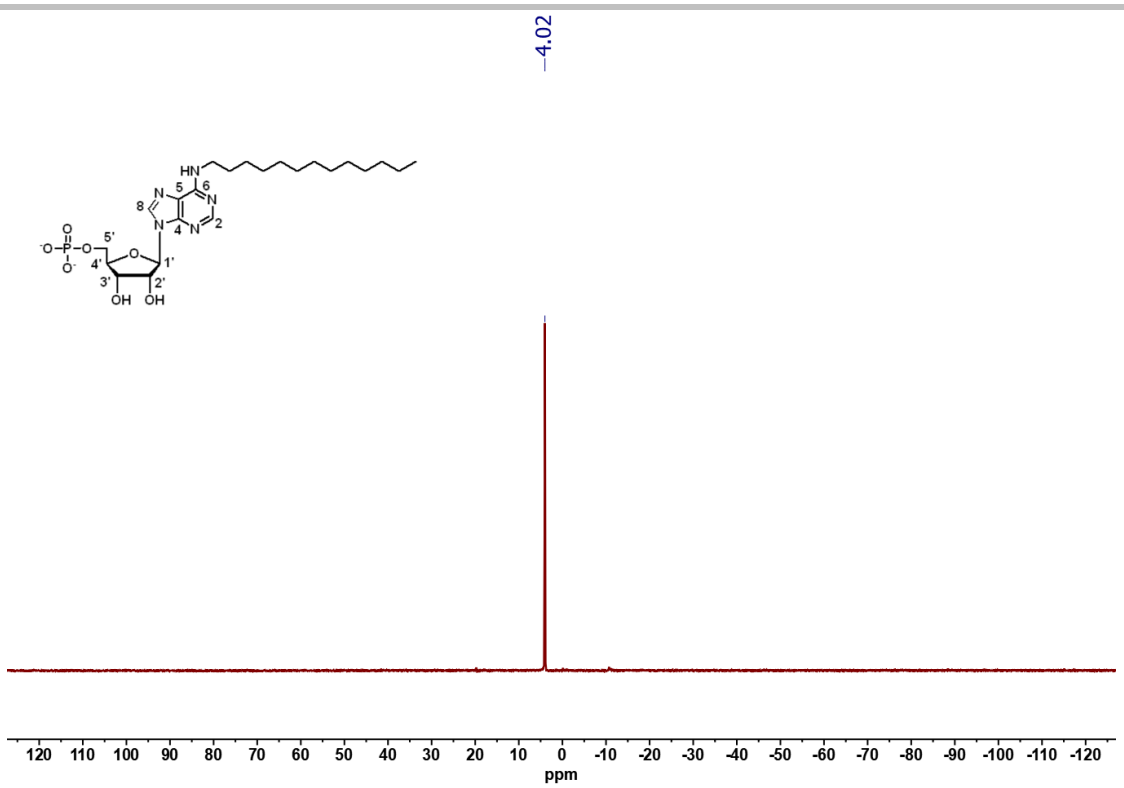

Figure S67. ^{31}P NMR spectrum of compound **21** (D_2O, 243 MHz, 295 K).

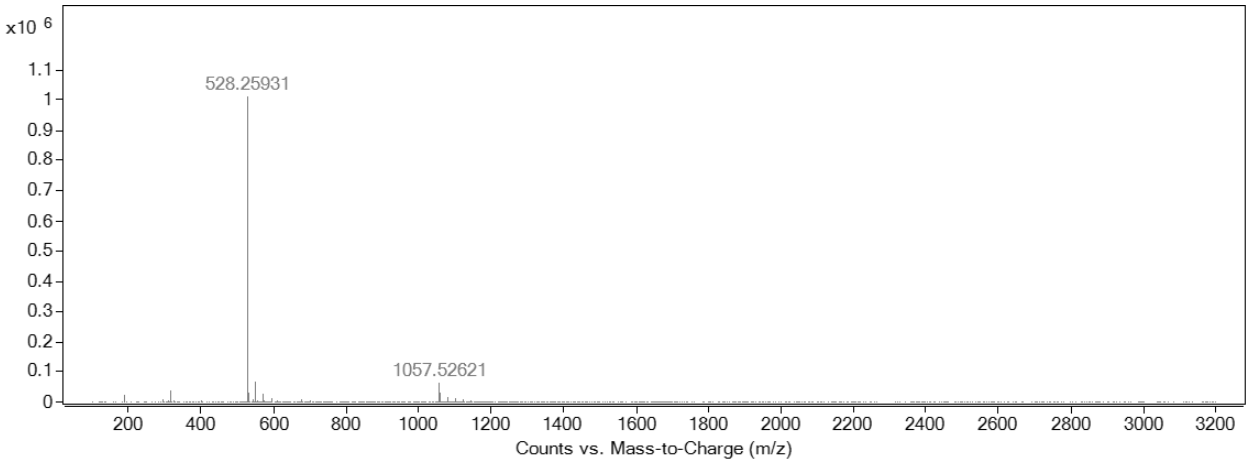

Figure S68. HR-MS (-) of compound **21**.

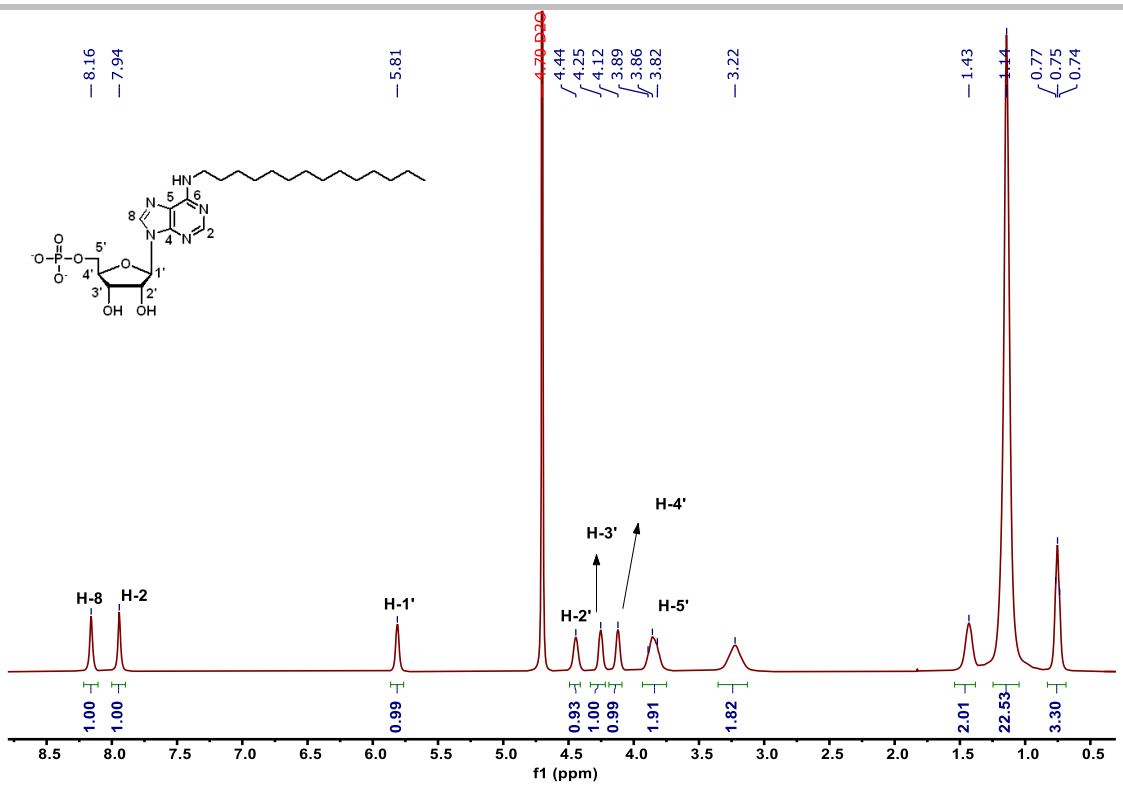

Figure S69. ^{1}H NMR spectrum of compound **22** (D_2O, 400 MHz, 295 K).

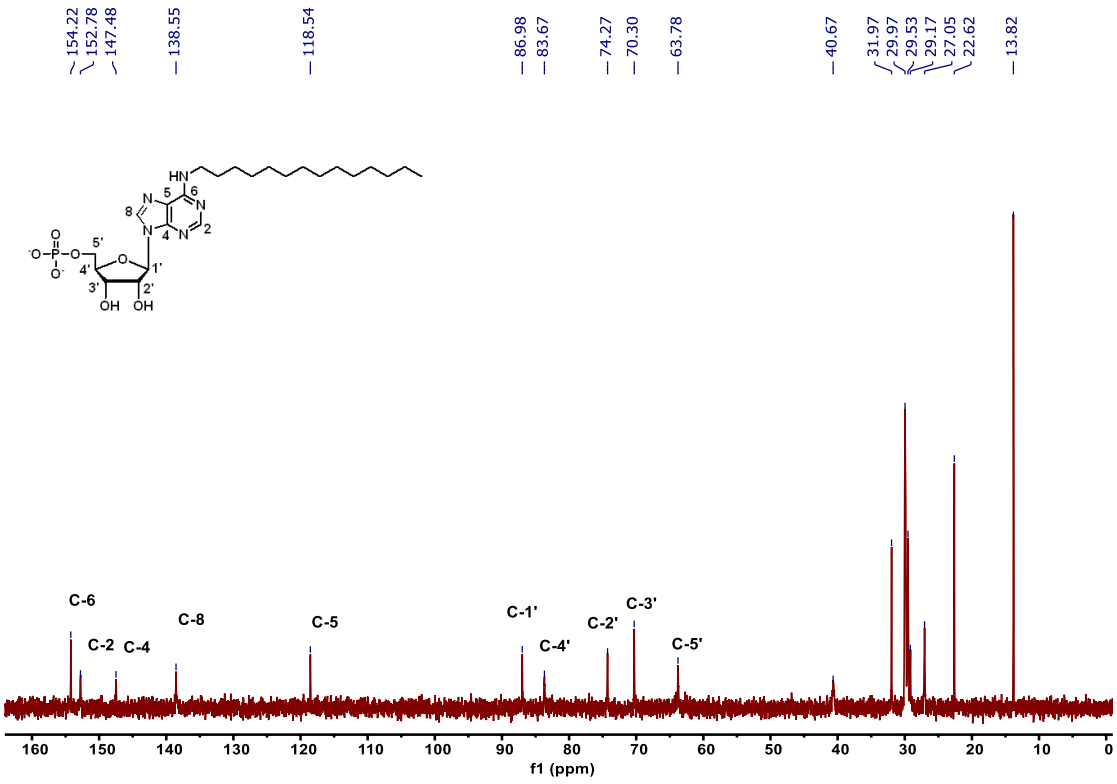

Figure S70. ^{13}C NMR spectrum of compound **22** (D_2O, 100 MHz, 295 K).

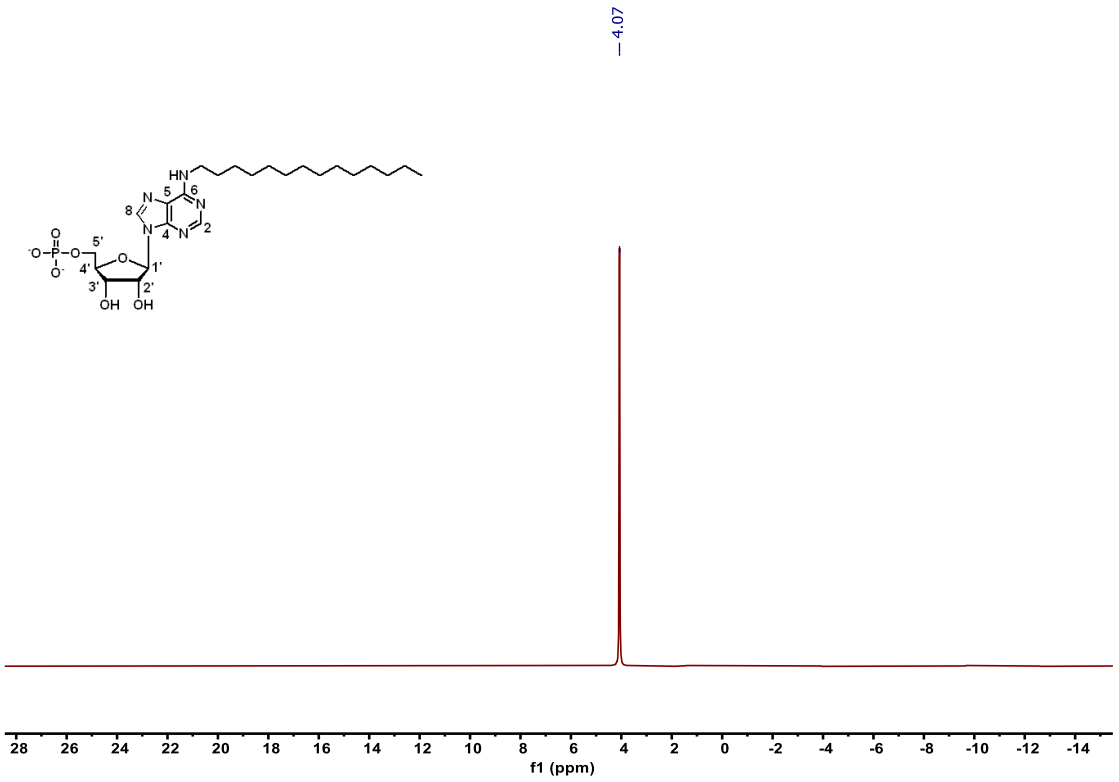

Figure S71. ^{31}P NMR spectrum of compound **22** (D_2O, 162 MHz, 295 K).

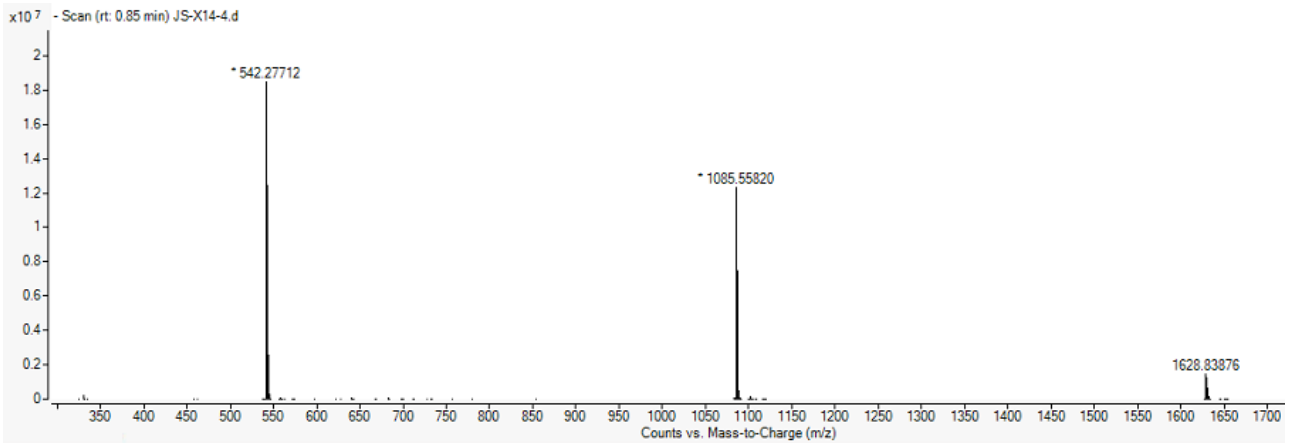

Figure S72. HR-MS (-) of compound **22**.

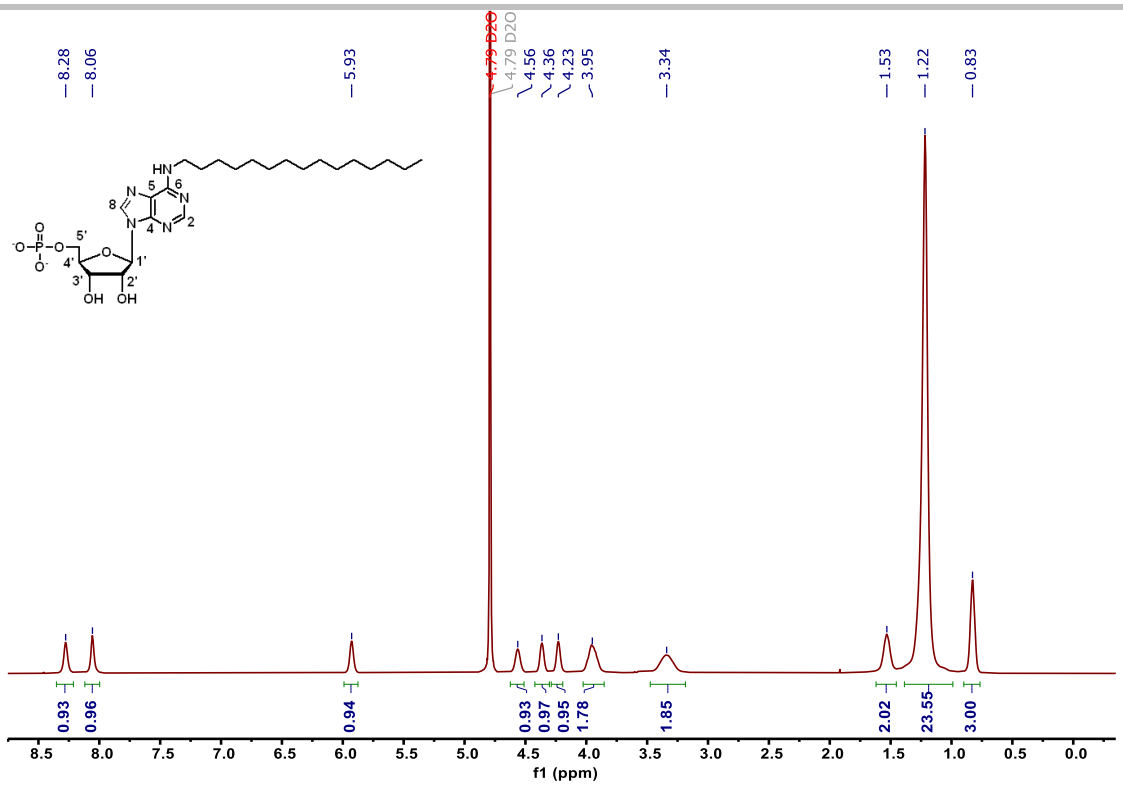

Figure S73. ^{1}H NMR spectrum of compound **23** (D_2O, 400 MHz, 295 K).

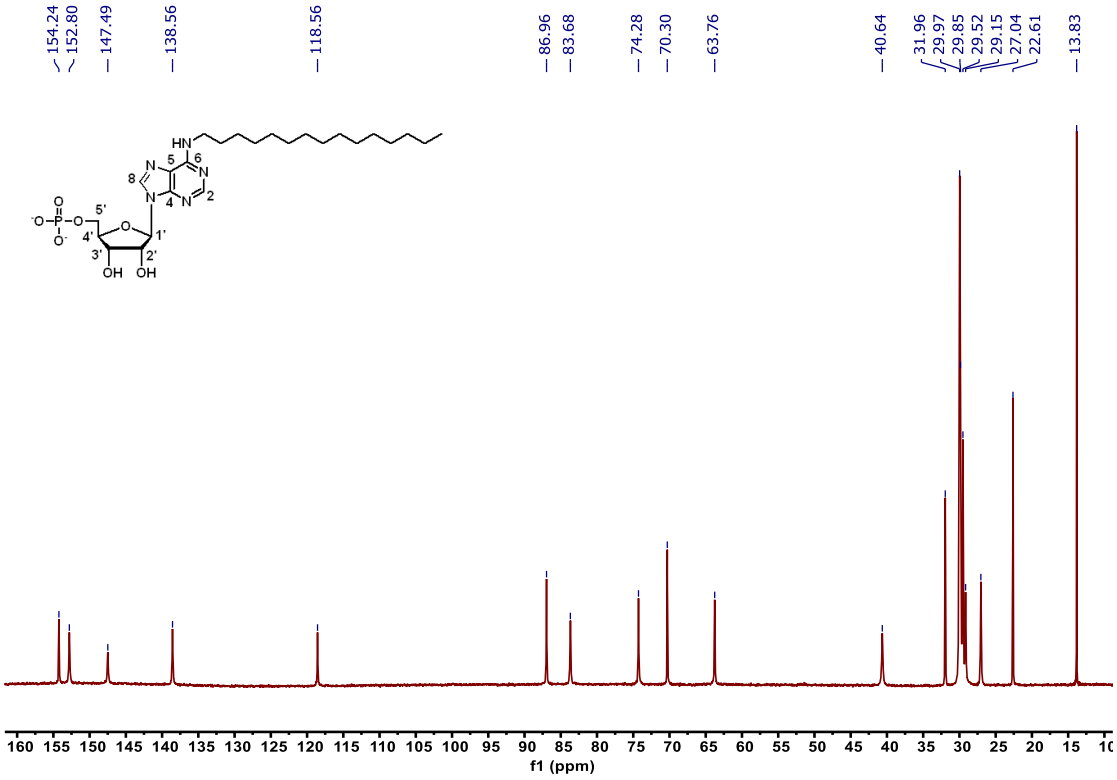

Figure S74. ^{13}C NMR spectrum of compound **23** (D_2O, 100 MHz, 295 K).

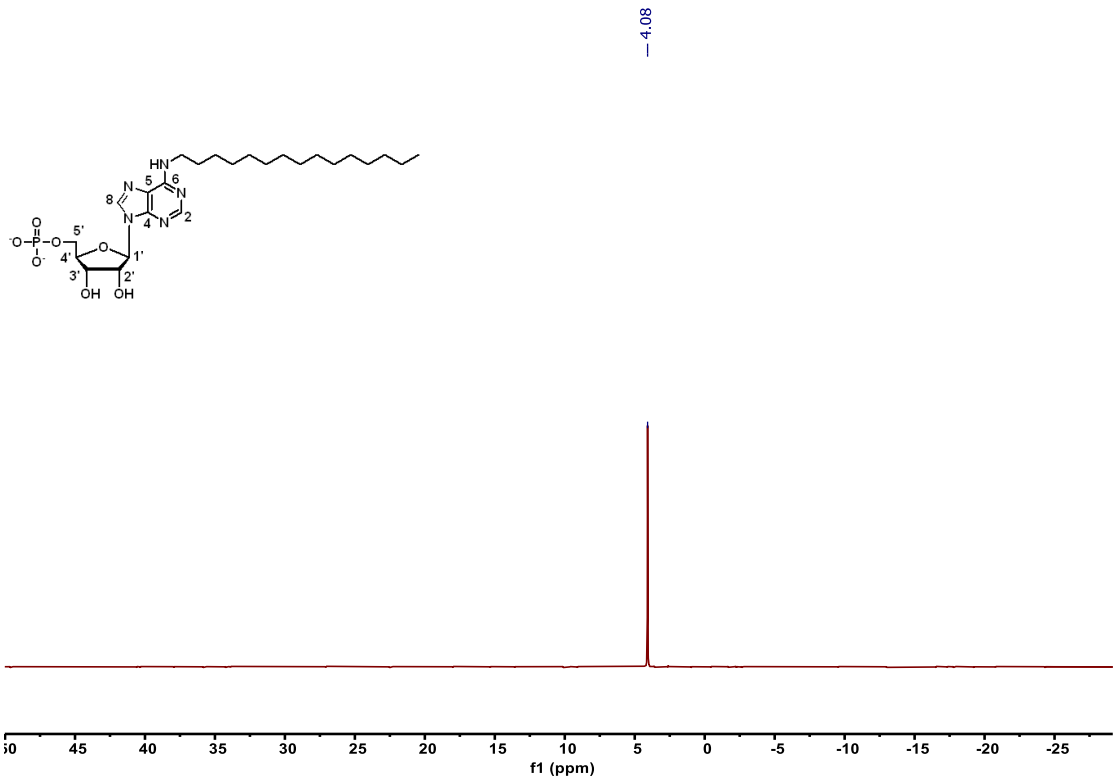

Figure S75. ^{31}P NMR spectrum of compound **23** (D_2O, 162 MHz, 295 K).

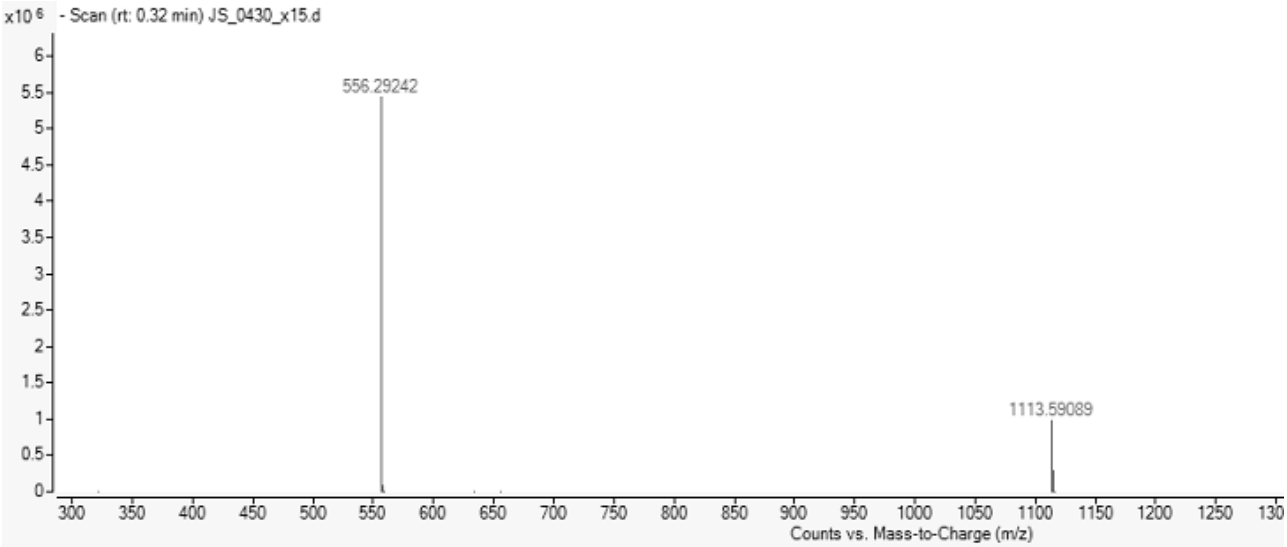

Figure S76. HR-MS (-) of compound **23**.

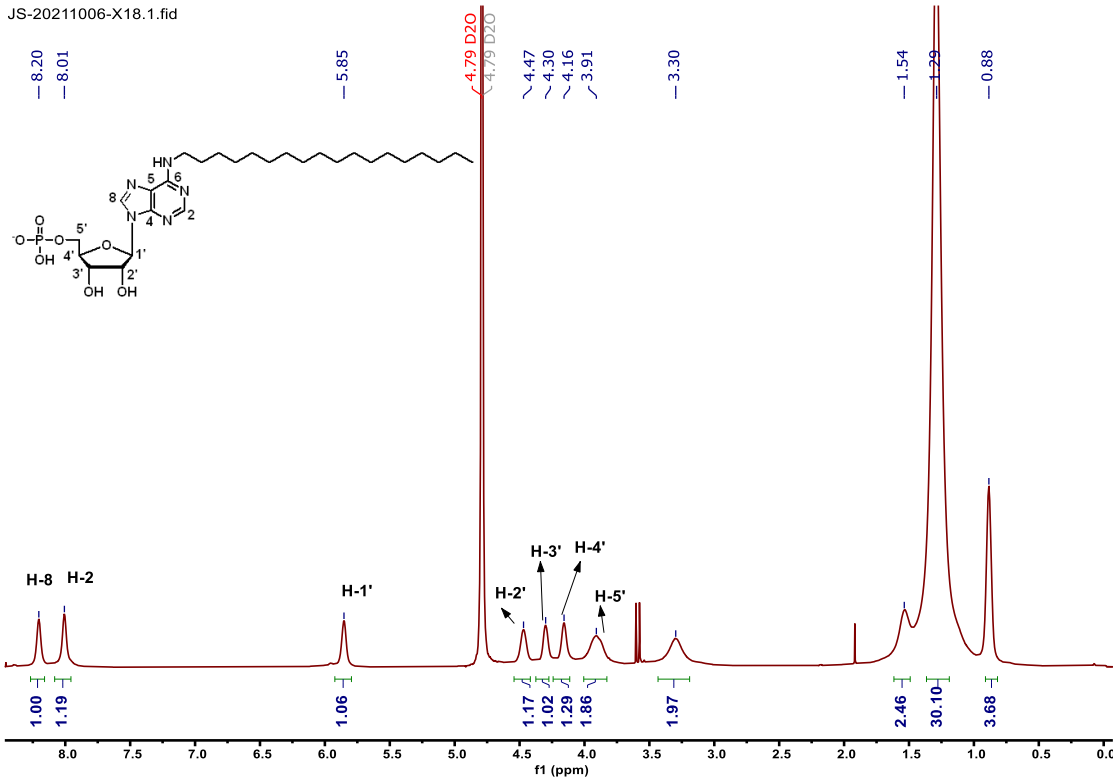

Figure S77. ^{1}H NMR spectrum of compound **24** (D_2O, 400 MHz, 295 K).

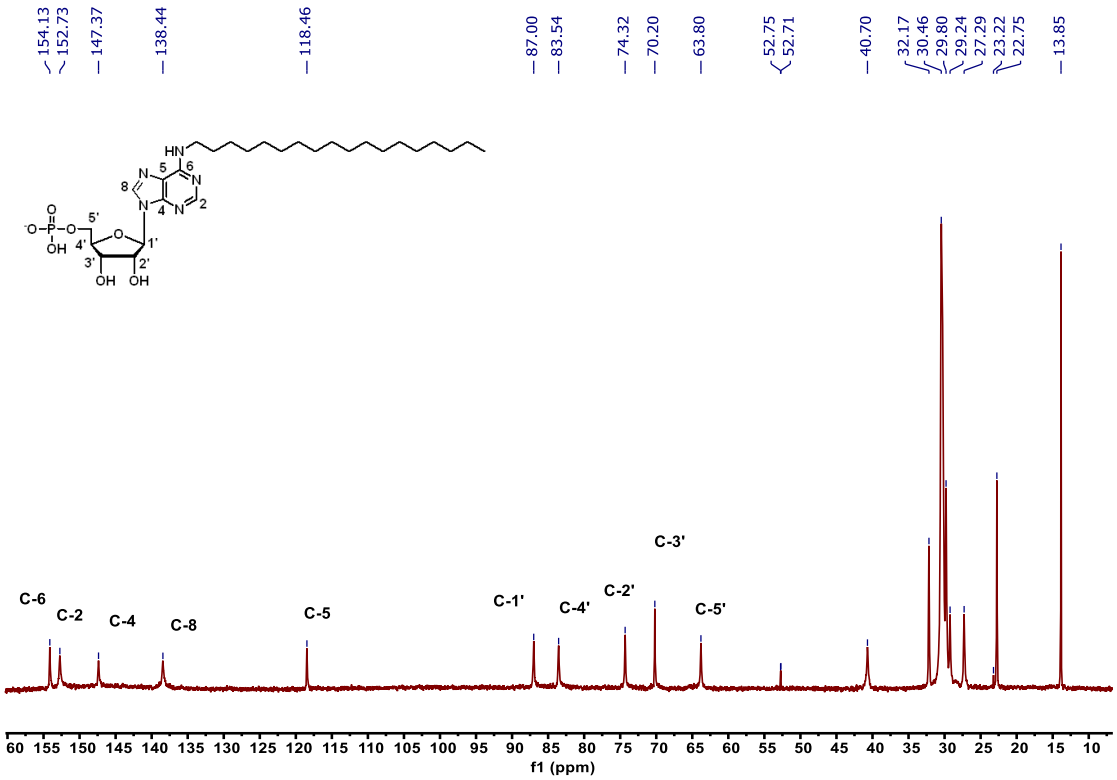

Figure S78. ^{13}C NMR spectrum of compound **24** (D_2O, 100 MHz, 295 K).

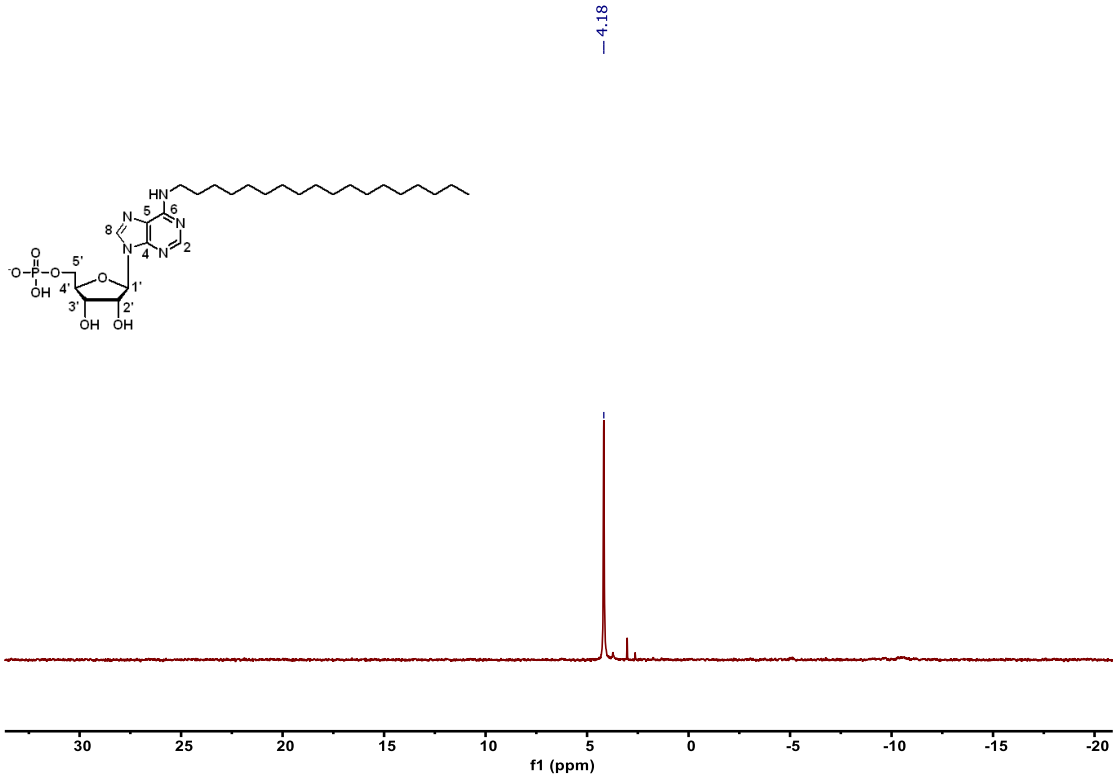

Figure S79. ^{31}P NMR spectrum of compound **24** (D_2O, 162 MHz, 295 K).

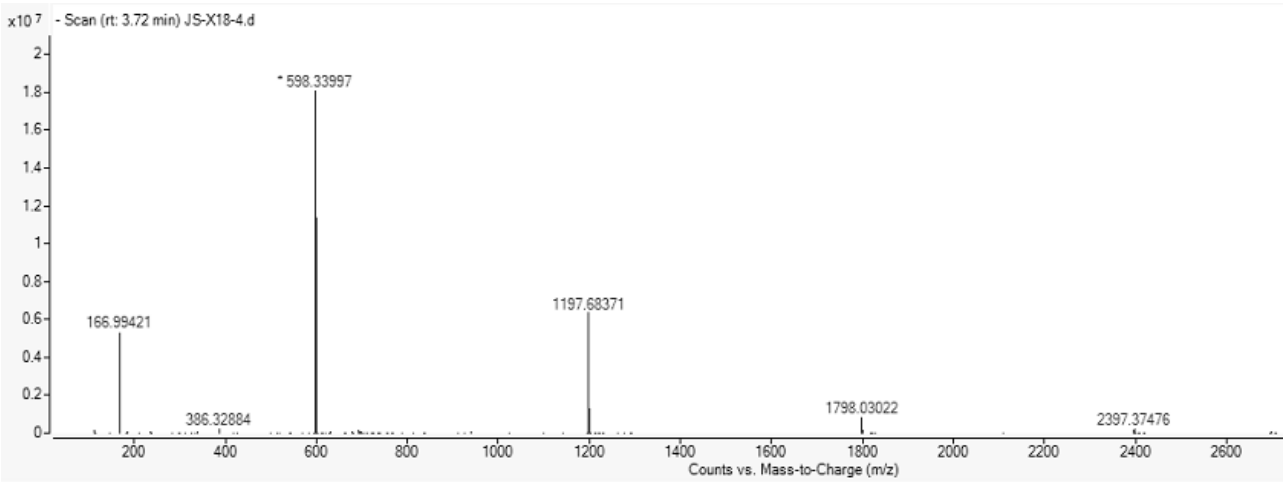

Figure S80. HR-MS (-) of compound **24**.

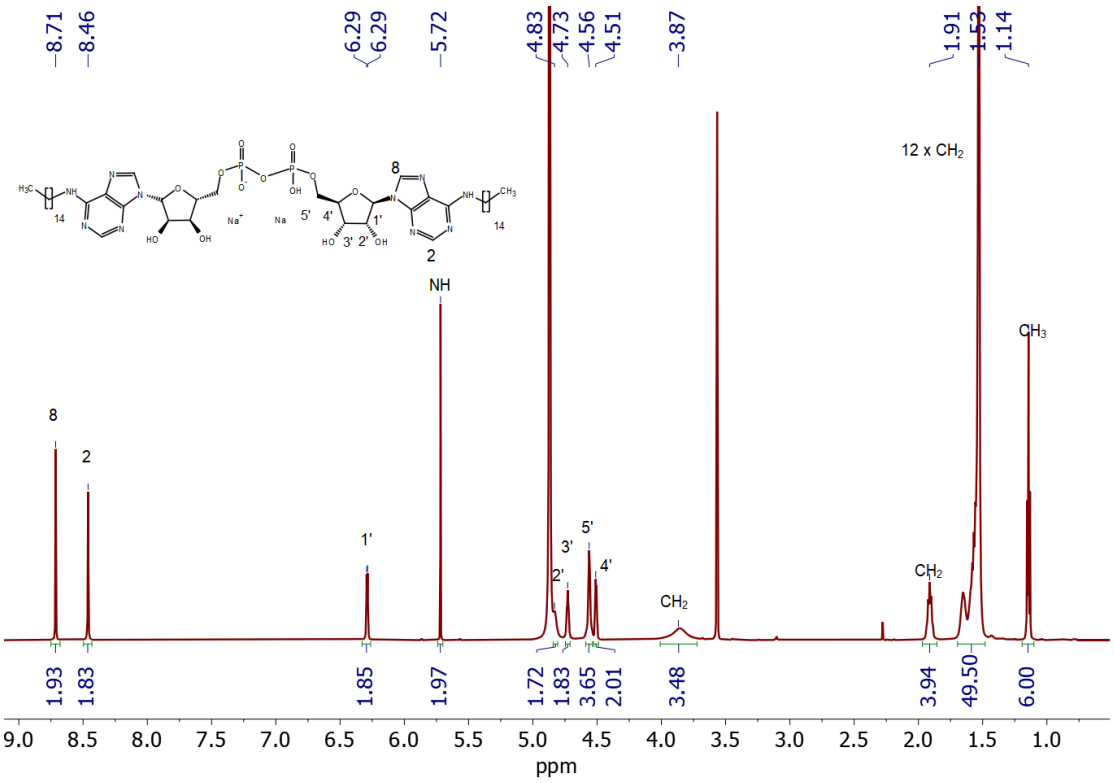

Figure S81. ^{1}H NMR spectrum of **X15ppX15** (MeOH-d$_4$, 600 MHz, 323 K).

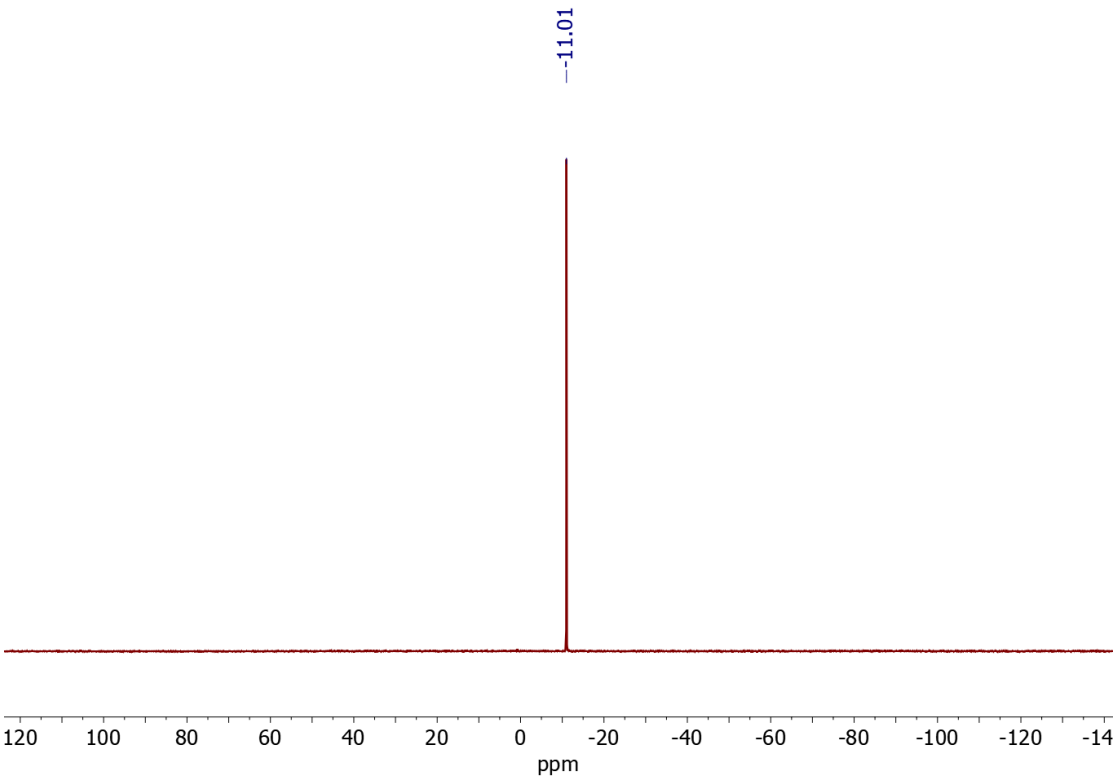

Figure 82. ^{31}P NMR spectrum of **X15ppX15** (MeOH-d$_4$, 243 MHz, 323 K).

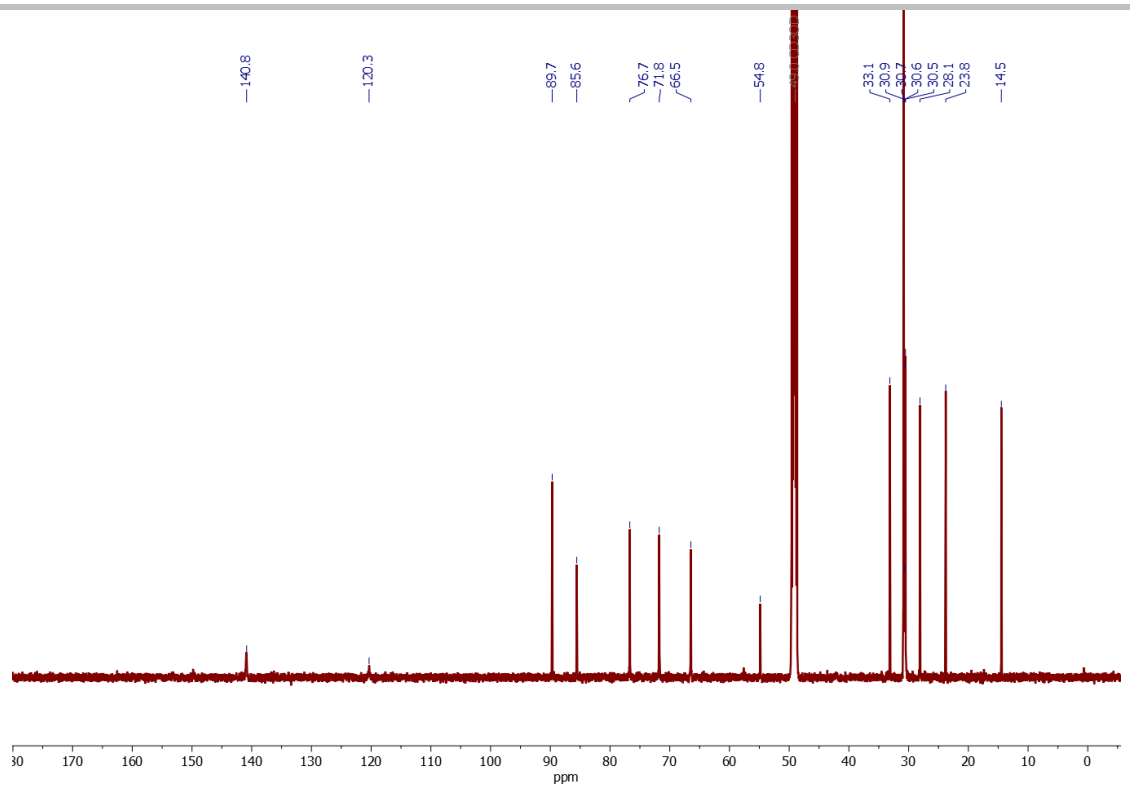

Figure 83. ^{13}C NMR spectrum of **X15ppX15** (MeOH-d_4, 150 MHz, 323 K).

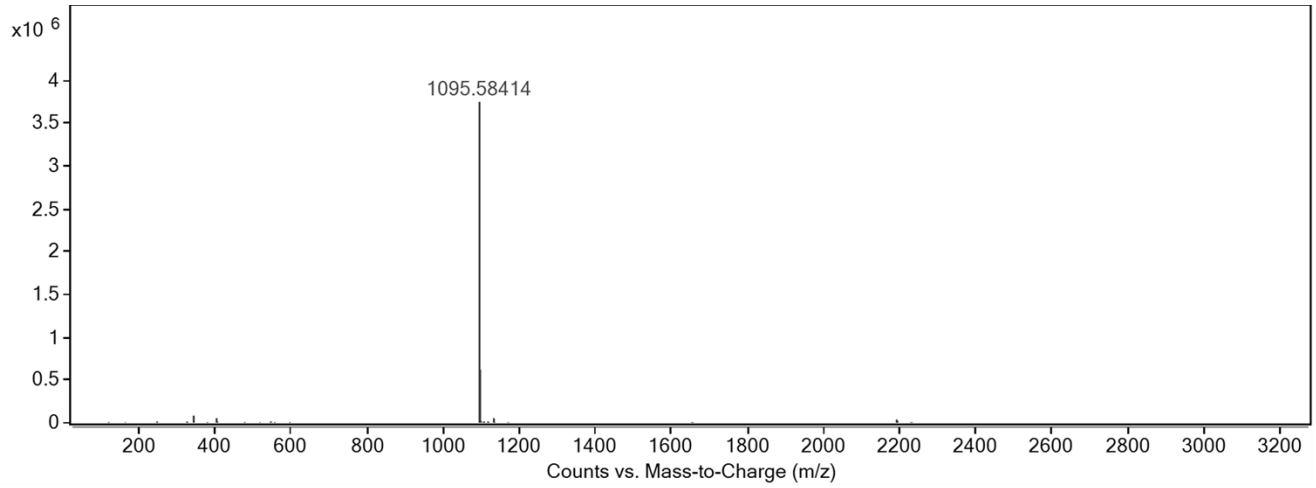

Figure 84. HR-MS (-) of **X15ppX15.**

References

[1] S. B. Salunke, N. S. Babu, C. T. Chen, *Chem. Commun.* **2011**, *47*, 10440–10442.

[2] K. El Akri, K. Bougrin, J. Balzarini, A. Faraj, R. Benhida, *Bioorg. Med. Chem. Lett.* **2007**, *17*, 6656–6659.

[3] B. L. Wilkinson, H. Long, E. Sim, A. J. Fairbanks, *Bioorg. Med. Chem. Lett.* **2008**, *18*, 6265–6267.

[4] S. Wallrodt, A. Buntz, Y. Wang, A. Zumbusch, A. Marx, *Angew. Chem. Int. Ed.* **2016**, *55*, 7660–7664.

3.2 A Ribonucleotide ↔ Phosphoramidate Reaction Network Optimized by Computer-Aided Design

Julian Vogel, Andreas Englert, Tim Bergner, Jessica Loske and Max von Delius, *J. Am. Chem. Soc.* **2022**, *144*, 15266-12374. DOI: https://doi.org/10.1021/jacs.2c05861.
This article is licensed and reprinted under a Creative Commons Attribution 4.0 International License (CC BY 4.0), https://creativecommons.org/licenses/by/4.0/

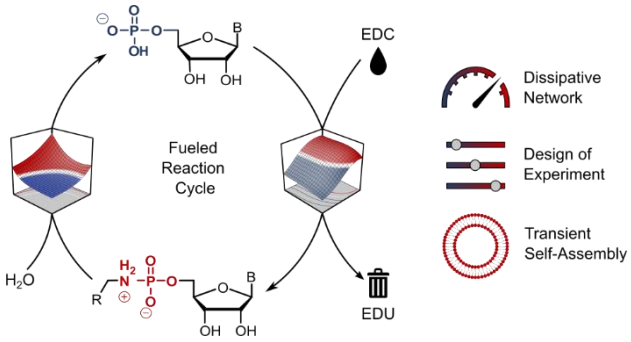

Abstract:
A growing number of out-of-equilibrium systems have been created and investigated in chemical laboratories over the past decade. One way to achieve this is to create a reaction cycle, in which the forward reaction is driven by a chemical fuel and the backward reaction follows a different pathway. Such dissipative reaction networks are still relatively rare, however, and most non-enzymatic examples are based on the carbodiimide-driven generation of carboxylic acid anhydrides. In this work, we describe a dissipative reaction network that comprises the chemically fueled formation of phosphoramidates from natural ribonucleotides (e.g., GMP or AMP) and phosphoramidate hydrolysis as a mild backward reaction. Because the individual reactions are subject to a multitude of interconnected parameters, the software-assisted tool "Design of Experiment" (DoE) was a great asset for optimizing and understanding the network. One notable insight was the stark effect of the nucleophilic catalyst 1-ethylimidazole (EtIm) on the hydrolysis rate, which is reminiscent of the action of the histidine group in phosphoramidase enzymes (e.g., HINT1). We were also able to use the reaction cycle to generate transient self-assemblies, which were characterized by dynamic light scattering (DLS), confocal microscopy (CLSM) and cryogenic transmission electron microscopy (cryo-TEM). Because these compartments are based on prebiotically plausible building blocks, our findings may have relevance for origin of life scenarios.

Own contributions:
The initial idea to use phosphoramidates for reactions cycles stems from Andreas Englert. I developed the concept for the corresponding dissipative self-assembly. Andreas Englert investigated phosphoramidate condensation and hydrolysis by means of DoE. I carried out and optimized the dissipative self-assembly (e.g., different amines, phosphates, and conditions). Furthermore, I characterized the corresponding (four) reaction cycles by HPLC, DLS, CLSM and TEM. Tim Bergner recorded cryo-TEM images and Jessica Loske assisted with experiments for the DoE. Writing of the first draft (incl. graphics) and the SI was equally shared by me and Andreas Englert. Max von Delius edited the manuscript.

JACS
JOURNAL OF THE AMERICAN CHEMICAL SOCIETY
pubs.acs.org/JACS
Article

A Ribonucleotide ↔ Phosphoramidate Reaction Network Optimized by Computer-Aided Design

Andreas Englert,[§] Julian F. Vogel,[§] Tim Bergner, Jessica Loske, and Max von Delius*

Cite This: J. Am. Chem. Soc. 2022, 144, 15266−15274
Read Online
ACCESS | Metrics & More | Article Recommendations | Supporting Information

ABSTRACT: A growing number of out-of-equilibrium systems have been created and investigated in chemical laboratories over the past decade. One way to achieve this is to create a reaction cycle, in which the forward reaction is driven by a chemical fuel and the backward reaction follows a different pathway. Such dissipative reaction networks are still relatively rare, however, and most non-enzymatic examples are based on the carbodiimide-driven generation of carboxylic acid anhydrides. In this work, we describe a dissipative reaction network that comprises the chemically fueled formation of phosphoramidates from natural ribonucleotides (e.g., GMP or AMP) and phosphoramidate hydrolysis as a mild backward reaction. Because the individual reactions are subject to a multitude of interconnected parameters, the software-assisted tool "Design of Experiments" (DoE) was a great asset for optimizing and understanding the network. One notable insight was the stark effect of the nucleophilic catalyst 1-ethylimidazole (EtIm) on the hydrolysis rate, which is reminiscent of the action of the histidine group in phosphoramidase enzymes (e.g., HINT1). We were also able to use the reaction cycle to generate transient self-assemblies, which were characterized by dynamic light scattering (DLS), confocal microscopy (CLSM), and cryogenic transmission electron microscopy (cryo-TEM). Because these compartments are based on prebiotically plausible building blocks, our findings may have relevance for origin-of-life scenarios.

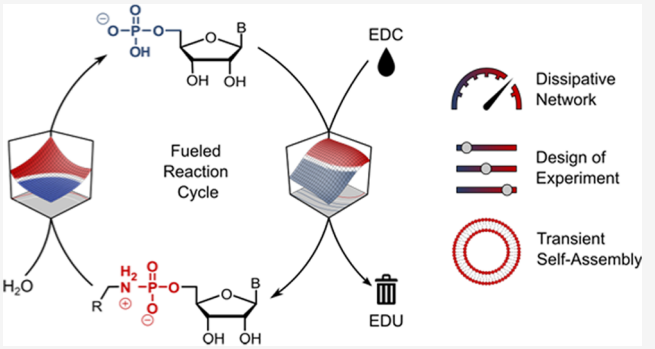

Downloaded via UNIV ULM on September 22, 2022 at 09:19:46 (UTC).
See https://pubs.acs.org/sharingguidelines for options on how to legitimately share published articles.

INTRODUCTION

At the molecular level, life is an out-of-equilibrium state that is characterized by a multitude of interconnected networks, each exhibiting complex collective behavior.[1] The emergent functions of such systems can only be maintained as long as energy is dissipated in the form of the consumption of high-energy molecules that stem from metabolic pathways.[2] In some cases, most notably in actin filaments[3] and microtubules,[4] chemical fuels drive the self-assembly of organic building blocks into transient supramolecular scaffolds. Over the past decade, researchers in the field of systems chemistry[5−7] have begun to mimic these natural processes, using artificial building blocks, chemical fuels,[8] and catalysts.[9−13]

Because the most widespread fuels in nature are adenosine triphosphate (ATP) and guanosine triphosphate (GTP), it is not surprising that artificial dissipative self-assemblies (DSA) have been realized with these compounds.[14−19] However, research on artificial systems is not limited to natural fuels. Pioneering work by Boekhoven, Eelkema, and van Esch[20,21] for instance has been based on the alkylating agent dimethyl sulfate. Other fuels used to generate DSA include dithionate,[22] perborate,[23] cyclodextrin,[24] acetic anhydride,[25] and amino acids.[26] Arguably, the most popular chemical fuels in artificial dissipative networks, especially in those that do not require enzyme catalysis, are carbodiimides such as 1-ethyl-3-(3-dimethylaminopropyl) carbodiimide (EDC).[27] Although the prebiotic plausibility of carbodiimide fuels is questionable,[28−30] EDC is valuable as a model reagent because of its water solubility, slow background reaction with water, and its exceptionally well-understood reaction profile.[31] For these reasons, EDC has been successfully used in a large number of recent studies on transient behavior. Dynamic vesicles have been formed by EDC-fueled self-assembly[32] and were shown to give rise to selective behavior due to phase separation.[33] Comparable systems were shown to facilitate transient macrocyclization (including host−guest chemistry),[34,35] time-controlled tuning of polymer properties,[36,37] control over molecular emission,[38] and fueled self-regulating hydrogels.[39−41] In all cases, EDC is used to transform carboxylic acids into the corresponding anhydrides.

Furthermore, carbodiimides recently fueled the ratcheted and directional motion of molecular machines.[42,43] Mimicking

Received: June 2, 2022
Published: August 11, 2022



© 2022 The Authors. Published by American Chemical Society

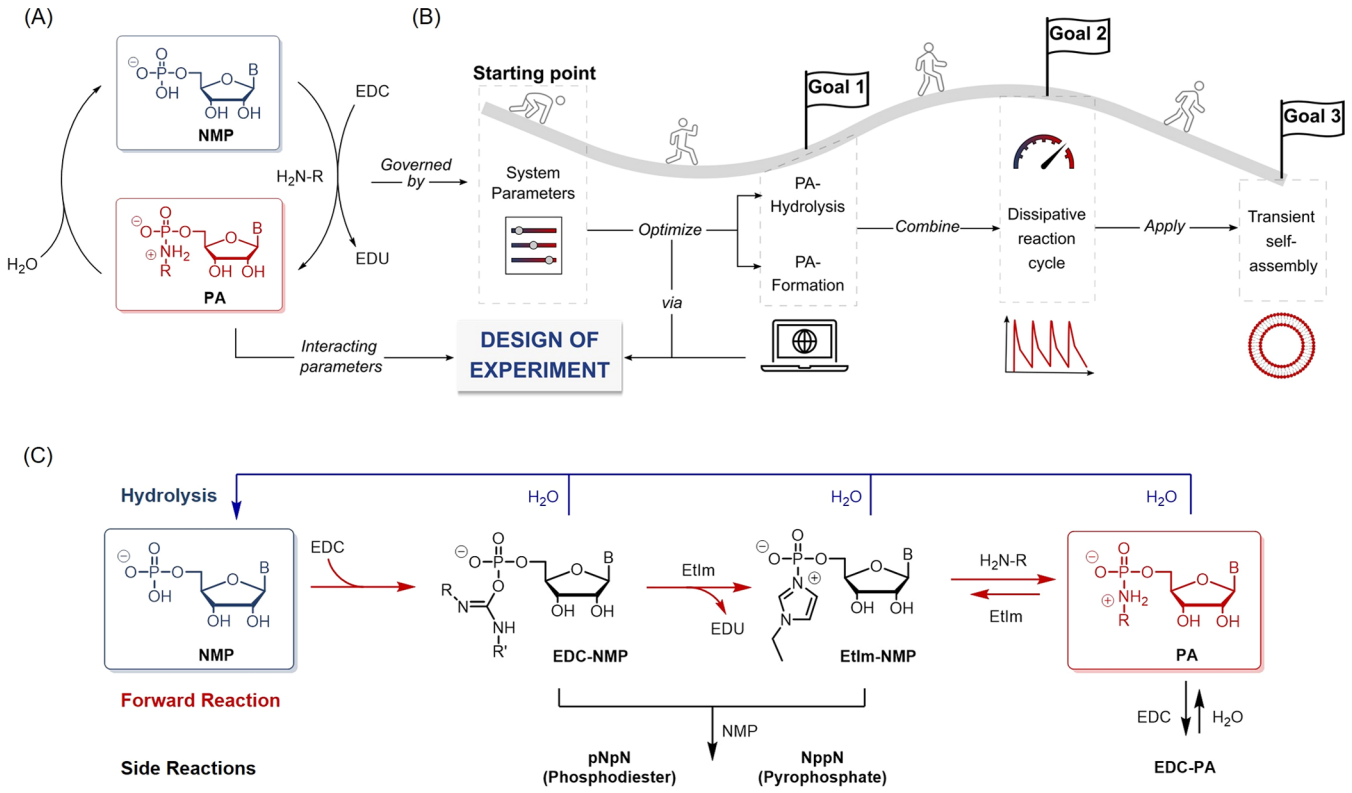

Figure 1. Reaction scheme and outline. (A) General scheme of the dissipative reaction cycle. (B) Objectives of this study and role of design of experiments (DoE). (C) Detailed reaction scheme of the reaction network, including the forward reaction from monophosphates NMP to phosphoramidates PA (red arrows), hydrolysis pathways (blue arrows), and side reactions (black arrows). B: nucleobase.

nature's dissipative systems can be crucial to understanding the origins of life, which requires out-of-equilibrium systems featuring self-replication, metabolism, and compartmentalization.[23,44,45] Recently, phosphoramidates have been identified as a compound class with prebiotic relevance. For example, efficient non-enzymatic primer extension of 3′-NP DNA[46,47] and template-directed synthesis of 3N′-5P′-RNA[48] have been reported (self-replication). Moreover, it was shown that prebiotically plausible stereoselective aminoacyl-RNA synthesis[28] and even ribosome-like translation[49] (metabolism) contain phosphoramidate intermediates. Both the formation[50−53] and the hydrolysis[54−57] as well as the self-assembly[58,59] of phosphoramidates have been studied individually. However, a fueled reaction network based on phosphoramidates and DSA controlled by this chemistry is elusive.

Herein, we present a dissipative reaction cycle, in which phosphoramidates are formed by the EDC-driven reaction of natural ribonucleotides with primary amines (Figure 1A). The hydrolytic backward reaction proceeds under relatively mild conditions, as long as it is catalyzed by 1-ethylimidazole (EtIm). Both the forward and the backward reaction were investigated by a broad design of experiments (DoE) approach (Figure 1B), which not only helped optimize the two fundamental processes but also revealed unexpected interactions between system parameters. Establishing ideal conditions for the full reaction cycle allowed us to demonstrate the transient self-assembly of rudimentary compartments comprising prebiotically plausible building blocks.

RESULTS AND DISCUSSION

Phosphoramidate-Based Reaction Cycle. The reaction network comprises a three-step forward reaction from natural ribonucleotide monophosphate (NMP) to the corresponding phosphoramidate (PA, red arrows in Figure 1C). First, the phosphate group of the NMPs reacts with the chemical fuel 1-ethyl-3-(3-dimethylaminopropyl) carbodiimide (EDC) to form an activated phosphate (EDC-NMP). Richert and co-workers have shown that this intermediate is highly sensitive to hydrolysis, while 1-ethylimidazole (EtIm) is used as a catalyst to capture the EDC-NMP and form a more stable EtIm-activated phosphate (EtIm-NMP).[60]

Nucleophilic attack of a primary amine leads to the formation of a phosphoramidate. As we describe below in more details, the conversion of the PA back to the EtIm-NMP plays a crucial role in the (mild) hydrolysis of the PA, which is required to close the dissipative reaction cycle. Hydrolysis can occur for all intermediates along the forward reaction (blue arrows in Figure 1C). Additionally, some side reactions need to be taken into account (black arrows in Figure 1C). The activated phosphates can undergo a nucleophilic attack with the 2′- or 3′-hydroxy group of another ribose to form a phosphodiester (pNpN) or with a second 5′-phosphate to form a pyrophosphate (NppN). As previously reported by our group, pyrophosphates can form rapidly and are kinetically stable toward hydrolysis,[61] which makes this side-reaction a problematic kinetic sink, while phosphodiesters hydrolyze more readily and played a negligible role in this study. Finally, we observed small amounts of *O*-acyl- and *N*-acyl-adducts (EDC-PA) between PA and EDC. The full chemical structures of these side products are depicted in Scheme S1. We refer to

https://doi.org/10.1021/jacs.2c05861
J. Am. Chem. Soc. 2022, 144, 15266−15274

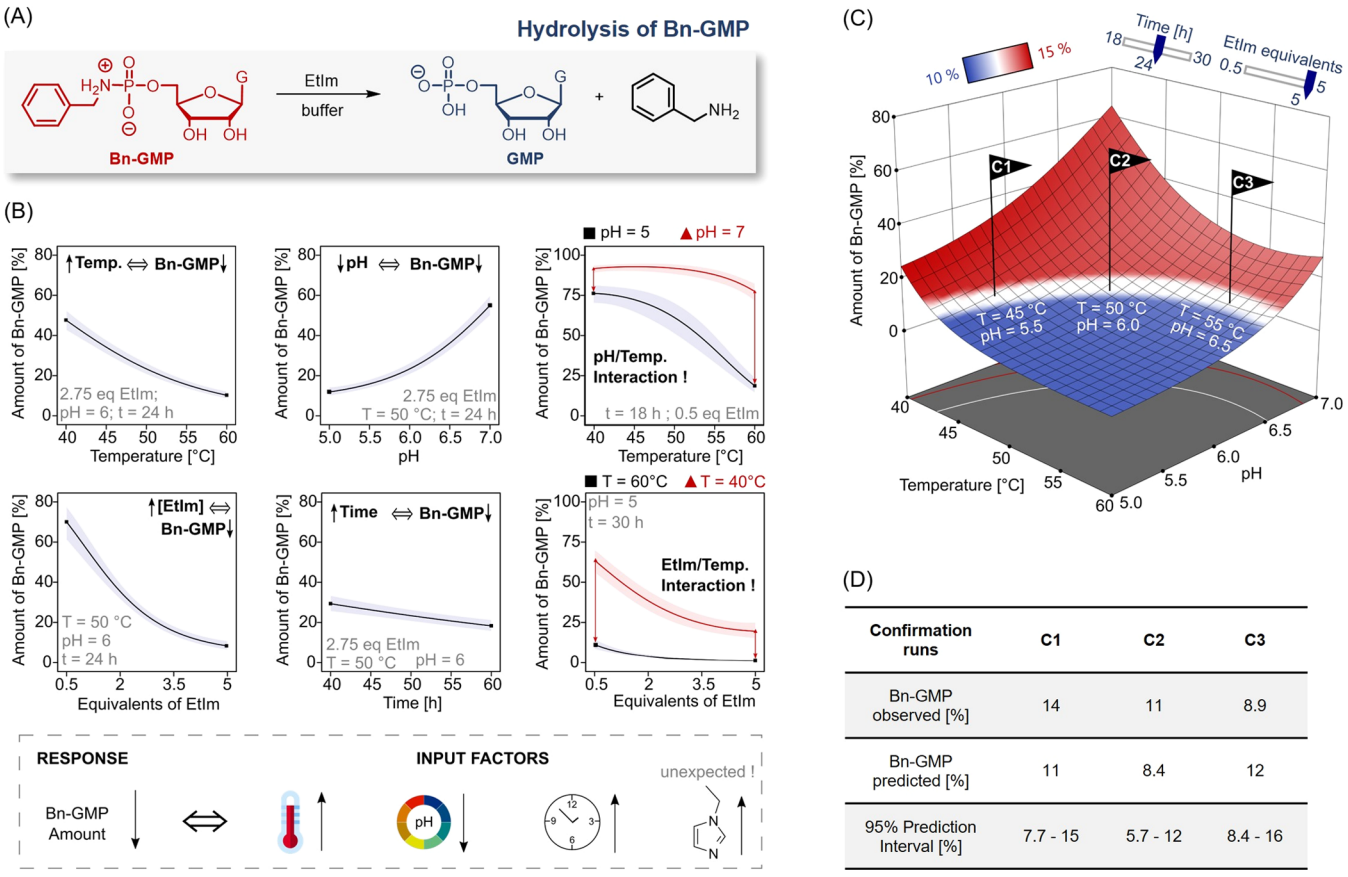

Confirmation runs	C1	C2	C3
Bn-GMP observed [%]	14	11	8.9
Bn-GMP predicted [%]	11	8.4	12
95% Prediction Interval [%]	7.7 - 15	5.7 - 12	8.4 - 16

Figure 2. (A) Reaction scheme of Bn-GMP hydrolysis. (B) One-factor diagrams and interaction diagrams with 95% confidence intervals (shaded area). The constant parameter sets for each diagram are indicated. General trends observed for the hydrolysis reaction are summarized at the bottom. (C) Predicted response surface of the hydrolysis reaction. The flags C1, C2, and C3 indicate the experimental confirmation runs of the model. (D) Table of the confirmation runs, comparing the experimentally observed values with the response predicted by DoE.

EDC as a "chemical fuel" to signify that the difference in free energy between EDC and the corresponding urea waste (EDU) is used to maintain a certain function,[8] e.g., the generation of transient vesicles. In a proof-of-principle experiment, we show that continuous addition of the fuel leads to an out-of-equilibrium steady state, where fuel is dissipated over a long period of time (see the Supporting Information, Section VII).

The three main objectives of this work are illustrated in Figure 1B. We first aimed to investigate and optimize the PA hydrolysis and PA formation reactions individually. Parameter optimization for chemical reactions can be a time-consuming and difficult endeavor, especially when parameters are involved that interact with each other and thus cannot be considered independently. Classical "One Factor at a Time" (OFAT) strategies are not able to reveal such interactions and do not lead to efficient experimental designs.[62,63] Particularly, in dissipative systems that possess two different reaction pathways, an OFAT approach might not be advisable. Computer-assisted design tools such as design of experiments (DoE) are well suited for the efficient evaluation of systems made up of interacting parameters and are applied in modern synthesis laboratories for the characterization and optimization of reactions.[64,65] Furthermore, by conducting a sufficient number of runs, response surface methods (RSM) can be used within a DoE to establish a predictive description model. To the best of our knowledge, the use of DoE has not yet been reported in the context of dissipative reaction cycles.

Our second objective was to combine the findings of both DoEs to find a parameter set that satisfies all criteria to allow several reaction cycles upon chemical fueling. Finally, we aimed to use the reaction cycle for the dissipative self-assembly of prebiotically relevant compartments.

Optimizing and Understanding the Hydrolysis of Phosphoramidates. To establish a dissipative reaction cycle, the backward reaction should proceed at a reasonable rate. We used the hydrolysis reaction depicted in Figure 2A as a reference system to evaluate whether phosphoramidates of primary amines fulfill this requirement. Bn-GMP was chosen as a model compound, and the respective reactions were performed at 25 mM concentration. The amount of Bn-GMP was determined by HPLC (with an internal standard) and was monitored throughout experiments to assess the degree of hydrolysis. To determine general trends and construct a predictive description model, we applied the DoE methodology to this system. More specifically, the reactions were performed in two blocks according to a central composite design (CCD) (Table S3), correlating the influence of the input factors temperature, pH, EtIm concentration, and time with the amount of unhydrolyzed Bn-GMP. The description model and the respective fit statistics are shown and discussed in detail in the Supporting Information (Section IV).

The observed trends are depicted schematically in Figure 2B. An increase in temperature, a more acidic pH, longer reaction times, and an increased amount of EtIm result in

https://doi.org/10.1021/jacs.2c05861
J. Am. Chem. Soc. 2022, 144, 15266−15274

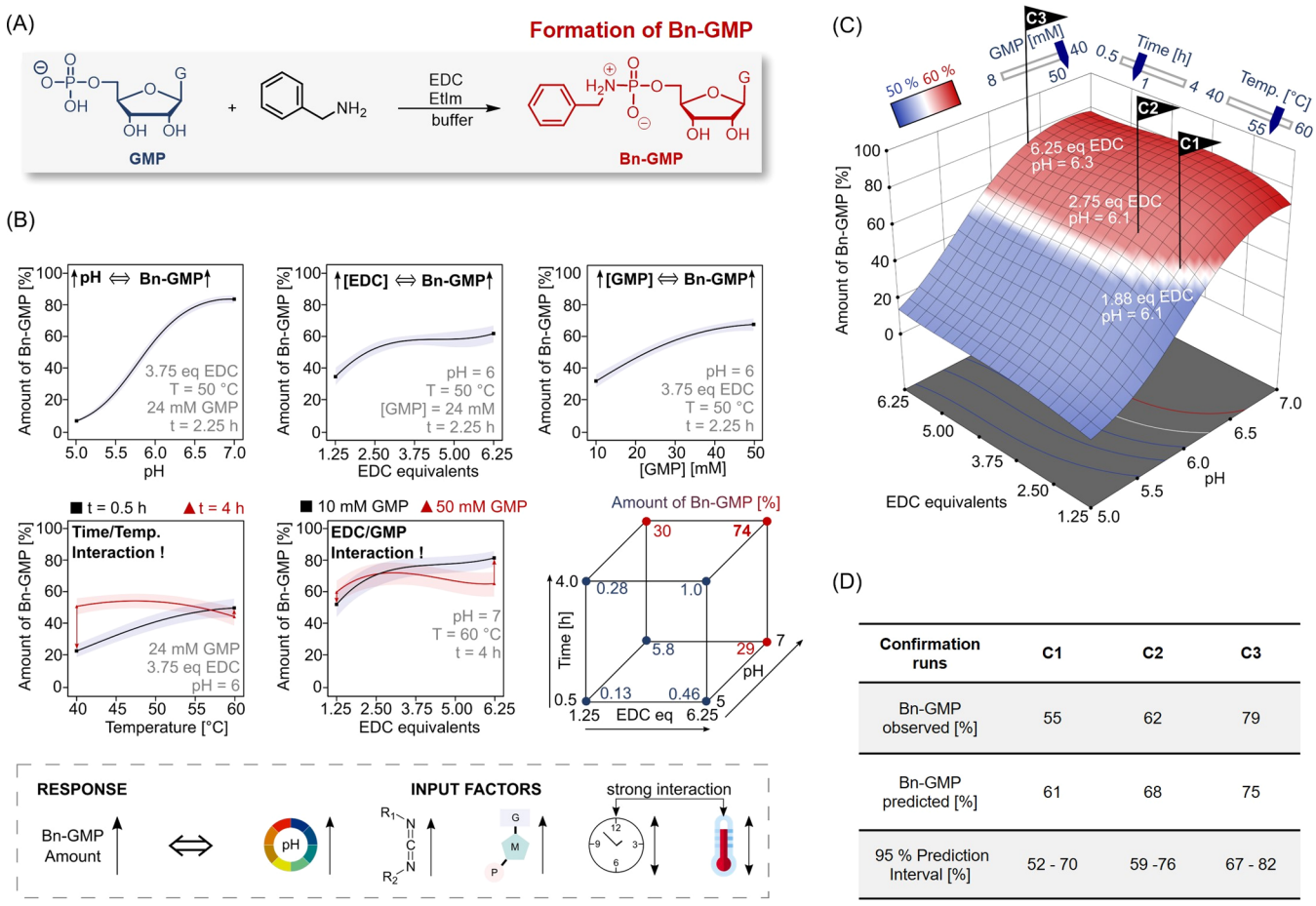

(D)

Confirmation runs	C1	C2	C3
Bn-GMP observed [%]	55	62	79
Bn-GMP predicted [%]	61	68	75
95 % Prediction Interval [%]	52 - 70	59 -76	67 - 82

Figure 3. (A) Reaction scheme of Bn-GMP formation. (B) One-factor diagrams and interaction diagrams with 95% confidence intervals (shaded area). All experiments were performed containing five equivalents of EtIm. Further parameter sets held constant are stated for each diagram. In the full factorial representation (cube), the data given here correspond to a temperature of 40 °C and an 8 mM GMP concentration. The general trends of the PA formation reaction are summarized at the bottom. (C) Predicted response surface of the formation reaction. The flags C1, C2, and C3 indicate the experimental confirmation runs of the model. (D) Table of the confirmation runs, comparing the experimentally observed values with the response predicted by DoE.

faster hydrolysis. The one-factor diagrams and interaction diagrams in Figure 2B show the quantitative effect of the individual factors on the response for different factor settings. While the correlation of reaction progress with temperature and time is unremarkable, the effect of pH is more interesting. In principle, we can explain this finding by the higher degree of protonation of the basic nitrogen atoms in the phosphoramidate and the phosphorimidazolide intermediate. This protonation is known to affect the rate of elimination of the leaving group in this "S_N2-like" reaction.[55] The pronounced influence of the EtIm amount on the hydrolysis was surprising, even though it had been reported previously that imidazole derivatives can play a role in the hydrolysis of phosphoramidates.[57] EtIm as a hydrolysis catalyst offers a great advantage compared to other degradation reactions of dissipative reaction cycles since it serves as an additional parameter allowing one to fine-tune the reaction.

One benefit of DoE analysis is that factors are not treated independently, and it therefore accounts for the fact that adjusting one factor may be highly dependent on the setting of another factor. We observed this behavior clearly in the pH/temperature and EtIm/temperature interactions depicted in Figure 2B (right-hand side). The more the red and blue slopes in the interaction diagrams differ from each other, the stronger the interaction. For instance, increasing the pH at 60 °C leads to starkly increased hydrolysis when compared to the moderate increase observed at 40 °C. Because such interactions are likely to exist also in other reaction networks, we believe the DoE methodology can generally be applied to help identify suitable reaction conditions.

We chose DoE based on RSM designs for the analysis of the system because this approach not only reveals trends within the recorded data set but also allows predictions based on the description model. This predictive capacity is demonstrated in the temperature-pH-response surface shown in Figure 2C. As mentioned above, the goal of this DoE was to achieve nearly complete hydrolysis of the reference compound within a reasonable timeframe. Therefore, three confirmation runs (C1−C3) were performed under conditions where a Bn-GMP amount below 15% after 24 h was predicted by the model. The mean values of the experimentally observed Bn-GMP amount of three parallel measurements are depicted in Figure 2D. All three confirmation runs are in good agreement with the predictions and within the interval of the prediction error, thus corroborating that we can predict diverse conditions for reasonably fast hydrolysis.

Optimizing and Understanding the EDC-Driven Formation of Phosphoramidates. After evaluating the

https://doi.org/10.1021/jacs.2c05861
J. Am. Chem. Soc. 2022, 144, 15266−15274

hydrolysis of phosphoramidates (backward reaction), we turned our attention to the forward reaction. To ensure comparability, we used the same model compounds as above, and the only crucial difference from the hydrolysis reaction is the presence of EDC (Figure 3A). Again, the amount of Bn-GMP was determined by HPLC and used as a response to evaluate the efficiency of the reaction. This response was correlated with the five input factors pH, temperature, concentration of GMP, time, and equivalents of EDC. The factor settings, the experimental design, and the respective fit statistics of the description model are shown in the Supporting Information (Section V). As shown in Figure 3B, increasing the pH, equivalents of EDC, and the concentration of GMP results in a more efficient Bn-GMP formation. The impact of these factors is illustrated in Figure 3B in the one-factor and interaction diagrams. Especially, the pH turned out to influence the reaction tremendously (steep curve in Figure 3B, top left). Under acidic conditions, the protonated state of the amine is favored, which impedes its effective nucleophilicity. Additionally, as the hydrolysis of Bn-GMP proceeds faster at a lower pH, it is reasonable to assume that the reactive intermediates (EDC-GMP and EtIm-GMP) also hydrolyze faster at a lower pH. The influence of EDC and GMP can be explained accordingly. Increasing the amount of the activation agent EDC counterbalances the hydrolysis of reactive intermediates, while a higher GMP concentration naturally increases the forward rate (according to collision theory).

In the case of the input factors temperature and time, no general trend could be established, as shown in the first interaction diagram of Figure 3B (for further time interactions, see Figure S8). The inverse slopes of the two graphs indicate that high Bn-GMP yields are observed after long reaction times at relatively low temperatures, while high yields can also be observed after short reaction times at relatively high temperatures. Such a behavior is characteristic of dissipative reaction cycles as the backward reaction dominates earlier at high temperatures. Moreover, we found that side reactions are also capable of diminishing the yield of the reaction, as illustrated in the second interaction diagram (Figure 3B).

Even though EDC reacts preferentially with the phosphate, a high excess of this reagent leads to the formation of EDC adducts (as shown in the reaction scheme in Figure 1C) and therefore an otherwise unexplainable decrease in Bn-GMP formation. The importance of multifactor interactions is further highlighted by the cubic representation of the parameters time, EDC, and pH (cube in Figure 3B).[66] Only careful adjustment of all three parameters allowed a considerable increase of the reaction efficiency. Figure 3C shows the EDC-pH-response surface of the investigated reaction as predicted by DoE. As with the hydrolysis reaction, confirmation runs (C1−C3) were conducted at conditions where the reaction yields were predicted to be above 50%. All three confirmation runs agree with the predictions and are within the interval of the prediction error (Figure 3D).

Closing the Dissipative Reaction Cycle. By conducting the DoEs, we found general system trends and description models. With these results in hand, our next objective was to use the reference system to establish a dissipative reaction cycle by combining the above findings. Figure 4A shows a contour plot that combines both models and was used to identify conditions suited for an efficient dissipative reaction cycle. Specifically, the green-shaded area represents conditions under which the PA hydrolysis occurs nearly completely within

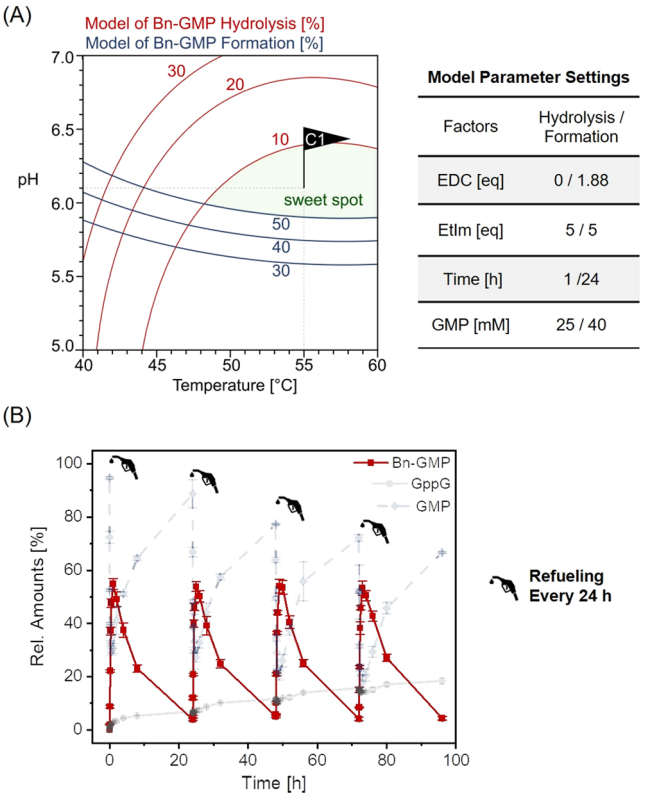

Figure 4. Combination of PA hydrolysis and PA formation (DoE). (A) Graphical optimization of temperature and pH for a dissipative reaction cycle. The desired conditions allow for hydrolysis below 10% of the residual Bn-GMP within 24 h (red lines) and sufficient (over 50%) Bn-GMP formation (blue lines) at the same time. The table specifies the remaining system parameters. (B) Four dissipative reaction cycles under optimized conditions. Relative amounts of Bn-GMP (red), GMP (blue, dotted line), and GppG (light gray) as determined by HPLC. Error bars indicate standard deviation based on triplicate reaction runs. Data points are connected to guide the eye.

24 h, but the PA formation is still quite effective (yield higher than 50%). To test the validity of the model, we fueled the dissipative system four times with EDC under these conditions (55 °C, pH = 6.1; see Table in Figure 4A). Figure 4B shows the relative amount of Bn-GMP over four cycles, validating that the predicted conditions are suited to establish a dissipative reaction cycle. It must be noted, however, that side products such as the pyrophosphate GppG form and accumulate over the course of several reaction cycles. For applications targeting many cycles in dissipative systems, the exploration of catalysts that enable the hydrolysis of pyrophosphates may be necessary.[61]

Transient Self-Assembly. Having optimized the dissipative reaction cycle, we wondered whether the combination of an alkylamine with a monophosphate could give rise to the transient self-assembly of compartments (Figure 5A). Due to the simplicity of all building blocks (except perhaps the fuel), such a system may have prebiotic relevance.[28,47,49] Furthermore, the use of an alkylamine rather than benzylamine demonstrates the relatively broad scope of the approach. Using alkylamines required only moderate adjustment of the reaction conditions, probably due to differences in pK_a.[67] We dissolved the natural ribonucleotide adenosine 5'-monophosphate (AMP) (75 mM) in a buffer, containing 5 equiv EtIm and added 1.5 equiv heptylamine. After adjusting the pH to 6.5 (at

https://doi.org/10.1021/jacs.2c05861
J. Am. Chem. Soc. 2022, 144, 15266−15274

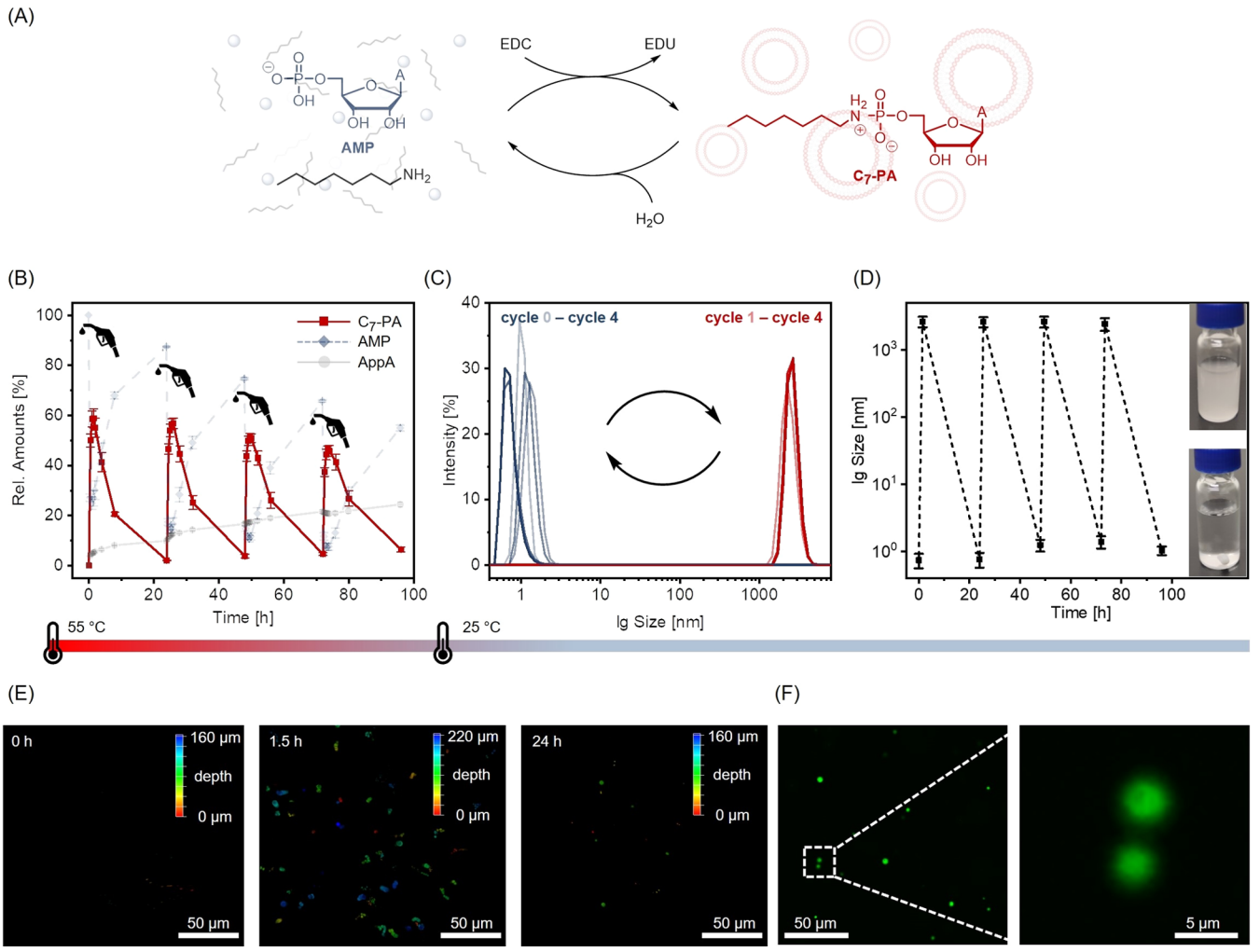

Figure 5. Transient self-assembly of compartments. (A) Reaction scheme of the EDC-driven reaction cycle. (B) Four dissipative reaction cycles (performed at 55 °C). Relative amounts of C_7-PA (red), AMP (blue, dotted line), and AppA (light gray) as determined by HPLC. Error bars indicate standard deviation based on triplicate reaction runs. Data points are connected to guide the eye. (C) DLS measurements at different time points during the four cycles (measured at 25 °C). The average distributions in mean hydrodynamic diameter of five parallel measurements are shown. (D) Average size of the aggregates at different time points as measured by DLS. Error bars indicate one standard deviation. Dotted lines are displayed to guide the eye. Inlets show clear solutions in the non-aggregated and turbid solutions in the aggregated state, respectively (at 25 °C). (E) 3D-CLSM images during one reaction cycle, measured at 25 °C and along the whole *z*-axis. The color code indicates the depth of the aggregates in the sample. (F) 2D-CLSM image of vesicular structures after 1.5 h with magnification. As a fluorescent dye 2.5 μM C153 was used.

55 °C) we obtained a clear, molecularly dissolved solution. Addition of 2 equiv EDC led to the rapid formation of the corresponding phosphoramidate (C_7-PA), as determined by quantitative HPLC (Figures 5B and S12). After 1.5 h, 60% of the AMP was converted to C_7-PA. As soon as the fuel was depleted, C_7-PA began to hydrolyze, and its amount dropped below 10% within 24 h. These results imply that the "sweet spot" identified in Figure 4A for benzyl amine is also viable for alkyl amines with only minor adjustments, and the stage was therefore set for the coupling of dissipative cycles with hydrophobic self-assembly. As shown in Figure 5B, we were able to demonstrate that this reaction cycle can be (re-)fueled at least four times. The main side-reaction is the formation of adenosine pyrophosphate (AppA). While the reaction was performed at 55 °C, we were only able to observe transient self-assembly at lower temperatures, e.g., at 25 °C. When quickly cooling the reaction mixture to 25 °C after 1.5 h, we obtained a turbid solution, and dynamic light scattering (DLS) revealed the formation of aggregates with an average hydrodynamic diameter of around 2.6 μm (Figures 5C,D and S13). After 24 h, the solutions were clear at 25 °C, and DLS indicated that the aggregates had vanished upon hydrolysis. Figure 5C shows the hydrodynamic diameter as an average of five measurements, corroborating the good reversibility of the self-assembly during four reaction cycles. Finally, confocal laser scanning microscopy (CLSM) with 2.5 μM "Cumarin 153" (C153) as a fluorescent dye was used to directly visualize the transient formation of aggregates (Figures 5E,F and S14). We scanned the sample along the whole z-axis to obtain a three-dimensional image of the solution (the color code in Figure 5E indicates the depth of the vesicle along the *z*-axis). While we initially observed no aggregates, a large number of spherical objects with diameters of approx 1−5 μm were visible 1.5 h after the addition of EDC. After 24 h, when most of the C_7-PA had hydrolyzed, there were only very few aggregates left. Figure 5F shows an enlarged two-dimensional CLSM image (after 1.5 h) of two aggregates, which would be consistent with a vesicular or colloidal structure. Cryogenic

https://doi.org/10.1021/jacs.2c05861
J. Am. Chem. Soc. 2022, 144, 15266−15274

transmission electron microscopy (cryo-TEM, Figures S15 and S16) is rather indicative of vesicles. Irrespective of the aggregate structure, the DLS and CLSM measurements reveal how the phosphoramidate-based reaction cycle we introduce herein can lead to compartmentalization under primordial conditions with prebiotically plausible building blocks such as ribonucleotides[68] and primary amines.[69] Our finding that the activation chemistry proceeded most efficiently at 55 °C, whereas compartments were only present at 25 °C, is interesting in the context of studies on thermophoresis, which showed that temperature gradients (e.g., at hydrothermal vents)[70] can lead to the enrichment of prebiotic molecules[71] and large oligomers[72] as well as the fission of lipid vesicles that can serve as a model for protocells.[73] Despite the use of EDC as a model reagent, our work therefore suggests that temperature gradients could have prebiotic relevance not only for physical or simple chemical processes but also for the regulation of individual processes in chemical reaction cycles and for the dynamic kinetic stability of dissipative compartments.

CONCLUSIONS

We report an out-of-equilibrium reaction cycle based on natural ribonucleotides and their corresponding phosphoramidates. For the first time, the software-assisted tool design of experiments (DoE) was used to optimize and better understand a fuel-driven chemical reaction cycle. For instance, we discovered a strong influence of 1-ethylimidazole on the hydrolysis of phosphoramidates. Such catalysis is reminiscent of the action of the histidine group in phosphoramidase enzymes (e.g., HINT1)[74] and has been used strategically before by others.[25,60] In the case of the phosphoramidate formation, we identified the pH value as the most important parameter and revealed interesting time/temperature interactions that are characteristic of dissipative systems. Furthermore, we were able to identify a "sweet spot" set of reaction conditions for both the forward and the backward reaction to enable an efficient dissipative reaction cycle. In all cases, we found the modeled predictions to be in good agreement with our experimental results. We expect that the DoE approach will become more commonplace in systems chemistry due to its ability to reveal useful insights into chemical systems governed by a complex set of parameters.

We also designed and realized a system capable of undergoing transient self-assembly. While both self-replicating and metabolic phosphoramidate-based systems have been reported recently,[28,47,49] to the best of our knowledge, we report the first example of transient compartmentalization using this particular chemistry. Despite some limitations related to the fuel (EDC) and the accumulation of a side product (pyrophosphate), this work therefore underscores the potential importance of phosphoramidates in prebiotic chemistry.

ASSOCIATED CONTENT

Supporting Information

The Supporting Information is available free of charge at https://pubs.acs.org/doi/10.1021/jacs.2c05861.

Reaction conditions, DoE data (such as factor settings, experimental design, and respective fit statistics of the description model), and additional measurements such as HPLC, DLS, CLSM, and (cryo-)TEM (PDF)

Raw_Data (XLSX)

AUTHOR INFORMATION

Corresponding Author

Max von Delius − *Institute of Organic Chemistry, Ulm University, 89081 Ulm, Germany*; orcid.org/0000-0003-1852-2969; Email: max.vondelius@uni-ulm.de

Authors

Andreas Englert − *Institute of Organic Chemistry, Ulm University, 89081 Ulm, Germany*

Julian F. Vogel − *Institute of Organic Chemistry, Ulm University, 89081 Ulm, Germany*

Tim Bergner − *Central Facility for Electron Microscopy, Ulm University, 89081 Ulm, Germany*

Jessica Loske − *Institute of Organic Chemistry, Ulm University, 89081 Ulm, Germany*

Complete contact information is available at: https://pubs.acs.org/10.1021/jacs.2c05861

Author Contributions

§A.E. and J.V. contributed equally and worked closely together on all concepts, experiments, and the preparation of the manuscript. All authors have given approval to the final version of the manuscript.

Notes

The authors declare no competing financial interest.

ACKNOWLEDGMENTS

This work was supported by the European Union (ERCstg 802428 "'SUPRANET"'). The authors would like to thank Prof. Paul Walther for help with (cryo-)TEM measurements and Aileen Klaus for valuable support during CLSM measurements.

REFERENCES

(1) Ruiz-Mirazo, K.; Briones, C.; De La Escosura, A. Prebiotic Systems Chemistry: New Perspectives for the Origins of Life. *Chem. Rev.* **2014**, *114*, 285−366.

(2) Giuseppone, N.; Walther, A.*Out-of-Equilibrium (Supra)Molecular Systems and Materials*, Wiley-VCH, 2021; pp 167−169 DOI: 10.1002/9783527821990.

(3) Pollard, T. D.; Blanchoin, L.; Mullins, R. D. Molecular Mechanism Controlling Actin Filament Dynamics in Nonmuscle Cells. *Annu. Rev. Biophys. Biomol. Struct.* **2000**, *29*, 545−576.

(4) Conde, C.; Cáceres, A. Microtubule Assembly, Organization and Dynamics in Axons and Dendrites. *Nat. Rev. Neurosci.* **2009**, *10*, 319−332.

(5) Ashkenasy, G.; Hermans, T. M.; Otto, S.; Taylor, A. F. Systems Chemistry. *Chem. Soc. Rev.* **2017**, *46*, 2543−2554.

(6) Mattia, E.; Otto, S. Supramolecular Systems Chemistry. *Nat. Nanotechnol.* **2015**, *10*, 111−119.

(7) Miljanić, O. S. Small-Molecule Systems Chemistry. *Chem* **2017**, *2*, 502−524.

(8) Borsley, S.; Leigh, D. A.; Roberts, B. M. W. Chemical Fuels for Molecular Machinery. *Nat. Chem.* **2022**, *14*, 728−738.

(9) Das, K.; Gabrielli, L.; Prins, L. J. Chemically Fueled Self-Assembly in Biology and Chemistry. *Angew. Chem., Int. Ed.* **2021**, *60*, 20120−20143.

(10) Rieß, B.; Grötsch, R. K.; Boekhoven, J. The Design of Dissipative Molecular Assemblies Driven by Chemical Reaction Cycles. *Chem* **2020**, *6*, 552−578.

(11) Wang, G.; Liu, S. Strategies to Construct a Chemical-Fuel-Driven Self-Assembly. *ChemSystemsChem* **2020**, *2*, No. e1900046.

(12) De, S.; Klajn, R. Dissipative Self-Assembly Driven by the Consumption of Chemical Fuels. *Adv. Mater.* **2018**, *30*, No. 1706750.
(13) Weißenfels, M.; Gemen, J.; Klajn, R. Perspective Dissipative Self-Assembly: Fueling with Chemicals versus Light. *Chem* **2021**, *7*, 23−37.
(14) Heinen, L.; Walther, A. Programmable Dynamic Steady States in ATP-Driven Nonequilibrium DNA Systems. *Sci. Adv.* **2019**, *5*, No. eaaw059.
(15) Deng, J.; Walther, A. ATP-Responsive and ATP-Fueled Self-Assembling Systems and Materials. *Adv. Mater.* **2020**, *32*, No. 2002629.
(16) Sorrenti, A.; Leira-Iglesias, J.; Sato, A.; Hermans, T. M. Non-Equilibrium Steady States in Supramolecular Polymerization. *Nat. Commun.* **2017**, *8*, No. 15899.
(17) Maiti, S.; Fortunati, I.; Ferrante, C.; Scrimin, P.; Prins, L. J. Dissipative Self-Assembly of Vesicular Nanoreactors. *Nat. Chem.* **2016**, *8*, 725−731.
(18) Cardona, M. A.; Prins, L. J. ATP-Fuelled Self-Assembly to Regulate Chemical Reactivity in the Time Domain. *Chem. Sci.* **2020**, *11*, 1518−1522.
(19) Chen, R.; Neri, S.; Prins, L. J. Enhanced Catalytic Activity under Non-Equilibrium Conditions. *Nat. Nanotechnol.* **2020**, *15*, 868−874.
(20) Boekhoven, J.; Brizard, A. M.; Kowlgi, K. N. K.; Koper, G. J. M.; Eelkema, R.; Van Esch, J. H. Dissipative Self-Assembly of a Molecular Gelator by Using a Chemical Fuel. *Angew. Chem., Int. Ed.* **2010**, *49*, 4825−4828.
(21) Boekhoven, J.; Hendriksen, W. E.; Koper, G. J. M.; Eelkema, R.; Esch, J. H. Van. Transient Assembly of Active Materials Fueled by a Chemical Reaction. *Science* **2015**, *349*, 1075−1080.
(22) Singh, N.; Lainer, B.; Formon, G. J. M.; Piccoli, S.; De; Hermans, T. M. Re-Programming Hydrogel Properties Using a Fuel-Driven Reaction Cycle. *J. Am. Chem. Soc.* **2020**, *142*, 4083−4087.
(23) Yang, S.; Schaeffer, G.; Mattia, E.; Markovitch, O.; Liu, K.; Hussain, A. S.; Ottelé, J.; Sood, A.; Otto, S. Chemical Fueling Molecular Complexification of Self-Replicators. *Angew. Chem., Int. Ed.* **2021**, *60*, 1344−11349.
(24) Lu, H.; Hao, J.; Wang, X. Host-Fueled Transient Supramolecular Hydrogels. *ChemSystemsChem* **2022**, *4*, No. e202100050.
(25) Helm, M. P.; Wang, C. L.; Fan, B.; Macchione, M.; Mendes, E.; Eelkema, R. Organocatalytic Control over a Fuel-Driven Transient-Esterification Network. *Angew. Chem., Int. Ed.* **2020**, *59*, 20604−20611.
(26) Debnath, S.; Roy, S.; Ulijn, R. V. Peptide Nanofibers with Dynamic Instability through Nonequilibrium Biocatalytic Assembly. *J. Am. Chem. Soc.* **2013**, *135*, 16789−16792.
(27) Schwarz, P. S.; Tena-solsona, M.; Dai, K.; Boekhoven, J. Carbodiimide-Fueled Catalytic Reaction Cycles to Regulate Supramolecular Processes. *Chem. Commun.* **2022**, *58*, 1284−1297.
(28) Roberts, S. J.; Liu, Z.; Sutherland, J. D. Potentially Prebiotic Synthesis of Aminoacyl-RNA via a Bridging Phosphoramidate-Ester Intermediate. *J. Am. Chem. Soc.* **2022**, *144*, 4254−4259.
(29) Song, E. Y.; Jiménez, E. I.; Lin, H.; Le Vay, K.; Krishnamurthy, R.; Mutschler, H. Prebiotically Plausible RNA Activation Compatible with Ribozyme-Catalyzed Ligation. *Angew. Chem., Int. Ed.* **2021**, *60*, 2952−2957.
(30) Duvernay, F.; Chiavassa, T.; Borget, F.; Aycard, J. P. Experimental Study of Water-Ice Catalyzed Thermal Isomerization of Cyanamide into Carbodiimide: Implication for Prebiotic Chemistry. *J. Am. Chem. Soc.* **2004**, *126*, 7772−7773.
(31) Williams, A.; Ibrahim, I. T. Carbodiimide Chemistry: Recent Advances. *Chem. Rev.* **1981**, *81*, 589−636.
(32) Wanzke, C.; Jussupow, A.; Kohler, F.; Dietz, H.; Kaila, V. R. I.; Boekhoven, J. Dynamic Vesicles Formed by Dissipative Self-Assembly. *ChemSystemsChem* **2020**, *2*, No. e190004.
(33) Tena-Solsona, M.; Wanzke, C.; Riess, B.; Bausch, A. R.; Boekhoven, J. Self-Selection of Dissipative Assemblies Driven by Primitive Chemical Reaction Networks. *Nat. Commun.* **2018**, *9*, No. 2044.
(34) Kariyawasam, L. S.; Hartley, C. S. Dissipative Assembly of Aqueous Carboxylic Acid Anhydrides Fueled by Carbodiimides. *J. Am. Chem. Soc.* **2017**, *139*, 11949−11955.
(35) Hossain, M. M.; Atkinson, J. L.; Hartley, C. S. Dissipative Assembly of Macrocycles Comprising Multiple Transient Bonds. *Angew. Chem., Int. Ed.* **2020**, *59*, 13807−13813.
(36) Zhang, B.; Jayalath, I. M.; Ke, J.; Sparks, J. L.; Hartley, C. S.; Konkolewicz, D. Chemically Fueled Covalent Crosslinking of Polymer Materials. *Chem. Commun.* **2019**, *55*, 2086−2089.
(37) Würbser, M. A.; Schwarz, P. S.; Heckel, J.; Bergmann, A. M.; Walther, A.; Boekhoven, J. Chemically Fueled Block Copolymer Self-Assembly into Transient Nanoreactors. *ChemSystemsChem* **2021**, *3*, No. e2100015.
(38) Zong, Z.; Zhang, Q.; Qiu, S. H.; Wang, Q.; Zhao, C.; Zhao, C. X.; Tian, H.; Qu, D. H. Dynamic Timing Control over Multicolor Molecular Emission by Temporal Chemical Locking. *Angew. Chem., Int. Ed.* **2022**, *61*, No. e2021164.
(39) Bal, S.; Das, K.; Ahmed, S.; Das, D. Chemically Fueled Dissipative Self-Assembly That Exploits Cooperative Catalysis. *Angew. Chem., Int. Ed.* **2019**, *58*, 244−247.
(40) Panja, S.; Dietrich, B.; Adams, D. J. Chemically Fuelled Self-Regulating Gel-to-Gel Transition. *ChemSystemsChem* **2019**, *1900038*, 2−7.
(41) Heckel, J.; Loescher, S.; Mathers, R. T.; Walther, A. Chemically Fueled Volume Phase Transition of Polyacid Microgels. *Angew. Chem., Int. Ed.* **2021**, *60*, 7117−7125.
(42) Borsley, S.; Leigh, D. A.; Roberts, B. M. W. A Doubly Kinetically-Gated Information Ratchet Autonomously Driven by Carbodiimide Hydration. *J. Am. Chem. Soc.* **2021**, *143*, 4414−4420.
(43) Borsley, S.; Kreidt, E.; Leigh, D. A.; Roberts, B. M. W. Autonomous Fuelled Directional Rotation about a Covalent Single Bond. *Nature* **2022**, *604*, 80−85.
(44) Adamski, P.; Eleveld, M.; Sood, A.; Kun, Á.; Szilágyi, A.; Czárán, T.; Szathmáry, E.; Otto, S. From Self-Replication to Replicator Systems En Route to de Novo Life. *Nat. Rev.* **2020**, *4*, 386−403.
(45) Otto, S. An Approach to the De Novo Synthesis of Life. *Acc. Chem. Res.* **2022**, *55*, 145−155.
(46) Zhang, S.; Zhang, N.; Blain, J. C.; Szostak, J. W. Synthesis of N3′-P5′-Linked Phosphoramidate DNA by Nonenzymatic Template-Directed Primer Extension. *J. Am. Chem. Soc.* **2013**, *135*, 924−932.
(47) Zhou, L.; Szostak, J. W. Nonenzymatic Template-Directed Synthesis of Mixed-Sequence 3′-NP-DNA up to 25 Nucleotides Long Inside Model Protocells. *J. Am. Chem. Soc.* **2019**, *141*, 10481−10488.
(48) Kaiser, A.; Spies, S.; Lommel, T.; Richert, C. Template-Directed Synthesis in 3′- and 5′-Direction with Reversible Termination. *Angew. Chem., Int. Ed.* **2012**, *51*, 8299−8303.
(49) Jash, B.; Tremmel, P.; Jovanovic, D.; Richert, C. Single Nucleotide Translation without Ribosomes. *Nat. Chem.* **2021**, *13*, 751−757.
(50) Gryaznov, S. M.; Lloyd, D. H.; Chen, J.; Schultz, R. G.; Dedionisio, L. A.; Ratmeyert, L.; Wilson, W. D. Oligonucleotide N3′-P5′ Phosphoramidates. *Proc. Natl. Acad. Sci. U.S.A.* **1995**, *92*, 5798−5802.
(51) Chen, J.-K.; Schultz, R. G.; Lioyd, D. H.; Gryaznov, S. M. Synthesis of Oligodeoxyribonucleotide N3′→P5′ Phosphoramidates. *Nucleic Acids Res.* **1995**, *23*, 2661−2668.
(52) Griesser, H.; Tremmel, P.; Kervio, E.; Pfeffer, C.; Steiner, U. E.; Richert, C. Ribonucleotides and RNA Promote Peptide Chain Growth. *Angew. Chem., Int. Ed.* **2017**, *56*, 1219−1223.
(53) Griesser, H.; Bechthold, M.; Tremmel, P.; Kervio, E.; Richert, C. Amino Acid-Specific, Ribonucleotide-Promoted Peptide Formation in the Absence of Enzymes. *Angew. Chem., Int. Ed.* **2017**, *56*, 1224−1228.
(54) Lonnberg, T.; Ora, M.; Lonnberg, H. Hydrolytic Reactions of Nucleoside Phosphoramidates: Kinetics and Mechanisms. *Org. Chem.* **2010**, *7*, 33−43.
(55) Maiti, M.; Michielssens, S.; Dyubankova, N.; Maiti, M.; Lescrinier, E.; Ceulemans, A.; Herdewijn, P. Influence of the

https://doi.org/10.1021/jacs.2c05861
J. Am. Chem. Soc. 2022, 144, 15266−15274

Nucleobase and Anchimeric Assistance of the Carboxyl Acid Groups in the Hydrolysis of Amino Acid Nucleoside Phosphoramidates. *Chem. - Eur. J.* **2012**, *18*, 857−868.
(56) Choy, C. J.; Ley, C. R.; Davis, A. L.; Backer, B. S.; Geruntho, J. J.; Clowers, B. H.; Berkman, C. E. Second-Generation Tunable PH-Sensitive Phosphoramidate-Based Linkers for Controlled Release. *Bioconjugate Chem.* **2016**, *27*, 2206−2213.
(57) Jovanovic, D.; Tremmel, P.; Pallan, P. S.; Egli, M.; Richert, C. The Enzyme-Free Release of Nucleotides from Phosphoramidates Depends Strongly on the Amino Acid. *Angew. Chem., Int. Ed.* **2020**, *59*, 20154−20160.
(58) Gangadhara, K. L.; Srivastava, P.; Rozenski, J.; Mattelaer, H. P.; Leen, V.; Dehaen, W.; Hofkens, J.; Lescrinier, E.; Herdewijn, P. Design and Synthesis of Nucleolipids as Possible Activated Precursors for Oligomer Formation via Intramolecular Catalysis: Stability Study and Supramolecular Organization. *J. Syst. Chem.* **2014**, *5*, No. 5.
(59) West, H. T.; Csizmar, C. M.; Wagner, C. R. Tunable Supramolecular Assemblies from Amphiphilic Nucleoside Phosphoramidate Nanofibers by Enzyme Activation. *Biomacromolecules* **2018**, *19*, 2650−2656.
(60) Tremmel, P.; Griesser, H.; Steiner, U. E.; Richert, C. How Small Heterocycles Make a Reaction Network of Amino Acids and Nucleotides Efficient in Water. *Angew. Chem., Int. Ed.* **2019**, *58*, 13087−13092.
(61) Sun, J.; Vogel, J.; Chen, L.; Schleper, A. L.; Bergner, T.; Kuehne, A. J. C.; von Delius, M. Carbodiimide-Driven Dimerization and Self-Assembly of Artificial, Ribose-Based Amphiphiles. *Chem. - Eur. J.* **2022**, *28*, No. e202104116.
(62) Dejaegher, B.; Heyden, Y. Vander. Experimental Designs and Their Recent Advances in Set-up, Data Interpretation, and Analytical Applications. *J. Pharm. Biomed. Anal.* **2011**, *56*, 141−158.
(63) Weissman, S. A.; Anderson, N. G. Design of Experiments (DoE) and Process Optimization. A Review of Recent Publications. *Org. Process Res. Dev.* **2015**, *19*, 1605−1633.
(64) Aggarwal, V. K.; Staubitz, A. C.; Owen, M. Optimization of the Mizoroki - Heck Reaction Using Design of Experiment (DoE). *Org. Process Res. Dev.* **2006**, *10*, 64−69.
(65) Bowden, G. D.; Pichler, B. J.; Maurer, A. A Design of Experiments (DoE) Approach Accelerates the Optimization of Copper-Mediated F-Fluorination Reactions of Arylstannanes. *Sci. Rep.* **2019**, *9*, No. 11370.
(66) When following one axis starting from different corners, it becomes evident that there are different relative improvements of the reaction yields (numbers on the corners) depending on the starting point.
(67) The scope does not include arylamines like aniline, which form phosphoramidates that are mostly stable towards hydrolysis.
(68) Becker, S.; Feldmann, J.; Wiedemann, S.; Okamura, H.; Schneider, C.; Iwan, K.; Crisp, A.; Rossa, M.; Amatov, T.; Carell, T. Unified Prebiotically Plausible Synthesis of Pyrimidine and Purine RNA Ribonucleotides. *Science* **2019**, *366*, 76−82.
(69) Mullen, L. B.; Sutherland, J. D. Formation of Potentially Prebiotic Amphiphiles by Reaction of β-Hydroxy-n-Alkylamines with Cyclotriphosphate. *Angew. Chem., Int. Ed.* **2007**, *46*, 4166−4168.
(70) Arndt, N. T.; Nisbet, E. G. Processes on the Young Earth and the Habitats of Early Life. *Annu. Rev. Earth Planet. Sci.* **2012**, *40*, 521−549.
(71) Morasch, M.; Liu, J.; Dirscherl, C. F.; Ianeselli, A.; Kühnlein, A.; Le Vay, K.; Schwintek, P.; Islam, S.; Corpinot, M. K.; Scheu, B.; Dingwell, D. B.; Schwille, P.; Mutschler, H.; Powner, M. W.; Mast, C. B.; Braun, D. Heated Gas Bubbles Enrich, Crystallize, Dry, Phosphorylate and Encapsulate Prebiotic Molecules. *Nat. Chem.* **2019**, *11*, 779−788.
(72) Mast, C. B.; Schink, S.; Gerland, U.; Braun, D. Escalation of Polymerization in a Thermal Gradient. *Proc. Natl. Acad. Sci. U.S.A.* **2013**, *110*, 8030−8035.
(73) Kudella, P. W.; Preißinger, K.; Morasch, M.; Dirscherl, C. F.; Braun, D.; Wixforth, A.; Westerhausen, C. Fission of Lipid-Vesicles by Membrane Phase Transitions in Thermal Convection. *Sci. Rep.* **2019**, *9*, No. 18808.
(74) Zhou, X.; Chou, T.; Aubol, B. E.; Park, C. J.; Wolfenden, R.; Adams, J.; Wagner, C. R. Kinetic Mechanism of Human Histidine Triad Nucleotide Binding Protein 1. *Biochemistry* **2013**, *52*, 3588−3600.

Recommended by ACS

Template-Free Assembly of Functional RNAs by Loop-Closing Ligation
Long-Fei Wu, John D. Sutherland, *et al.*
JULY 26, 2022
JOURNAL OF THE AMERICAN CHEMICAL SOCIETY
READ

Optical Control of MicroRNA Function in Zebrafish Embryos
Wes Brown, Alexander Deiters, *et al.*
SEPTEMBER 08, 2022
JOURNAL OF THE AMERICAN CHEMICAL SOCIETY
READ

Aminooxy Click Chemistry as a Tool for Bis-homo and Bis-hetero Ligand Conjugation to Nucleic Acids
Dhrubajyoti Datta, Muthiah Manoharan, *et al.*
JUNE 17, 2022
ORGANIC LETTERS
READ

Stochastic Emergence of Two Distinct Self-Replicators from a Dynamic Combinatorial Library
Gaël Schaeffer, Sijbren Otto, *et al.*
MARCH 31, 2022
JOURNAL OF THE AMERICAN CHEMICAL SOCIETY
READ

Get More Suggestions >

https://doi.org/10.1021/jacs.2c05861
J. Am. Chem. Soc. 2022, 144, 15266−15274

Supporting Information

A Ribonucleotide ↔ Phosphoramidate Reaction Network Optimized by Computer-Aided Design

Andreas Englert[a‡], Julian F. Vogel[a‡], Tim Bergner[b], Jessica Loske[a], Max von Delius[a]*

[a]Institute of Organic Chemistry, Ulm University, Albert-Einstein-Allee 11, 89081 Ulm, Germany

[b]Central Facility for Electron Microscopy, Ulm University, Albert-Einstein-Allee 11, 89081 Ulm, Germany

E-Mail: max.vondelius@uni-ulm.de

Table of Contents

General **3**

Abbreviations **4**

Synthesis **6**

N,N,N,N′,N′,N′,-hexaethyl-2,7-benzenedimethanammonium dibromide 6

Bn-GMP 6

Optimizing Bn-GMP Hydrolysis by DoE **7**

Objectives and Responses 7

Input factors 8

Experimental Procedure and Design 9

Data Analysis 10

Additional interaction diagrams regarding the time variable 24

Graphical optimization 14

Optimizing the formation of Bn-GMP by DoE **15**

Objectives and responses 15

Input factors 16

Experimental Procedure and Design 17

Data Analysis 20

Graphical Optimization 24

Combining Hydrolysis and Formation of Bn-GMP and Closing the Dissipative Reaction Cycle **26**

Reaction cycle 26

HPLC Analysis 26

Further experiments **27**

Bn-GMP Reaction cycle at Room Temperature 27

Steady-State Experiment 27

Transient Self-Assembly with AMP and Heptylamine **29**

Reaction cycle 29

HPLC Analysis 29

Dynamic Light Scattering (DLS) 30

Confocal Laser Scanning Microscopy (CLSM) 31

Transmission Electron Microscopy (TEM) 32

Cryogenic Transmission Electron Microscopy (cryo-TEM) 33

References **34**

Supplementary Data **35**

General

All chemicals were purchased from Merck Sigma Aldrich, TCI, AcrosOrganics, FisherScientific, VWR or chemPUR and were used without further purifications. In the case of guanosine 5'-monophosphate, the disodium salt hydrate was purchased. The guanosine 5'-monophosphate content (without crystal water) was determined by quantitative NMR (with internal standard) to be 80%. Since EDC is hygroscopic and susceptible to hydrolysis, it was stored in the freezer and its purity was determined regularly by quantitative HPLC and found to be around 99%.

BrukerAvance 400 and 600 NEO spectrometers were used to record NMR spectra (^{1}H: 400 or 600 Hz, ^{13}C: 101 Hz, ^{31}P: 162 or 243 Hz). The respective spectra were referenced to the residual solvent peaks (1H: 4.79 ppm. Chemical shifts (δ) are denoted in ppm and coupling constants (J) in Hz. Peak multiplicities are indicated as s = singlet, d = doublet, t = triplet and m = multiplet.)

Chromatograms and HRMS were recorded on an Agilent 1260 Infinity II system containing the following modules: G7117C 1260 DAD HS, G7116A 1260 MCT, G7167A 1260 Multisampler, G7104C 1260 flexible pump and 6546 LC/QTOF. HILIC was used as separation mode throughout this study. The UPLC column ACQUITY PRM BEHAmide (100 x 2.1 mm, 1.7 µm, 130 Å) was purchased from Waters and used as stationary phase.

Transmission Electron Microscopy (TEM) measurements were performed on a ZEISS EM10 microscope with an acceleration voltage of 120 kV.

Cryo-TEM grids were analyzed on a JEM-2100F (JEOL) at 200 kV and a temperature of -150 °C using a Gatan cryo-holder.

Dynamic light scattering (DLS) was performed on a Nano-Zetasizer (Malvern Instruments) at 25 °C with a 173° backscatter angle at λ = 633 nm.

Confocal laser scanning microscopy (CLSM) images were recorded with a TCS SP8 confocal microscope using the Leica Application Suite X (LASX) with the LIGHTNING wizard.

DesignExpert 13 (version 13.0.10.0), Wolfram Mathematica (version 12.3.0.0), and OriginPro 2021b (version 9.8.5.201) were used for analyzing and displaying data.

Abbreviations

Abbreviation	Name
ACN	Acetonitrile
AICc	Akaike Information Criterion
AMP	Adenosine-5'-monophosphate
ANOVA	Analysis of Variance
AppA	*P,P*-Di(adenosine-5') pyrophosphate (see structure below)
BIC	Bayesian Information Criterion
Bn-GMP	((2R,3S,5R)-5-(2-amino-6-oxo-1,6-dihydro-9H-purin-9-yl)-3-hydroxytetrahydrofuran-2-yl)methyl benzylphosphoramidate
C153	Cumarin 153 (see structure below)
CCD	Central Composite Design
CLSM	Confocal Laser Scanning Microscopy
DAD	Diode Array Detector
DLS	Dynamic Light Scattering
DOE	Design Of Experiment
EDC	1-Ethyl-3-(3-dimethylaminopropyl)carbodiimide (see structure below)
EDC-PA	EDC adducts (see structure below)
EDU	1-(3-(dimethylamino)propyl)-3-ethylurea (see structure below)
EIC	Extracted Ion Chromatogram
ESI	Electrospray Ionisation
EtIm	1-Ethylimidazole
FFD	Full Factorial Design
GMP	Guanosine-5'-monophosphate
GppG	*P,P*-Di(guanosine-5') pyrophosphate (see structure below)
HILIC	Hydrophilic Liquid Interaction Chromatography
HINT1	Histidine Triad Nucleotide Binding Protein 1
HPLC	High Performance Liquid Chromatography
HRMS	High Resolution Mass Spectrometry
ISDT	Internal Standard
MES	4-Morpholino-ethansulfonic acid
MOPS	3-Morpholino-propansulfonic acid
NMR	Nuclear Magnetic Resonance
OFAT	One Factor at a Time
PA	Phosphoramidate
PRESS	Predicted Residual Sum of Squares
TIC	Total Ion Count
UV/VIS	Ultraviolet/Visible
TEM	Transmission Electron Microscopy

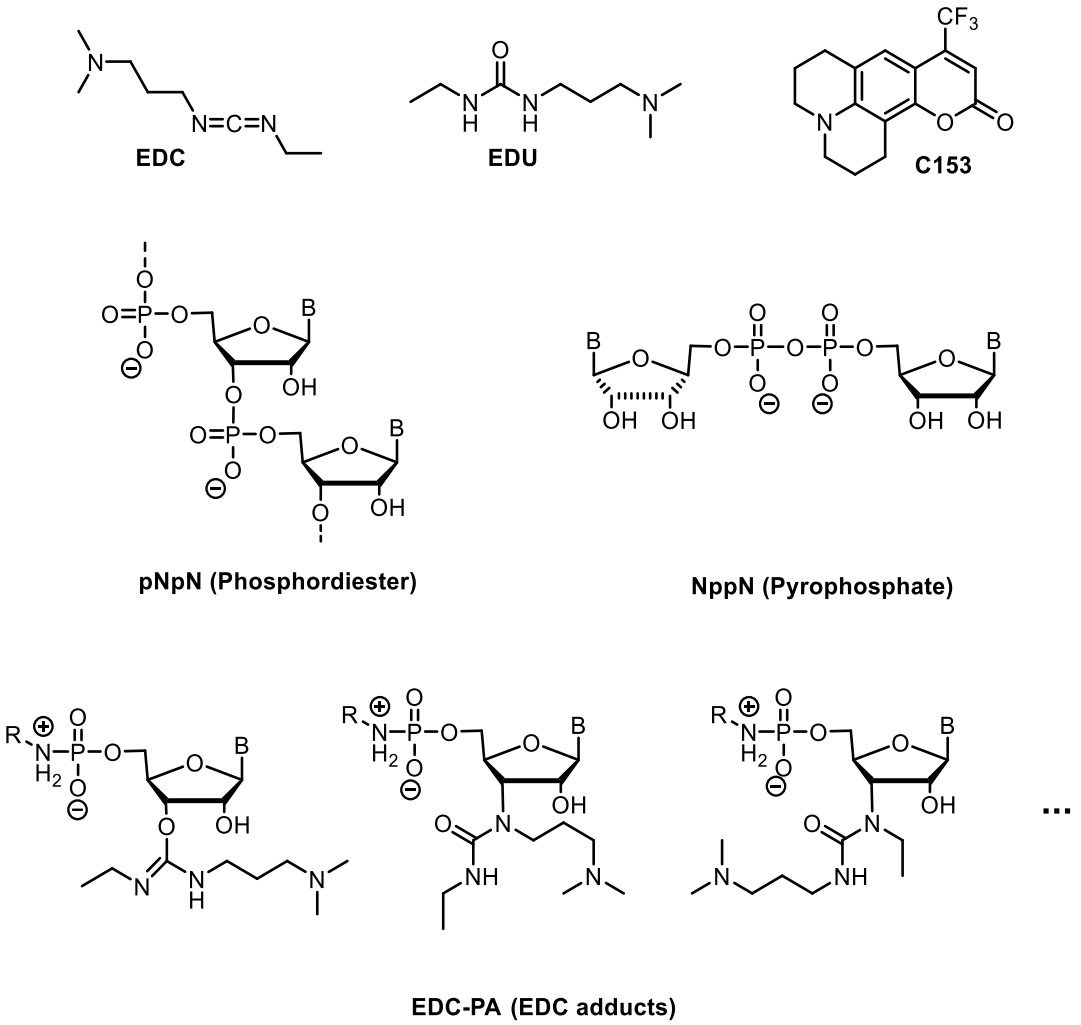

Scheme S1: Full molecular structures and abbreviations for key compounds.

Synthesis

N,N,N,N',N',N',-hexaethyl-2,7-benzenedimethanammonium dibromide

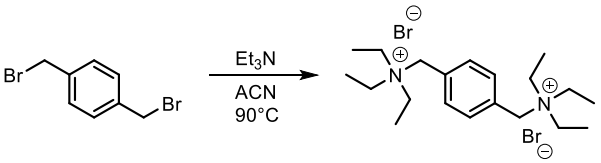

The reaction was performed according to a modified protocol of Chu *et al.*.[1] In a pressure tube 3.00 g (11.4 mmol) 1,4-dibromoxylol were suspended in 15 mL acetonitrile. After addition of 4.75 mL (34.0 mmol, 3 equiv.) triethylamine the mixture was stirred at 90 °C for 24 h. The precipitate was filtered off and washed with cold acetonitrile and diethyl ether. 4.60 g (9.90 mmol 87%) were obtained as a colorless solid.

^{1}H NMR (400 MHz, D_2O, 298 K): δ [ppm] = 7.67 (s, 4 H, phenylic), 4.51 (s, 4 H, benzylic), 3.28 (q, ^{3}J= 7.24 Hz, 12 H, CH_2), 1.43 (t, ^{3}J= 7.22 Hz, 18 H, CH_3)

^{13}C NMR (101 MHz, D_2O, 298 K): δ [ppm] = 133.1, 129.5, 59.1, 52.4, 7.0

HRMS (ESI^+) ($C_{20}H_{38}N_2Br_1^+$, calc.: *m/z* = 385.2218): m/z = 385.2216

Bn-GMP

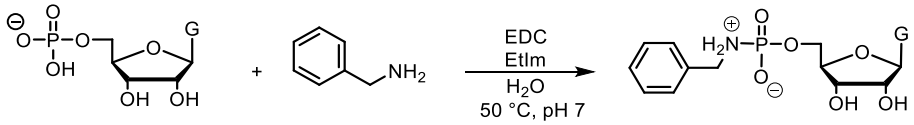

In a 100 mL round bottom flask, 1.43 g guanosine-5'-monophosphate disodium salt (3.50 mmol) were dissolved in 70 mL demineralized water. After addition of 0.46 mL benzylamine (4.20 mmol, 1.2 equiv.), and 1.35 mL 1-ethylimidazole (14.0 mmol, 4.0 equiv.) the reaction mixture was heated to 50 °C. The sample was set to pH = 7 by addition of concentrated HCl. 1.34 g EDC*HCl (7.00 mmol, 2 equiv.) were added and the mixture was stirred at 50 °C for two hours. The reaction mixture was diluted with Acetonitrile (approx. 1:1) and directly injected into a silica-based cartridge (separation mode HILIC, Interchim PF-15HIT-F0025) where the product was eluted by applying a gradient of ACN and NH_4HCO_3 buffer. Combining the respective fractions and lyophilization yielded 1.10 g (2.42 mmol 69%) of Bn-GMP.

^{1}H NMR (400 MHz, D_2O, 298 K): δ [ppm] = 7.97 (s, 1 H, guanosinic), 7.16 (m, 5 H, phenylic), 5.81 (d, 1 H, ^{3}J= 5.71 Hz, 1'), 4.77 (m, 1 H, 2'), 4.36 (m, 1 H, 3'), 4.25 (m, 1 H, 4'), 3.98 (m, 2 H, 5'), 3.75 (m, 2 H, benzylic)

^{13}C NMR (101 MHz, D_2O, 298 K): δ [ppm] = 158.6, 153.6, 140.5 (d), 137.4, 128.1, 127.0, 126.7, 116.3, 86.9, 84.0 (d), 73.0, 70.4, 63.9 (d), 44.9

^{31}P NMR (162 MHz, D_2O, 298 K): δ [ppm] = 8.85

HRMS (ESI^+) ($C_{17}H_{22}N_6O_7P_1^+$, calc.: *m/z* = 453.1288): m/z = 453.1285

Optimizing Bn-GMP Hydrolysis by DoE

Objectives and Responses

The hydrolysis of Bn-GMP was investigated, focusing on revealing general trends and optimizing reaction conditions. More specifically, the overall goal of the DOE was to achieve nearly complete hydrolysis (Bn-GMP content < 10-15%) within 24 hours.

Based on this objective the response of interest was chosen to be the relative amount of unhydrolyzed Bn-GMP. The amount was determined by HPLC-MS and *N,N,N,N',N',N'*,-hexaethyl-2,7-benzenedimethanammonium dibromide was used as internal standard. Here, a calibration was conducted where different concentration ratios of the internal standard and Bn-GMP were plotted against the respective intensity ratios. The calibration and the respective chromatograms are depicted in **Figure S1 and Table S1**.

Table S1: Internal Standard Calibration of Bn-GMP.

Run	[Bn-GMP] [mM]	[ISDT] [mM]	[Bn-GMP] / [ISDT]	ISTD intensity	Bn-GMP intensity	R(PA)/R(ISTD)
1	0.1	0.50	0.2	800.87	46.93	0.06
	0.5	0.50	1	824.67	516.08	0.63
	1	0.50	2	803.96	1039.01	1.29
	1.5	0.50	3	792.85	1475.83	1.86
2	0.1	0.50	0.2	799.17	47.89	0.06
	0.5	0.50	1	819.11	517.41	0.63
	1	0.50	2	802.6	1050.13	1.31
	1.5	0.50	3	798.3	1475.6	1.85
3	0.1	0.50	0.2	813.42	45.45	0.06
	0.5	0.50	1	797.54	503.8	0.63
	1	0.50	2	787.42	1031.6	1.31
	1.5	0.50	3	784.49	1458.94	1.86

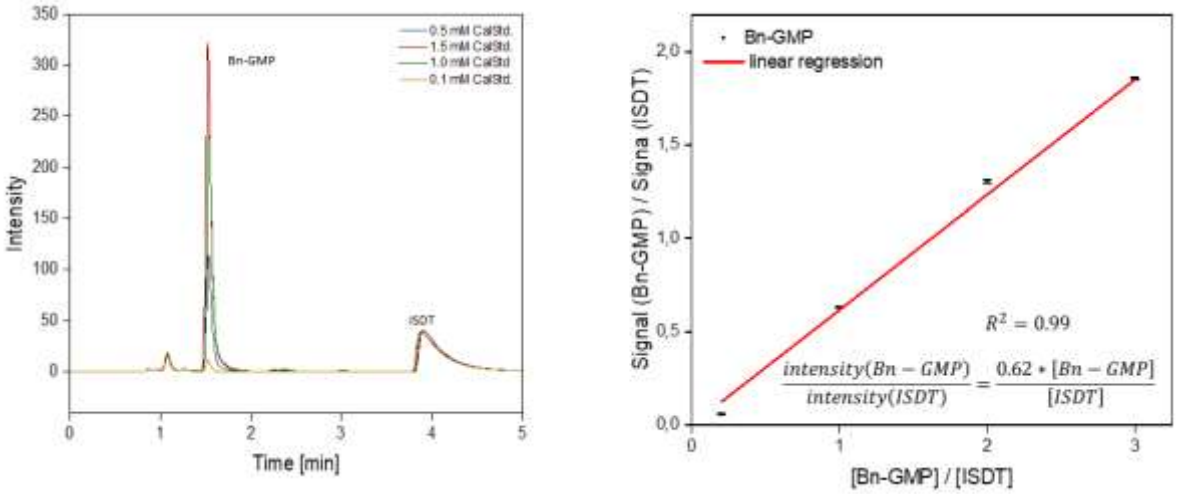

Figure S1: HPLC-based Internal Standard Calibration of Bn-GMP

Input factors

The input factors used in the designed experiment are shown in **Table S2 and Figure S2.**

Table S2: Input factors and ranges used in the designed experiment.

Factor	Name	Units	Type	SubType	Minimum	Maximum	Coded Low	Coded High
A	Temperature	°C	Numeric	Continuous	35.9	64.1	-1 ↔ 40.00	+1 ↔ 60.00
B	pH		Numeric	Continuous	4.6	7.4	-1 ↔ 5.00	+1 ↔ 7.00
C	Time	h	Numeric	Continuous	15.5	32.5	-1 ↔ 18.00	+1 ↔ 30.00
D	Equivalents of EtIm		Numeric	Continuous	0.5	5.93	-1 ↔ 0.50	+1 ↔ 5.00

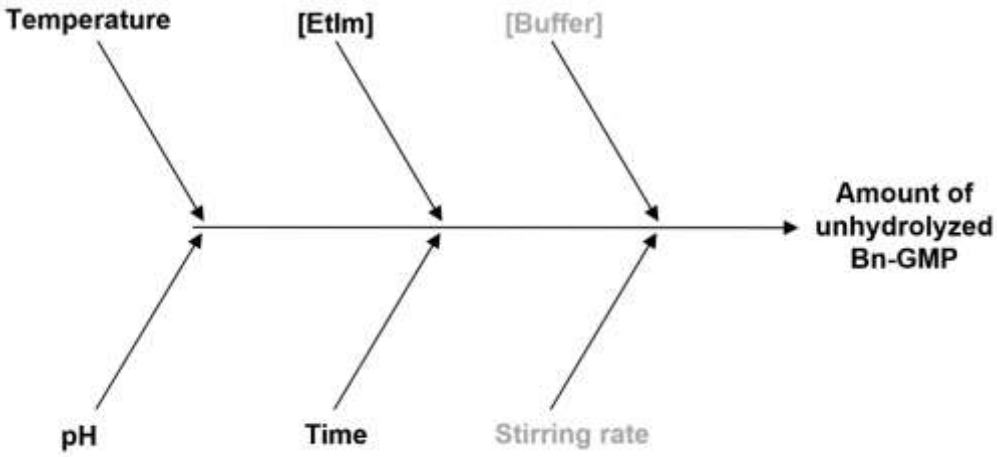

Figure S2: Fishbone diagram of the respective input factors (red), controlled/constant factors (blue) and responses (green).

Experimental Procedure and Design

Stock solutions of MOPS/MES (0.5 M), ISDT (0.05 M), EtIm (1.0 M), and Bn-GMP (0.25 M) were prepared in advance and used during the study. The reactions were performed in a closed reaction vessel equipped with a stirring bar. The reaction mixtures were prepared by pipetting and mixing the desired amounts of stock solutions in the order of buffer, ISDT, demineralized water, EtIm and Bn-GMP. Subsequently the sample was heated, and the pH adjusted by addition of concentrated HCl at the desired temperature. After the respective reaction time, an aliquot was taken from the mixture and analyzed via LC-MS. For HPLC, 50 µL were dissolved in 950 µL MeCN/H_2O (1:1) and 1 µL was injected on a Waters ACQUITY PRM BEHAmide (100 x 2.1 mm, 1.7 µm, 130 Å) column. Eluent: 70% MeCN, 30% aqueous NH_4HCO_3 solution (170 mM, total: 50 mM), flow rate = 0.3 mL/min, temp. = 60 °C.

From previous experiments it was known that the response will not behave in a linear manner based on factor changes. Therefore, an experimental design sufficient of filling a full quadratic description model was used as starting point. In concrete terms this means a CCD design was chosen, where in the first block 20 runs (containing a full factorial design with additional 4 center points) and in the second block 10 runs (containing the axial star points with two additional center points) were conducted as shown in **Table S3**.

Table S3: Experimental Design.

Block	Run	Temperature [°C]	pH	Time [h]	Equivalents of EtIm	Amount of Bn-GMP
Block 1	1	40	7	18	0.5	91
Block 1	2	40	7	18	5	69.9
Block 1	3	50	6	24	2.75	23.48
Block 1	4	60	5	18	5	1.96
Block 1	5	40	5	18	5	35.26
Block 1	6	40	5	30	5	19.31
Block 1	7	50	6	24	2.75	23.71
Block 1	8	60	5	18	0.5	24.8
Block 1	9	40	5	18	0.5	76.23
Block 1	10	60	7	18	0.5	72.26
Block 1	11	50	6	24	2.75	21.8
Block 1	12	60	7	30	0.5	70.77
Block 1	13	60	7	18	5	37.8
Block 1	14	40	7	30	0.5	87.71
Block 1	15	50	6	24	2.75	23.78
Block 1	16	60	5	30	5	1.42
Block 1	17	40	5	30	0.5	63.99

Block 1	18	40	7	30	5	55.43
Block 1	19	60	7	30	5	23.33
Block 1	20	60	5	30	0.5	10.69
Block 2	21	50	6	15.5	2.75	39.53
Block 2	22	50	6	32.5	2.75	16.26
Block 2	23	50	6	24	2.75	18.29
Block 2	24	50	4.6	24	2.75	7.87
Block 2	25	64.1	6	24	2.75	5.73
Block 2	26	50	6	24	0.5	68.38
Block 2	27	50	7.4	24	2.75	74.53
Block 2	28	50	6	24	5.93	6.05
Block 2	29	35.9	6	24	2.75	62.13
Block 2	30	50	6	24	2.75	23.97

Data Analysis

Since the system of interest represents a chemical reaction, the response is limited between boundaries of 0 and 100%. For this reason, the data were at first transformed via a logit function. Based on this, the description model was chosen by applying an AICc model reduction algorithm of all not aliased terms available. **Table S4** shows the respective model and the analysis of variance.

Table S4: ANOVA of the considered description model.

Source	Sum of Squares	df	Mean Square	F-value	p-value	
Block	1.59	1	1.59			
Model	74.47	11	6.77	144.98	< 0.0001	significant
A-Temperature	21.91	1	21.91	469.18	< 0.0001	
B-pH	24.57	1	24.57	526.18	< 0.0001	
C-Time	1.93	1	1.93	41.29	< 0.0001	
D-Equivalents of 1-Ethylimidazole	6.71	1	6.71	143.66	< 0.0001	
AB	2.18	1	2.18	46.62	< 0.0001	
AD	0.1321	1	0.1321	2.83	0.1108	
BD	0.2378	1	0.2378	5.09	0.0375	
A^2	0.0284	1	0.0284	0.6082	0.4462	
B^2	0.7301	1	0.7301	15.64	0.001	
D^2	0.9806	1	0.9806	21	0.0003	
A^2D	0.9759	1	0.9759	20.9	0.0003	

Residual	0.7938	17	0.0467			
Lack of Fit	0.7266	13	0.0559	3.33	0.1276	not significant
Pure Error	0.0672	4	0.0168			
Cor Total	76.85	29				

The regression model and its individual terms (factor effects and interactions) except A^2 and AD are statistically significant and exhibit large F and low p-values. This indicates that the variation explained by the model and its individual terms are large compared to the unexplained variance of the Residual. The model terms A^2 and AD were kept in the model for hierarchy reasons. The high F and low p value of the lack-of-fit test imply that the Lack of Fit is not significant. Further Model statistics are shown in **Table S5**. The predicted coefficient of determination (Predicted R^2) is close to 1 which is caused by a low predicted residual sum of squares (PRESS). This means that the variation explained by the model in "new data" is high, indicating that the model is suited for making predictions. The same holds true for the adjusted coefficient of determination (Adjusted R^2) which measures the variation around the mean explained by the regression taking a penalty for an increasing number of model parameters into account. The difference between Adjusted R^2 and Predicted R^2 is less than 0.2, and therefore in reasonable agreement. The adequate precision can be regarded as a signal-to-noise ratio, where the predicted values of the design points are compared to the average prediction error. As a rule of thumb, a ratio greater than four is desirable which means that the observed ratio of 48.28 indicates an adequate signal.

Table S5: Model Fit Statistics.

Std. Dev.	0.2161	R^2	0.9895
Mean	-0.712	Adjusted R^2	0.9826
C.V. %	30.35	Predicted R^2	0.9568
		Adeq Precision	48.2764

The regression model with the coded factors is depicted in **Table S6**.

Table S6: Coefficients as coded factors of the model regression.

Factor	Coefficient Estimate	df	Standard Error	95% CI Low	95% CI High	VIF
Intercept	-1.2	1	0.0748	-1.36	-1.04	
Block 1	0.034	1				
Block 2	-0.034					
A-Temperature	-1.05	1	0.0483	-1.15	-0.9452	1.00
B-pH	1.11	1	0.0484	1.01	1.21	1.00
C-Time	-0.3104	1	0.0483	-0.4123	-0.2085	1.00
D-Equivalents of EtIm	-1.64	1	0.1366	-1.92	-1.35	7.58
AB	0.3689	1	0.054	0.2549	0.4828	1.00
AD	-0.0909	1	0.054	-0.2048	0.0231	1.00
BD	0.1219	1	0.054	0.0079	0.2359	1.00
A^2	0.0571	1	0.0732	-0.0973	0.2115	1.22
B^2	0.2926	1	0.074	0.1365	0.4486	1.23
D^2	0.4216	1	0.092	0.2275	0.6157	1.62
A^2D	0.6714	1	0.1469	0.3615	0.9812	7.39

Figure S3A-E displays diagnostic graphs of the description model. **Figure S3A** represents the normal Plot of Residuals. Since all data points are following a straight line, it can be assumed that the residuals are normally distributed. Random Fluctuations within the data are not supposed to be systematic and are expected therefore to follow a normal distribution. Potential outliers (not caused by random fluctuations) would have been detected within this plot by strongly deviating from this line. **Figure S3B** shows the predicted and transformed response plotted against their residuals. The data points are randomly scattered, indicating no expanding variance. **Figure S3C** shows the calculated Residuals against the individual run number. The residuals are randomly scattered indicating that no time depending uncontrolled variables are apparent. **Figure S3D** depicts the Residuals within each block. Both blocks exhibit similar ranges of scattering with no specific pattern apparent. **Figure S3E** shows an intuitive way of looking at the performance of the description model in terms of a comparison of predicted and observed response values. A major part of the data variation is explained by the description model. The data scatters around the first bisector. This means that observed responses are in good agreement with the predicted ones. **Figure S3F** represents the Cook's distance and is an example of an influence graph. In this plot, the difference in the predictions of the respective data with and without the run under consideration is calculated, squared, and put in proportion to the estimated variance and the model constant. Thus, the Cook's distance directly shows how much a measured value or potential outlier influences the whole model. Since all runs were below the threshold and no data point stood out in the normal plot either, no further runs were considered as outliers.

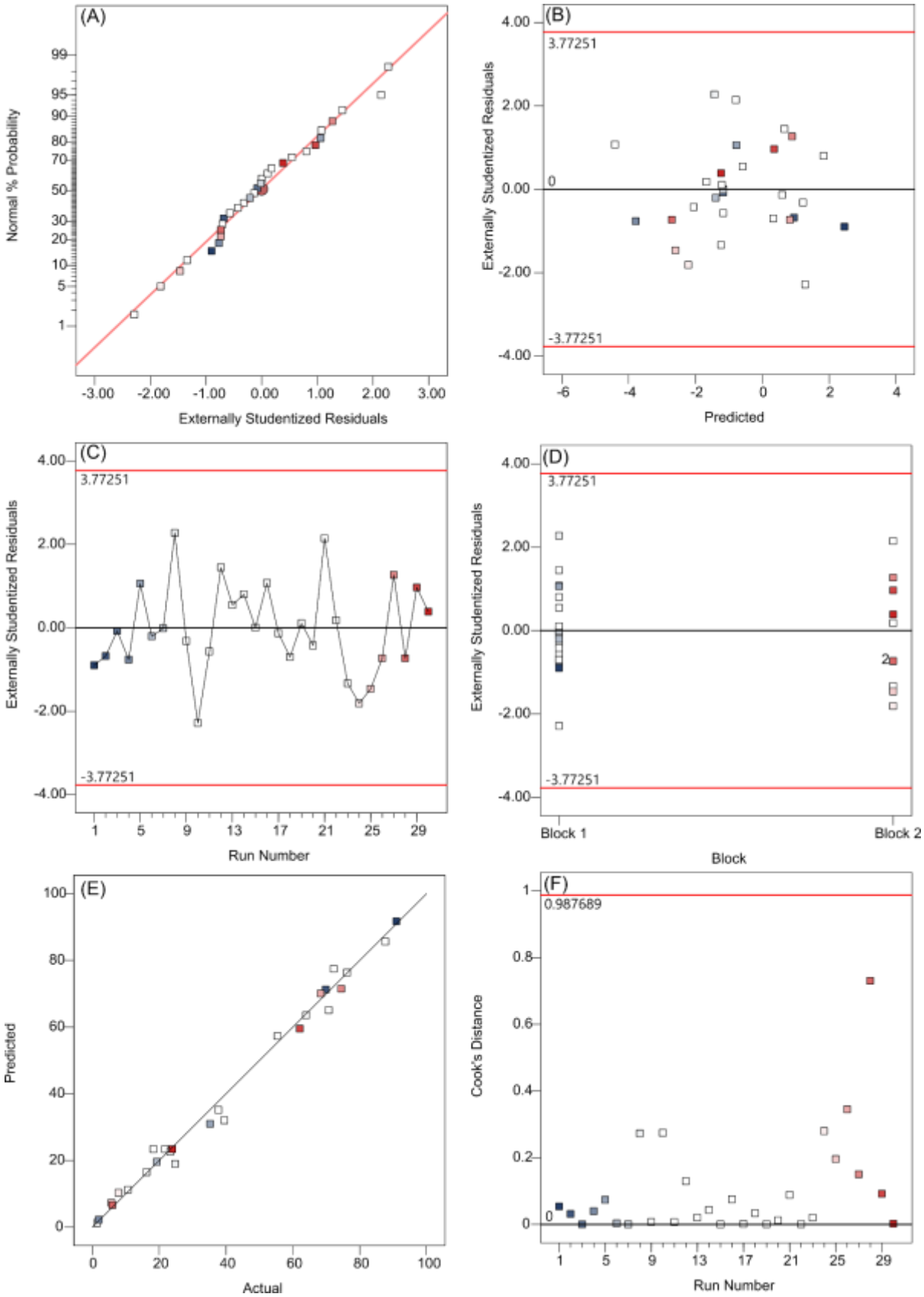

Figure S3: Diagnostic and influence plots. The color of the data points was chosen in accordance with the run number. (blue = 0, red = 30, white = in between). (A) Normal-Plot of Residuals. (B) Residuals vs. Predicted. (C) Residuals vs Runs. (D) Residuals vs. Block. (E) Predicted vs. Actual. (F) Cook's Distance.

Graphical optimization

Figure S4 shows the graphical optimization process of the designed experiment after 24 h and with 5 equiv. of EtIm. In the yellow area the predicted response is smaller than 15%. The adjacent brown area indicates where the 95% confidence interval is below 15%. On this basis, three Confirmation runs (C1, C2 and C3) were conducted (see Figure 2C in the manuscript).

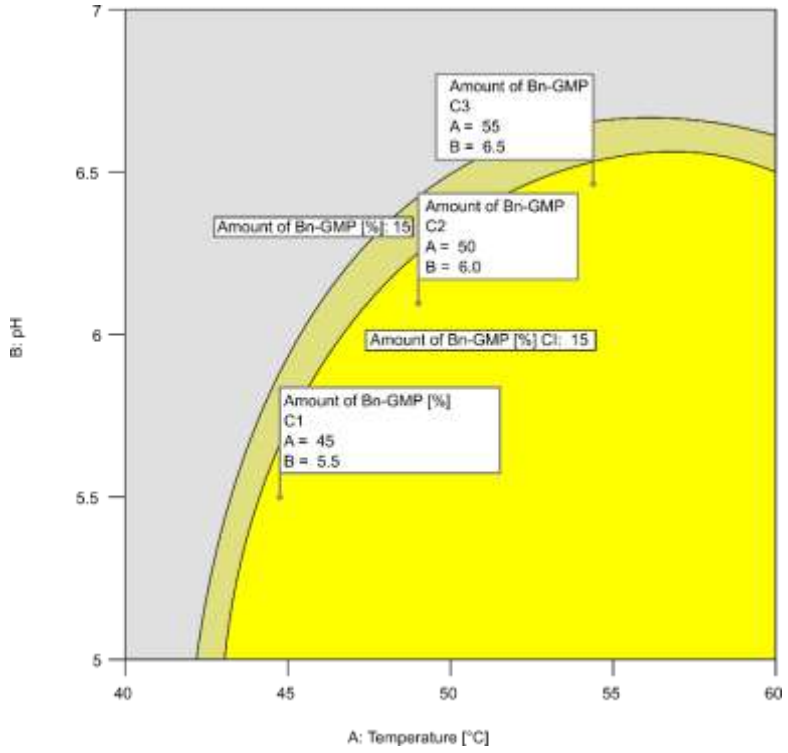

Figure S4: Graphical Optimization of Bn-GMP hydrolysis.

Optimizing the formation of Bn-GMP by DoE

Objectives and responses

The second DoE dealt with the formation of Bn-GMP and the optimization of the forward reaction. In concrete terms this means that the objective was to evaluate if this reaction is suitable to obtain more than at least 50% Bn-GMP.

Based on this objective, the response of interest was chosen to be the relative amount of Bn-GMP formed. RNA and DNA quantification is commonly performed at 260 nm (e.g. OD260 measurements).[2] It was assumed that at this wavelength the only significant absorbing moiety within our system is the purine unit of the nucleotides. To verify this assumption, the Bn-GMP amount determined by internal standard calibration of the previous DOE was compared with the relative area percentage of the Bn-GMP peak in the chromatogram. As depicted in **Table S7**, the relative amount of Bn-GMP formed in the previous DOE was nearly identical with the relative area percentage of the Bn-GMP in the chromatogram at 260 nm, corroborating the validity of our assumption.

Table S7: Bn-GMP amount determinations.

Run	Amount of Bn-GMP [%] determined with ISDT	Relative area percent of Bn-GMP [%]
1	91.00	88.39
14	87.71	85.68
29	62.13	62.34
18	55.43	53.29
7	23.71	22.89
20	10.69	11.48

Based on this observation, it was assumed that the amount of Bn-GMP and other species present can be reasonably determined as relative area percentages in the chromatogram at 260 nm. To further prove the validity of this assumption and to exclude that other species (that were potentially not observed in the chromatographic analysis) are present, a test run was performed to determine the relative amount of Bn-GMP and GMP using quantitative ^{31}P NMR (with TMP as an internal standard). The results were compared with the relative area percentages of the respective LC-MS analysis (see **Table S8**). Even when using a different analytical technique to determine the amount of each species, the relative area percentages in the chromatogram are well comparable to the ones determined by this method. The deviations are within the necessary accuracy for analyzing the reaction network. Furthermore, it becomes apparent that the species observed in the ^{31}P spectra are similar to those monitored in the respective chromatograms, indicating that no (potentially new) species were overlooked that could cause an error in the chromatographic analysis.

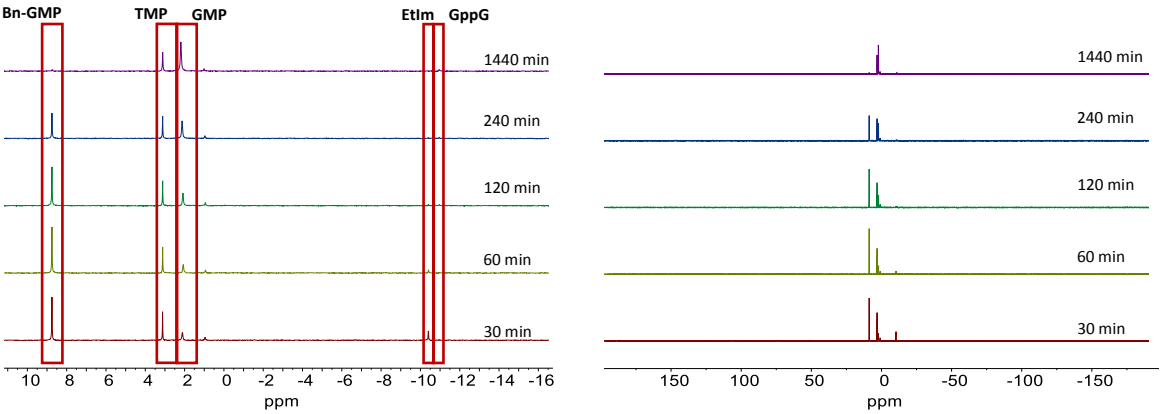

Figure S5: ^{31}P NMR spectra of Bn-GMP.

Table S8: Comparison of the relative amounts of observed species determined by NMR and HPLC.

t [min]	Bn-GMP [%] NMR	Bn-GMP [%] LC	GMP [%] NMR	GMP [%] LC
30	56.67	47.67	22.91	29.32
60	61.51	54.86	24.21	30.50
120	56.11	49.13	33.07	41.09
240	41.48	37.55	50.78	51.02
1440	3.82	3.90	84.95	88.62

Input factors

The input factors used in the designed experiment are shown in **Table S9** and **Figure S6**.

Table S9: Input factors and ranges used in the designed experiment.

Factor	Name	Units	Type	SubType	Minimum	Maximum	Coded Low	Coded High
A	Temperature	°C	Numeric	Continuous	35	65	-1 ↔ 40.00	+1 ↔ 60.00
B	pH		Numeric	Continuous	4.5	7.5	-1 ↔ 5.00	+1 ↔ 7.00
C	Time	min	Numeric	Continuous	30	292	-1 ↔ 30.00	+1 ↔ 240.00
D	Equivalents of EDC		Numeric	Continuous	1.25	7.50	-1 ↔ 1.25	+1 ↔ 6.25
E	[GMP]	mM	Numeric	Continuous	8	48	-1 ↔ 8.00	+1 ↔ 40.00

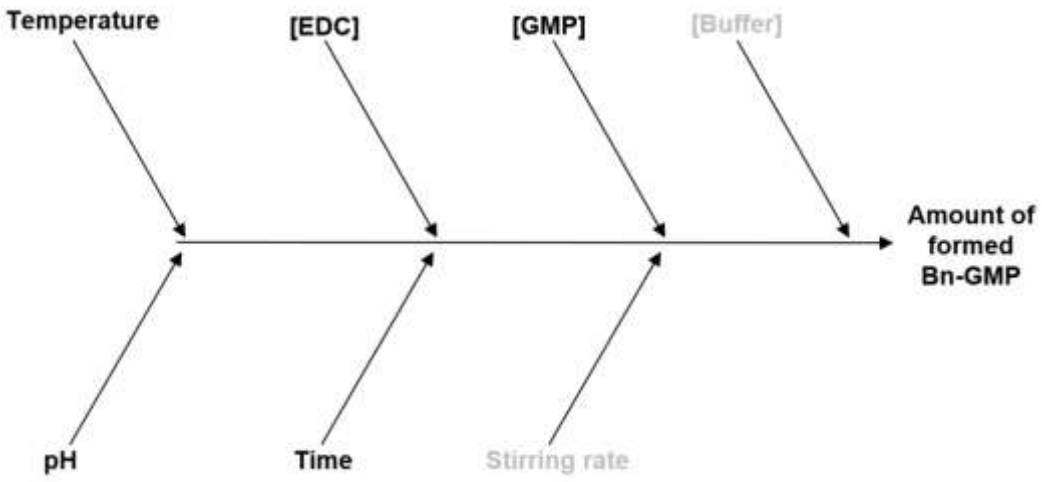

Figure S6: Fishbone diagram of the respective input factors (red), controlled/constant factors (blue) and responses (green).

Experimental Procedure and Design

Stock solutions of MOPS/MES (0.5 M), EtIm (1.0 M), GMP (0.4 M), $BnNH_2$ (1.0 M) were prepared in advance and used during this study. The EDC stock solution (1.25 M) was freshly prepared every day and stored at 7 °C until use. The reactions were performed in HPLC vials containing stirring bars. Reaction mixtures were prepared by pipetting and mixing the desired amounts of stock solutions in the order of buffer, GMP, $BnNH_2$, demineralized water, and EtIm.[3] In all cases, 1.5 equiv. of $BnNH_2$ were used. The sample was heated to the desired temperature and the pH was adjusted with concentrated HCl. The reaction was started by adding the appropriate amount of EDC stock solution to the reaction mixture. For HPLC, 50 µL were dissolved in 950 µL MeCN/H_2O (1:1) and 1 µL was injected on a Waters ACQUITY PRM BEHAmide (100 x 2.1 mm, 1.7 µm, 130 Å) column. Eluent: 70% MeCN, 30% aqueous NH_4HCO_3 solution (170 mM, total: 50 mM), flow rate = 0.3 mL/min, temp. = 60 °C.

From previous experiments it was known that factor changes will not result in a linear change of the response. Therefore, it was assumed that a linear description model would be not sufficient to represent the considered system well. As starting point of the DOE an experimental design was used that is suitable to fill a full quadratic description model. In concrete terms this means a CCD design was chosen, where in the first two blocks 40 runs (containing a full factorial design with additional 8 center points) and the third block 13 runs (containing the axial star points and additional 3 center points) were conducted. Since a full quadratic model was not suited to describe the present system, the experimental design was augmented by optimal exchange methods (Point exchange using an I-optimality criterion). As depicted in **Table S10**, this resulted in an experimental design of 87 runs suitable to fill a full cubic model.

Table S10: Experimental design.

Block	Run	Temperature [°C]	pH	Time [min]	Equivalents of EDC	[GMP] [mM]	Amount of Bn-GMP
Block 1	1	60	5	240	6.25	40	2.55
Block 1	2	60	5	240	1.25	8	1.1
Block 1	3	60	7	30	6.25	40	78.29
Block 1	4	40	7	240	6.25	40	83.21
Block 1	5	40	7	30	6.25	8	26.46
Block 1	6	50	6	135	3.75	24	58.12
Block 1	7	40	5	30	1.25	8	0.18
Block 1	8	40	5	240	1.25	40	2.81
Block 1	9	60	7	240	1.25	40	65.06
Block 1	10	60	5	30	1.25	40	4.12
Block 1	11	40	7	240	1.25	8	34.42
Block 1	12	40	5	30	6.25	40	5.55
Block 1	13	50	6	135	3.75	24	55.07
Block 1	14	60	7	30	1.25	8	32.52
Block 1	15	50	6	135	3.75	24	54.64
Block 1	16	40	5	240	6.25	8	0.87
Block 1	17	40	7	30	1.25	40	36.78
Block 1	18	60	7	240	6.25	8	79.76
Block 1	19	50	6	135	3.75	24	50.94
Block 1	20	60	5	30	6.25	8	1.93
Block 2	21	40	7	30	1.25	8	4.19
Block 2	22	40	5	240	6.25	40	13.67
Block 2	23	60	5	30	1.25	8	0.49
Block 2	24	60	7	240	6.25	40	65.76
Block 2	25	40	7	30	6.25	40	66.59
Block 2	26	50	6	135	3.75	24	61.04
Block 2	27	60	7	30	1.25	40	66.36
Block 2	28	60	7	30	6.25	8	65.03
Block 2	29	60	7	240	1.25	8	49.24
Block 2	30	40	7	240	1.25	40	84.64
Block 2	31	60	5	240	1.25	40	1.11
Block 2	32	60	5	30	6.25	40	14.6
Block 2	33	60	5	240	6.25	8	1.54
Block 2	34	50	6	135	3.75	24	62.15
Block 2	35	40	5	30	1.25	40	1.62
Block 2	36	40	5	240	1.25	8	0.18
Block 2	37	40	5	30	6.25	8	0.52
Block 2	38	40	7	240	6.25	8	73.32
Block 2	39	50	6	135	3.75	24	56.29
Block 2	40	50	6	135	3.75	24	62.44
Block 3	41	50	7.5	135	3.75	24	70.52
Block 3	42	50	6	135	3.75	24	49.36

Block 3	43	50	6	135	3.75	8	29.51
Block 3	44	35	6	135	3.75	24	41.07
Block 3	45	50	6	30	3.75	24	40.31
Block 3	46	50	6	135	3.75	24	61.38
Block 3	47	50	6	292	3.75	24	49.86
Block 3	48	65	6	135	3.75	24	44.58
Block 3	49	50	4.5	135	3.75	24	1.14
Block 3	50	50	6	135	7.5	24	72.1
Block 3	51	50	6	135	3.75	48	72.92
Block 3	52	50	6	135	1.25	24	31.15
Block 3	53	50	6	135	3.75	24	59.69
Block 4	54	40	6.3	240	4.625	40	75.63
Block 4	55	40	6.3	240	2.875	8	31.28
Block 4	56	40	5	170	6.25	29.36	9.34
Block 4	57	53	6.3	30	6.25	8	29.14
Block 4	58	55	6.5	82.5	3.75	32	79.51
Block 4	59	47	5	30	6.25	29.36	7.27
Block 4	60	47	7	170	6.25	8	82.38
Block 4	61	55	5.5	82.5	2.5	32	24.78
Block 4	62	40	7	30	6.25	24	50.48
Block 4	63	47	5	240	1.25	8	0.5
Block 4	64	55	6.5	82.5	3.75	32	84.41
Block 4	65	40	7	240	1.25	24	59.71
Block 4	66	53	7	240	2.875	8	70.72
Block 4	67	55	6.5	82.5	2.5	16	64.86
Block 4	68	40	6.3	100	6.25	40	72.89
Block 4	69	40	7	30	4.625	18.64	35.66
Block 4	70	60	6.3	240	1.25	40	37.38
Block 4	71	45	5.5	135	2.5	32	23.95
Block 4	72	45	6.5	82.5	2.5	32	73.55
Block 4	73	40	7	170	1.25	8	27.12
Block 4	74	55	5.5	187.5	5	16	17.74
Block 4	75	40	7	240	6.25	18.64	90
Block 4	76	40	6.3	240	6.25	29.36	81.49
Block 4	77	40	5	240	2.875	29.36	4.95
Block 4	78	55	6.5	82.5	2.5	16	71.65
Confirmation	79	55	6.1	60	1.88	40	57.13
Confirmation	80	55	6.1	60	1.88	40	53.8
Confirmation	81	55	6.1	60	1.88	40	53.66
Confirmation	82	55	6.1	60	2.75	40	64
Confirmation	83	55	6.1	60	2.75	40	61.6
Confirmation	84	55	6.1	60	2.75	40	61.43
Confirmation	85	55	6.3	60	6.25	40	80.01
Confirmation	86	55	6.3	60	6.25	40	78
Confirmation	87	55	6.3	60	6.25	40	79.07

Data Analysis

Since the forward reaction represents a chemical reaction, the response is limited between the boundaries of 0 and 100%. For this reason, the data was transformed via a logit function. Based on this, the description model was chosen by applying an AICc model reduction algorithm of all not aliased terms available. **Table S11** shows the analysis of variance of the respective model.

Table S11: ANOVA of the considered description model.

Source	Sum of Squares	df	Mean Square	F-value	p-value	
Block	29.38	3	9.79			
Model	330.22	22	15.01	213.55	< 0.0001	significant
A-Temperature	2.71	1	2.71	38.49	< 0.0001	
B-pH	37.38	1	37.38	531.81	< 0.0001	
C-Time	3.25	1	3.25	46.19	< 0.0001	
D-EDC	0.0526	1	0.0526	0.7476	0.3912	
E-GMP	26.13	1	26.13	371.74	< 0.0001	
AC	5.65	1	5.65	80.33	< 0.0001	
AD	0.5545	1	0.5545	7.89	0.007	
AE	3.83	1	3.83	54.5	< 0.0001	
BC	3.29	1	3.29	46.77	< 0.0001	
BD	0.0411	1	0.0411	0.5848	0.4479	
BE	1.4	1	1.4	19.87	< 0.0001	
CE	1.81	1	1.81	25.77	< 0.0001	
DE	0.5115	1	0.5115	7.28	0.0094	
A^2	0.9146	1	0.9146	13.01	0.0007	
B^2	10.34	1	10.34	147.15	< 0.0001	
C^2	1.82	1	1.82	25.86	< 0.0001	
D^2	1.15	1	1.15	16.33	0.0002	
E^2	1.2	1	1.2	17.08	0.0001	
ACE	0.974	1	0.974	13.86	0.0005	
BDE	1.17	1	1.17	16.64	0.0002	
B^3	0.9125	1	0.9125	12.98	0.0007	
D^3	0.5411	1	0.5411	7.7	0.0077	
Residual	3.66	52	0.0703			
Lack of Fit	3.27	42	0.0778	2.01	0.1189	not significant
Pure Error	0.388	10	0.0388			
Cor Total	363.25	77				

The regression model and most of its individual terms (factor effects and higher order interactions) are statistically significant and exhibit large F and low p-values. This indicates that the variation explained by the model as well as its individual terms are quite large compared to the unexplained variance of the Residual. Seemingly insignificant model terms like BD and D were kept within the model for hierarchy reasons. Conversely, the high F and low p-value of the lack-of-fit test imply that the Lack of Fit is not significant. Further Model statistics are shown in **Table S12**. The predicted coefficient of

determination (Predicted R^2) is close to 1 which is caused by a low PRESS. This means that the variation explained by the model in "new data" is high, indicating that the model is suited for making predictions. The same holds true for the adjusted coefficient of determination (Adjusted R^2) which measures the variation around the mean explained by the regression taking a penalty for an increasing number of model parameters into account. The difference between Adjusted R^2 and Predicted R^2 is less than 0.2 meaning that they are in reasonable agreement. The adequate precision can be regarded as a signal-to-noise ratio, where the predicted values of the design points are compared to the average prediction error. As a rule of thumb, a ratio greater than 4 is suited which means that the observed ratio of 578.089 indicates an adequate signal.

Table S12: Model Fit Statistics.

Std. Dev.	0.2651	**R^2**	0.9891
Mean	-0.8844	**Adjusted R^2**	0.9844
C.V. %	29.98	**Predicted R^2**	0.9651
		Adeq Precision	57.8089

The regression model with the coded factors is shown in **Table S13**.

Table S13: Coefficients in terms of coded factors of the model regression.

Factor	Coefficient Estimate	df	Standard Error	95% CI Low	95% CI High	VIF
Intercept	0.3233	1	0.0658	0.1913	0.4554	
Block 1	-0.0163	3				
Block 2	0.0144					
Block 3	-0.0289					
Block 4	0.0308					
A-Temperature	0.2442	1	0.0394	0.1652	0.3232	1.1
B-pH	2.53	1	0.1098	2.31	2.75	8.5
C-Time	0.2642	1	0.0389	0.1862	0.3422	1.08
D-EDC	0.1378	1	0.1593	-0.1819	0.4574	17.8
E-GMP	0.766	1	0.0397	0.6862	0.8457	1.05
AC	-0.3766	1	0.042	-0.4609	-0.2923	1.05
AD	-0.1202	1	0.0428	-0.2061	-0.0343	1.07
AE	-0.3201	1	0.0434	-0.4072	-0.2331	1.03
BC	0.2871	1	0.042	0.2029	0.3714	1.03
BD	-0.0321	1	0.042	-0.1163	0.0521	1.03
BE	-0.1971	1	0.0442	-0.2859	-0.1084	1.04
CE	-0.2192	1	0.0432	-0.3058	-0.1326	1.04
DE	-0.1158	1	0.0429	-0.202	-0.0297	1.03
A^2	-0.2585	1	0.0717	-0.4023	-0.1147	1.56
B^2	-0.8627	1	0.0711	-1.01	-0.72	1.55
C^2	-0.4144	1	0.0815	-0.5779	-0.2509	1.78
D^2	-0.3977	1	0.0984	-0.5951	-0.2002	2.66
E^2	-0.3228	1	0.0781	-0.4795	-0.1661	1.68
ACE	-0.1664	1	0.0447	-0.256	-0.0767	1.02

BDE	-0.1831	1	0.0449	-0.2732	-0.0931	1.03
B^3	-0.3408	1	0.0946	-0.5306	-0.151	8.37
D^3	0.4323	1	0.1558	0.1196	0.7449	19.36

Figure S7A-E displays the diagnostic graphs of the model. **Figure S7A** depicts the normal Plot of Residuals. Since all data points are following a straight line, it can be assumed that the residuals are normally distributed. Random Fluctuations within data are not supposed to be systematic and must therefore follow a normal distribution. A potential outlier (not caused by random fluctuations) would have been detected here by deviating from this line. **Figure S7B** shows the predicted transformed response plotted against their residuals. The data points are randomly scattered indicating no expanding variance. **Figure S7C** shows the calculated Residuals against the individual run number. The residuals are randomly scattered indicating that no time depending uncontrolled variables are apparent. **Figure S7D** depicts the Residuals within each block. Both blocks exhibit similar ranges of scattering with no specific pattern apparent. **Figure S7E** depicts an intuitive way of looking at the performance of the description model in terms of a comparison of predicted and observed response values. A great part of the variation of the data is explained by the description model. The data scatters slightly around the first bisector. This means that observed responses are in good agreement with the predicted ones. **Figure S7F** represents Cook's distance and is an example of an influence graph. In this plot, the difference in the predictions of the respective data with and without the run under consideration is calculated, squared, and put in proportion to the estimated variance and the model constant. Thus, the Cook's distance directly shows how much a measured value or potential outlier influences the whole model. Since all runs were below the threshold and no data point stood out in the normal plot either, no further runs were considered as outliers.

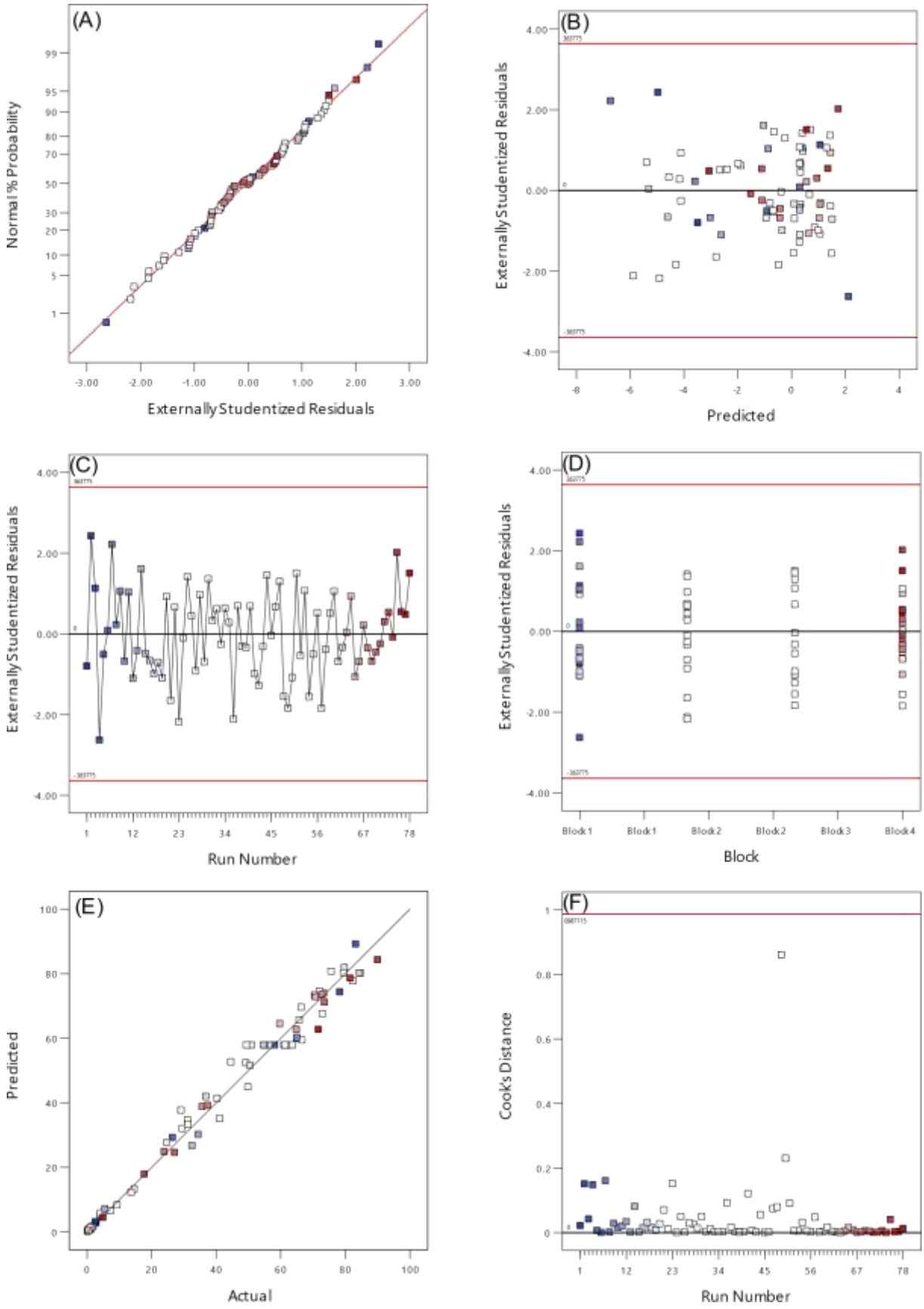

Figure S7: Diagnostic and influence plots. The color of the data points was chosen in accordance with the run number. (blue = 0, red = 78, white = in between). (A) Normal-Plot of Residuals. (B) Residuals vs. Predicted. (C) Residuals vs Runs. (D) Residuals vs. Block. (E) Predicted vs. Actual. (F) Cook's Distance.

Additional interaction diagrams regarding the time variable

The “optimal time” (where the Bn-GMP concentrations is at its peak) varies for every set of parameters. We chose 2.25 h for all diagrams in Fig. 3B; the general trends in the one-factor diagrams, however, do not change significantly when plotted at 1.5 h or 3.5 h instead. The variation of the “optimal time” is especially strong when varying a parameter with strong interactions like the temperature (see interaction diagram in Fig. 3B). Weak but considerable interaction can be found with the parameters [GMP] and pH. In principle, in can be stated that parameter sets that favor hydrolysis (like high temperatures, low pH and high concentration of GMP (where EDC is used up faster)) reach the “optimal time” for the Bn-GMP formation earlier. This can be seen in the two additional interaction diagrams below:

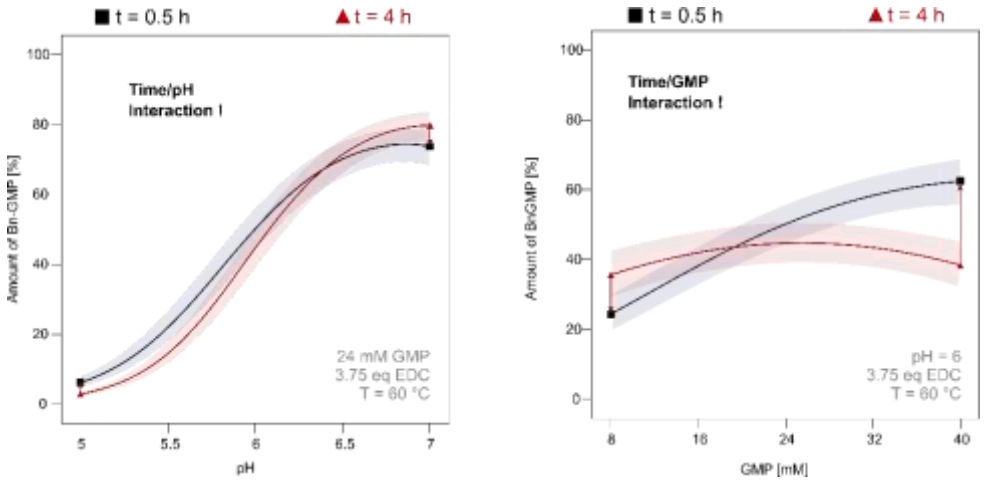

Figure S8: Interaction diagrams of the time/pH and time/[GMP] interaction, respectively.

Graphical Optimization

Figure S9 shows the graphical optimization process of the designed experiment after 60 min, at 55 °C, with 5 equiv. EtIm and with 40 mM GMP. In the yellow area the predicted response (amount of Bn-GMP) is larger than 50%. The adjacent brown area indicates where the 95% confidence interval is larger than 50%. On this basis, three Confirmation runs (C1, C2 and C3) were conducted (see Figure 3C in the manuscript).

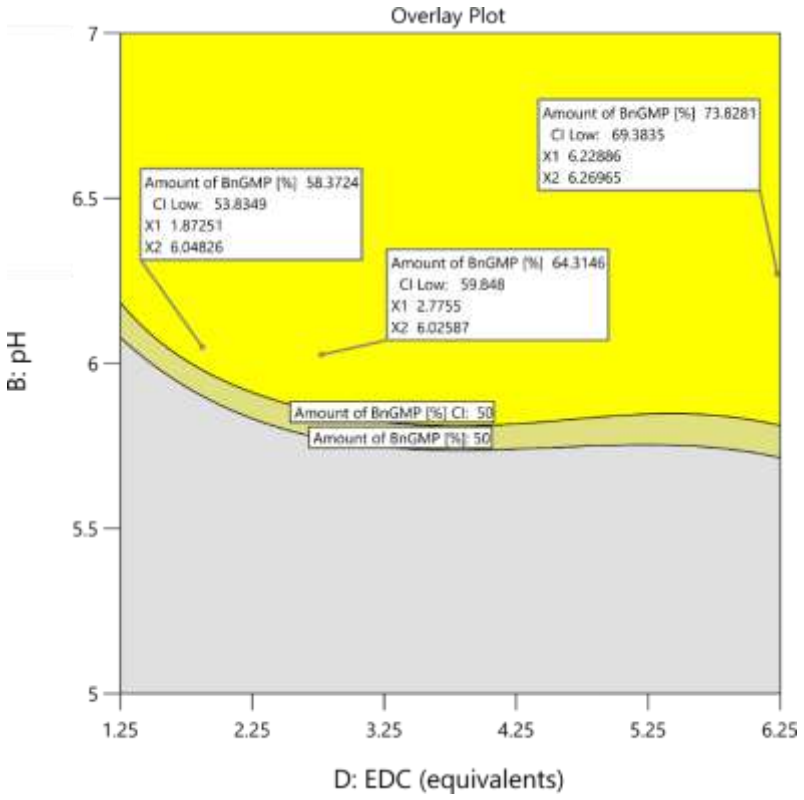

Figure S9: Graphical Optimization and Confirmation of Bn-GMP formation.

Combining Hydrolysis and Formation of Bn-GMP and Closing the Dissipative Reaction Cycle

Reaction cycle

Stock solutions of MOPS/MES (0.5 M), EtIm (1.0 M), GMP (0.4 M), $BnNH_2$ (1.0 M) were prepared in advance and used during this study. To 340 µL water, 100 µL GMP (0.04 mmol, 40 mM, 1 equiv.), 300 µL MOPS/MES buffer (0.15 mmol, 150 mM, 3 equiv.), 60 µL benzylamine (0.06 mmol, 60 mM, 1.5 equiv.) and 200 µL EtIm (0.2 mmol, 200 mM, 5 equiv.) stock solutions were added. The pH was adjusted to pH = 6.1 at 55 °C with conc. hydrochloric acid and 14.4 mg (75.2 µmol, 1.88 equiv.) 1-ethyl-3-(3-dimethylaminopropyl) carbodiimide hydrochloride (EDC) were added at the beginning of each fueled cycle (every 24 h). The reaction mixture was stirred at 55 °C in a tightly closed vial.

HPLC Analysis

The reaction cycle was run according to the procedure described above. For HPLC, 5 µL were dissolved in 995 µL MeCN/H_2O (1:1) and 1 µL was injected on a Waters ACQUITY PRM BEHAmide (100 x 2.1 mm, 1.7 µm, 130 Å) column. Eluent: 70% MeCN, 30% aqueous NH_4HCO_3 solution (170 mM, total: 50 mM), flow rate = 0.3 mL/min, temp. = 60 °C. Compounds were detected at 260 nm with a diode array detector (DAD) and the relative areas of the formed species were used for analysis. Three parallel experiments were performed to obtain error bars as the standard deviation of the three experiments.

Further experiments

Bn-GMP Reaction cycle at Room Temperature

16.3 mg (40 µmol, 40 mM) guanosine 5'-monophosphate (GMP) and 6.5 µL (60 µmol, 60 mM, 1.5 equiv.) benzylamine were dissolved in 1 mL of a freshly prepared aqueous reaction buffer (200 mM 3-morpholinopropionic acid, 200 mM 2-morpholin-4-ylethanesulfonic acid and 200 mM 1-ethylimidazole (5 equiv.)). The pH was adjusted to pH = 6.1 at room temperature with conc. hydrochloric acid. 15.3 mg (80 µmol, 2 equiv.) 1-ethyl-3-(3-dimethylaminopropyl)-carbodiimide hydrochloride (EDC) were added at the beginning to start the reaction. The reaction mixture was stirred at 55 °C in a tightly closed vial.

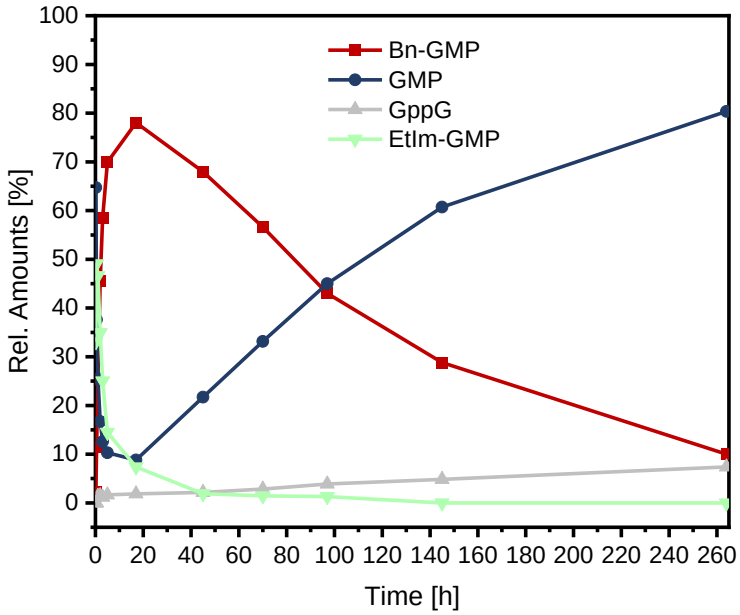

Figure S10: Concentration of GMP, Bn-GMP as well as EtIm-GMP and GppG over 145 h at 25 °C (under otherwise standard conditions).

If the reaction is performed at 25 °C, the formation of Bn-GMP is still rather efficient. The hydrolysis, however, is slowed down significantly with a half-life of the Bn-GMP of around 80 h. This corroborates, that the transient self-assembly could in principle be performed without cycling between two temperatures, albeit with very slow deactivation.

Steady-State Experiment

16.3 mg (40 µmol, 40 mM) guanosine 5'-monophosphate (GMP) and 6.5 µL (60 µmol, 60 mM, 1.5 equiv.) benzylamine were dissolved in 1 mL of a freshly prepared aqueous reaction buffer (200 mM 3-morpholinopropionic acid, 200 mM 2-morpholin-4-ylethanesulfonic acid and 200 mM (5 equiv.) 1-ethylimidazole). The pH was adjusted to pH = 6.1 at 55 °C with conc. hydrochloric acid. With a syringe pump 0.2 equiv. h^{-1} of EDC were added continuously (flowrate = 4 µL h^{-1}, EDC stock = 2 M).

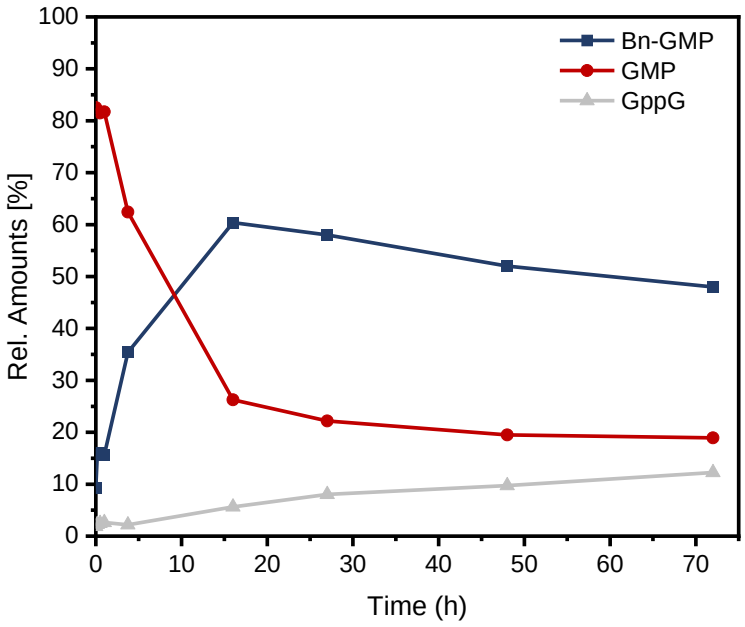

Figure S11: *Concentration of GMP, Bn-GMP and GppG over 72 h under standard conditions with a continuous supply of EDC (0.2 equiv. h^{-1}).*

Continuous addition of the fuel EDC leads to an out-of-equilibrium steady state.

Transient Self-Assembly with AMP and Heptylamine

Reaction cycle

29.4 mg (75 µmol, 75 mM) adenosine 5'-monophosphate (AMP) and 17 µL (0.11 mmol, 113 mM, 1.5 equiv.) heptylamine were dissolved in 1 mL of a freshly prepared aqueous MOPS buffer (200 mM 3-morpholinopropionic acid, 375 mM (5 equiv.) 1-ethylimidazole) and the pH was adjusted to pH = 6.5 at 55 °C with ca. 25 µL conc. hydrochloric acid. 29.0 mg (150 µmol, 2 equiv.) 1-ethyl-3-(3-dimethylaminopropyl)-carbodiimide hydrochloride (EDC) were added at the beginning of each fueled cycle (every 24 h). The reaction mixture was stirred at 55 °C in a tightly closed vial.

HPLC Analysis

The reaction cycle was run according to the procedure described above. For HPLC, 5 µL were dissolved in 995 µL MeCN/H_2O (3:1) and 2 µL were injected on a Waters ACQUITY PRM BEHAmide (100 x 2.1 mm, 1.7 µm, 130 Å) column. Eluent: 75% MeCN, 25% aqueous NH_4HCO_3 solution (170 mM, total: 50 mM), flow rate = 0.3 mL/min, temp. = 60 °C. Compounds were detected at 260 nm with a diode array detector (DAD) and the relative areas of the formed species were used for analysis. Three parallel experiments were performed to obtain error bars as the standard deviation of the three experiments.

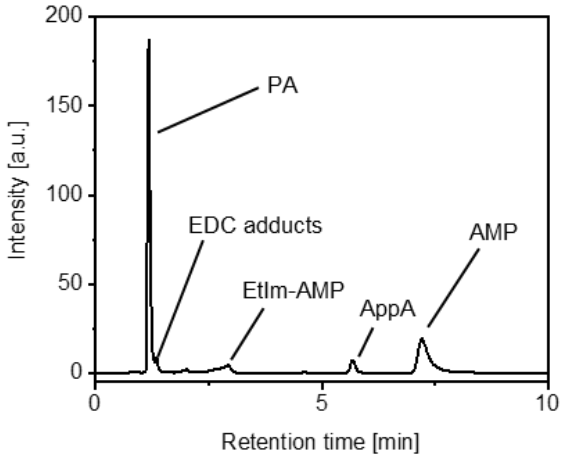

Figure S12: Typical HPLC trace of the reaction cycle with AMP and heptylamine.

Dynamic Light Scattering (DLS)

Samples for DLS were filtered through a 0.45 µm syringe filter before starting the first cycle according to the procedure described above. Dynamic light scattering was performed 1.5 h and 24 h after start of each cycle on a Nano-Zetasizer (Malvern Instruments) at 25 °C with a 173° backscatter angle at λ = 633 nm. At each time point, ten DLS runs were measured. The number mean of five representative measurements each are shown below. The hydrodynamic diameter was obtained as an average of these five measurements while the standard deviations was calculated from the same set of measurements.

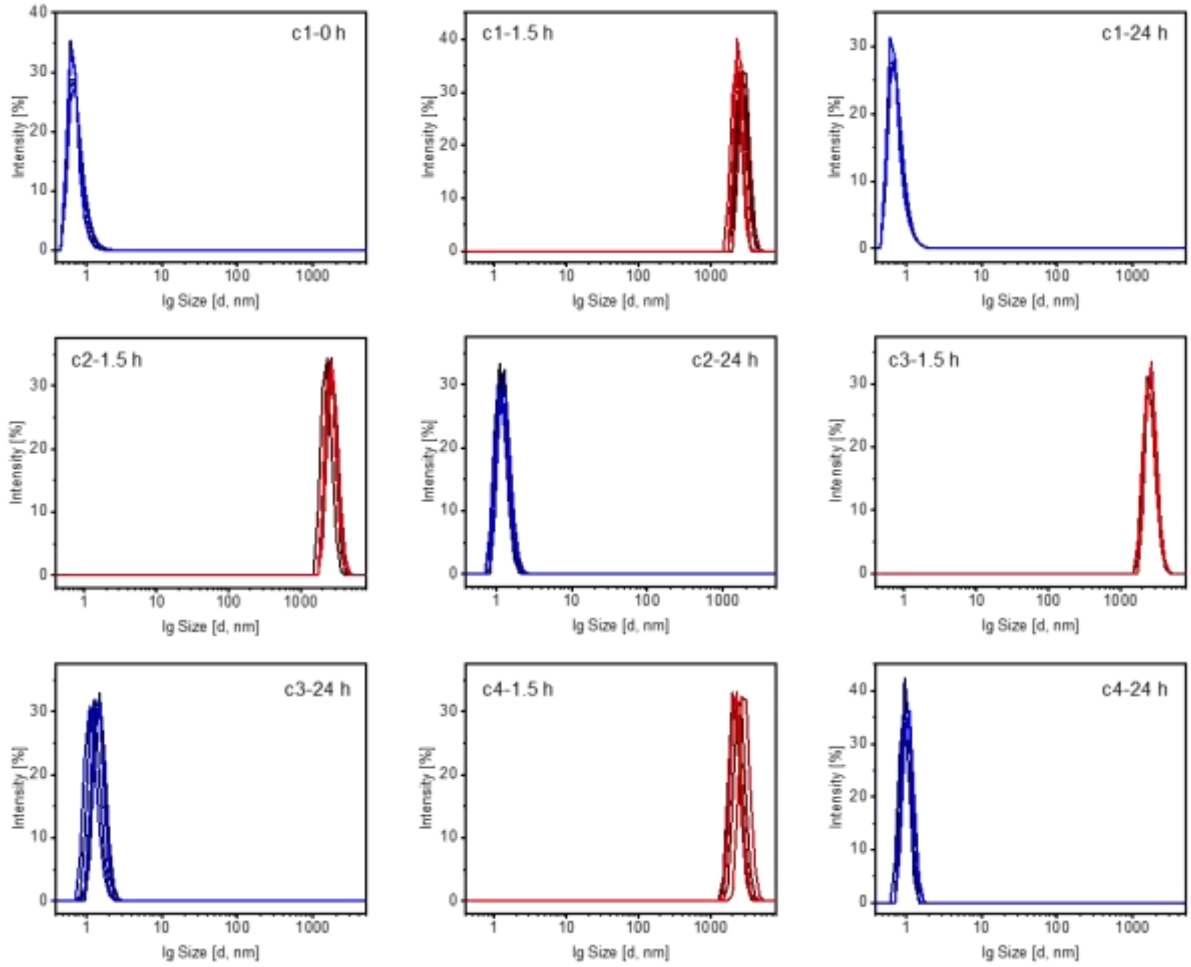

Figure S13: DLS measurements of four dissipative reaction cycles. At each time point five parallel measurements were performed.

Confocal Laser Scanning Microscopy (CLSM)

The reaction cycle was run according to the procedure described above. Before addition of EDC, 1.5 h and 24 h after starting the reaction cycle, samples for CLSM were prepared as follows: 0.5 µL of a 5 mM solution of C153 in THF were added to 1 mL of the sample (final concentration of C153 = 2.5 µM) at 25 °C. A drop of the prepared sample was placed on a freshly cleaned microscope glass slide with a 1 mm well and covered with a cover glass slip. CLSM images were recorded with a TCS SP8 confocal microscope using the Leica Application Suite X (LASX). The fluorescent dye was excited at 405 nm.

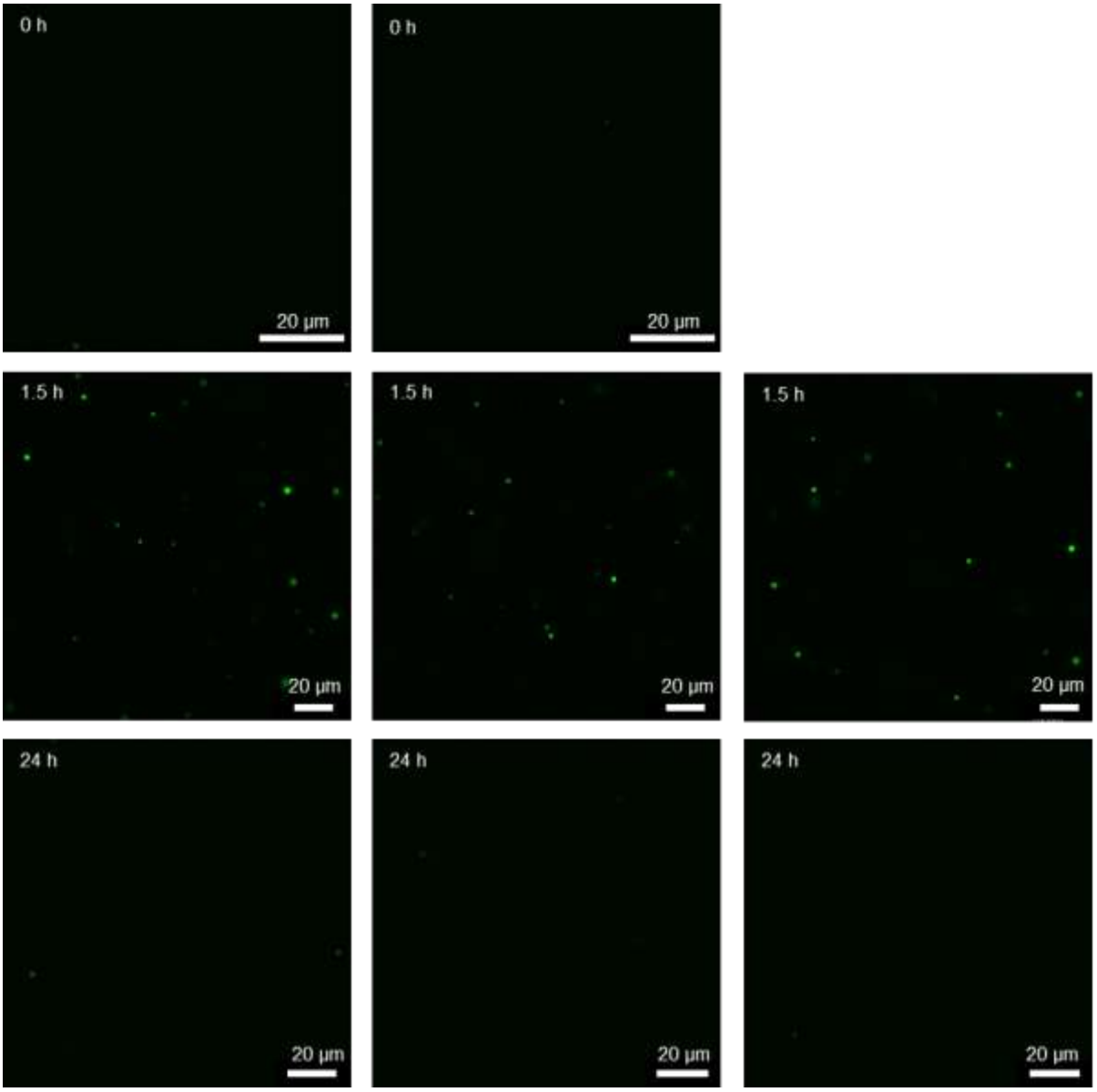

Figure S14: Additional confocal images of the transient self-assembly before EDC addition (top), after 1.5 h (middle) and after 24 h (bottom).

Transmission Electron Microscopy (TEM)

The reaction cycle was run according to the procedure described above. 5 µL of the reaction mixture before (control) and 1.5 h after (aggregated) addition of EDC were deposited on a copper grid at 25 °C. Negative staining with uranyl acetate was performed. TEM measurements were performed on a ZEISS EM10 microscope with an acceleration voltage of 120 kV.

Control experiments showed no aggregates inside the black areas of the stain. After 1.5 h, spherical objects were observed. Their size around 50 – 100 nm differed from the size of the aggregates observed in solution (~ 3 µm), which indicates that they collapse on the surface when being dried.

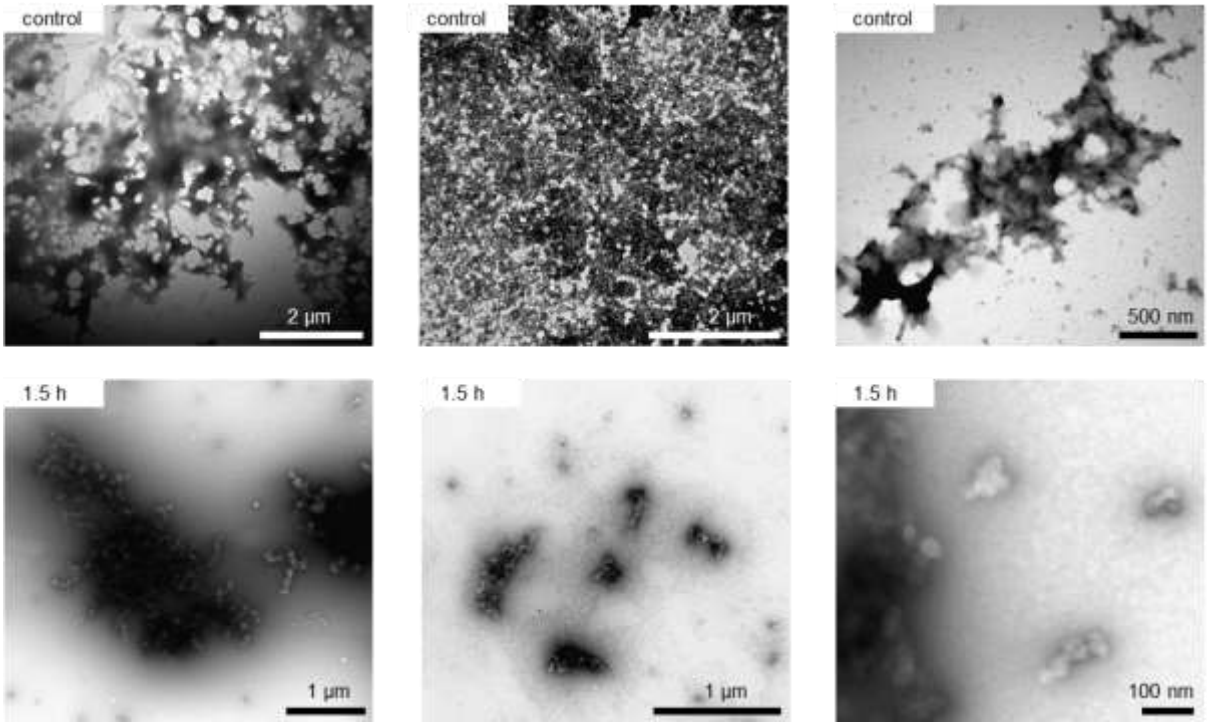

Figure S15: Top: TEM images of the control (before addition of EDC). No aggregates can be observed. Bottom: TEM images 1.5 h after addition of EDC. Clusters of spherical aggregates of about 50 – 100 nm size can be observed.

Cryogenic Transmission Electron Microscopy (cryo-TEM)

The reaction cycle was run according to the procedure described above. 5 µL of the reaction mixture before (control) and 1.5 h after (aggregated) addition of EDC were adhered to a freshly glow-discharged holey carbon grid. After blotting, the grids were vitrified in liquid ethane by a Vitrobot FP 5350/60 (FEI, Eindhoven, Netherlands). The cryo-TEM grids were analyzed on a JEM-2100F (JEOL) at 200 kV and a temperature of -150 °C using a Gatan cryo-holder.

Control experiments showed no aggregates inside the round area of the grid. After 1.5 h, spherical objects were observed. Their size of around one µm differed from the size of the aggregates observed in solution (~ 3 µm), which indicates that they shrink upon freezing. The shape and dark outline is rather indicative for vesicles.

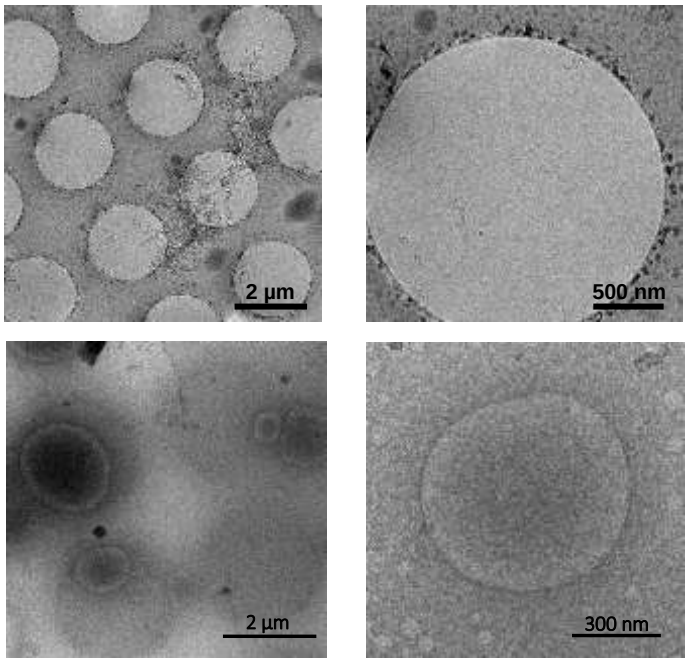

Figure S16: Top: cryo-TEM images of the control (before addition of EDC). No aggregates can be observed. Bottom: cryo-TEM images 1.5 h after addition of EDC. Spherical aggregates of about 200 – 500 nm size can be observed.

References

(1) Fuoss, R. M.; Chu, V. F. H.; Chu, F. H. Conductance of 1,3- 1,4- and 1,5 Di-(Trimethylammonium)-Polymethylene Halides in Water and in Methanol. *J. Am. Chem. Soc.* **1951**, *73*, 949–952.

(2) Barbas, C. F.; Burton, D. R.; Scott, J. K.; Silver, G. L. Quantification of DNA and RNA. *Cold Spring Harb Protoc.* **2007**.

(3) Tremmel, P.; Griesser, H.; Steiner, U. E.; Richert, C. How Small Heterocycles Make a Reaction Network of Amino Acids and Nucleotides Efficient in Water. *Angew. Chem., Int. Ed.* **2019**, *58*, 13087–13092.

Supplementary Data

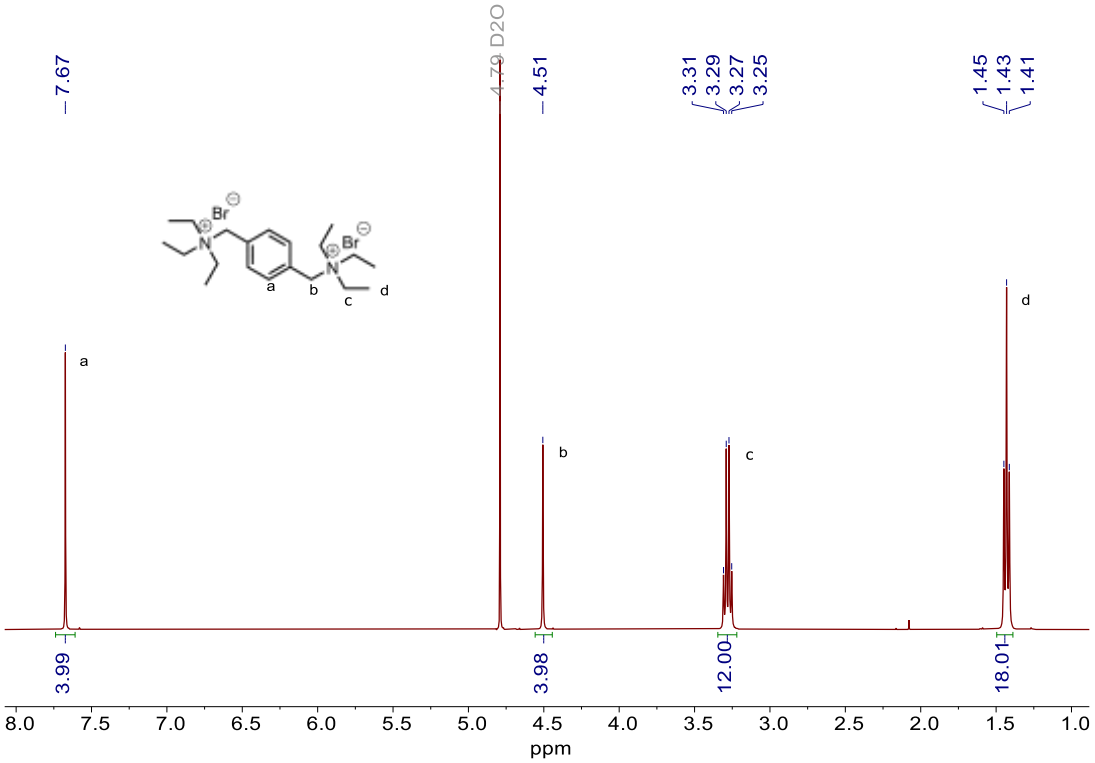

Figure S17: ^{1}H-NMR (400 MHz, D_2O, 298 K) of N,N,N,N',N',N',-hexaethyl-2,7-benzenedimethanammonium dibromide.

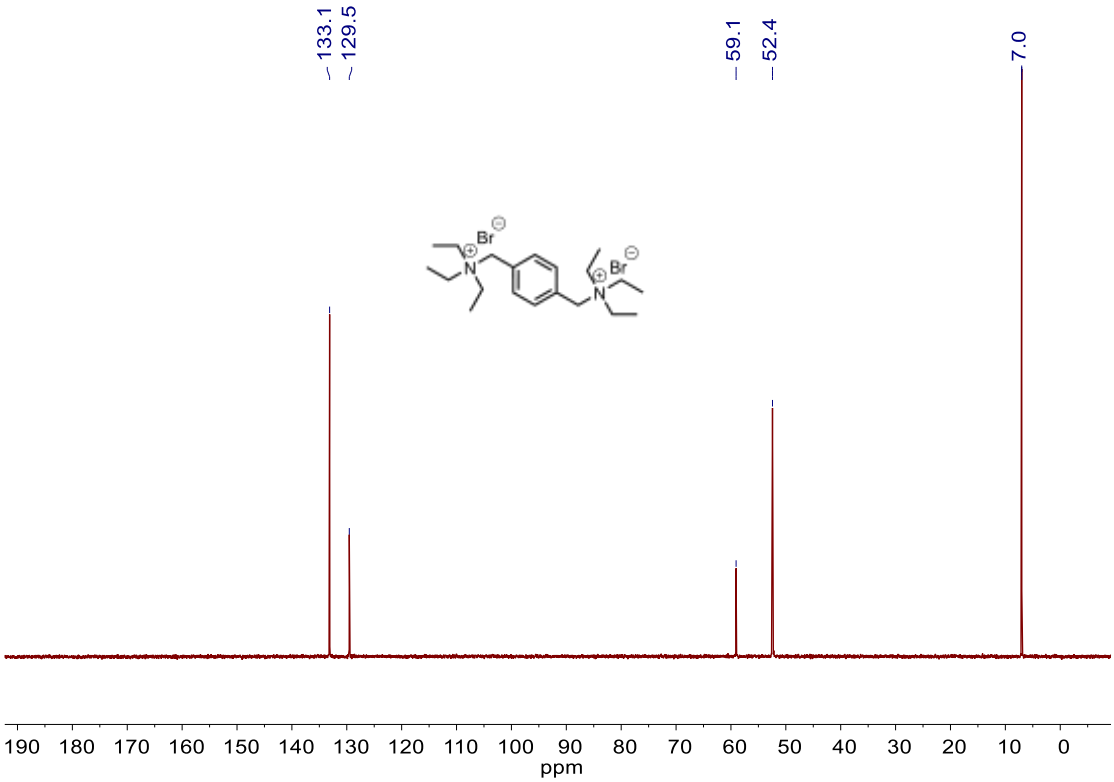

Figure S18: ^{13}C-NMR (101 MHz, D_2O, 298 K) of N,N,N,N',N',N',-hexaethyl-2,7-benzenedimethanammonium dibromide.

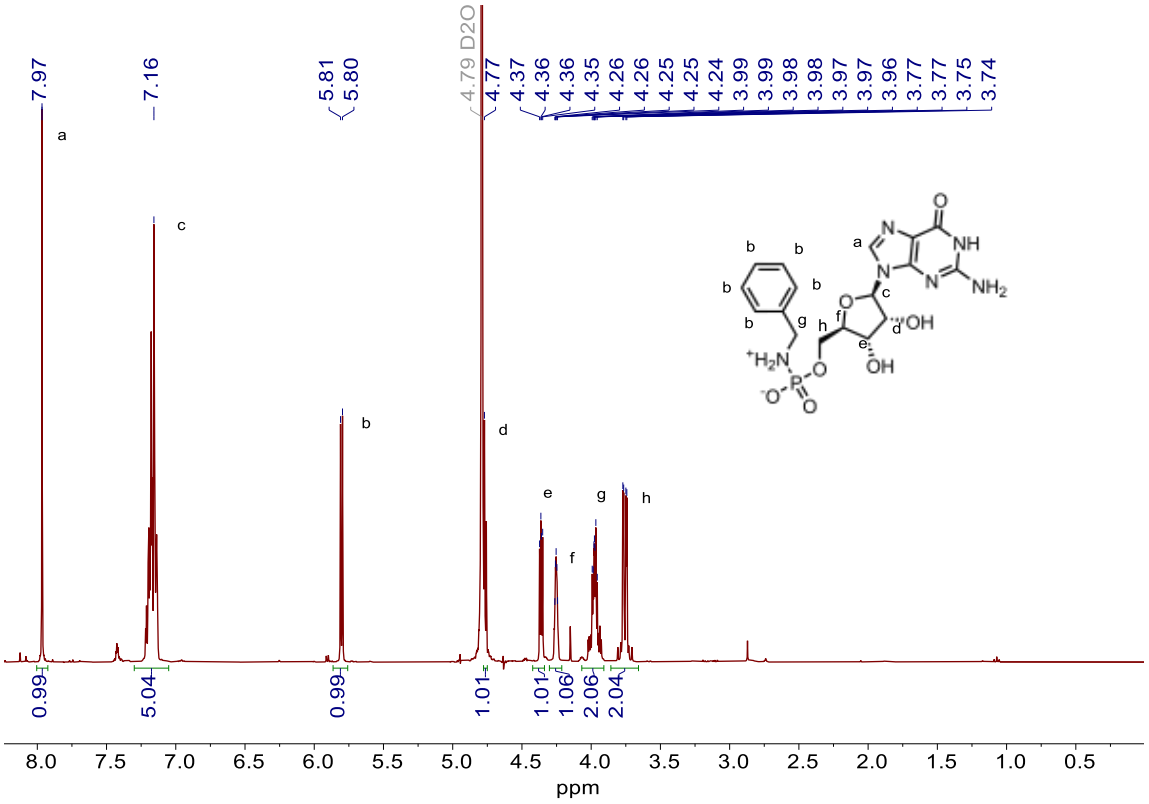

Figure S19: ^{1}H-NMR (400 MHz, D_2O, 298 K) of Bn-GMP.

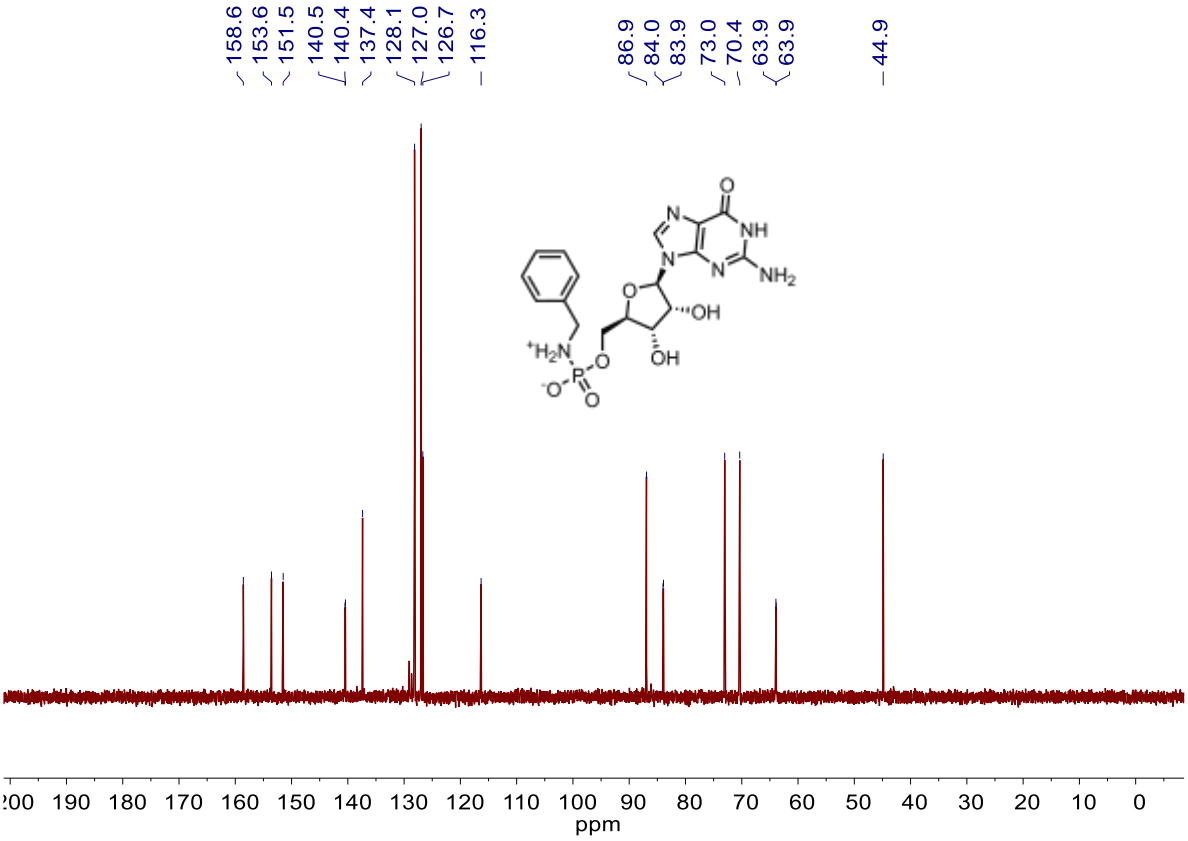

Figure S20: ^{13}C-NMR (101 MHz, D_2O, 298 K) of Bn-GMP.

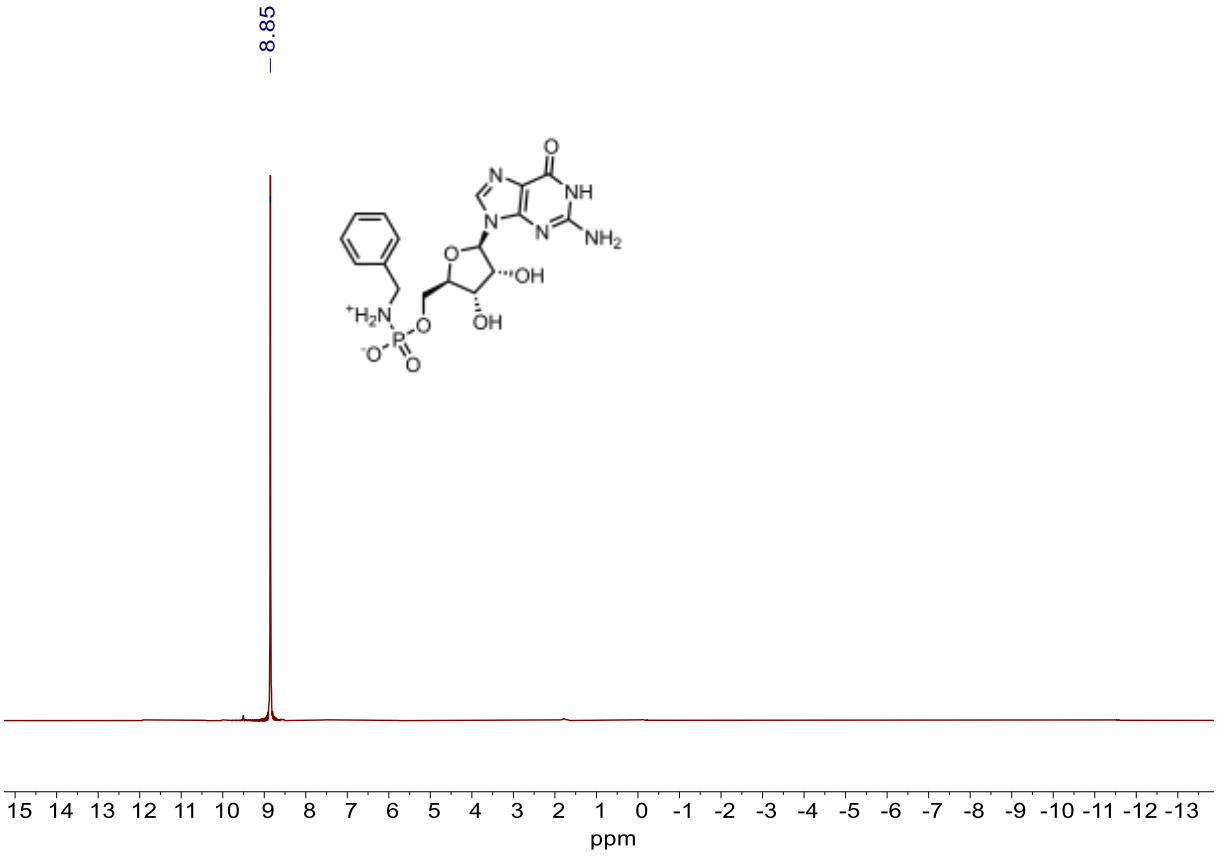

Figure S21: *^{31}P-NMR (162 MHz, D_2O, 298 K) of Bn-GMP.*

3.3 Steric Control over the Threading of Pyrophosphonates with One or Two Cyanostar Macrocycles during Pseudorotaxane Formation

Julian Vogel, Yusheng Chen, Rachel E. Fadler, Amar H. Flood and Max von Delius, *Chem. Eur. J.* **2023**, e202300899. DOI: https://doi.org/10.1002/chem.202300899.
This article is licensed and reprinted under a Creative Commons Attribution 4.0 International License (CC BY 4.0), https://creativecommons.org/licenses/by/4.0/

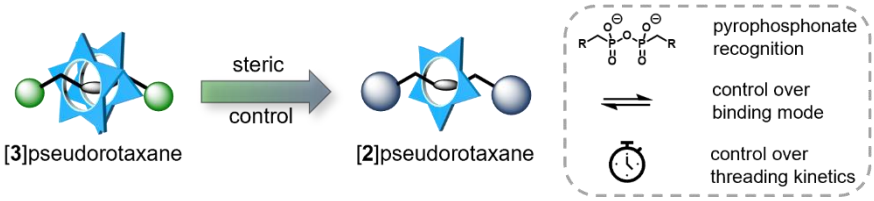

Abstract:
The supramolecular recognition of anions is increasingly harnessed to achieve the self-assembly of supramolecular architectures, ranging from cages and polymers to (pseudo)rotaxanes. The cyanostar (CS) macrocycle has previously been shown to form 2:1 complexes with organophosphate anions that can be turned into [3]rotaxanes by stoppering. Here we achieved steric control over the assembly of pseudorotaxanes comprising the cyanostar macrocycle and a thread based, for the first time, on organo-pyrophosphonates. Subtle differences in steric bulk on the threads allowed formation of either [3]pseudorotaxanes or [2]pseudorotaxanes. We demonstrate that the threading kinetics are governed by the steric demand of the organo-pyrophosphonates and in one case, slows down to the timescale of minutes. Calculations show that the dianions sterically offset inside the macrocycles. Our findings broaden the scope of cyanostar-anion assemblies and may have relevance for the design of molecular machines whose directionality is a result of relatively slow slipping.

Own contributions:
The initial idea to study the self-assembly of cyanostar to pyrophosphonates with different steric bulk stems from Rachel Fadler and me. I conducted all presented experiments including the synthesis and characterization of the pyrophosphonates, thermodynamic studies (NMR titrations, binding constants, HRMS and NOE-NMR experiments, VT NMR experiments) and kinetic studies. Yusheng Chen and Rachel Fadler were assisting during my time in their lab in Indiana, USA. Yusheng Chen provided the cyanostar macrocycle and performed DFT calculations. I wrote the first draft (incl. graphics) and the SI with help from Yusheng Chen und Rachel Fadler. Amar Flood and Max von Delius edited the manuscript.

Check for updates

Chemistry–A European Journal
Research Article
doi.org/10.1002/chem.202300899
Chemistry Europe
European Chemical Societies Publishing
www.chemeurj.org

Steric Control over the Threading of Pyrophosphonates with One or Two Cyanostar Macrocycles during Pseudorotaxane Formation

Julian Vogel,[a] Yusheng Chen,[b] Rachel E. Fadler,[b] Amar H. Flood,*[b] and Max von Delius*[a]

Abstract: The supramolecular recognition of anions is increasingly harnessed to achieve the self-assembly of supramolecular architectures, ranging from cages and polymers to (pseudo)rotaxanes. The cyanostar (**CS**) macrocycle has previously been shown to form 2:1 complexes with organophosphate anions that can be turned into [3]rotaxanes by stoppering. Here we achieved steric control over the assembly of pseudorotaxanes comprising the cyanostar macrocycle and a thread that is based, for the first time, on organo-pyrophosphonates. Subtle differences in steric bulk on the threads allowed formation of either [3]pseudorotaxanes or [2]pseudorotaxanes. We demonstrate that the threading kinetics are governed by the steric demand of the organo-pyrophosphonates and in one case, slows down to the timescale of minutes. Calculations show that the dianions are sterically offset inside the macrocycles. Our findings broaden the scope of cyanostar-anion assemblies and may have relevance for the design of molecular machines whose directionality is a result of relatively slow slipping.

Introduction

Since the first reports half a century ago,[1–4] the field of supramolecular anion recognition[5,6] and anion receptor chemistry[7–13] has made significant advances. Notable applications[14] of anion recognition include sensing,[15–17] membrane transport,[18,19] catalysis[20–24] and increasingly the self-assembly of supramolecular architectures.[25–34] Anion recognition has also been used to synthesize mechanically interlocked molecules.[35–38] In most of these interlocked examples, anions play the role of a template, such that the anion is not part of either the thread or the macrocycle and can be removed after synthesis.[39–42] Following one pioneering example based on a phenolate in the thread,[43] dialkyl phosphates have been pursued as promising binding sites to furnish anion-containing rotaxanes. While this approach comes with its challenges,[44] Flood and coworkers reported a strategy for the synthesis of [3]rotaxanes that are based on dialkyl phosphates and large anion-binding macrocycles (Figure 1A).[45,46]

The recognition of phosphorylated molecules,[47,48] including phosphates[49–52] and inorganic pyrophosphate[53–57] has been investigated extensively. By contrast, the supramolecular chemistry of organic pyrophosphates is underexplored[48,58,59] and, to the best of our knowledge, the recognition of organic pyrophosphonates is unexplored. As dianions with tunable organic substituents, these compounds would extend the scope of anion recognition towards designer guest molecules,[60–62] which could play a role in carbodiimide-driven chemical reaction cycles.[63–69]

A promising candidate for the binding of such large anions is the cyanostar (**CS**) macrocycle (Figure 1A)[45] that has a positively polarized central cavity in which it can bind anions

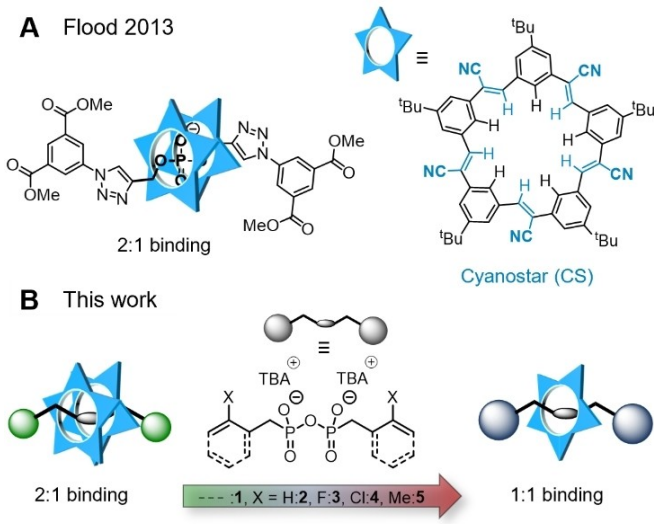

Figure 1. Overview on (A) previous work and (B) the scope of this study.

[a] J. Vogel, Prof. Dr. M. von Delius
Institute of Organic Chemistry, Ulm University
Albert-Einstein-Allee 11, 89081 Ulm (Germany)
E-mail: max.vondelius@uni-ulm.de
[b] Y. Chen, Dr. R. E. Fadler, Prof. Dr. A. H. Flood
Department of Chemistry, Indiana University
800 E. Kirkwood Avenue, Bloomington, IN 47405 (USA)
E-mail: aflood@indiana.edu

Supporting information for this article is available on the WWW under https://doi.org/10.1002/chem.202300899

© 2023 The Authors. Chemistry - A European Journal published by Wiley-VCH GmbH. This is an open access article under the terms of the Creative Commons Attribution License, which permits use, distribution and reproduction in any medium, provided the original work is properly cited.

© 2023 The Authors. Chemistry - A European Journal published by Wiley-VCH GmbH

through multiple CH hydrogen bonds. Cyanostar has been reported to bind organophosphates and organophosphonates in co-assemblies, where two (or more) macrocycles π-stack in a dimeric fashion with multiple equilibria.[61,70–73] This relatively strong interaction has enabled supramolecular polymerization[72] and reversible adhesion.[62] The 1:1 binding of only one cyanostar to an anion has only been observed once for a bulky derivative (i.e., cyanosolo),[74] but never for the parent macrocycle.

Herein, we report that control over the stoichiometry and kinetics of **CS**:anion binding can be achieved by modifying the steric bulk on organo-pyrophosphonate threads. A series of five pyrophosphonates was synthesized (Figure 1B) and their thermodynamics and kinetics of binding with cyanostar were studied. We found that binding can be switched between the 2:1 and the 1:1 stoichiometry, which represents the selective formation of [3]- and [2]pseudorotaxanes, respectively.

Results and Discussion

To study their interaction with the cyanostar macrocycle, we synthesized five different pyrophosphonates (**PP**) as *bis*-tetrabutylammonium (TBA) salts by condensation of the corresponding phosphonate with diisopropylcarbodiimide (DIC). Full synthesis procedures and characterization by NMR spectroscopy (including ^{31}P NMR) and high-resolution mass spectrometry (HRMS) is provided in the Supporting Information. The pyrophosphonates differ in their steric bulk, ranging from the least sterically demanding homoallyl-PP **1** to benzyl-PPs with different substituents in the *ortho*-position. Substitution with –H (**2**), –F (**3**) and –Cl (**4**) atoms or the methyl group (–Me, **5**) provides a subtle stepwise increase in steric demand. The dianionic pyrophosphonate in the center of the dumbbell-like structure can act as a binding site for the cyanostar macrocycle. The structures are depicted in Figure 1B. The cyanostar was synthesized as reported previously[45] (Figure S45–46).

Thermodynamics of binding

To investigate complexation, we performed ^{1}H NMR titrations by adding the pyrophosphonate threads to the cyanostar (0.5 mM, DCM-d_2, Figure 2A). As depicted by the cartoons in Figure 2A, there are three different binding modes possible: Either a threaded 2:1 complex (green, [3]pseudorotaxane), a threaded 1:1 complex (blue, [2]pseudorotaxane) or a perched 1:1 complex (cyan), in which the cyanostar is associated with the pyrophosphonate binding site but not threaded with it. In the case of the least sterically demanding homoallyl-PP thread **1** (Figure 2B), we observed the expected formation of the characteristic peaks for the cyanostar dimer (green) that are in slow exchange on the NMR timescale as reported previously.[70,72] Because the macrocycle dimer can arrange either as a *chiral* (') or as a *meso* isomer, two sets of diastereomeric peaks can be observed (structures shown in Figure S69). Due to its larger pseudo-stopper, addition of the benzyl-PP **2** to cyanostar (Figure 2C) yielded the [3]pseudorotaxane (2:1 binding) only in minor amounts. Instead, we observed a new set of ^{1}H NMR signals (blue) that belongs to the 1:1 binding mode corresponding to a [2]pseudorotaxane. In both complexes we observed a strong downfield shift for protons H_a and H_d that point inside the binding cavity and is consistent with CH hydrogen bonding to the pyrophosphonate anions. Interestingly, the [3]pseudorotaxane displays shifts in H_a and H_d that more closely resemble the shifts seen upon complexation of dianions[70] rather than monoanions.[45] The minor shift seen for protons H_b and H_c are consistent with their locations on the outside of the macrocycles. Likewise, we exclusively observed the formation of [2]pseudorotaxane when performing the analogous titration with F-benzyl-PP **3** (Figure 2D), where the steric demand is further increased. Binding also leads to a new set of signals for the pyrophosphonates phenyl protons (grey, shifted upfield under the influence of cyanostar's π-system). When increasing the equivalents of the pyrophosphonate up to 50, we could observe that the equilibrium is shifted towards the [2]pseudorotaxane even in the case of homoallyl-PP **1** (Figure S64 and Figure S70), because the cyanostar availability is decreased.

For all investigated threads, the signals of the unthreaded cyanostar (cyan) broaden upon addition of excess pyrophosphonate as a result of forming a perched complex that is in fast exchange with the free cyanostar on the NMR timescale.The sharp signals for both the 2:1 and the 1:1 pseudorotaxanes indicate slow exchange on the NMR timescale. For the two most sterically demanding pyrophosphonates **4** and **5** (–Cl, –Me), no evidence of threading was observed. Even at increased temperatures up to 403 K (VT NMR, Figure S67), ^{1}H NMR spectroscopy did not indicate any rotaxane formation in $C_2D_2Cl_4$ (upon cooling to ambient temperature), from which we conclude that even the Cl-substituted stopper is already too large to allow slipping of cyanostar. Further fine-tuning of the stoppers (e.g., five-membered rings) could potentially facilitate a convenient synthesis of cyanostar rotaxanes by a slipping approach (heating followed by cooling).[75,76]

To complete the characterization of the complexes, we measured high resolution mass spectra (HRMS) of the pseudorotaxanes and found corresponding signals to be in good agreement with the calculated isotopic patterns (Figures S74–75). When applying a collision voltage to the pseudorotaxane in the gas-phase, the signal decreased in favor of the free pyrophosphonates indicating dethreading (Figure S76). The binding of the cyanostar to the pyrophosphonates in solution was further corroborated by ^{1}H–^{1}H NOE NMR spectroscopy, where a cross-peak between the inner protons of the cyanostar (H_a and H_d) and the benzyl protons of the pyrophosphonate was observed (Figure S73).

The binding was investigated further by ^{31}P NMR spectroscopy. In a titration experiment, we added cyanostar to benzyl-PP **2** and F-benzyl-PP **3** (2.5 mM, DCM-d_2 or $CDCl_3$) and monitored the decreasing peak of the free pyrophosphonate and the increasing peak of [2]pseudorotaxanes. As the species are in slow exchange, we were able to integrate the two peaks

© 2023 The Authors. Chemistry - A European Journal published by Wiley-VCH GmbH

15213765, 0, Downloaded from https://chemistry-europe.onlinelibrary.wiley.com/doi/10.1002/chem.202300899 by KIZ der Universitat Ulm, Wiley Online Library on [06/07/2023]. See the Terms and Conditions (https://onlinelibrary.wiley.com/terms-and-conditions) on Wiley Online Library for rules of use; OA articles are governed by the applicable Creative Commons License

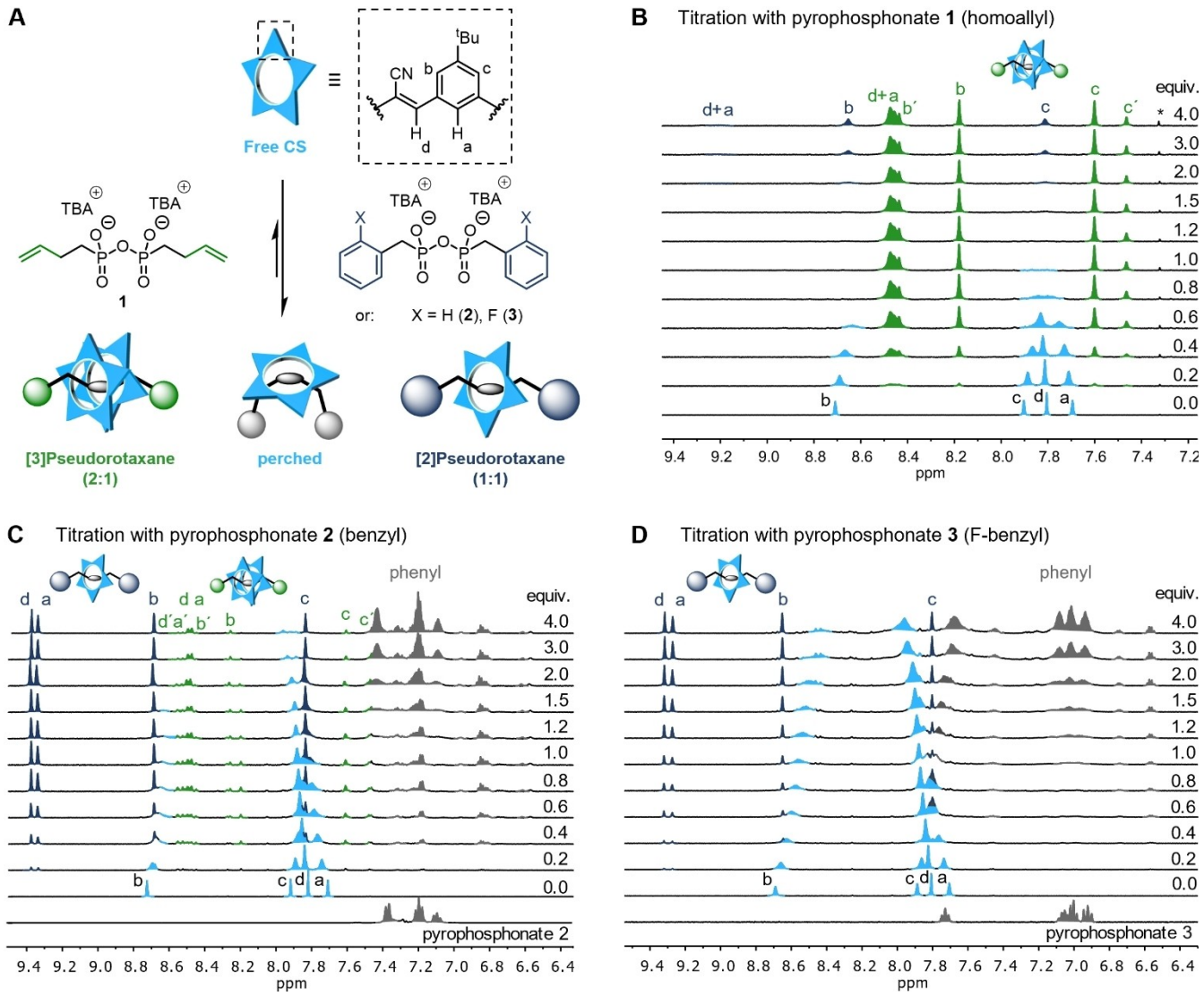

Figure 2. ^{1}H NMR titrations. (A) Schematic illustration of experiments leading to either [*n*]pseudorotaxanes ($n = 2, 3$) or the perched complex. (B) Titration of homoallyl-PP **1** into a solution of **CS** leads to the formation of [3]pseudorotaxane (2:1 complex). (C) Titration of benzyl-PP **2** to **CS** leads to a mixture of 1:1 and 2:1 complexes. (D) Titration of F-benzyl-PP **3** to **CS** leads exclusively to the formation of [2]pseudorotaxane (1:1 complex). The corresponding signals are color-coded as follows: free and perched **CS** generate a single fast-exchange signature colored cyan, the 2:1 complex is green, and the 1:1 complex is blue, while the phenyl-protons (free and bound) are grey. ^{1}H NMR titrations (600 MHz) were performed with 0.5 mM **CS**, at 298 K in DCM-d_2.

and determine binding constants by applying the mass action law (Figures S77–S80). All binding constants are moderate and on the order of 10^3 M^{-1} (see Table 1). Unfavorable steric interactions could account for the weaker binding compared to previously studied anions.[45,74]

Table 1. Summary of binding thermodynamics and kinetics of the [2]pseudorotaxanes.[87,88]

Pyrophosphonate	A value[a]	K_A [M^{-1}][b]	t_{50}[c]
1 (homoallyl)	n.a.	n.d.	< 20 s
2 (benzyl)	H: 0.0	2600 ± 300 ($CDCl_3$)	< 20 s
3 (F-benzyl)	F: 0.15	1300 ± 300 ($CDCl_3$) 4400 ± 500 (CD_2Cl_2)	~3.5 min
4 (Cl-benzyl)	Cl: 0.43	No threading[d]	
5 (Me-benzyl)	Me: 1.70	No threading[d]	

[a] Indicates the size of the *ortho*-substituent on the phenyl group.[89,90] [b] At 298 K, 2.5 mM. Only $CDCl_3$ was used for benzyl-PP **2** where no 2:1 binding was observed due to the lower polarity of this solvent (compared to CD_2Cl_2). [c] At 298 K, 1 mM in CD_2Cl_2. [d] Up to 333 K in $CDCl_3$ or up to 403 K in $C_2D_2Cl_4$ (S52). n.a.: not applicable. n.d.: not determined (complex mixture).

Kinetics of binding

We also explored the kinetics of threading cyanostar macrocycles onto the pyrophosphonates. As illustrated in Figure 3A, we added the pyrophosphonates (2 mM) to a solution of cyanostar in DCM-d_2 (1 mM) and monitored the formation of the corresponding pseudorotaxanes by ^{1}H NMR spectroscopy. For homoallyl-PP **1** (Figure S58) and benzyl-PP **2** (Figure 3B and

© 2023 The Authors. Chemistry - A European Journal published by Wiley-VCH GmbH

15213765, 0, Downloaded from https://chemistry-europe.onlinelibrary.wiley.com/doi/10.1002/chem.202300899 by KIT der Universitat Ulm, Wiley Online Library on [06/07/2023]. See the Terms and Conditions (https://onlinelibrary.wiley.com/terms-and-conditions) on Wiley Online Library for rules of use; OA articles are governed by the applicable Creative Commons License

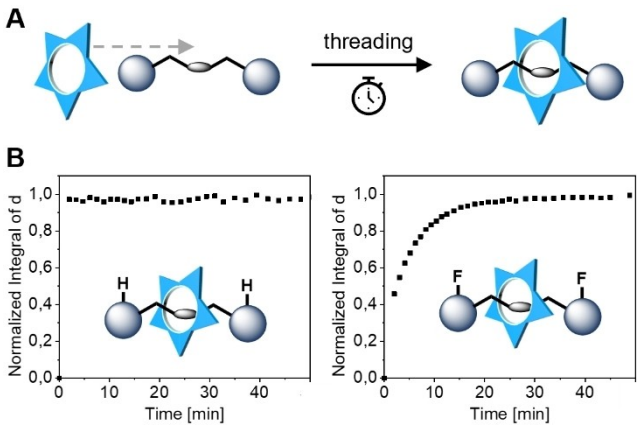

Figure 3. Binding kinetics. (A) Illustration of the experiment: The threading kinetics of cyanostar on the pyrophosphonates is monitored. (B) Formation of the [2]pseudorotaxane (1:1 binding) over time (as indicated by the integral of the characteristic H_d proton) with pyrophosphonates **2** and **3**, respectively. All kinetic experiments were performed at 298 K, 1 mM in DCM-d_2.

S59) the threading is too fast to be observed in these experiments. Taking the delay between addition of the pyrophosphonate and the first measurement into account, the time until 50% of the final equilibrium is reached (t_{50}) is therefore below 20 s. When we studied the de-threading kinetics of the 1:1 complex between cyanostar and benzyl-PP **2**, we found that it made a difference whether we initiated de-threading by addition of PF_6^- (relatively slow de-threading with $t_{50} \approx 120$ s; Figure S61) or water (fast de-threading with $t_{50} < 20$ s, Figure S62). The steric demand of F-benzyl-PP **3** (Figure 3B and Figure S60) slowed down the threading significantly and we determined $t_{50} \approx 3.5$ min. Equilibrium is reached after approximately 15 min (Figures S48–49), so this compound can be considered a borderline case between pseudorotaxane and rotaxane.[77] Such relatively slow threading kinetics could be interesting for the design of directional molecular machines,[78–82] in which a ratcheting step relies on a molecular "valve".[83–86]

Variable temperature (VT) NMR spectroscopy was performed (Figures S50–S53) to gain insights into the kinetics associated with formation of the perched interaction from the free cyanostar. As mentioned above, formation of this perched structure is fast on the NMR time scale at 298 K. Decreasing the temperature to 233 K slows down this process significantly, as indicated by peak splitting of the cyanostar signals into those that can be assigned to the free and perched structures (Figure S65). At 333 K, on the other hand, sharp peaks are observed for free cyanostar indicating fast kinetics (in $CDCl_3$).

The results of both the thermodynamic and the kinetic studies are summarized in Table 1. We found that increasing the steric bulk of the pyrophosphonates - as indicated here by the A values[89–91] - decreases the threading kinetics over (at least) one order of magnitude. The binding thermodynamics (2:1 vs. 1:1 vs. no binding) is strongly dependent on the size of the pseudo-stoppers, with the K_A value of the more sterically demanding F-benzyl-PP **3** being slightly lower than benzyl-PP **2** (in $CDCl_3$).

Molecular modeling

In order to investigate how the steric demand of the pyrophosphonate dianions contribute to differences in the 1:1 and 2:1 binding modes, we performed density functional theory (DFT) calculations on the [3]pseudorotaxane with homoallyl-PP **1** and the [2]pseudorotaxane with F-benzyl-PP **3** (RB3LYP/6-31G(D), gas phase). Optimized geometries (Figure 4) were generated with the TBA^+ cation but it was omitted in parts of the figure for the purpose of clarity (see Figures S81–85). Consistent with reported (pseudo)rotaxanes formed between phosphate threads and cyanostar,[45,46,61] both structures show C–H···O hydrogen bonds between the polar cyanostar CH donors and the oxygen atoms on the pyrophosphonate threads. The [2]pseudorotaxane with F-benzyl-PP **3** shows an average hydrogen bond distance of 2.4 Å while the [3]pseudorotaxane with homoallyl PP **1** has an average hydrogen bond distance of 2.5 Å. In the case of the [3]pseudorotaxane with homoallyl PP **1**, we also observe a very short interaction ($d_{H\cdots O} = 2.1$ Å) between α-proton of one TBA^+ cation and an oxygen from the pyrophosphonate (Figure S83). This contact is consistent with reported crystal data of cyanostar and TBA-bisulfate[92] or TBA-organophosphate[70] complexes.

Interestingly, we observe that the π-stacked cyanostar dimer is not centered on the homoallyl PP **1** thread but shifted non-symmetrically to one side. To investigate the origin of this off-center position, we modelled binding of the simplest dianionic pyrophosphonate, $H_2P_2O_5^{2-}$, with the cyanostar dimer (Figure S84). Here we also observe the non-symmetric binding

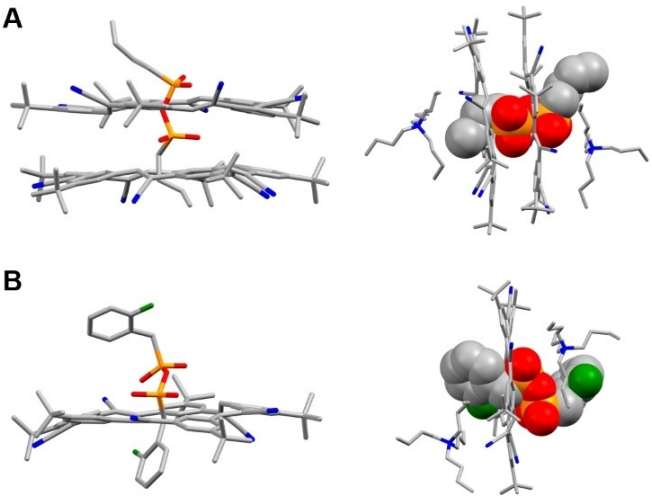

Figure 4. Equilibrium geometries of (A) the [3]pseudorotaxane comprised of two CS macrocycles and homoallyl-PP **1** and (B) the [2]pseudorotaxane comprised of one CS and F-benzyl-PP **3** shown as stick (left) and space-filling models (right). Equilibrium geometries were optimized using density functional theory (RB3LYP/6-31G(D)). Hydrogen atoms and TBA counter ions are omitted from the images on the left for clarity. Color code: C (grey), N (blue), O (red), F (green), P (orange).

© 2023 The Authors. Chemistry - A European Journal published by Wiley-VCH GmbH

15213765, 0, Downloaded from https://chemistry-europe.onlinelibrary.wiley.com/doi/10.1002/chem.202300899 by KIZ der Universitat Ulm, Wiley Online Library on [06/07/2023]. See the Terms and Conditions (https://onlinelibrary.wiley.com/terms-and-conditions) on Wiley Online Library for rules of use; OA articles are governed by the applicable Creative Commons License

mode even without substituents, indicating the steric profile of pyrophosphonate itself does not allow centralization inside the cyanostar dimer. This steric outcome naturally leads to a more limited stabilization of the dianionic pyrophosphonate by the cyanostar(s) with the available external oxygen atom shown to form the short contact with the TBA^+ cation. When the steric profile of the anionic thread becomes even more demanding, as with F-benzyl-PP **3** (Figure 4B and Figure S85), only one cyanostar can bind to the pyrophosphonate. This preference for one macrocycle emerges from the combination of the pyrophosphonate's steric profile and the steric proximity of the fluorophenyl.

Conclusions

We report the first example of organo-pyrophosphonate recognition and characterize their threading inside cyanostar macrocycles, which is modulated by the size of the organic substituent to afford pseudorotaxanes with one or two macrocycles (Figure 5). We synthesized a series of five short threads, explored their non-covalent C–H···O hydrogen bonding interactions with the anion-binding cyanostar macrocycle and characterized both thermodynamics and kinetics of threading. Using NMR titrations, we found that the previously reported propensity for cyanostar to form 2:1 complexes can be switched off completely by fine-tuning the steric profile of the pyrophosphonate. While DFT shows the pyrophosphonate anion is unable to perfectly fit inside two macrocycles, experiments show the homoallyl-PP alone can form a [3]pseudorotaxane. Increasing the steric demand yielded the successful assembly of a [2]pseudorotaxane with the F-benzyl-PP pyrophosphonate in chlorinated solvents. This first example of a 1:1 **CS**:anion complex was further corroborated by HRMS and NOESY NMR. We therefore demonstrate an approach to make use of substituents in designer anions with different steric demand to tune supramolecular recognition. Furthermore, we gained steric control not only over the thermodynamic binding mode, but also over the threading kinetics, which vary over at least one order of magnitude. Threading kinetics on the minutes-to-hours timescale represent the boundary between pseudorotaxanes and rotaxanes[77] and can be harnessed to create directional molecular machines, which will be at the focus of future work.

Experimental Section

Synthesis of pyrophosphonates (PP): Tetrabutylammonium phosphonates were dissolved in DCM and 10 equivalents of *N,N'*-diisopropylcarbodiimide (DIC) were added. The mixture was stirred at room temperature for 48 h. DCM was evaporated and the residue was purified by reversed-phase column chromatography. Lyophilization yielded the desired pyrophosphonates in 29–46 %.

^{1}H NMR titrations: All compounds were dried for 24 h under oil pump vacuum before use. A 0.5 mM solution of cyanostar in DCM-d_2 (dried over 3 Å molecular sieves) was prepared. A freshly prepared stock solution of the corresponding pyrophosphonate (25 mM, DCM-d_2) was added in a stepwise titration (1 μL = 0.1 equiv). The solutions were equilibrated according to their binding kinetics (see below) before measurement. All measurements were performed on a Bruker Avance 600 NEO spectrometer (600 MHz).

High Resolution Mass Spectrometry Electrospray Ionization (HRMS-ESI): A 200 μM solution of a 1:1 mixture of cyanostar and the pyrophosphonate in HPLC-grade DCM was prepared and HRMS was measured with ESI in the negative ion mode on an Agilent 1260 Infinity II system with a 6546 LC/QTOF mass spectrometer. In the 2D-MS experiment a collision voltage of 10–30 V was applied to the [2]pseudorotaxane in the gas phase.

^{31}P NMR titrations and determination of binding constants (K_A): 500 μL of a 2.5 mM solution of the corresponding pyrophosphonate was prepared in $CDCl_3$ or DCM-d_2. A 50 mM solution of cyanostar in $CDCl_3$ or DCM-d_2 was added in a stepwise titration (5 μL = 0.2 equiv. cyanostar). ^{31}P NMR was measured and the ratio of free pyrophosphonate and [2]pseudorotaxane was obtained by relative integration. Concentrations (including cyanostar) were calculated

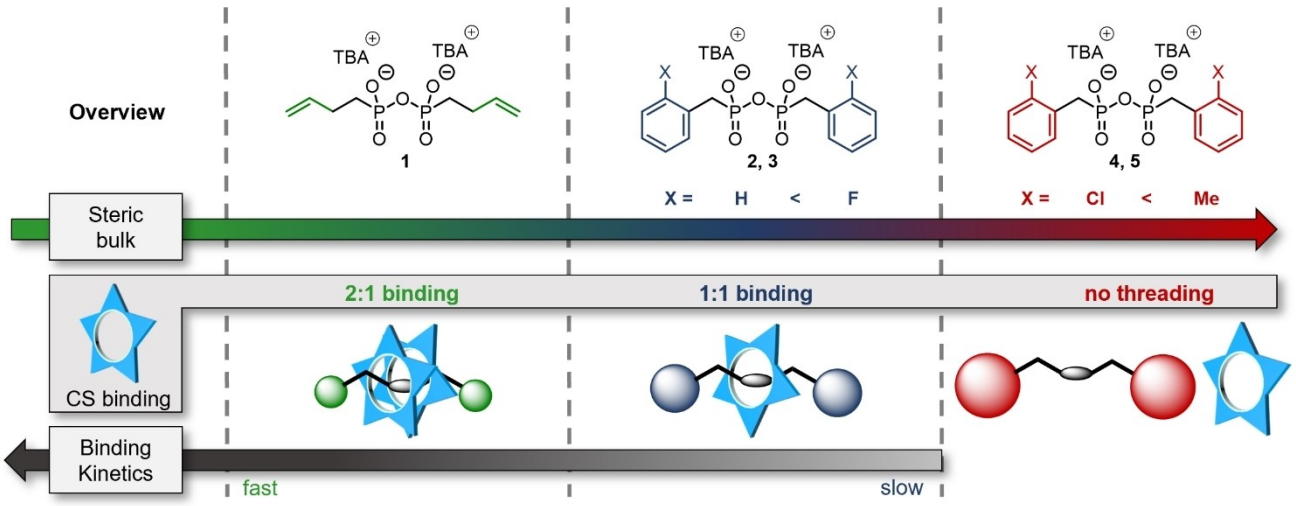

Figure 5. Overview of key findings of this study. Five different pyrophosphonates divided into three categories by their steric bulk.

© 2023 The Authors. Chemistry - A European Journal published by Wiley-VCH GmbH

15213765, 0, Downloaded from https://chemistry-europe.onlinelibrary.wiley.com/doi/10.1002/chem.202300899 by KIT der Universitat Ulm, Wiley Online Library on [06/07/2023]. See the Terms and Conditions (https://onlinelibrary.wiley.com/terms-and-conditions) on Wiley Online Library for rules of use; OA articles are governed by the applicable Creative Commons License

considering the total volume. Binding constants (K_A) were determined (as a mean value of seven measurements with the standard deviation as error) under the reasonable assumption that exchange is slow on the NMR time scale [Eq. (1)]:

$$K_A = \frac{[HG]}{[G] \times [H]} = \frac{[pseudorotaxane]}{[pyrophosphonate] \times [CS]} \quad (1)$$

Binding kinetics by ^{1}H NMR monitoring: 25 μL of a cyanostar stock solution (20 mM in DCM-d_2) was diluted with 435 μL DCM-d_2. 40 μL of a stock solution (25 mM in DCM-d_2) of the corresponding pyrophosphonate (**PP**) were added (1 mM **CS** + 2 mM **PP**) and a series of NMR spectra were recorded. A lag time of 120 s between addition of pyrophosphonate and the first measurement was taken into account. A characteristic peak for the formation of the [*n*]pseudorotaxane was monitored over time.

Variable temperature (VT) NMR studies: 25 μL of a 20 mM cyanostar stock solution (in $CDCl_3$) and 40 μL of a 25 mM stock solution of the corresponding pyrophosphonate (in $CDCl_3$) were diluted to 500 μL with $CDCl_3$ (1 mM **CS** + 2 mM **PP**). VT ^{1}H NMR was measured starting from the lower temperature. The temperature was equilibrated for 5 min before each measurement.

DFT calculations: A restricted hybrid HF-DFT SCF calculation was performed using Pulay DIIS + geometric direct minimization SPARTAN'20 on the RB3LYP functional with a 6–31G(D) basis set for the geometry optimization.

Acknowledgements

This work was supported by the European Union (ERCstg 802428 "SUPRANET"). Open Access funding enabled and organized by Projekt DEAL. We acknowledge support from the National Science Foundation (CHE 2105848). YC thanks the Slagle Fellowship for support. REF thanks the Raymond Siedle Materials Fellowship for support and the National Institutes of Health (T32GM109825) for support through the training grant entitled "Graduate Program in Quantitative and Chemical Biology at Indiana University Bloomington". We thank the staff of the Indiana University Mass Spectrometry Facility.

Conflict of Interests

The authors declare no conflict of interest.

Data Availability Statement

The data that support the findings of this study are available from the corresponding author upon reasonable request.

Keywords: anion binding · host-guest chemistry · macrocycles · phosphorus chemistry · rotaxanes

[1] H. E. Simmons, C. H. Park, *J. Am. Chem. Soc.* **1968**, *90*, 2428–2429.
[2] H. E. Simmons, C. H. Park, *J. Am. Chem. Soc.* **1968**, *90*, 2429–2431.
[3] H. E. Simmons, C. H. Park, *J. Am. Chem. Soc.* **1968**, *90*, 2431–2432.
[4] J.-M. Lehn, E. Sonveaux, A. K. Willard, *J. Am. Chem. Soc.* **1978**, *100*, 4914–4916.
[5] P. Molina, F. Zapata, A. Caballero, *Chem. Rev.* **2017**, *117*, 9907–9972.
[6] S. A. Boer, E. M. Foyle, C. M. Thomas, N. G. White, *Chem. Soc. Rev.* **2019**, *48*, 2596–2614.
[7] F. P. Schmidtchen, M. Berger, *Chem. Rev.* **1997**, *97*, 1609–1646.
[8] S. O. Kang, J. M. Llinares, V. W. Day, K. Bowman-James, *Chem. Soc. Rev.* **2010**, *39*, 3980–4003.
[9] L. Chen, S. N. Berry, X. Wu, E. N. W. Howe, P. A. Gale, *Chem* **2020**, *6*, 61–141.
[10] L. K. Macreadie, A. M. Gilchrist, D. A. McNaughton, W. G. Ryder, M. Fares, P. A. Gale, *Chem* **2022**, *8*, 46–118.
[11] N. H. Evans, P. D. Beer, *Angew. Chem. Int. Ed.* **2014**, *53*, 11716–11754.
[12] P. A. Gale, N. Busschaert, C. J. E. Haynes, L. E. Karagiannidis, I. L. Kirby, *Chem. Soc. Rev.* **2014**, *43*, 205–241.
[13] P. A. Gale, E. N. W. Howe, X. Wu, *Chem* **2016**, *1*, 351–422.
[14] N. Busschaert, C. Caltagirone, W. Van Rossom, P. A. Gale, *Chem. Rev.* **2015**, *115*, 8038–8155.
[15] N. Kaur, G. Kaur, U. A. Fegade, A. Singh, S. K. Sahoo, A. S. Kuwar, N. Singh, *TrAC Trends Anal. Chem.* **2017**, *95*, 86–109.
[16] M. T. Albelda, J. C. Frías, E. García-España, H. J. Schneider, *Chem. Soc. Rev.* **2012**, *41*, 3859–3877.
[17] A. R. Benasco, J. Tropp, V. Kaphle, Y. Chen, W. Zhao, N. Eedugurala, T. N. Ng, A. H. Flood, J. D. Azoulay, *Adv. Electron. Mater.* **2022**, *8*, 2101353.
[18] Z. Liu, L. F. Wu, J. Xu, C. Bonfio, D. A. Russell, J. D. Sutherland, *Nat. Chem.* **2020**, *12*, 1023–1028.
[19] J. T. Davis, O. Okunola, R. Quesada, *Chem. Soc. Rev.* **2010**, *39*, 3843–3862.
[20] Z. Zhang, P. R. Schreiner, *Chem. Soc. Rev.* **2009**, *38*, 1187–1198.
[21] R. J. Phipps, G. L. Hamilton, F. D. Toste, *Nat. Chem.* **2012**, *4*, 603–614.
[22] Y. Zhao, Y. Cotelle, L. Liu, J. López-Andarias, A. B. Bornhof, M. Akamatsu, N. Sakai, S. Matile, *Acc. Chem. Res.* **2018**, *51*, 2255–2263.
[23] C. Kwamen, J. Niemeyer, *Chem. Eur. J.* **2021**, *27*, 175–186.
[24] K. Kang, J. A. Lohrman, S. Nagarajan, L. Chen, P. Deng, X. Shen, K. Fu, W. Feng, D. W. Johnson, L. Yuan, *Org. Lett.* **2019**, *21*, 652–655.
[25] J. Zhao, D. Yang, X. J. Yang, B. Wu, *Coord. Chem. Rev.* **2019**, *378*, 415–444.
[26] D. Yang, J. Zhao, X. J. Yang, B. Wu, *Org. Chem. Front.* **2018**, *5*, 662–690.
[27] S. Hollstein, O. Shyshov, M. Hanževački, J. Zhao, T. Rudolf, C. M. Jäger, M. von Delius, *Angew. Chem. Int. Ed.* **2022**, *61*, e202201831.
[28] W. Zhang, J. Zhao, D. Yang, *ChemPlusChem* **2022**, *87*, e202200294.
[29] G. F. Feng, J. Geng, F. Da Feng, W. Huang, *Sci. Rep.* **2020**, *10*, 2–6.
[30] G. Zhang, M. Mastalerz, *Chem. Soc. Rev.* **2014**, *43*, 1934–1947.
[31] A. Thevenet, R. Custelcean, B. A. Moyer, S. Jansone-Popova, *Chem. Eur. J.* **2020**, *26*, 14290–14294.
[32] F. C. Parks, E. G. Sheetz, S. R. Stutsman, A. Lutolli, S. Debnath, K. Raghavachari, A. H. Flood, *J. Am. Chem. Soc.* **2022**, *144*, 1274–1287.
[33] C. J. Massena, D. A. Decato, O. B. Berryman, *Angew. Chem.* **2018**, *130*, 16341–16345.
[34] A. Dhara, R. E. Fadler, Y. Chen, L. A. Köttner, D. Van Craen, V. Carta, A. H. Flood, *Chem. Sci.* **2023**, *14*, 2585–2595.
[35] M. S. Vickers, P. D. Beer, *Chem. Soc. Rev.* **2007**, *36*, 211–225.
[36] A. Caballero, F. Zapata, P. D. Beer, *Coord. Chem. Rev.* **2013**, *257*, 2434–2455.
[37] A. W. Heard, S. M. Goldup, *ACS Cent. Sci.* **2020**, *6*, 117–128.
[38] J. Riebe, J. Niemeyer, *Eur. J. Org. Chem.* **2021**, *2021*, 5106–5116.
[39] G. M. Hübner, J. Gläser, C. Seel, F. Vögtle, *Angew. Chem. Int. Ed.* **1999**, *38*, 383–386.
[40] J. A. Wisner, P. D. Beer, M. G. B. Drew, M. R. Sambrook, *J. Am. Chem. Soc.* **2002**, *124*, 12469–12476.
[41] M. R. Sambrook, P. D. Beer, M. D. Lankshear, R. F. Ludlow, J. A. Wisner, *Org. Biomol. Chem.* **2006**, *4*, 1529–1538.
[42] J. Y. C. Lim, T. Bunchuay, P. D. Beer, *Chem. Eur. J.* **2017**, *23*, 4700–4707.
[43] P. Ghosh, O. Mermagen, C. A. Schalley, *Chem. Commun.* **2002**, *2*, 2628–2629.
[44] T. Fiala, V. Sindelar, *Supramol. Chem.* **2016**, *28*, 810–816.
[45] S. Lee, C. H. Chen, A. H. Flood, *Nat. Chem.* **2013**, *5*, 704–710.
[46] B. Qiao, Y. Liu, S. Lee, M. Pink, A. H. Flood, *Chem. Commun.* **2016**, *52*, 13675–13678.
[47] A. E. Hargrove, S. Nieto, T. Zhang, J. L. Sessler, E. V. Anslyn, *Chem. Rev.* **2011**, *111*, 6603–6782.
[48] H. T. Ngo, X. Liu, K. A. Jolliffe, *Chem. Soc. Rev.* **2012**, *41*, 4928–4965.
[49] S. Pal, T. K. Ghosh, R. Ghosh, S. Mondal, P. Ghosh, *Coord. Chem. Rev.* **2020**, *405*, 213128.
[50] J. V. Gavette, N. S. Mills, L. N. Zakharov, C. A. Johnson, D. W. Johnson, M. M. Haley, *Angew. Chem.* **2013**, *125*, 10460–10464.

© 2023 The Authors. Chemistry - A European Journal published by Wiley-VCH GmbH

15213765, 0, Downloaded from https://chemistry-europe.onlinelibrary.wiley.com/doi/10.1002/chem.202300899 by KIZ der Universitat Ulm, Wiley Online Library on [06/07/2023]. See the Terms and Conditions (https://onlinelibrary.wiley.com/terms-and-conditions) on Wiley Online Library for rules of use; OA articles are governed by the applicable Creative Commons License

[51] S. J. Wezenberg, M. Vlatković, J. C. M. Kistemaker, B. L. Feringa, *J. Am. Chem. Soc.* **2014**, *136*, 16784–16787.
[52] D. R. Rice, P. Vacchina, B. Norris-Mullins, M. A. Morales, B. D. Smith, *Antimicrob. Agents Chemother.* **2016**, *60*, 2932–2940.
[53] K. I. M. S. Kyung, L. E. E. Dong Hoon, J. I. N. Hong, J. Yoon, *Acc. Chem. Res.* **2009**, *42*, 23–31.
[54] S. Lee, K. K. Y. Yuen, K. A. Jolliffe, J. Yoon, *Chem. Soc. Rev.* **2015**, *44*, 1749–1762.
[55] P. Sokkalingam, D. S. Kim, H. Hwang, J. L. Sessler, C. H. Lee, *Chem. Sci.* **2012**, *3*, 1819–1824.
[56] M. Ali, I. Ahmed, P. Ramirez, S. Nasir, C. M. Niemeyer, S. Mafe, W. Ensinger, *Small* **2016**, *12*, 2014–2021.
[57] K. A. Jolliffe, *Acc. Chem. Res.* **2017**, *50*, 2254–2263.
[58] C. Ma, C. Lin, Y. Wang, X. Chen, *TrAC Trends Anal. Chem.* **2016**, *77*, 226–241.
[59] K. Fujita, S. Fujiwara, T. Yamada, Y. Tsuchido, T. Hashimoto, T. Hayashita, *J. Org. Chem.* **2017**, *82*, 976–981.
[60] E. G. Sheetz, Z. Zhang, A. Marogil, M. Che, M. Pink, V. Carta, K. Raghavachari, A. H. Flood, *Chem. Eur. J.* **2022**, *28*, e202201584.
[61] R. E. Fadler, A. Al Ouahabi, B. Qiao, V. Carta, F. K. Niklas, X. Gao, *J. Org. Chem.* **2021**, *86*, 4532–4546.
[62] W. Zhao, J. Tropp, B. Qiao, M. Pink, J. D. Azoulay, A. H. Flood, *J. Am. Chem. Soc.* **2020**, *142*, 2579–2591.
[63] J. Sun, J. Vogel, L. Chen, A. L. Schleper, T. Bergner, A. J. C. Kuehne, M. von Delius, *Chem. Eur. J.* **2022**, *28*, e202104116.
[64] A. Englert, J. F. Vogel, T. Bergner, J. Loske, M. Von Delius, *J. Am. Chem. Soc.* **2022**, *144*, 15266–15274.
[65] S. Borsley, D. A. Leigh, B. M. W. Roberts, *Nat. Chem.* **2022**, *14*, 728–738.
[66] N. Singh, G. J. M. Formon, S. De Piccoli, T. M. Hermans, *Adv. Mater.* **2020**, *32*, 1906834.
[67] K. Das, L. Gabrielli, L. J. Prins, *Angew. Chem. Int. Ed.* **2021**, *60*, 20120–20143.
[68] S. A. P. Van Rossum, M. Tena-Solsona, J. H. Van Esch, R. Eelkema, J. Boekhoven, *Chem. Soc. Rev.* **2017**, *46*, 5519–5535.
[69] S. De, R. Klajn, *Adv. Mater.* **2018**, *30*, 1706750.
[70] W. Zhao, B. Qiao, C. H. Chen, A. H. Flood, *Angew. Chem. Int. Ed.* **2017**, *56*, 13083–13087.
[71] E. M. Fatila, M. Pink, E. B. Twum, J. A. Karty, A. H. Flood, *Chem. Sci.* **2018**, *9*, 2863–2872.
[72] W. Zhao, B. Qiao, J. Tropp, M. Pink, J. D. Azoulay, A. H. Flood, *J. Am. Chem. Soc.* **2019**, *141*, 4980–4989.
[73] W. Zhao, A. H. Flood, N. G. White, *Chem. Soc. Rev.* **2020**, *49*, 7893–7906.
[74] B. Qiao, J. R. Anderson, M. Pink, A. H. Flood, *Chem. Commun.* **2016**, *52*, 8683–8686.
[75] M. Xue, Y. Yang, X. Chi, X. Yan, F. Huang, *Chem. Rev.* **2015**, *115*, 7398–7501.
[76] A. J. McConnell, P. D. Beer, *Chem. Eur. J.* **2011**, *17*, 2724–2733.
[77] A. Affeld, G. M. Hühner, C. Seel, C. A. Schalley, *Eur. J. Org. Chem.* **2001**, *15*, 2877–2890.
[78] S. Erbas-Cakmak, D. A. Leigh, C. T. McTernan, A. L. Nussbaumer, *Chem. Rev.* **2015**, *115*, 10081–10206.
[79] D. A. Leigh, J. K. Y. Wong, F. Dehez, F. Zerbetto, *Nature* **2003**, *424*, 174–179.
[80] A. Coskun, M. Banaszak, R. D. Astumian, J. F. Stoddart, B. A. Grzybowski, *Chem. Soc. Rev.* **2012**, *41*, 19–30.
[81] C. J. Bruns, *Nat. Nanotechnol.* **2022**, *17*, 1231–1234.
[82] I. Aprahamian, *ACS Cent. Sci.* **2020**, *6*, 347–358.
[83] C. Cheng, P. R. McGonigal, S. T. Schneebeli, H. Li, N. A. Vermeulen, C. Ke, J. F. Stoddart, *Nat. Nanotechnol.* **2015**, *10*, 547–553.
[84] Y. Qiu, L. Zhang, C. Pezzato, Y. Feng, W. Li, M. T. Nguyen, C. Cheng, D. Shen, Q. H. Guo, Y. Shi, K. Cai, F. M. Alsubaie, R. D. Astumian, J. F. Stoddart, *J. Am. Chem. Soc.* **2019**, *141*, 17472–17476.
[85] L. Zhang, Y. Qiu, W. G. Liu, H. Chen, D. Shen, B. Song, K. Cai, H. Wu, Y. Jiao, Y. Feng, J. S. W. Seale, C. Pezzato, J. Tian, Y. Tan, X. Y. Chen, Q. H. Guo, C. L. Stern, D. Philp, R. D. Astumian, W. A. Goddard III, J. F. Stoddart, *Nature* **2023**, *613*, 280–286.
[86] S. Corra, M. T. Bakić, J. Groppi, M. Baroncini, S. Silvi, E. Penocchio, M. Esposito, A. Credi, *Nat. Nanotechnol.* **2022**, *17*, 746–751.
[87] The free energy of hydration of phosphates is reported to be relatively high, compared to other anions.[88] It is likely that this is also true for pyrophosphonates. We found that addition of water can completely shut down the CS:PP binding (Figure S69) due to competitive solvation of the PP dianions. We therefore dried all substances under vacuum prior to use and performed sample preparation under exclusion of moisture.
[88] Y. Marcus, *J. Chem. Soc. Faraday Trans.* **1993**, *89*, 2995–2999.
[89] E. L. Eliel, S. H. Wilen, L. N. Mander, Stereochemistry of Organic Compounds, *John Wiley&Sons, New York* **1994**.
[90] E. Solel, M. Ruth, P. R. Schreiner, *J. Am. Chem. Soc.* **2021**, *143*, 20837–20848.
[91] E. Solel, M. Ruth, P. R. Schreiner, *J. Org. Chem.* **2021**, *86*, 7701–7713.
[92] E. M. Fatila, E. B. Twum, A. Sengupta, M. Pink, J. A. Karty, K. Raghavachari, A. H. Flood, *Angew. Chem. Int. Ed.* **2016**, *55*, 14057–14062.

Manuscript received: March 21, 2023
Accepted manuscript online: May 8, 2023
Version of record online: ■■, ■■

© 2023 The Authors. Chemistry - A European Journal published by Wiley-VCH GmbH

15213765, 0, Downloaded from https://chemistry-europe.onlinelibrary.wiley.com/doi/10.1002/chem.202300899 by KIZ der Universitat Ulm, Wiley Online Library on [06/07/2023]. See the Terms and Conditions (https://onlinelibrary.wiley.com/terms-and-conditions) on Wiley Online Library for rules of use; OA articles are governed by the applicable Creative Commons License



J. Vogel, Y. Chen, Dr. R. E. Fadler, Prof. Dr. A. H. Flood, Prof. Dr. M. von Delius**

1 – 8

Steric Control over the Threading of Pyrophosphonates with One or Two Cyanostar Macrocycles during Pseudorotaxane Formation

Control over the binding stoichiometry and the threading kinetics is achieved in pseudorotaxanes comprising the anion-binding cyanostar macrocycle and organic pyrophosphonates with fine-tuned steric bulk. The approach allowed the selective assembly of [3]pseudorotaxanes and [2]pseudorotaxanes, and it provided insights that are valuable for future work on anion recognition and the design of molecular machines.

15213765, 0, Downloaded from https://chemistry-europe.onlinelibrary.wiley.com/doi/10.1002/chem.202300899 by KIZ der Universitat Ulm, Wiley Online Library on [06/07/2023]. See the Terms and Conditions (https://onlinelibrary.wiley.com/terms-and-conditions) on Wiley Online Library for rules of use; OA articles are governed by the applicable Creative Commons License

Chemistry–A European Journal

Supporting Information

Steric Control over the Threading of Pyrophosphonates with One or Two Cyanostar Macrocycles during Pseudorotaxane Formation

Julian Vogel, Yusheng Chen, Rachel E. Fadler, Amar H. Flood,* and Max von Delius*

Table of Contents

General Methods **3**

Synthesis **4**

NMR Kinetic Experiments **47**

NMR Variable Temperature (VT) Experiments **50**

^{1}H NMR Titrations **54**

NOESY NMR spectrum of [2]pseudorotaxane **57**

Mass Spectrometry (MS) Experiments **58**

^{31}P NMR titrations and binding constants **60**

DFT calculations **66**

References **77**

General Methods

All reagents were obtained from commercial suppliers (Merck Sigma Aldrich, TCI, AcrosOrganics, FisherScientific or VWR) and used as received.

Phosphonate deprotection,[1] formation of TBA salts,[2] and cyanostar synthesis[3] were performed according to literature procedures with some modifications.

Reversed-phase chromatography was performed on an Advion Interchim Scientific Puriflash 430, using HPLC-grade solvents and an Interchim PF-15C18HP-F0025 C18 column. For lyophilization a Christ Alpha 3-4 LSCbasic was used.

Nuclear magnetic resonance (NMR) spectra were recorded on BrukerAvance 400 or 600 NEO spectrometers (^{1}H: 400 or 600 Hz, ^{13}C: 101 Hz, ^{31}P: 162 or 243 Hz) at room temperature (298 K). Chemical shifts were referenced on residual solvent peaks ($CDCl_3$: 7.26 ppm, $C_2D_2Cl_4$: 6.00 ppm, DCM-d_2: 5.32 ppm, DMSO-d_6: 2.50 ppm). ^{31}P-NMR chemicals shifts were referenced on 85% H_3PO_4 (0.00 ppm). Chemical shifts (δ) are denoted in ppm and coupling constants (*J*) in Hz. Peak multiplicities are indicated as s = singlet, d = doublet, t = triplet and m = multiplet.

High resolution electrospray ionization mass spectroscopy (HRMS – ESI) was performed on an Agilent 1260 Infinity II system with a 6546 LC/QTOF mass spectrometer.

Materials for all studies were dried at least 24 h under vacuum and the sample preparation was performed in a MBraun glovebox to exclude moisture. Deuterated solvents were dried over 3 Å molecular sieves for at least three days prior to use. All NMR studies were performed on a BrukerAvance 600 NEO spectrometer.

The following abbreviations were used: CS: Cyanostar, DFT: Density Functional Theory, DIC: *N,N*-diisopropylcarbodiimide, DCM: dichloromethane, DMSO: dimethylsulfoxide, ESI: electrospray ionization, HPLC: high-performance liquid chromatography, HRMS: high-resolution mass spectrometry, MeCN: acetonitrile, MPLC: medium-performance liquid chromatography, NMR: nuclear magnetic resonance, NOESY: Nuclear Overhauser effect spectroscopy, PP: pyrophosphonate, TBA: tetrabutylammonium, VT: variable temperature.

Synthesis

Synthesis overview

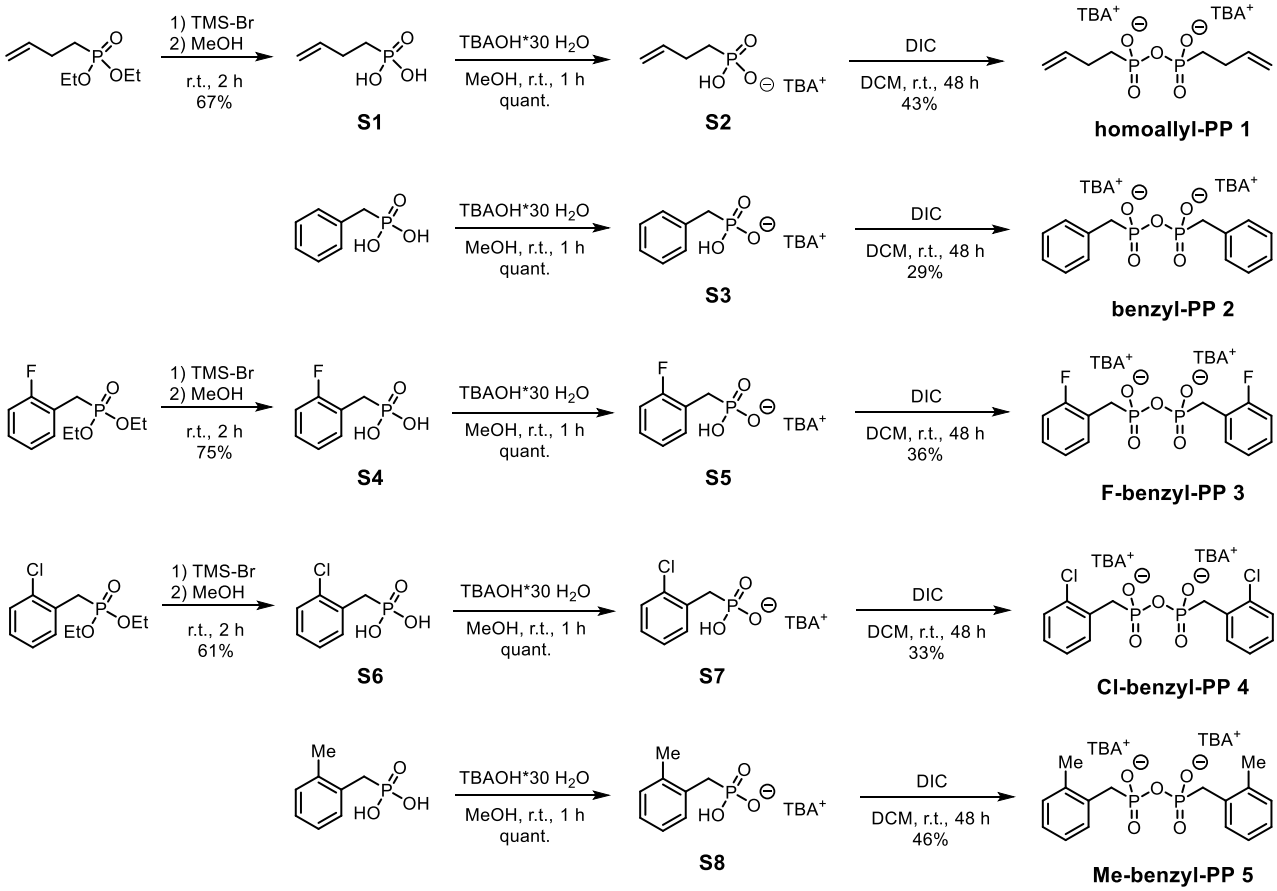

Scheme S1: Synthesis overview.

Synthesis of 3-butenylphosphonic acid S1

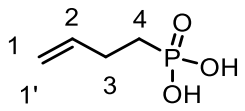

S1

1.00 mL (5.20 mmol) diethyl 3-butenylphosphonate were dissolved in 50 mL anhydrous DCM and 6.91 mL (52.0 mmol, 10 equiv.) trimethylsilylbromide were added. The mixture was stirred for 2 h at room temperature under inert atmosphere until TLC (DCM, 5% MeOH, stained with $KMnO_4$) indicated full conversion. DCM was evaporated and the residue was stirred for 1 h in anhydrous MeOH before the solvent was removed. MPLC on an Interchim PF-15C18HP-F0025 C18 column with a mobile phase of MeCN and 25 mM formic acid (5-10% MeCN) and subsequent lyophilization yielded 474 mg (3.48 mmol, 67%) of the desired product as a colourless solid.

^{1}H-NMR (400 MHz, DMSO-d_6): δ [ppm] = 5.92-5.82 (m, 1 H, **2**), 5.03 (dd, ^{3}J = 17.2 Hz, ^{2}J = 1.68 Hz, 1 H, **1'**), 4.94 (dd, ^{3}J = 10.2 Hz, ^{2}J = 1.40 Hz, 1 H, **1**), 2.20 (m, 2 H, **3**), 1.59 (m, 2 H, **4**).

^{13}C-NMR (101 MHz, DMSO-d_6): δ [ppm] = 138.4 (d), 114.7, 27.0 (d), 26.8 (d).

^{31}P-NMR (162 MHz, DMSO-d_6, external standard: 85% H_3PO_4): δ [ppm] = 27.30.

HRMS(ESI (-)): m/z = 135.02179 (calc. 135.02165, δm/m = 1.04 ppm) $[M-H]^-$

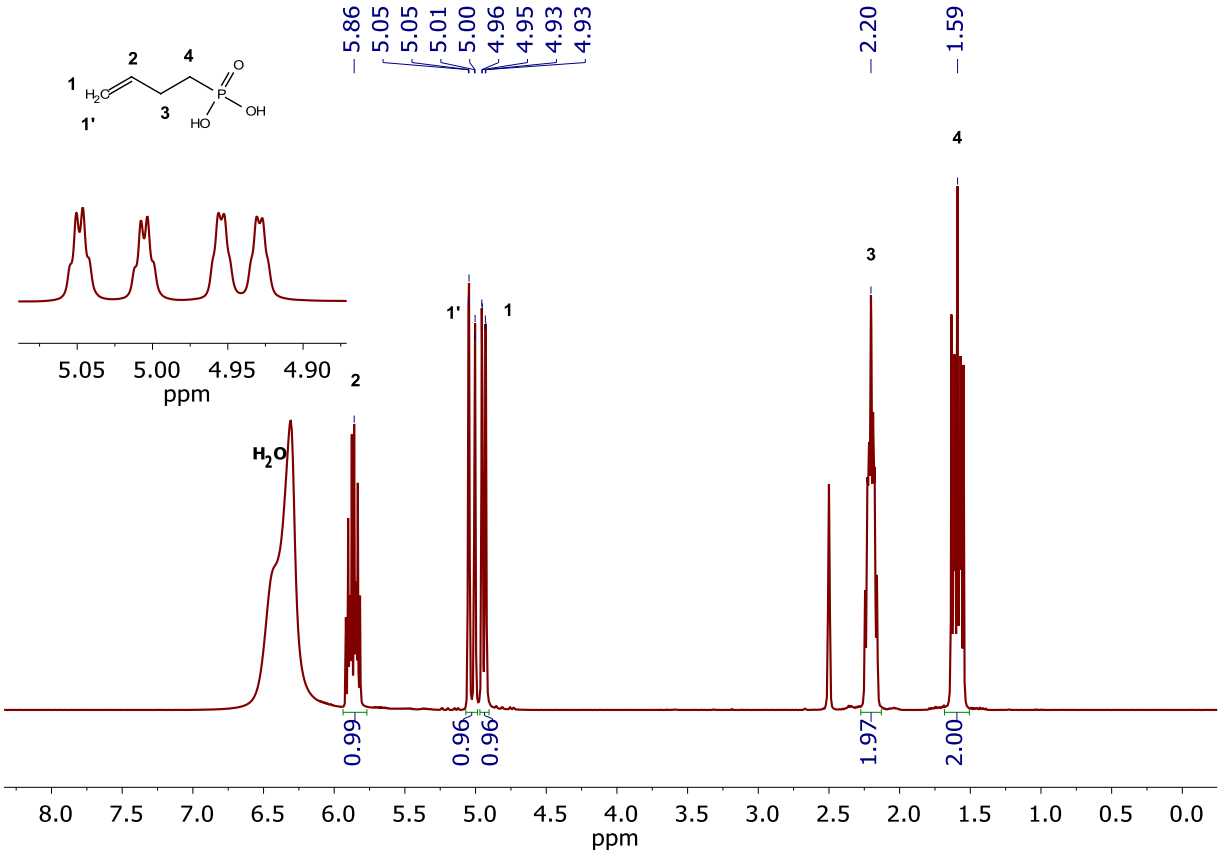

Figure S1: ^{1}H NMR (400 MHz, DMSO-d_6, 298 K) of 3-butenylphosphonic acid **S1**.

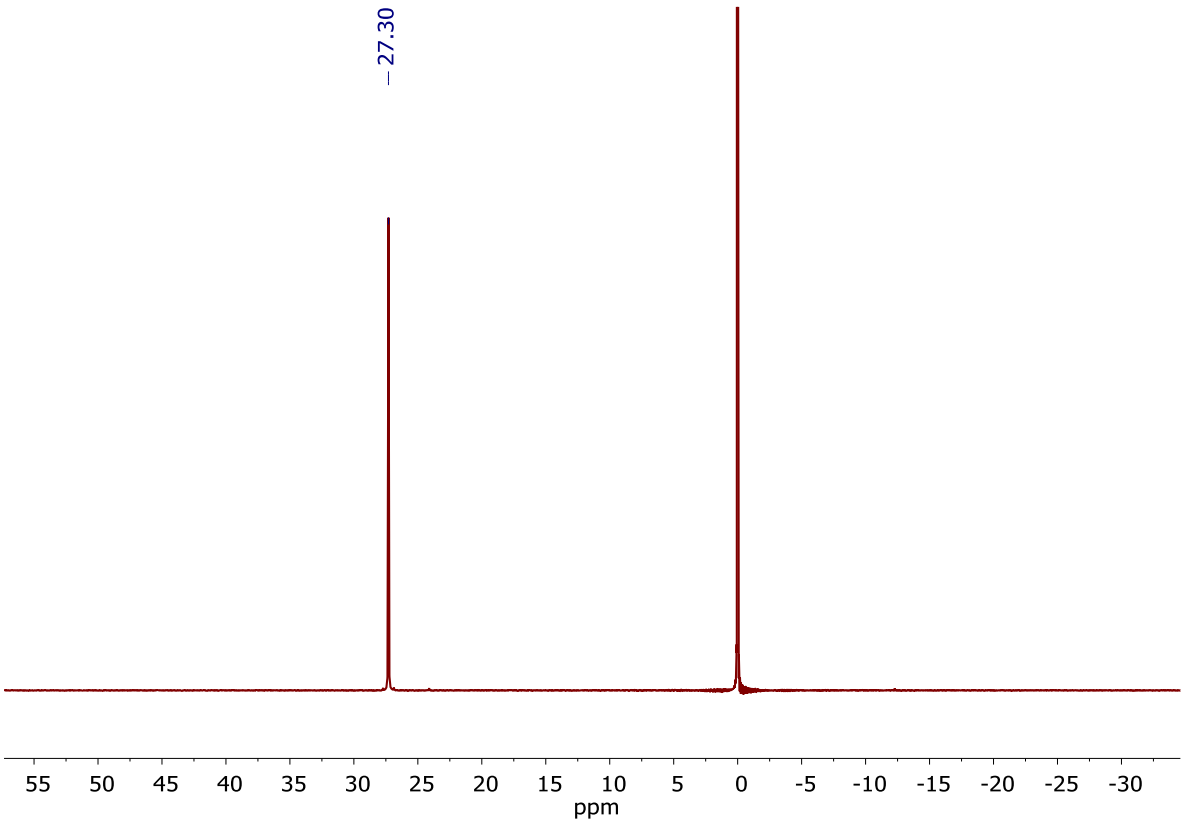

Figure S2: ^{31}P NMR (162 MHz, DMSO-d_6, 298 K, 85% H_3PO_4) of 3-butenylphosphonic acid **S1**.

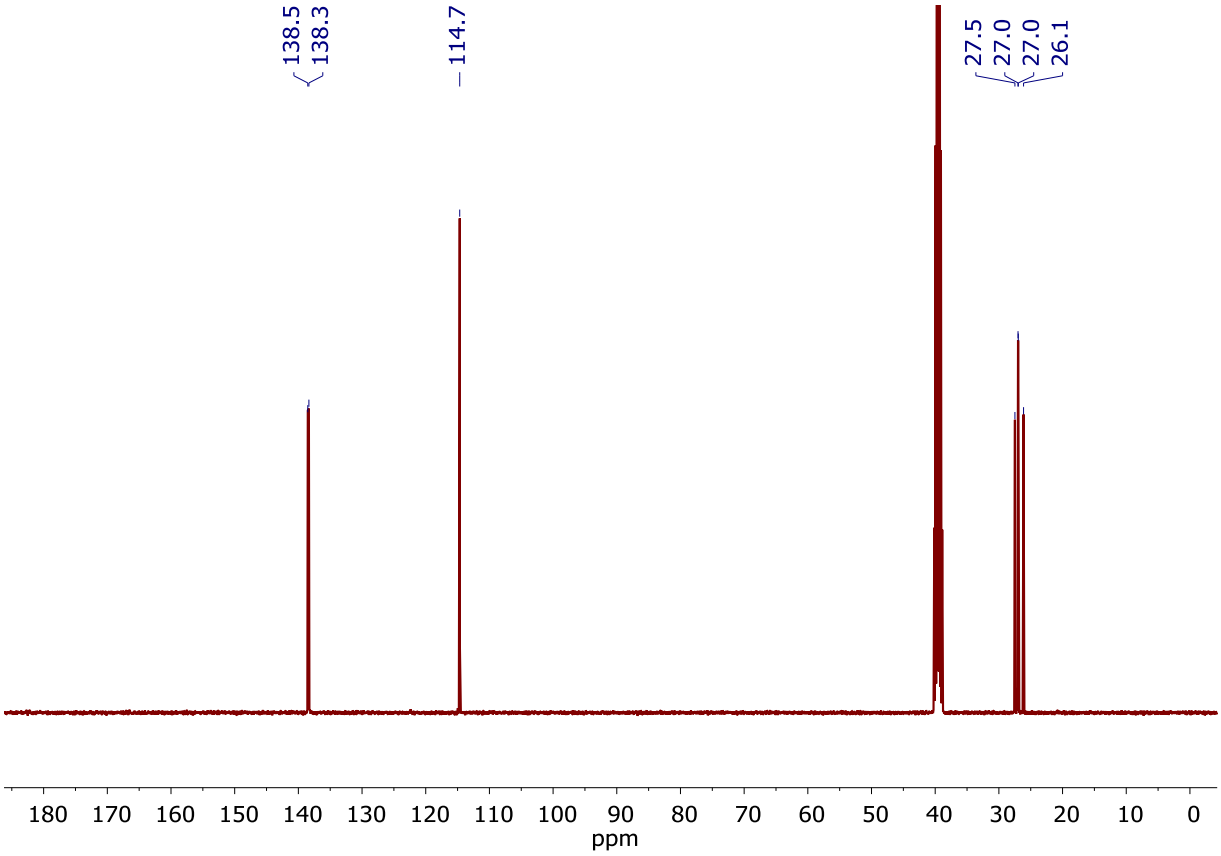

Figure S3: ^{13}C NMR (101 MHz, DMSO-d_6, 298 K) of 3-butenylphosphonic acid **S1**.

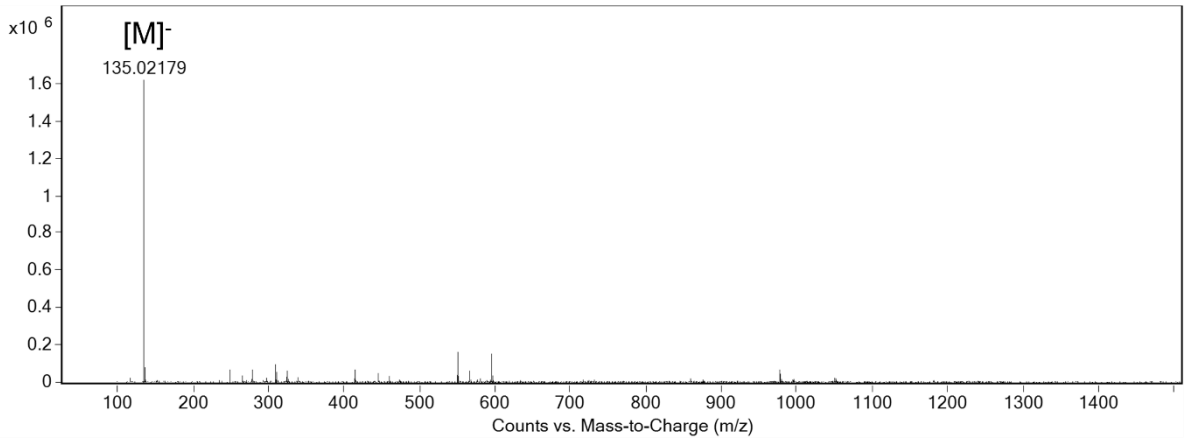

Figure S4: HRMS (ESI, negative mode) of 3-butenylphosphonic acid **S1**.

Synthesis of tetrabutylammonium 3-butenyl phosphonate S2

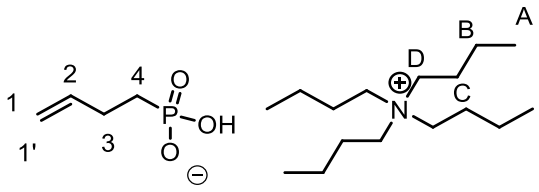

S2

450 mg (3.30 mmol) 3-butenylphosphonic acid **S1** and 2.64 g (3.30 mmol, 1.0 equiv.) TBAOH · 30 H_2O were combined in a round bottom flask and dissolved in 40 mL MeOH. The mixture was stirred for 1 h at room temperature, before the solvent was removed and the product was dried in vacuo to afford 1.25 g (3.30 mmol, quant.) of the desired TBA salt as a colourless solid.

^{1}H-NMR (400 MHz, $CDCl_3$): δ [ppm] = 5.93-5.82 (m, 1 H, **2**), 4.90 (dd, ^{3}J = 17.2 Hz, ^{2}J = 1.83 Hz, 1 H, **1'**), 4.74 (d_{br}, ^{3}J = 10.8 Hz, 1 H, **1**), 3.31-3.27 (m, 8 H, **D**), 2.35 (m, 2 H, **3**), 1.63-1.58 (m, 8 H, **C**), 1.53 (m, 2 H, **4**), 1.45-1.36 (m, 8 H, **B**), 0.93 (t, ^{3}J = 7.36 Hz, 12 H, **A**).

^{13}C-NMR (101 MHz, $CDCl_3$): δ [ppm] = 141.4 (d), 112.3, 58.7, 29.6 (d), 29.4 (d), 24.2, 19.8, 13.8.

^{31}P-NMR (162 MHz, $CDCl_3$, external standard: 85% H_3PO_4): δ [ppm] = 21.78.

HRMS(ESI (-)): m/z = 135.02236 (calc. 135.02165, δm/m = 5.26 ppm) $[M]^-$, 512.32897 (calc. 512.32753, δm/m = 2.81 ppm) $[2M+TBA]^-$.

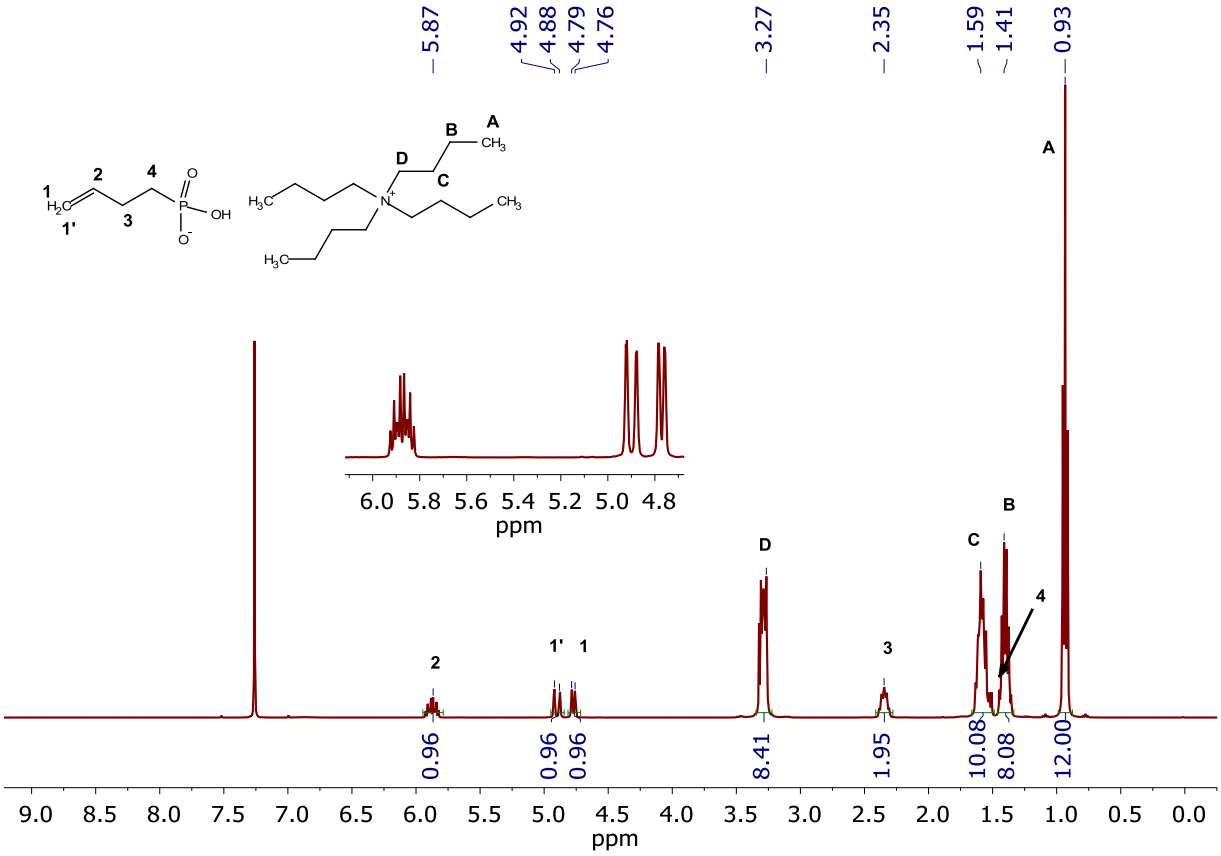

Figure S5: ^{1}H NMR (400 MHz, $CDCl_3$, 298 K) of tetrabutylammonium 3-butenyl phosphonate **S2**.

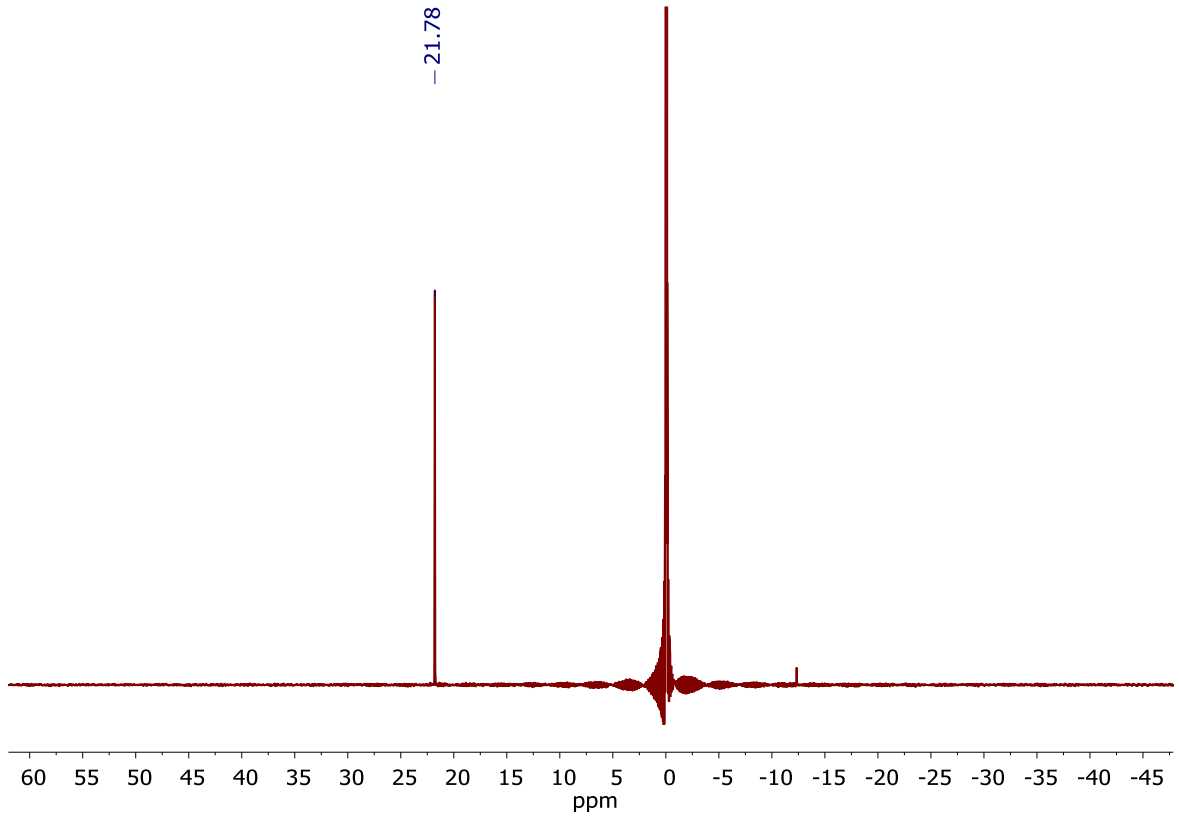

Figure S6: ^{31}P NMR (162 MHz, $CDCl_3$, 298 K, 85% H_3PO_4) of tetrabutylammonium 3-butenyl phosphonate **S2**. Peak at -12.6 ppm, belongs to an impurity in the internal standard.

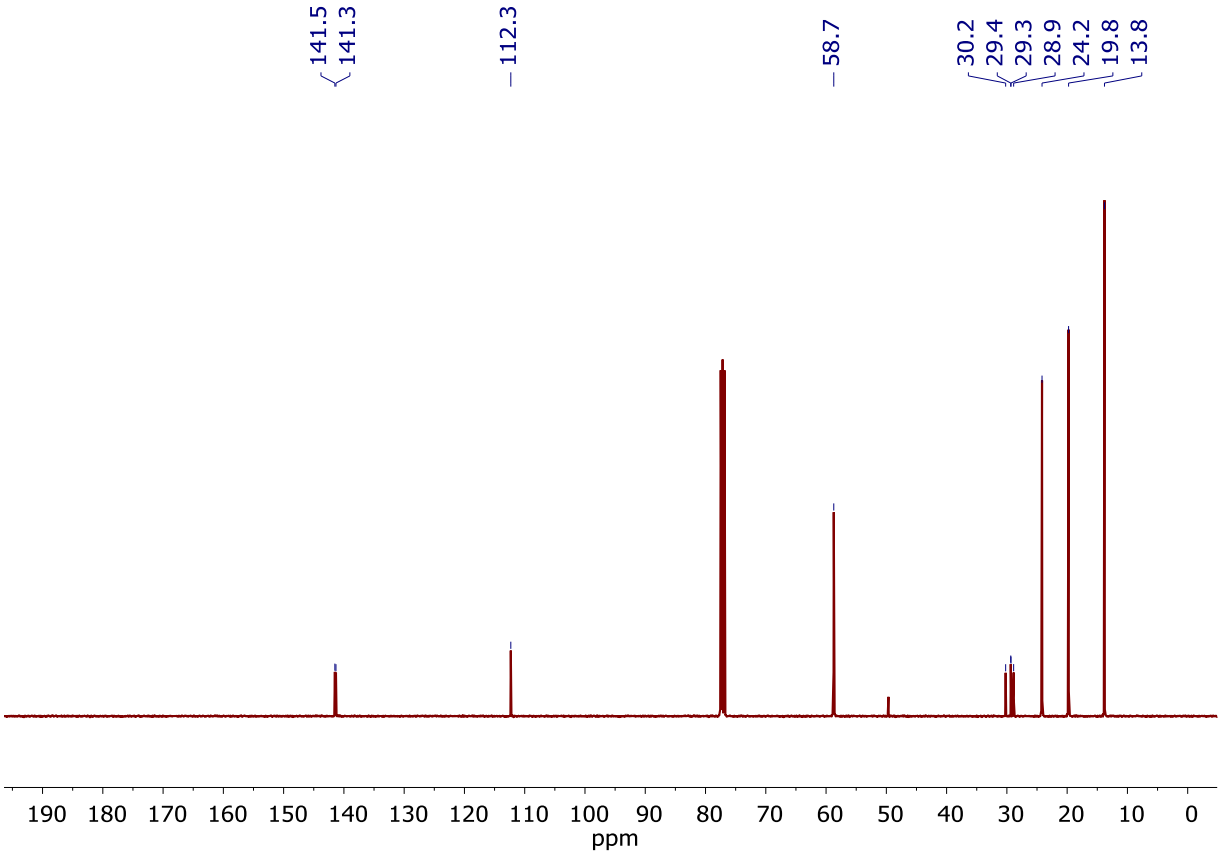

Figure S7: ^{13}C NMR (101 MHz, $CDCl_3$, 298 K) of tetrabutylammonium 3-butenyl phosphonate **S2**.

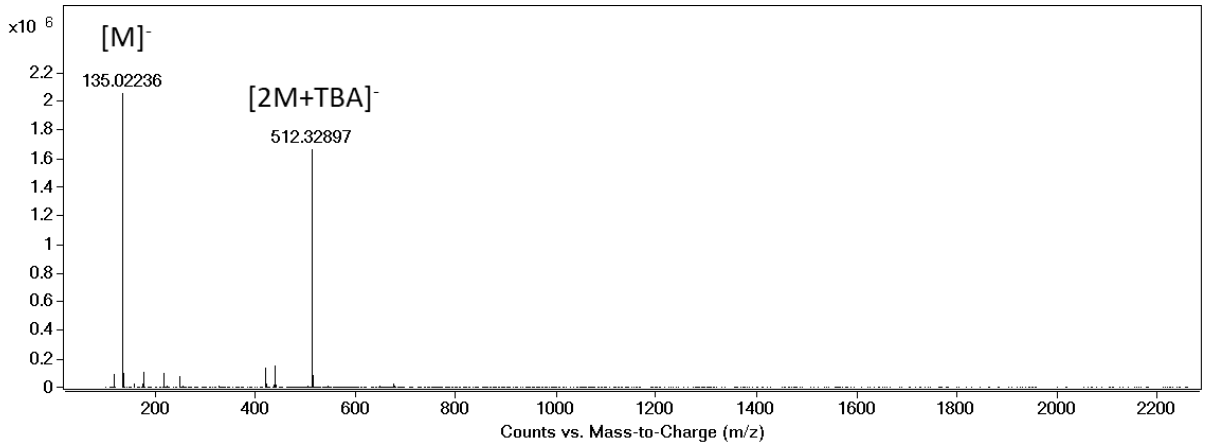

Figure S8: HRMS (ESI, negative mode) of tetrabutylammonium 3-butenyl phosphonate **S2**.

Synthesis of *bis*-tetrabutylammonium 3-butenyl pyrophosphonate (homoallyl-PP) 1

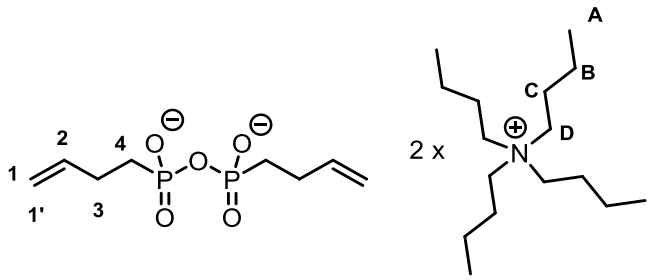

1

350 mg (0.93 mmol) tetrabutylammonium 3-butenyl phosphonate **S2** were dissolved in 40 mL DCM and 1.41 mL (9.30 mmol, 10 equiv.) *N,N'*-diisopropylcarbodiimide (DIC) were added. The mixture was stirred at room temperature for 48 h. DCM was evaporated and the residue was dissolved in 4 mL H_2O / MeCN (3:1) mixture. MPLC on an Interchim PF-15C18HP-F0025 C18 column with a mobile phase of MeCN and water (20-30% MeCN) and subsequent lyophilization yielded 150 mg (0.20 mmol, 43%) of the dimer as a colourless oil.

^{1}H-NMR (400 MHz, $CDCl_3$): δ [ppm] = 5.94-5.85 (m, 2 H, **2**), 4.95 (dd, ^{3}J = 17.1 Hz, ^{2}J = 1.85 Hz, 2 H, **1'**), 4.82 (d_{br}, ^{3}J = 10.2 Hz, 2 H, **1**), 3.39-3.33 (m, 16 H, **D**), 2.39 (m, 4 H, **3**), 1.74 (m, 4 H, **4**), 1.63-1.59 (m, 16 H, **C**), 1.47-1.39 (m, 16 H, **B**), 0.96 (t, ^{3}J = 7.30 Hz, 24 H, **A**).

^{13}C-NMR (101 MHz, $CDCl_3$): δ [ppm] = 141.1 (t), 112.6, 58.7, 30.1 (d), 28.9 (d), 24.2, 19.8, 13.8.

^{31}P-NMR (162 MHz, $CDCl_3$, external standard: 85% H_3PO_4): δ [ppm] = 13.64.

HRMS(ESI (-)): m/z = 253.04108 (calc. 253.04002, δm/m = 4.19 ppm) $[M]^-$, 494.31733 (calc. 494.31697, δm/m = 0.73 ppm) $[2M+TBA]^-$.

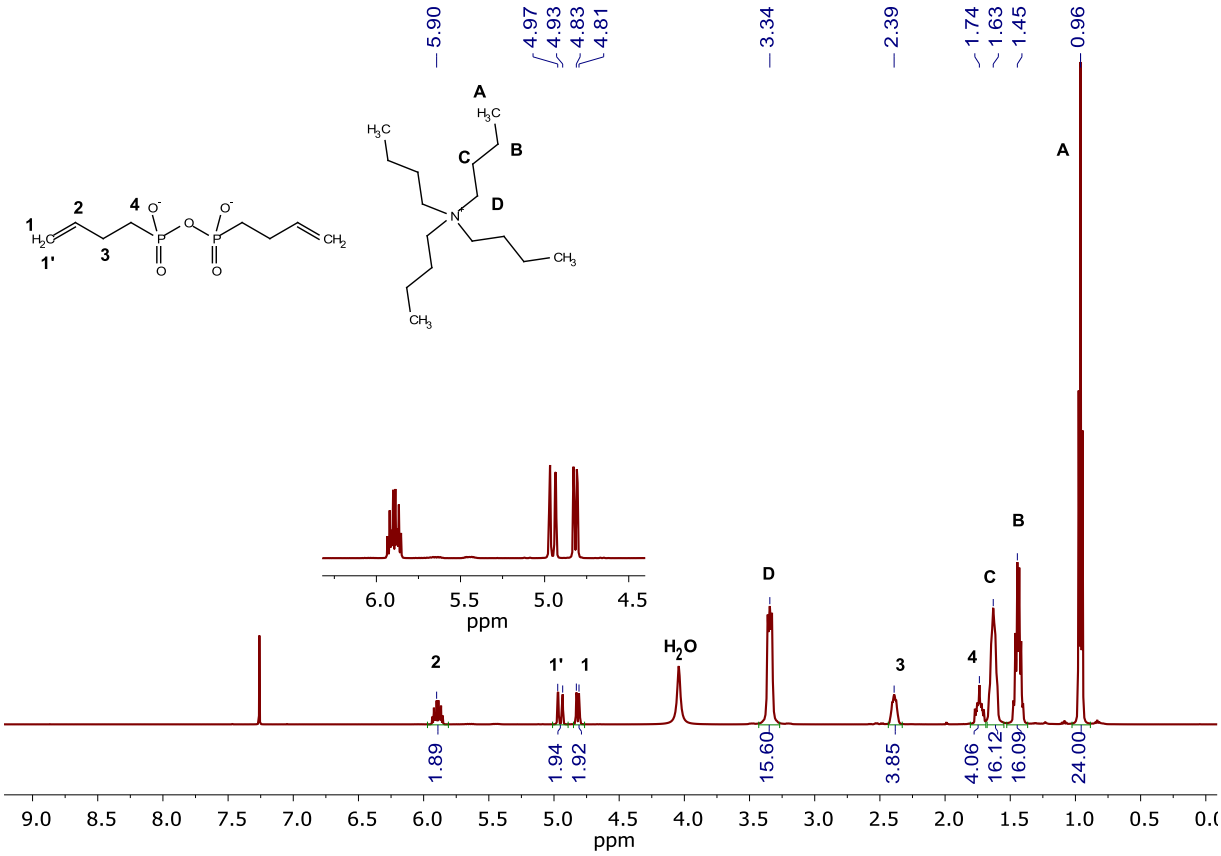

Figure S9: ^{1}H NMR (400 MHz, $CDCl_3$, 298 K) of *bis*-tetrabutylammonium 3-butenyl pyrophosphonate **1**.

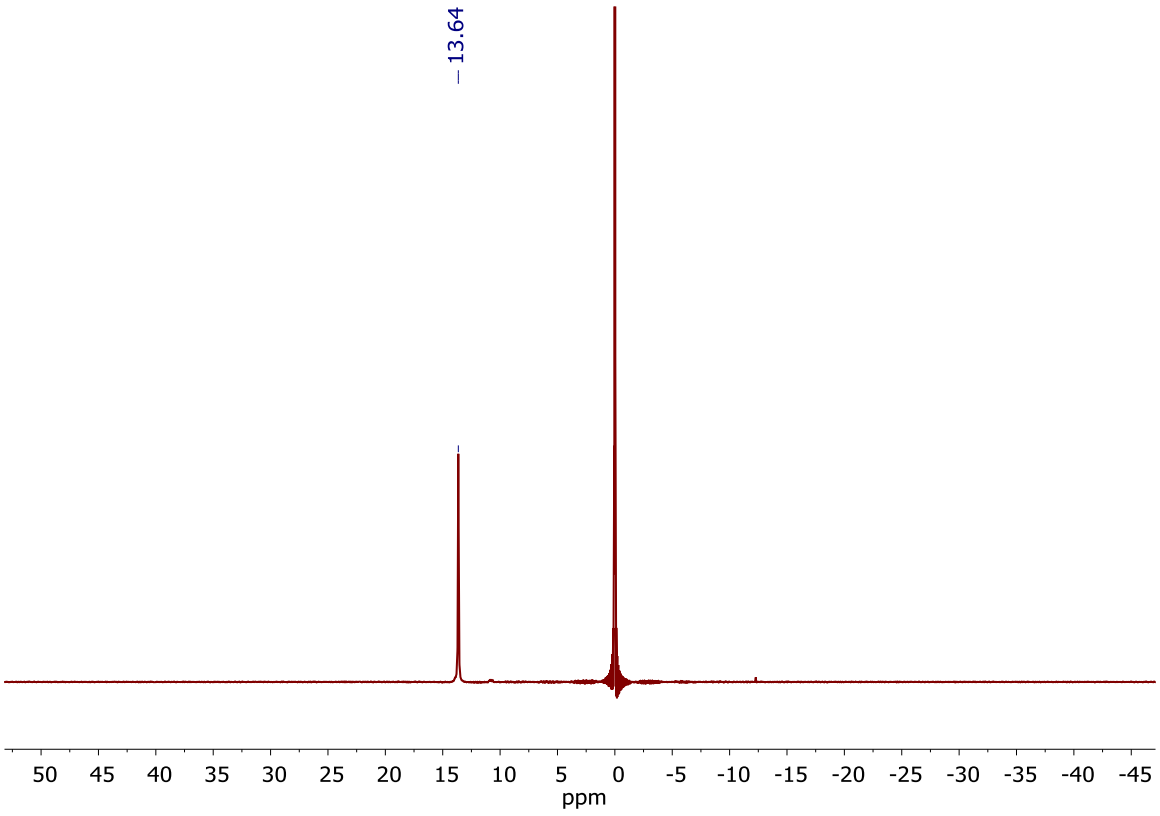

Figure S10: ^{31}P NMR (162 MHz, $CDCl_3$, 298 K, 85% H_3PO_4) of *bis*-tetrabutylammonium 3-butenyl pyrophosphonate **1**.

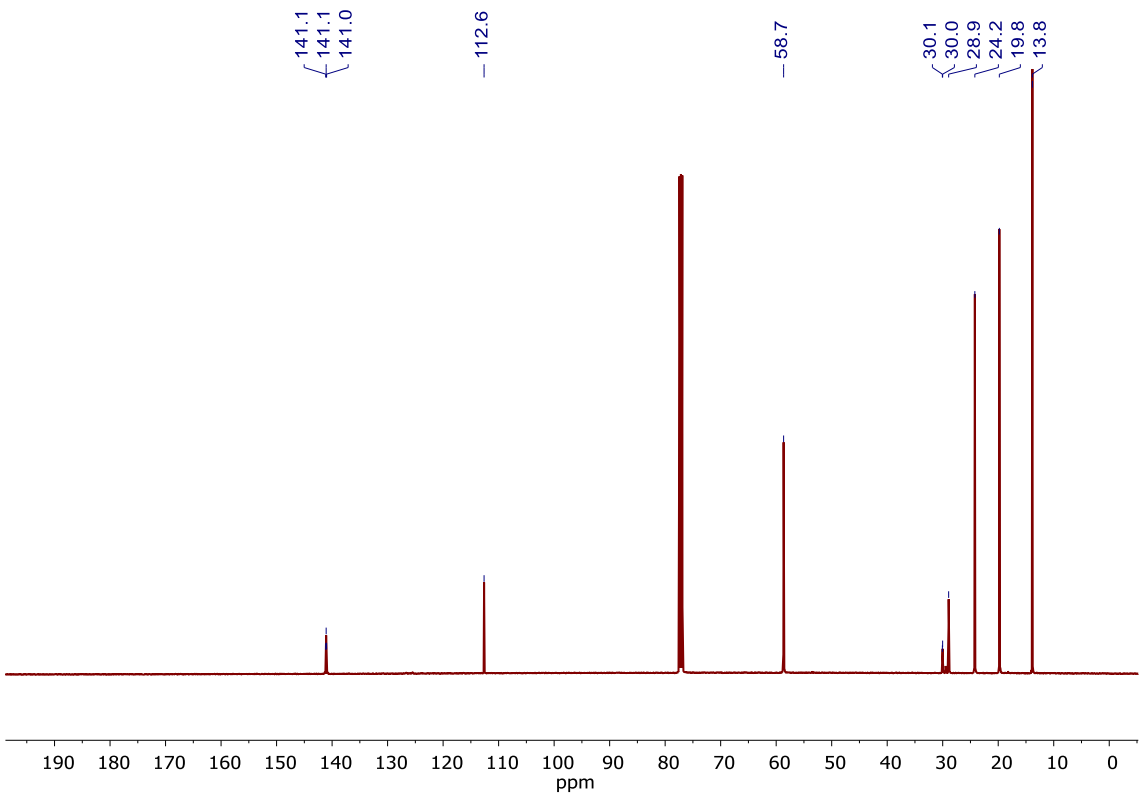

Figure S11: ^{13}C NMR (101 MHz, $CDCl_3$, 298 K) of *bis*-tetrabutylammonium 3-butenyl pyrophosphonate **1**.

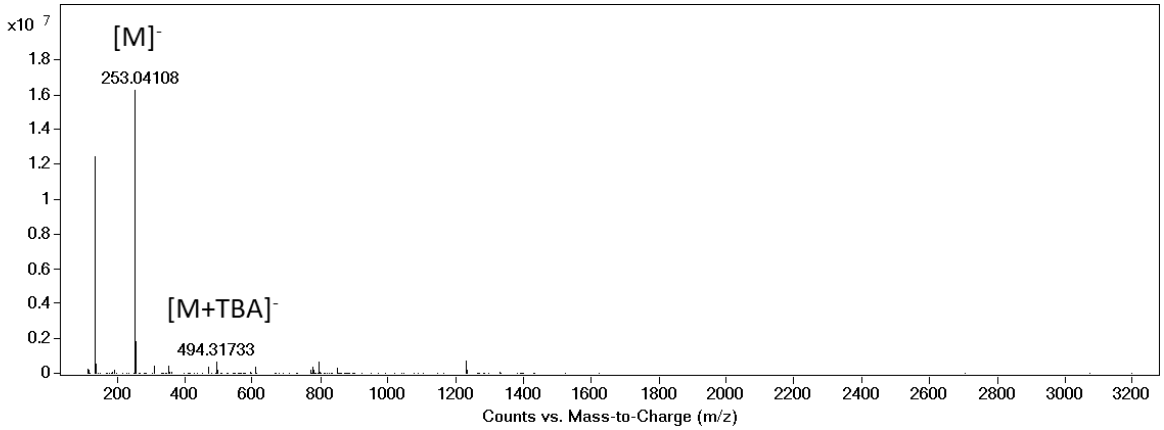

Figure S12: HRMS (ESI, negative mode) of *bis*-tetrabutylammonium 3-butenyl pyrophosphonate **1**.

Synthesis of tetrabutylammonium benzyl phosphonate S3

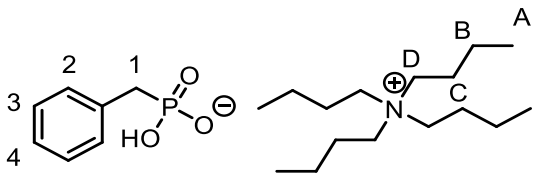

S3

200 mg (1.16 mmol) benzylphosphonic acid and 928 mg (1.16 mmol, 1.0 equiv.) TBAOH · 30 H_2O were combined in a round bottom flask and dissolved in 12 mL MeOH. The mixture was stirring for 1 h at room temperature, before the solvent was removed and the product was dried in vacuo to afford 483 mg (1.16 mmol, quant.) of the desired TBA salt as a colourless solid.

^{1}H-NMR (400 MHz, $CDCl_3$): δ [ppm] = 7.42-7.36 (m, 2 H, **3**), 7.16 (t, ^{3}J = 7.59 Hz, 2 H, **2**), 7.08-7.04 (dt, ^{3}J = 7.48 Hz, ^{4}J = 1.36 Hz, 1 H, **4**), 3.20-3.09 (m, 8 H, **D**), 2.93 (d, $^{2}J_{H\text{-}P}$ = 20.7 Hz, 2 H, **1**), 1.60-1.44 (m, 8 H, **C**), 1.42-1.30 (m, 8 H, **B**), 0.95 (t, ^{3}J = 7.35 Hz, 12 H, **A**).

^{13}C-NMR (101 MHz, $CDCl_3$): δ [ppm] = 138.4 (d), 130.3 (d), 127.6 (d), 124.7 (d), 58.8, 37.8 (d), 24.2, 19.8, 13.9.

^{31}P-NMR (162 MHz, $CDCl_3$, external standard: 85% H_3PO_4): δ [ppm] = 16.71.

HRMS(ESI (-)): m/z = 171.02168 (calc. 171.02165, δm/m = 0.18 ppm) $[M]^-$, 584.32771 (calc. 584.32754, δm/m = 0.34 ppm) $[2M+TBA]^-$.

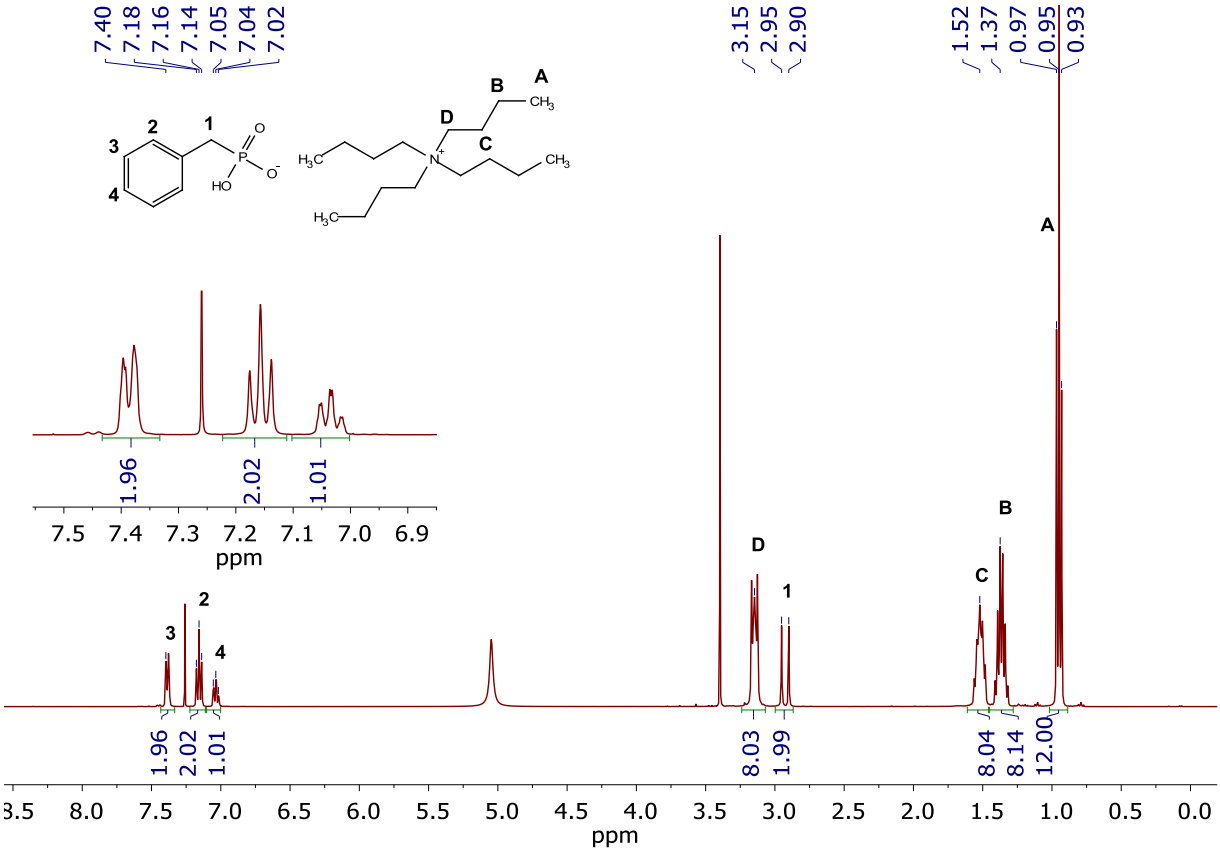

Figure S13: ^{1}H NMR (400 MHz, $CDCl_3$, 298 K) of tetrabutylammonium benzyl phosphonate **S3**.

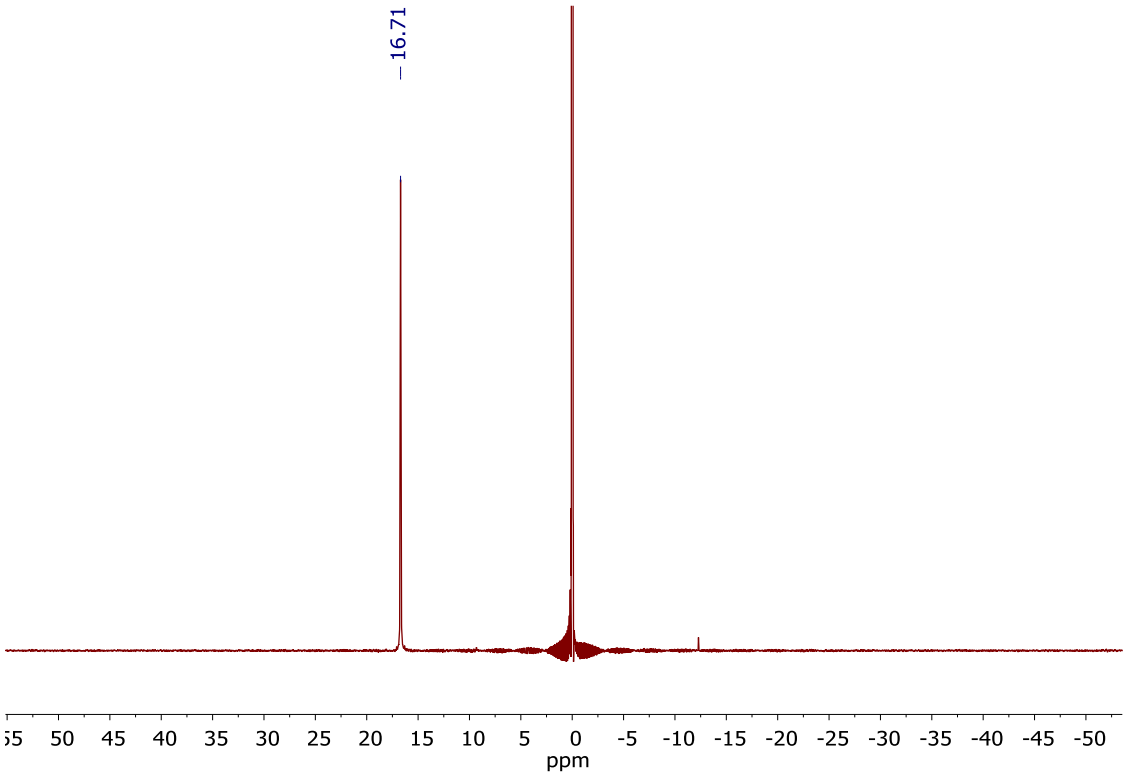

Figure S14: ^{31}P NMR (162 MHz, $CDCl_3$, 298 K, 85% H_3PO_4) of tetrabutylammonium benzyl phosphonate **S3**. Peak at -12.6 ppm, belongs to an impurity in the internal standard.

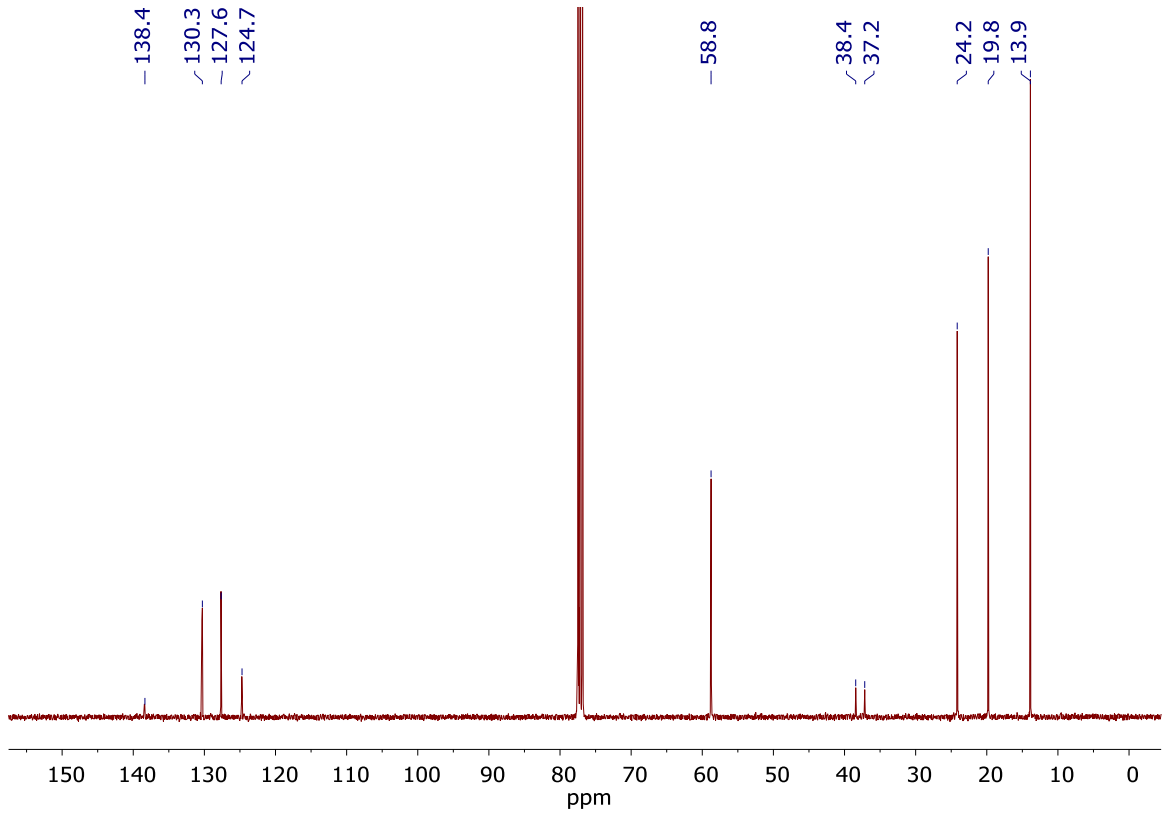

Figure S15: ^{13}C NMR (101 MHz, $CDCl_3$, 298 K) of tetrabutylammonium benzyl phosphonate **S3**.

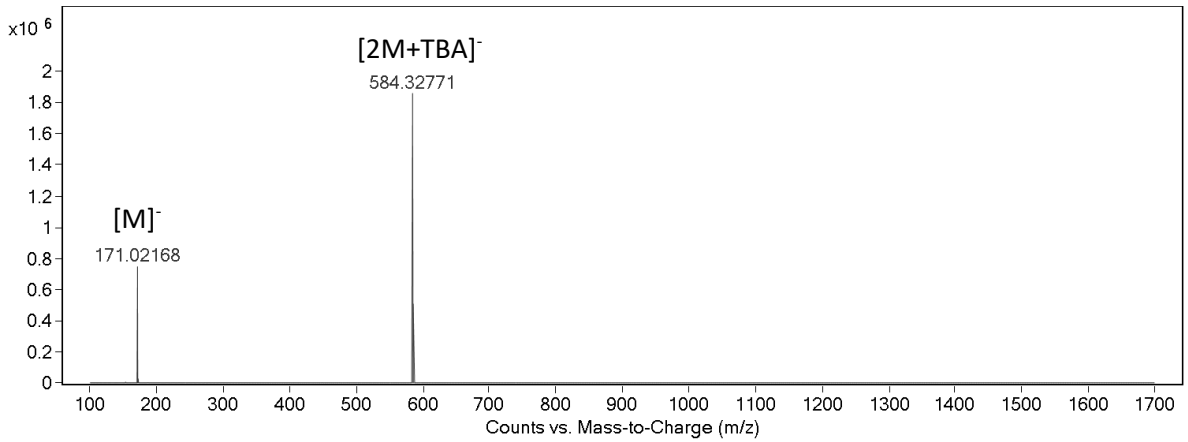

Figure S16: HRMS (ESI, negative mode) of tetrabutylammonium benzyl phosphonate **S3**.

Synthesis of *bis*-tetrabutylammonium benzyl pyrophosphonate (benzyl-PP) 2

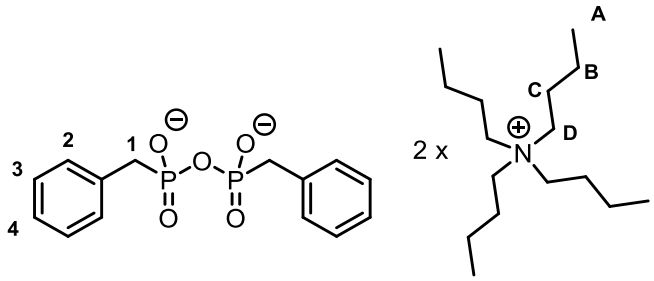

2

150 mg (0.35 mmol) benzyl phosphonate **S3** were dissolved in 15 mL DCM and 558 µL (3.50 mmol, 10 equiv.) *N,N'*-diisopropylcarbodiimide (DIC) were added. The mixture was stirred at room temperature for 48 h. DCM was evaporated and the residue was dissolved in 4 mL H_2O / MeCN (1:1) mixture and MPLC on an Interchim PF-15C18HP-F0025 C18 column with a mobile phase of MeCN and water (20-30% MeCN) and subsequent lyophilization yielded 40 mg (0.05 mmol, 29%) of the dimer as a colourless oil.

^{1}H-NMR (400 MHz, DMSO-d_6): δ [ppm] = 7.32-7.28 (m, 4 H, **3**), 7.11 (t, ^{3}J = 7.63 Hz, 4 H, **2**), 7.04-6.98 (m, 2 H, **4**), 3.22-3.12 (m, 16 H, **D**), 2.93-2.85 (m, 4 H, **1**), 1.63-1.52 (m, 16 H, **C**), 1.35-1.26 (m, 16 H, **B**), 0.93 (t, ^{3}J = 7.41 Hz, 24 H, **A**).

^{13}C-NMR (101 MHz, DMSO-d_6): δ [ppm] = 139.8 (t), 130.0 (t), 127.0, 123.8, 57.5, 37.6 (d), 23.1, 19.2, 13.5.

^{31}P-NMR (162 MHz, DMSO-d_6, external standard: 85% H_3PO_4): δ [ppm] = 6.84.

HRMS(ESI (-)): m/z = 325.04006 (calc. 325.04002, δm/m = 0.12 ppm) $[M]^-$, 566.31640 (calc. 566.31697, δm/m = 1.01 ppm) $[2M+TBA]^-$.

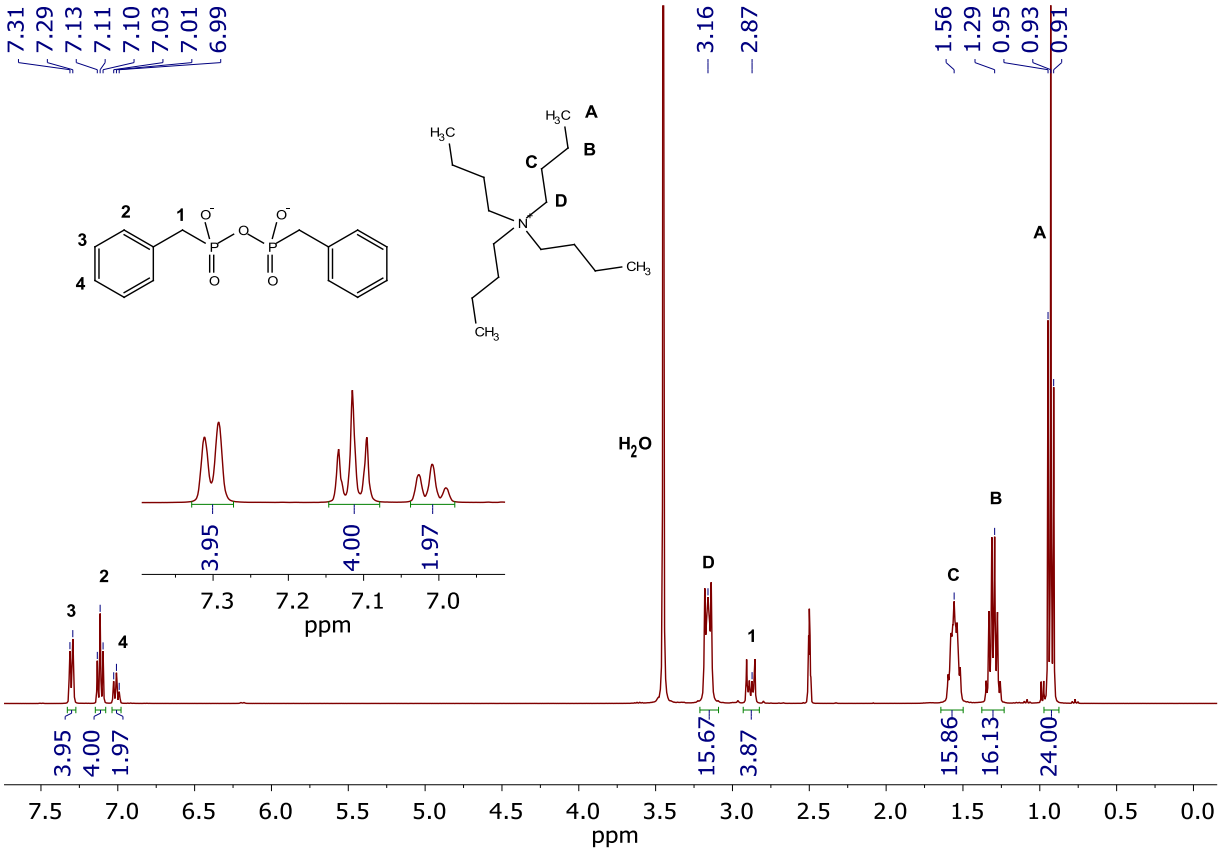

Figure S17: ^{1}H NMR (400 MHz, DMSO-d$_6$, 298 K) of *bis*-tetrabutylammonium benzyl pyrophosphonate **2**.

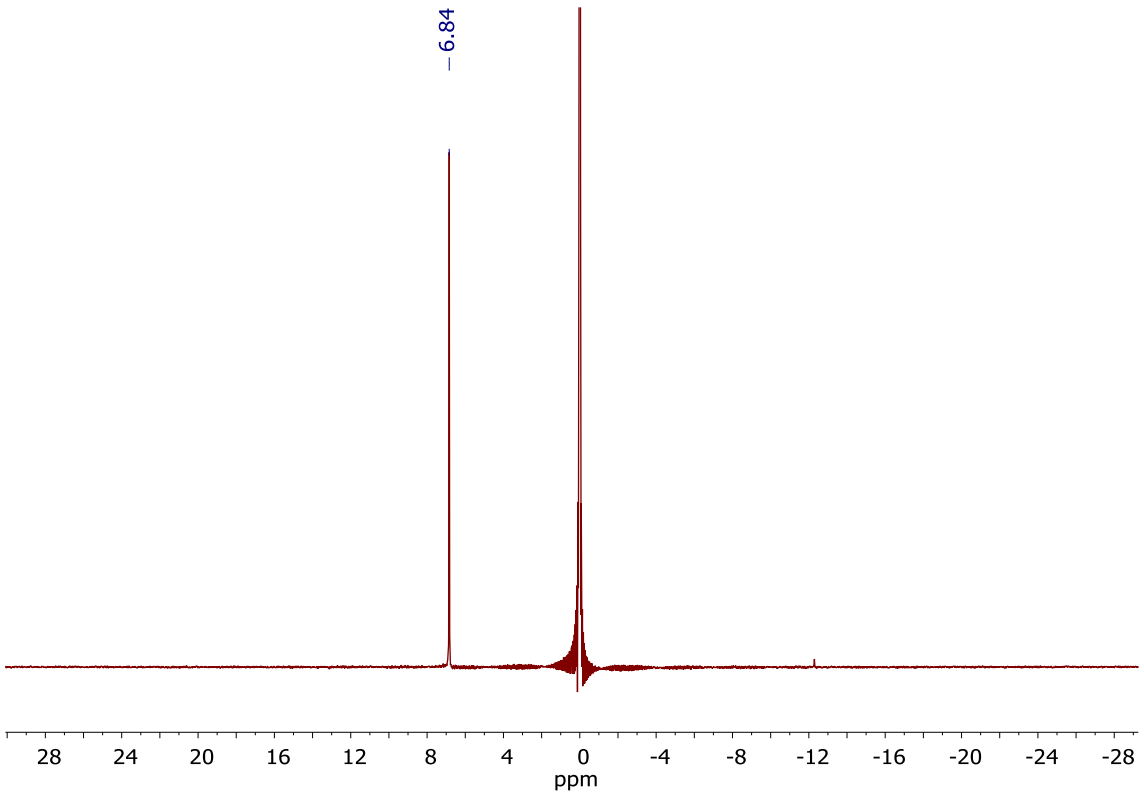

Figure S18: ^{31}P NMR (162 MHz, DMSO-d$_6$, 298 K, 85% H_3PO_4) of *bis*-tetrabutylammonium benzyl pyrophosphonate **2**. Peak at -12.6 ppm, belongs to an impurity in the internal standard.

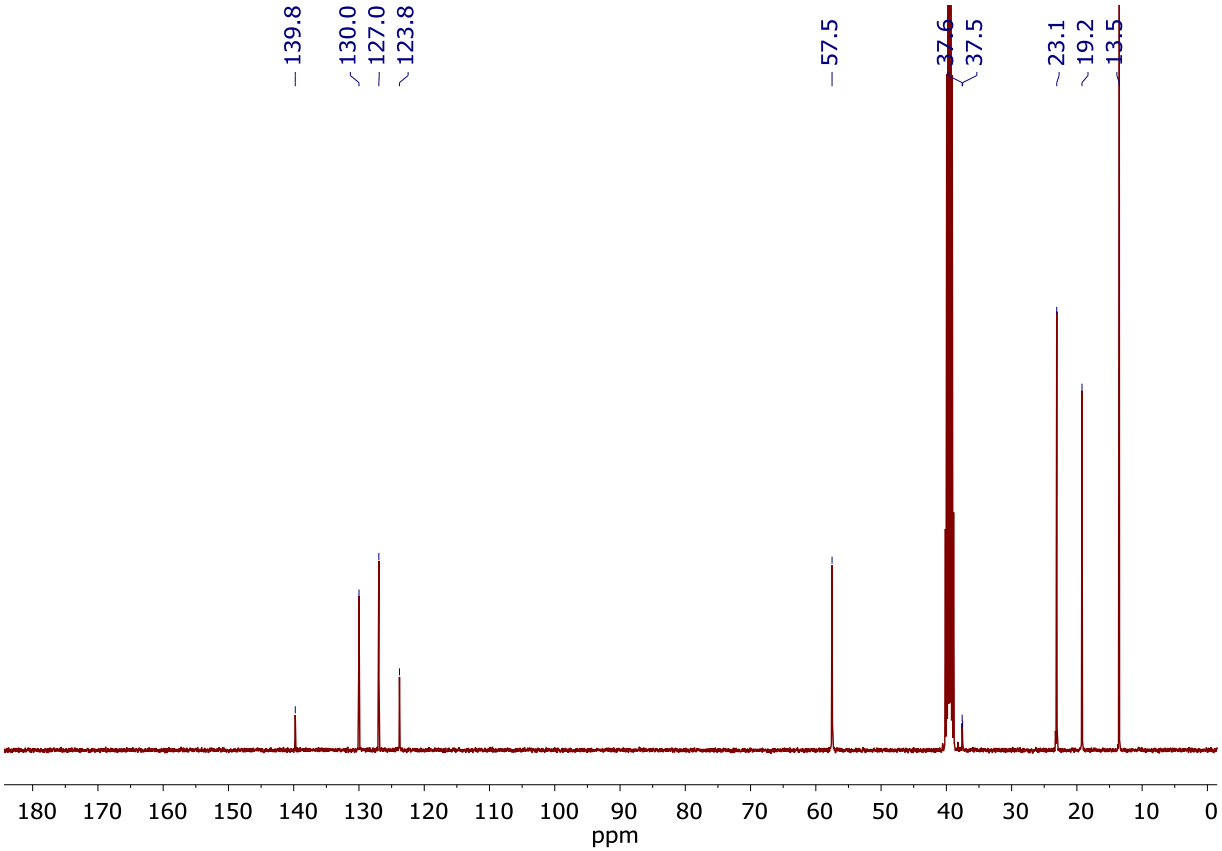

Figure S19: ^{13}C NMR (101 MHz, DMSO-d_6, 298 K) of *bis*-tetrabutylammonium benzyl pyrophosphonate **2**.

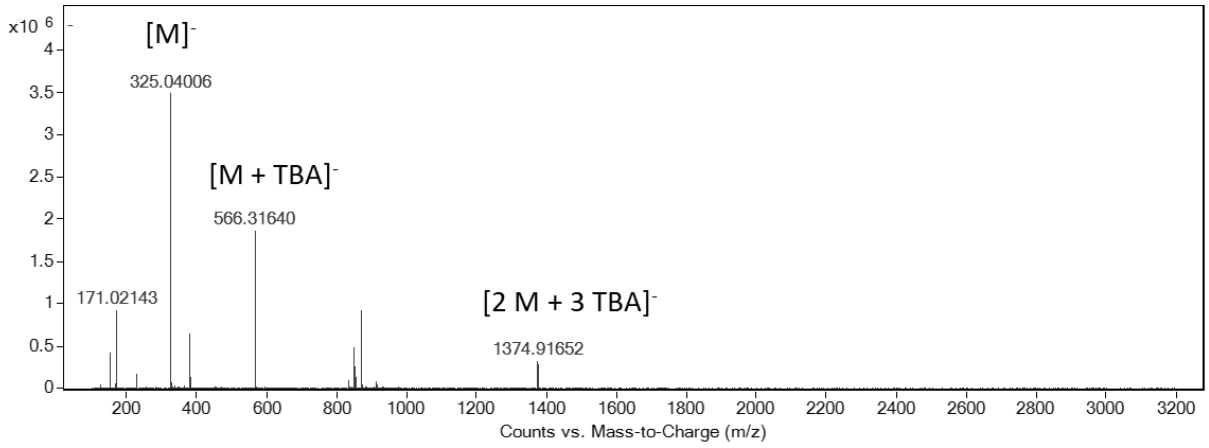

Figure S20: HRMS (ESI, negative mode) of *bis*-tetrabutylammonium benzyl pyrophosphonate **2**.

Synthesis of 2-fluorobenzylphosphonic acid S4

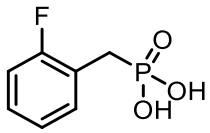

S4

450 mg (1.83 mmol) diethyl 2-fluorobenzylphosphonate were dissolved in 20 mL anhydrous DCM and 1.70 mL (12.8 mmol, 7 equiv.) trimethylsilylbromide were added. The mixture was stirred for 2 h at room temperature under inert atmosphere. DCM was evaporated and the residue was stirred for 1 h in anhydrous MeOH before the solvent was removed. MPLC on an Interchim PF-15C18HP-F0025 C18 column with a mobile phase of MeCN and 25 mM formic acid (5-35% MeCN) and subsequent lyophilization yielded 260 mg (1.36 mmol, 75%) of the desired product as a colourless solid.

^{1}H-NMR (400 MHz, DMSO-d_6): δ [ppm] = 7.35 (m, 1 H, **Ar**), 7.23 (m, 1 H, **Ar**), 7.12 (m, 2 H, **Ar**), 2.96 (d, $^{2}J_{H\text{-}P}$ = 21.2 Hz, 2 H, **CH_2**).

^{13}C-NMR (101 MHz, DMSO-d_6): δ [ppm] = 161.7 – 159.2 (dd), 132.1 (t), 128.1 (dd), 124.0 (t), 121.4 (dd), 115.0 (dd), 28.8 – 27.5 (dd).

^{31}P-NMR (162 MHz, DMSO-d_6, external standard: 85% H_3PO_4): δ [ppm] = 20.95.

^{19}F-NMR (367 MHz, DMSO-d_6): δ [ppm] = -117.3.

HRMS(ESI (-)): m/z = 189.01210 (calc. 189.01223, δm/m = 0.69 ppm) $[M\text{-}H]^-$

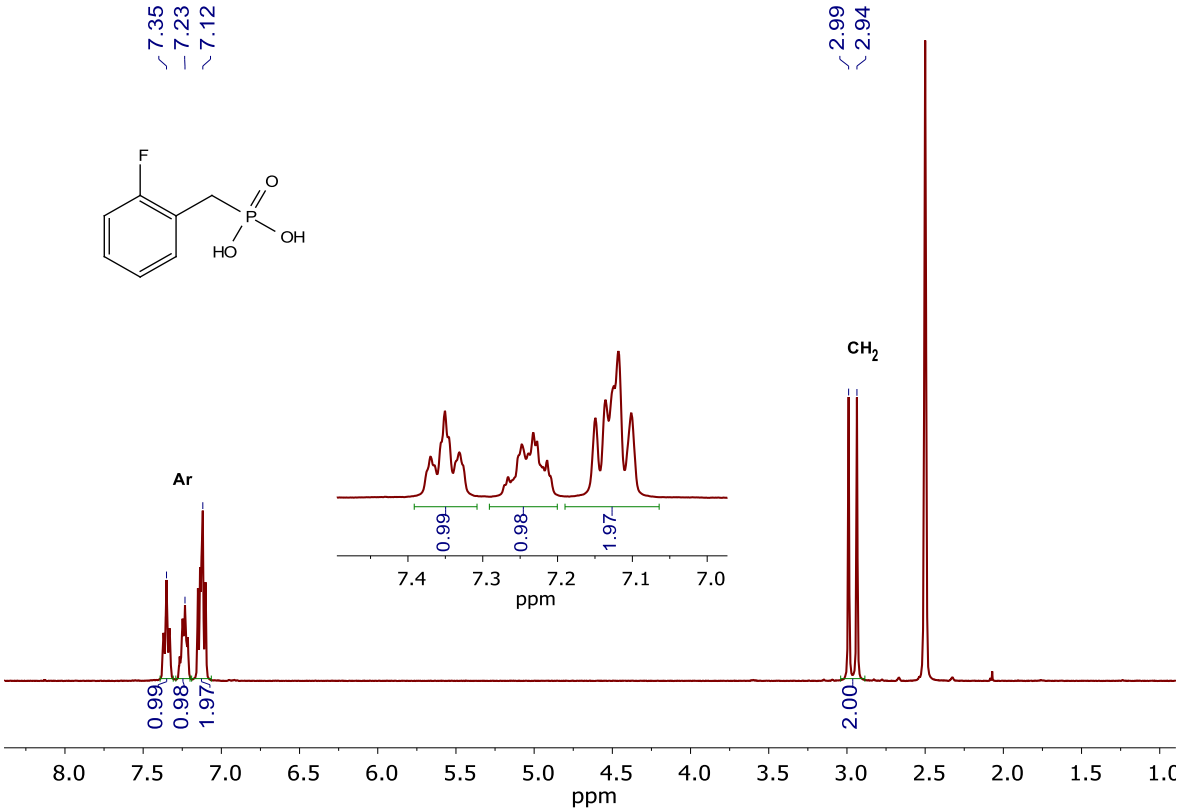

Figure S21: ^{1}H NMR (400 MHz, DMSO-d_6, 298 K) of 2-fluorobenzylphosphonic acid **S4**.

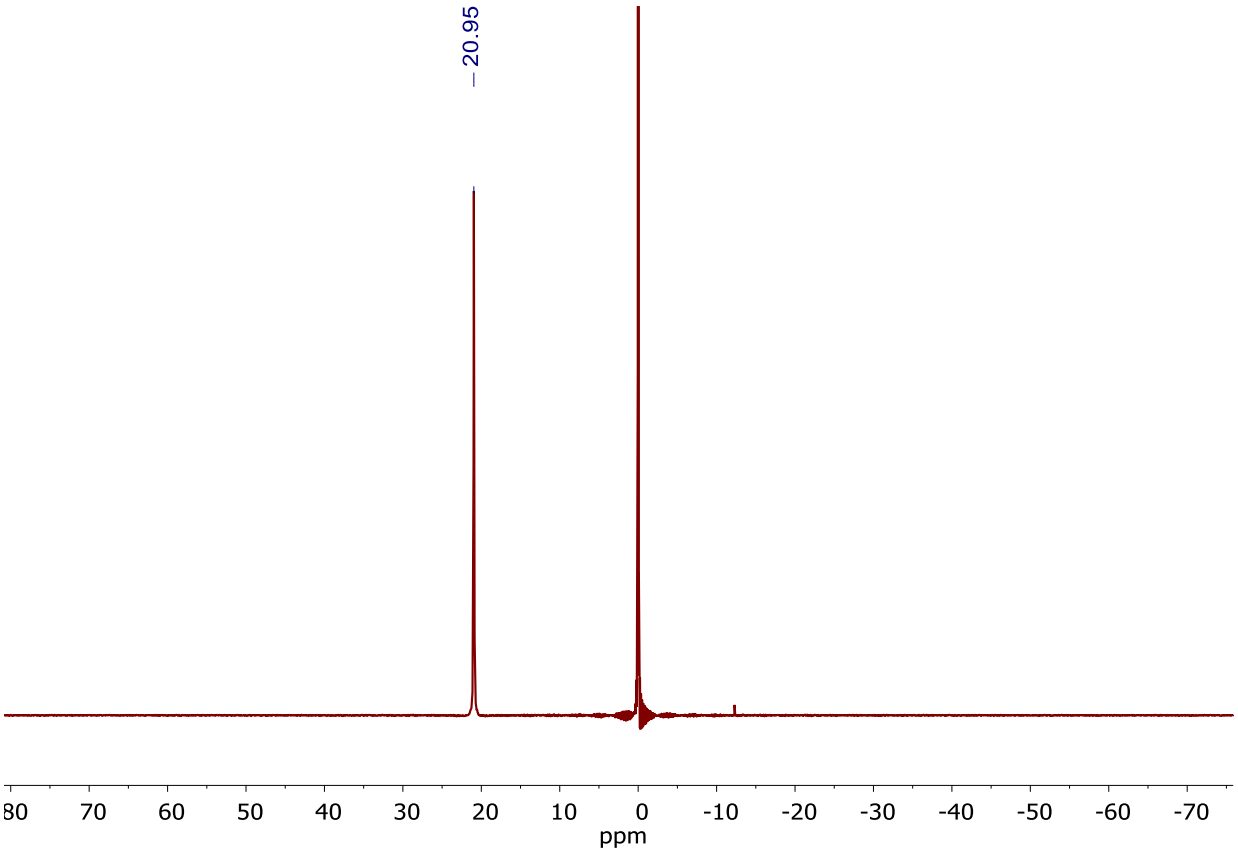

Figure S22: ^{31}P NMR (162 MHz, DMSO-d_6, 298 K, 85% H_3PO_4) of 2-fluorobenzylphosphonic acid **S4**. Peak at -12.6 ppm, belongs to an impurity in the internal standard.

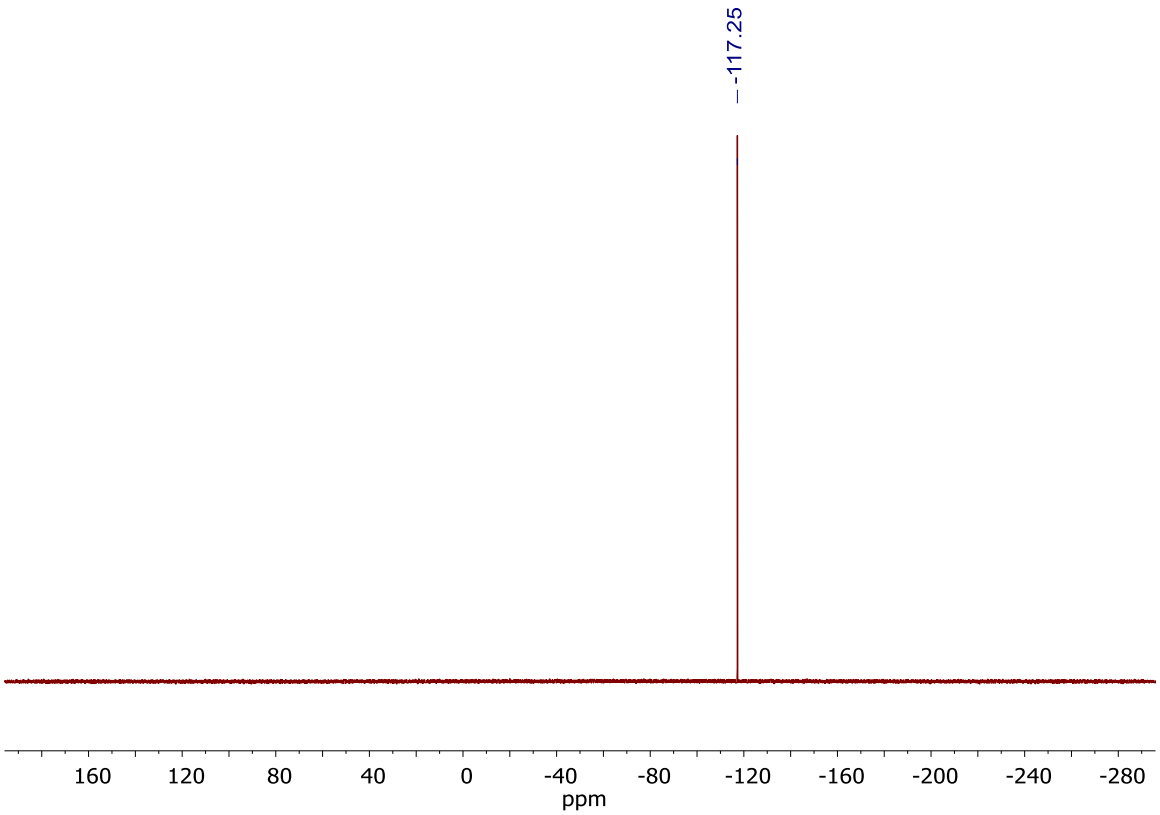

Figure S23: ^{19}F NMR (367 MHz, DMSO-d_6, 298 K) of 2-fluorobenzylphosphonic acid **S4**.

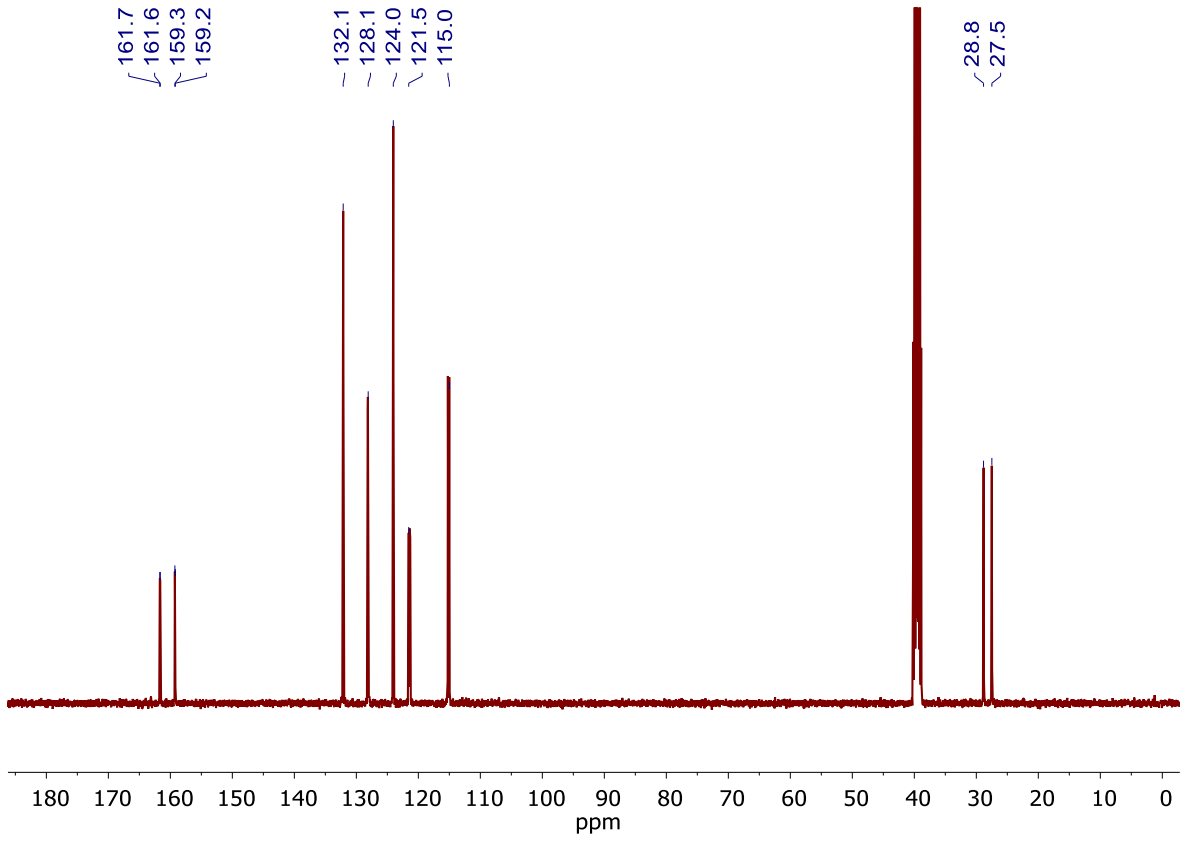

Figure S24: ^{13}C NMR (101 MHz, DMSO-d_6, 298 K) of 2-fluorobenzylphosphonic acid **S4**.

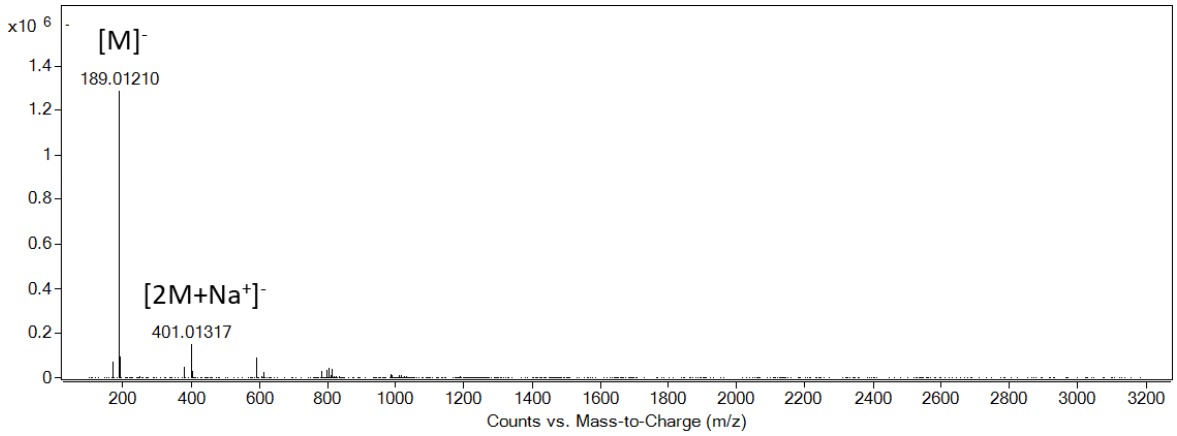

Figure S25: HRMS (ESI, negative mode) of 2-fluorobenzylphosphonic acid **S4**.

Synthesis of tetrabutylammonium 2-fluorobenzyl phosphonate S5

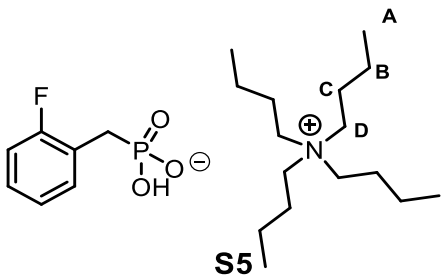

S5

120 mg (0.63 mmol) 2-fluorobenzylphosphonic acid **S4** and 505 mg (0.63 mmol, 1.0 equiv.) TBAOH · 30 H_2O were combined in a round bottom flask and dissolved in 8 mL MeOH. The mixture was stirring for 1 h at room temperature, before the solvent was removed and the product was dried in vacuo to afford 265 mg (0.62 mmol, quant.) of the desired TBA salt as a colourless solid.

^{1}H-NMR (400 MHz, $CDCl_3$): δ [ppm] = 7.70 (m, 1 H, **Ar**), 6.96 (m, 2 H, **Ar**), 6.86 (m, 1 H, **Ar**), 3.26 – 3.22 (m, 8 H, **D**), 2.93 (d, $^{2}J_{H\text{-}P}$ = 20.3 Hz, 2 H, **CH_2**), 1.56 (m, 8 H, **C**), 1.43 – 1.34 (m, 8 H, **B**), 0.95 (t, ^{3}J = 7.24 Hz, 12 H, **A**).

^{13}C-NMR (101 MHz, $CDCl_3$): δ [ppm] = 162.4 (d), 160.0 (d) 133.0 (t), 125.9 (d), 123.3 (t), 114.4 (d), 58.8, 29.8 (d), 24.2, 19.8, 13.9.

^{31}P-NMR (162 MHz, $CDCl_3$, external standard: 85% H_3PO_4): δ [ppm] = 15.98.

^{19}F-NMR (367 MHz, $CDCl_3$): δ [ppm] = -117.6.

HRMS(ESI (-)): m/z = 189.01262 (calc. 189.01223, δm/m = 2.06 ppm) $[M\text{-}H]^-$, 620.30897 (calc. 620.30869, δm/m = 0.45 ppm) $[2M+TBA]^-$.

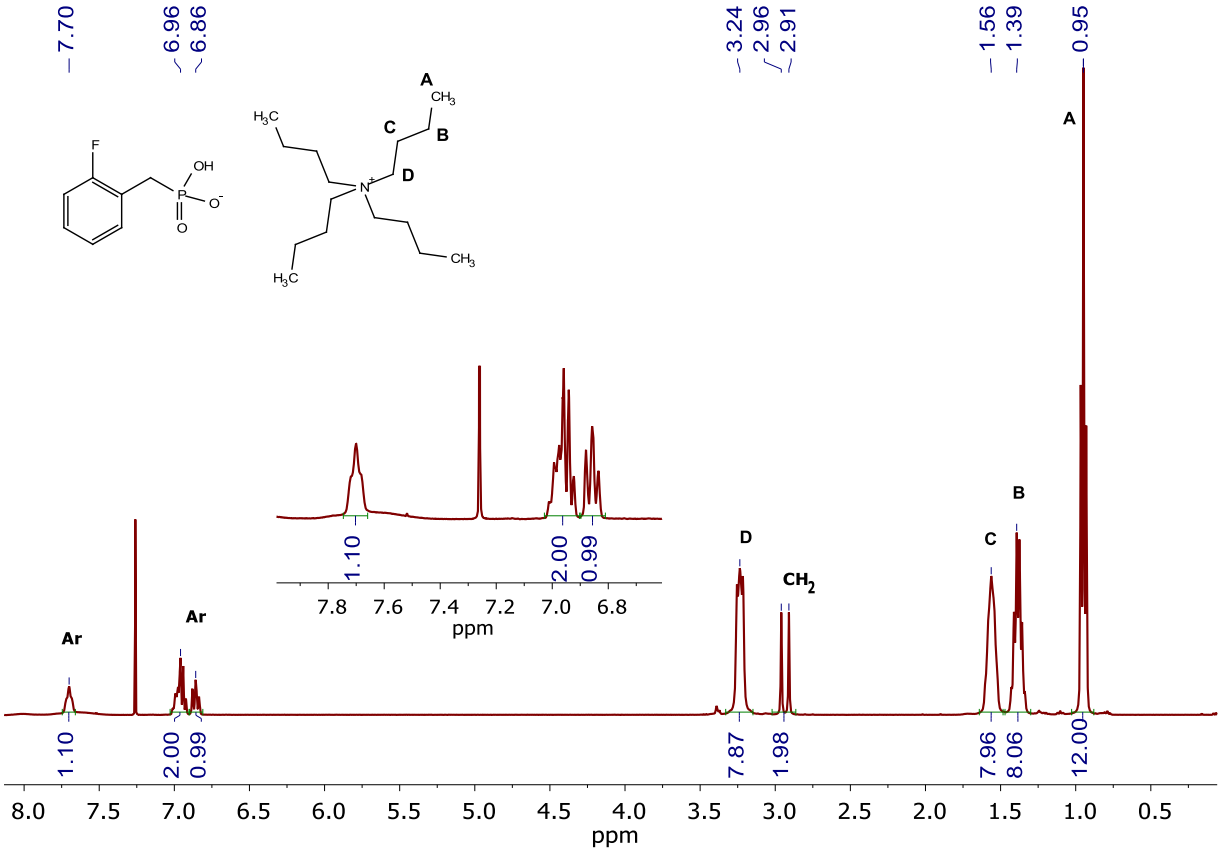

Figure S26: ^{1}H NMR (400 MHz, $CDCl_3$, 298 K) of tetrabutylammonium 2-fluorobenzyl phosphonate **S5**.

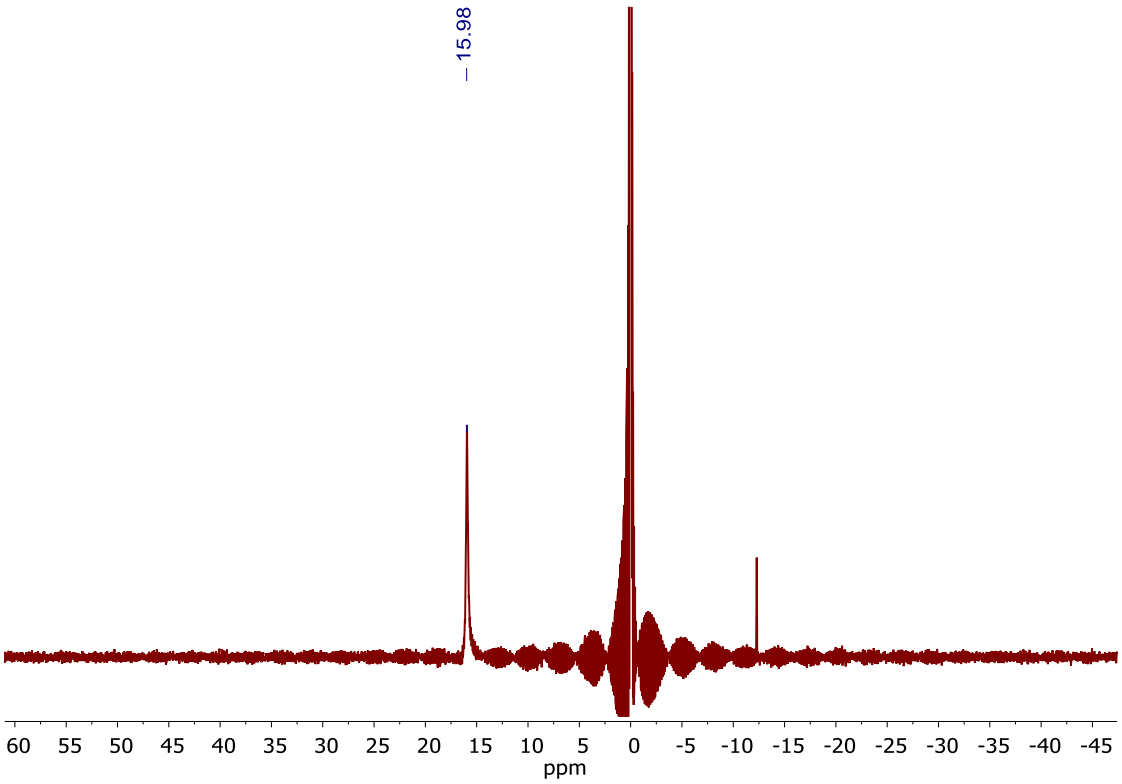

Figure S27: ^{31}P NMR (162 MHz, $CDCl_3$, 298 K, 85% H_3PO_4) of tetrabutylammonium 2-fluorobenzyl phosphonate **S5**. Peak at -12.6 ppm, belongs to an impurity in the internal standard.

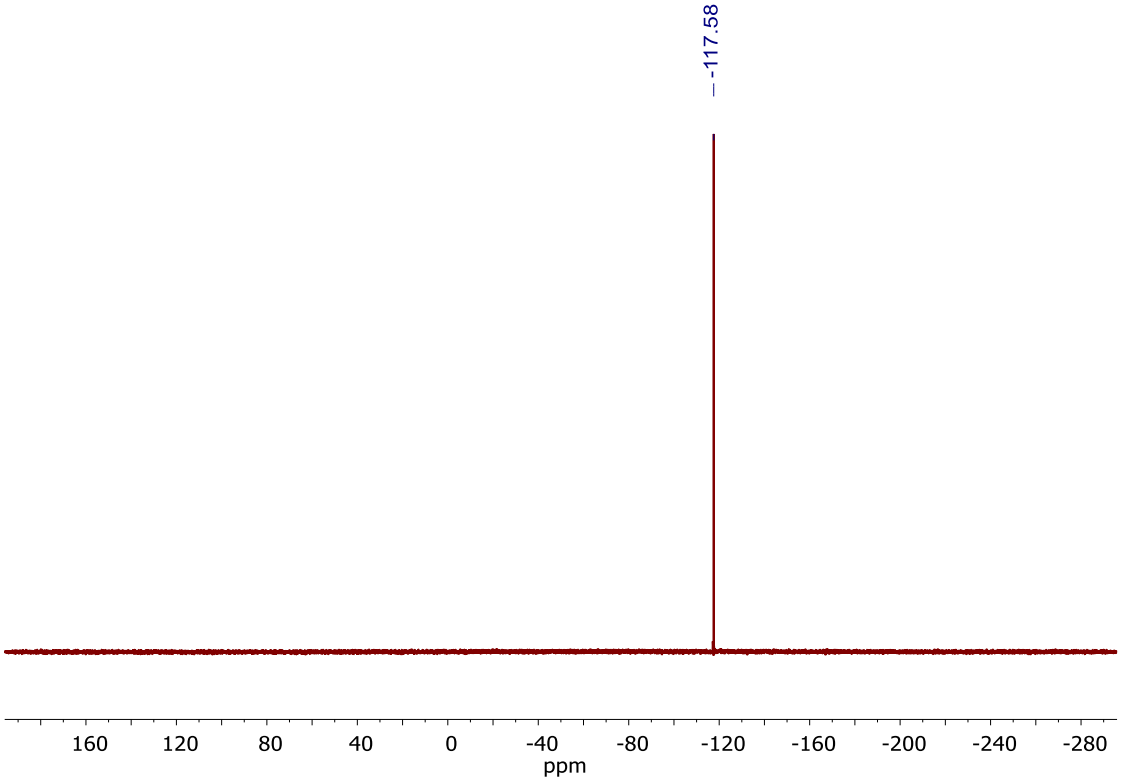

Figure S28: ^{19}F NMR (367 MHz, $CDCl_3$, 298 K) of tetrabutylammonium 2-fluorobenzyl phosphonate **S5**.

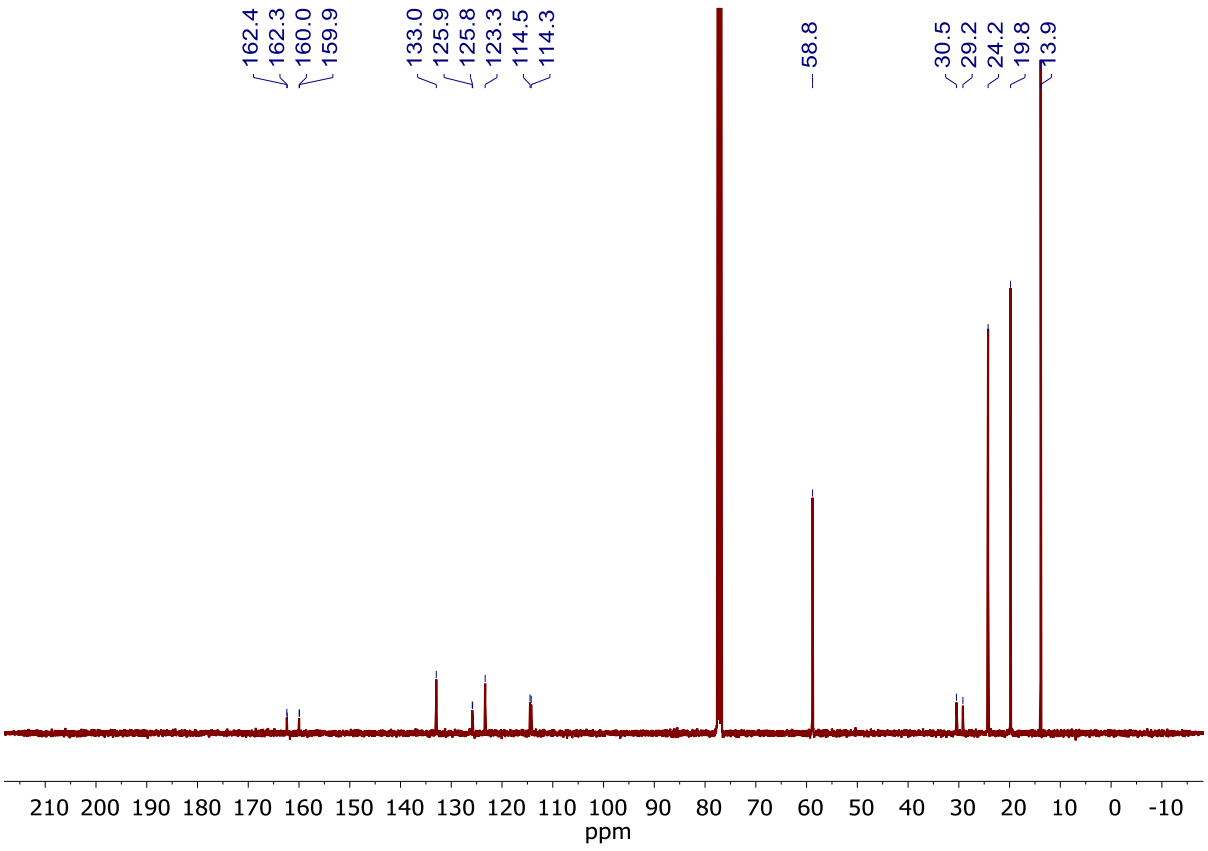

Figure S29: ^{13}C NMR (101 MHz, $CDCl_3$, 298 K) of tetrabutylammonium 2-fluorobenzyl phosphonate **S5**.

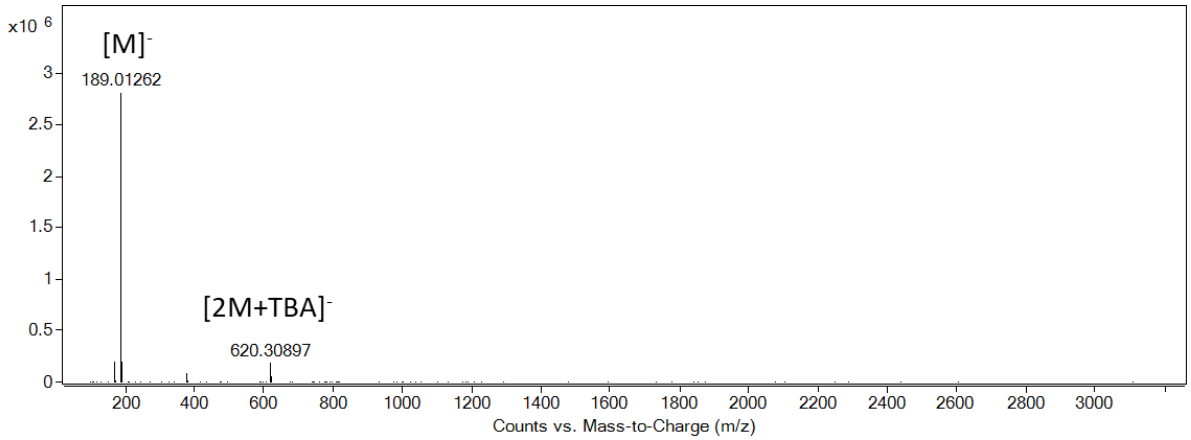

Figure S30: HRMS (ESI, negative mode) of tetrabutylammonium 2-fluorobenzyl phosphonate **S5**.

Synthesis of *bis*-tetrabutylammonium 2-fluorobenzyl pyrophosphonate (F-benzyl-PP) 3

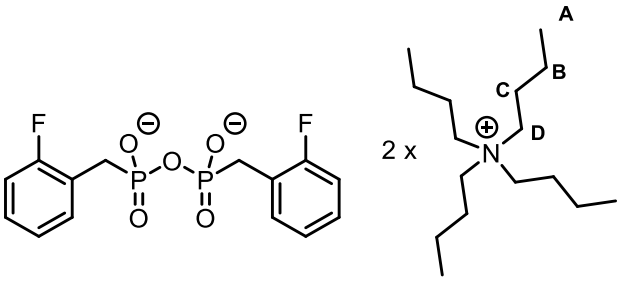

3

130 mg (0.30 mmol) tetrabutylammonium 2-fluorobenzyl phosphonate **S5** were dissolved in15 mL DCM and 560 µL (3.00 mmol, 10 equiv.) *N,N'*-diisopropylcarbodiimide (DIC) were added. The mixture was stirred at room temperature for 48 h. DCM was evaporated and the residue was dissolved in 4 mL of a H_2O / MeCN (3:1) mixture. MPLC on an Interchim PF-15C18HP-F0025 C18 column with a mobile phase of MeCN and water (20-30% MeCN) and subsequent lyophilization yielded 46 mg (0.054 mmol, 36%) of the dimer as a colourless oil.

^{1}H-NMR (400 MHz, DMSO-d_6): δ [ppm] = 7.74 (m, 2 H, **Ar**), 7.08-7.03 (m, 2 H, **Ar**), 6.97-6.93 (m, 4 H, **Ar**), 3.19-3.15 (m, 16 H, **D**), 2.97-2.92 (m, 4 H, **CH_2**), 1.60-1.52 (m, 16 H, **C**), 1.35-1.26 (m, 16 H, **B**), 0.93 (t, ^{3}J = 7.34 Hz, 24 H, **A**).

^{13}C-NMR (101 MHz, DMSO-d_6): δ [ppm] = 161.7 - 159.2 (dt), 132.6 (d), 126.7 (d), 125.5 (d), 122.9 (d), 113.9 (d), 57.5, 30.2 – 28.8 (dd), 23.1, 19.2, 13.5.

^{31}P-NMR (162 MHz, DMSO-d_6, external standard: 85% H_3PO_4): δ [ppm] = 5.56.

^{19}F-NMR (367 MHz, **$CDCl_3$):** δ [ppm] = -117.9

HRMS(ESI (-)): m/z = 361.02120 (calc. 361.02118, δm/m = 0.06 ppm) $[M]^-$, 602.29745 (calc. 602.29813, δm/m = 1.13 ppm) $[M+TBA]^-$

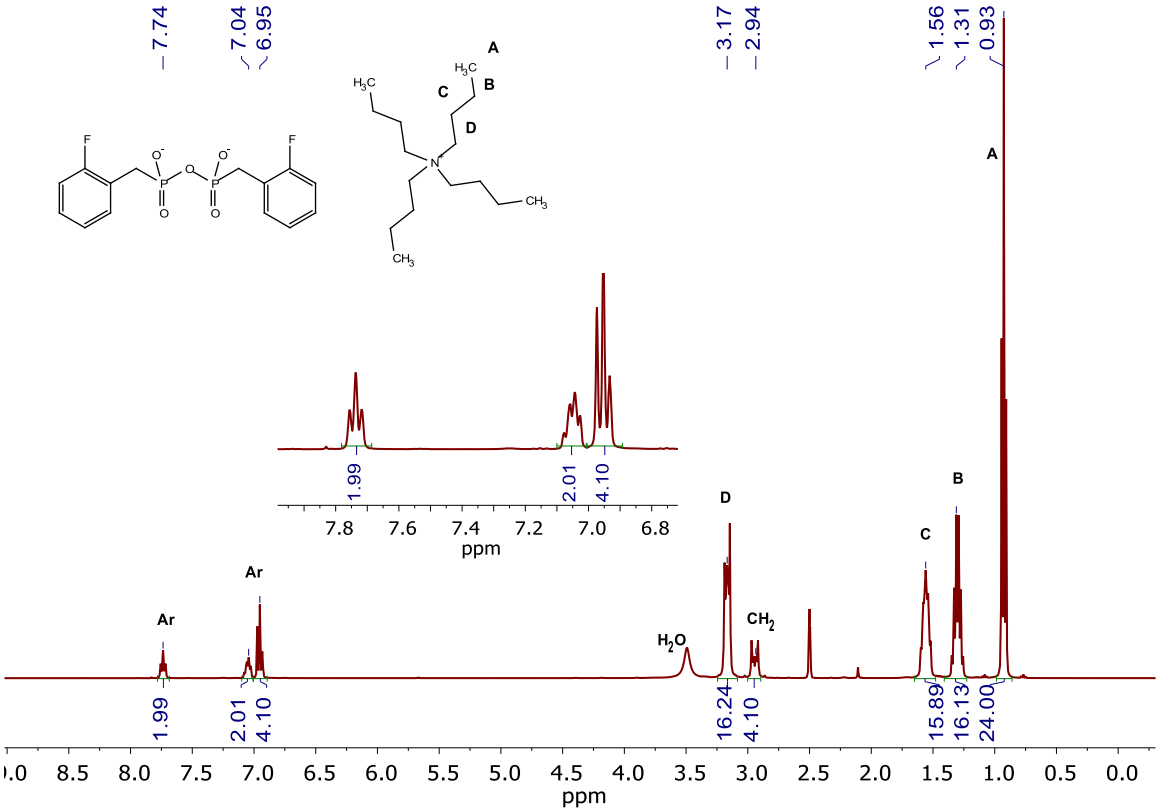

Figure S31: ^{1}H NMR (400 MHz, DMSO-d_6, 298 K) of *bis*-tetrabutylammonium 2-fluorobenzyl pyrophosphonate **3**.

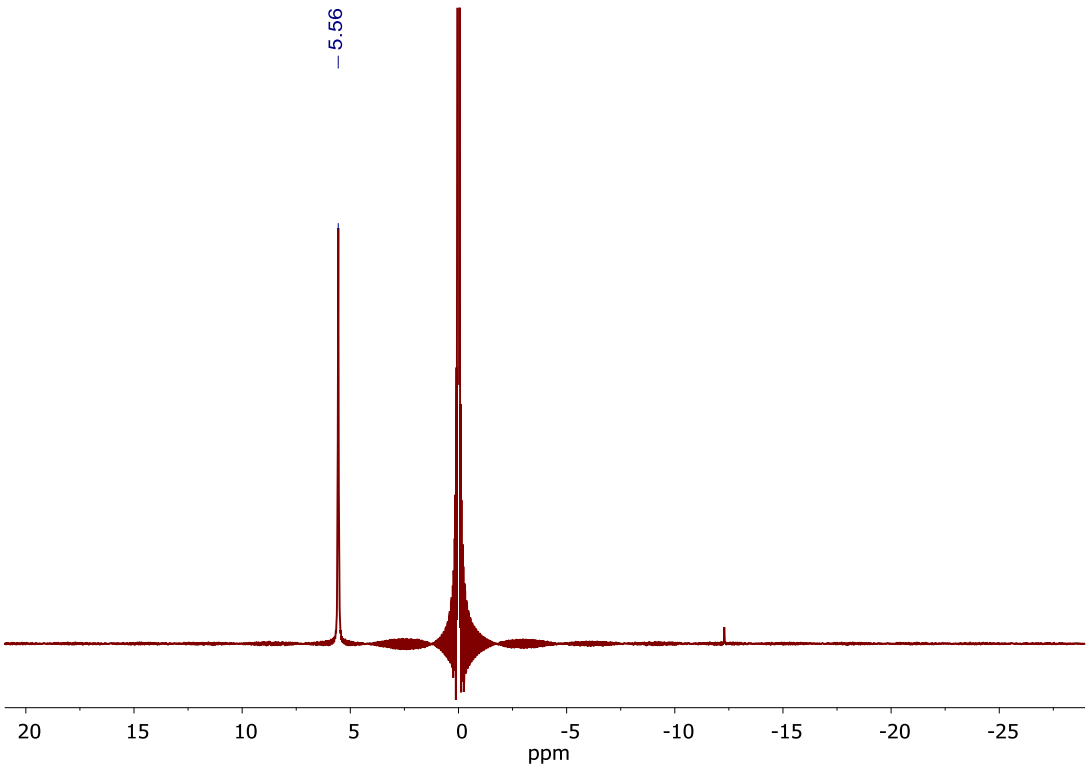

Figure S32: ^{31}P NMR (162 MHz, DMSO-d_6, 298 K, 85% H_3PO_4) of *bis*-tetrabutylammonium 2-fluorobenzyl pyrophosphonate **3**. Peak at -12.6 ppm, belongs to an impurity in the internal standard.

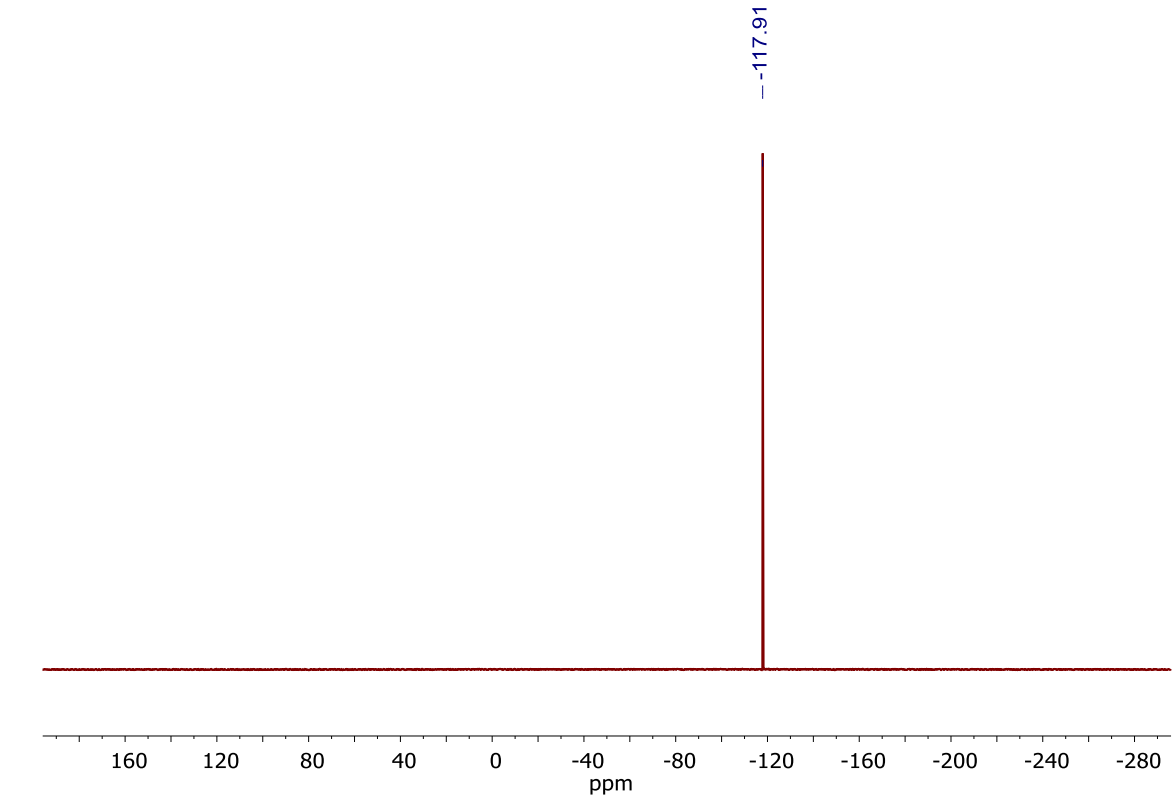

Figure S33: ^{19}F NMR (367 MHz, DMSO-d_6, 298 K) of *bis*-tetrabutylammonium 2-fluorobenzyl pyrophosphonate **3**.

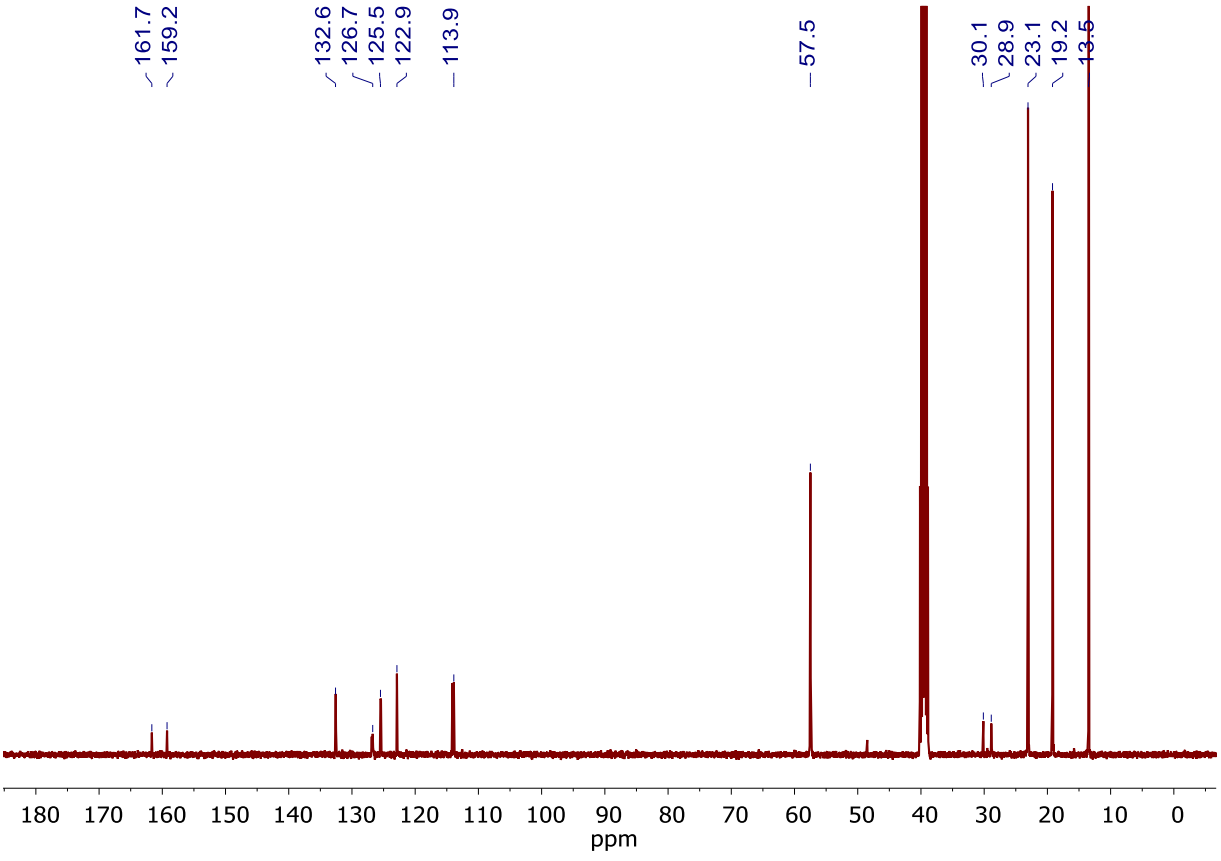

Figure S34: ^{13}C NMR (101 MHz, DMSO-d_6, 298 K) of *bis*-tetrabutylammonium 2-fluorobenzyl pyrophosphonate **3**.

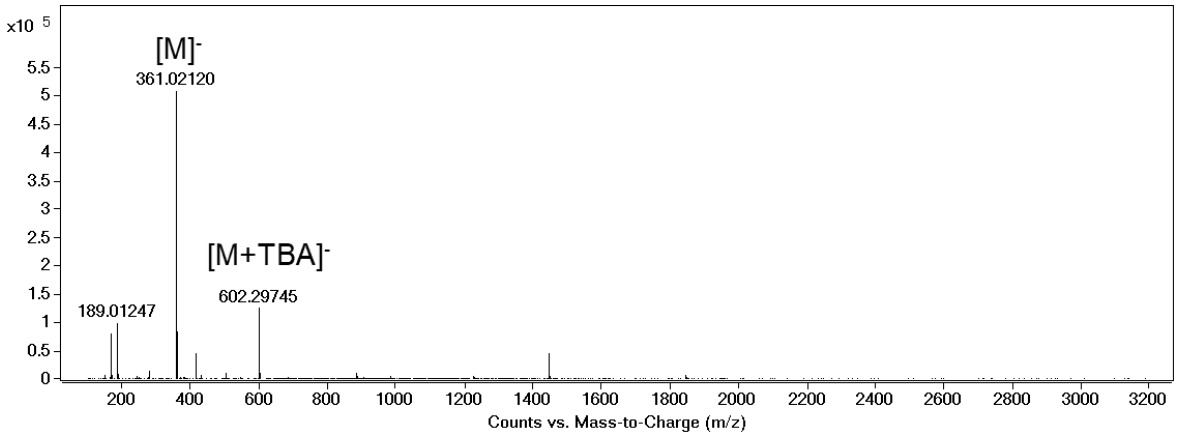

Figure S35: HRMS (ESI, negative mode) of *bis*-tetrabutylammonium 2-fluorobenzyl pyrophosphonate **3**.

Synthesis of 2-chlorobenzylphosphonic acid S6

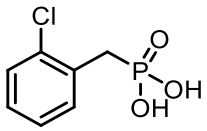

S6

431 µL (500 mg, 1.90 mmol) diethyl 2-chlorobenzylphosphonate were dissolved in 20 mL anhydrous DCM and 2.49 mL (19.0 mmol, 10 equiv.) trimethylsilylbromide were added. The mixture was stirred for 2 h at room temperature under inert atmosphere. DCM was evaporated and the residue was stirred for 1 h in anhydrous MeOH before the solvent was removed. MPLC on an Interchim PF-15C18HP-F0025 C18 column with a mobile phase of MeCN and 25 mM formic acid (5-35% MeCN) and subsequent lyophilization yielded 240 mg (1.16 mmol, 61%) of the desired product as a colourless solid.

^{1}H-NMR (400 MHz, DMSO-d_6): δ [ppm] = 7.42 (m, 2 H, **Ar**), 7.29 – 7.20 (m, 2 H, **Ar**), 3.14 (d, $^{2}J_{H\text{-}P}$ = 21.7 Hz, 2 H, **CH_2**).

^{13}C-NMR (101 MHz, DMSO-d_6): δ [ppm] = 133.4 – 132.3 (dd), 131.9 (d), 129.1 (d), 127.8 (d), 126.8 (d), 33.2 – 31.9 (d).

^{31}P NMR (162 MHz, DMSO-d_6, external standard: 85% H_3PO_4): δ [ppm] = 20.44.

HRMS(ESI (-)): m/z = 204.98322 (calc. 204.98268, δm/m = 3.12 ppm) $[M\text{-}H]^-$

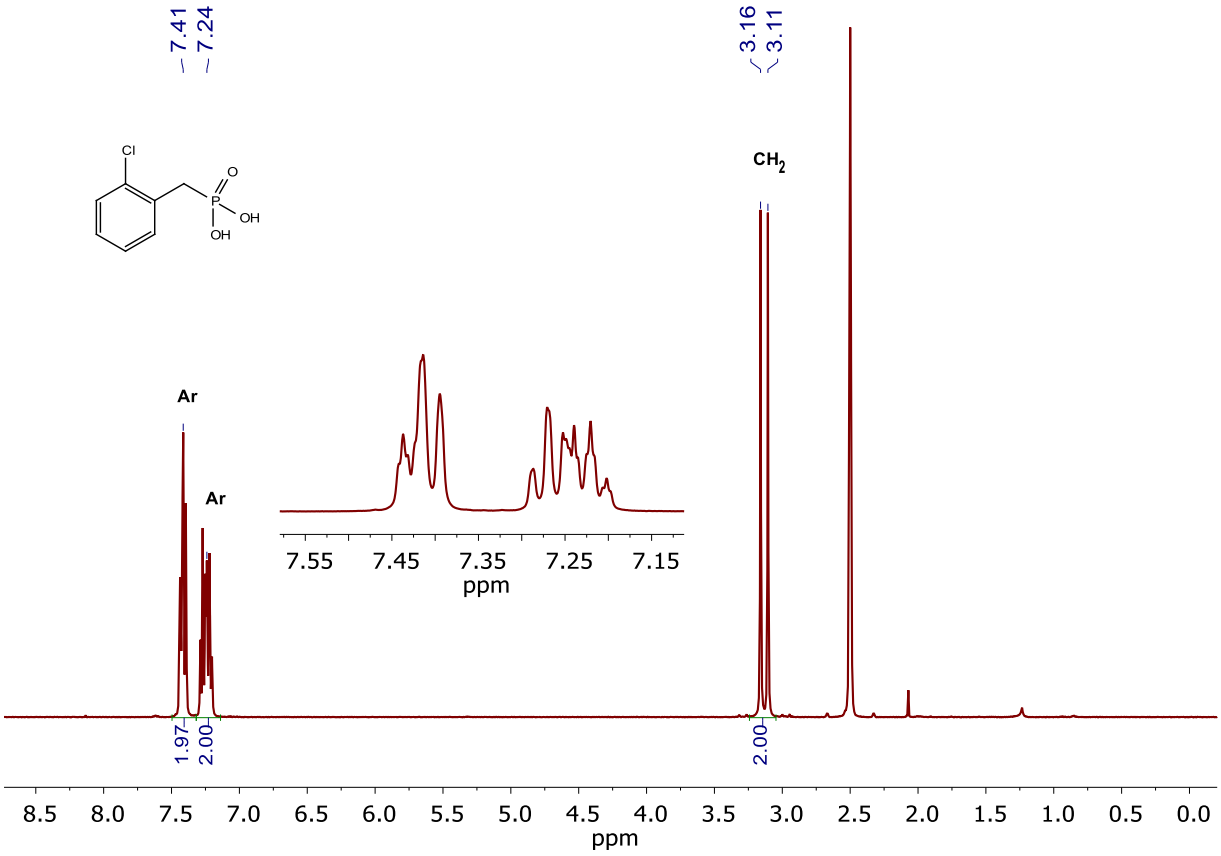

Figure S36: ^{1}H NMR (400 MHz, DMSO-d_6, 298 K) of 2-chlorobenzylphosphonic acid **S6**.

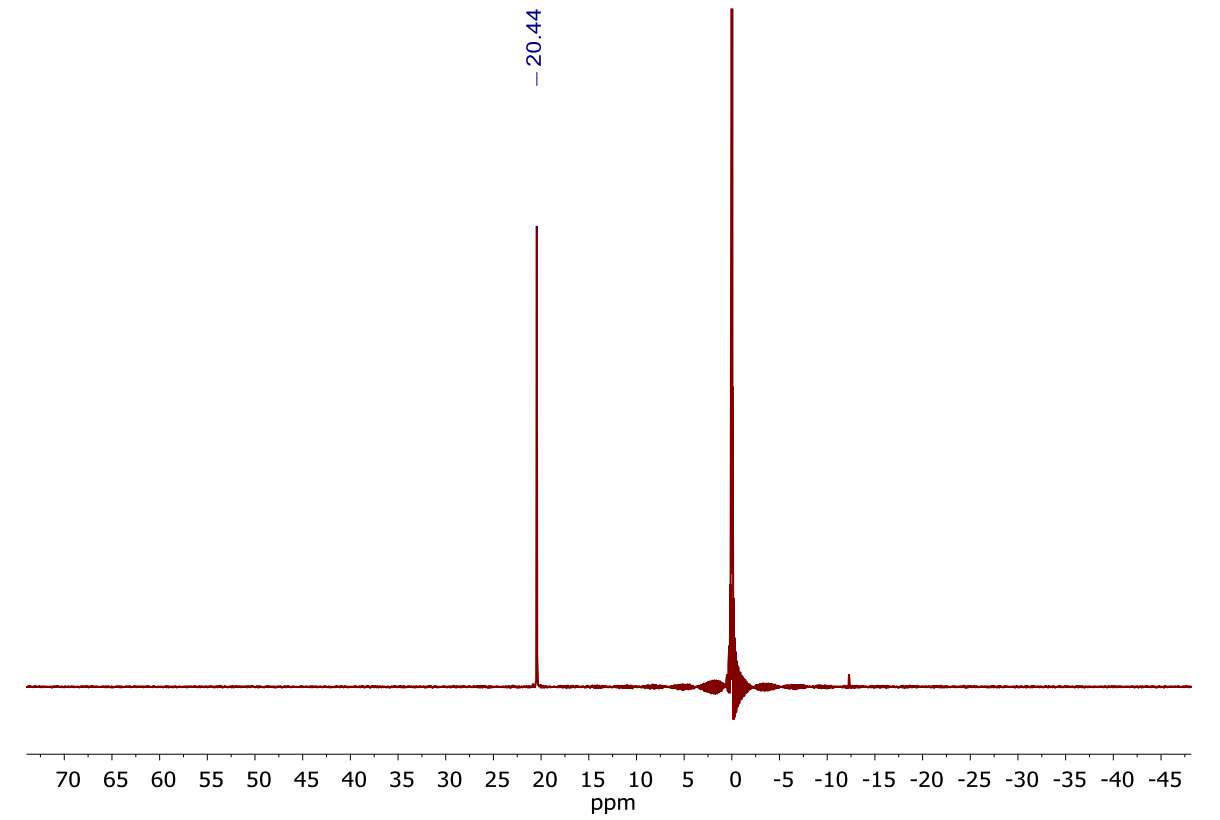

Figure S37: ^{31}P NMR (162 MHz, DMSO-d_6, 298 K, 85% H_3PO_4) of 2-chlorobenzylphosphonic acid **S6**. Peak at -12.6 ppm, belongs to an impurity in the internal standard.

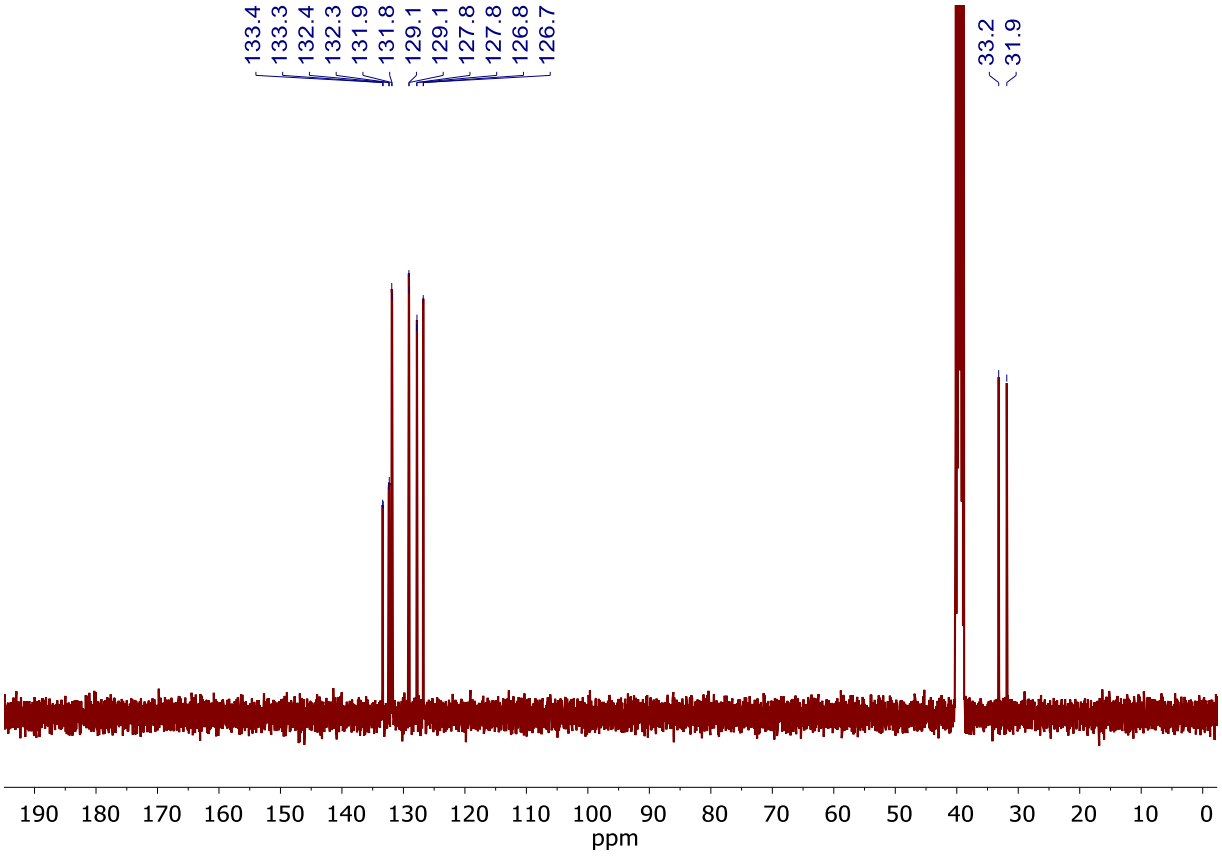

Figure S38: ^{13}C NMR (101 MHz, DMSO-d_6, 298 K) of 2-chlorobenzylphosphonic acid **S6**.

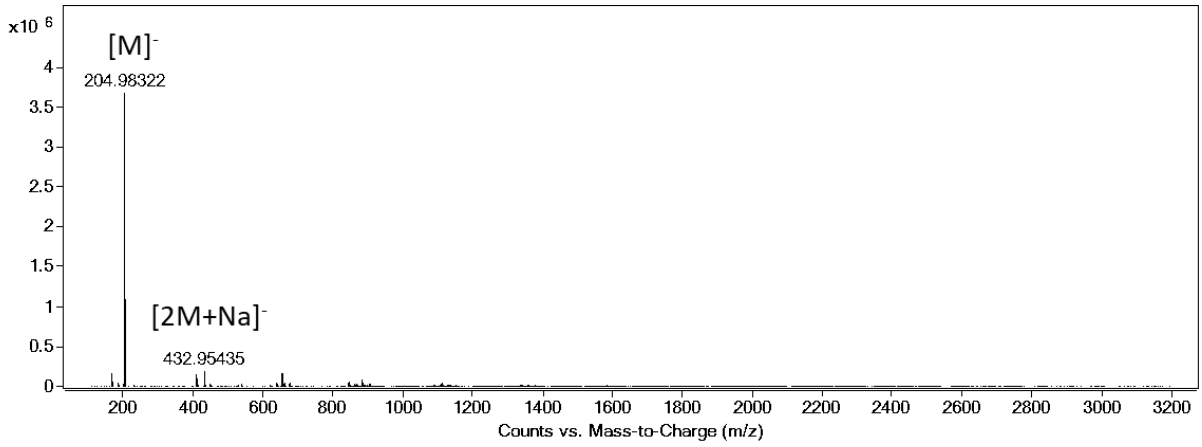

Figure S39: HRMS (ESI, negative mode) of 2-chlorobenzylphosphonic acid **S6**.

Synthesis of tetrabutylammonium 2-chlorobenzyl phosphonate S7

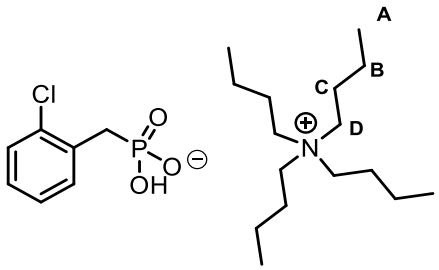

S7

225 mg (1.09 mmol) 2-chlorobenzylphosphonic acid **S6** and 872 mg (1.09 mmol, 1.0 equiv.) TBAOH · 30 H_2O were combined in a round bottom flask and dissolved in 15 mL MeOH. The mixture was stirring for 1 h at room temperature, before the solvent was removed and the product was dried in vacuo to afford 490 mg (1.09 mmol, quant.) of the desired TBA salt as a colourless solid.

^{1}H-NMR (400 MHz, $CDCl_3$): δ [ppm] = 7.82 (m, 1 H, **Ar**), 7.20 (m, 1 H, **Ar**), 7.08 (m, 1 H, **Ar**), 6.96 (m, 1 H, **Ar**), 3.23 – 3.19 (m, 8 H, **D**), 3.11 (d, $^{2}J_{H\text{-}P}$ = 20.5 Hz, 2 H, **CH_2**), 1.55 (m, 8 H, **C**), 1.42 – 1.33 (m, 8 H, **B**), 0.95 (t, ^{3}J = 7.31 Hz, 12 H, **A**).

^{13}C-NMR (101 MHz, $CDCl_3$): δ [ppm] = 137.2 (d), 134.4 (d) 132.6 (d), 128.6 (d), 126.1 (d), 125.9 (d), 58.8, 34.7 (d), 24.2, 19.8, 13.9.

^{31}P-NMR (162 MHz, $CDCl_3$, external standard: 85% H_3PO_4): δ [ppm] = 15.89.

HRMS(ESI (-)): m/z = 204.98344 (calc. 204.98213, δm/m = 6.39 ppm) $[M]^-$, 652.25043 (calc. 652.24904, δm/m = 2.13 ppm) $[2M+TBA]^-$.

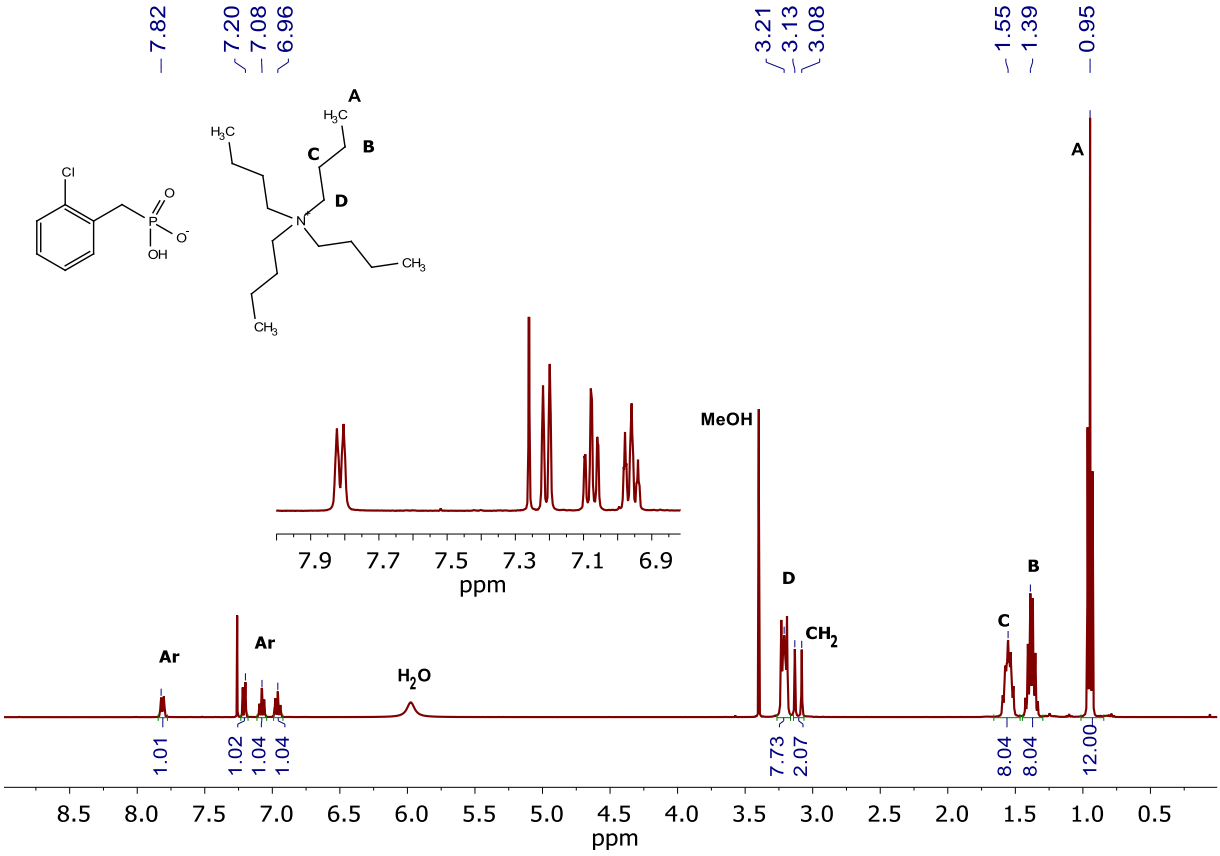

Figure S40: ^{1}H NMR (400 MHz, $CDCl_3$, 298 K) of tetrabutylammonium 2-chlorobenzyl phosphonate **S7**.

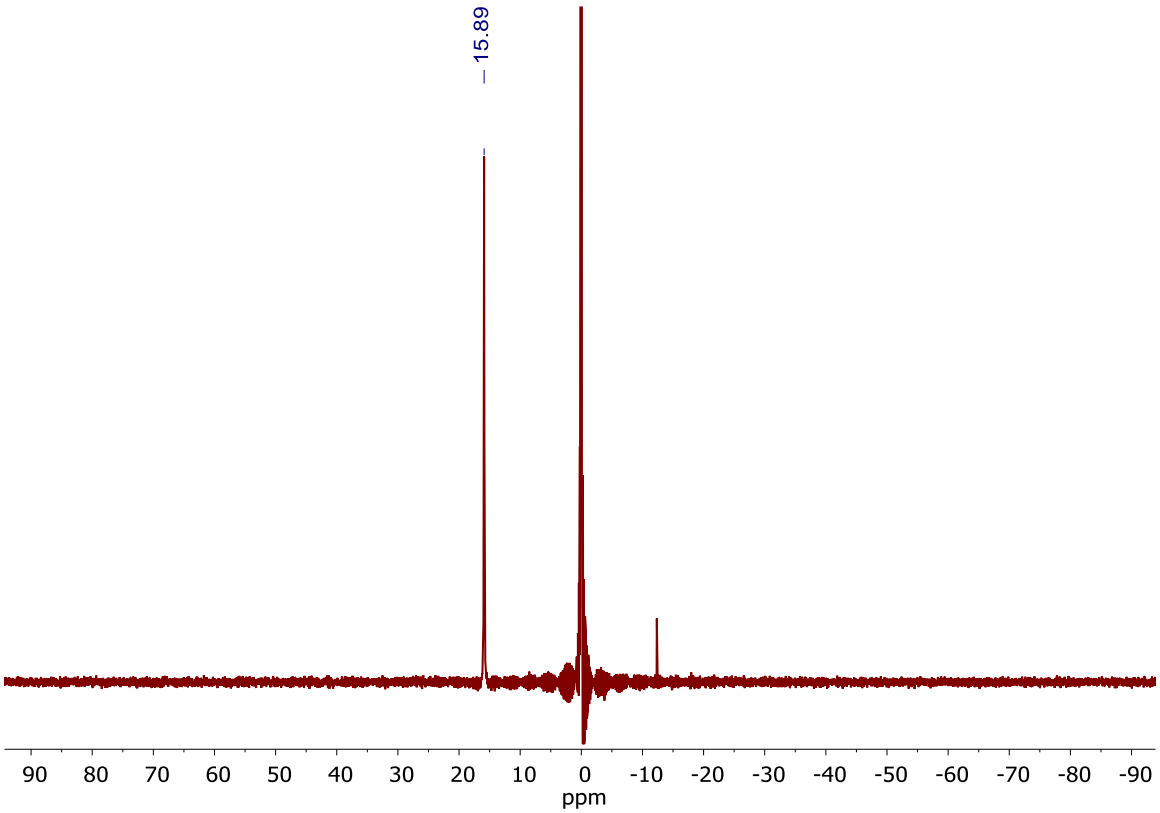

Figure S41: ^{31}P NMR (162 MHz, $CDCl_3$, 298 K, 85% H_3PO_4) of tetrabutylammonium 2-chlorobenzyl phosphonate **S7**. Peak at -12.6 ppm, belongs to an impurity in the internal standard.

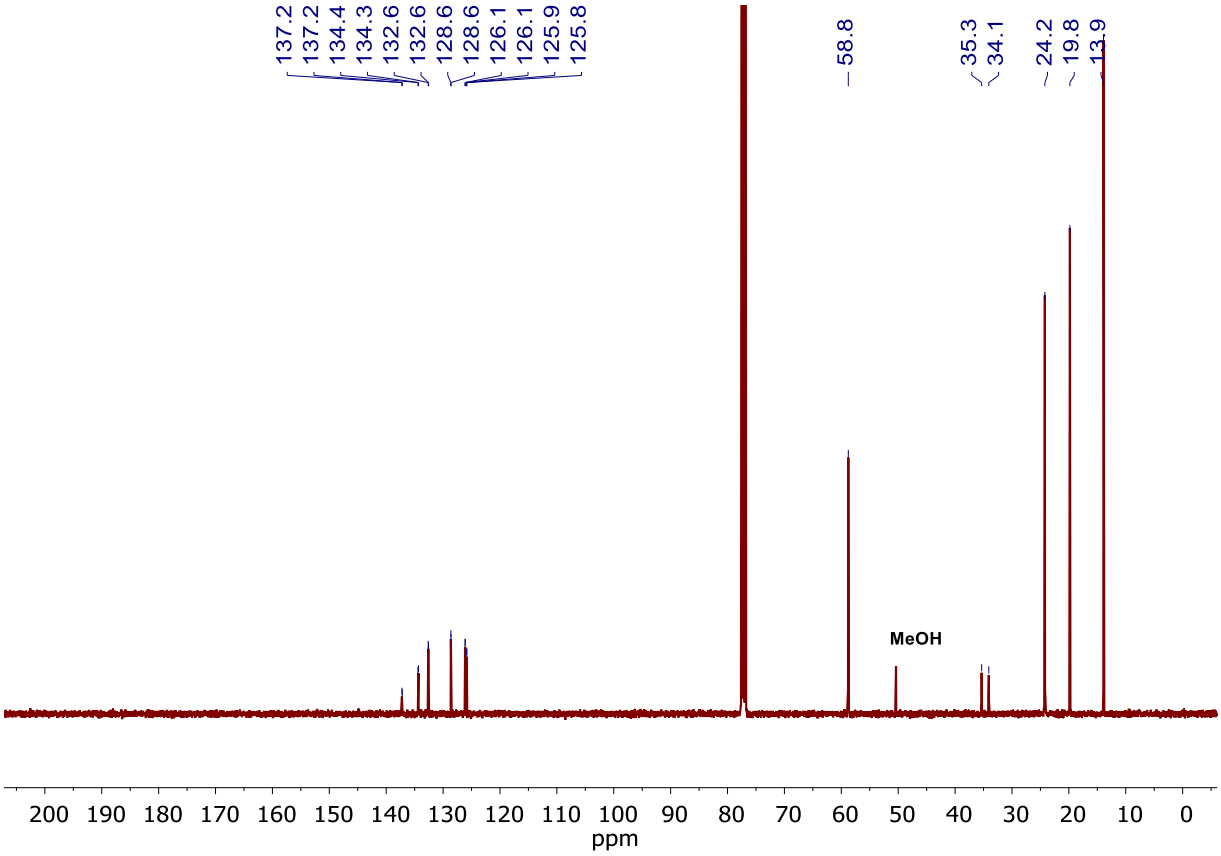

Figure S42: ^{13}C NMR (101 MHz, $CDCl_3$, 298 K) of tetrabutylammonium 2-chlorobenzyl phosphonate **S7**.

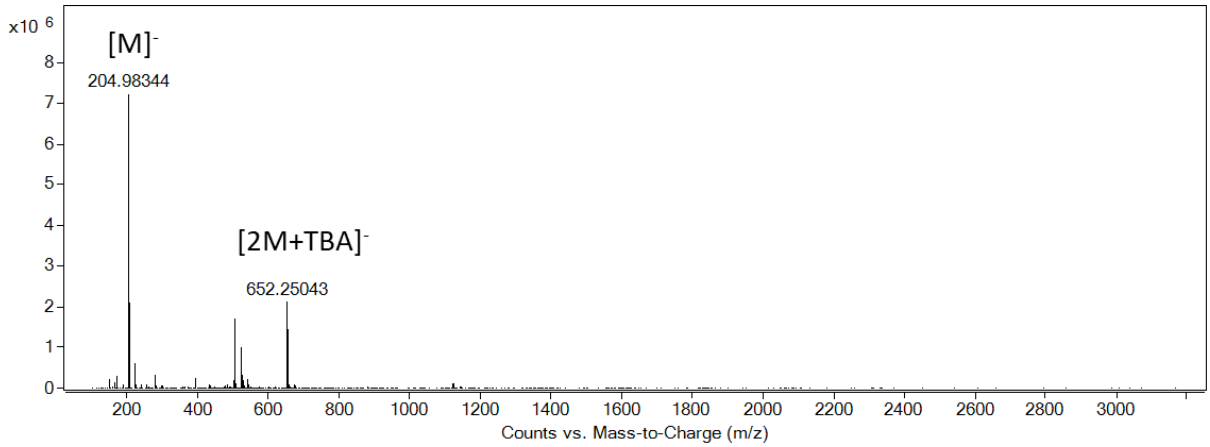

Figure S43: HRMS (ESI, negative mode) of tetrabutylammonium 2-chlorobenzyl phosphonate **S7**.

Synthesis of *bis*-tetrabutylammonium 2-chlorobenzyl pyrophosphonate (Cl-benzyl-PP) 4

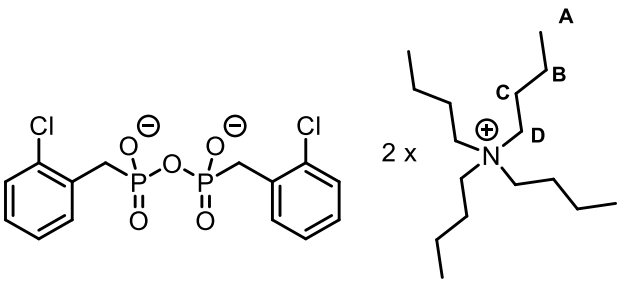

4

490 mg (1.09 mmol) tetrabutylammonium 2-chlorobenzyl phosphonate **S7** were dissolved in 30 mL DCM and 1.71 mL (10.9 mmol, 10 equiv.) *N,N'*-diisopropylcarbodiimide (DIC) were added. The mixture was stirred at room temperature for 48 h. DCM was evaporated and the residue was dissolved in 4 mL of a H_2O / MeCN (3:1) mixture. MPLC on an Interchim PF-15C18HP-F0025 C18 column with a mobile phase of MeCN and water (20-30% MeCN) and subsequent lyophilization yielded 160 mg (0.18 mmol, 33%) of the dimer as a colourless oil.

^{1}H-NMR (400 MHz, $CDCl_3$): δ [ppm] = 7.83 (m, 2 H, **Ar**), 7.19 (m, 2 H, **Ar**), 7.06 (m, 2 H, **Ar**), 6.96 (m, 2 H, **Ar**), 3.28 – 3.19 (m, 16 H, **D**), 3.30 – 3.26 (m, 4 H, **CH_2**), 1.59-1.51 (m, 16 H, **C**), 1.41-1.32 (m, 16 H, **B**), 0.92 (t, ^{3}J = 7.35 Hz, 24 H, **A**).

^{13}C-NMR (101 MHz, $CDCl_3$): δ [ppm] = 136.6, 134.4 (t), 132.6, 128.6, 126.2 (d), 126.0 (d), 58.7, 35.3 – 33.9 (dd), 24.2, 19.8, 13.8.

^{31}P-NMR (162 MHz, $CDCl_3$, external standard: 85% H_3PO_4): δ [ppm] = 8.52.

HRMS(ESI (-)): m/z = 392.96248 (calc. 392.96208, δm/m = 1.02 ppm) $[M]^-$, 634.23973 (calc. 634.23848, δm/m = 1.97 ppm) $[M+TBA]^-$

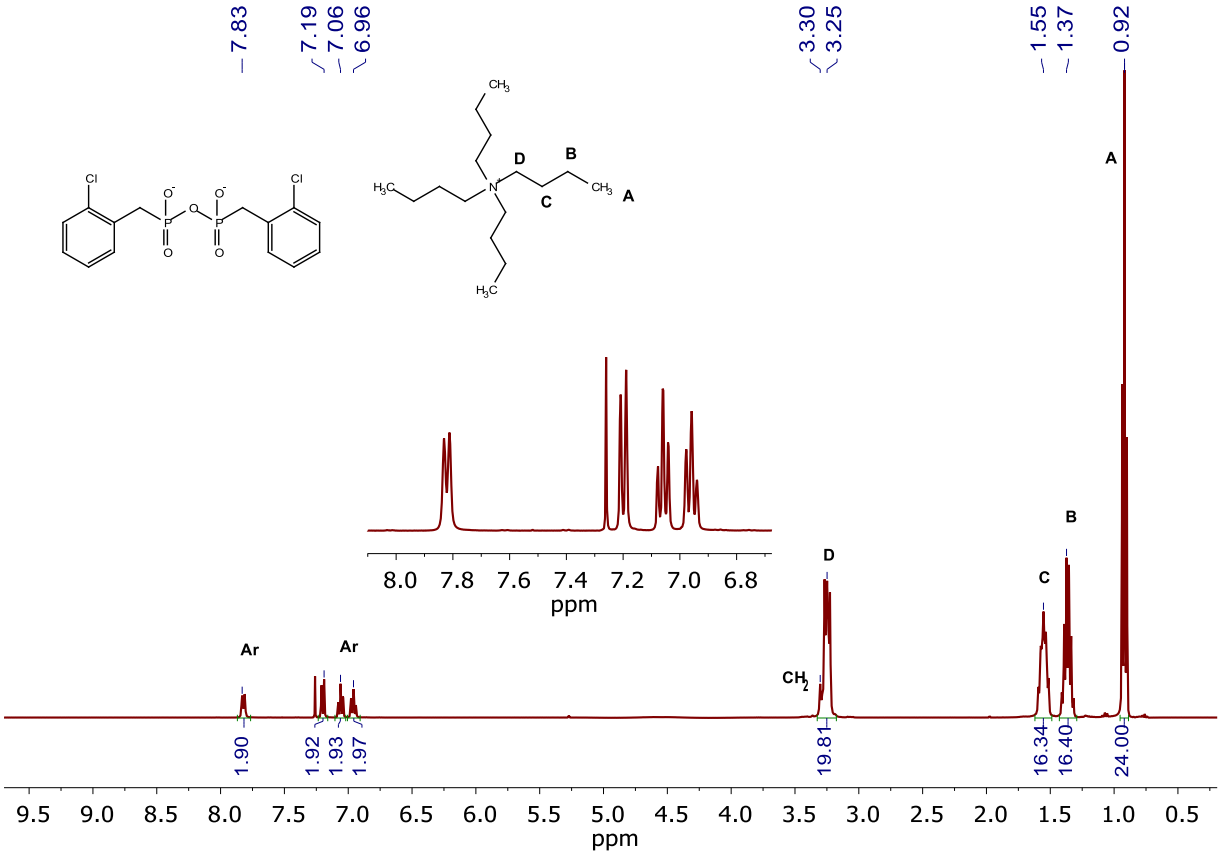

Figure S44: ^{1}H NMR (400 MHz, $CDCl_3$, 298 K) of *bis*-tetrabutylammonium 2-chlorobenzyl pyrophosphonate **4**.

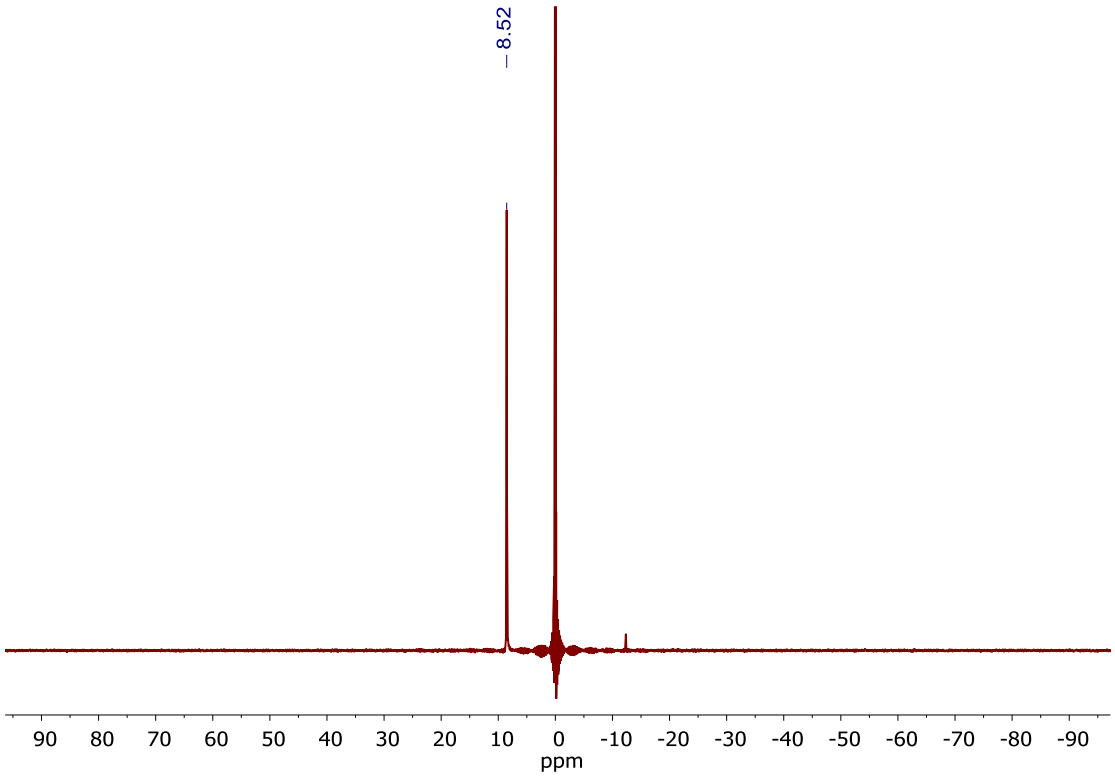

Figure S45: ^{31}P NMR (162 MHz, $CDCl_3$, 298 K, 85% H_3PO_4) of *bis*-tetrabutylammonium 2-chlorobenzyl pyrophosphonate **4**. Peak at -12.6 ppm, belongs to an impurity in the internal standard.

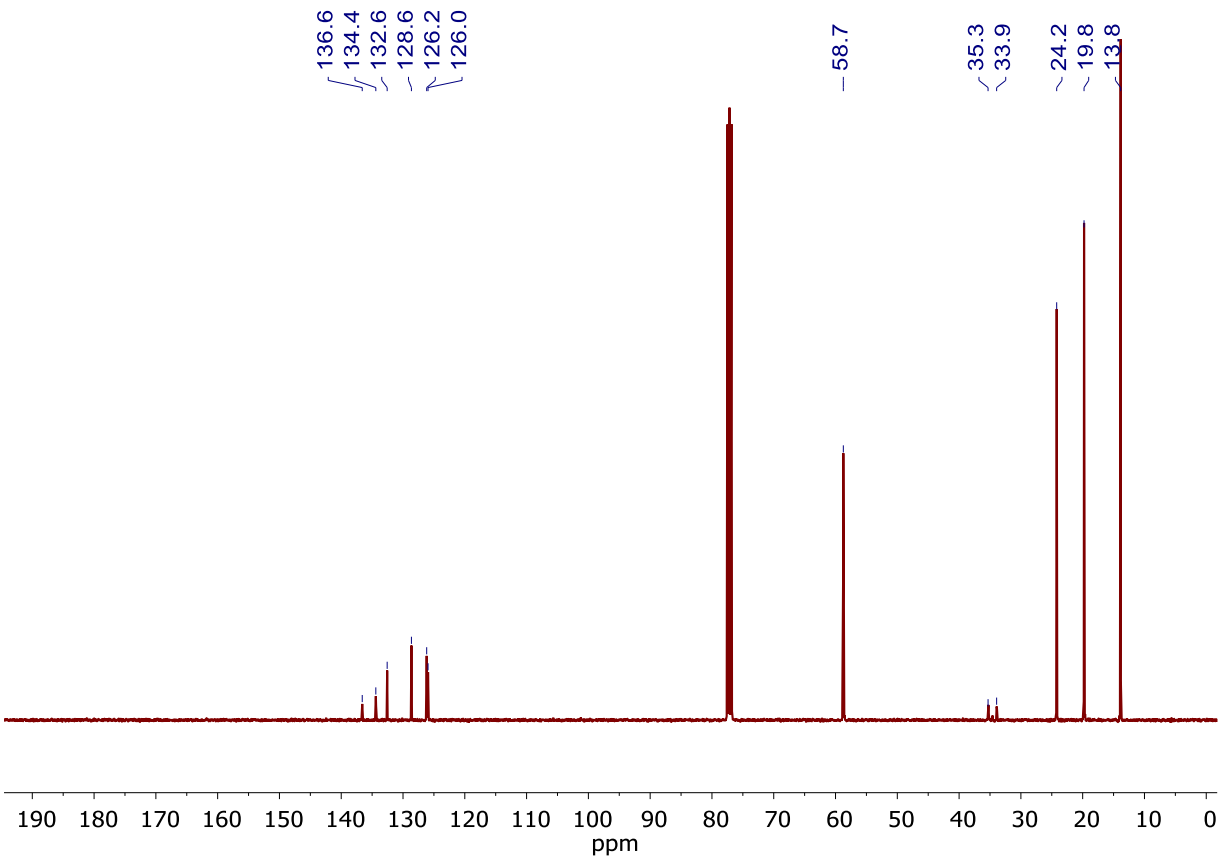

Figure S46: ^{13}C NMR (101 MHz, $CDCl_3$, 298 K) of *bis*-tetrabutylammonium 2-chlorobenzyl pyrophosphonate **4**.

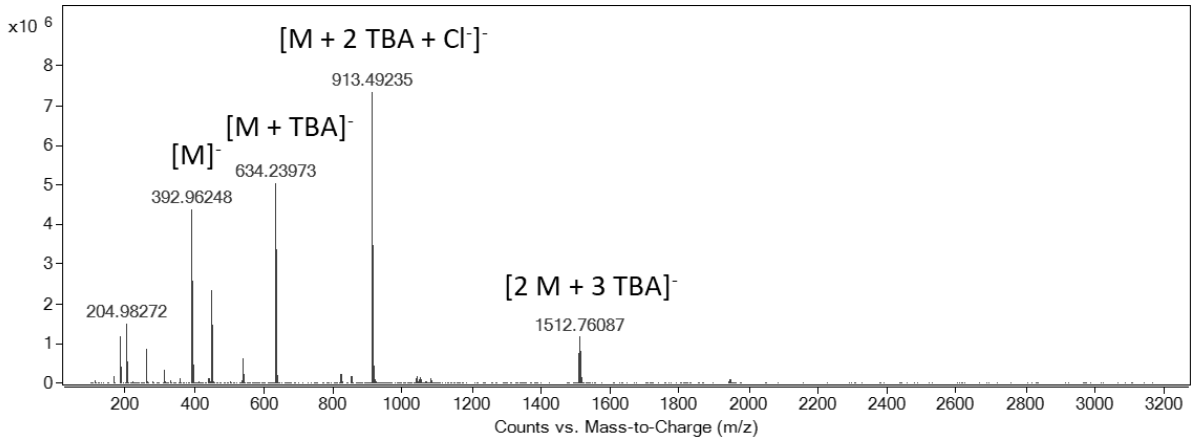

Figure S47: HRMS (ESI, negative mode) of *bis*-tetrabutylammonium 2-chlorobenzyl pyrophosphonate **4**.

Synthesis of tetrabutylammonium 2-methylbenzyl phosphonate S8

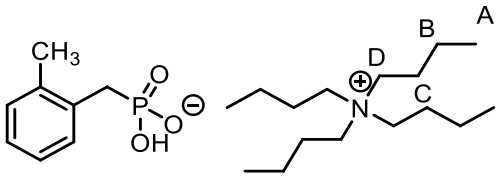

S8

300 mg (1.63 mmol) 2-methylbenzylphosphonic acid and 1.30 g (1.63 mmol, 1.0 equiv.) TBAOH · 30 H_2O were combined in a round bottom flask and dissolved in 20 mL MeOH. The mixture was stirring for 1 h at room temperature, before the solvent was removed and the product was dried in vacuo to afford 720 mg (1.63 mmol, quant.) of the desired TBA salt as a colourless solid.

^{1}H-NMR (400 MHz, $CDCl_3$): δ [ppm] = 7.42 (m, 1 H, **Ar**), 6.99 (m, 2 H, **Ar**), 6.92 (m, 1 H, **Ar**), 3.16-3.12 (m, 8 H, **D**), 2.96 (d, $^{2}J_{H\text{-}P}$ = 20.9 Hz, 2 H, **CH_2**), 2.44 (s, 3 H, **CH_3**), 1.64-1.46 (m, 8 H, **C**), 1.41-1.31 (m, 8 H, **B**), 0.94 (t, ^{3}J = 7.29 Hz, 12 H, **A**).

^{13}C-NMR (101 MHz, $CDCl_3$): δ [ppm] = 138.3 (d), 137.3 (d), 131.2 (d), 129.4 (d), 125.0 (d), 124.3 (d), 58.6, 36.2 – 34.9 (d), 24.2, 20.8, 19.8, 13.9.

^{31}P-NMR (162 MHz, $CDCl_3$, external standard: 85% H_3PO_4): δ [ppm] = 16.77.

HRMS(ESI (-)): m/z = 185.03761 (calc. 185.03730, δm/m = 1.68 ppm) $[M]^-$, 612.35852 $[2M+TBA]^-$.

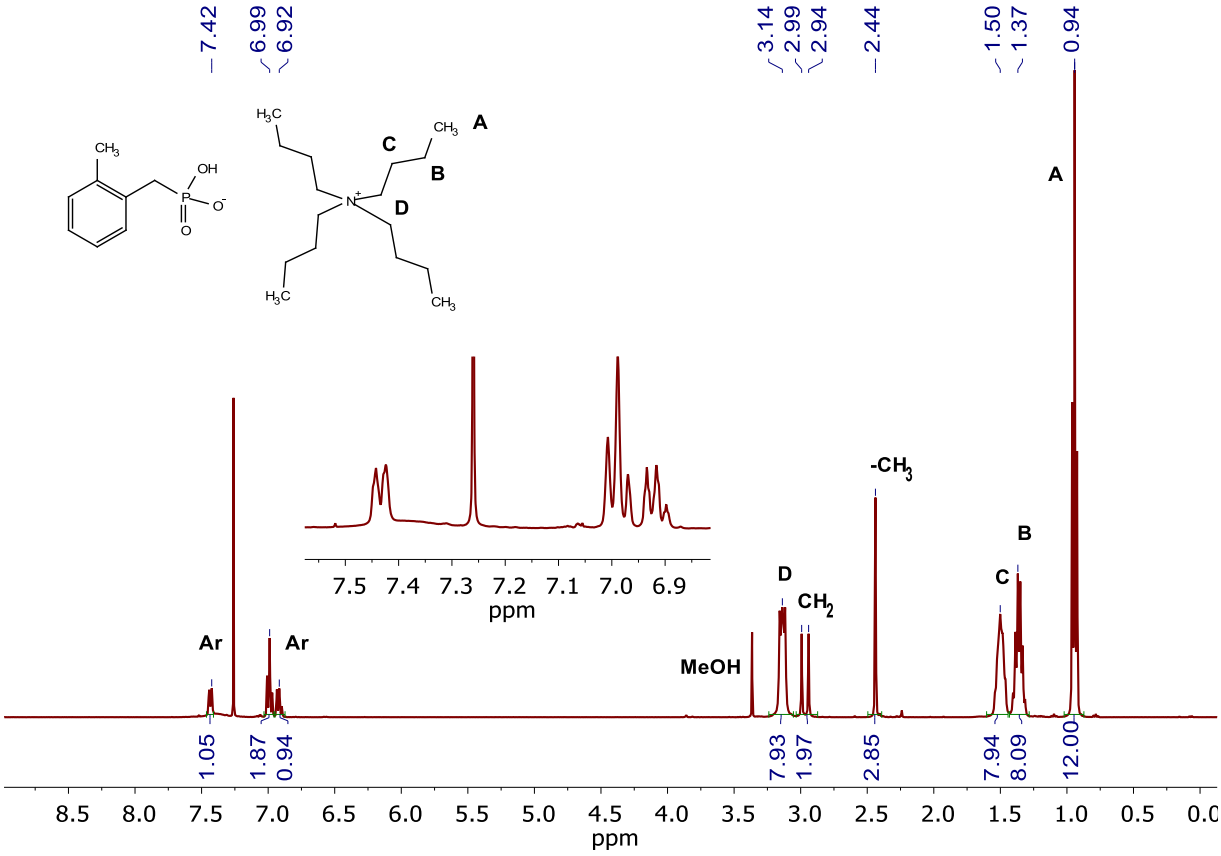

Figure S48: ^{1}H NMR (400 MHz, $CDCl_3$, 298 K) of tetrabutylammonium 2-methylbenzyl phosphonate **S8**.

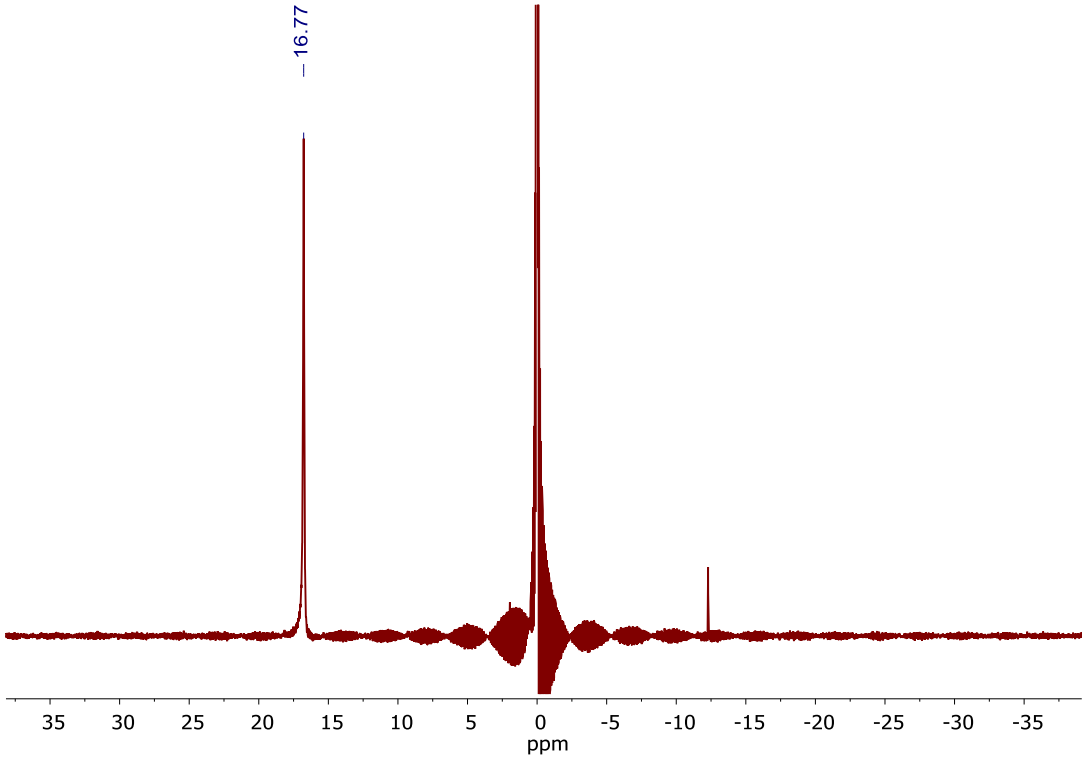

Figure S49: ^{31}P NMR (162 MHz, $CDCl_3$, 298 K, 85% H_3PO_4) of tetrabutylammonium 2-methylbenzyl phosphonate **S8**. Peak at -12.6 ppm, belongs to an impurity in the internal standard.

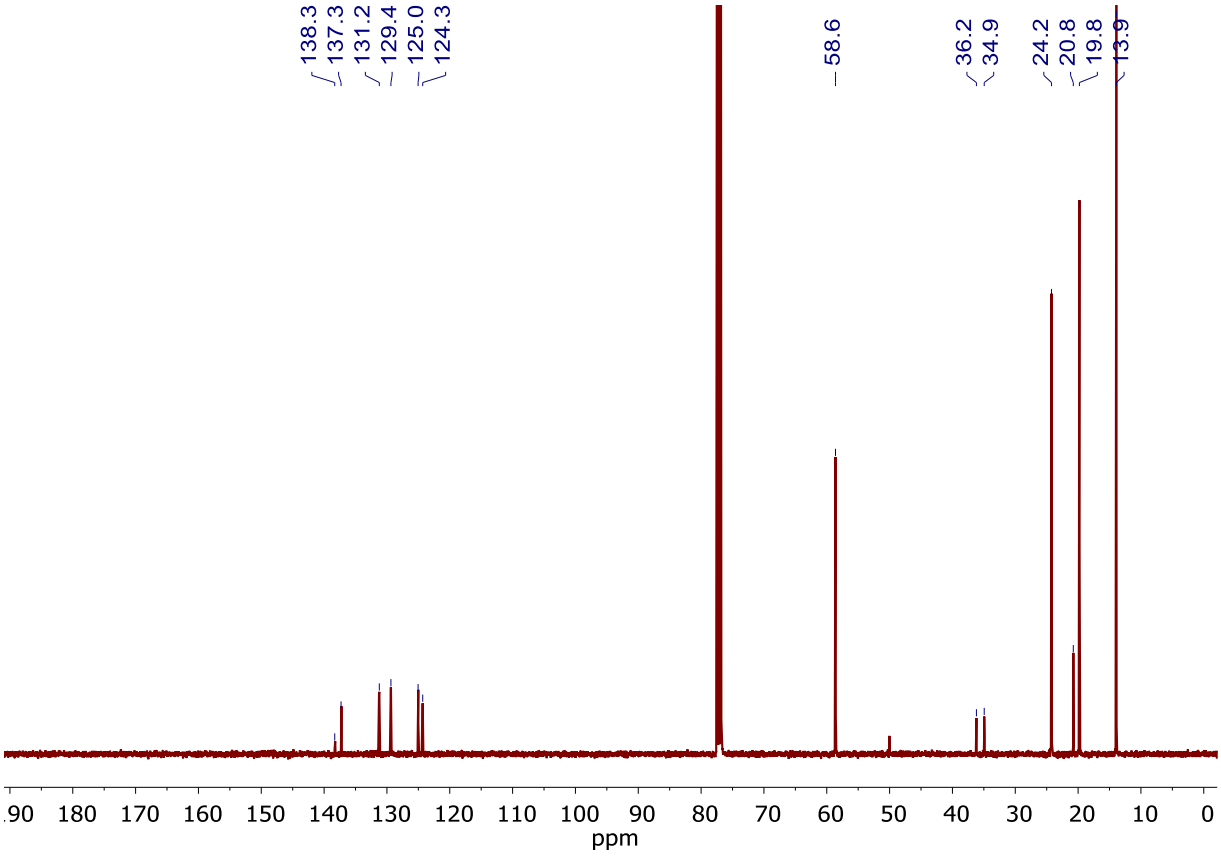

Figure S50: ^{13}C NMR (101 MHz, $CDCl_3$, 298 K) of tetrabutylammonium 2-methylbenzyl phosphonate **S8**.

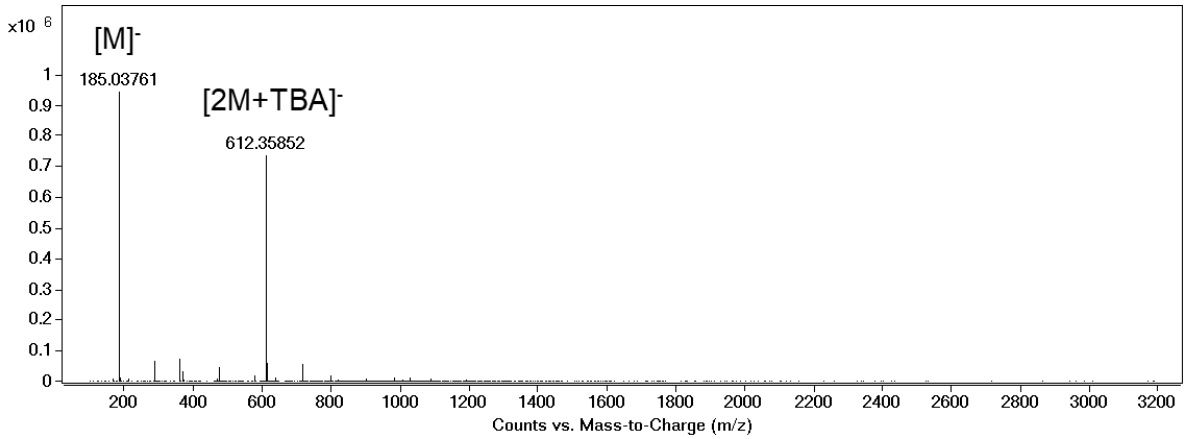

Figure S51: HRMS (ESI, negative mode) of tetrabutylammonium 2-methylbenzyl phosphonate **S8**.

Synthesis of *bis*-tetrabutylammonium 2-methylbenzyl pyrophosphonate (Me-benzyl-PP) 5

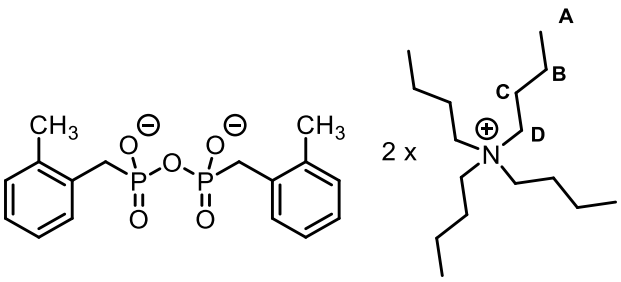

5

200 mg (0.61 mmol) 2-methylbenzyl phosphonate **S8** were dissolved in 20 mL DCM and 705 µL (4.53 mmol, 10 equiv.) *N,N'*-diisopropylcarbodiimide (DIC) were added. The mixture was stirred at room temperature for 48 h. DCM was evaporated and the residue was dissolved in 4 mL of a H_2O / MeCN (3:1) mixture. MPLC on an Interchim PF-15C18HP-F0025 C18 column with a mobile phase of MeCN and water (20-30% MeCN) and subsequent lyophilization yielded 119 mg (0.14 mmol, 46%) of the dimer as a colourless oil.

^{1}H-NMR (400 MHz, DMSO-d_6): δ [ppm] = 7.39 (m, 2 H, **Ar**), 6.98 – 6.87 (m, 6 H, **Ar**), 3.24 - 3.10 (m, 16 H, **D**), 2.95 – 2.89 (m, 4 H, **CH_2**), 2.34 (s, 3 H, **CH_3**) 1.59 – 1.52 (m, 16 H, **C**), 1.34 -1.26 (m, 16 H, **B**), 0.93 (t, ^{3}J = 7.34 Hz, 24 H, **A**).

^{13}C-NMR (101 MHz, DMSO-d_6): δ [ppm] = 138.8 (t), 136.3 (t), 130.6, 128.7, 124.4, 123.6, 57.5, 23.1, 20.3, 19.2, 13.5.

^{31}P-NMR (162 MHz, DMSO-d_6, external standard: 85% H_3PO_4): δ [ppm] = 6.45.

HRMS(ESI (-)): m/z = 353.07163 (calc. 353.07132, δm/m = 0.88 ppm) $[M]^-$, 594.34748 (calc. 594.34827, δm/m = 1.33 ppm) $[2M+TBA]^-$.

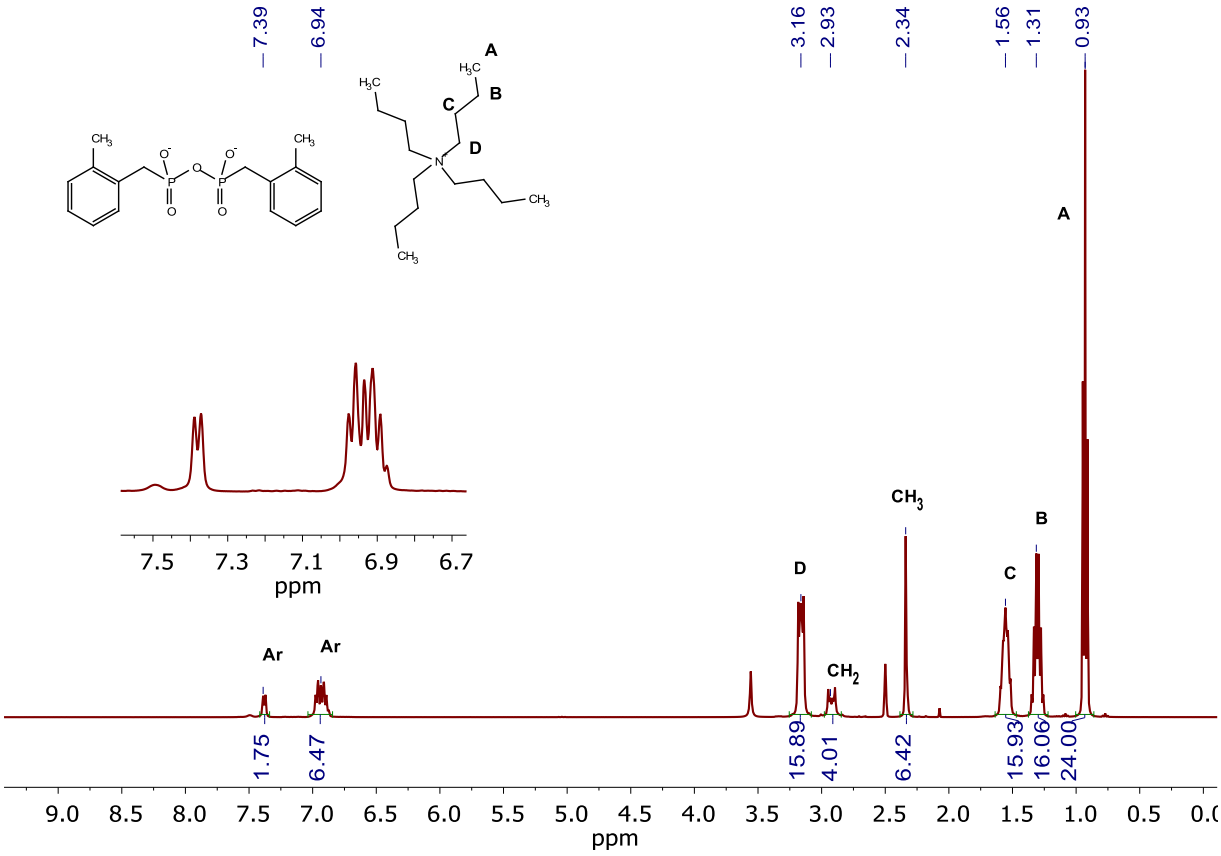

Figure S52: ^{1}H NMR (400 MHz, DMSO-d$_6$, 298 K) of *bis*-tetrabutylammonium 2-methylbenzyl pyrophosphonate **5**.

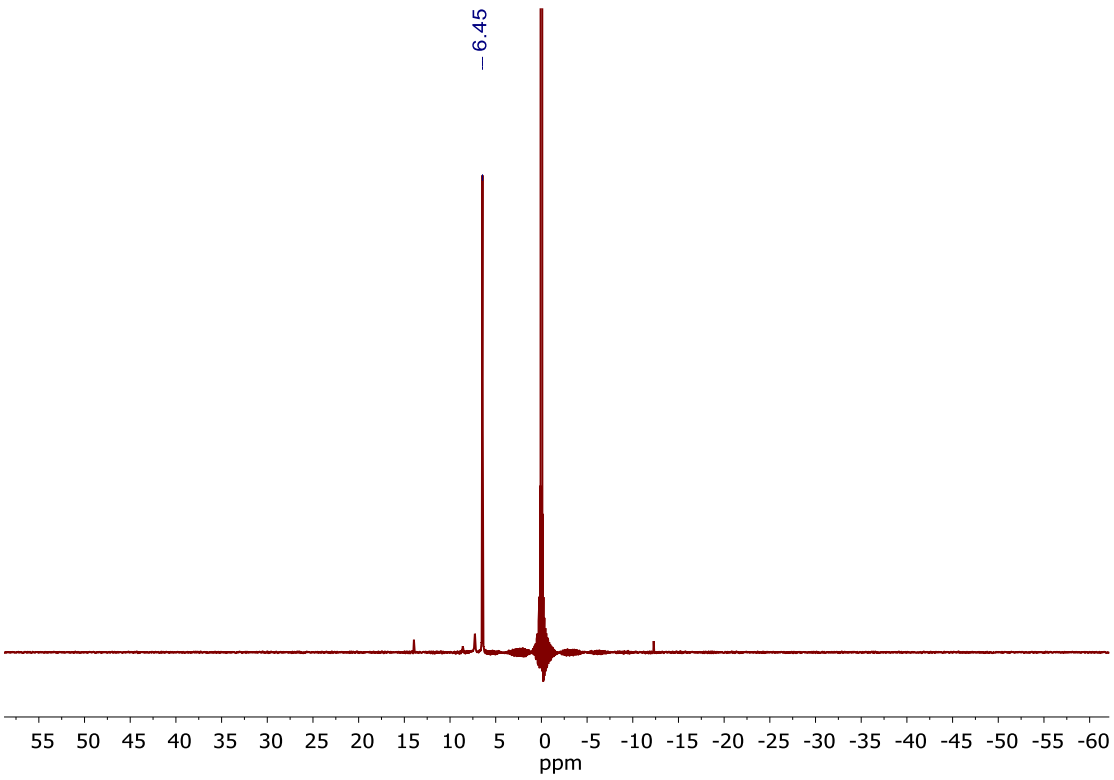

Figure S53: ^{31}P NMR (162 MHz, DMSO-d$_6$, 298 K, 85% H_3PO_4) of *bis*-tetrabutylammonium 2-methylbenzyl pyrophosphonate **5**.

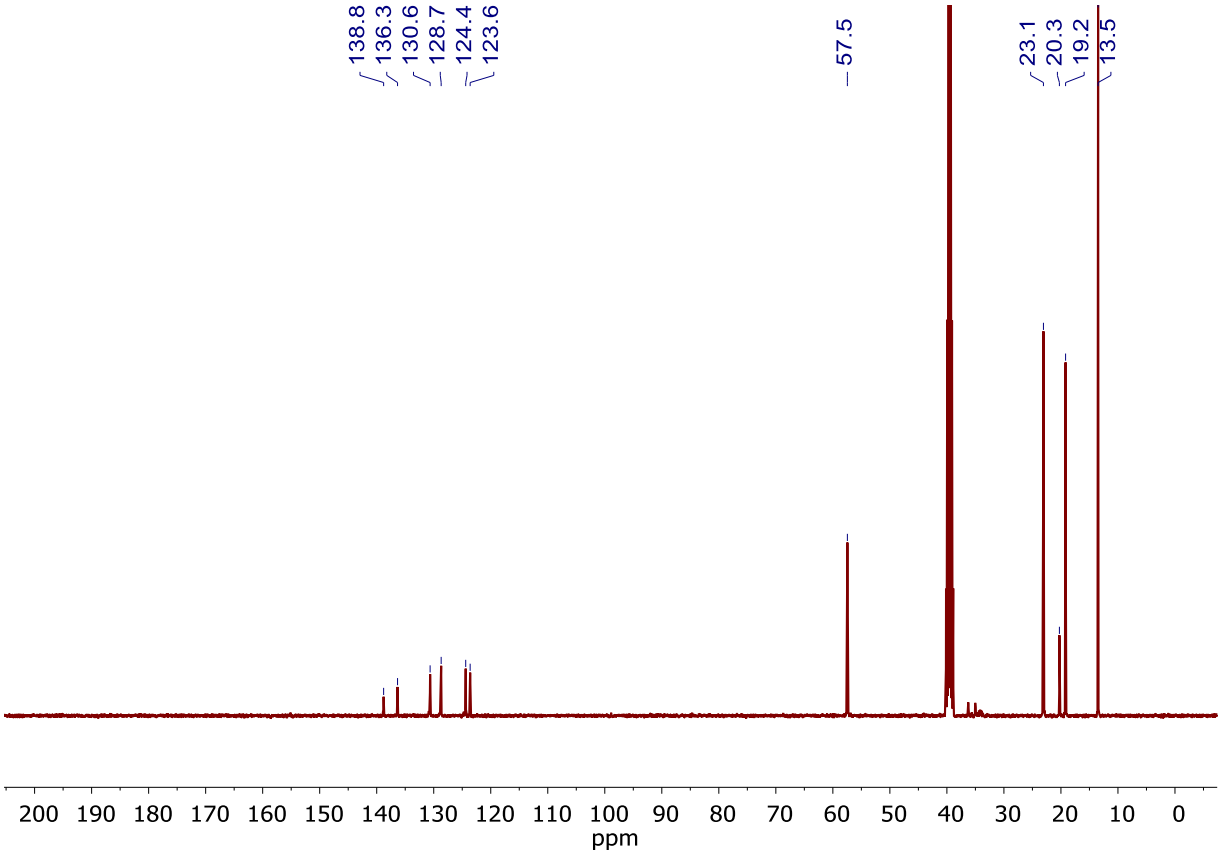

Figure S54: ^{13}C NMR (101 MHz, DMSO-d_6, 298 K) of *bis*-tetrabutylammonium 2-methylbenzyl pyrophosphonate **5**.

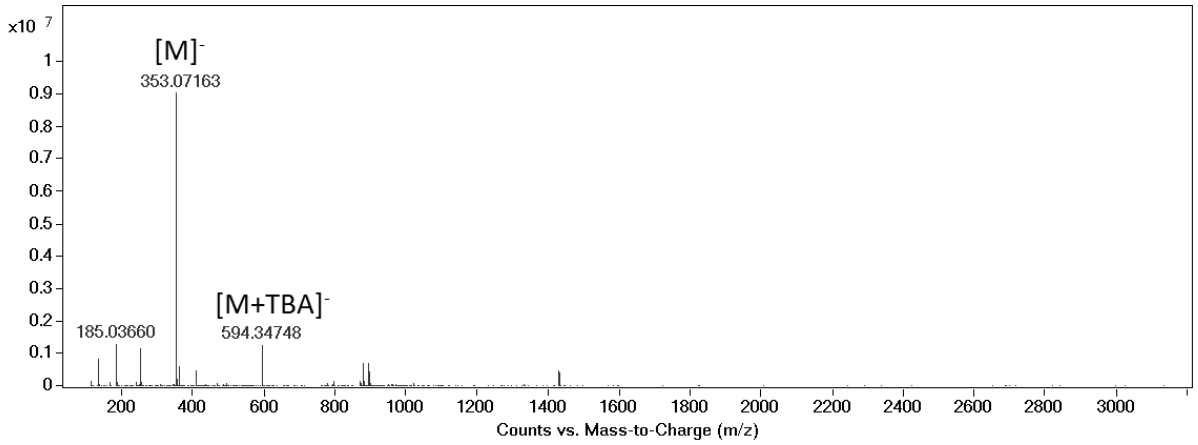

Figure S55: HRMS (ESI, negative mode) of *bis*-tetrabutylammonium 2-methylbenzyl pyrophosphonate **5**.

Synthesis of Cyanostar

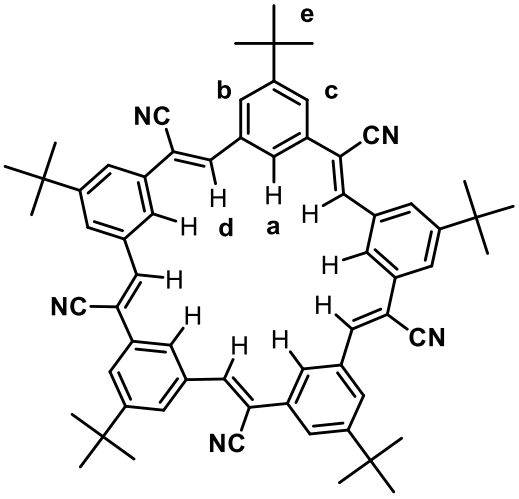

CS

Cyanostar (**CS**) was synthesized according to a published procedure.[3]

^{1}H NMR (400 MHz, CD_2Cl_2): δ [ppm] = 8.67 (s, 5 H, **b**), 7.88 (s, 5 H, **c**), 7.78 (s, 5 H, **d**), 7.70 (s, 5 H, **a**), 1.49 (s, 45 H, **e**).

^{13}C NMR (101 MHz, CD_2Cl_2): δ [ppm] = 154.3, 142.3, 135.1, 134.3, 127.2, 126.4, 124.6, 117.9, 111.3, 35.9, 31.4

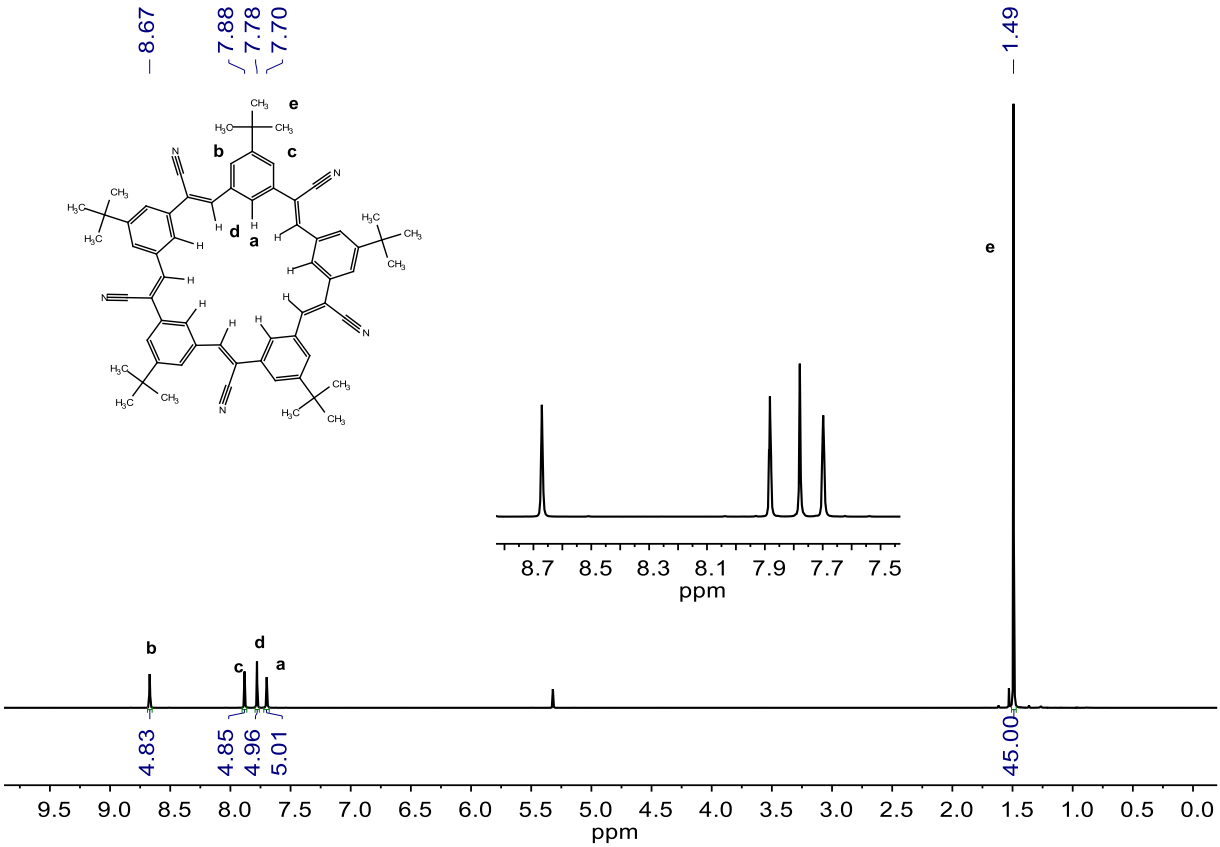

Figure S56: ^{1}H NMR (400 MHz, CD_2Cl_2, 298 K) of Cyanostar (**CS**).

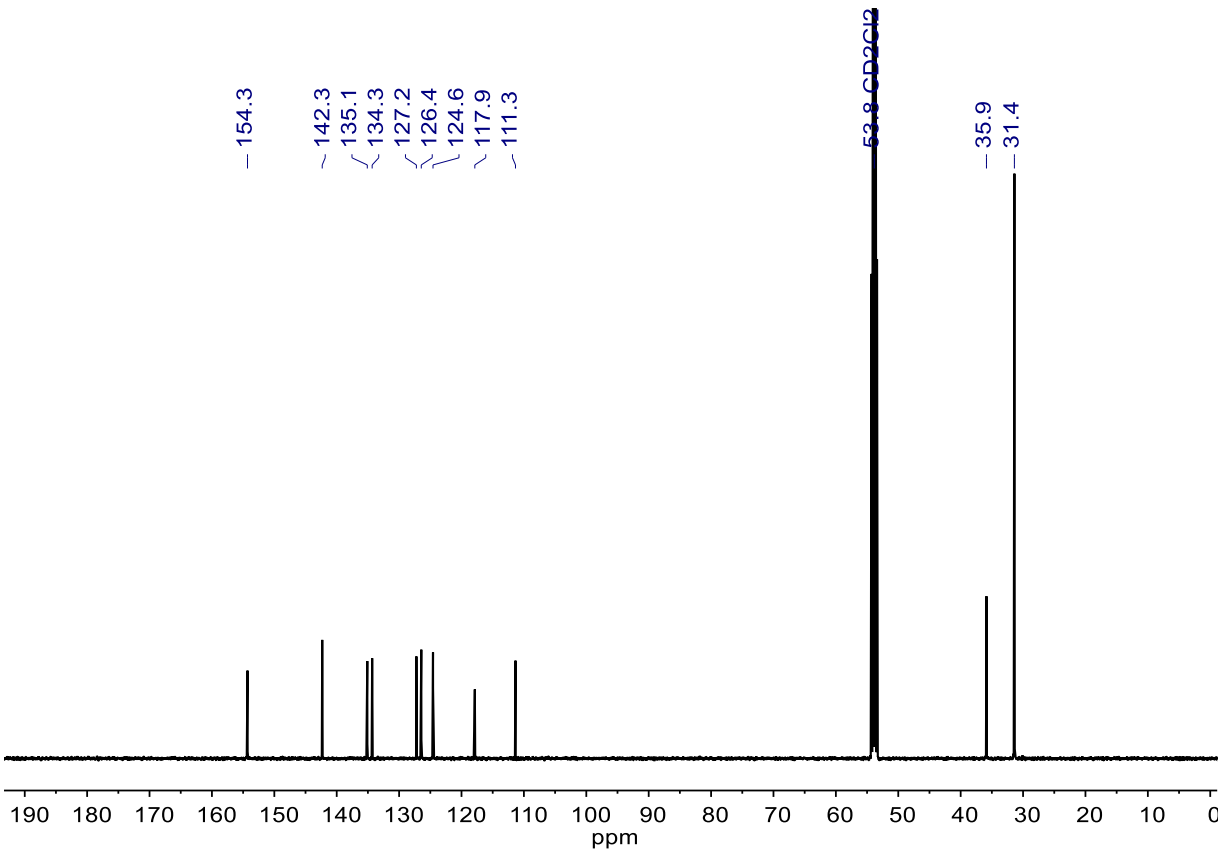

Figure S57: ^{13}C NMR (101 MHz, CD_2Cl_2, 298 K) of Cyanostar (**CS**).

NMR Kinetic Experiments

25 µL of a **CS** stock solution (20 mM in CD_2Cl_2) were diluted with 435 µL CD_2Cl_2 and an initial ^{1}H-NMR (number of scans = 16, delay = 1s) was measured. 40 µL of a stock solution (25 mM in CD_2Cl_2) of the corresponding pyrophosphonate (**PP**) were added to obtain a final concentration of 2 mM **PP** and 1 mM **CS**. A series of NMR spectra were recorded. The lack time of 120 s between addition of **PP** and the first measurement was taken into account. The experiments were performed at 298 K. In case of 2:1-binding (**1**), the peak at 7.61 ppm (corresponding to the c-proton of the meso **CS** in the [3]pseudorotaxane), and in case of 1:1-binding (**2** & **3**), the peak at 9.32 ppm (corresponding to the d-proton of **CS** in the [2]pseudorotaxane) was monitored over time.

Kinetics of the binding of CS to homoallyl-PP 1

The binding between homoallyl-PP **1** and 2 x **CS** leading to the formation of the [3]pseudorotaxane (2:1 binding) reaches its equilibrium fast (i.e. no delay time could be observed).

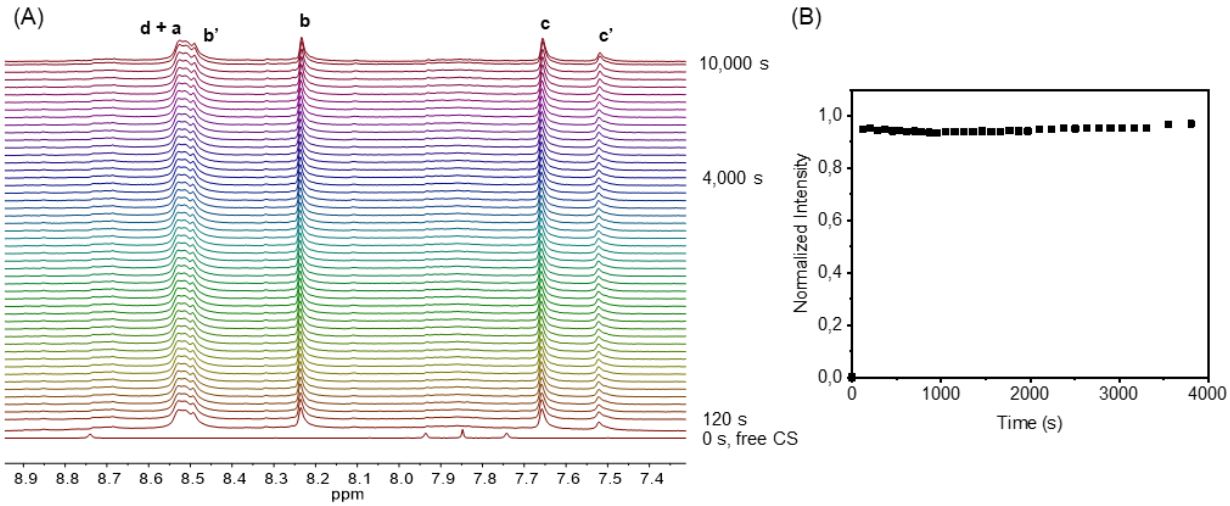

Figure S58: Binding kinetics. (A) Stacked ^{1}H NMR spectra at t=0 to t=3 h. (B) Normalized intensity of c-proton over the first 4000 s. No change can be observed, indicating that the equilibrium is reached fast (< 120 s). 298 K, DCM-d_2.

Binding Kinetics of CS on benzyl-PP 2

The binding between benzyl-PP **2** and **CS** leading to the formation of the [2]pseudorotaxane (1:1 binding) reaches its equilibrium fast (i.e. no delay time could be observed).

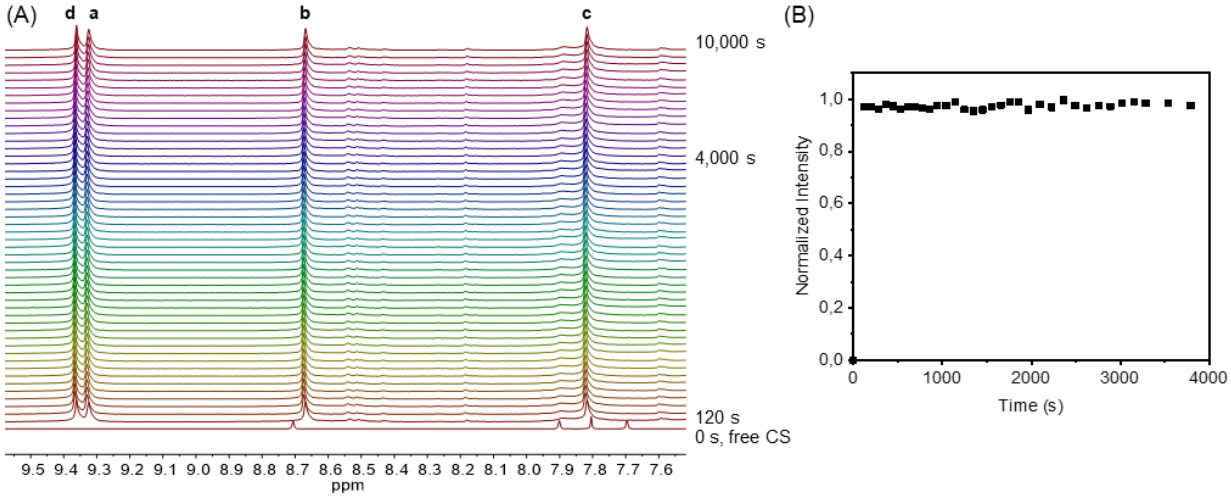

Figure S59: Binding kinetics. (A) Stacked NMR spectra at t=0 to t=3 h. (B) Normalized intensity of d-proton over the first 4000 s. No change can be observed, indicating that the equilibrium is reached fast (< 120 s). 298 K, DCM-d_2.

Binding Kinetics of CS on F-benzyl-PP 3

The binding between F-benzyl-PP **3** and **CS** leading to the formation of the [2]pseudorotaxane (1:1 binding) reaches its equilibrium within approx. 15 min.

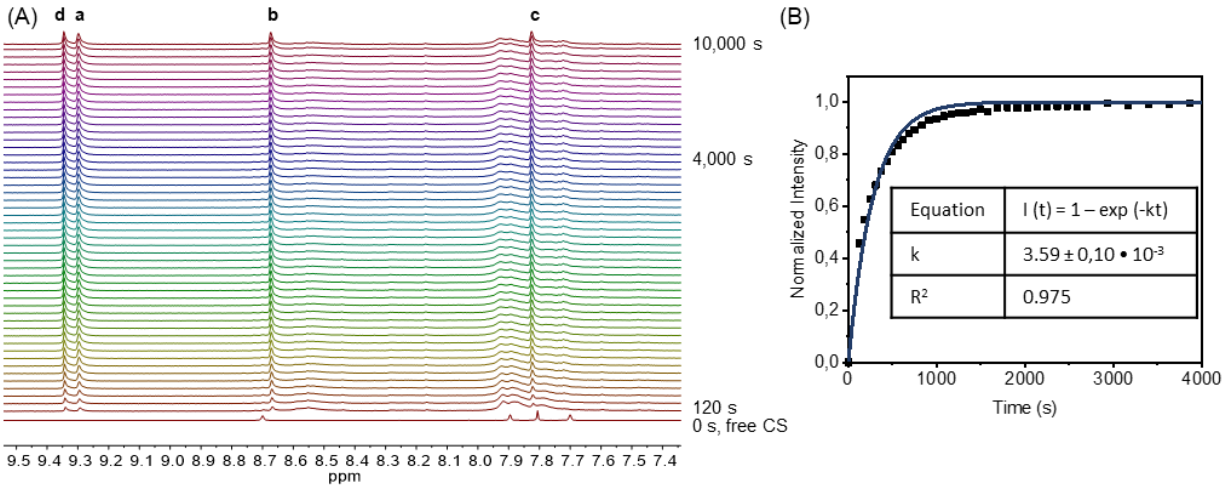

Figure S60: Binding kinetics. (A) Stacked NMR spectra at t=0 – t=3 h. (B) Normalized intensity of d-proton over the first 4000 s. The intensity increased and reached a plateau after approx. 15 min, indicating that the equilibrium is reached. Data points were fitted to a first order kinetics. 298 K, DCM-d_2.

The kinetic curve in Fig. S60B was fitted as follows: $I_t = 1 - e^{kt}$ (R^2= 0.975) and the rate constant was determined to be k_{obs} = 0.215 min^{-1} or k_{obs} = 3.59 • 10^{-3} s^{-1}. According to $t_{50} = \frac{\ln(2)}{k}$ the time where 50% of the final equilibrium of the [2]pseudorotaxane formation is reached is t_{50} = 3.22 min = 193 s.

In case of pyrophosphonates **1** and **2** (Fig. S58 and S59) the plateau was already reached after 120 s. This corresponds to five times a t_{50} of 24 s after which 97% of the plateau would be reached. This indicates that the t_{50} of formation is below 24 s.

De-threading Kinetics

Assuming that the kinetics of de-threading might be slower and therefore measurable, we prepared the 1:1 complex of benzyl phosphonate **2** and **CS** in $CDCl_3$ and triggered de-threading by addition of either $TBAPF_6$ (Fig. S61) or H_2O (Fig. S62). A mixture of 2 mM pyrophosphonate **2** and 1 mM **CS** was prepared in $CDCl_3$. After a first ^1H NMR measurement, 2 mM PF_6^- or 30 mM H_2O, respectively were added and further NMR spectra were recorded.

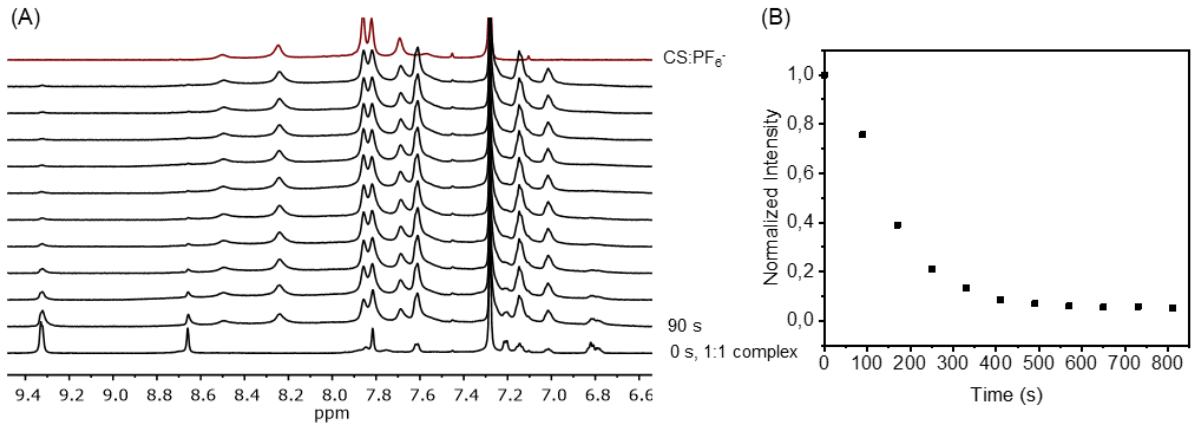

Figure S61: De-threading kinetics triggered by $TBAPF_6$ addition. (A) Stacked NMR spectra at t=0 – t= 800 s. (B) Normalized intensity of d&a-protons. The intensity increased and reached a plateau after approx. 6 min after addition of $TBAPF_6$, indicating that equilibrium is reached. A half life of ca. 120 s was determined (please note that PF_6^- is likely involved in the de-threading mechanism). 298 K, $CDCl_3$.

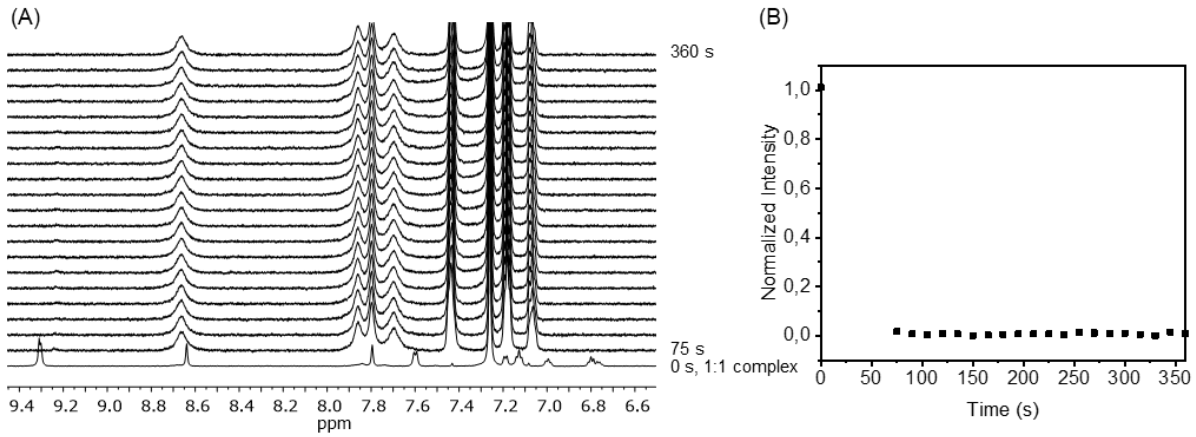

Figure S62: De-threading kinetics triggered by addition of H_2O. (A) Stacked NMR spectra at t=0 – t= 360 s. (B) Normalized intensity of d&a-proton. The signals of the 1:1 complex vanished after addition of H2O already at the first measurement after 75 s. 298 K, $CDCl_3$.

NMR Variable Temperature (VT) Experiments

A series of VT ^{1}H NMR spectra of free **CS** under the same conditions as below were measured for comparison. 25 µL of a 20 mM **CS** stock solution were diluted with 475 µL $CDCl_3$ to give a 1 mM **CS** solution. VT ^{1}H NMR spectra (number of scans = 16, delay = 1 s) were measured starting from the lower temperature.

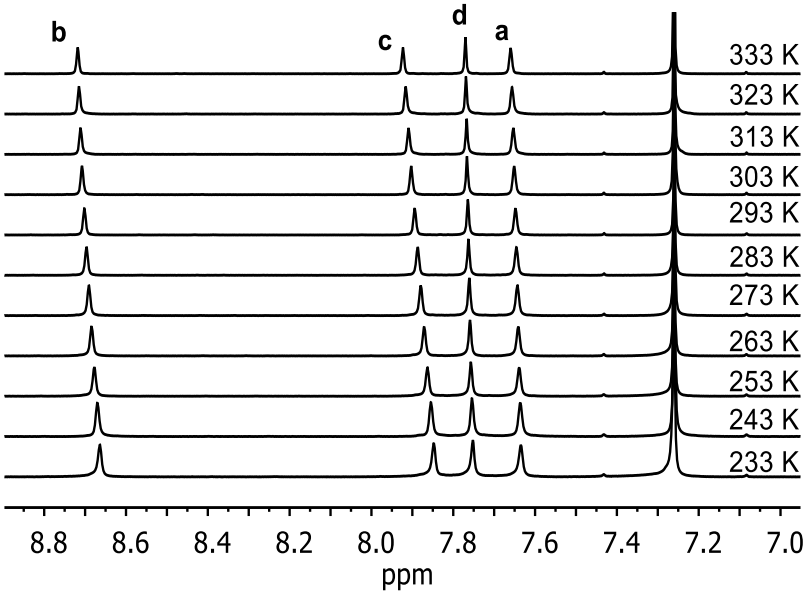

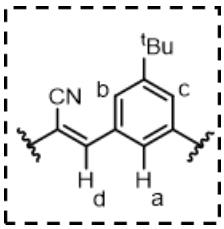

Figure S63: VT ^{1}H NMR spectra ($CDCl_3$) of **CS**.

VT ^{1}H NMR spectra of CS – PP complexes

General procedure. 25 µL of a 20 mM **CS** stock solution (in $CDCl_3$) and 40 µL of a 25 mM stock solution of the corresponding pyrophosphonate (in $CDCl_3$) were diluted to obtain a total volume of 500 µL (1 mM **CS** + 2 mM **PP**). VT ^{1}H NMR spectra (number of scans = 16, delay = 1s) were measured starting from the lower temperature. The temperature was equilibrated for 5 min before each measurement. Signals of the free and the perched **CS** are depicted in cyan and aromatic signals of the pyrophosphonates are grey. The signals of the [2]pseudorotaxane are blue and the meso and chiral signals (see Fig. S67) of [3]pseudorotaxane are depicted in green.

VT NMR spectra of the CS / homoallyl-PP 1 complex

Note: Study was performed in DCM-d_2 rather than $CDCl_3$.

At lower temperatures the d and a signal of [2]pseudorotaxane (blue) sharpen up (see magnification), indicating fast exchange on the NMR time scale at room temperature (where the signals are broad). Most of the **CS** is bound in the [3]pseudorotaxane (green), where only the d and a signal sharpen upon warming, while the b and c signals remain mostly unchanged.

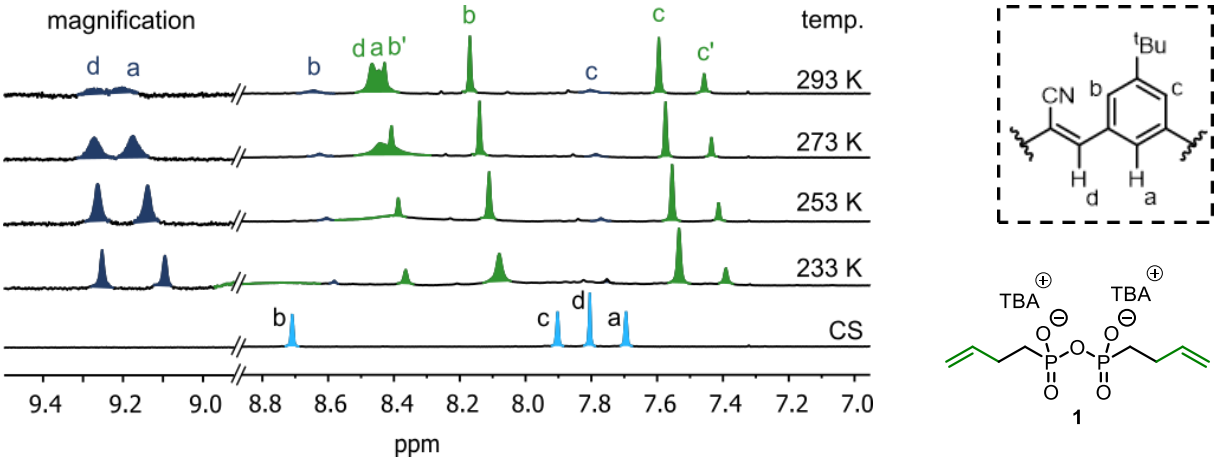

Figure S64: VT NMR spectra (DCM-d_2) of a mixture of **CS** and homoallyl-PP **1**.

VT NMR spectra of the CS / F-benzyl-PP 3 complex

The signals of the [2]pseudorotaxane (blue) shift upon temperature variation (especially signal a), but do not change otherwise. At higher temperatures (333 K) the perched interaction is (mostly) overcome and only four signals of the free **CS** remain (cyan). At 233 K, on the other hand, all these signals split into two, indicating that the perched interaction is slowed down with reference to the NMR time scale.

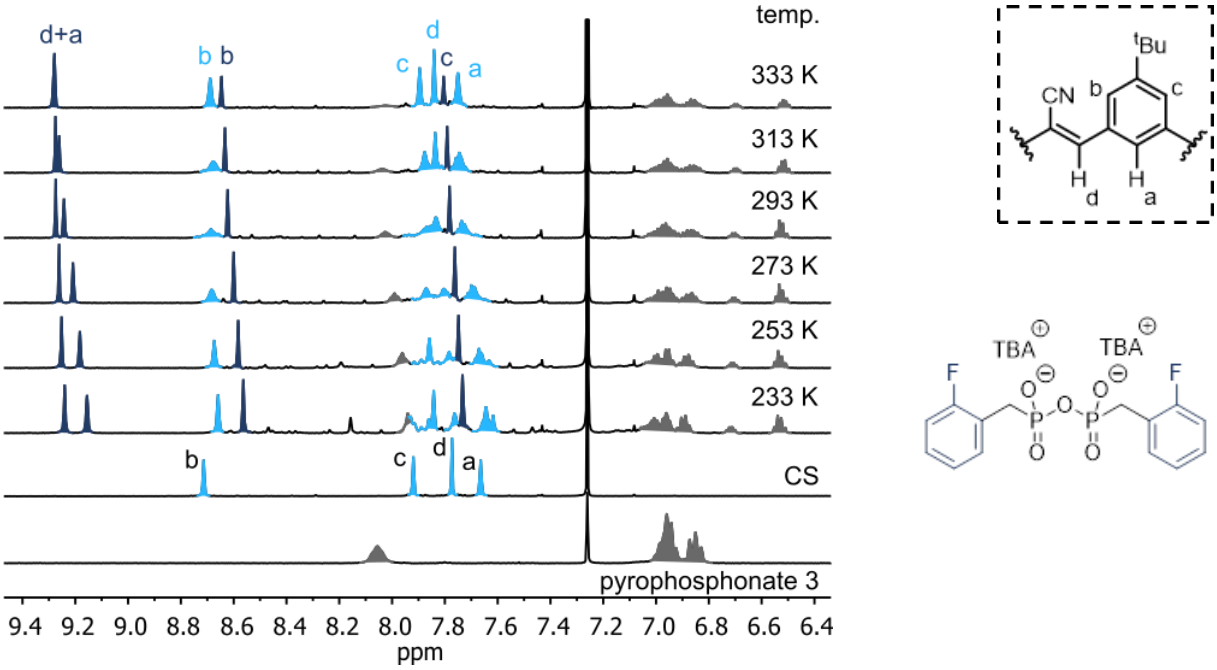

Figure S65: VT NMR spectra ($CDCl_3$) of a mixture of **CS** and F-benzyl-PP **3**.

VT NMR of CS with Cl-benzyl-PP 4

VT NMR was performed in $CDCl_3$ up to 333 K and in $C_2D_2Cl_4$ up to 403 K. Only the broad signals of the free and perched **CS** (cyan), that sharpen as the weak perched interaction is overcome, can be observed. This indicates that even at higher temperatures threading is not occurring.

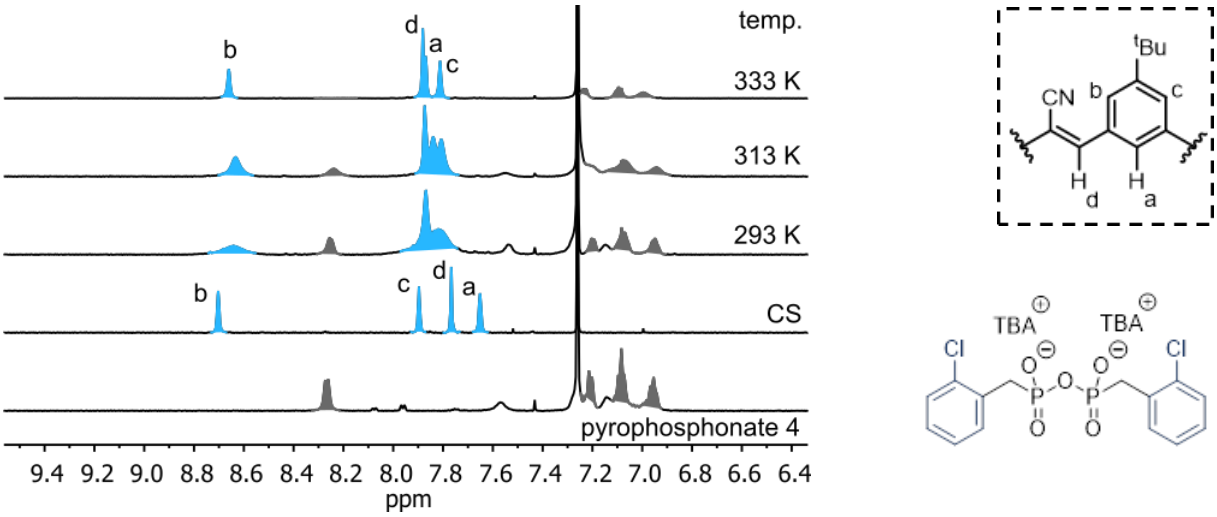

Figure S66: VT NMR spectra ($CDCl_3$) of a mixture of **CS** and Cl-benzyl-PP **4**. No threading was observed.

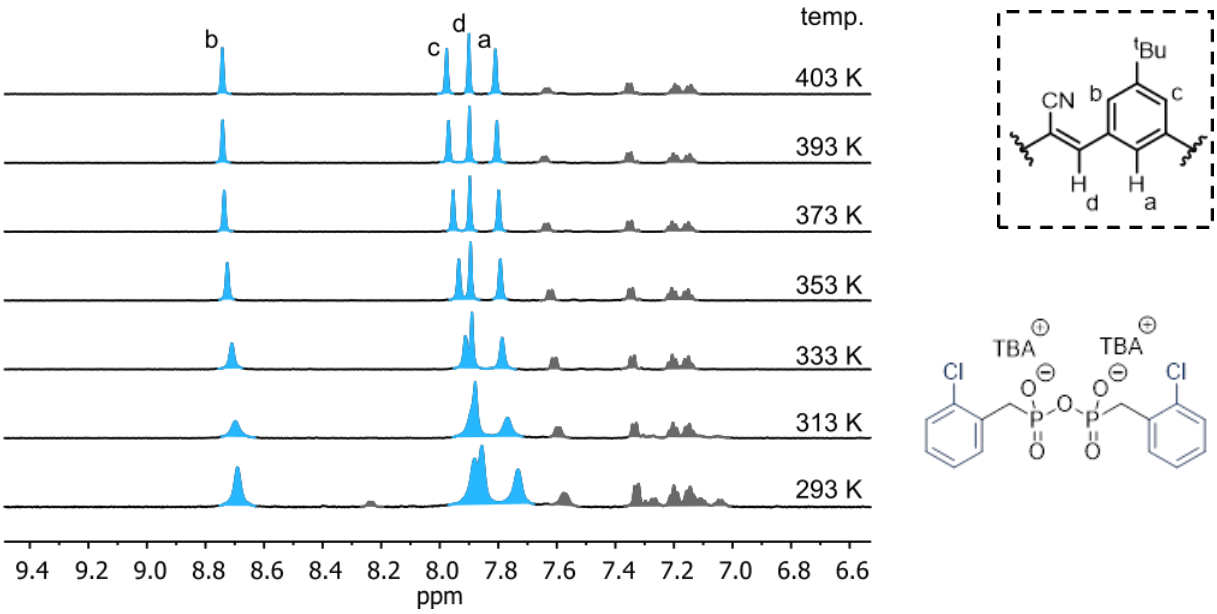

Figure S67: VT NMR spectra ($C_2D_2Cl_4$) of a mixture of **CS** and Cl-benzyl-PP **4**. No threading was observed.

VT NMR of CS with Me-benzyl-PP 5

Only the broad signals of the free and perched **CS** (cyan), that sharpen up as the perched interaction is reduced, can be observed. This indicates that even at higher temperatures threading is not occurring.

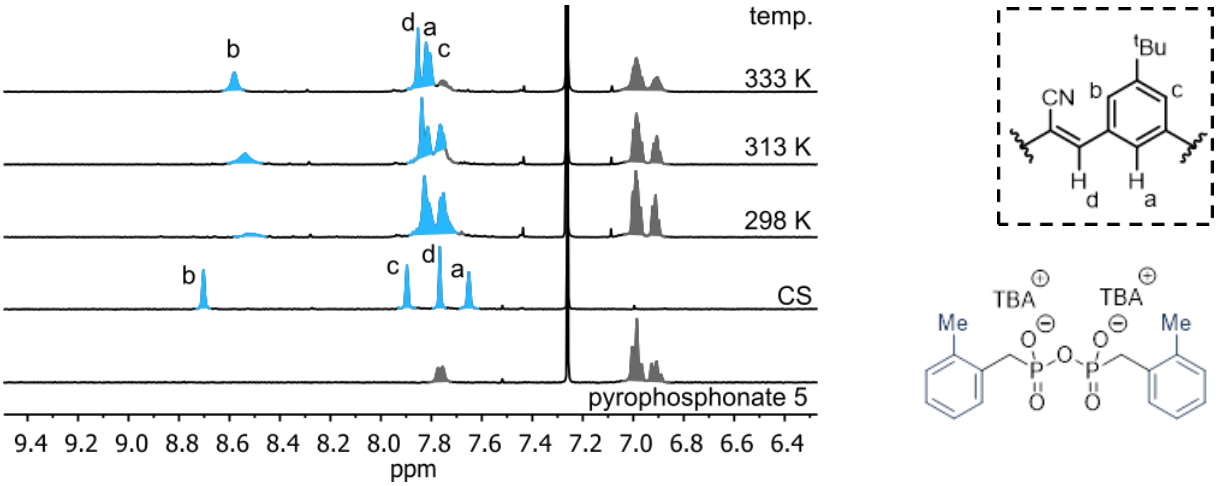

Figure S68: VT NMR ($CDCl_3$) of a mixture of **CS** and Me-benzyl-PP **5**. No threading was observed.

^{1}H NMR Titrations

12.5 µL of a 20 mM **CS** stock solution (in DCM-d_2) was diluted to 500 µL with DCM-d_2 to obtain a 0.5 mM solution (0.25 µmol **CS**). A freshly prepared stock solution of the corresponding pyrophosphonate (25 mM, DCM-d_2) was added in a stepwise titration (1 µL = 0.1 equiv.). The solutions were equilibrated according to their binding kinetics (see p. S47-49) before ^{1}H NMR spectra were measured (number of scans = 16, delay time = 1 s).

On one hand, the characteristic signals of the binding of **two CS** to the pyrophosphonate can be observed (depicted in green). They split into two sets of signals, because the **CS dimer** can arrange both in a chiral (‘) and in a *meso* isomer, as published previously[2,4] and depicted in Figure S67.

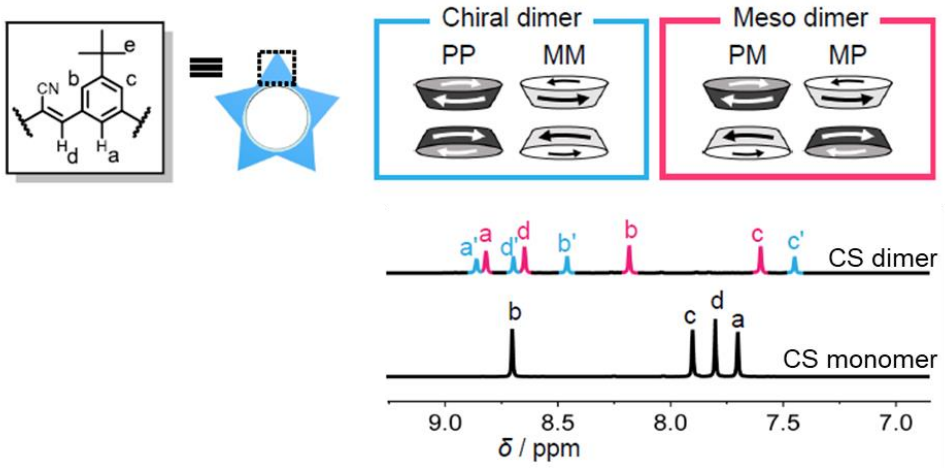

Figure S69: Visual representation of the formation of a chiral and a meso **CS** dimer and the resulting peaks in ^{1}H NMR spectra (DCM-d_2), compared to a free **CS** monomer. Adapted from Ref. [4].

On the other hand, a set of signals (depicted in blue) forms that corresponds to the binding of **one CS** on the pyrophosphonate (1:1 binding). The signals of free and perched cyanostar **CS** are depicted in cyan, aromatic signals of the pyrophosphonate are grey.

Additional data on the binding titration of CS to homoallyl-PP 1

To see, whether the equilibrium can be further pushed from the [3]pseudo- towards the [2]pseudorotaxane, more equivalents of homoallyl-PP **1** were added (as depicted in Fig. 2 of the manuscript). At 50 equiv. there is only little amount of the [3]pseudorotaxane left.

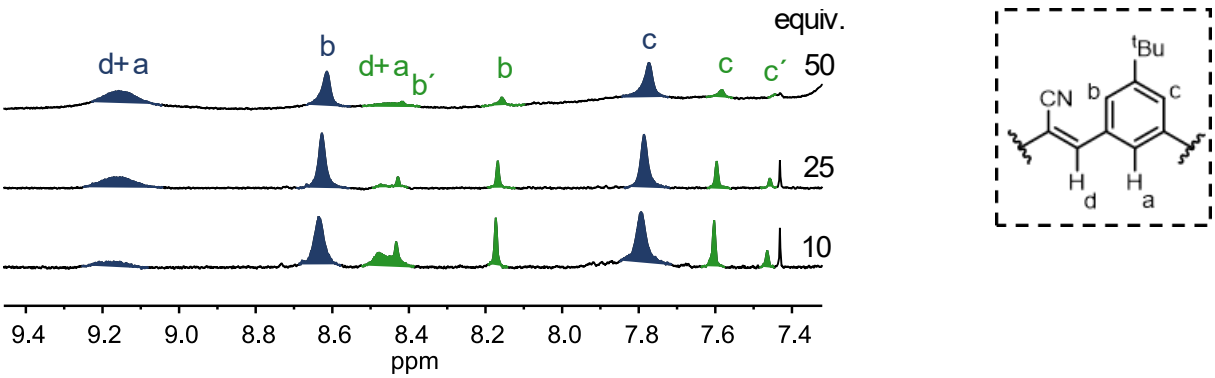

Figure S70: Additional data on the binding titration as depicted in Fig. 2 of the manuscript. Increasing the equivalents of homoallyl-PP **1**, further shifts the equilibrium from [3]pseudorotaxane (green) to [2]pseudorotaxane (blue).

While the addition **CS** to benzyl and F-benzyl PP **2** and **3** led to the formation of a 1:1 complex and a downfield shift of the corresponding ^{31}P NMR signal (see Fig. S77), an upfield shift of the ^{31}P NMR signal was observed upon formation of the 2:1 complex in case of homoallyl-PP **1**. The signal also broadened significantly, which is consistent with the broadening of the inner protons of the cyanostar macrocycle in the ^{1}H NMR spectrum (see Fig. 2B in the manuscript).

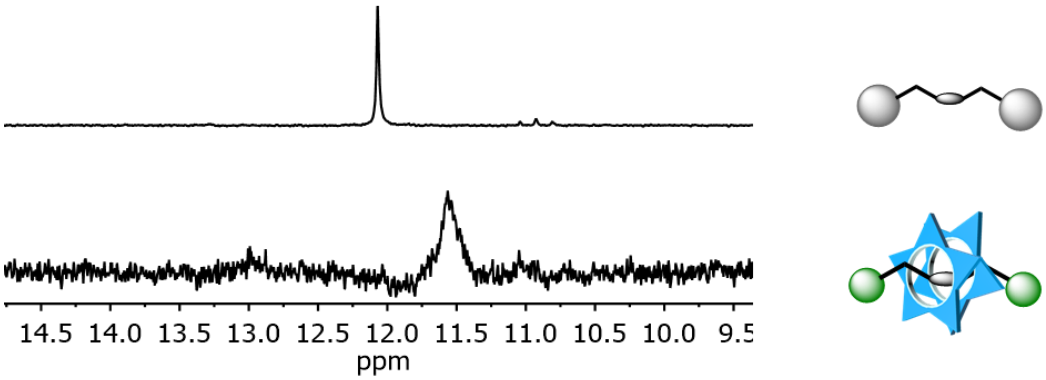

Figure S71: ^{31}P NMR (243 MHz, $CDCl_3$, 298 K) of free homoallyl-PP **1** and the 2:1 complex with **CS**.

Water-Sensitivity of binding

The free energy of hydration of phosphates is reported to be relatively high, compared to other anions.[5] It is likely that this is also true for pyrophosphonates. At the same time, binding of **CS** to pyrophosphonates is governed by hydrogen bonding. This experiment shows whether competitive hydrogen bonding of water interferes with the binding investigated in this study.

A 1 mM solution of **CS** and 2 equiv. F-benzyl-PP **3** (dried under vacuum for 48 h) was prepared in $CDCl_3$ (500 µL, stored over molecular sieves) and equilibrated for 15 min. A ^1H NMR spectrum was measured before and after addition of 10 µL (2% v.v.) of water (saturating chloroform).

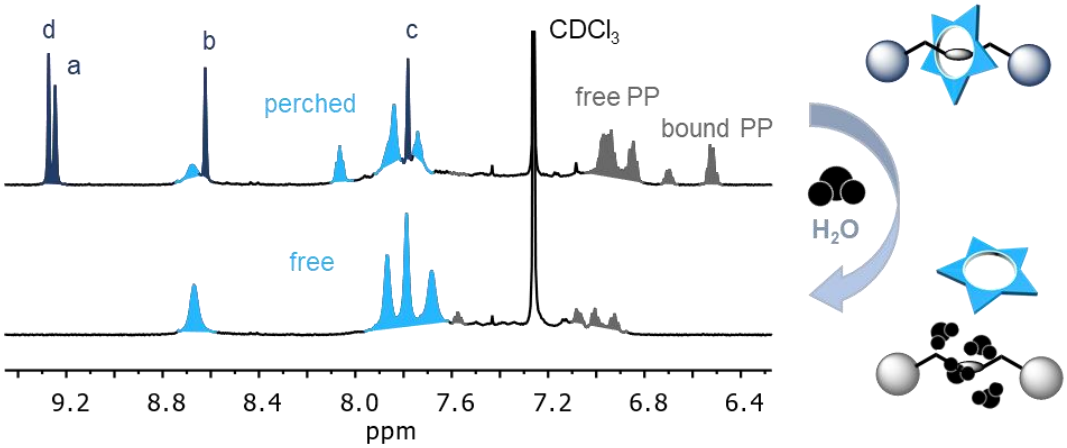

Figure S72: ^1H NMR spectra (in $CDCl_3$) of typical 1:1 binding (blue signals) under anhydrous conditions and after addition of 2% v.v. of water, indicating that water is shutting down the binding completely.

NOESY NMR spectrum of [2]pseudorotaxane

A 2:1 mixture of F-benzyl-PP **3** (10 mM) and **CS** (5 mM) in $CDCl_3$ was prepared and equilibrated for 15 minutes. A ^1H-^1H-NOESY NMR spectrum (number of scans = 32, mixing time = 0.3 s) was measured.

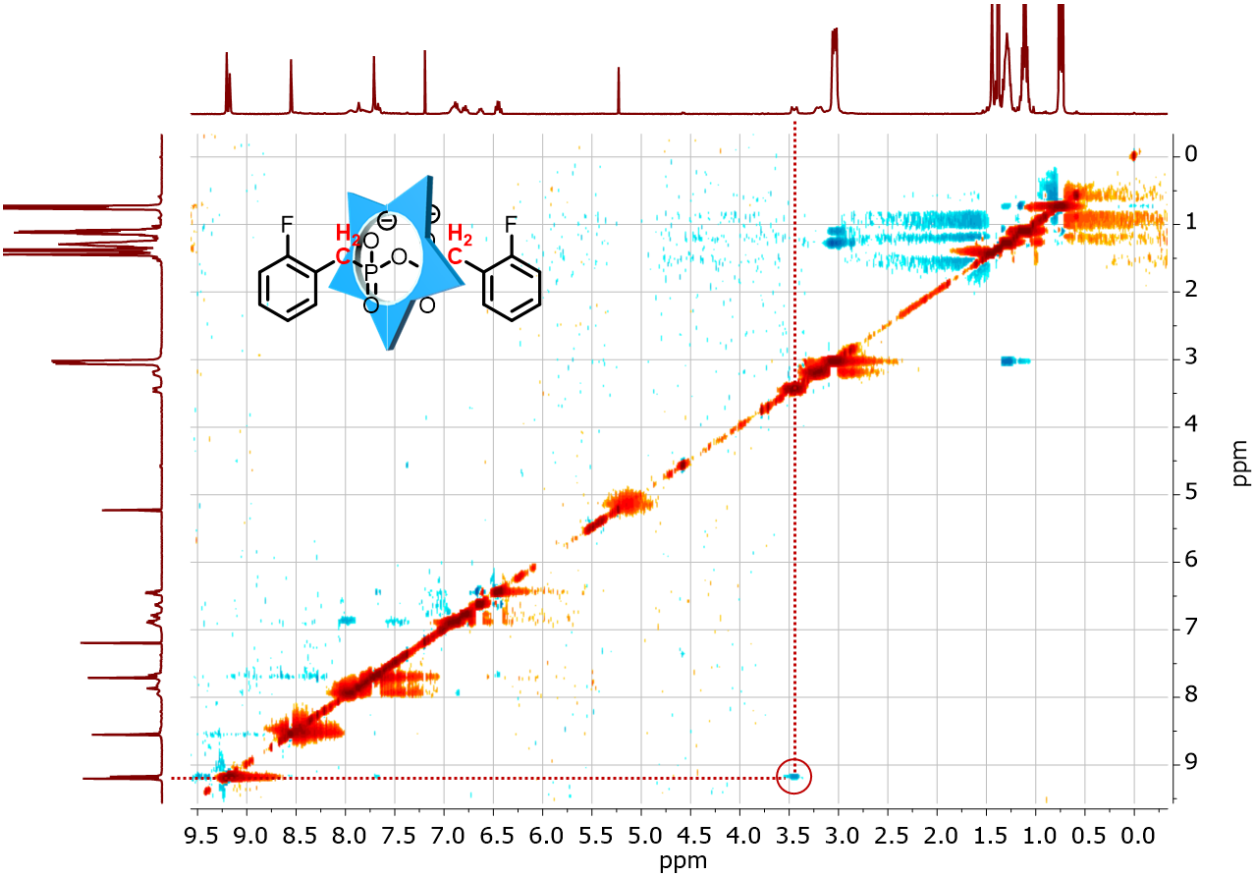

Figure S73: ^1H-^1H-NOESY spectrum of the [2]pseudorotaxane of F-benzyl-PP **3** and **CS**.

Conclusion: The cross peak between the d and a signals of the **CS** (~ 9.35 ppm) in the [2]pseudorotaxane and the benzyl signals of the bound pyrophosphonate (~ 3.45 ppm) corroborates the formation of the [2]pseudorotaxane.

Mass Spectrometry (MS) Experiments

A 200 µM solution of a 1:1 mixture of **CS** and the pyrophosphonate was prepared in HPLC-grade DCM and high-resolution mass spectrometry (HRMS) was measured with electrospray ionization (ESI) in the negative mode. Additional signals can be assigned as follows: 950.49 = CS + Cl^-; 1867.02 = 2 CS + Cl^-; 1877.05 = 2 CS + HCO_2^-; 1891.06 = 2 CS + OAc^-.

The measured isotopic patterns of the [3]pseudorotaxane (in case of homoallyl-PP **1**) and the [2]pseudorotaxane (in case of the F-benzyl-PP **3**) were compared to the calculation to corroborate their formation. mMass software[6] was used for the simulation of the isotopic patterns.

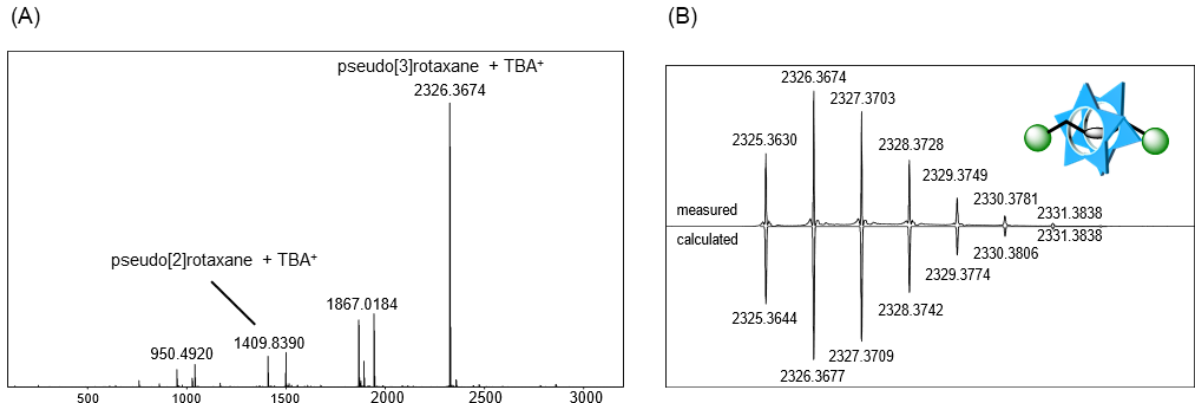

Figure S74: (A) Mass spectrum of a 1:1 mixture of homoallyl-PP **1** and **CS**. (B) Measured vs. calculated spectrum of the corresponding [3]pseudorotaxane (+TBA^+).

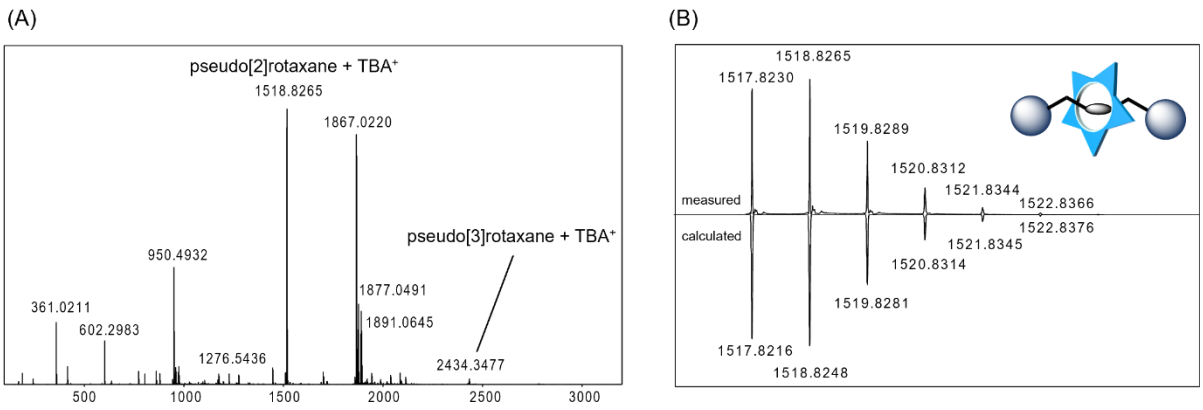

Figure S75: (A) Mass spectrum of a 1:1 mixture of F-benzyl-PP **3** and **CS**. (B) Measured vs. calculated spectrum of the corresponding [2]pseudorotaxane (+ TBA^+).

With [2]pseudorotaxane (H^+ instead of TBA^+) of **3** and **CS**, a 2D-MS experiment was performed. A collision voltage (0 – 30 V) was applied to the species in gas phase. With increasing collision voltage, the signal intensity (1276.54) reduces in favor of the free pyrophosphonate (361.02) as the **CS** is gradually slipped off. This behaviour is typical for a pseudorotaxane.

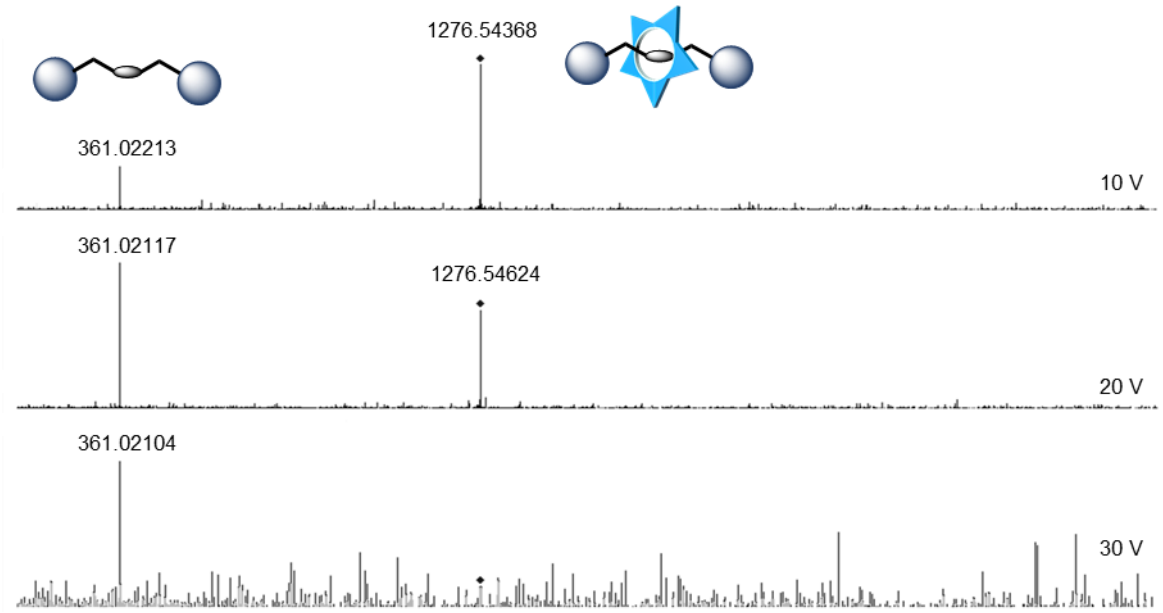

Figure S76: 2D-MS experiment with [2]pseudorotaxane of benzyl-PP **3** and **CS**. The signal of the [2]pseudorotaxane (1276.54) decreases with increasing collision voltage.

^{31}P NMR titrations and binding constants

Titrations of **CS** to the corresponding pyrophosphonate were performed. In all titration experiments, the peak of the free pyrophosphonate (G, grey) decreased upon addition of **CS** (H) in the ^{31}P NMR spectrum. It also broadend up, indicating the perched interaction which is fast on the NMR time scale. At the same time, a new peak (HG, blue) of the [2]pseudorotaxane increased. It is sharp, as the threading/dethreading is slow on the NMR time scale. The concentrations of free pyrophosphonate and [2]pseudorotaxane can be obtained by integration of the NMR peaks under the reasonable assumption that the **exchange is slow on the NMR time scale**. (We further assumed no further species, signal overlap or decomposition.) The concentration of the free **CS** can be calculated. According to the mass action law, the binding constants can be calculated as follows: $K_A = \frac{[HG]}{[G]*[H]} = \frac{[pseudorotaxane]}{[pyrophosphonate]*[CS]}$.

Binding constant of CS to benzyl-PP 2

500 µL of a 2.5 mM solution of benzyl-PP **2** was prepared in $CDCl_3$. ^{31}P NMR spectra (number of scans = 64, delay time = 3 s) were measured. A 50 mM solution of **CS** in $CDCl_3$ was added in a stepwise titration (5 µL = 0.2 eq **CS**). In $CDCl_3$ no formation of the [3]pseudorotaxane was observed (see Fig. S78), as the interaction between the pyrophosphonate and the TBA counterion is stronger in the less polar solvent $CDCl_3$, favoring the 1:1 binding mode. Furthermore, in the more polar solvent CD_2Cl_2, the cyanostar macrocycle is more prone to dimerize due to the solvophobic effect.

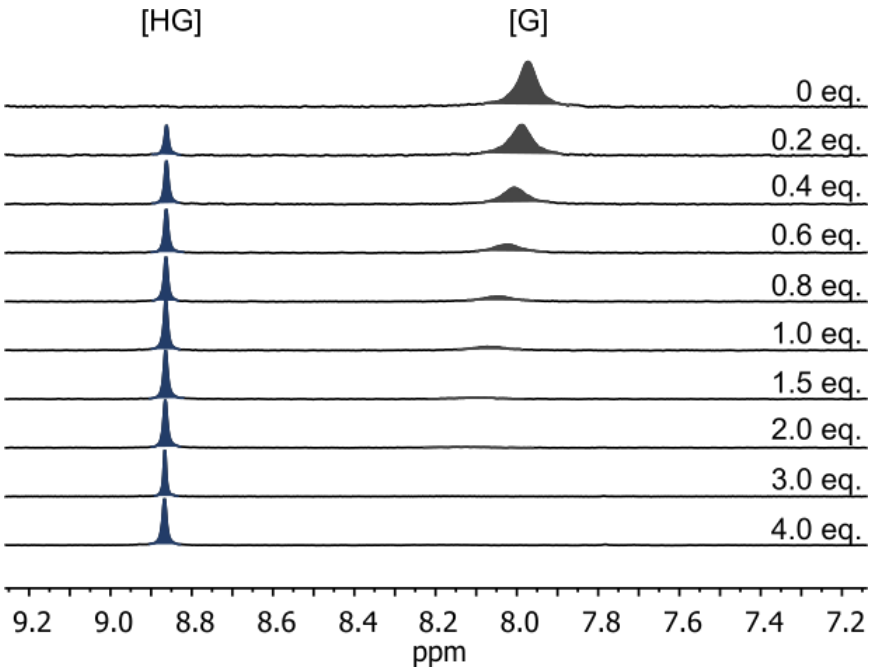

Figure S77: ^{31}P NMR titration of **CS** to pyrophosphonate **2** (2.5 mM, $CDCl_3$).

Table S1: ^{31}P NMR titration. Ratios of G and HG were determined by NMR integration, directly giving the amounts of G, HG and H and the corresponding concentrations by considering the total volume. K_A values were determined according to the mass action law.

Equiv. CS	**0.0**	**0.2**	**0.4**	**0.6**	**0.8**	**1.0**	**1.5**	**2.0**	**3.0**	**4.0**
Total volume	500	505	510	515	520	525	537,5	550	575	600
				free pyrophosphonate (G)						
Ratio	1.00	0.84	0.68	0.55	0.44	0.33	0.17	0.12	0.05	0.04
Amount [µmol]	1.25	1.05	0.85	0.68	0.55	0.41	0.21	0.14	0.07	0.05
Conc. [mM]	2.50	2.07	1.66	1.33	1.05	0.78	0.40	0.26	0.12	0.09
				[2]pseudorotaxane (HG)						
Ratio	0.00	0.16	0.32	0.45	0.56	0.67	0.83	0.89	0.95	0.96
Amount [µmol]	0.00	0.21	0.40	0.57	0.70	0.84	1.04	1.11	1.18	1.20
Conc. [mM]	0.00	0.41	0.79	1.10	1.35	1.60	1.93	2.01	2.06	1.99
				free CS (H)						
Amount [µmol]	0.00	0.05	0.10	0.18	0.30	0.41	0.84	1.39	2.57	3.81
Conc. [mM]	0.00	0.09	0.19	0.35	0.57	0.78	1.56	2.53	4.47	6.34
				K_A [M^{-1}]						
$\frac{[HG]}{[G] * [H]}$	-	2200	2440	2350	2260	2640	3110	3040	3920	3510

The last two data points were left out as the integration accuracy decreased. K_A was determined as the mean value of the first seven data points with the standard deviation as error to be:

K_A = 2.58 ± 0.34 • 10^3 M^{-1}

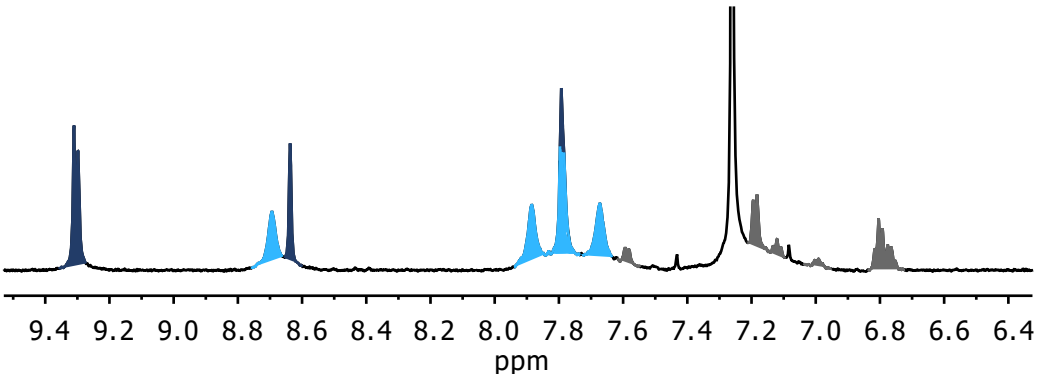

Figure S78: ^{1}H NMR spectrum of a mixture of 1 mM **CS** and 0.5 mM benzyl-PP **2** in $CDCl_3$ at 298 K. No signals of [3]pseudorotaxane are observed.

Binding constant of CS to F-benzyl-PP 3 (in $CDCl_3$)

500 µL of a 5.0 mM solution of F-benzyl-PP **3** was prepared in $CDCl_3$. ^{31}P NMR (number of scans = 64, delay time = 3 s) was measured. A 50 mM solution of **CS** in $CDCl_3$ was added in a stepwise titration (10 µL = 0.2 eq **CS**). The mixture was equilibrated for 15 min before measurement to allow the binding to equilibrate (compare Fig. S60).

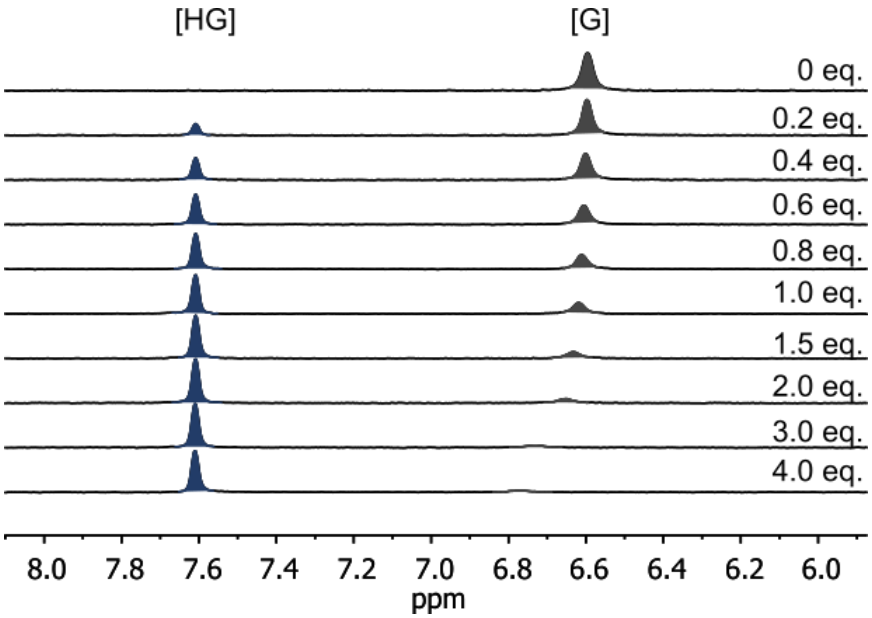

Figure S79: ^{31}P NMR titration of **CS** to F-benzyl-PP **3** (5.0 mM, $CDCl_3$).

Table S2: ^{31}P NMR titration in $CDCl_3$. Ratios of G and HG were determined by NMR integration, directly giving the amounts of G, HG and H and the corresponding concentrations by considering the total volume. K_A values were determined according to the mass action law.

Equiv. CS	**0.0**	**0.2**	**0.4**	**0.6**	**0.8**	**1.0**	**1.5**	**2.0**	**3.0**	**4.0**
Total volume	500	510	520	530	540	550	575	600	650	700
				free pyrophosphonate (G)						
Ratio	1.00	0.83	0.66	0.52	0.42	0.35	0.24	0.18	0.12	0.10
Moles [µmol]	2.50	2.08	1.65	1.31	1.05	0.87	0.59	0.46	0.30	0.24
Conc. [mM]	5.00	4.08	3.18	2.46	1.94	1.57	1.03	0.76	0.46	0.34
				[2]pseudorotaxane (HG)						
Ratio	0.00	0.17	0.34	0.48	0.58	0.65	0.76	0.82	0.88	0.91
Moles [µmol]	0.00	0.42	0.85	1.20	1.46	1.64	1.91	2.05	2.20	2.26
Conc. [mM]	0.00	0.82	1.63	2.25	2.69	2.97	3.32	3.41	3.39	3.23
				free CS (H)						
Moles [µmol]	0.00	0.08	0.15	0.31	0.55	0.87	1.84	2.96	5.30	7.74
Conc. [mM]	0.00	0.16	0.29	0.58	1.01	1.57	3.20	4.93	8.15	11.1
				K_A **[M^{-1}]**						
$\frac{[HG]}{[G] * [H]}$	-	1240	1750	1590	1380	1200	1010	913	908	862

The last two data points were left out as the integration accuracy decreased. K_A was determined as the mean value of the first seven data point with the standard deviation as error to be:

K_A = 1.30 ± 0.28 • 10^3 M^{-1}

Binding constant of CS to F-benzyl-PP 3 (in DCM-d_2)

500 µL of a 2.5 mM solution of F-benzyl-PP **3** was prepared in $CDCl_3$. ^{31}P NMR (number of scans = 64, delay time = 3 s) was measured. A 50 mM solution of **CS** in $CDCl_3$ was added in a stepwise titration (5 µL = 0.2 eq **CS**). The mixture was equilibrated for 15 min before measurement to allow the binding to equilibrate (compare Fig. S60).

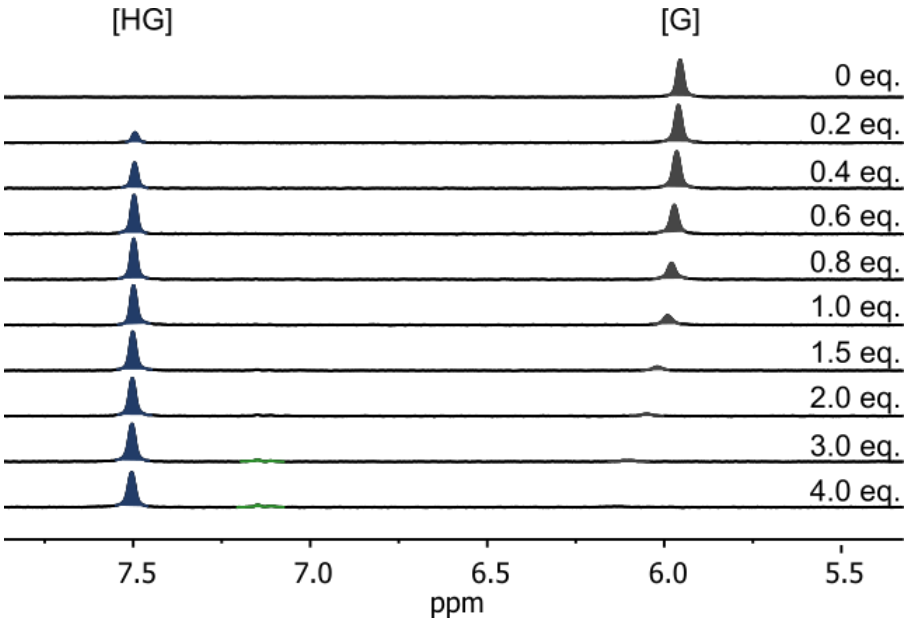

Figure S80: ^{31}P NMR titration of **CS** to F-benzyl-PP **3** (2.5 mM, DCM-d_2).

Table S3: ^{31}P NMR titration in DCM-d_2. Ratios of G and HG were determined by NMR integration, directly giving the amounts of G, HG and H and the corresponding concentrations by considering the total volume. K_A values were estimated according to the mass action law.

Equiv. CS	**0.0**	**0.2**	**0.4**	**0.6**	**0.8**	**1.0**	**1.5**	**2.0**	**3.0**	**4.0**
Total volume	500	505	510	515	520	525	537.5	550	575	600
				free pyrophosphonate (G)						
Ratio	1.00	0.83	0.65	0.49	0.36	0.26	0.12	0.08	-	-
Moles [µmol]	1.25	1.04	0.81	0.61	0.45	0.15	0.10	0.46	-	-
Conc. [mM]	2.50	2.05	1.59	1.19	0.87	0.62	0.28	0.18	-	-
				[2]pseudorotaxane (HG)						
Ratio	0.00	0.17	0.35	0.51	0.64	0.74	0.88	0.92	-	-
Moles [µmol]	0.00	0.21	0.44	0.64	0.80	0.93	1.10	1.15	-	-
Conc. [mM]	0.00	0.82	1.63	2.25	2.69	2.97	3.32	3.41	-	-
				free CS (H)						
Moles [µmol]	0.00	0.04	0.06	0.11	0.20	0.33	0.78	1.35	-	-
Conc. [mM]	0.00	0.07	0.12	0.22	0.38	0.62	1.44	2.45	-	-
				K_A [M^{-1}]						
$\frac{[HG]}{[G] * [H]}$	-	2760	4390	4760	4620	4600	5090	4690	-	-

The last two data points were left out as the integration accuracy decreased and small amounts of 2:1 binding were observed. K_A was determined as the mean value of the first seven data point with the standard deviation as error to be:

K_A = 4.42 ± 0.7 • 10^3 M^{-1}

DFT calculations

A restricted hybrid HF-DFT SCF calculation was performed using Pulay DIIS + Geometric Direct Minimization with a SPARTAN'20 Quantum Mechanics Driver Software on the RB3LYP function with a 6-31G(D) basis set for the optimized geometries.

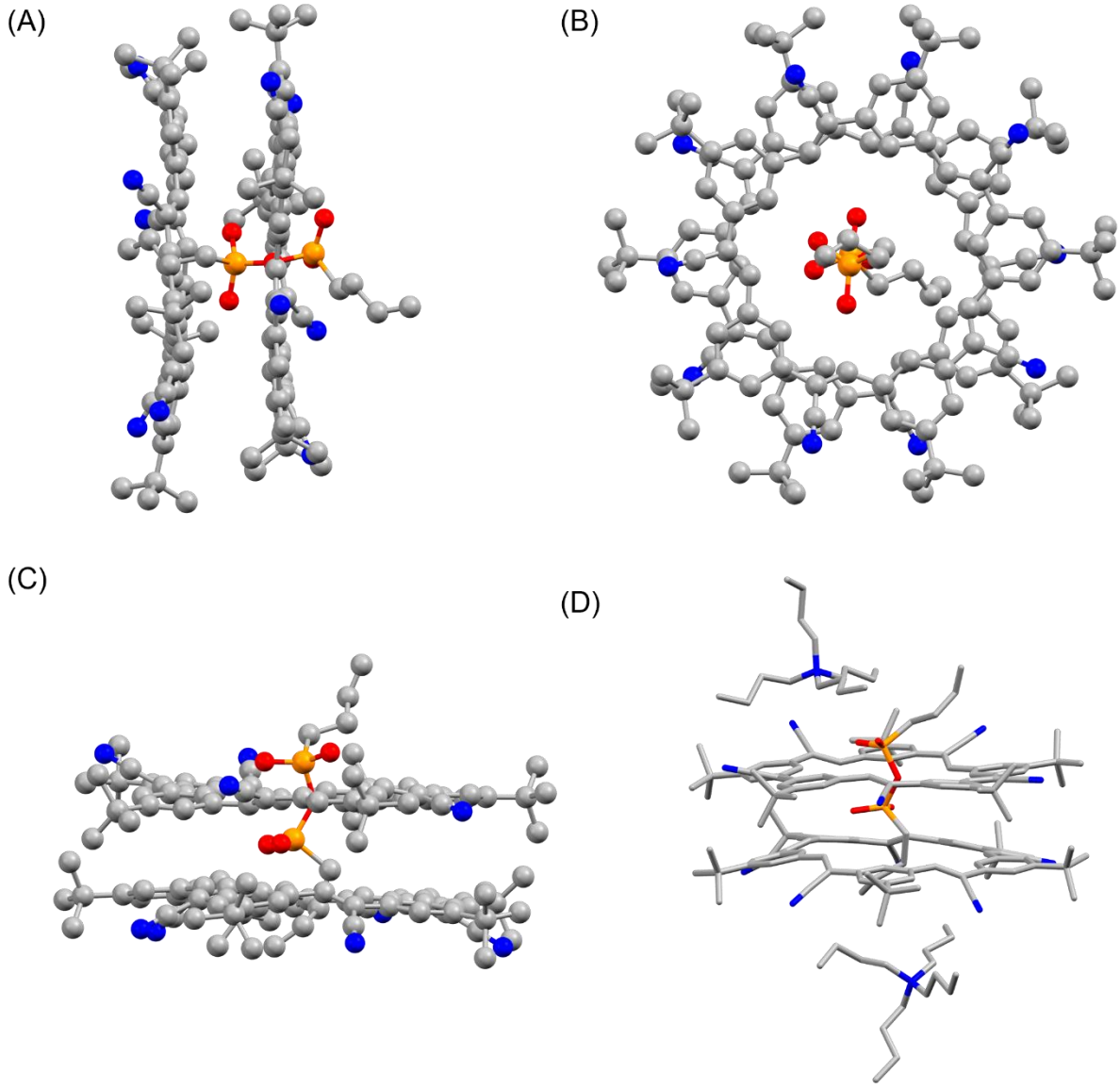

Figure S81: Additional images of [3]pseudorotaxane, assembled of 2x **CS** and homoallyl-PP **1**. Equilibrium geometries were optimized using density functional theory (RB3LYP/6-31G(D), gas phase). Hydrogen atoms and TBA counter ions were omitted for clarity. Color code: C (grey), N (blue), O (red), P (orange).

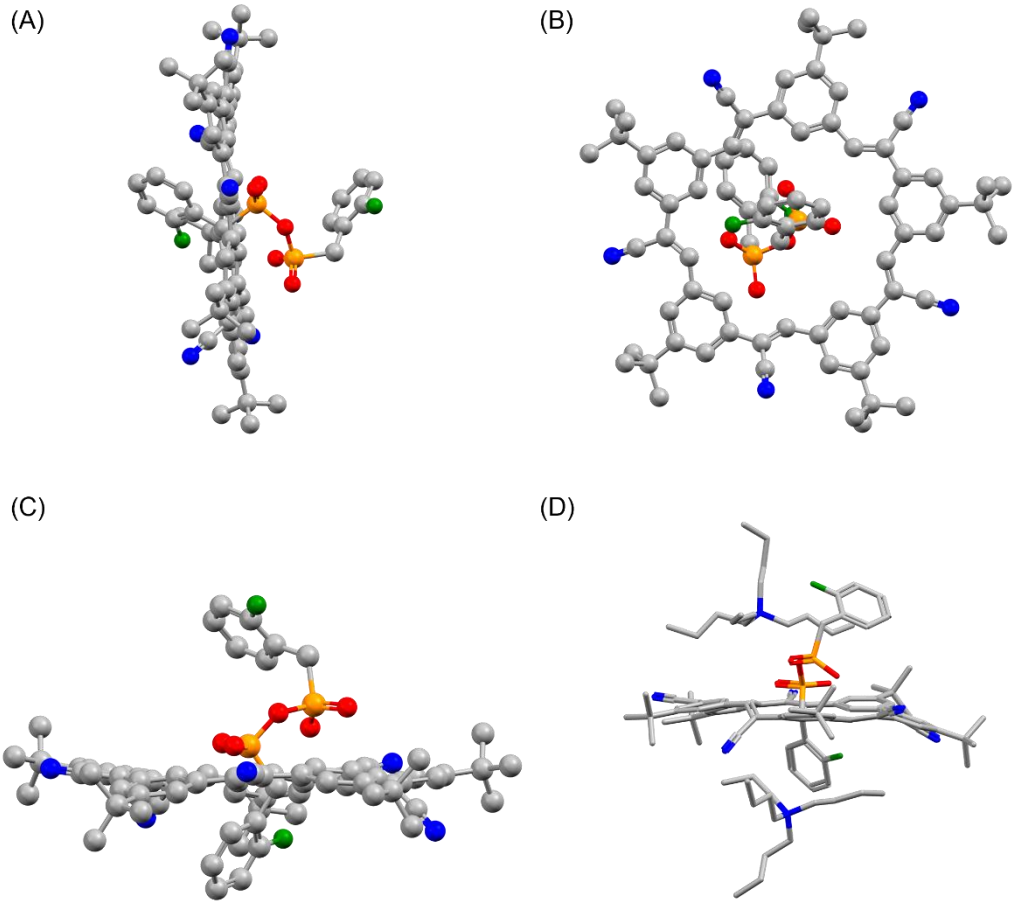

Figure S82: Additional images of [2]pseudorotaxane, assembled of **CS** and F-benzyl-PP **3**. Equilibrium geometries were optimized using density functional theory (RB3LYP/6-31G(D), gas phase). Hydrogen atoms and TBA counter ions were omitted for clarity. Color code: C (grey), N (blue), O (red), F (green), P (orange).

Table S4: Cartesian coordinates of the [3]pseudorotaxane (2x **CS** on homoallyl-PP **1**) in the gas phase, according to density functional theory (RB3LYP/6-31G(D), gas phase).

Atom	Cartesian Coordinates			Atom	Cartesian Coordinates		
H	5.59100	4.15000	-5.50900	H	6.35200	9.88300	3.17300
C	5.38200	3.60800	-4.59000	C	2.47500	6.94800	2.43900
C	4.16100	3.15300	-4.30400	H	1.70300	6.17400	2.43100
C	3.78700	2.39200	-3.06200	H	2.02800	7.85700	2.04200
C	2.66900	3.08800	-2.26500	C	3.01400	7.18200	3.86800
H	1.75000	3.16500	-2.85800	H	2.61500	8.14400	4.21400
H	2.97800	4.12000	-2.05800	H	4.10300	7.30900	3.86100
P	2.25100	2.37400	-0.61400	C	2.63300	6.10500	4.89500
O	1.44200	3.42200	0.13200	H	1.54100	6.00000	4.91200
O	3.49100	1.77800	0.02000	H	3.02100	5.12800	4.58300
O	1.24900	1.08900	-1.05100	C	3.14400	6.43000	6.30000
P	-0.21700	0.67400	-0.37400	H	2.86100	5.63900	7.00000
O	-0.16700	0.75400	1.14000	H	4.23800	6.51700	6.31700
O	-1.32200	1.36400	-1.15500	H	2.73100	7.37900	6.66700
C	-0.24400	-1.10600	-0.85400	N	-3.23500	-7.45600	0.77900
H	0.52100	-1.62400	-0.26400	C	-3.12300	-6.72500	-0.57100
H	0.05900	-1.18300	-1.90500	H	-3.49700	-7.44500	-1.30500
C	-1.62800	-1.76600	-0.67900	H	-2.05400	-6.59400	-0.75100
C	-2.11000	-1.93300	0.73700	C	-3.85800	-5.39700	-0.74700
H	-1.38400	-2.32300	1.44900	H	-3.42300	-4.60900	-0.12400
C	-3.34700	-1.67000	1.16700	H	-4.91300	-5.48700	-0.46500
H	-3.63100	-1.81500	2.20600	C	-3.80100	-4.96500	-2.22700
H	-4.10600	-1.24800	0.51300	H	-4.18000	-5.78200	-2.85700
H	3.34800	3.33400	-5.01100	H	-2.75800	-4.80500	-2.52700
H	6.22400	3.44300	-3.91900	C	-4.62200	-3.69900	-2.49200
H	-1.59000	-2.76800	-1.13400	H	-4.26600	-2.85500	-1.89100
H	-2.37300	-1.19600	-1.24600	H	-4.55600	-3.40600	-3.54400
H	4.66200	2.25600	-2.41800	H	-5.68000	-3.85600	-2.25400
H	3.45600	1.38800	-3.35000	C	-2.58200	-8.83800	0.60800
C	5.69100	-3.58000	-2.41200	H	-2.83000	-9.39300	1.51300
C	4.01000	-1.58400	-1.34600	H	-3.11000	-9.30700	-0.22600
C	5.75700	-3.22200	-1.06100	C	-1.07100	-8.90400	0.38900
C	4.76200	-2.92100	-3.22200	H	-0.75300	-8.35300	-0.50200
C	3.91900	-1.91400	-2.71400	H	-0.53700	-8.47200	1.24300
C	4.92400	-2.23300	-0.50800	C	-0.66400	-10.38500	0.23600
H	3.36100	-0.81000	-0.95000	H	-1.09000	-10.77700	-0.69800
C	4.97700	-1.94700	0.95600	H	-1.11300	-10.97100	1.05100
C	4.40600	-0.84700	1.52700	C	0.85200	-10.59300	0.23700
H	3.99200	-0.10500	0.84400	H	1.28800	-10.29300	1.19700
C	5.62900	-2.95700	1.73800	H	1.09300	-11.65100	0.08200
N	6.19200	-3.79500	2.32100	H	1.33800	-10.01000	-0.55000
C	4.50900	-0.74900	5.34500	C	-2.51100	-6.71000	1.91200
C	3.26500	0.53300	3.16500	H	-1.58800	-6.32300	1.47300
C	3.54900	0.25700	5.54100	H	-2.22900	-7.47900	2.63100

C	4.81800	-1.11700	4.03500	C	-3.26400	-5.59300	2.63700
C	4.19500	-0.49600	2.93200	H	-4.23400	-5.94700	3.00200
C	2.91300	0.90300	4.47200	H	-3.44800	-4.74400	1.97300
H	2.84200	1.04200	2.30500	C	-2.44000	-5.11000	3.85200
C	1.90900	1.97600	4.72800	H	-2.87800	-4.16700	4.19700
C	0.99100	2.37800	3.80500	H	-1.42100	-4.86600	3.52900
H	0.99100	1.85500	2.85000	C	-2.39200	-6.09500	5.02700
C	1.98500	2.58900	6.02300	H	-1.94800	-7.06000	4.75300
N	2.08200	3.05600	7.08700	H	-1.78100	-5.68700	5.83700
C	-1.41000	5.09500	5.01300	H	-3.39800	-6.28900	5.42000
C	-0.39100	3.98700	2.62400	C	-4.71400	-7.68300	1.09100
C	-1.75300	5.62700	3.75700	H	-5.11600	-8.18300	0.20500
C	-0.53900	4.00200	5.04700	H	-5.16500	-6.69600	1.14500
C	0.00600	3.46300	3.86300	C	-5.03700	-8.49300	2.36500
C	-1.28200	5.06900	2.56000	H	-5.77500	-7.92400	2.94200
H	0.04600	3.57000	1.72000	H	-4.16200	-8.56900	3.02000
C	-1.72500	5.60700	1.24100	C	-5.61000	-9.89300	2.09000
C	-1.73100	4.84400	0.11400	H	-6.50000	-9.79100	1.45500
H	-1.36500	3.82800	0.22500	H	-4.89100	-10.48900	1.51200
C	-2.11100	6.98800	1.22300	C	-5.98000	-10.63900	3.37400
N	-2.38600	8.12100	1.24900	H	-6.42000	-11.61500	3.14600
C	-3.35100	6.42200	-2.95800	H	-5.10200	-10.81000	4.00700
C	-1.57900	4.34800	-2.25600	H	-6.71100	-10.07400	3.96400
C	-2.75700	5.60700	-3.93600	C	-5.91200	3.98200	1.47000
C	-3.02200	6.19100	-1.62100	C	-4.09500	2.08000	0.45800
C	-2.12800	5.16400	-1.25700	C	-5.96400	3.57000	0.13300
C	-1.87700	4.56700	-3.60700	C	-4.95500	3.39000	2.30300
H	-0.92400	3.54200	-1.94900	C	-4.05600	2.42500	1.82100
C	-1.26900	3.71800	-4.67100	C	-5.06200	2.62700	-0.39200
C	-0.71400	2.49900	-4.41800	H	-3.36900	1.37100	0.08000
H	-0.77000	2.15700	-3.38600	C	-5.17800	2.18900	-1.81500
C	-1.26600	4.29100	-5.98700	C	-4.16900	1.57700	-2.49700
N	-1.29100	4.79500	-7.03700	H	-3.22300	1.47200	-1.96600
C	0.63000	0.68900	-7.49800	C	-6.47100	2.39500	-2.40600
C	0.87600	0.66600	-4.69100	N	-7.53400	2.58300	-2.84600
C	1.51700	-0.18100	-6.85400	C	-5.06300	0.63300	-6.09200
C	-0.12300	1.56200	-6.70600	C	-3.20400	-0.02200	-4.08300
C	0.00000	1.57800	-5.30700	C	-4.12800	-0.39000	-6.28000
C	1.66000	-0.21000	-5.45400	C	-5.07700	1.29400	-4.85900
H	0.94900	0.68900	-3.60900	C	-4.17300	0.96800	-3.83300
C	2.65600	-1.13100	-4.83100	C	-3.19000	-0.73700	-5.28900
C	2.93500	-1.16400	-3.49500	H	-2.46100	-0.20100	-3.31400
C	3.35800	-1.97700	-5.75400	C	-2.23800	-1.86000	-5.53900
N	3.89400	-2.65300	-6.53600	C	-1.37800	-2.35500	-4.60400
C	-1.98400	5.73500	6.29100	H	-1.42700	-1.87100	-3.63500
C	5.17800	-1.40400	6.56800	C	-2.31100	-2.46000	-6.84200
C	-4.34000	7.52000	-3.38900	N	-2.40100	-2.93700	-7.90100

C	0.47800	0.73600	-9.03100	C	0.87100	-5.26000	-5.68600
C	6.58900	-4.67400	-3.02100	C	0.04900	-3.89700	-3.37600
C	-0.99400	0.46200	-9.42000	C	1.29800	-5.67000	-4.41100
H	-1.30900	-0.54100	-9.11000	C	0.01000	-4.16200	-5.77500
H	-1.67800	1.18800	-8.96800	C	-0.43100	-3.47400	-4.62600
H	-1.11100	0.53000	-10.50900	C	0.91400	-4.98900	-3.24800
C	1.36300	-0.30400	-9.74300	H	-0.28000	-3.36600	-2.49200
H	1.11500	-1.32800	-9.44100	C	1.39700	-5.42800	-1.90400
H	1.21000	-0.23400	-10.82600	C	1.47100	-4.59800	-0.82700
H	2.42900	-0.13800	-9.55000	H	1.17900	-3.57100	-1.02000
C	0.88400	2.14500	-9.52700	C	1.73400	-6.81700	-1.80400
H	0.26600	2.93100	-9.08100	N	1.97300	-7.95700	-1.77300
H	1.93000	2.36000	-9.27900	C	2.96200	-6.09800	2.35000
H	0.77400	2.20900	-10.61700	C	1.32000	-3.96400	1.53200
H	-0.82400	2.23600	-7.18200	C	2.38600	-5.21900	3.28100
H	2.12000	-0.85700	-7.44800	C	2.67100	-5.90300	0.99700
C	-5.52400	6.87400	-4.14800	C	1.83900	-4.84800	0.57000
H	-6.24900	7.64000	-4.44700	C	1.57400	-4.14000	2.89900
H	-5.19300	6.35800	-5.05600	H	0.68700	-3.14800	1.20300
H	-6.04400	6.14200	-3.51800	C	0.94800	-3.26500	3.93800
C	-3.61900	8.52100	-4.32300	C	0.46200	-2.01100	3.70700
H	-2.79400	9.02000	-3.80000	H	0.61200	-1.60500	2.70900
H	-3.20500	8.03000	-5.20900	C	0.79100	-3.89700	5.21700
H	-4.31800	9.29300	-4.66600	N	0.67200	-4.47300	6.22300
C	-4.90600	8.30200	-2.18900	C	-1.19600	-0.39400	6.74100
H	-5.59000	9.08000	-2.54600	C	-1.20600	-0.24900	3.92300
H	-4.11900	8.79300	-1.60600	C	-2.09400	0.43600	6.05700
H	-5.47300	7.65200	-1.51200	C	-0.33000	-1.18900	5.98200
C	-1.46800	7.19100	6.39800	C	-0.33600	-1.14000	4.57700
H	-1.74300	7.78700	5.52100	C	-2.11700	0.52400	4.65300
H	-1.89300	7.68100	7.28300	H	-1.15700	-0.17500	2.84300
H	-0.37600	7.21200	6.49400	C	-3.12500	1.38700	3.96900
C	-1.56100	4.98000	7.56500	C	-3.07700	1.70400	2.64400
H	-0.47300	4.95800	7.69500	C	-4.21800	1.81500	4.79500
H	-1.99200	5.47500	8.44300	N	-5.08000	2.13600	5.51200
H	-1.92400	3.94500	7.55900	C	1.33600	-6.03800	-6.93100
C	-3.53000	5.74700	6.23200	C	-6.07200	1.04500	-7.18000
H	-3.93800	6.19800	7.14500	C	3.84800	-7.25600	2.84700
H	-3.90100	6.33200	5.38400	C	-1.15300	-0.47900	8.27900
H	-3.93200	4.73200	6.14800	C	-6.87300	5.03800	2.04900
C	5.89100	-0.31900	7.40900	C	-1.49800	-1.92300	8.71600
H	6.36500	-0.77100	8.28900	H	-2.51100	-2.19700	8.39800
H	6.67200	0.18200	6.82500	H	-0.80400	-2.65600	8.29200
H	5.19600	0.44900	7.76600	H	-1.45200	-2.00800	9.80800
C	4.09800	-2.09100	7.43700	C	-2.15200	0.48100	8.95000
H	3.34700	-1.37800	7.79600	H	-3.18800	0.26100	8.66900
H	4.55700	-2.55700	8.31800	H	-2.07800	0.38400	10.03900

H	3.57300	-2.87500	6.87800	H	-1.94400	1.52700	8.69800
C	6.22000	-2.46400	6.16800	C	0.26700	-0.12000	8.77800
H	7.03700	-2.03400	5.57800	H	1.02200	-0.80500	8.37700
H	5.78000	-3.27900	5.58400	H	0.54900	0.89900	8.48700
H	6.66100	-2.90400	7.07000	H	0.30900	-0.18500	9.87200
C	5.70100	-5.83400	-3.53200	H	0.37100	-1.84100	6.48700
H	5.00000	-5.50200	-4.30400	H	-2.79700	1.03800	6.61900
H	5.11900	-6.27300	-2.71300	C	2.94000	-8.30500	3.53300
H	6.32500	-6.62500	-3.96400	H	3.54300	-9.14000	3.91000
C	7.58900	-5.24900	-2.00100	H	2.39600	-7.87200	4.38000
H	7.08500	-5.71600	-1.14700	H	2.20200	-8.71100	2.82900
H	8.27000	-4.48100	-1.61600	C	4.89300	-6.74400	3.86500
H	8.19900	-6.02000	-2.48400	H	5.50800	-5.95100	3.43200
C	7.39100	-4.08400	-4.20500	H	4.42800	-6.35700	4.77800
H	8.02000	-3.24900	-3.87600	H	5.54800	-7.57100	4.16400
H	8.04500	-4.85100	-4.63800	C	4.60900	-7.93800	1.69200
H	6.73800	-3.71500	-5.00300	H	5.24100	-8.73800	2.09400
H	4.69100	-3.19900	-4.26300	H	5.26200	-7.22800	1.17400
H	6.46400	-3.71900	-0.40800	H	3.93700	-8.39300	0.95600
H	5.56100	-1.88200	3.86100	C	2.87700	-6.17700	-6.93000
H	3.29100	0.55000	6.55300	H	3.24100	-6.73600	-6.06200
H	-0.28300	3.55200	5.99400	H	3.19900	-6.72200	-7.82600
H	-2.42300	6.48000	3.70500	H	3.36100	-5.19500	-6.93500
H	-3.47000	6.79600	-0.84500	C	0.92500	-5.33900	-8.24100
H	-2.99200	5.77700	-4.98200	H	1.35800	-4.33600	-8.31200
H	2.34900	-0.48600	-2.88000	H	1.29400	-5.91900	-9.09400
N	3.50500	6.50600	1.40300	H	-0.16200	-5.25300	-8.35000
C	2.80200	6.26300	0.05400	C	0.69300	-7.44500	-6.89900
H	2.17200	5.37600	0.20000	H	1.01400	-8.03000	-7.76900
H	3.60800	5.97400	-0.62500	H	0.98000	-8.00100	-5.99900
C	1.99700	7.40700	-0.55900	H	-0.40100	-7.37700	-6.92000
H	2.62700	8.27900	-0.77100	C	-5.92600	0.20600	-8.46400
H	1.19400	7.73600	0.11000	H	-6.66600	0.53700	-9.20200
C	1.36000	6.93300	-1.87900	H	-4.93500	0.31700	-8.91800
H	0.75100	6.04400	-1.68300	H	-6.09900	-0.86000	-8.28000
H	2.15200	6.62100	-2.57400	C	-7.51000	0.85600	-6.63900
C	0.49900	8.01800	-2.53000	H	-7.70000	-0.19600	-6.39600
H	1.09100	8.91000	-2.77400	H	-8.24100	1.16500	-7.39700
H	0.05000	7.64900	-3.45700	H	-7.69500	1.44600	-5.73600
H	-0.31700	8.32400	-1.86600	C	-5.85100	2.53200	-7.54500
C	4.07500	5.14800	1.85500	H	-4.83400	2.70100	-7.92000
H	4.46600	5.32100	2.86000	H	-6.00300	3.19200	-6.68300
H	3.21700	4.47400	1.91200	H	-6.55700	2.83800	-8.32700
C	5.15900	4.52000	0.97800	C	-7.70400	4.39800	3.18700
H	4.72500	4.13800	0.05100	H	-7.07200	4.02500	4.00000
H	5.94500	5.24100	0.72000	H	-8.29400	3.55300	2.81200
C	5.79300	3.33300	1.72600	H	-8.39600	5.13500	3.61000

H	4.99600	2.65000	2.04000
H	6.29400	3.70000	2.63400
C	6.78300	2.56300	0.85000
H	7.58300	3.21500	0.47400
H	7.25200	1.74800	1.41200
H	6.25800	2.12400	-0.00300
C	4.65400	7.50700	1.27300
H	5.10700	7.31200	0.29800
H	5.38700	7.22600	2.03100
C	4.32600	8.99600	1.41000
H	3.95800	9.21400	2.41900
H	3.53700	9.29000	0.71400
C	5.57100	9.86500	1.13400
H	5.24500	10.91200	1.12800
H	5.94300	9.65800	0.12100
C	6.70800	9.70500	2.15100
H	7.16000	8.70600	2.12400
H	7.50900	10.42300	1.94900
C	-7.84700	5.59100	0.99100
H	-8.49200	4.80900	0.57600
H	-7.31800	6.07400	0.16100
H	-8.49500	6.34400	1.45200
C	-6.05800	6.22500	2.61500
H	-5.45500	6.70400	1.83600
H	-6.73500	6.98100	3.03200
H	-5.38100	5.91200	3.41700
H	-4.89600	3.69500	3.34000
H	-6.71100	3.99200	-0.53000
H	-5.79400	2.08700	-4.69600
H	-4.11800	-0.93200	-7.21700
H	-0.32400	-3.82900	-6.74500
H	1.95800	-6.52700	-4.32100
H	3.11200	-6.55400	0.25500
H	2.58200	-5.36700	4.33700
H	-2.21900	1.33400	2.08500

Table S5: Cartesian coordinates of the [2]pseudorotaxane (1 x **CS** on F-benzyl-PP **3**) in the gas phase, according to density functional theory (RB3LYP/6-31G(D), gas phase).

Atom	Cartesian Coordinates			Atom	Cartesian Coordinates		
H	3.78700	6.03800	-3.26400	H	1.85000	-2.82500	7.89800
C	3.44900	5.06100	-3.59400	C	2.49000	-4.85600	6.14600
C	2.65100	2.50200	-4.37200	H	1.40700	-4.77000	6.29800
C	2.65400	4.89800	-4.72900	H	2.88700	-5.53700	6.91000
C	3.81800	3.93100	-2.87600	H	2.65400	-5.31500	5.16600
C	3.46200	2.63000	-3.23200	C	4.69500	-3.63200	6.06600
C	2.24800	3.61600	-5.10800	H	5.20700	-2.66500	6.12600
H	2.32500	1.50600	-4.65300	H	4.93900	-4.08000	5.09700
H	2.35200	5.76700	-5.30700	H	5.10800	-4.28400	6.84500
H	1.61600	3.48100	-5.98000	C	3.18500	-7.35400	-3.95600
F	4.57500	4.12600	-1.74500	H	2.57100	-6.89900	-4.74000
C	3.96800	1.43400	-2.47000	H	2.51300	-7.84000	-3.23700
H	4.63800	1.74100	-1.66500	H	3.80200	-8.13300	-4.42200
H	4.56300	0.80100	-3.14100	C	4.97500	-7.03400	-2.23300
P	2.72900	0.24600	-1.77000	H	4.38500	-7.55900	-1.47300
O	3.50500	-0.75800	-0.94800	H	5.65300	-6.34100	-1.72300
O	1.75300	-0.18700	-2.83700	H	5.58900	-7.77900	-2.75100
O	1.90800	1.20900	-0.65900	C	5.00000	-5.63700	-4.30500
P	0.29300	1.41800	-0.39700	H	5.65300	-4.89500	-3.83200
O	0.24200	1.94300	1.04000	H	5.63400	-6.39300	-4.78700
O	-0.37300	2.20200	-1.49600	H	4.42900	-5.13100	-5.09000
C	-0.38800	-0.30700	-0.40200	H	2.34500	-4.62600	-4.47300
H	0.13700	-0.87500	0.37600	H	3.84300	-5.57100	-0.56100
H	-0.09600	-0.72000	-1.36500	H	3.32300	-3.78400	3.56300
C	-1.88000	-0.41200	-0.19600	H	1.74100	-1.09300	6.49000
C	-4.69100	-0.64900	0.18100	H	-1.30200	2.45900	6.36300
C	-2.52900	0.15500	0.91500	H	-3.68600	5.41500	4.36900
C	-2.70700	-1.10400	-1.08500	H	-4.20600	6.41600	-0.37300
C	-4.08200	-1.23300	-0.92900	H	-4.45300	5.06700	-4.43100
C	-3.90700	0.04300	1.10700	H	-0.01800	-1.99000	-2.98000
H	-5.76600	-0.72800	0.31400	N	2.72000	4.81200	1.69200
H	-1.92700	0.70300	1.62900	C	1.90800	4.61000	0.39600
H	-4.65100	-1.77200	-1.68200	H	1.10500	3.92300	0.67100
H	-4.36700	0.50700	1.97500	H	2.57500	4.07100	-0.27400
F	-2.14900	-1.72700	-2.16700	C	1.36800	5.85700	-0.30500
C	3.19000	-5.23500	-2.59300	H	2.18800	6.44200	-0.74000
C	1.55300	-3.25300	-1.47500	H	0.83100	6.51600	0.38900
C	3.19400	-4.99700	-1.21200	C	0.39700	5.44700	-1.42700
C	2.35000	-4.45500	-3.40400	H	-0.41900	4.85500	-1.00500
C	1.52600	-3.45300	-2.86900	H	0.90200	4.77700	-2.13000
C	2.39500	-3.98900	-0.64400	C	-0.16800	6.65700	-2.17400
H	0.92700	-2.48600	-1.04200	H	0.62400	7.23400	-2.67000
C	2.40300	-3.71400	0.83100	H	-0.87700	6.33300	-2.94300
C	2.41000	-2.45600	1.36100	H	-0.70300	7.33400	-1.49600
H	2.52300	-1.64600	0.63200	C	3.17500	3.42000	2.16600
C	2.28700	-4.89200	1.64000	H	3.57600	3.57900	3.16900
N	2.14300	-5.89300	2.22400	H	2.26000	2.82500	2.22800
C	2.60700	-2.54500	5.16500	C	4.20600	2.68400	1.31100
C	1.63300	-0.86800	3.10900	H	3.72900	2.29800	0.40900

C	1.90700	-1.37000	5.45700	H	5.03300	3.33700	1.00900
C	2.77700	-2.88400	3.81800	C	4.77900	1.50300	2.11900
C	2.28400	-2.07600	2.78000	H	3.95400	0.87400	2.47600
C	1.40100	-0.52300	4.45200	H	5.28400	1.89400	3.01600
H	1.30900	-0.20900	2.30800	C	5.74900	0.64500	1.30100
C	0.60400	0.67900	4.86100	H	6.56900	1.25300	0.89700
C	-0.19800	1.38000	4.00700	H	6.19400	-0.13500	1.92900
H	-0.13300	1.09000	2.96300	H	5.22900	0.15400	0.47000
C	0.71600	1.06300	6.23900	C	3.94300	5.69400	1.45000
N	0.84800	1.37700	7.35400	H	4.29700	5.43500	0.45000
C	-2.53500	4.00600	5.52500	H	4.70500	5.36900	2.16100
C	-1.58700	3.12000	3.03700	C	3.75000	7.21000	1.56900
C	-2.97300	4.59800	4.32600	H	3.51700	7.48300	2.60400
C	-1.62700	2.94600	5.45500	H	2.91200	7.54300	0.95300
C	-1.13200	2.49500	4.21200	C	5.01700	7.96800	1.12500
C	-2.52700	4.15800	3.07200	H	4.78100	9.03900	1.13300
H	-1.14900	2.79600	2.10000	H	5.24200	7.71500	0.08000
C	-3.04700	4.75700	1.80200	C	6.25700	7.72200	1.99300
C	-2.93300	4.12500	0.59500	H	6.60300	6.68300	1.94200
H	-2.43000	3.16500	0.62900	H	7.08800	8.35400	1.66500
C	-3.69500	6.02700	1.94500	H	6.05700	7.95800	3.04600
N	-4.20100	7.06200	2.12200	C	1.79400	5.37700	2.76600
C	-4.40200	5.90300	-2.44700	H	0.95400	4.68000	2.81500
C	-3.10300	3.50200	-1.75000	C	1.41200	6.31500	2.36700
C	-4.14100	4.90700	-3.40300	C	2.41300	5.59400	4.16400
C	-4.00900	5.67000	-1.12900	H	2.13000	6.60100	4.49700
C	-3.36200	4.47000	-0.76100	H	3.50900	5.60800	4.11300
C	-3.48600	3.71000	-3.08100	C	1.96000	4.58800	5.23400
H	-2.57300	2.59900	-1.47700	H	0.86600	4.61200	5.30500
C	-3.24800	2.67300	-4.13800	H	2.21700	3.56700	4.92600
C	-2.18100	1.82000	-4.14200	C	2.56900	4.86900	6.61000
H	-1.47000	1.94900	-3.32500	H	2.21500	4.13500	7.34200
C	-4.27100	2.63700	-5.14300	H	3.66400	4.81400	6.58400
N	-5.13100	2.65500	-5.93100	H	2.29500	5.86800	6.97200
C	-2.14200	-0.58200	-7.12700	N	-1.73500	-6.69300	-0.17000
C	-0.84300	-0.18100	-4.65100	C	-1.49100	-6.38200	-1.65800
C	-1.17200	-1.47900	-6.66800	H	-1.67500	-7.33000	-2.17400
C	-2.47400	0.50200	-6.30300	H	-0.42800	-6.15300	-1.74500
C	-1.85000	0.71800	-5.06100	C	-2.32400	-5.27900	-2.31100
C	-0.53000	-1.30700	-5.42900	H	-2.07500	-4.29300	-1.90800
H	-0.27400	0.02600	-3.74900	H	-3.39400	-5.44400	-2.14500
C	0.44400	-2.33500	-4.94900	C	-2.07800	-5.26100	-3.83200
C	0.62400	-2.57400	-3.62100	H	-2.22900	-6.27000	-4.24200
C	1.16100	-3.06400	-5.95200	H	-1.03500	-4.99100	-4.02900
N	1.71000	-3.67300	-6.78000	C	-3.01100	-4.27100	-4.53700
C	-3.06600	4.54700	6.86700	H	-2.93000	-3.27400	-4.09500
C	3.16900	-3.47100	6.25900	H	-2.76200	-4.18600	-5.59900
C	-5.10100	7.20500	-2.88400	H	-4.05700	-4.59400	-4.46200
C	-2.86300	-0.74800	-8.47800	C	-0.99400	-7.99500	0.15400
C	4.08100	-6.30600	-3.25400	H	-1.23600	-8.21900	1.19400
C	-4.38300	-0.90200	-8.23000	H	-1.46400	-8.76000	-0.47200
H	-4.59000	-1.79000	-7.62000	C	0.52200	-8.01100	-0.02200

H	-4.80200	-0.03400	-7.71200
H	-4.91500	-1.01400	-9.18300
C	-2.37100	-1.98400	-9.25600
H	-2.56400	-2.91500	-8.70900
H	-2.89700	-2.05100	-10.21500
H	-1.29700	-1.93200	-9.47100
C	-2.61600	0.50400	-9.35300
H	-2.98000	1.41500	-8.86800
H	-1.54700	0.63500	-9.55800
H	-3.13900	0.40500	-10.31200
H	-3.22000	1.20400	-6.64700
H	-0.89500	-2.33600	-7.27200
C	-6.48600	6.87000	-3.48400
H	-6.99100	7.78900	-3.80700
H	-6.41000	6.21000	-4.35400
H	-7.12400	6.37500	-2.74300
C	-4.23500	7.91200	-3.95300
H	-3.24300	8.15400	-3.55200
H	-4.09400	7.29100	-4.84300
H	-4.71100	8.84800	-4.27100
C	-5.30800	8.18200	-1.71200
H	-5.81000	9.08700	-2.07400
H	-4.35900	8.49100	-1.25900
H	-5.93300	7.75100	-0.92100
C	-2.62400	6.02100	7.02400
H	-3.00000	6.64900	6.20900
H	-3.00000	6.43400	7.96700
H	-1.53100	6.10000	7.03200
C	-2.53300	3.75100	8.07300
H	-1.44000	3.78100	8.14100
H	-2.93400	4.18000	8.99900
H	-2.84200	2.70000	8.03600
C	-4.61200	4.46900	6.88700
H	-4.99800	4.83400	7.84600
H	-5.06600	5.07500	6.09600
H	-4.95200	3.43500	6.75700
C	2.91900	-2.92300	7.67800
H	3.34500	-3.61200	8.41600
H	3.38800	-1.94500	7.82800
H	0.80500	-7.89300	-1.07400
H	0.99100	-7.19900	0.54200
C	1.07600	-9.34800	0.50900
H	0.62000	-10.18500	-0.04000
H	0.77800	-9.46300	1.56000
C	2.60100	-9.42900	0.40700
H	3.07000	-8.61800	0.97500
H	2.96900	-10.38000	0.80700
H	2.93500	-9.35400	-0.63500
C	-1.19700	-5.57000	0.74400
H	-0.30200	-5.18800	0.24900
H	-0.87300	-6.06200	1.66100
C	-2.15100	-4.42300	1.08000
H	-3.06300	-4.80400	1.55400
H	-2.45400	-3.88400	0.17800
C	-1.48900	-3.42400	2.05300
H	-2.15800	-2.56000	2.12400
H	-0.55700	-3.04800	1.61600
C	-1.21700	-3.97700	3.45800
H	-0.41400	-4.72300	3.47100
H	-0.90400	-3.16900	4.12600
H	-2.12000	-4.43000	3.88800
C	-3.22500	-6.94300	0.04700
H	-3.50800	-7.68100	-0.71000
H	-3.72200	-6.01000	-0.20400
C	-3.64600	-7.41700	1.45300
H	-4.53300	-6.83700	1.73500
H	-2.88700	-7.15300	2.19900
C	-3.99600	-8.91100	1.56200
H	-4.76900	-9.14800	0.81800
H	-3.12700	-9.53100	1.30700
C	-4.49800	-9.28700	2.95900
H	-4.76000	-10.34900	3.01000
H	-3.73500	-9.09500	3.72300
H	-5.39000	-8.70900	3.22800
H	0.98779	6.14463	1.39957
H	2.21238	7.02054	2.28628
H	0.66035	6.70183	3.02295

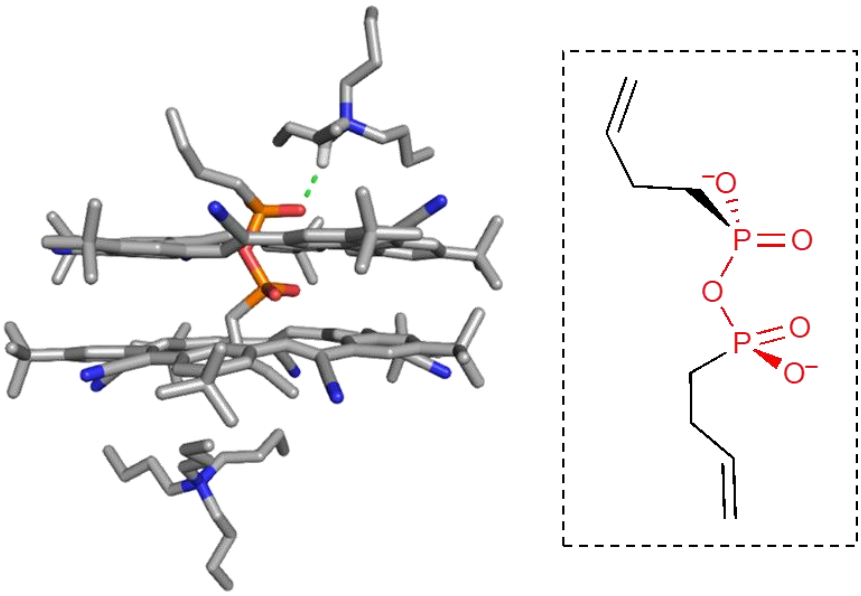

Figure S83: Geometry optimization showing the hydrogen bonding between the α-proton of TBA^+ and the oxygen of the pyrophosphonates moiety in the [3]pseudorotaxane of homoallyl-PP **1** and cyanostar.

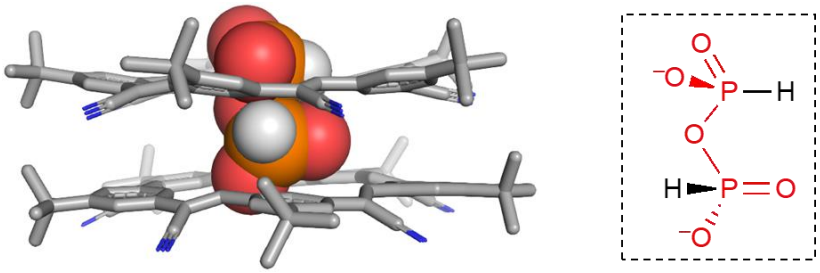

Figure S84: Geometry optimization of a 2:1 complex between cyanostar and $H_2P_2O_5^{2-}$ (RB3LYP/6-31G(D), gas phase).

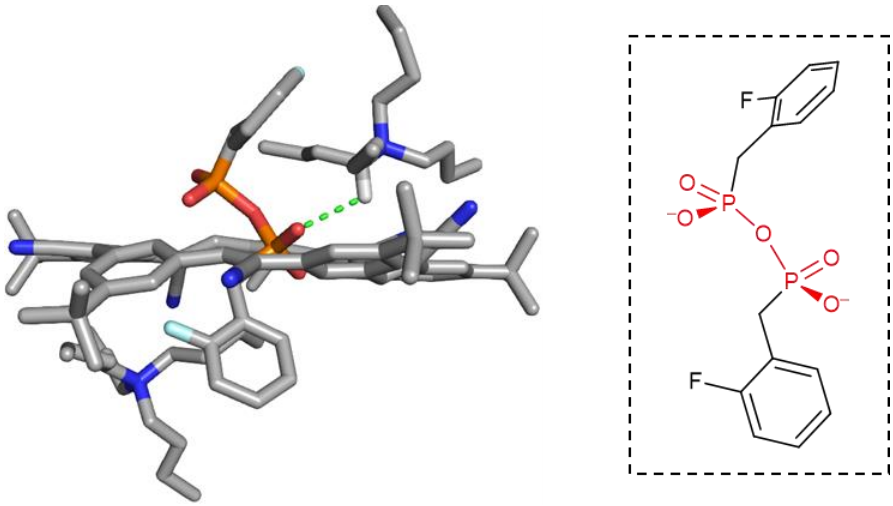

Figure S85: Geometry optimization showing the hydrogen bonding between the α-proton of TBA^+ and the oxygen of the pyrophosphonates moiety in the [2]pseudorotaxane of F-benzyl-PP **3** and cyanostar.

References

[1] L. Du, L. Ma, F. Qi, X. Zheng, C. Jiang, A. Li, X. Wan, S.-J. Liu, S. Li, *J. Bio. Chem.* **2016**, 291, 6583-6594

[2] W. Zhoa, B. Qiao, J. Tropp, M. Pink, J. D. Azoulay, A. H. Flood, *J. Am. Chem. Soc.* **2019**, 141, 4980-4989

[3] S. Lee, C.-H. Chen, A. H. Flood, *Nat. Chem.* **2013**, 5, 704-710

[4] W. Zhao, B. Qiao, C.-H. Chen, A. H. Flood, *Angew. Chem. Int. Ed*. **2017**, 56, 13083-13087

[5] Y. Marcus, *J. Chem. Soc. Faraday Trans.* **1991**, 87, 2995-2999

[6] http://www.mmass.org/, Jan.2023

4 Summary and Outlook

Spatiotemporal control over the self-organization of matter is a key characteristic of all living entities. This principle extends from the self-assembly of lipid membranes at thermodynamic equilibrium to the dissipative self-assembly of microtubules. The latter require a constant input of chemical energy to maintain their out-of-equilibrium state. Inspired by nature, scientists in the past decade strived to design artificial chemically fueled systems that exhibit complex emergent behavior. Non-equilibrium systems chemistry promises applications in the field of new life-like materials and is crucial in unraveling the mystery of the origins of life. Thus, the aim of this thesis was to design new chemically fueled dissipative systems, based on the versatile chemistry of organic phosphates and especially ribonucleotides, the building blocks of RNA.

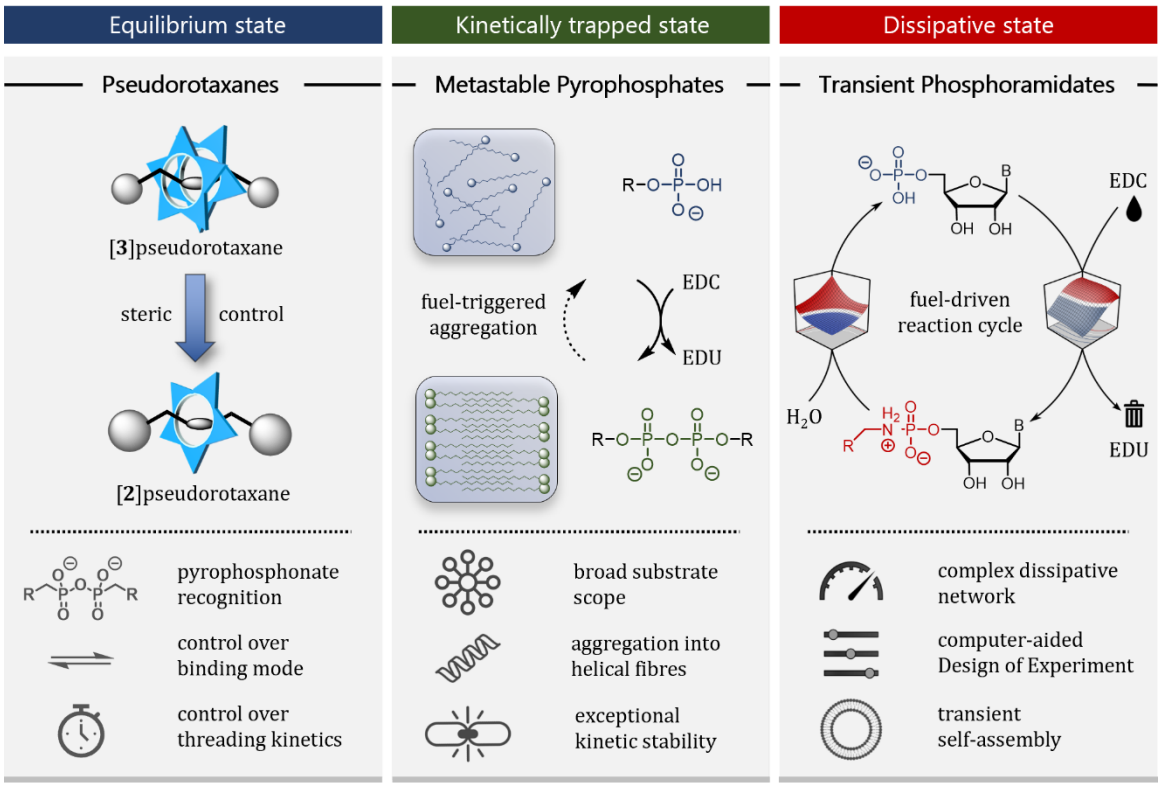

Figure 29: Summary of this work. The three projects can be assigned to different thermodynamic regimes: Steric control over pyrophosphonate pseudorotaxanes at thermodynamic equilibrium, *in situ* aggregation of kinetically trapped pyrophosphates and dissipative self-assembly of phosphoramidates.

Since different phosphate derivatives occupy different states on the energy landscape, not all systems proofed suitable for dissipative reaction cycles. Throughout this work, self-assembly along all three thermodynamic regimes (equilibrium, kinetically trapped and dissipative states) was investigated (Figure 29). By that means, a broad understanding of the chemistry of organic phosphates for the design of complex chemical systems was established and initial misconceptions were erased. Eventually, a dissipative reaction cycle based on phosphoramidates was developed that enabled transient self-assembly. Overall, my work features three peer-reviewed publications on the self-assembly of organophosph(on)ates.

At the beginning of our studies, we planned to use 1-ethyl-3-(3-dimethylaminopropyl) carbodiimide (EDC) to dimerize a series of ribonucleotide-based amphiphiles for transient self-assembly. EDC is a high-energy condensation agent that has been used as a chemical fuel before. Ribonucleotides can either form phosphodiesters or pyrophosphates, upon the condensation of two 5'-phosphates. We could show that addition of EDC to molecularly dissolved amphiphiles lead to rapid dimerization under the formation of a pyrophosphate bond. 25-fold reduction of the critical aggregation concentration upon dimerization triggered spontaneous self-assembly into helical fibers (Figure 29, middle). However, the organic pyrophosphates are kinetically stable and the dissipative reaction cycle could thus not be closed. A comprehensive hydrolysis study was performed and revealed promising results with lanthanide salt catalysis. However, depurination under (Lewis) acidic conditions made this resolution for the kinetic trap inaccessible. Nevertheless, this first study contained valuable lessons for the design of phosphate-based reaction cycles.

Turning our attention from pyrophosphates to pyrophosphonates, allowed harsher conditions for the hydrolysis, but too acidic media tempered with the carbodiimide activation chemistry. Despite that, we identified pyrophosphonates as interesting binding sites for anion-binding macrocycles and decided to study their thermodynamically controlled self-assembly with the cyanostar macrocycle into pseudorotaxanes. We synthesized five different pyrophosphonates with varying steric demand and gained control over their binding stoichiometry from a 2:1 binding (i.e., [3]pseudorotaxane) to a 1:1 binding (i.e., [2]pseudorotaxane) (Figure 29, left). Therefore, this study broadened the scope of anion recognition towards designer anions that facilitate control over supramolecular interactions. Furthermore, steric control over the threading kinetics on the time scale of minutes laid the foundation for chemically fueled artificial molecular motors (see below).

Finally, we were able to enter the dissipative regime, when predominantly suppressing the pyrophosphate formation by introducing amines as strong nucleophiles. EDC-activation allowed rapid transfer of the RNA nucleotides AMP and GMP to their corresponding phosphoramidates in the presence of primary amines. Even under mild conditions, the phosphoramidates hydrolyzed back to the phosphate, when the chemical fuel (EDC) was depleted (Figure 29, right). We investigated and optimized both the phosphoramidate formation and hydrolysis, making use of a software-assisted statistical tool, that allowed us to elucidate unexpected multi-parameter interactions. The newly developed phosphate ↔ phosphoramidate reaction cycle facilitated transient self-assembly of vesicles which has implications for non-equilibrium compartmentalization from prebiotically plausible building blocks.

In conclusion, my work produced insights into the versatile chemistry of organic phosph(on)ates that facilitated supramolecular self-assembly under thermodynamic and kinetic control and culminated in the design of a new dissipative reaction cycle. As such, this work sets the stage for future work of the Delius group on phosphate-based systems towards applications in dissipative reaction cycles and artificial molecular motors.

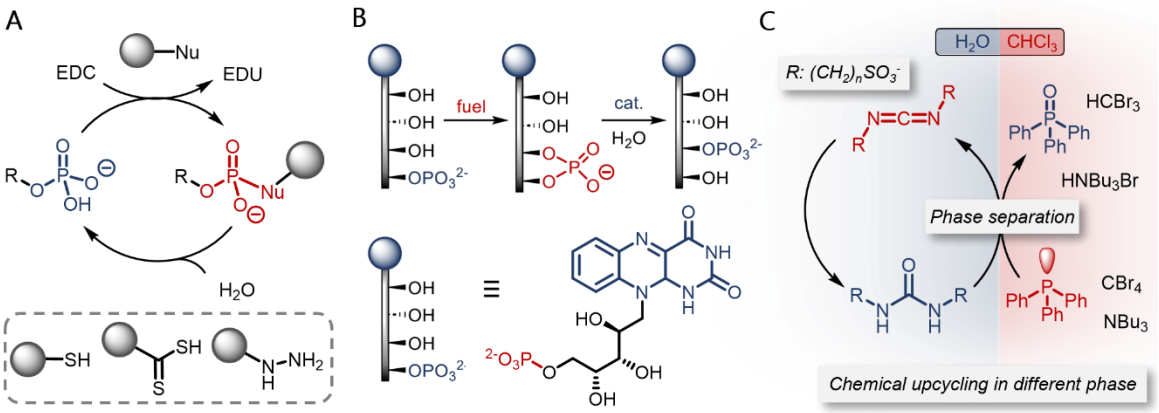

Figure 30: Outlook on EDC-driven reaction cycles. **(A)** The introduction of new nucleophiles like thiols, dithiocarboxylic acids or hydrazines yields new phosphate reaction cycles. **(B)** A fueled phosphodiester walker on a chiral riboflavin track. **(C)** Chemical upcycling of urea waste with PPh_3 as terminal fuel. Terminal waste products accumulate in a different phase from the actual carbodiimide-fueled reaction cycle.

The difference between the kinetically trapped pyrophosphate and the transient phosphoramidate (projects 1 and 2) highlights the stark effect of the nucleophile on the properties of the corresponding phosphate-based reaction cycle. In the future, new reaction cycles for the transient complexation of heavy metal ions could be developed with nucleophiles like thiols and dithiocarboxylic acids (e.g., dithiocarbamates). Hydrazines resemble alkylamine in terms of basicity and nucleophilicity and might be interesting due to their well-known propensity to form hydrogels in guanosine derivatives[251] (Figure 30A). Hydroxy groups as nucleophiles facilitate labile diester bonds that can be used for the design of a simple chemically fueled molecular walker,[252] as depicted in Figure 30B. Riboflavin[253] is a suitable track with four hydroxy footholds that is desymmetrized by a chromophore. Cyclic phosphodiesters are formed intramolecularly, when a carbodiimide is added and subsequent hydrolysis can yield a 5'- or a 4'-monophosphate. The formation of the latter is equivalent to one step of the phosphate moiety. Directional bias on the chiral track could potentially be introduced, using chiral carbodiimides and chiral hydrolysis catalysts.[95]
Arguably the most severe disadvantage of chemically fueled reaction cycles for molecular machines and transient organic materials is the accumulation of waste (like EDU) that eventually inhibits the systems function. One possible remedy could be the thermodynamic upcycling of the waste back to be fuel. For carbodiimide-driven systems, triphenylphosphine (PPh_3) could act as a terminal fuel, as it is known to generate carbodiimides from the corresponding urea.[93] In a two-phase system, as proposed in Figure 30C, the new terminal waste products stay in the organic phase ($CDCl_3$), while the actual carbodiimide-fueled reaction cycle takes place in the aqueous phase and remains intact for many cycles. Adjusting the partition coefficient[254] of all components is crucial for a reliable waste separation and upcycling at the water/chloroform interface.

Inspired by the work of *Leigh* and *Stoddart* on molecular motors that harvest energy to perform directional motion,[255] biased by a molecular "valve",[247–249] I furthermore propose a similar but very simple catenane motor (Figure 31). Its structure and mechanism are based on the insights on sterically controlled slipping kinetics that we obtained in the third project (chapter 2.3). The proposed catenane comprises the two macrocycles depicted in Figure 31A.

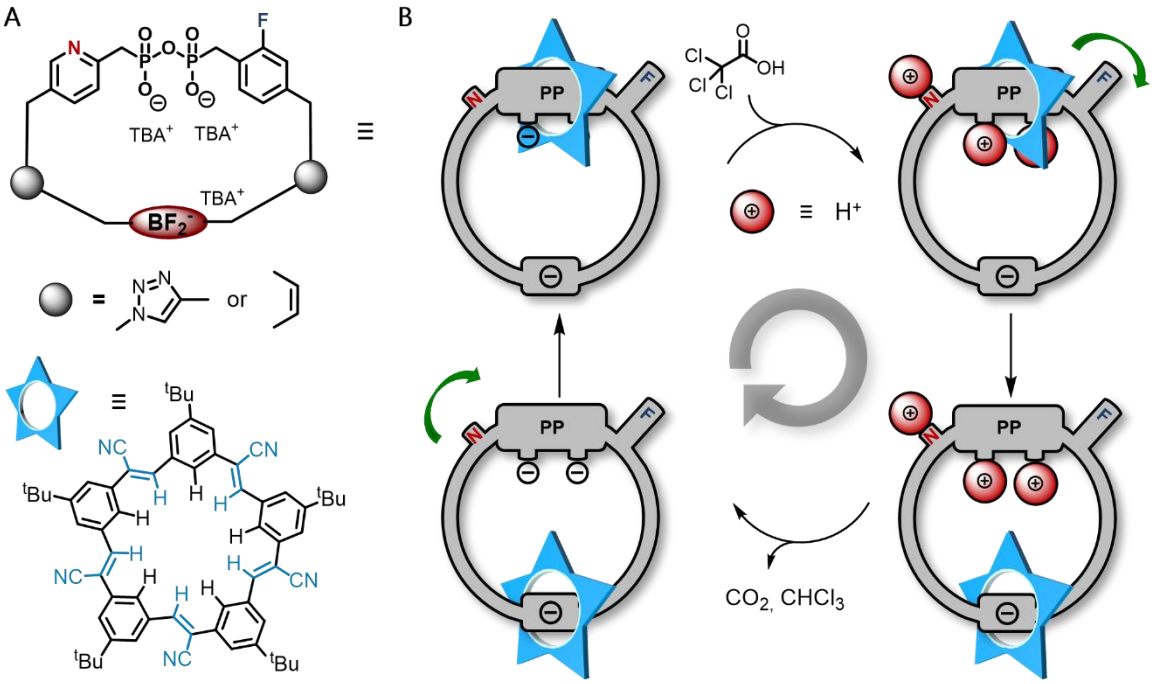

Figure 31: Proposed directional molecular motor. **(A)** Structure of the proposed pyrophosphonate (PP) macrocycle and the cyanostar (CS) macrocycle that form the functional catenane. **(B)** Illustration of the mechanism of net directional motion of CS around the PP macrocycle, chemically fueled by the transient trichloroacetic acid. TBA = tetrabutylammonium.

The static macrocycle contains a pyrophosphonate moiety (PP) similar to the F-benzyl-PP in project 3. However, the pseudo-stopper on one side is replaced by a pyridine. Additional to the PP, the macrocycle also contains a non-pH-sensitive weak binding site like a $BF_2R_2^-$ group. Cyanostar (CS) is used as the mobile macrocycle. A corresponding catenane could be synthesized by Cu(I)-catalyzed azide-alkyne cycloaddition or ring-closing metathesis. The mechanism of the envisaged chemically fueled directional motion is illustrated in Figure 31B. Initially, the cyanostar macrocycle resides on the deprotonated PP binding site. Addition of a transient acid like trichloroacetic acid[160,161] protonates both the PP and the pyridine moiety. The CS macrocycle can now move to the weaker binding site. Due to electrostatic repulsion between the pyridinium and the positively polarized CS cavity, the ring will move clockwise. Eventually, the transient acid decarboxylates and restores the neutral pyridine and the deprotonated PP binding site. The mobile CS can move back to the PP either over the pyridine moiety or over the fluorobenzyl pseudo-stopper. Since the latter retains the slipping on the time scale of several minutes (see chapter 2.3[3]), the ring will preferentially continue moving clockwise over the pyridine. Repetitive addition of the chemical fuel drives the net directional motion of cyanostar around the static macrocycle by an energy ratchet mechanism.

References

(1) Sun, J.; Vogel, J.; Chen, L.; Schleper, A. L.; Bergner, T.; Kuehne, A. J. C.; von Delius, M. Carbodiimide-Driven Dimerization and Self-Assembly of Artificial, Ribose-Based Amphiphiles. *Chem. Eur. J.* **2022**, *28*, e202104116.

(2) Englert, A.; Vogel, J. F.; Bergner, T.; Loske, J.; Von Delius, M. A Ribonucleotide ↔ Phosphoramidate Reaction Network Optimized by Computer-Aided Design. *J. Am. Chem. Soc.* **2022**, *144*, 15266–15274.

(3) Vogel, J.; Chen, Y.; Fadler, R. E.; Flood, A. H.; von Delius, M. Steric Control over the Threading of Pyrophosphonates with One or Two Cyanostar Macrocycles during Pseudorotaxane Formation. *Chem. Eur. J.* **2023**, *e202300899*.

(4) Hollstein, S.; Ali, L. M. A.; Coste, M.; Vogel, J.; Bettache, N. A Triazolium-Anchored Self-Immolative Linker Enables Self- Assembly-Driven SiRNA Binding and Esterase-Induced Release. *Chem. Eur. J.* **2022**, *29*, e202203311.

(5) *https://chat.openai.com/chat*. 15.02.23.

(6) Nitschke, J. R. Systems Chemistry: Molecular Networks Come of Age. *Nature* **2009**, *462*, 736–738.

(7) Ludlow, R. F.; Otto, S. Systems Chemistry. *Chem. Soc. Rev.* **2008**, *37*, 101–108.

(8) Ashkenasy, G.; Hermans, T. M.; Otto, S.; Taylor, A. F. Systems Chemistry. *Chem. Soc. Rev.* **2017**, *46*, 2543–2554.

(9) Miljanić, O. Small-Molecule Systems Chemistry. *Chem* **2017**, *2*, 502–524.

(10) Semenov, S. N.; Kraft, L. J.; Ainla, A.; Zhao, M.; Baghbanzadeh, M.; Campbell, V. E.; Kang, K.; Fox, J. M.; Whitesides, G. M. Autocatalytic, Bistable, Oscillatory Networks of Biologically Relevant Organic Reactions. *Nature* **2016**, *537*, 656–660.

(11) Györgyi, L.; Turányi, T.; Field, R. J. Mechanistic Details of the Oscillatory Belousov-Zhabotinskii Reaction. *J. Phys. Chem.* **1990**, *94*, 7162–7170.

(12) Mattia, E.; Otto, S. Supramolecular Systems Chemistry. *Nat. Nanotechnol.* **2015**, *10*, 111–119.

(13) Van Esch, J. H.; Klajn, R.; Otto, S. Chemical Systems out of Equilibrium. *Chem. Soc. Rev.* **2017**, *46*, 5474–5475.

(14) Stoddart, J. F. Mechanically Interlocked Molecules (MIMs)—Molecular Shuttles, Switches, and Machines (Nobel Lecture). *Angew. Chem. Int. Ed.* **2017**, *56*, 11094–11125.

(15) Adamski, P.; Eleveld, M.; Sood, A.; Kun, Á.; Szilágyi, A.; Czárán, T.; Szathmáry, E.; Otto, S. From Self-Replication to Replicator Systems En Route to de Novo Life. *Nat. Rev. Chem.* **2020**, *4*, 386–403.

(16) Ottelé, J.; Hussain, A. S.; Mayer, C.; Otto, S. Chance Emergence of Catalytic Activity and Promiscuity in a Self-Replicator. *Nat. Catal.* **2020**, *3*, 547–553.

(17) Li, J.; Nowak, P.; Otto, S. Dynamic Combinatorial Libraries: From Exploring Molecular Recognition to Systems Chemistry. *J. Am. Chem. Soc.* **2013**, *135*, 9222–9239.

(18) Kriebisch, B. A. K.; Kriebisch, C. M. E.; Bergmann, A. M.; Wanzke, C.; Tena-Solsona, M.; Boekhoven, J. Tuning the Kinetic Trapping in Chemically Fueled Self-Assembly. *ChemSystemsChem* **2023**, *5*, e202200035.

(19) Wagner, N.; Ashkenasy, G. Rhythm before Life. *Nat. Chem.* **2019**, *11*, 681–683.

(20) Ruiz-Mirazo, K.; Briones, C.; De La Escosura, A. Prebiotic Systems Chemistry: New Perspectives for the Origins of Life. *Chem. Rev.* **2014**, *114*, 285–366.

(21) Otto, S. An Approach to the de Novo Synthesis of Life. *Acc. Chem. Res.* **2022**, *55*, 145–155.

(22) Islam, S.; Powner, M. W. Prebiotic Systems Chemistry: Complexity Overcoming Clutter.

Chem **2017**, *2*, 470–501.

(23) Kroiss, D.; Ashkenasy, G.; Braunschweig, A. B.; Tuttle, T.; Ulijn, R. V. Catalyst: Can Systems Chemistry Unravel the Mysteries of the Chemical Origins of Life? *Chem* **2019**, *5*, 1917–1920.

(24) Danger, G.; d'Hendecourt, L. L. S.; Pascal, R. On the Conditions for Mimicking Natural Selection in Chemical Systems. *Nat. Rev. Chem.* **2020**, *4*, 102–109.

(25) Merindol, R.; Walther, A. Materials Learning from Life: Concepts for Active, Adaptive and Autonomous Molecular Systems. *Chem. Soc. Rev.* **2017**, *46*, 5588–5619.

(26) Freeman, R.; Han, M.; Álvarez, Z.; Lewis, J. A.; Wester, J. R.; Stephanopoulos, N.; McClendon, M. T.; Lynsky, C.; Godbe, J. M.; Sangji, H.; Luijten, E.; Stupp, S. I. Reversible Self-Assembly of Superstructured Networks. *Science* **2018**, *362*, 808–813.

(27) Aida, T.; Meijer, E. W.; Stupp, S. I. Functional Supramolecular Polymers. *Science* **2012**, *335*, 813–817.

(28) Deng, J.; Bezold, D.; Jessen, H. J.; Walther, A. Multiple Light Control Mechanisms in ATP-Fueled Non-Equilibrium DNA Systems. *Angew. Chem. Int. Ed.* **2020**, *59*, 12084–12092.

(29) Weißenfels, M.; Gemen, J.; Klajn, R. Dissipative Self-Assembly: Fueling with Chemicals versus Light. *Chem* **2021**, *7*, 23–37.

(30) Ragazzon, G.; Malferrari, M.; Arduini, A.; Secchi, A.; Rapino, S.; Silvi, S.; Credi, A. Autonomous Non-Equilibrium Self-Assembly and Molecular Movements Powered by Electrical Energy. *Angew. Chem. Int. Ed.* **2023**, *62*, e202214265.

(31) Barpuzary, D.; Hurst, P. J.; Patterson, J. P.; Guan, Z. Waste-Free Fully Electrically Fueled Dissipative Self-Assembly System. *J. Am. Chem. Soc.* **2023**, *145*, 3727–3735.

(32) De, S.; Klajn, R. Dissipative Self-Assembly Driven by the Consumption of Chemical Fuels. *Adv. Mater.* **2018**, *30*, 1706750.

(33) Das, K.; Gabrielli, L.; Prins, L. J. Chemically Fueled Self-Assembly in Biology and Chemistry. *Angew. Chem. Int. Ed.* **2021**, *60*, 20120–20143.

(34) Van Ravensteijn, B. G. P.; Voets, I. K.; Kegel, W. K.; Eelkema, R. Out-of-Equilibrium Colloidal Assembly Driven by Chemical Reaction Networks. *Langmuir* **2020**, *36*, 10639–10656.

(35) Ragazzon, G.; Prins, L. J. Energy Consumption in Chemical Fuel-Driven Self-Assembly. *Nat. Nanotechnol.* **2018**, *13*, 882–889.

(36) Kariyawasam, L. S.; Hossain, M. M.; Hartley, C. S. The Transient Covalent Bond in Abiotic Nonequilibrium Systems. *Angew. Chem. Int. Ed.* **2021**, *60*, 12648–12658.

(37) Sorrenti, A.; Leira-Iglesias, J.; Markvoort, A. J.; De Greef, T. F. A.; Hermans, T. M. Non-Equilibrium Supramolecular Polymerization. *Chem. Soc. Rev.* **2017**, *46*, 5476–5490.

(38) Van Rossum, S. A. P.; Tena-Solsona, M.; Van Esch, J. H.; Eelkema, R.; Boekhoven, J. Dissipative Out-of-Equilibrium Assembly of Man-Made Supramolecular Materials. *Chem. Soc. Rev.* **2017**, *46*, 5519–5535.

(39) Wang, G.; Liu, S. Strategies to Construct a Chemical-Fuel-Driven Self-Assembly. *ChemSystemsChem* **2020**, *2*, e1900046.

(40) Singh, N.; Formon, G. J. M.; De Piccoli, S.; Hermans, T. M. Devising Synthetic Reaction Cycles for Dissipative Nonequilibrium Self-Assembly. *Adv. Mater.* **2020**, *32*, 1906834.

(41) Rieß, B.; Grötsch, R. K.; Boekhoven, J. The Design of Dissipative Molecular Assemblies Driven by Chemical Reaction Cycles. *Chem* **2020**, *6*, 552–578.

(42) Afrose, S. P.; Ghosh, C.; Das, D. Substrate Induced Generation of Transient Self-Assembled Catalytic Systems. *Chem. Sci.* **2021**, *12*, 14674–14685.

(43) Sharko, A.; Livitz, D.; De Piccoli, S.; Bishop, K. J. M.; Hermans, T. M. Insights into Chemically Fueled Supramolecular Polymers. *Chem. Rev.* **2022**, *122*, 11759–11777.

(44) Giuseppone, A. N.; Walther, A. *Out-of-Equilibrium (Supra)Molecular Systems and Materials*; 2021.

(45) Aprahamian, I.; Goldup, S. M. Off Detailed Balance: Non-Equilibrium Steady States in Catalysis, Molecular Motors and Supramolecular Materials. *ChemRXiv* **2022**, 1–14.

(46) Kassem, S.; Van Leeuwen, T.; Lubbe, A. S.; Wilson, M. R.; Feringa, B. L.; Leigh, D. A. Artificial Molecular Motors. *Chem. Soc. Rev.* **2017**, *46*, 2592–2621.

(47) Erbas-Cakmak, S.; Leigh, D. A.; McTernan, C. T.; Nussbaumer, A. L. Artificial Molecular Machines. *Chem. Rev.* **2015**, *115*, 10081–10206.

(48) Coskun, A.; Banaszak, M.; Astumian, R. D.; Stoddart, J. F.; Grzybowski, B. A. Great Expectations: Can Artificial Molecular Machines Deliver on Their Promise? *Chem. Soc. Rev.* **2012**, *41*, 19–30.

(49) Bruns, C. J. Moving Forward in the Semantic Soup of Artificial Molecular Machine Taxonomy. *Nat. Nanotechnol.* **2022**, *17*, 1231–1234.

(50) Aprahamian, I. The Future of Molecular Machines. *ACS Cent. Sci.* **2020**, *6*, 347–358.

(51) Pezzato, C.; Cheng, C.; Stoddart, J. F.; Astumian, R. D. Mastering the Non-Equilibrium Assembly and Operation of Molecular Machines. *Chem. Soc. Rev.* **2017**, *46*, 5491–5507.

(52) Biagini, C.; Di Stefano, S. Abiotic Chemical Fuels for the Operation of Molecular Machines. *Angew. Chemie* **2020**, *132*, 8420–8430.

(53) Borsley, S.; Leigh, D. A.; Roberts, B. M. W. Chemical Fuels for Molecular Machinery. *Nat. Chem.* **2022**, *14*, 728–738.

(54) Amano, S.; Esposito, M.; Kreidt, E.; Leigh, D. A.; Penocchio, E.; Roberts, B. M. W. Using Catalysis to Drive Chemistry Away from Equilibrium: Relating Kinetic Asymmetry, Power Strokes, and the Curtin-Hammett Principle in Brownian Ratchets. *J. Am. Chem. Soc.* **2022**, *144*, 20153–20164.

(55) van der Helm, M. P.; de Beun, T.; Eelkema, R. On the Use of Catalysis to Bias Reaction Pathways in Out-of-Equilibrium Systems. *Chem. Sci.* **2021**, *12*, 4484–4493.

(56) Karsenti, E. Self-Organization in Cell Biology: A Brief History. *Nat. Rev. Mol. Cell Biol.* **2008**, *9*, 255–262.

(57) Nédélec, F. J.; Surrey, T.; Maggs, A. C.; Leibler, S. Self-Organization of Microtubules and Motors. *Nature* **1997**, *389*, 305–308.

(58) Pollard, T. D.; Blanchoin, L.; Mullins, R. D. Molecular Mechanisms Controlling Actin Filament Dynamics in Nonmuscle Cells. *Annu. Rev. Biophys. Biomol. Struct.* **2000**, *29*, 545–576.

(59) Reisler, E.; Egelman, E. H. Actin Structure and Function: What We Still Do Not Understand. *J. Biol. Chem.* **2007**, *282*, 36133–36137.

(60) Conde, C.; Cáceres, A. Microtubule Assembly, Organization and Dynamics in Axons and Dendrites. *Nat. Rev. Neurosci.* **2009**, *10*, 319–332.

(61) Hess, H.; Ross, J. L. Non-Equilibrium Assembly of Microtubules: From Molecules to Autonomous Chemical Robots. *Chem. Soc. Rev.* **2017**, *46*, 5570–5587.

(62) Desai, A.; Mitchison, T. J. Microtubule Polymerization Dyamics. *Annu. Rev. Cell Dev. Biol.* **1997**, *13*, 83–117.

(63) Hollstein, S.; von Delius, M. Über Den Trend Vom Molekül Zum System. *Nachrichten aus der Chemie* **2019**, *67*, 62–65.

(64) Sugden, A. M.; Hurtley, S. M.; Lopez, B.; Funk, M. A.; Stajic, J.; Kelly, P. N.; Yeston, J. Editor's Choice. *Science* **2020**, *367*, 1439–1440.

(65) Ferreira, L. T.; Orr, B.; Rajendraprasad, G.; Pereira, A. J.; Lemos, C.; Lima, J. T.; Boldú, C. G.; Ferreira, J. G.; Barisic, M.; Maiato, H. α-Tubulin Detyrosination Impairs Mitotic Error Correction by Suppressing MCAK Centromeric Activity. *J. Cell Biol.* **2020**, *219*, e201910064.

(66) Etienne-Manneville, S. Microtubules in Cell Migration. *Annu. Rev. Cell Dev. Biol.* **2013**, *29*, 471–499.

(67) Nogales, E. Structural Insights Into Microtubule Function. *Annu. Rev. Biophys. Biomol.*

Struct. **2001**, *30*, 397–420.

(68) Boekhoven, J.; Brizard, A. M.; Kowlgi, K. N. K.; Koper, G. J. M.; Eelkema, R.; Van Esch, J. H. Dissipative Self-Assembly of a Molecular Gelator by Using a Chemical Fuel. *Angew. Chem. Int. Ed.* **2010**, *49*, 4825–4828.

(69) Boekhoven, J.; Hendriksen, W. E.; Koper, G. J. M.; Eelkema, R.; Van Esch, J. H. Transient Assembly of Active Materials Fueled by a Chemical Reaction. *Science* **2015**, *349*, 1075–1079.

(70) Maiti, S.; Fortunati, I.; Ferrante, C.; Scrimin, P.; Prins, L. J. Dissipative Self-Assembly of Vesicular Nanoreactors. *Nat. Chem.* **2016**, *8*, 725–731.

(71) Chen, R.; Das, K.; Cardona, M. A.; Gabrielli, L.; Prins, L. J. Progressive Local Accumulation of Self-Assembled Nanoreactors in a Hydrogel Matrix through Repetitive Injections of ATP. *J. Am. Chem. Soc.* **2022**, *144*, 2010–2018.

(72) della Sala, F.; Maiti, S.; Bonanni, A.; Scrimin, P.; Prins, L. J. Fuel-Selective Transient Activation of Nanosystems for Signal Generation. *Angew. Chem. Int. Ed.* **2018**, *57*, 1611–1615.

(73) Deng, J.; Walther, A. ATP-Responsive and ATP-Fueled Self-Assembling Systems and Materials. *Adv. Mater.* **2020**, *32*, 2002629.

(74) Chandrabhas, S.; Olivo, M.; Prins, L. J. Template-Dependent (Ir)Reversibility of Noncovalent Synthesis Pathways. *ChemSystemsChem* **2020**, *2*, e1900063.

(75) Chandrabhas, S.; Maiti, S.; Fortunati, I.; Ferrante, C.; Gabrielli, L.; Prins, L. J. Nucleotide-Selective Templated Self-Assembly of Nanoreactors under Dissipative Conditions. *Angew. Chem. Int. Ed.* **2020**, *59*, 22223–22229.

(76) Das, K.; Kar, H.; Chen, R.; Fortunati, I.; Ferrante, C.; Scrimin, P.; Gabrielli, L.; Prins, L. J. Formation of Catalytic Hotspots in ATP-Templated Assemblies. *J. Am. Chem. Soc.* **2023**, *145*, 898–904.

(77) Cardona, M. A.; Prins, L. J. ATP-Fuelled Self-Assembly to Regulate Chemical Reactivity in the Time Domain. *Chem. Sci.* **2020**, *11*, 1518–1522.

(78) Heinen, L.; Walther, A. Programmable Dynamic Steady States in ATP-Driven Nonequilibrium DNA Systems. *Sci. Adv.* **2019**, *5*, 32–37.

(79) Deng, J.; Walther, A. Programmable ATP-Fueled DNA Coacervates by Transient Liquid-Liquid Phase Separation. *Chem* **2020**, *6*, 3329–3343.

(80) Deng, J.; Walther, A. Autonomous DNA Nanostructures Instructed by Hierarchically Concatenated Chemical Reaction Networks. *Nat. Commun.* **2021**, *12*, 5132.

(81) Deng, J.; Liu, W.; Sun, M.; Walther, A. Dissipative Organization of DNA Oligomers for Transient Catalytic Function. *Angew. Chem. Int. Ed.* **2022**, *61*, e202113477.

(82) Sorrenti, A.; Leira-Iglesias, J.; Sato, A.; Hermans, T. M. Non-Equilibrium Steady States in Supramolecular Polymerization. *Nat. Commun.* **2017**, *8*, 15899.

(83) Dhiman, S.; Jain, A.; George, S. J. Transient Helicity: Fuel-Driven Temporal Control over Conformational Switching in a Supramolecular Polymer. *Angew. Chem.* **2017**, *129*, 1349–1353.

(84) Tena-Solsona, M.; Rieß, B.; Grötsch, R. K.; Löhrer, F. C.; Wanzke, C.; Käsdorf, B.; Bausch, A. R.; Müller-Buschbaum, P.; Lieleg, O.; Boekhoven, J. Non-Equilibrium Dissipative Supramolecular Materials with a Tunable Lifetime. *Nat. Commun.* **2017**, *8*, 15895.

(85) Kariyawasam, L. S.; Hartley, C. S. Dissipative Assembly of Aqueous Carboxylic Acid Anhydrides Fueled by Carbodiimides. *J. Am. Chem. Soc.* **2017**, *139*, 11949–11955.

(86) Schwarz, P. S.; Tena-Solsona, M.; Dai, K.; Boekhoven, J. Carbodiimide-Fueled Catalytic Reaction Cycles to Regulate Supramolecular Processes. *Chem. Commun.* **2022**, *58*, 1284–1297.

(87) Mikolajczyk, M.; Kielbasinski, P. Recent Developments in the Carbodiimide Chemistry. *Tetrahedron* **1981**, *37*, 233–284.

(88) Williams, A.; Ibrahim, I. T. Carbodiimide Chemistry: Recent Advances. *Chem. Rev.* **1981**, *81*, 589–636.

(89) Tordini, F.; Bencini, A.; Bruschi, M.; Gioia, L. De; Zampella, G.; Fantucci, P. Theoretical Study of Hydration of Cyanamide and Carbodiimide. *J. Phys. Chem. A* **2003**, *107*, 1188–1196.

(90) Gajewski, E.; Steckler, D. K.; Goldberg, R. N. Thermodynamics of the Hydrolysis of Adenosine 5'-Triphosphate to Adenosine 5'-Diphosphate. *J. Biol. Chem.* **1986**, *261*, 12733–12737.

(91) Berg, J. M.; Tymoczko, J. L.; Stryer, L. *Biochemistry, 6th Edition*; 2007.

(92) Taniguchi, T.; Suzuki, T.; Satoh, H.; Shichibu, Y.; Konishi, K.; Monde, K. Preparation of Carbodiimides with One-Handed Axial Chirality. *J. Am. Chem. Soc.* **2018**, *140*, 15577–15581.

(93) Brunner, T. S.; Benndorf, P.; Gamer, M. T.; Kno, N.; Gugau, K.; Roesky, P. W. Enantiopure Amidinate Complexes of the Rare-Earth Elements. *Organometallics* **2016**, *35*, 3474–3487.

(94) Borsley, S.; Leigh, D. A.; Roberts, B. M. W. A Doubly Kinetically-Gated Information Ratchet Autonomously Driven by Carbodiimide Hydration. *J. Am. Chem. Soc.* **2021**, *143*, 4414–4420.

(95) Borsley, S.; Kreidt, E.; Leigh, D. A.; Roberts, B. M. W. Autonomous Fuelled Directional Rotation about a Covalent Single Bond. *Nature* **2022**, *604*, 80–85.

(96) Williams, A.; Ibrahim, I. T. A New Mechanism Involving Cyclic Tautomers for the Reaction with Nucleophiles of the Water-Soluble Peptide Coupling Reagent 1-Ethyl-3-(3-(Dimethylamino)Propyl)Carbodiimide (EDC). *J. Am. Chem. Soc.* **1981**, *103*, 7090–7095.

(97) Donau, C.; Boekhoven, J. The Chemistry of Chemically Fueled Droplets. *Trends Chem.* **2023**, *5*, 45–60.

(98) Wanzke, C.; Jussupow, A.; Kohler, F.; Dietz, H.; Kaila, V. R. I.; Boekhoven, J. Dynamic Vesicles Formed By Dissipative Self-Assembly. *ChemSystemsChem* **2020**, *2*, e190004.

(99) Hossain, M. M.; Jayalath, I. M.; Baral, R.; Hartley, C. S. Carbodiimide-Induced Formation of Transient Polyether Cages. *ChemSystemsChem* **2022**, *4*, e202200016.

(100) Tena-Solsona, M.; Boekhoven, J. Dissipative Self-Assembly of Peptides. *Isr. J. Chem.* **2019**, *59*, 898–905.

(101) Yao, Z.-F.; Kuang, Y.; Kohl, P.; Li, Y.; Ardoña, H. A. M. Carbodiimide-Fueled Assembly of Π-Conjugated Peptides Regulated by Electrostatic Interactions. *ChemSystemsChem* **2023**, e202300003.

(102) Kriebisch, B. A. K.; Jussupow, A.; Bergmann, A. M.; Kohler, F.; Dietz, H.; Kaila, V. R. I.; Boekhoven, J. Reciprocal Coupling in Chemically Fueled Assembly: A Reaction Cycle Regulates Self-Assembly and Vice Versa. *J. Am. Chem. Soc.* **2020**, *142*, 20837–20844.

(103) Tena-Solsona, M.; Wanzke, C.; Riess, B.; Bausch, A. R.; Boekhoven, J. Self-Selection of Dissipative Assemblies Driven by Primitive Chemical Reaction Networks. *Nat. Commun.* **2018**, *9*, 2044.

(104) Schwarz, P. S.; Laha, S.; Janssen, J.; Huss, T.; Boekhoven, J.; Weber, C. A. Parasitic Behavior in Competing Chemically Fueled Reaction Cycles. *Chem. Sci.* **2021**, *12*, 7554–7560.

(105) Wanzke, C.; Tena-Solsona, M.; Rieß, B.; Tebcharani, L.; Boekhoven, J. Active Droplets in a Hydrogel Release Drugs with a Constant and Tunable Rate. *Mater. Horizons* **2020**, *7*, 1397–1403.

(106) Hossain, M. M.; Atkinson, J. L.; Hartley, C. S. Dissipative Assembly of Macrocycles Comprising Multiple Transient Bonds. *Angew. Chem. Int. Ed.* **2020**, *59*, 13807–13813.

(107) Zong, Z.; Zhang, Q.; Qiu, S. H.; Wang, Q.; Zhao, C.; Zhao, C. X.; Tian, H.; Qu, D. H. Dynamic Timing Control over Multicolor Molecular Emission by Temporal Chemical Locking.

Angew. Chem. Int. Ed. **2022**, *61*, e202116414.

(108) Jayalath, I. M.; Wang, H.; Mantel, G.; Kariyawasam, L. S.; Hartley, C. S. Chemically Fueled Transient Geometry Changes in Diphenic Acids. *Org. Lett.* **2020**, *22*, 7567–7571.

(109) Heckel, J.; Loescher, S.; Mathers, R. T.; Walther, A. Chemically Fueled Volume Phase Transition of Polyacid Microgels. *Angew. Chem. Int. Ed.* **2021**, *60*, 7117–7125.

(110) Kriebisch, C. M. E.; Bergmann, A. M.; Boekhoven, J. Fuel-Driven Dynamic Combinatorial Libraries. *J. Am. Chem. Soc.* **2021**, *143*, 7719–7725.

(111) Jayalath, I. M.; Gerken, M. M.; Mantel, G.; Hartley, C. S. Substituent Effects on Transient, Carbodiimide-Induced Geometry Changes in Diphenic Acids. *J. Org. Chem.* **2021**, *86*, 12024–12033.

(112) Vale, R. D.; Milligan, R. A. The Way Things Move : Looking Under the Hood of Molecular Motor Proteins. *Science* **2000**, *288*, 88–95.

(113) Wang, H.; Oster, G. Energy Transduction in the F1 Motor of ATP Synthase. *Nature* **1998**, *396*, 279–282.

(114) Heckel, J.; Batti, F.; Mathers, R. T.; Walther, A. Spinodal Decomposition of Chemically Fueled Polymer Solutions. *Soft Matter* **2021**, *17*, 5401–5409.

(115) Würbser, M. A.; Schwarz, P. S.; Heckel, J.; Bergmann, A. M.; Walther, A.; Boekhoven, J. Chemically Fueled Block Copolymer Self-Assembly into Transient Nanoreactors. *ChemSystemsChem* **2021**, *3*, e2100015.

(116) Rodon-Fores, J.; Würbser, M. A.; Kretschmer, M.; Rieß, B.; Bergmann, A. M.; Lieleg, O.; Boekhoven, J. A Chemically Fueled Supramolecular Glue for Self-Healing Gels. *Chem. Sci.* **2022**, *13*, 11411–11421.

(117) Cheng, M.; Qian, C.; Ding, Y.; Chen, Y.; Xiao, T.; Lu, X.; Jiang, J.; Wang, L. Writable and Self-Erasable Hydrogel Based on Dissipative Assembly Process from Multiple Carboxyl Tetraphenylethylene Derivative. *ACS Mater. Lett.* **2020**, *2*, 425–429.

(118) Bai, S.; Niu, X.; Wang, H.; Wei, L.; Liu, L.; Liu, X.; Eelkema, R.; Guo, X.; van Esch, J. H.; Wang, Y. Chemical Reaction Powered Transient Polymer Hydrogels for Controlled Formation and Free Release of Pharmaceutical Crystals. *Chem. Eng. J.* **2021**, *414*, 128877.

(119) Panja, S.; Dietrich, B.; Adams, D. J. Chemically Fuelled Self-Regulating Gel-to-Gel Transition. *ChemSystemsChem* **2020**, *2*, e1900038.

(120) Zhang, B.; Jayalath, I. M.; Ke, J.; Sparks, J. L.; Hartley, C. S.; Konkolewicz, D. Chemically Fueled Covalent Crosslinking of Polymer Materials. *Chem. Commun.* **2019**, *55*, 2086–2089.

(121) Dodo, O. J.; Petit, L.; Rajawasam, C. W. H.; Hartley, C. S.; Konkolewicz, D. Tailoring Lifetimes and Properties of Carbodiimide-Fueled Covalently Cross-Linked Polymer Networks. *Macromolecules* **2021**, *54*, 9860–9867.

(122) Rajawasam, C. W. H.; Tran, C.; Weeks, M.; McCoy, K. S.; Ross-Shannon, R.; Dodo, O. J.; Sparks, J. L.; Hartley, C. S.; Konkolewicz, D. Chemically Fueled Reinforcement of Polymer Hydrogels. *J. Am. Chem. Soc.* **2023**, *1*45, 5553-5560

(123) Xu, H.; Bai, S.; Gu, G.; Gao, Y.; Sun, X.; Guo, X.; Xuan, F.; Wang, Y. Bioinspired Self-Resettable Hydrogel Actuators Powered by a Chemical Fuel. *ACS Appl. Mater. Interfaces* **2022**, *14*, 43825–43832.

(124) Del Giudice, D.; Spatola, E.; Valentini, M.; Ercolani, G.; Di Stefano, S. Dissipative Dynamic Libraries (DDLs) and Dissipative Dynamic Combinatorial Chemistry (DDCC). *ChemSystemsChem* **2022**, *4*, e202200023.

(125) Van Ravensteijn, B. G. P.; Hendriksen, W. E.; Eelkema, R.; Van Esch, J. H.; Kegel, W. K. Fuel-Mediated Transient Clustering of Colloidal Building Blocks. *J. Am. Chem. Soc.* **2017**, *139*, 9763–9766.

(126) Cheng, M.; Chen, D.; Zhang, L.; Xiao, T.; Jiang, J.; Wang, L. Chemical Fuel-Driven Gelation with Dissipative Assembly-Induced Emission. *Org. Chem. Front.* **2023**,

10.1039/d2qo01888h.

(127) Mei, J.; Leung, N. L. C.; Kwok, R. T. K.; Lam, J. W. Y.; Tang, B. Z. Aggregation-Induced Emission: Together We Shine, United We Soar! *Chem. Rev.* **2015**, *115*, 11718–11940.

(128) Hong, Y.; Lam, J. W. Y.; Tang, B. Z. Aggregation-Induced Emission. *Chem. Soc. Rev.* **2011**, *40*, 5361–5388.

(129) Mei, J.; Hong, Y.; Lam, J. W. Y.; Qin, A.; Tang, Y.; Tang, B. Z. Aggregation-Induced Emission: The Whole Is More Brilliant than the Parts. *Adv. Mater.* **2014**, *26*, 5429–5479.

(130) Su, B.; Chi, T.; Ye, Z.; Xiang, Y.; Dong, P.; Liu, D.; Addonizio, C. J.; Webber, M. J. Transient and Dissipative Host–Guest Hydrogels Regulated by Consumption of a Reactive Chemical Fuel. *Angew. Chem.* **2023**, e202216537.

(131) van der Helm, M. P.; Wang, C. L.; Fan, B.; Macchione, M.; Mendes, E.; Eelkema, R. Organocatalytic Control over a Fuel-Driven Transient-Esterification Network. *Angew. Chem. Int. Ed.* **2020**, *59*, 20604–20611.

(132) Bal, S.; Das, K.; Ahmed, S.; Das, D. Chemically Fueled Dissipative Self-Assembly That Exploits Cooperative Catalysis. *Angew. Chem.* **2019**, *131*, 250–253.

(133) Klemm, B.; Lewis, R. W.; Piergentili, I.; Eelkema, R. Temporally Programmed Polymer – Solvent Interactions Using a Chemical Reaction Network. *Nat. Commun.* **2022**, *13*, 6242.

(134) Lewis, R. W.; Klemm, B.; Macchione, M.; Eelkema, R. Fuel-Driven Macromolecular Coacervation in Complex Coacervate Core Micelles. *Chem. Sci.* **2022**, *13*, 4533–4544.

(135) Wu, B.; Lewis, R. W.; Li, G.; Gao, Y.; Fan, B.; Klemm, B.; Huang, J.; Wang, J.; Cohen Stuart, M. A.; Eelkema, R. Chemical Signal Regulated Injectable Coacervate Hydrogels. *Chem. Sci.* **2023**, *14*, 1512–1523.

(136) Afrose, S. P.; Mahato, C.; Sharma, P.; Roy, L.; Das, D. Nonequilibrium Catalytic Supramolecular Assemblies of Melamine- and Imidazole-Based Dynamic Building Blocks. *J. Am. Chem. Soc.* **2022**, *144*, 673–678.

(137) Goswami, S.; Reja, A.; Pal, S.; Singh, A.; Das, D. Nonequilibrium Amyloid Polymers Exploit Dynamic Covalent Linkage to Temporally Control Charge-Selective Catalysis. *J. Am. Chem. Soc.* **2022**, *144*, 19248–19252.

(138) Bal, S.; Ghosh, C.; Ghosh, T.; Vijayaraghavan, R. K.; Das, D. Non-Equilibrium Polymerization of Cross-β Amyloid Peptides for Temporal Control of Electronic Properties. *Angew. Chem. Int. Ed.* **2020**, *59*, 13506–13510.

(139) Grötsch, R. K.; Angı, A.; Mideksa, Y. G.; Wanzke, C.; Tena-Solsona, M.; Feige, M. J.; Rieger, B.; Boekhoven, J. Dissipative Self-Assembly of Photoluminescent Silicon Nanocrystals. *Angew. Chem. Int. Ed.* **2018**, *57*, 14608–14612.

(140) Grötsch, R. K.; Wanzke, C.; Speckbacher, M.; Angl, A.; Rieger, B.; Boekhoven, J. Pathway Dependence in the Fuel-Driven Dissipative Self-Assembly of Nanoparticles. *J. Am. Chem. Soc.* **2019**, *141*, 9872–9878.

(141) Liu, K.; Blokhuis, A. W. P.; Dijt, S. J.; Hamed, S.; Kiani, A.; Matysiak, B. M.; Otto, S. Systems Chemistry across Multiple Length Scales: Macroscopic Flow via Dissipative Co-Assemblies Featuring Transient Amides. *ChemRXiv* **2022**, 1–20.

(142) Chen, C.; Valera, J. S.; Adachi, T. B. M.; Hermans, T. M. Efficient Photoredox Cycles to Control Perylenediimide Self-Assembly. *Chem. Eur. J.* **2023**, *29*, e202202849.

(143) Monreal Santiago, G.; Liu, K.; Browne, W. R.; Otto, S. Emergence of Light-Driven Protometabolism on Recruitment of a Photocatalytic Cofactor by a Self-Replicator. *Nat. Chem.* **2020**, *12*, 603–607.

(144) Chen, C.; Guan, Z. Precise Control of Dissipative Self-Assembly by Light and Electricity. *Chem. Eur. J.* **2023**, e202300347.

(145) Morrow, S. M.; Colomer, I.; Fletcher, S. P. A Chemically Fuelled Self-Replicator. *Nat. Commun.* **2019**, *10*, 1011.

(146) Engwerda, A. H. J.; Southworth, J.; Lebedeva, M. A.; Scanes, R. J. H.; Kukura, P.; Fletcher,

S. P. Coupled Metabolic Cycles Allow Out-of-Equilibrium Autopoietic Vesicle Replication. *Angew. Chem. Int. Ed.* **2020**, *59*, 20361–20366.

(147) Howlett, M. G.; Engwerda, A. H. J.; Scanes, R. J. H.; Fletcher, S. P. An Autonomously Oscillating Supramolecular Self-Replicator. *Nat. Chem.* **2022**, *14*, 805–810.

(148) Ogden, W. A.; Guan, Z. Redox Chemical-Fueled Dissipative Self-Assembly of Active Materials. *ChemSystemsChem* **2019**, *1*, e1900030.

(149) Yang, S.; Schaeffer, G.; Mattia, E.; Markovitch, O.; Liu, K.; Hussain, A. S.; Ottelé, J.; Sood, A.; Otto, S. Chemical Fueling Enables Molecular Complexification of Self-Replicators. *Angew. Chem. Int. Ed.* **2021**, *60*, 11344–11349.

(150) Liu, B.; Wu, J.; Geerts, M.; Markovitch, O.; Pappas, C. G.; Liu, K.; Otto, S. Out-of-Equilibrium Self-Replication Allows Selection for Dynamic Kinetic Stability in a System of Competing Replicators. *Angew. Chem. Int. Ed.* **2022**, *61*, e202117605.

(151) Altay, Y.; Pijpers, I. A. B.; Abdelmohsen, L. K. E. A.; van Hest, J. C. M. Dynamic Assembly of Micellar Mesostructures. *ChemSystemsChem* **2020**, *2*, e190004.

(152) Del Grosso, E.; Prins, L. J.; Ricci, F. Transient DNA-Based Nanostructures Controlled by Redox Inputs. *Angew. Chem. Int. Ed.* **2020**, *59*, 13238–13245.

(153) Singh, N.; Lainer, B.; Formon, G. J. M.; De Piccoli, S.; Hermans, T. M. Re-Programming Hydrogel Properties Using a Fuel-Driven Reaction Cycle. *J. Am. Chem. Soc.* **2020**, *142*, 4083–4087.

(154) Vries, J. G. De; Kellogg, R. M. Reduction of Aldehydes and Ketones by Sodium Dithionite. *J. Org. Chem.* **1980**, *45*, 4126–4129.

(155) Singh, N.; Lopez-Acosta, A.; Formon, G. J. M.; Hermans, T. M. Chemically Fueled Self-Sorted Hydrogels. *J. Am. Chem. Soc.* **2022**, *144*, 410–415.

(156) Jo, H.; Selmani, S.; Guan, Z.; Sim, S. Sugar-Fueled Dissipative Living Materials. *J. Am. Chem. Soc.* **2023**, *145*, 1811–1817.

(157) Lu, H.; Hao, J.; Wang, X. Host-Fueled Transient Supramolecular Hydrogels. *ChemSystemsChem* **2022**, *4*, e202100050.

(158) Debnath, S.; Roy, S.; Ulijn, R. V. Peptide Nanofibers with Dynamic Instability through Nonequilibrium Biocatalytic Assembly. *J. Am. Chem. Soc.* **2013**, *135*, 16789–16792.

(159) Sawczyk, M.; Klajn, R. Out-of-Equilibrium Aggregates and Coatings during Seeded Growth of Metallic Nanoparticles. *J. Am. Chem. Soc.* **2017**, *139*, 17973–17978.

(160) Del Giudice, D.; Frateloreto, F.; Sappino, C.; Di Stefano, S. Chemical Tools for the Temporal Control of Water Solution PH and Applications in Dissipative Systems. *European J. Org. Chem.* **2022**, *33*, e202200407.

(161) Olivieri, E.; Quintard, A. Out of Equilibrium Chemical Systems Fueled by Trichloroacetic Acid. *ACS Org. Inorg. Au* **2023**, *3*, 4–12.

(162) Ghosh, A.; Paul, I.; Adlung, M.; Wickleder, C.; Schmittel, M. Oscillating Emission of [2]Rotaxane Driven by Chemical Fuel. *Org. Lett.* **2018**, *20*, 1046–1049.

(163) Borodin, O.; Shchukin, Y.; Robertson, C. C.; Richter, S.; Delius, M. von. Self-Assembly of Stimuli-Responsive [2]Rotaxanes by Amidinium Exchange. *J. Am. Chem. Soc.* **2021**, *143*, 16448–16457.

(164) Kirby, A. J.; Nome, F. Fundamentals of Phosphate Transfer. *Acc. Chem. Res.* **2015**, *48*, 1806–1814.

(165) Dürr-Mayer, T.; Qiu, D.; Eisenbeis, V. B.; Steck, N.; Häner, M.; Hofer, A.; Mayer, A.; Siegel, J. S.; Baldridge, K. K.; Jessen, H. J. The Chemistry of Branched Condensed Phosphates. *Nat. Commun.* **2021**, *12*, 5368.

(166) Westheimer, F. H. Why Nature Chose Phosphates. *Science* **1987**, *235*, 1173–1178.

(167) Liu, Z.; Rossi, J. C.; Pascal, R. How Prebiotic Chemistry and Early Life Chose Phosphate. *Life* **2019**, *9*, 1–16.

(168) Liu, Z.; Wu, L. F.; Xu, J.; Bonfio, C.; Russell, D. A.; Sutherland, J. D. Harnessing Chemical

Energy for the Activation and Joining of Prebiotic Building Blocks. *Nat. Chem.* **2020**, *12*, 1023–1028.

(169) Deck, C.; Jauker, M.; Richert, C. Efficient Enzyme-Free Copying of All Four Nucleobases Templated by Immobilized RNA. *Nat. Chem.* **2011**, *3*, 603–608.

(170) Kervio, E.; Sosson, M.; Richert, C. The Effect of Leaving Groups on Binding and Reactivity in Enzyme-Free Copying of DNA and RNA. *Nucleic Acids Res.* **2016**, *44*, 5504–5514.

(171) Li, L.; Prywes, N.; Tam, C. P.; Oflaherty, D. K.; Lelyveld, V. S.; Izgu, E. C.; Pal, A.; Szostak, J. W. Enhanced Nonenzymatic RNA Copying with 2-Aminoimidazole Activated Nucleotides. *J. Am. Chem. Soc.* **2017**, *139*, 1810–1813.

(172) Zhang, S. J.; Duzdevich, D.; Szostak, J. W. Potentially Prebiotic Activation Chemistry Compatible with Nonenzymatic RNA Copying. *J. Am. Chem. Soc.* **2020**, *142*, 14810–14813.

(173) Wright, T. H.; Giurgiu, C.; Zhang, W.; Radakovic, A.; O'Flaherty, D. K.; Zhou, L.; Szostak, J. W. Prebiotically Plausible "Patching" of RNA Backbone Cleavage through a 3-5 Pyrophosphate Linkage. *J. Am. Chem. Soc.* **2019**, *141*, 18104–18112.

(174) Jauker, M.; Griesser, H.; Richert, C. Copying of RNA Sequences without Pre-Activation. *Angew. Chem. Int. Ed.* **2015**, *54*, 14559–14563.

(175) Tremmel, P.; Griesser, H.; Steiner, U. E.; Richert, C. How Small Heterocycles Make a Reaction Network of Amino Acids and Nucleotides Efficient in Water. *Angew. Chem. Int. Ed.* **2019**, *58*, 13087–13092.

(176) Komiyama, M.; Takeda, N.; Shigekawa, H.; Ce, T. Hydrolysis of DNA and RNA by Lanthanide Ions : Mechanistic Studies Leading to New Applications. *Chem. Commun.* **1999**, 1443–1451.

(177) Ahmad, F.; Kelso, W. I. Pyrophosphate As a Source of Phosphorus: Hydrolysis Under Different Conditions. *J. res. Sci* **2001**, *12*, 130–139.

(178) Perreault, D. M.; Anslyn, E. V. Unifying the Current Data on the Mechanism of Cleavage-Transesterification of RNA. *Angew. Chem. Int. Ed. Engl.* **1997**, *36*, 432–450.

(179) Oivanen, M.; Kuusela, S.; Lönnberg, H. Kinetics and Mechanisms for the Cleavage and Isomerization of the Phosphodiester Bonds of RNA by Bronsted Acids and Bases. *Chem. Rev.* **1998**, *98*, 961–990.

(180) Morrow, J. R.; Buttrey, L. A.; Shelton, V. M.; Berback, K. A. Efficient Catalytic Cleavage of RNA by Lanthanide(III) Macrocyclic Complexes: Toward Synthetic Nucleases for in Vivo Applications. *J. Am. Chem. Soc.* **1992**, *114*, 1903–1905.

(181) Hurst, P.; Takasaki, B. K.; Chin, J. Rapid Cleavage of RNA with a La(III) Dimer. *J. Am. Chem. Soc.* **1996**, *118*, 9982–9983.

(182) Sumaoka, J. Progress towards Synthetic Enzymes for Phosphoester. *Curr. Opin. Chem. Biol.* **1998**, *2*, 751–757.

(183) Wazer, J. R. V.; Griffith, E. J.; McCullough, J. F. Structure and Properties of the Condensed Phosphates. VII. Hydrolytic Degradation of Pyro- and Tripolyphosphate. *J. Am. Chem. Soc.* **1955**, *77*, 287–291.

(184) Chen, J.; Schultz, R. G.; Lloyd, D. H.; Gryaznov, S. M. Synthesis of Oligodeoxyribonucleotide N3'-P5' Phosphoramidates. *Nucleic Acids* **1995**, *23*, 2661–2668.

(185) Oligonucleotide, N.; Gryaznov, S. M.; Lloyd, D. H.; Chen, J.; Schultz, R. G.; Dedionisio, L. A.; Ratmeyert, L.; Wilsont, W. D. Oligonucleotide N3'-P5' Phosphoramidates. *Proc. Natl. Acad. Sci. USA* **1995**, *92*, 5798–5802.

(186) Zhang, S.; Zhang, N.; Blain, J. C.; Szostak, J. W. Synthesis of N3′-P5′-Linked Phosphoramidate DNA by Nonenzymatic Template-Directed Primer Extension. *J. Am. Chem. Soc.* **2013**, *135*, 924–932.

(187) O'Flaherty, D. K.; Zhou, L.; Szostak, J. W. Nonenzymatic Template-Directed Synthesis of

Mixed-Sequence 3′-NP-DNA up to 25 Nucleotides Long inside Model Protocells. *J. Am. Chem. Soc.* **2019**, *141*, 10481–10488.

(188) Orgel, L. E.; Zielinski, W. S. Autocatalytic Synthesis of a Tetranucleotide Analog. *Nature* **1987**, *327*, 346–347.

(189) Griesser, H.; Bechthold, M.; Tremmel, P.; Kervio, E.; Richert, C. Amino Acid-Specific, Ribonucleotide-Promoted Peptide Formation in the Absence of Enzymes. *Angew. Chem. Int. Ed.* **2017**, *56*, 1224–1228.

(190) Jash, B.; Tremmel, P.; Jovanovic, D.; Richert, C. Single Nucleotide Translation without Ribosomes. *Nat. Chem.* **2021**, *13*, 751–757.

(191) Roberts, S. J.; Liu, Z.; Sutherland, J. D. Potentially Prebiotic Synthesis of Aminoacyl-RNA via a Bridging Phosphoramidate-Ester Intermediate. *J. Am. Chem. Soc.* **2022**, *144*, 4254–4259.

(192) Garrison, A. W.; Boozer, C. E. The Acid-Catalyzed Hydrolysis of a Series of Phosphoramidates. *J. Am. Chem. Soc.* **1968**, *90*, 3486–3494.

(193) Ora, M.; Mattila, K.; Lönnberg, T.; Oivanen, M.; Lönnberg, H. Hydrolytic Reactions of Diribonucleoside the P - O and P - N Bond Cleavage Of. *J. Am. Chem. Soc.* **2002**, *124*, 14364–14372.

(194) Lönnberg, T.; Ora, M.; Lönnberg, H. Hydrolytic Reactions of Nucleoside Phosphoramidates : Kinetics and Mechanisms. *Org. Chem.* **2010**, *7*, 33–43.

(195) Brown, C.; Boudreau, J.; Hewitson, B.; Hudson, R. F. Alkaline Hydrolysis of Cyclic Phosphoramidates. *J.C.S. Chem. Comm.* **1975**, 504–505.

(196) Jung, H.; Shin, S. H.; Kee, J. Recent Updates on Protein N -Phosphoramidate Hydrolases. *ChemBioChem* **2019**, *20*, 623–633.

(197) Zhou, X.; Chou, T. F.; Aubol, B. E.; Park, C. J.; Wolfenden, R.; Adams, J.; Wagner, C. R. Kinetic Mechanism of Human Histidine Triad Nucleotide Binding Protein 1. *Biochemistry* **2013**, *52*, 3588–3600.

(198) Jovanovic, D.; Tremmel, P.; Pallan, P. S.; Egli, M.; Richert, C. The Enzyme-Free Release of Nucleotides from Phosphoramidates Depends Strongly on the Amino Acid. *Angew. Chem. Int. Ed.* **2020**, *59*, 20154–20160.

(199) Wang, Y.; Nie, J.; Fang, W.; Yang, L.; Hu, Q.; Wang, Z.; Sun, J. Z.; Tang, B. Z. Sugar-Based Aggregation-Induced Emission Luminogens: Design, Structures, and Applications. *Chem. Rev.* **2020**, *120*, 4534–4577.

(200) Crick, F. H. The Origin of the Genetic Code. *J. Mol. Biol.* **1968**, *38*, 367–379.

(201) Orgel, L. E. Evolution of the Genetic Apparatus. *J. Mol. Biol.* **1968**, *38*, 381–393.

(202) De Duve, C. The Onset of Selection. *Nature* **2005**, *433*, 581–582.

(203) Vázquez-Salazar, A.; Lazcano, A. Early Life: Embracing the RNA World. *Curr. Biol.* **2018**, *28*, 220–222.

(204) Preiner, M.; Asche, S.; Becker, S.; Betts, H. C.; Boniface, A.; Camprubi, E.; Chandru, K.; Erastova, V.; Garg, S. G.; Khawaja, N.; Kostyrka, G.; Machné, R.; Moggioli, G.; Muchowska, K. B.; Neukirchen, S.; Peter, B.; Pichlhöfer, E.; Radványi, Á.; Rossetto, D.; Salditt, A.; Schmelling, N. M.; Sousa, F. L.; Tria, F. D. K.; Vörös, D.; Xavier, J. C. The Future of Origin of Life Research: Bridging Decades-Old Divisions. *Life* **2020**, *10*, 1–25.

(205) Weissman, S. A.; Anderson, N. G. Design of Experiments (DoE) and Process Optimization. A Review of Recent Publications. *Org. Process Res. Dev.* **2015**, *19*, 1605–1633.

(206) Dejaegher, B.; Vander Heyden, Y. Experimental Designs and Their Recent Advances in Set-up, Data Interpretation, and Analytical Applications. *J. Pharm. Biomed. Anal.* **2011**, *56*, 141–158.

(207) Aggarwal, V. K.; Staubitz, A. C.; Owen, M. Optimization of the Mizoroki-Heck Reaction Using Design of Experiment (DoE). *Org. Process Res. Dev.* **2006**, *10*, 64–69.

(208) Becker, S.; Feldmann, J.; Wiedemann, S.; Okamura, H.; Schneider, C.; Iwan, K.; Crisp, A.; Rossa, M.; Amatov, T.; Carell, T. Unified Prebiotically Plausible Synthesis of Pyrimidine and Purine RNA Ribonucleotides. *Science* **2019**, *366*, 76–82.

(209) Mullen, L. B.; Sutherland, J. D. Formation of Potentially Prebiotic Amphiphiles by Reaction of β-Hydroxy-n-Alkylamines with Cyclotriphosphate. *Angew. Chem. Int. Ed.* **2007**, *46*, 4166–4168.

(210) Borsley, S.; Leigh, D. A.; Roberts, B. M. W. A Doubly Kinetically-Gated Information Ratchet Autonomously Driven by Carbodiimide Hydration. *J. Am. Chem. Soc.* **2021**, *143*, 4414–4420.

(211) Biagini, C.; Fielden, S. D. P.; Leigh, D. A.; Schaufelberger, F.; Di Stefano, S.; Thomas, D. Dissipative Catalysis with a Molecular Machine. *Angew. Chem.* **2019**, *131*, 9981–9985.

(212) Ghosh, A.; Paul, I.; Schmittel, M. Multitasking with Chemical Fuel: Dissipative Formation of a Pseudorotaxane Rotor from Five Distinct Components. *J. Am. Chem. Soc.* **2021**, *143*, 5319–5323.

(213) Lee, S.; Chen, C. H.; Flood, A. H. A Pentagonal Cyanostar Macrocycle with Cyanostilbene CH Donors Binds Anions and Forms Dialkylphosphate [3]Rotaxanes. *Nat. Chem.* **2013**, *5*, 704–710.

(214) Gale, P. A.; Howe, E. N. W.; Wu, X. Anion Receptor Chemistry. *Chem* **2016**, *1*, 351–422.

(215) Chen, L.; Berry, S. N.; Wu, X.; Howe, E. N. W.; Gale, P. A. Advances in Anion Receptor Chemistry. *Chem* **2020**, *6*, 61–141.

(216) Macreadie, L. K.; Gilchrist, A. M.; McNaughton, D. A.; Ryder, W. G.; Fares, M.; Gale, P. A. Progress in Anion Receptor Chemistry. *Chem* **2022**, *8*, 46–118.

(217) Molina, P.; Zapata, F.; Caballero, A. Anion Recognition Strategies Based on Combined Noncovalent Interactions. *Chem. Rev.* **2017**, *117*, 9907–9972.

(218) Kang, S. O.; Llinares, J. M.; Day, V. W.; Bowman-James, K. Cryptand-like Anion Receptors. *Chem. Soc. Rev.* **2010**, *39*, 3980–4003.

(219) Busschaert, N.; Caltagirone, C.; Van Rossom, W.; Gale, P. A. Applications of Supramolecular Anion Recognition. *Chem. Rev.* **2015**, *115*, 8038–8155.

(220) Evans, N. H.; Beer, P. D. Advances in Anion Supramolecular Chemistry: From Recognition to Chemical Applications. *Angew. Chem. Int. Ed.* **2014**, *53*, 11716–11754.

(221) Yang, D.; Zhao, J.; Yang, X. J.; Wu, B. Anion-Coordination-Directed Self-Assemblies. *Org. Chem. Front.* **2018**, *5*, 662–690.

(222) Hollstein, S.; Shyshov, O.; Hanževački, M.; Zhao, J.; Rudolf, T.; Jäger, C. M.; von Delius, M. Dynamic Covalent Self-Assembly of Chloride- and Ion-Pair-Templated Cryptates. *Angew. Chem. Int. Ed.* **2022**, *61*, e202201831.

(223) Zhang, W.; Zhao, J.; Yang, D. Anion-Coordination-Driven Assembly: From Discrete Supramolecular Self-Assemblies to Functional Soft Materials. *ChemPlusChem* **2022**, *87*, e202200294.

(224) Zhang, G.; Mastalerz, M. Organic Cage Compounds-from Shape-Persistency to Function. *Chem. Soc. Rev.* **2014**, *43*, 1934–1947.

(225) Vickers, M. S.; Beer, P. D. Anion Templated Assembly of Mechanically Interlocked Structures. *Chem. Soc. Rev.* **2007**, *36*, 211–225.

(226) Caballero, A.; Zapata, F.; Beer, P. D. Interlocked Host Molecules for Anion Recognition and Sensing. *Coord. Chem. Rev.* **2013**, *257*, 2434–2455.

(227) Hübner, G. M.; Gläser, J.; Seel, C.; Vögtle, F. High-Yielding Rotaxane Synthesis with an Anion Template. *Angew. Chem. Int. Ed.* **1999**, *38*, 383–386.

(228) Wisner, J. A.; Beer, P. D.; Drew, M. G. B.; Sambrook, M. R. Anion-Templated Rotaxane Formation. *J. Am. Chem. Soc.* **2002**, *124*, 12469–12476.

(229) Sambrook, M. R.; Beer, P. D.; Lankshear, M. D.; Ludlow, R. F.; Wisner, J. A. Anion-Templated Assembly of [2]Rotaxanes. *Org. Biomol. Chem.* **2006**, *4*, 1529–1538.

(230) Ghosh, P.; Mermagen, O.; Schalley, C. A. Novel Template Effect for the Preparation of [2]Rotaxanes with Functionalised Centre Pieces. *Chem. Commun.* **2002**, *2*, 2628–2629.

(231) Qiao, B.; Liu, Y.; Lee, S.; Pink, M.; Flood, A. H. A High-Yield Synthesis and Acid-Base Response of Phosphate-Templated [3]Rotaxanes. *Chem. Commun.* **2016**, *52*, 13675–13678.

(232) Zhao, W.; Qiao, B.; Chen, C. H.; Flood, A. H. High-Fidelity Multistate Switching with Anion–Anion and Acid–Anion Dimers of Organophosphates in Cyanostar Complexes. *Angew. Chem. Int. Ed.* **2017**, *56*, 13083–13087.

(233) Zhao, W.; Tropp, J.; Qiao, B.; Pink, M.; Azoulay, J. D.; Flood, A. H. Tunable Adhesion from Stoichiometry-Controlled and Sequence-Defined Supramolecular Polymers Emerges Hierarchically from Cyanostar-Stabilized Anion-Anion Linkages. *J. Am. Chem. Soc.* **2020**, *142*, 2579–2591.

(234) Fatila, E. M.; Pink, M.; Twum, E. B.; Karty, J. A.; Flood, A. H. Phosphate-Phosphate Oligomerization Drives Higher Order Co-Assemblies with Stacks of Cyanostar Macrocycles. *Chem. Sci.* **2018**, *9*, 2863–2872.

(235) Zhao, W.; Qiao, B.; Tropp, J.; Pink, M.; Azoulay, J. D.; Flood, A. H. Linear Supramolecular Polymers Driven by Anion-Anion Dimerization of Difunctional Phosphonate Monomers Inside Cyanostar Macrocycles. *J. Am. Chem. Soc.* **2019**, *141*, 4980–4989.

(236) Qiao, B.; Anderson, J. R.; Pink, M.; Flood, A. H. Size-Matched Recognition of Large Anions by Cyanostar Macrocycles Is Saved When Solvent-Bias Is Avoided. *Chem. Commun.* **2016**, *52*, 8683–8686.

(237) Sheetz, E. G.; Zhang, Z.; Marogil, A.; Che, M.; Pink, M.; Carta, V.; Raghavachari, K.; Flood, A. H. High-Fidelity Recognition of Organotrifluoroborate Anions (R–BF3–) as Designer Guest Molecules. *Chem. Eur. J.* **2022**, *28*, e202201584.

(238) Hargrove, A. E.; Nieto, S.; Zhang, T.; Sessler, J. L.; Anslyn, E. V. Artificial Receptors for the Recognition of Phosphorylated Molecules. *Chem. Rev.* **2011**, *111*, 6603–6782.

(239) Ngo, H. T.; Liu, X.; Jolliffe, K. A. Anion Recognition and Sensing with Zn(II)–Dipicolylamine Complexes. *Chem. Soc. Rev.* **2012**, *41*, 4928–4965.

(240) Pal, S.; Ghosh, T. K.; Ghosh, R.; Mondal, S.; Ghosh, P. Recent Advances in Recognition, Sensing and Extraction of Phosphates: 2015 Onwards. *Coord. Chem. Rev.* **2020**, *405*, 213128.

(241) Wezenberg, S. J.; Vlatković, M.; Kistemaker, J. C. M.; Feringa, B. L. Multi-State Regulation of the Dihydrogen Phosphate Binding Affinity to a Light- and Heat-Responsive Bis-Urea Receptor. *J. Am. Chem. Soc.* **2014**, *136*, 16784–16787.

(242) Kyung, K. I. M. S.; Dong Hoon, L. E. E.; Hong, J. I. N.; Yoon, J. Chemosensors for Pyrophosphate. *Acc. Chem. Res.* **2009**, *42*, 23–31.

(243) Lee, S.; Yuen, K. K. Y.; Jolliffe, K. A.; Yoon, J. Fluorescent and Colorimetric Chemosensors for Pyrophosphate. *Chem. Soc. Rev.* **2015**, *44*, 1749–1762.

(244) Sokkalingam, P.; Kim, D. S.; Hwang, H.; Sessler, J. L.; Lee, C. H. A Dicationic Calix[4]Pyrrole Derivative and Its Use for the Selective Recognition and Displacement-Based Sensing of Pyrophosphate. *Chem. Sci.* **2012**, *3*, 1819–1824.

(245) Ali, M.; Ahmed, I.; Ramirez, P.; Nasir, S.; Niemeyer, C. M.; Mafe, S.; Ensinger, W. Label-Free Pyrophosphate Recognition with Functionalized Asymmetric Nanopores. *Small* **2016**, *12*, 2014–2021.

(246) Jolliffe, K. A. Pyrophosphate Recognition and Sensing in Water Using Bis[Zinc(II)Dipicolylamino]-Functionalized Peptides. *Acc. Chem. Res.* **2017**, *50*, 2254–2263.

(247) Cheng, C.; McGonigal, P. R.; Schneebeli, S. T.; Li, H.; Vermeulen, N. A.; Ke, C.; Stoddart, J. F. An Artificial Molecular Pump. *Nat. Nanotechnol.* **2015**, *10*, 547–553.

(248) Zhang, L.; Qiu, Y.; Liu, W. G.; Chen, H.; Shen, D.; Song, B.; Cai, K.; Wu, H.; Jiao, Y.; Feng, Y.; Seale, J. S. W.; Pezzato, C.; Tian, J.; Tan, Y.; Chen, X. Y.; Guo, Q. H.; Stern, C. L.; Philp, D.;

Astumian, R. D.; Goddard, W. A.; Stoddart, J. F. An Electric Molecular Motor. *Nature* **2023**, *613*, 280–286.

(249) Qiu, Y.; Zhang, L.; Pezzato, C.; Feng, Y.; Li, W.; Nguyen, M. T.; Cheng, C.; Shen, D.; Guo, Q. H.; Shi, Y.; Cai, K.; Alsubaie, F. M.; Astumian, R. D.; Stoddart, J. F. A Molecular Dual Pump. *J. Am. Chem. Soc.* **2019**, *141*, 17472–17476.

(250) Corra, S.; Bakić, M. T.; Groppi, J.; Baroncini, M.; Silvi, S.; Penocchio, E.; Esposito, M.; Credi, A. Kinetic and Energetic Insights into the Dissipative Non-Equilibrium Operation of an Autonomous Light-Powered Supramolecular Pump. *Nat. Nanotechnol.* **2022**, *17*, 746–751.

(251) Bhattacharyya, T.; Saha, P.; Dash, J. Guanosine-Derived Supramolecular Hydrogels: Recent Developments and Future Opportunities. *ACS Omega* **2018**, *3*, 2230–2241.

(252) Delius, M. Von; Leigh, D. A. Walking Molecules. *Chem. Soc. Rev.* **2011**, *40*, 3656–3676.

(253) Nielsen, P.; Harksen, J.; Bacher, A. Hydrolysis and Rearrangement Reactions of Riboflavin Phosphates: An Explicit Kinetic Study. *Eur. J. Biochem.* **1985**, *152*, 465–473.

(254) Dearden, J. C.; Bresnen, G. M. The Measurement of Partition Coefficients. *Quant. Struct.-Act. Relat.* **1988**, *7*, 133–144.

(255) Wilson, M. R.; Solà, J.; Carlone, A.; Goldup, S. M.; Lebrasseur, N.; Leigh, D. A. An Autonomous Chemically Fuelled Small-Molecule Motor. *Nature* **2016**, *534*, 235–240.

List of Publications

1. Sun, J.;* Vogel, J.;* Chen, L.; Schleper, A. L.; Bergner, T.; Kuehne, A. J. C.; von Delius, M. Carbodiimide-Driven Dimerization and Self-Assembly of Artificial, Ribose-Based Amphiphiles. *Chem. Eur. J.* **2022**, *28* (13), e202104116.

2. Englert, A.;* Vogel, J. F.;* Bergner, T.; Loske, J.; von Delius, M. A Ribonucleotide ↔ Phosphoramidate Reaction Network Optimized by Computer-Aided Design. *J. Am. Chem. Soc.* **2022**, *144* (33), 15266–15274.

3. Vogel, J.; Chen Y.; Fadler R. E.; Flood, A. H.; von Delius, M. Steric Control over the Threading of Pyrophosphonates with One or Two Cyanostar Macrocycles during Pseudorotaxane Formation, *Chem. Eur. J.* **2023**, e202300899.

4. Hollstein, S.; Lamiaa, M. A.; Coste, M,; Vogel, J.; Bettache N.; Ulrich S.; von Delius, M. A Triazolium-Anchored Self-Immovaltive Linker Enables Self-Assembly-Driven siRNA Binding and Esterase-Induced Release. *Chem. Eur. J.* **2022**, 29, e202203311

*Authors contributed equally to this work.

Curriculum Vitae

Ausbildung	
Seit 07/2019	Promotion (Dr. rer. nat.) am Institut für Organische Chemie I, Universität Ulm, AK Prof. Dr. Max von Delius
03/2019	M. Sc. Wirtschaftschemie, Ulm, ø 1,1
12/2016	B. Sc. Wirtschaftschemie, Ulm, ø 2,0
06/2012	Abitur am Erasmus-Widman-Gymnasium, Schwäbisch Hall, ø 1,6
Auslandserfahrung	
04 – 07 /2022	Forschungsaufenthalt an der Indiana University, USA in der Gruppe von Prof. Dr. Amar H. Flood
10/2012 – 04/2013	Work&Travel Neuseeland
Berufliche Erfahrungen	
2020 – 2022	Freiberuflicher Berater bei Merck KGaA, Bereich Future Insights
04 – 07 / 2017	Praktikum in F&E MANZ CIGS Technology GmbH
Auszeichnungen	
2019	Studienpreis Wirtschaftschemie der VCW
2018	Stipendium für die Masterarbeit der Stiftung Industrieforschung
2012	Sozialpreis für herausragendes schulischen Engagement
Liste Konferenzbeiträge	
2023	Poster: Frühjahrssymposium, Gießen, Deutschland
2022	Poster: Systems Chemistry Gordons Conference, Maine, USA
2022	Poster: Frühjahrssymposium, Hannover, Deutschland
2020	Poster: ASRC – Virtual Symposium on Systems Chemistry, online
Publikationsliste	
2023	Vogel, J,; Chen Y.; Fadler R. E.; Flood, A. H.; von Delius, M. Steric Control over the Threading of Pyrophosphonates with One or Two Cyanostar Macrocycles during Pseudorotaxane Formation, *Chem. Eur. J.* **2023**, e202300899.
2022	Hollstein, S.; Lamiaa, M. A.; Coste, M.; Vogel, J.; Bettache N.; Ulrich S.; von Delius, M. A Triazolium Anchored Self-Immolative Linker Enables Self Assembly Driven siRNA Binding and Esterase Induced Release. *Chem. Eur. J.* **2022**, 29, e202203311.
2022	Englert, A.;* Vogel, J. F.;* Bergner, T.; Loske, J.; von Delius, M. A Ribonucleotide ↔Phosphoramidate Reaction Network optimized by Computer Aided Design. *J. Am. Chem. Soc.* **2022**, 144 (33), 15266 -15274.
2022	Sun, J.;* Vogel, J.;* Chen, L.; Schleper, A. L.; Bergner, T.; Kuehne, A. J. C.; von Delius, M. Carbodiimide Driven Dimerization and Self Assembly of Artificial, Ribose Based Amphiphiles. *Chem. Eur. J.* **2022**, 28 (13), e202104116.

Acknowledgments / Danksagung

Mein erster Dank geht an meinen Doktorvater Prof. Dr. Max von Delius. Max, vielen Dank für die Möglichkeit bei dir auf einem superspannenden Thema promovieren zu können, für all die fachliche Unterstützung und dafür, dass deine Tür im wahrsten Sinne des Wortes immer offen stand!

Für die Begutachtung meiner Arbeit und die Übernahme des Prüfungsvorsitzes meiner Promotionsverteidigung danke ich Prof. Dr. Alexander Kühne. Außerdem danke ich den beiden weiteren Prüfer:innen Prof. Dr. Paul Walther und Jun.-Prof. Dr. Andrea Pannwitz.

Meine Forschungsarbeit war geprägt von fruchtvollen Kollaborationen und Teamarbeiten. So gilt mein Dank den Arbeitsgruppen, in deren Zusammenarbeit meine Publikationen entstanden sind und deren Professoren: Das sind Prof. Kühne (Organische Chemie III, Ulm), Prof. Walther (Z. E. Elektronenmikroskopie, Ulm) und Prof. Amar Flood (Organic Chemistry, Indiana, USA). Genauso danke ich allen Koautoren für die reibungslose Zusammenarbeit. Das sind insbesondere Jing Sun und Andreas Englert, aber auch Lisa Chen, Lennart Respondek (geb. Schleper), Tim Bergner, Jessica Loske, Yusheng Chen und Rachel Fadler.

Für die Finanzierung meiner Arbeit danke ich dem European Research Council (ERC) und dem Land Baden-Württemberg und der Universität Ulm für die entsprechende Infrastruktur.

Für sprachliche und stilistische Korrekturen meiner Arbeit danke ich Andreas Englert, Jannik Schießl, Fabian Schwer, Sarah Spiewok und besonders Frank Dissinger.

For my wonderful time in Bloomington at the Indiana University, I want to thank Prof. Amar Flood and his whole group. Yusheng, Rachel, Alteka, Nabarupa, Andrew, Liz, Zhao, Yan, Michaela and Amanda, thanks for making this an unforgettable experience. Many thank also to my roommates Sarah and Jacob.

Ein Arbeitsplatz steht und fällt mit den Kollegen. Für die entspannte Arbeitsatmosphäre und viele spaßige Aktionen möchte ich mich bei allen ehemaligen und aktuellen Kolleg:innen bedanken. Hier in alphabetischer Reihenfolge: Anna, Andreas E., Andreas U., Bala, Fabian S., Fabian St., Jan, Jie, Jing, Juanita, Henrik, Lizzy, Oleg, Oleksandr, Pascal, Sebastian, Selina, Shyam, Yev, Youzhi.

Ganz besonders danke ich Henrik, Selina, Fabi, Anna, Aileen und Sarah, die alle mehr als nur Kollegen geworden sind und die immer da waren, um die Höhen und Tiefen einer Promotion zusammen zu meistern. Danke für die coole Zeit!

Zu besonderem Dank verpflichtet bin ich auch den Mitarbeiter:innen der OC I, die das Institut am laufen halten und eine hervorragende Grundlage für meine Forschung geschaffen haben. Danke, Dr. Frank Dissinger, Christian Tontsch, Birgit Mögenburg und Nora Bendleder-Grimm!

Lionel Kroner und Samuel Blessing danke ich für die Kristallstrukturmessungen und Markus Wunderlin für massenspektrometrische Messungen. Bei vielen NMR-Messungen war mir Christian Tontsch eine große Hilfe.

In Form von Bachelor, oder Projektarbeiten an meiner Forschung mitgewirkt haben Mario Löw, Dominik Jage, Jannik Schießl, Izzy Sedwick und Steffen Volk. Danke für euer Engagement.

Zum Schluss geht ein besonderes Dankeschön an meine Eltern, die mich mit allem unterstützt haben, was man sich für sein Studium und eine Promotionszeit wünschen kann. In gleichem Maße geht mein Dank an den Rest meiner Familie und insbesondere an meine Patentante. Ich bin froh, dass ich immer auf euren Rückhalt zählen konnte!